



**HAL**  
open science

# Development of processes for the valorization of lignocellulosic biomass based on renewable energies

Daniele Di Menno Di Bucchianico

► **To cite this version:**

Daniele Di Menno Di Bucchianico. Development of processes for the valorization of lignocellulosic biomass based on renewable energies. Chemical and Process Engineering. Normandie Université; Università degli studi (Bologne, Italie), 2023. English. NNT : 2023NORMIR27 . tel-04555625

**HAL Id: tel-04555625**

**<https://theses.hal.science/tel-04555625v1>**

Submitted on 23 Apr 2024

**HAL** is a multi-disciplinary open access archive for the deposit and dissemination of scientific research documents, whether they are published or not. The documents may come from teaching and research institutions in France or abroad, or from public or private research centers.

L'archive ouverte pluridisciplinaire **HAL**, est destinée au dépôt et à la diffusion de documents scientifiques de niveau recherche, publiés ou non, émanant des établissements d'enseignement et de recherche français ou étrangers, des laboratoires publics ou privés.



Normandie Université

# THÈSE

**Pour obtenir le diplôme de doctorat**

Spécialité **GENIE DES PROCÉDES**

Préparée au sein de l'**INSA Rouen Normandie**

En cotutelle internationale avec l'**Université de Bologne ITALIE, ITALIE**

**Development of processes for the valorization of lignocellulosic biomass based on renewable energies**

Présentée et soutenue par

**DANIELE DI MENNO DI BUCCHIANICO**

**Thèse soutenue le 18/10/2023**

devant le jury composé de :

MME CATHERINE AZZARO-PANTEL	PROFESSEUR DES UNIVERSITÉS - INP ENSIACET, Toulouse	Rapporteur
M. JORIS THYBAUT	PROFESSEUR - Ghent University, Belgique	Rapporteur
M. JEAN-CHRISTOPHE BUVAT	MAÎTRE DE CONFÉRENCES - INSA de Rouen Normandie	Membre Co-encadrant
MME VALERIA CASSON MORENO	PROFESSEUR - University of Pisa, Italy	Membre
MME NADINE GABAS	PROFESSEUR DES UNIVERSITÉS - INP ENSIACET, Toulouse	Membre
M. ERIC SCHAER	PROFESSEUR DES UNIVERSITÉS - ENSIC - LRGP, Nancy	Président du jury
M. SEBASTIEN LEVENEUR	MAITRE DE CONFERENCES DES UNIVERSITES HDR - INSA de Rouen Normandie	Directeur de thèse
M. ALESSANDRO TUGNOLI	ASSOCIATE PROFESSOR - UNIVERSITE DE BOLOGNE ITALIE	Directeur de thèse

Thèse dirigée par **SEBASTIEN LEVENEUR** (LABORATOIRE DE SECURITE DES PROCÉDES CHIMIQUES) et **ALESSANDRO TUGNOLI** (LABORATORY OF INDUSTRIAL SAFETY AND ENVIRONMENTAL SUSTAINABILITY)







Normandie Université

# THESE

**Pour obtenir le diplôme de doctorat**

**Spécialité Génie des Procédés**

Préparée au sein de « l'Institut National des Sciences Appliquées de Rouen Normandie » et de  
« l'Université de Bologne »

**“Development of processes for the valorization of lignocellulosic  
biomass based on renewable energies”**

**Présentée et soutenue par**

**Daniele DI MENNO DI BUCCHIANICO**

**Thèse soutenue publiquement le 18/10/2023**

**devant le jury compose de**

Joris THYBAUT	Professeur, Ghent University, Belgium	Rapporteur
Catherine AZZARO-PANTEL	Professeure, INP-ENSIACET-LGC, Toulouse, France	Rapporteur
Nadine GABAS	Professeure, INP-ENSIACET-LGC, Toulouse, France	Examineur
Eric SCHAEER	Professeur, ENSIC – LRGP, Nancy, France	Examineur
Sophie THIEBAUD-ROUX	Professeure, INP-ENSIACET-LCA, Toulouse, France	Invitée
Alessandro TUGNOLI	Professeur, University of Bologna, Italy	Co-Directeur de thèse
Jean-Christophe BUVAT	MCF, INSA Rouen, France	Encadrant de thèse
Valeria CASSON MORENO	Professeure, University of Pisa, Italy	Co-Directrice de thèse
Sébastien LEVENEUR	MCF-HDR, LSPC, INSA Rouen, France	Directeur de thèse

**Thèse dirigée par Sébastien LEVENEUR (INSA Rouen Normandie)**

et Alessandro TUGNOLI (University of Bologna)



*And when you look back,  
it will all become clear...  
...that this was always the path you were meant to walk.*

**To my family**

# Curriculum Vitae

## Daniele Di Menno Di Bucchianico

Born in 1995, Lanciano, Italy

### Formation:

- 10.2020 – 09.2023: PhD candidate in Chemical and Process Engineering at the LSPC (Laboratoire de Sécurité des Procédés Chimiques) of the National Institute of Applied Sciences in Rouen (INSA-Rouen) and at the Department of Civil, Chemical, Environmental and Materials Engineering (DICAM) of the University of Bologna, Italy.
- 10.2017 – 03.2020: Master's degree in Chemical and Process Engineering at the University of Bologna, Italy.
- 09.2014 – 10.2017: Bachelor's degree in Chemical and Biochemical Engineering at the University of Bologna, Italy

### Teaching and supervision experiences:

- Teaching assistant in the course "Unit operations in the process industry", academic year 2022/2023 in the Bachelor degree in Chemical and Biochemical Engineering, University of Bologna.
- 09.2021 – 02.2022: Supervision of research project (master student, Antonella Cipolla, University of Bologna) on "Kinetic Modeling of 5-HMF solvolysis to n-butyl levulinate".
- 02.2022 – 07.2022: Supervision of research project (master student, Emy Encarnacion Munoz, INSA-Rouen) on "Production of platform molecules: Alkyl levulinates, kinetic study".
- 09.2022 – 11.2022: Supervision of research project (master student, Laura Bernacchioni, University of Bologna) on "Experimental investigation of the Heating Value of Biofuels".

### Research Activities:

- 11.2022 – 09.2023: doctoral research activities in the laboratory LISES (Laboratory of Industrial Safety and Environmental Sustainability) of the University of Bologna, concerning process simulation and multi-criteria sustainability assessment.

- 10.2020 – 10-2022: doctoral research activities in the laboratory LSPC (Laboratoire de Sécurité des Procédés Chimiques) of INSA-Rouen, concerning the experimental research of lignocellulosic biomass valorization reactions, kinetic modelling, and calorimetric analyses.
- 09.2019 – 02-2020: research project in the laboratory LSPC (Laboratoire de Sécurité des Procédés Chimiques) of INSA-Rouen, on the experimental and kinetic research of hydrogen peroxide decomposition, in the context of the valorization of vegetable oils.
- 05.2017 – 09-2017: research project in the laboratory and research center CENTRO CERAMICO (Bologna), concerning the experimental research into geopolymer-based adhesive formulations, in the context of the circular economy and decarbonization of the construction sector.

## Publications and Communications:

List of publications related to the thesis:

1. Di Menno Di Bucchianico, D.; Wang, Y.; Buvat, J.-C.; Pan, Y.; Casson Moreno, V.; Leveneur, S. Production of Levulinic Acid and Alkyl Levulinates: A Process Insight. *Green Chem.*, 2022,24, 614-646.
2. Di Menno Di Bucchianico, D.; Buvat, J.-C.; Mignot, M.; Casson Moreno, V.; Leveneur, S. Role of Solvent in Enhancing the Production of Butyl Levulinate from Fructose. *Fuel*, 2022, 318, 123703.
3. Di Menno Di Bucchianico, D.; Cipolla, A.; Buvat, J.-C.; Mignot, M.; Casson Moreno, V.; Leveneur, S. Kinetic study and model assessment for the n-butyl levulinate production from the alcoholysis of 5-HMF over Amberlite IR-120. *Ind. Eng. Chem. Res.* 2022, 61, 30, 10818–10836.
4. Di Menno Di Bucchianico, D.; Buvat, J.-C.; Mignot, M.; Casson Moreno, V.; Leveneur, S. Production of butyl levulinate from the solvolysis of high-gravity fructose over heterogeneous catalyst: In-depth kinetic modeling, *Chemical Engineering Journal* 2023, 465, 142914.

Other publications:

1. Di Menno Di Bucchianico, D.; Perez-Sena, W.Y.; Casson Moreno, V.; Salmi, T.; Leveneur, S. Model Discrimination for Hydrogen Peroxide Consumption towards  $\gamma$ -Alumina in Homogeneous Liquid and Heterogeneous Liquid-Liquid Systems. *Processes* 2021, 9, 1476.

Communications:

1. Di Menno Di Bucchianico, D.; Buvat, J.-C.; Casson Moreno, V.; Leveneur, S. Inside the mechanism for transforming cellulose into biofuels: kinetic and calorimetry investigation of 5-hmf alcoholysis to n-butyl levulinate over solid catalyst. **Oral presentation** for ISGC2022 - The International Symposium on Green Chemistry, 16<sup>th</sup>-20<sup>th</sup> May, 2022, La Rochelle, France.
2. Di Menno Di Bucchianico, D.; Buvat, J.-C.; Casson Moreno, V.; Leveneur, S. Alcoholysis of Fructose to N-Butyl Levulinate in Gamma-Valerolactone solvent: kinetic and calorimetry investigation. **Oral**



**presentation** for WasteEng22 – The 9th Conference of Engineering for Waste and Biomass Valorization, 27<sup>th</sup>-30<sup>th</sup> June 2022, Copenhagen, Denmark.

3. Di Menno Di Bucchianico, D.; Buvat, J.-C.; Casson Moreno, V.; Leveneur, S. - butyl levulinate production from the alcoholysis of 5-HMF. **Oral presentation** for CHISA – The 26th International Congress of Chemical and Process Engineering, 21<sup>th</sup>-25<sup>th</sup> August 2022, Prague, Czech Republic.
4. Di Menno Di Bucchianico, D.; Buvat, J.-C.; Casson Moreno, V.; Leveneur, S. Biofuel candidate n-butyl levulinate from fructose solvolysis: Detailed kinetic investigation under high gravity conditions. **Oral presentation** for MECCE15- The 15th Mediterranean Congress in Chemical Engineering, 30<sup>th</sup> May - 2<sup>nd</sup> June 2023, Barcelona, Spain.
5. Di Menno Di Bucchianico, D.; Scarponi, G.E.; Buvat, J.-C.; Leveneur, S; Casson Moreno, V. Evaluating the economic feasibility of lignocellulosic biomass valorization through green-hydrogen: a case study in Normandy. **Poster presentation** for EUCBE31 - The 31th European Biomass Conference & Exhibition, 5<sup>th</sup>-8<sup>th</sup> June 2023, Bologna, Italy.
6. Di Menno Di Bucchianico, D.; Buvat, J.-C.; Casson Moreno, V.; Leveneur, S. High-Gravity solvolysis to n-Butyl levulinate. **Oral presentation** for ISCRE27 - The 27th International Symposium for Chemical Reaction Engineering, 11<sup>th</sup>-14<sup>th</sup> June 2023, Quebec City, Canada.

# Remerciements

Je tiens à remercier la Région Normandie pour le soutien apporté à ma thèse de doctorat, réalisée dans le cadre du projet ARBRE RIN 100% et des activités de recherche du pôle CTM (Continuum Terre-Mer) de Normandie Université. L'activité de recherche a été réalisée dans le cadre du projet ARBRE, cofinancé par l'Union Européenne à travers le Fonds Européen de Développement Régional (FEDER) et la Région Normandie, à travers le soutien du "pôle CTM (Continuum Terre-Mer) et EP2M (Énergies, Propulsion, Matière, Matériaux) de Normandie université". Je tiens également à remercier l'Université Franco-Italienne (Università Italo Francese) pour avoir soutenu ma thèse de doctorat, lors de ma période de mobilité en cotutelle entre la France et l'Italie, à travers le "Programme Vinci".

J'exprime ma gratitude à mon directeur de thèse, le Dr. Sébastien Leveneur, pour m'avoir accompagné et conseillé dans ce parcours, en m'introduisant dans le monde de la recherche et de l'université. J'ai apprécié sa disponibilité sans faille et "sa porte" toujours ouverte aux questions, recommandations et discussions.

Je tiens également à exprimer ma gratitude à la codirectrice de cette thèse, le Professeur Valeria Casson Moreno, pour m'avoir guidée et aidée dans les différentes étapes de ma recherche et pour m'avoir donné des conseils et des éclairages sincères et constructifs, ainsi que pour m'avoir orientée dans le choix d'entreprendre le doctorat.

J'aimerais remercier les co-superviseurs, le Dr. Jean-Christophe Buvat, et en particulier le Professeur Alessandro Tugnoli, pour avoir pris en charge les tâches administratives pendant mon séjour à Bologne, ainsi que les suggestions de recherche.

J'exprime ma sincère gratitude au Dr. Giordano Emrys Scarponi qui m'a guidé, conseillé pendant ma période de recherche à l'Université de Bologne, et qui a apporté une contribution fondamentale à différentes étapes de mon activité de recherche.

Je voudrais remercier tous les membres du jury d'avoir accepté de participer à la soutenance de ma thèse de doctorat: Joris Thybaut, Catherine Azzaro-Pantel, Nadine Gabas, Eric Schaer, et Sophie Thiebaud-Roux, pour leur temps et leur disponibilité.

Un grand merci à tout le personnel de l'INSA et du laboratoire LSPC, à commencer par le directeur Alain Ledoux, pour sa gentillesse et sa serviabilité, au personnel technique du laboratoire Bruno Daronat, Sylvie Poubelle. Je remercie tout particulièrement Maria Pereira De Araujo pour son extrême gentillesse, sa serviabilité et son attention à l'égard de tous les doctorants que nous sommes.

Je voudrais également remercier Mélanie Mignot pour sa gentillesse et sa contribution fondamentale à l'évaluation des méthodes analytiques pour ma recherche, qui a été constamment disponible pour des conseils et des questions pendant mon travail ; un grand merci également à Christine Devouge-Boyer et Laura Bom pour m'avoir guidé et toujours aidé avec tous les aspects techniques des différents équipements analytiques.

Je remercie tout particulièrement tous mes collègues qui m'ont accompagné au fil des années ; mon ami et collègue Sindi pour tous les moments passés ensemble, les pauses café à l'université et les nombreux fous rires au laboratoire, ainsi que tous mes autres collègues de thèse à l'INSA.

Je remercie également tous les collègues que j'ai rencontrés dans le laboratoire LISES de l'université de Bologne, qui m'ont chaleureusement accueillie et m'ont immédiatement fait me sentir chez moi, rendant ainsi ma troisième année de doctorat moins difficile.

Les plus grands remerciements vont à ma famille ; à mes parents qui sont le noyau de mon identité et qui m'ont enseigné les valeurs de sacrifice, de persévérance et de gentillesse, à qui je dédie toutes mes réalisations ; à ma sœur que j'aime infiniment et qui croit toujours en moi ; à mon petit neveu Alessandro qui m'a réservé un sourire à chaque moment difficile de la rédaction de cette thèse ; et à mon partenaire Quentin, mon bon côté, je te remercie de m'avoir soutenue, motivée et protégée tout au long de ces années, cette réalisation est aussi la tienne.

Enfin, merci à mes amis de toujours qui m'ont supporté, moi et mes plaintes, aussi loin que je me souviens ; à mes amis Irene, Giada, Marco, Cepo, SimonSalvo, Naomi, Ermelinda, e Chiara.

# Ringraziamenti

Desidero ringraziare la Regione Normandia per il sostegno alla mia tesi di dottorato, svolta nell'ambito di "ARBRE RIN 100%" e delle attività di ricerca del "pôle CTM (Continuum Terre-Mer) de Normandie Université". L'attività di ricerca è stata svolta nell'ambito del progetto ARBRE, cofinanziato dall'Unione Europea attraverso il Fondo Europeo di Sviluppo Regionale (FESR) e dalla Regione Normandia, attraverso il supporto del "pôle CTM (Continuum Terre-Mer) e EP2M (Énergies, Propulsion, Matière, Matériaux) de Normandie université".

Desidero inoltre ringraziare l'Université Franco-Italienne (Università Italo Francese) per aver sostenuto la mia tesi di dottorato, durante il periodo di mobilità cotutela tra Francia e Italia, attraverso il "Programma Vinci".

Esprimo la mia gratitudine al mio direttore di tesi, il dottor Sébastien Leveueur, per avermi accompagnato e consigliato in questo percorso, introducendomi al mondo della ricerca e dell'università. Ho apprezzato la sua immancabile disponibilità e la "sua porta" sempre aperta a domande, consigli e discussioni.

Desidero inoltre esprimere la mia gratitudine alla co-relatrice di questa tesi, la professoressa Valeria Casson Moreno, per avermi guidato e aiutato nelle diverse fasi della mia ricerca e per avermi dato consigli e spunti sinceri e costruttivi, oltre ad avermi orientato nella scelta di intraprendere il dottorato.

Desidero ringraziare i co-supervisor, il professor Jean-Christophe Buvat e in particolare il professor Alessandro Tugnoli, soprattutto per essersi occupati delle incombenze amministrative durante la mia permanenza a Bologna, insieme ai suggerimenti per la ricerca.

Esprimo la mia sincera gratitudine al dottor Giordano Emrys Scarponi, che mi ha guidato e consigliato durante il mio periodo di ricerca all'Università di Bologna, e che ha contribuito in modo fondamentale in diverse fasi della mia attività di ricerca.

Vorrei ringraziare tutti i membri della giuria per aver accettato di far parte della difesa della mia tesi di dottorato: Joris Thybaut, Catherine Azzaro-Pantel, Nadine Gabas, Eric Schaer e Sophie Thiebaud-Roux, per il loro tempo e la loro disponibilità.

Un enorme ringraziamento va a tutto il personale dell'INSA e del laboratorio LSPC, a partire dal direttore Alain Ledoux, per la sua gentilezza e disponibilità, al personale tecnico di laboratorio Bruno Daronat, Sylvie Poubelle. Un ringraziamento particolare a Maria Pereira De Araujo per la sua estrema gentilezza, disponibilità e attenzione verso tutti noi dottorandi.

Vorrei anche ringraziare Melanie Mignot per la sua gentilezza e il suo fondamentale contributo alla valutazione dei metodi analitici per la mia ricerca, che è stata costantemente disponibile per consigli e domande durante il mio lavoro; un grande ringraziamento anche a Christine Devouge-Boyer e Laura Bom per avermi guidato e sempre aiutato con tutti gli aspetti tecnici delle diverse apparecchiature analitiche.

Un ringraziamento speciale va a tutti i colleghi che mi hanno accompagnato in questi anni; alla mia amica e collega Sindi per tutti i momenti passati insieme, le pause caffè all'università e le tante risate in laboratorio, e a tutti gli altri colleghi di dottorato dell'INSA.

Un ringraziamento speciale va anche a tutti i colleghi che ho incontrato nel laboratorio LISES dell'Università di Bologna, che mi hanno accolto calorosamente e mi hanno fatto sentire subito a casa, rendendo meno duro il mio terzo anno di dottorato.

Il ringraziamento più grande va alla mia famiglia; ai miei genitori che sono il fulcro della mia identità e che mi hanno insegnato i valori del sacrificio, della perseveranza e della gentilezza, a loro dedico tutti i miei successi; a mia sorella che amo immensamente e che crede sempre in me; al mio nipotino Alessandro che mi ha riservato un sorriso in ogni momento difficile della stesura di questa tesi; e al mio compagno Quentin, il mio lato buono, ti ringrazio per avermi sostenuto, motivato e protetto in tutti questi anni; questo risultato è anche tuo.

Infine, grazie ai miei amici di sempre che hanno sopportato me e le mie lamentele da sempre; ai miei amici Irene, Giada, Marco, Cepo, SimonSalvo, Naomi, Ermelinda e Chiara.

# Acknowledgements

I would like to thank the Normandy Region for supporting my doctoral thesis, which was carried out as part of "ARBRE RIN 100%" and part of the research activities of the "pôle CTM (Continuum Terre-Mer) de Normandie Université. The research activity was carried out in the context of the ARBRE project, co-financed by the European Union through the European Regional Development Fund (ERDF) and the Normandy Region, through the support of the " pôle CTM (Continuum Terre-Mer) and EP2M (Énergies, Propulsion, Matière, Matériaux) de Normandie université".

I would like also to thank the Université Franco-Italienne (Università Italo Francese) for supporting my doctoral thesis, during my cotutela mobility period between France and Italy, through the "Programme Vinci".

I express my gratitude to my thesis director, Dr. Sébastien Leveneur for having accompanied and advised me along this path, introducing me to the world of research and academia. I appreciated his unfailing availability and "his door" always open for questions, recommendations and discussion.

I would also like to express my gratitude to the co-director of this thesis, Professor Valeria Casson Moreno, for guiding and helping me through the different stages of my research and for giving me sincere and constructive advice and insights, as well as orienting me in the choice to undertake the PhD.

I would like to thank the co-supervisors, Professor Jean-Christophe Buvat, and in particular Professor Alessandro Tugnoli, especially for taking care of administrative duties during my stay in Bologna, along with research suggestions.

I express my sincere gratitude to Dr. Giordano Emrys Scarponi who guided me, advised me during my research period at the University of Bologna, and who contributed fundamentally at different stages of my research activity.

I would like to thank all of jury members for accepting to be part of my doctoral thesis defense: Joris Thybaut, Catherine Azzaro-Pantel, Nadine Gabas, Eric Schaer, and Sophie Thiebaud-Roux, for your time and availability.

A huge thank you goes out to all the staff at INSA and the LSPC laboratory, starting with the director Alain Ledoux, for his kindness and helpfulness, to the technical laboratory staff Bruno Daronat, Sylvie Poubelle. Special thanks to Maria Pereira De Araujo for her extreme kindness, helpfulness and care for all of us PhD students.

I would also like to thank Melanie Mignot for her kindness and fundamental contribution to the evaluation of analytical methods for my research, who was constantly available for advice and questions during my work; a big thank you also to Christine Devouge-Boyer and Laura Bom for guiding me and always helping me with all the technical aspects of the different analytical equipment.

My special thanks go to all my colleagues who have accompanied me over the years; to my friend and colleague Sindi for all the times we spent together, the coffee breaks at university and the many laughs in the lab, and to all my other PhD colleagues at INSA.

Special thanks also to all the colleagues I met in the LISES lab at the University of Bologna, who warmly welcomed me and immediately made me feel at home, making my third year of PhD less tough.

The biggest thanks go to my family; to my parents who are the core of my identity and who taught me the values of sacrifice, perseverance and kindness, to them I dedicate all my achievements; to my sister whom I love immeasurably and who always believes in me; to my little nephew Alessandro who reserved a smile for me at every difficult moment in the writing of this thesis; and to my partner Quentin, my good side, I thank you for supporting, motivating and protecting me throughout these years, this achievement is also yours.

Finally, thanks to my lifelong friends who have put up with me and my complaints for as long as I can remember; to my friends Irene, Giada, Marco, Cepo, SimonSalvo, Naomi, Ermelinda, e Chiara.

# Résumé

Comme prévu, le monde est confronté aux effets tangibles du changement climatique, conséquence d'une économie basée sur les combustibles fossiles depuis des centaines d'années. En plus de faire face et de prendre des mesures correctives pour limiter les effets du réchauffement climatique, l'Europe est confrontée à une grave crise énergétique, révélant la fragilité du système énergétique européen, qui dépend principalement des importations de combustibles fossiles.

La géopolitique des ressources fossiles a déclenché la nécessaire refonte de l'économie énergétique européenne, qui s'oriente "à marche forcée" vers les sources d'énergie renouvelables pour devenir une économie neutre en termes de ressources fossiles et de carbone. Dans le panorama des énergies renouvelables, les ressources les plus exploitées sont l'énergie solaire, l'énergie éolienne et l'énergie de la biomasse. Outre la production de bioénergie, la biomasse est une source inestimable de biocarbone, qui peut être exploitée et valorisée pour la production de molécules à haute valeur ajoutée pouvant être utilisées dans divers secteurs industriels, pour la production de carburants, de produits chimiques, de matériaux, et en remplaçant les produits correspondants d'origine fossile. Dans ce contexte, des systèmes innovants de bioraffinage de la biomasse de deuxième génération ont été développés pour transformer et déconstruire la structure complexe de la biomasse en molécules plateformes plus simples, qui peuvent ensuite être transformées en molécules à fort potentiel. Parmi celles-ci, les lévulinate d'alkyle ont été identifiés pour leur potentiel considérable en tant que bio-additifs et biocarburants. Esters de l'acide lévulinique, ces composés peuvent être obtenus à partir de dérivés de la biomasse, tels que les monosaccharides de sucre, selon différentes voies de réaction ; parmi celles-ci, la solvolysse acide des sucres hexagonaux pourrait être une voie de production prometteuse et rentable, qui nécessite des recherches plus approfondies qui n'ont pas encore été trouvées dans la littérature.

Le potentiel du lévulinate d'alkyle réside également dans la possibilité d'un traitement ultérieur par hydrogénation pour produire de la  $\gamma$ -valérolactone (GVL), une molécule dont le marché est prometteur en tant que biosolvant en raison de ses propriétés de stabilité, d'écotoxicité et de biodégradabilité. L'utilisation d'hydrogène moléculaire est la voie la plus courante pour l'hydrogénation de la GVL, mais, en plus d'être un réactif chimique fondamental, l'hydrogène est également l'un des principaux acteurs de la transition énergétique. En effet, en tant que vecteur énergétique, l'hydrogène peut permettre la pénétration complète des sources d'énergie renouvelables sur le marché de l'énergie, en constituant un complément tampon pour le stockage des énergies renouvelables intermittentes, grâce à la conception de systèmes de stockage de l'énergie à base d'hydrogène (HydESS). Le stockage à long terme de l'hydrogène peut permettre la mise en place de systèmes d'énergie renouvelable autonomes, car il fait le lien entre la fonctionnalité des systèmes "Power-to-Hydrogen", capables d'absorber les surplus d'énergie provenant des énergies renouvelables et de les stocker, et celle des systèmes "Hydrogen-to-Power", qui restituent l'énergie renouvelable lorsque les sources d'énergie primaires ne sont pas disponibles. Dans cette perspective, le développement de ces systèmes peut conduire à l'intégration complète et stable des sources d'énergie renouvelables dans les actifs industriels existants, ainsi que dans de nouveaux marchés industriels, tels que les bioraffineries de biomasse lignocellulosique, promouvant le développement de réalités industrielles "vertes" en termes de transformation des matériaux et de l'énergie.



Le marché industriel mondial évolue vers la décarbonisation et le redéveloppement de divers actifs, grâce à des investissements dans l'efficacité énergétique et à l'introduction de processus verts pour la valorisation des sources renouvelables, mais la mise en œuvre à grande échelle de ces initiatives nécessite une analyse complète et approfondie de leur durabilité.

Des mesures et des outils d'évaluation de la durabilité ont été développés au fil des ans, en particulier pour guider les phases de conception ; l'application de ces mesures est particulièrement efficace dans le contexte de la conception précoce des processus, où une analyse décisionnelle basée sur des critères de durabilité permet d'orienter judicieusement les décisions de conception clés, telles que la technologie des processus, les conditions d'exploitation, la taille de l'usine, le site d'installation, vers les meilleures solutions possibles.

Les exigences de durabilité constituent donc la base de l'investissement dans la conception de nouveaux procédés et systèmes d'exploitation des énergies renouvelables et des bio-ressources carbonées, afin d'évaluer leur rentabilité économique, leur fiabilité technologique, leur sécurité sociale et leurs incidences sur l'environnement.

Dans ce contexte, le sujet de recherche de cette thèse se concentre sur l'étude technologique et l'évaluation de la durabilité d'un système de bioraffinage potentiel pour valoriser la biomasse lignocellulosique pour la production d'une molécule à haute valeur ajoutée, telle que le lévulinate de butyle et, par la suite, la  $\gamma$ -valérolactone, intégrée à des systèmes d'énergie renouvelable pour la production d'énergie et d'hydrogène.

Afin de répondre à la question de la durabilité de l'ensemble de la configuration du processus, la recherche présente une première section axée sur l'étude expérimentale de la technologie optimale pour la production de lévulinate de butyle. Pour combler les lacunes de la littérature concernant ce lévulinate d'alkyle prometteur, la solvolysé de l'hexose Fructose dérivé de la biomasse en lévulinate de butyle a été étudiée, en termes de conditions optimales de processus et de modélisation cinétique. Après avoir sélectionné un catalyseur hétérogène efficace, l'effet du solvant a été étudié, montrant les avantages de l'utilisation de la  $\gamma$ -valérolactone comme co-solvant, avec le butanol, sur la cinétique de conversion et de dissolution du fructose.

En tenant compte de l'utilisation du catalyseur sélectionné et du système de solvant optimal, la solvolysé en lévulinate de butyle a été étudiée en profondeur d'un point de vue cinétique, d'abord en proposant un modèle pour la solvolysé du 5-HMF, un intermédiaire dans la voie du fructose, et ensuite en étendant la modélisation à partir du fructose lui-même. Un modèle cinétique robuste, décrivant le mécanisme réactionnel de la solvolysé, a été défini et validé, en particulier dans des conditions de concentration initiale élevée en fructose (en appliquant le concept de haute gravité), et en incluant dans la modélisation la cinétique de dissolution et de dégradation du fructose dans des conditions acides.

Dans la deuxième partie de la recherche, la perspective technologique a été étendue à l'hydrogénation du lévulinate de butyle en  $\gamma$ -valérolactone, en utilisant des modèles cinétiques rapportés dans la littérature, afin de définir un schéma de processus optimal pour la conversion globale du fructose en GVL, via le lévulinate de butyle. À partir d'une phase de conception, le schéma du procédé a été défini pour inclure les unités de la réaction de solvolysé et de l'hydrogénation ultérieure, ainsi que les étapes de purification du produit final, le GVL, et la régénération du solvant butanol, au moyen d'une première étape de séparation de la teneur en eau produite et d'une décomposition ultérieure des traces de formiate de butyle, un produit secondaire de la réaction de solvolysé. Une fois le schéma de procédé de référence défini, il a été optimisé sur la base du concept d'intensification des procédés, visant à optimiser la

récupération des matières et de l'énergie ; une analyse énergétique a été réalisée pour définir la demande d'énergie du schéma, pour différentes tailles d'installations.

Outre l'optimisation du procédé de bio-raffinage, cette section s'est concentrée sur l'utilisation de l'hydrogène pour l'étape d'hydrogénation et comme vecteur énergétique, et donc sur la définition et la conception optimale du système de stockage de l'hydrogène, qui dépend de la demande en énergie et en hydrogène du procédé, mais aussi de la disponibilité des ressources énergétiques renouvelables et des technologies de conversion, c'est-à-dire des turbines éoliennes, etc.

L'analyse a donc été adaptée à une étude de cas, en considérant la région de Normandie (France) comme un site d'installation potentiel pour l'ensemble de la configuration, et en se concentrant sur la disponibilité locale de la biomasse lignocellulosique et de l'énergie éolienne.

Sur la base du potentiel des ressources renouvelables, de la demande énergétique du processus et des technologies de conversion de l'énergie éolienne et de production, de stockage et d'utilisation sur site de l'hydrogène, une méthode de conception et d'intégration du système d'approvisionnement en énergie au processus de production a été définie ; une conception optimale de la configuration présentée et différents scénarios d'intégration ont été définis en conséquence. Enfin, une méthodologie d'évaluation de la durabilité a été définie, à l'aide d'indicateurs de performance clés qui évaluent la durabilité pour chaque scénario sur la base de perspectives économiques, environnementales et sociales. L'application de méthodes de pondération et d'agrégation des indicateurs a été utilisée pour définir un indice global de durabilité agrégé, permettant de classer les scénarios en fonction de leur durabilité.

L'analyse de la durabilité par le biais de l'indice global final a démontré le potentiel des scénarios 6 et 7 avec un système de bioraffinerie GVL, intégré à l'énergie éolienne et à des systèmes de stockage d'énergie à base d'hydrogène, par rapport aux scénarios alimentés par des sources d'énergie conventionnelles. En particulier, l'analyse des perspectives individuelles a révélé la rentabilité économique élevée de ces scénarios, en raison de la synergie commerciale du GVL et de l'hydrogène vert, et de la réduction de l'impact sur l'environnement ; certaines critiques sont, en revanche, associées à la perspective sociale, exprimée en termes d'analyse de la sécurité inhérente au processus, motivée par la taille du stockage de l'hydrogène vert.

La robustesse de la méthodologie utilisée a été testée par des analyses de sensibilité basées sur la méthode de Monte Carlo, qui confirment la fiabilité et la robustesse des résultats. Bien qu'appliquée à une étude de cas spécifique, la méthodologie définie constitue un outil flexible et fiable qui peut être étendu à différentes technologies de processus, à différents sites, ainsi qu'à des systèmes hybrides énergie renouvelable plus complexes.

**Mots-clés** : Valorisation de la biomasse lignocellulosique, production des molécules plateformes, modélisation cinétique, simulation de procédé, analyse technico-économique, analyse de l'impact environnemental, analyse de la sécurité intrinsèque, évaluation de la durabilité.

# Riassunto

Come previsto, il mondo sta affrontando gli effetti tangibili del cambiamento climatico come conseguenza di un'economia basata sui combustibili fossili per centinaia di anni. Oltre a dover affrontare e adottare misure correttive per limitare gli effetti del riscaldamento globale, l'Europa sta affrontando una grave crisi energetica, che rivela la fragilità del sistema energetico europeo, prevalentemente dipendente dalle importazioni di combustibili fossili.

La geopolitica delle risorse fossili ha innescato la necessaria rimodulazione dell'economia energetica europea, che si sta spostando "forzatamente" verso le risorse energetiche rinnovabili per diventare un'economia fossile e a zero emissioni di carbonio. Nel panorama delle rinnovabili, le risorse più sfruttate sono l'energia solare, eolica e da biomassa. Oltre alla produzione di bioenergia, la biomassa è una fonte inestimabile di biocarbonio, che può essere sfruttata e valorizzata per la produzione di molecole ad alto valore aggiunto che possono essere utilizzate in vari settori industriali, per la produzione di carburanti, prodotti chimici, materiali e sostituendo i corrispondenti prodotti di origine fossile. In questo contesto, sono stati sviluppati sistemi innovativi di bioraffinazione della biomassa di seconda generazione per trasformare e decostruire la complessa struttura della biomassa in molecole piattaforma più semplici, che possono poi essere trasformate in molecole ad alto potenziale. Tra queste, gli alchil levulinati sono stati identificati per il loro notevole potenziale come bioadditivi e biocarburanti. Esteri dell'acido levulinico, questi composti possono essere ottenuti da derivati della biomassa, come i monosaccaridi dello zucchero, secondo diverse vie di reazione; tra queste, la solvolisi acida degli zuccheri esosi può essere una via di produzione promettente ed economicamente vantaggiosa, che richiede ulteriori indagini non ancora presenti in letteratura.

Il potenziale degli alchil levulinati risiede anche nella possibilità di un'ulteriore trasformazione mediante idrogenazione per produrre  $\gamma$ -valerolattone (GVL), una molecola con un mercato promettente come bio-solvente, grazie alle sue proprietà di stabilità, ecotossicità e biodegradabilità. L'uso dell'idrogeno gassoso è la via più comune per l'idrogenazione del GVL, ma, oltre a essere un reagente chimico fondamentale, l'idrogeno è anche uno dei principali protagonisti della transizione energetica. Infatti, come vettore energetico, l'idrogeno può portare alla piena penetrazione delle fonti energetiche rinnovabili nel mercato dell'energia, costituendo un complemento-tampone per lo stoccaggio delle energie rinnovabili intermittenti, attraverso la progettazione di sistemi di stoccaggio dell'energia dell'idrogeno (HydESS). L'accumulo di energia a idrogeno a lungo termine può consentire l'autosufficienza dei sistemi di energia rinnovabile, in quanto agisce da ponte tra le funzionalità dei sistemi Power-to-Hydrogen, in grado di assorbire i surplus energetici delle energie rinnovabili e di immagazzinarli, e quelle dei sistemi Hydrogen-to-Power, che restituiscono energia rinnovabile quando le fonti di energia primaria non sono disponibili. In quest'ottica, lo sviluppo di tali sistemi può portare all'integrazione completa e stabile delle fonti di energia rinnovabile in asset industriali già esistenti, così come in nuovi mercati industriali, come le bioraffinerie di biomassa lignocellulosica, promuovendo lo sviluppo di realtà industriali "verdi" in termini di trasformazione di materiali ed energia.

Il mercato industriale globale si sta evolvendo verso la decarbonizzazione e la riqualificazione di diversi asset, attraverso investimenti in efficienza energetica e l'introduzione di processi green per la valorizzazione delle fonti rinnovabili, ma l'implementazione su larga scala di queste iniziative richiede un'analisi completa e approfondita della loro sostenibilità.

Nel corso degli anni sono state sviluppate metriche e strumenti di valutazione della sostenibilità, in particolare per guidare le fasi iniziali di progettazione. L'applicazione di queste metriche è particolarmente efficace nel contesto della progettazione di nuovi processi, dove un'analisi decisionale basata su criteri di sostenibilità consente di orientare in modo sensato le decisioni di progettazione, quali le tecnologie di processo, condizioni operative, dimensioni dell'impianto, sito di installazione, indicando le alternative migliori.

I requisiti di sostenibilità sono, quindi, alla base delle scelte di investimento nella progettazione di nuovi processi e sistemi per lo sfruttamento delle energie rinnovabili e delle bio-risorse di carbonio, al fine di valutarne la redditività economica, l'affidabilità tecnologica, la sicurezza sociale e l'impatto ambientale.

In questo contesto, il tema di ricerca di questa tesi si concentra sull'indagine tecnologica e sulla valutazione della sostenibilità di un potenziale sistema di bioraffineria per la valorizzazione della biomassa lignocellulosica per la produzione di una molecola ad alto valore aggiunto, quale il butil levulinato e, successivamente, il  $\gamma$ -valerolattone, integrato con sistemi di energia rinnovabile per la produzione di energia e idrogeno.

Per rispondere alla domanda sulla sostenibilità dell'intera filiera di processo, la ricerca presenta una prima sezione incentrata sull'indagine sperimentale della tecnologia ottimale per la produzione di butil levulinato. Per colmare la lacuna in letteratura riguardo a questo promettente alchil levulinato, è stata studiata la solvolisi dell'esoso fruttosio derivato da biomassa a butil levulinato, in termini di condizioni ottimali di processo e modellazione cinetica. Selezionato un efficace catalizzatore eterogeneo, è stato studiato l'effetto del solvente, mostrando i benefici dell'utilizzo del  $\gamma$ -valerolattone come co-solvente, insieme al butanolo, sulla conversione e sulla cinetica di dissoluzione del fruttosio.

Considerando l'uso del catalizzatore selezionato e del sistema di solventi ottimale, la solvolisi a butil levulinato è stata studiata in modo approfondito da un punto di vista cinetico, proponendo dapprima un modello per la solvolisi del 5-HMF, intermedio nel percorso del fruttosio, e poi estendendo la modellazione della solvolisi dal fruttosio stesso.

È stato definito e validato un modello cinetico robusto, che descrive il meccanismo di reazione della solvolisi, in condizioni di elevata concentrazione iniziale di fruttosio (applicando il concetto di High-gravity) e includendo nella modellazione la cinetica di dissoluzione e degradazione del fruttosio in condizioni acide.

Nella seconda parte della ricerca, la prospettiva tecnologica è stata estesa all'idrogenazione del butil levulinato a  $\gamma$ -valerolattone, utilizzando modelli cinetici riportati in letteratura, al fine di definire uno schema di processo ottimale per la conversione complessiva del fruttosio in GVL, attraverso il butil levulinato. Partendo da una fase di progettazione concettuale, lo schema di processo è stato definito includendo le unità della reazione di solvolisi e successiva idrogenazione, nonché le fasi di purificazione del prodotto finale, GVL, e di rigenerazione del solvente butanolo, attraverso un primo stadio di separazione dal contenuto di acqua prodotto, e la successiva decomposizione delle tracce di butilformiato, un prodotto secondario della reazione di solvolisi. Una volta definito lo schema di processo di riferimento, questo è stato ottimizzato sulla base del concetto di intensificazione del processo, volto a ottimizzare il recupero di materia ed energia; è stata effettuata un'analisi energetica per definire la domanda di energia dello schema, per diverse dimensioni di impianto.

Oltre all'ottimizzazione dello schema del processo di bioraffinazione, questa sezione si è concentrata sull'uso dell'idrogeno per la fase di idrogenazione e come vettore energetico, e quindi sulla definizione e sulla progettazione

ottimale del sistema di stoccaggio dell'idrogeno, che dipende dalla domanda di energia e di idrogeno del processo, ma anche dalla disponibilità di risorse energetiche rinnovabili e di tecnologie di conversione, ad esempio turbine eoliche.

Essendo specifica del sito, la disponibilità di risorse energetiche rinnovabili dipende fortemente dalla località considerata; per questo motivo, l'analisi è stata adattata a un caso di studio, considerando la regione della Normandia (Francia) come potenziale sito di installazione per l'intera configurazione e concentrandosi sulla disponibilità locale di biomassa lignocellulosica e di energia eolica.

Sulla base del potenziale delle risorse rinnovabili, del fabbisogno energetico del processo e delle tecnologie per la conversione dell'energia eolica e per la produzione, lo stoccaggio e l'utilizzo in loco dell'idrogeno, è stato definito un metodo per la progettazione e l'integrazione del sistema di approvvigionamento energetico nel processo produttivo; è stato presentato un progetto ottimale della configurazione e sono stati definiti diversi scenari per l'integrazione.

Infine, è stata definita una metodologia di valutazione della sostenibilità, utilizzando indicatori chiave di prestazione che valutano la sostenibilità per ogni scenario sulla base di prospettive economiche, ambientali e sociali. L'applicazione di metodi di ponderazione e aggregazione degli indicatori è stata utilizzata per definire un indice di sostenibilità complessivo aggregato, che consente di valutare e confrontare la sostenibilità tra gli scenari.

L'analisi di sostenibilità attraverso l'indice aggregato finale ha dimostrato il potenziale degli scenari 6 e 7 con un sistema di bioraffineria GVL, integrato con sistemi di accumulo di energia eolica e idrogeno, rispetto agli scenari alimentati da fonti energetiche convenzionali. In particolare, l'analisi delle singole prospettive ha evidenziato l'elevata redditività economica di questi scenari, dovuta alla sinergia di mercato del GVL e dell'idrogeno verde, e il ridotto impatto ambientale; alcune criticità sono invece associate alla prospettiva sociale, espressa in termini di analisi della sicurezza intrinseca del processo, influenzata dalla dimensione dello stoccaggio di idrogeno.

La robustezza della metodologia utilizzata è stata testata con analisi di sensitività basate sul metodo Monte Carlo, che confermano l'affidabilità e la solidità dei risultati. Sebbene applicata a un caso di studio specifico, la metodologia definita costituisce uno strumento flessibile e affidabile che può essere esteso a diverse tecnologie di processo, siti di ubicazione e sistemi ibridi di energia rinnovabile più complessi.

**Parole chiave:** Valorizzazione della biomassa lignocellulosica, Produzione di molecole piattaforma, Modellazione cinetica, Simulazione di processo, Analisi tecno-economica, Analisi dell'impatto ambientale, Analisi della sicurezza intrinseca, Analisi di sostenibilità.

# Abstract

As expected, the world is facing the tangible effects of climate change as a consequence of an economy based on fossil fuels for hundreds of years. In addition to coping with and taking remedial action to limit the effects of global warming, Europe is facing a severe energy crisis, revealing the fragility of the European energy system, which is predominantly dependent on imported fossil fuels.

The geopolitics of fossil resources has triggered the necessary reshaping of the European energy economy, which is shifting 'forcibly' towards renewable energy resources to become a fossil- and carbon-neutral economy. In the panorama of renewables, the most exploited resources are solar, wind, and biomass energy. In addition to the production of bio-energy, biomass is an invaluable source of bio-carbon, which can be exploited and valorized for the production of high-value-added molecules that can be used in various industrial sectors, for the production of fuels, chemicals, materials, and by replacing the corresponding fossil-based products. In this context, innovative biorefining systems for second-generation biomass have been developed to transform and deconstruct the complex structure of biomass into simpler platform molecules, which can then be transformed into high-potential molecules. Among these, alkyl levulinates have been identified for their considerable potential as bio-additives and bio-fuels. Esters of levulinic acid, these compounds can be obtained from biomass derivatives, such as sugar monosaccharides, according to different reaction pathways; of these, acid solvolysis of hexose sugars may be a promising and cost-effective production route, which requires further investigation not yet found in the literature.

The potential of alkyl levulinate also lies in the possibility of further processing by hydrogenation to produce  $\gamma$ -valerolactone (GVL), a molecule with a promising market as a bio-solvent due to its stability, ecotoxicity and biodegradability properties. The use of molecular hydrogen is the most common route to hydrogenation to GVL, but, besides being a fundamental chemical reagent, hydrogen is also one of the main players in the energy transition. In fact, as energy carrier, hydrogen can lead to the full penetration of renewable energy sources into the energy market, constituting a buffer-complement for the storage of intermittent renewable energies, through the design of hydrogen energy storage systems (HydESS). Long-term hydrogen energy storage can enable self-sustaining renewable energy systems, as it acts to bridge the functionality of Power-to-Hydrogen systems, capable of absorbing energy surpluses from renewable-energies and storing them, and those of the Hydrogen-to-Power systems, that return renewable power when primary energy sources are unavailable. In this perspective, the development of such systems can lead to the complete and stable integration of renewable energy sources in already existing industrial assets, as well as, in new industrial markets, such as lignocellulosic biomass biorefineries, promoting the development of 'green' industrial realities in terms of material and energy transformation.

The global industrial market is evolving towards the decarbonization and redevelopment of various assets, through investment in energy efficiency and the introduction of green-processes for the valorization of renewable sources, but the full-scale implementation of these initiatives requires a complete and in-depth analysis of their sustainability.

Sustainability metrics and assessment tools have been developed over the years, in particular to guide design phases; the application of these metrics is particularly effective in the context of early process design, where a decision-

making analysis based on sustainability criteria allows for sensible steering of key design decisions, such as process technology, operating conditions, plant size, installation site, towards the best alternatives.

Sustainability requirements are, therefore, the basis for investing in the design of new processes and systems to exploit renewable energy, and carbon bio-resources, in order to assess their economic profitability, technological reliability, social safety and environmental impacts.

In this context, the research topic of this thesis focuses on the technological investigation and sustainability assessment of a potential biorefinery system to valorize the lignocellulosic biomass for the production of a high-value-added molecule, such as butyl levulinate and, subsequent,  $\gamma$ -valerolactone, integrated with renewable energy systems for the production of energy and hydrogen.

In order to answer the question of sustainability of the entire process configuration, the research presents a first section focused on the experimental investigation of the optimal technology for the production of butyl levulinate. To fill the gap in the literature regarding this promising alkyl levulinate, the solvolysis of the biomass-derived hexose Fructose to butyl levulinate was investigated, in terms of optimal process conditions and kinetic modelling. Selected an effective heterogeneous catalyst, the effect of the solvent was investigated, showing the benefits of using  $\gamma$ -valerolactone as co-solvent, together with butanol, on the conversion and dissolution kinetics of fructose.

Considering the use of the selected catalyst and the optimal solvent system, the solvolysis to butyl levulinate was studied in depth from a kinetic point of view, first by proposing a model for the solvolysis of 5-HMF, an intermediate in the fructose pathway, and then extending the modelling from fructose itself. A robust kinetic model, describing the reaction mechanism of solvolysis, was defined and validated, particularly under conditions of high initial fructose concentration (applying the concept of *High-gravity*), and including in the modelling the kinetics of dissolution, and degradation of fructose, under acidic conditions.

In the second part of the research, the technological perspective was extended to the hydrogenation of butyl levulinate to  $\gamma$ -valerolactone, by using kinetic models reported in the literature, in order to define an optimal process scheme for the overall conversion of fructose to GVL, via butyl levulinate. Starting from a conceptual design phase, the process scheme was defined to include the units of the solvolysis reaction, and subsequent hydrogenation, and the stages of purification of the final product, GVL, and regeneration of the butanol solvent, by means of a first stage of separation from the produced water content, and subsequent decomposition of the butyl formate traces, a secondary product of the solvolysis reaction. Once the reference process scheme was defined, it was then optimized on the basis of the process intensification concept, aimed at optimizing material and energy recovery; energy analysis was carried out to define the energy demand of the scheme, for different plant sizes.

In addition to the optimization of the bio-refining process scheme, this section focused on the use of hydrogen for the hydrogenation stage and also as energy carrier, and thus, on the definition and optimal design of the hydrogen energy storage system, which depends from the energy and hydrogen demand of the process, but also on the availability of renewable energy resources and conversion technologies, i.e. wind turbines, etc.

Being site-specific, the availability of renewable energy resources is highly dependent on the location considered; for this reason, the analysis has been adapted to a case study, considering the region Normandy (France) as a potential

installation-site for the entire configuration, and focusing on the local availability of lignocellulosic biomass and wind energy.

Based on the potential of renewable resources, the energy demand of the process, and the technologies for wind energy conversion and hydrogen production, storage and on-site use, a method for the design and integration of the energy-supply system to the production process was defined; an optimal design of the configuration presented and different scenarios for the integration were defined accordingly.

Finally, a sustainability assessment methodology was defined, using key performance indicators that assess sustainability for each scenario on the basis of economic, environmental, and social perspectives. The application of weighting and aggregation methods of the indicators was used to define an aggregated overall sustainability index, allowing the sustainability ranking among the scenarios.

The sustainability analysis through the final aggregate index demonstrated the potential of Scenarios 6 and 7 with a GVL biorefinery system, integrated with wind power and hydrogen energy storage systems, compared to scenarios powered by conventional energy sources. In particular, the analysis of the individual perspectives revealed the high economic profitability for these scenarios, due to the market synergy of GVL and green hydrogen, and the reduced environmental impact; some criticalities are, instead, associated with the social perspective, expressed in terms of inherent safety analysis of the process, driven by the size of the green hydrogen storage.

The robustness of the methodology used has been tested by sensitivity analyses based on the Monte Carlo method, which confirm the reliability and robustness of the results. Although applied to a specific case study, the defined methodology constitutes a flexible and reliable tool that can be extended to different process technologies, location sites, as well as more complex renewable energy-hybrid systems.

**Keywords:** Lignocellulosic biomass valorization, Platform molecules production, Kinetic modeling, Process simulation, Techno-economic analysis, Environmental impact analysis, Inherent safety analysis, Sustainability assessment.



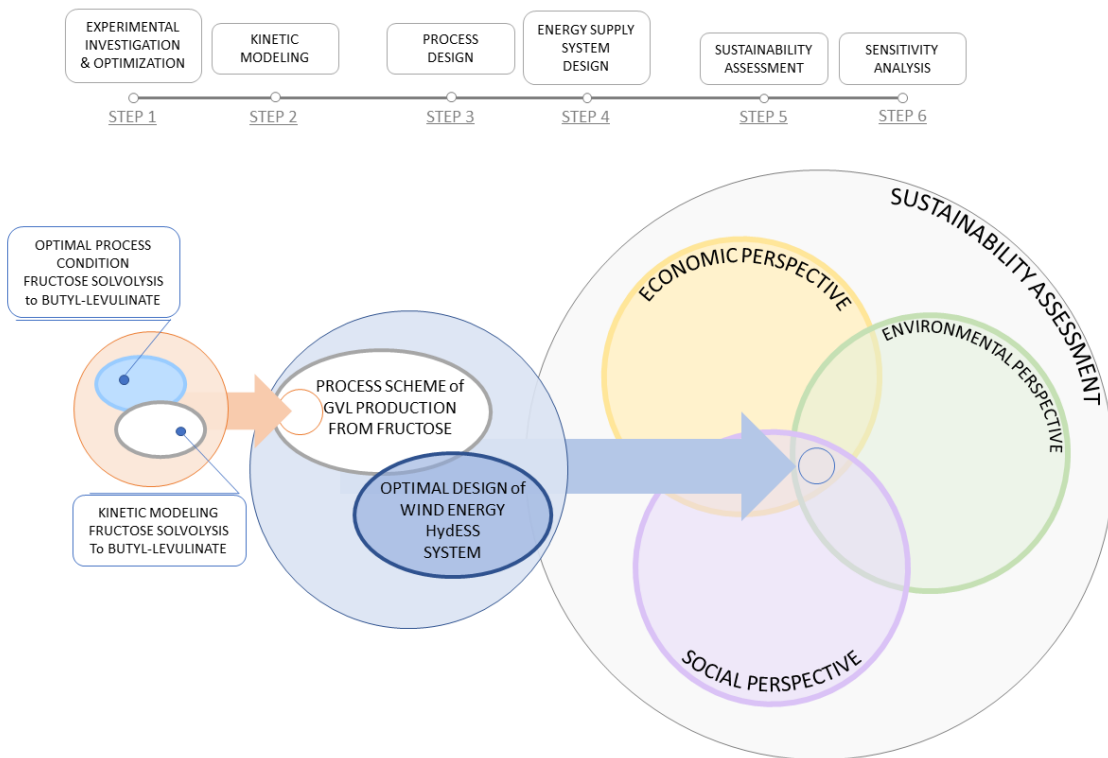


Fig. 1: Graphical Abstract of the research



# Table of Contents

<b>CHAPTER 1: Context of the study</b>	<b>1</b>
<b>1.1 Introduction</b>	<b>1</b>
<b>1.2 Lignocellulosic biomass (LCB) valorization</b>	<b>3</b>
<b>1.3 Levulinic acid and Alkyl levulinates: Synthesis and applications</b>	<b>5</b>
1.3.1 Production from hexoses and pentoses sugar monomers	5
1.3.2 Homogeneous and heterogeneous catalysts in the solvolysis of sugar monomers	7
1.3.3 Direct production of Levulinates from cellulose, hemicellulose and biomass	12
<b>1.4 <math>\gamma</math>-Valerolactone: Synthesis and applications</b>	<b>16</b>
<b>1.5 Integration of renewable energy sources (RESs)</b>	<b>19</b>
1.5.1 Wind and solar energy	19
1.5.2 Hydrogen	21
<b>1.6 Process Design and Sustainable Development</b>	<b>27</b>
1.6.1 Sustainability assessment	29
<b>1.7 Objectives and Outline of the thesis</b>	<b>31</b>
<b>CHAPTER 2 - Optimization of process conditions for the solvolysis of fructose to butyl levulinate: effect of catalyst and solvent</b>	<b>33</b>
<b>2.1 Introduction</b>	<b>33</b>
<b>2.2 Experimental and Analytical set up</b>	<b>35</b>
2.2.1 Chemicals	35
2.2.2 Analytical methods	35
2.2.3 Experimental set-up	36
2.2.3.1 Mass transfer resistance investigation	37
2.2.3.2 Experimental investigation on the solvent effect	37
2.2.3.3 Fructose dissolution investigation	38
<b>2.3 Experimental results and discussion</b>	<b>40</b>
2.3.1 Mass transfer limitations effect	40
2.3.2 Solvent effect: kinetics and swelling effect	42
2.3.2.1 Swelling effect	43
2.3.2.2 Co-solvent effect: Water	44
2.3.2.3 Co-solvents effect: GVL in presence of Water	45
2.3.2.4 Co-solvents effect: GVL in Butanol	47
2.3.2.5 Dissolution kinetics investigation	48

2.3.3 Comparison with literature	48
<b>2.4 Conclusions</b>	<b>50</b>
<b><i>CHAPTER 3 - Solvolysis of the platform molecule 5-Hydroxymethyl furfural (5-HMF) to butyl levulinate: kinetic modelling and model assessment</i></b>	
<b>3.1 Introduction</b>	<b>51</b>
<b>3.2 Experimental and Analytical set up</b>	<b>53</b>
3.2.1 Chemicals	53
3.2.2 Analytical methods	53
3.2.3 Kinetic experiments set-up	53
<b>3.3 Experimental results and discussion</b>	<b>54</b>
3.3.1 Effect of temperature	55
3.3.2 Effect of catalyst loading	56
3.3.3 Effect of 5-HMF loading	57
3.3.4 LA and FA esterification results	59
3.3.5 Deactivation catalyst effect	60
3.3.6 Repeatability of kinetic experiments	60
<b>3.4 Kinetic Modelling</b>	<b>60</b>
3.4.1 Models	62
3.4.1.1 Model 1	62
3.4.1.2 Model 2	63
3.4.1.3 Model 3	63
3.4.1.4 Model 4	64
<b>3.5 Modelling results and discussion</b>	<b>64</b>
3.5.1 Regression methods and strategy	64
3.5.2 Regression models results	66
3.5.3 Cross-Validation method and results	71
<b>3.6 Conclusions</b>	<b>72</b>
<b><i>CHAPTER 4 - In-depth kinetic modelling of butyl levulinate production from Fructose in High-Gravity condition</i></b>	
<b>4.1 Introduction</b>	<b>74</b>
<b>4.2 Experimental and Analytical set up</b>	<b>77</b>
4.2.1 Chemicals	77
4.2.2 Analytical methods	77
4.2.3 Kinetic experiments set-up	77
4.2.4 Solubility measurement	79

<b>4.3 Experimental results and discussion</b>	<b>80</b>
4.3.1 Temperature effect	80
4.3.2 Catalyst loading	82
4.3.3 Deactivation catalyst effect	83
4.3.4 Fructose initial loading	85
4.3.5 Solubility measurement	86
4.3.6 Repeatability	87
<b>4.4 Kinetic Modelling</b>	<b>89</b>
4.4.1 Models	91
4.4.1.1 Model 1	92
4.4.1.2 Model 2	92
4.4.1.3 Model 3	93
<b>4.5 Modelling results and discussion</b>	<b>93</b>
4.5.1 Training phase	93
4.5.2 Model estimation results	94
4.5.3 Models validation results	97
4.5.4 Tuning of process conditions	98
<b>4.6 Conclusions</b>	<b>100</b>
<b><i>CHAPTER 5 - Sustainability assessment of <math>\gamma</math>-valerolactone production from fructose</i></b>	<b><i>101</i></b>
<b>5.1 Introduction</b>	<b>101</b>
<b>5.2 Methodology</b>	<b>103</b>
5.2.1 Assessing site-specific renewable energy sources	106
5.2.1.1: Lignocellulosic biomass availability	106
5.2.1.2: Wind data analysis and characteristic parameters	108
5.2.1.3: Wind potential assessment	109
5.2.2 Conceptual design of the chemical process	112
5.2.3 Process modelling for an intensified process flowsheet	114
5.2.3.1 Solvolysis Fructose to n-butyl levulinate	116
5.2.3.2 Hydrogenation of n-butyl levulinate to $\gamma$ -valerolactone	117
5.2.3.3 Water separation and butyl formate decomposition	117
5.2.4 Energy analysis	118
5.2.5 Integrating renewable energies into the GVL biorefinery	118
5.2.5.1 Alkaline electrolyzer (AEL)	119
5.2.5.2 Hydrogen Storage	120
5.2.5.3 Hydrogen Fuel Cell	121
5.2.6 Description of the scenarios analyzed	122
5.2.7 Conceptual design of the integration system for electricity and hydrogen from RES	125
5.2.8 Sustainability Assessment and Key Performance Indicators (KPIs)	128

5.2.8.1 Economic KPIs _____	128
5.2.8.2 Environmental impact KPIs _____	132
5.2.8.3 Inherent Safety KPIs _____	135
5.2.8.4 Overall Sustainability Index: Normalization, Weighting and Aggregation _____	139
<b>5.3 Results and discussion _____</b>	<b>143</b>
5.3.1 Results of the conceptual design of the process and RES system _____	143
5.3.2 Results of the economic analysis _____	148
5.3.2.1 Results of preliminary design and cost estimation of GVL-process scheme _____	148
5.3.2.2 Effect of parameters: wind farm size and storage system on economic indicators _____	151
5.3.2.3 Cost analysis and economic indicators: scenario comparison _____	159
5.3.2.4 Sensitivity analysis on the economic KPI _____	164
5.3.3 Results of the environmental impacts analysis _____	168
5.3.3.1 Sensitivity analysis on the environmental KPI _____	170
5.3.4 Results of the Inherent safety analysis _____	174
5.3.4.1 Sensitivity analysis on the inherent safety KPI _____	179
5.3.5 Overall sustainability index analysis _____	181
<b>5.4 Conclusions _____</b>	<b>183</b>
<b><i>CHAPTER 6 – Conclusions and perspectives _____</i></b>	<b><i>185</i></b>
<b><i>Appendix S1: Additional Data-Chapter 3 _____</i></b>	<b><i>188</i></b>
<b><i>Appendix S2: Additional Data-Chapter 4 _____</i></b>	<b><i>197</i></b>
<b><i>Appendix S3: Additional Data-Chapter 5 _____</i></b>	<b><i>203</i></b>
<b><i>References _____</i></b>	<b><i>211</i></b>
<b><i>Symbols and Units _____</i></b>	<b><i>234</i></b>
<b><i>Abbreviations _____</i></b>	<b><i>237</i></b>
<b><i>List of Figures _____</i></b>	<b><i>239</i></b>
<b><i>List of Tables _____</i></b>	<b><i>243</i></b>



# CHAPTER 1: Context of the study

Part of this chapter is adapted from the post-print of the following article:

Di Menno Di Bucchianico, D.; Wang, Y.; Buvat, J.-C.; Pan, Y.; Casson Moreno, V.; Leveneur, S. Production of Levulinic Acid and Alkyl Levulinates: A Process Insight. *Green Chem.*, 2022,24, 614-646.

Further permission for extracted material should be addressed to © Royal Society of Chemistry 2023.

## 1.1 Introduction

The energy industry is the largest source of emissions worldwide, followed by chemical industry and transport, and therefore, holds the key role in responding to the current global climate change. Up-to-date statistics for global primary energy production estimate it at 617 EJ ( $10^{18}$ J) [1] in 2019, with global energy-related CO<sub>2</sub>-emissions reaching 33.3 metric gigatons (Gt) per year. In 2022, global emissions in the energy sector reached a new high of 36.8 Gt/y [2], although the strong expansion of renewable energies partially mitigated the emission growth rate. The share of fossil fuels in the global energy mix was more than 80 per cent in 2019 (26.8 % of coal, 30.9 % of oil, and 23.2 % from natural gas), and it continues to be stubbornly high even today, as shown in Fig. 1: (a) Global primary energy consumption [4]; (b) Global energy investment in clean and fossil energy, 2015-2023[5](a) [3,4]. As reported by IEA in the World Energy Outlook 2022, “Global fossil fuel use has increased along with GDP since the start of the Industrial Revolution in the 18th century: reversing this increase by continuing to expand the global economy will be a crucial moment in the history of energy” [3]. In 2022, emissions growth was lower than global GDP growth (+3.2%), returning to a decades-long trend of decoupling emissions from economic growth, which was interrupted in 2021. Although investments in renewable and clean energy (USD 1.7 Trillion in 2023, Fig. 1: (a) Global primary energy consumption [4]; (b) Global energy investment in clean and fossil energy, 2015-2023[5](b)[5]), policy and technological changes since the

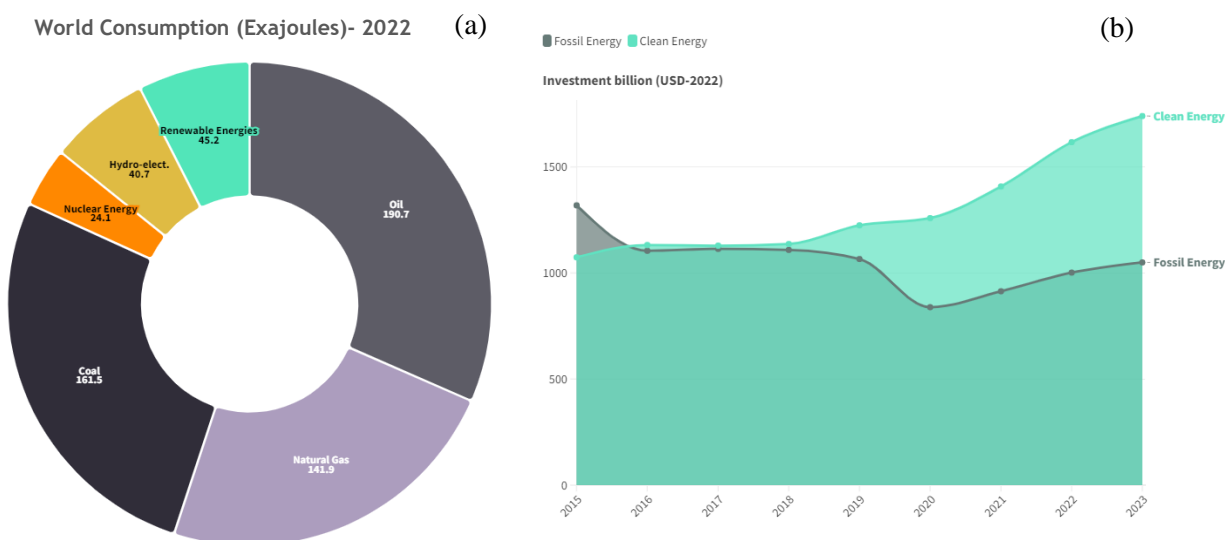


Fig. 1: (a) Global primary energy consumption [4]; (b) Global energy investment in clean and fossil energy, 2015-2023[5]



2015 Paris Agreement, have reduced the expected temperature rise, there are still many steps to reach the targets of climate neutrality by 2050 (NZE2050) and limit the global warming increase below 1.5 °C [3,6].

The exploitation of renewable energy resources is, therefore, the only way, together with the use of CO<sub>2</sub> mitigation and capture (CCS) techniques, to reduce emissions; among the renewable resources such as wind and solar energy, the lignocellulosic biomass (LCB) is the only carbon-fixing renewable resource, being generated from carbon dioxide and water, through photosynthesis. This renewable and abundant resource is a valuable source of bio-energy, which is the largest source of renewable energy, accounting for 55% of renewable energy and over 6% of the total energy supply, constituting an essential pillar of decarbonization in the energy transition as a near-zero emission power source [7].

Its potential lies in the flexibility of uses and sectors of this resource; from solid bioenergy and biogas burned for energy and heat, to liquid biofuels and additives used in the industry, transport and aviation sectors [7]. The high-potential of biomass is due to its cellular structure, consisting of bio-polymers (cellulose, hemicellulose, and lignin), which is particularly rich in hexose and pentose sugar monosaccharides, whose conversion, through different chemical pathways, leads to the production of value-added molecules, exploitable in hard-to-abate industrial sectors, such as chemical and petrochemical industry, as fuels, fuel additives, solvents, and polymers, replacing current chemical compounds of fossil origin [1][8,9].

Analogous to a refinery, which produces different fuels and products from oil, a biorefinery is a plant (or network of plants) that integrates biomass conversion processes and equipment to produce biofuels for transport, energy and chemicals from biomass [10–12]. Unlike traditional refineries, which are usually represented by large plants, where fossil feedstocks are entirely converted in a single site, many plants of different sizes, generally, characterize a biorefining system, and often, the economies of different bio-refineries are combined in order to fully exploit all components of the biomass; i.e., the production residue of one plant may be the feedstock of another, thus defining integrated bio-refinery systems [10]. The energy demand in a biorefinery plant can be met entirely or partly by biomass or process residues, although in some cases, the integration of different renewable energies can result in a more stable and cost-effective system [10,13]. In fact, compared to a single-renewable-source system, integrating multiple renewable sources allows to compensate the intermittency effects typical of renewables, avoiding interruption in the supply of energy to the process [13]. Although biomass is considered one of the most stable renewable energies, being less susceptible to meteorological conditions, it can be integrated within a bio-refinery using solar and wind energy [13]. Due to their fluctuating nature, a key aspect in the production of energy from renewables is the energy storage; besides the use of batteries, which have a limited storing-time, storage can also take place using more-stable energy carriers, among which hydrogen is gaining more and more interest and a growing market [14,15]. In fact, Hydrogen-based energy storage systems (HydESS) are gaining great interest as a cost-effective solution for storing large amounts of energy in the form of hydrogen, which can be stored,

transported and utilized efficiently [16]. Accounted as a key pillar in the targets of NZE2050 scenario by IEA [7], hydrogen is leading the way towards a fully renewable energy economy, called the “*hydrogen economy*” [16]. In the field of biomass conversion, hydrogen is also a valuable reagent for converting and upgrading biomass and its derivatives into a wide range of high-value-added products (i.e. hydrogenation of sugar monosaccharides to polyols [17], hydrogenation of furfural (Fur) to furfuryl alcohol (FA)[18], hydrogenation of levulinic acid and alkyl levulinates to  $\gamma$ -valerolactone (GVL)[19], GVL hydrogenation to Valeric acid (VA), 2-methyltetrahydrofuran (2-MTHF) [20], etc.).

In this context, the hydrogen economy can thus be integrated, together with the use of hybrid renewable energy systems, to the conversion of biomass in biorefineries for the production of energy and high value-added chemicals; expanding the green economy with economically, environmentally and socially sustainable industrial initiatives in line with the Sustainable Development Goals (SDGs), defined by the ONU [21,22].

## **1.2 Lignocellulosic biomass (LCB) valorization**

With a global annual production of 181.5 billion tons, the lignocellulosic biomass is the most abundant renewable resource of biogenic carbon and bio-energy [23]. Forestry is the main source of 2nd generation biomass for energy (logging residues, wood processing residues, firewood, etc.) and bio-conversion, followed by LCB wastes from agriculture, industry, and municipal sector or by biomass from specific crops [24]; currently about 0.2% of the world's total land (~25 million hectares) is used to cultivate bioenergy feedstocks [25]. In contrast to first-generation biomass, which may face competition with the food sector (“*food versus fuel*” debate)[26], LCB is an abundant, carbon-fixing and cost-effective alternative feedstock for the production of bio-fuels and bio-chemicals.

The main structural elements of LCB are: cellulose (25-55 wt%) a linear, highly crystalline bio-polymer consisting of only glucose units, hemicellulose (15-30 wt%) an amorphous oligomer consisting of bonds between C5-C6 monosaccharides, and lignin (10-35 wt%) a highly cross-linked polymer consisting of substituted phenols. Thus, the biomass will mainly consist of carbohydrates, subdivided into storage polysaccharides (e.g. starch and inulin), disaccharides, such as sucrose, and structural polysaccharides such as cellulose and hemicellulose. Other components of the biomass composition are triglycerides, proteins, terpenic hydrocarbons, waxes, tannins and other inorganic elements. Depending on the type of biomass, whether it is agricultural waste such as corn stover, cereals and straw, grass silage and bagasse, or forestry residue such as pine waste, short rotation crops such as switchgrass, miscanthus, aquatic plants or paper waste or other industrial and municipal waste, the composition in terms of these elements can vary considerably [1]. Pentose and hexose sugar monomers are fully exploitable considering two main conversion processes: thermo-chemical and chemical/bio-chemical [27].

The first category of conversion processes, such as pyrolysis and gasification, considers the simultaneous conversion of all sugars from the biomass feedstock, resulting in a process that is operationally simpler but less flexible than bio-conversion processes, which instead involve the

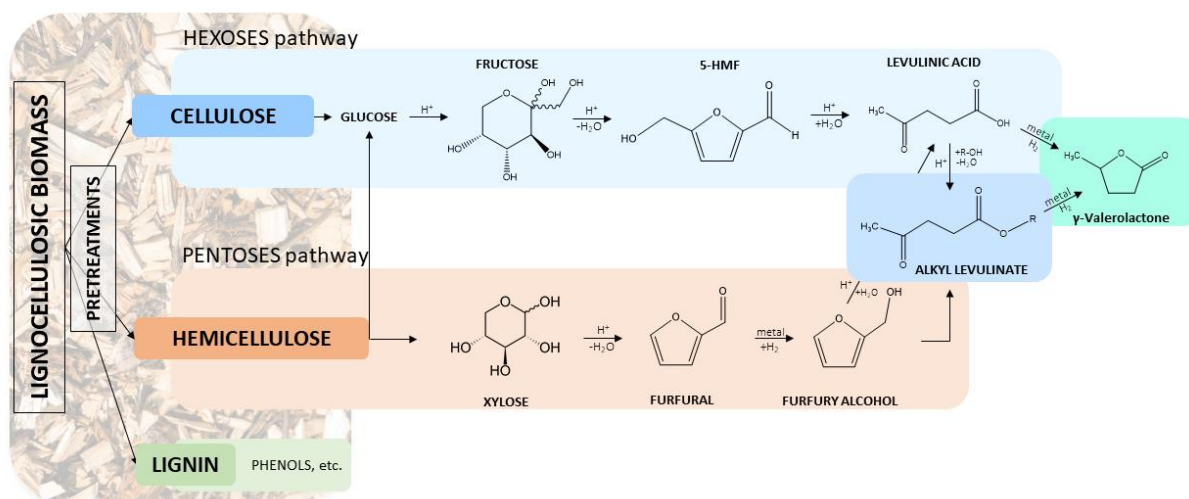


Fig. 2: Lignocellulosic biomass bio-components and conversion pathways.

fractionation of cellulose and hemicellulose and could consider a different valorization route for each fraction, offering a wide range of bio-products [28].

Regardless of the type of conversion process, the LCB must be pre-treated in order to open up its structure, remove the lignin in a reusable form, de-crystallize the cellulose fibers, and reduce the possible resistance to the mass transfer to allow the efficient use of a chemical or biological catalyst in the subsequent monosaccharide extraction steps [29–31]. Pre-treatment can be categorized as mechanical (e.g., milling, chipping, milling, etc.), chemical (e.g., acids, alkaline, organic solvents, ionic liquids), physical and/or physicochemical (steam explosion, wet air, oxidation, ammonia fiber explosion, etc.), or biological (e.g. by enzymes) [32]. The choice of pre-treatment method is crucial not only for production efficiency and yield but also for the economic feasibility of the process, as in some cases, pre-treatment costs can exceed 40% of the total cost [33]. Therefore, it is necessary to consider methods whose cost does not affect downstream processing steps and must balance the trade-off with the conversion process's operational, capital and biomass costs [33,34].

After fractionation of the two main bio-polymers, chemical methods take into account the different reactivities of C5- and C6-sugars, such as the conversion of C5 sugars through furfural-pathway, and the conversion of C6 sugars to levulinic acid and formic acid and other products [28,29]. In fact, although there are many pathways for the conversion of sugars, including fermentation, a high-potential conversion pathway focuses on solvolysis under acidic conditions and the production of furan and levulinic acid from hemicellulose and cellulose. Among the high-value platform molecules of this pathway, both 5-hydroxymethylfurfural (5-HMF) and levulinic acid (LA) have been identified by the US Department of Energy as top 10 platform chemicals on which to focus research for biorefining processes. Due to its reactivity, LA can react with numerous functional groups to produce various chemicals relevant to different market sectors [32]. Among LA derivatives, levulinic esters or alkyl levulinate (ALs), such as methyl levulinate, ethyl levulinate and butyl levulinate, have high potential as bio-fuels and additives for conventional fuels and are, therefore, the subject of numerous investigations

[35]. Furthermore, such platform molecules can be transformed by hydrogenation to  $\gamma$ -valerolactone (GVL), which has been identified by Horvath et al.[36] as a versatile molecule for the production of fuels and chemicals.

### 1.3 Levulinic acid and Alkyl levulinates: Synthesis and applications

Given the high versatility of levulinic acid and its derivative in different industrial sectors, the market demand has shown rapid growth in the last decades, with an estimated global LA market of US\$21.7 million in 2020 and a perspective that it will reach US\$30.8 million by 2027. The considerable interest in the market is due to the levulinates applications that extend to various sectors of the industrial market: pharmaceutical and cosmetics industry, agriculture and food industry, chemical industry, polymers and fuels. The alkyl levulinates have distinctive physicochemical properties, similar to fatty acid methyl esters, which make them suitable for use in traditional chemical and process industry applications, as solvents and crude oil additives, flavorings, fragrance agents and plasticizers. In addition, they are characterized by high stability and lubricity, characteristics that indicate the high potential as oxygenate additives for conventional diesel, gasoline fuels, (Fischer-Tropsch) gas oil-based fuels, and biodiesels [37–41]. For fuel applications, long alkyl chain levulinates are more suitable due to their higher solubility in the hydrocarbon fraction in conjunction with lower solubility in water; thus, most of the studies are mainly focus on ethyl levulinate (EL) and butyl levulinate (BL). Several investigations showed that the presence of these oxygenated compounds leads to cleaner combustion, with fewer smoke or NO<sub>x</sub> (nitrogen oxides) emissions, to improve cold flow properties, conductivity, and lubricity of diesel fuel and reduce its vapor pressure. Compared to ethyl levulinate, BL was found to have more benefits, such as higher cetane number and calorific value (LHV), to remain in solution with diesel up to the cloud point, and to be more compatible with elastomers, being less corrosive [42,43].

#### 1.3.1 Production from hexoses and pentoses sugar monomers

Depending on the content of hexoses and/or pentoses in the initial biomass substrate, levulinate syntheses can take place via the C<sub>6</sub>-sugar or C<sub>5</sub>-sugar chemical pathway, as illustrated in Fig. 2: Lignocellulosic biomass bio-components and conversion pathways..

Although LA and its esters can be produced from platform molecules, such as 5-HMF and Furfural, direct production from monosaccharides is more cost-effective due to the lower cost compared to furan intermediates [28]. Among these, hexose sugars are the most abundant monosaccharides, mainly glucose

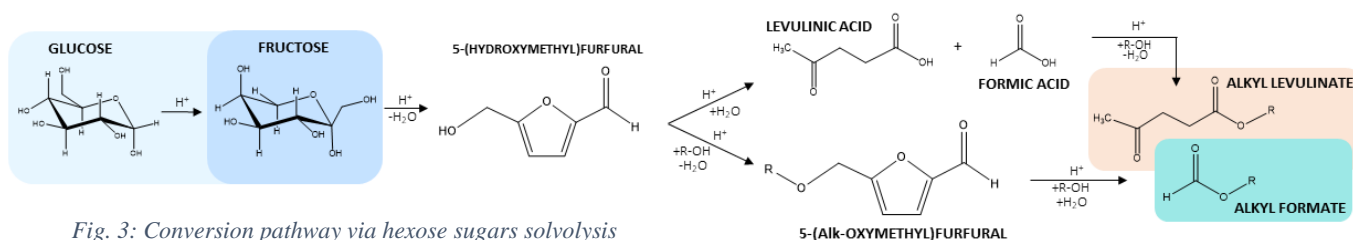


Fig. 3: Conversion pathway via hexose sugars solvolysis

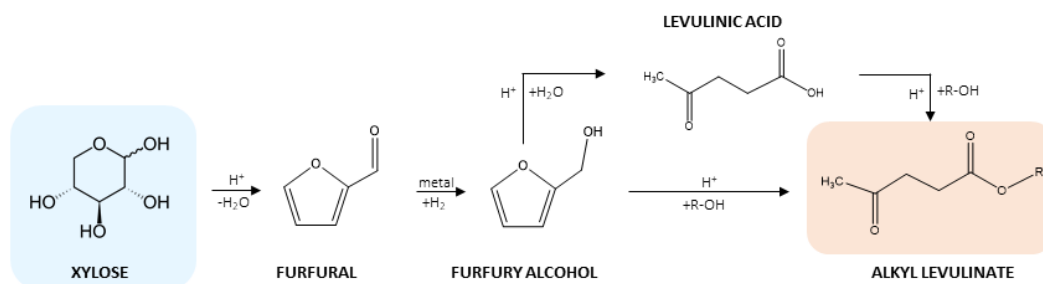


Fig. 4: Pentose sugars pathway to alkyl levulinates and levulinic acid

and fructose. Being the main building block of cellulose and hemicellulose, glucose is preferred over fructose due to its greater abundance in nature [32]. However, the conversion of fructose under acidic conditions gives a higher yield in levulinate products than glucose, due to its greater molecular instability, which leads to an easier opening of the ring structure. In general, the glucose conversion mechanism considers an isomerization step to fructose, prior to the formation of the furan intermediate 5-HMF (Fig. 3: Conversion pathway via hexose sugars solvolysis). While the production of LA, together with the secondary product formic acid (FA), is obtained by rehydration of 5-HMF, the mechanism of synthesis of alkyl levulinates considers the presence of an additional intermediate: ether-furanic, determined by the etherification of 5-HMF in the presence of alkyl groups, typically determined by the presence of alcohols as solvents (i. e. 5-(Ethoxymethyl)furfural in the presence of ethanol, 5-(Butoxymethyl)furfural corresponding butyl group for butanol solvent). From the conversion of this furan intermediate and, in parallel, the esterification of LA and FA, the corresponding levulinic and formic esters are synthesized; typically, in an equimolar ratio [32,35].

The pentose sugar route (mainly xylose), on the other hand, considers furfural as the first solvolysis intermediate corresponding to the 5-HMF of the hexose route (Fig. 4: Pentose sugars pathway to alkyl levulinates and levulinic acid); this intermediate is hydrogenated to furfuryl alcohol, which can be hydrolyzed to LA or converted by solvolysis to the corresponding alkyl levulinate. Compared to the hexose route, which only involves solvolysis steps, the need for catalysts for hydrogenation, the high-pressure conditions and the use of hydrogen makes this route both costly and unfavorable regarding process safety [1][18,35].

For the production of LA and ALs, various solvents, such as water and organic solvents, were tested. Sugars exhibit a high reactivity in water, which results in a good solvation environment, as well as it allows a high dissociation of acid catalysts and a high solubility of sugars.

Conversely, the high reactivity and instability exhibited by monomers in aqueous systems favors the occurrence of side degradation reactions to humins [44].

Humins are by-products of the degradation of sugars and the intermediate 5-HMF; an inevitable drawback in biomass conversion. They are carbonaceous, heterogeneous, polydisperse materials with a complex molecular structure [45], mainly consisting of furan rings and aldehydes, ketones and hydroxyls as the main functional groups [46]. Produced in insoluble or partially soluble forms, humins are responsible for lower yields in biomass conversion due to the consumption of reagents and fouling

of the reactor and catalyst, with a poisoning effect for heterogeneous catalysts. In this respect, the solvent system plays an important role and can be used to mitigate the degradation to humins; In levulinate solvolysis, several studies have shown that the use of alcohols (protic polar solvent) as solvent favors greater control of sugar conversion steps, higher yield and selectivity of LA, and notably that of alkyl levulinate, whereby the kinetics of solvolysis is favored in excess of the corresponding alcohol, which is also the solvolysis reagent. In addition, studies have also investigated the role of polar aprotic solvents, such as dimethylsulfoxide (DMSO), methylisobutylketone (MIBK), tetrahydrofuran (THF), carbon tetrachloride, ethyl acetate and GVL; They present a stabilizing effect on positively charged intermediates, with a reducing effect on secondary degradation reactions, notably such as the production of humins, and solubilizing effects on complex biomass matrices, making them available for catalytic activity, and of humins itself by reducing fouling phenomena for heterogeneous catalysts; for these reasons, they are certainly an interesting target for research.

### **1.3.2 Homogeneous and heterogeneous catalysts in the solvolysis of sugar monomers**

The conversion of biomass derivatives to levulinic acid and alkyl levulinate is mainly catalyzed by Brønsted acids, homogeneous and heterogeneous. Traditionally, the use of homogeneous acid catalysts, such as H<sub>2</sub>SO<sub>4</sub>, HCl, HNO<sub>3</sub> and H<sub>3</sub>PO<sub>4</sub>, is widespread in biomass valorization, due mainly to the easy and high contact with the substrate, combined with low cost, and good production yields. The use of H<sub>2</sub>SO<sub>4</sub> is widespread over hexose sugars, such as glucose [47,48] and fructose [49], achieving excellent LA yields, although associated with corrosion effects and cost- and energy-demand post-treatment phases. Sulfuric acid was also used by Rackemann et al. for the conversion of xylose to LA, obtaining a yield of 64.4 mol% and 61.6 mol% by using a mixture of xylose and glucose at high temperature and under a short reaction time [50]. Other homogeneous acids, such as HCl, trifluoroacetic acid (TFA) and PTSA, have also been tested for LA production. Heeres et al. investigated glucose conversion using TFA, with LA final yield of 35% and 45% from fructose [51]; Brasholz et al. tested HCl, obtaining 72 % of LA yield from fructose [52]. Some investigations have increased the yield from glucose by combining Brønsted and Lewis acids, since Lewis acids, typically, catalyze the isomerization of glucose to fructose in the conversion pathway; as in the work of Peng et al. in which transition metal chlorides, in particular CrCl<sub>3</sub>, were coupled with mineral acids, enhancing the final yield from glucose [53,54]. For the alkyl levulinates production catalyzed by homogeneous acids; Balakrishnan et al. reported the use of sulfuric acid for the conversion of fructose to ethyl levulinate with a yield of 56 mol% and a higher production yield for butyl levulinate of 64 mol% [55]; Peng et al. showed instead the production of methyl levulinate from glucose by using extremely low sulfuric acid ( $\leq 0.01$  mol/L), obtaining a production yield of 50 mol% [56].

By operating in excess of alcohol in solvolysis, homogeneous catalysts also favor the dehydration of the alcohol itself, with the formation of the corresponding di-alkyl-ether; this by-product can complicate the separation and isolation downstream steps of the product, and can be suppressed or limited by the use of much more selective heterogeneous catalysts [32,57].

Although homogeneous catalysts are still widely used today, they have many disadvantages, such as the difficulty in recovery and recycling, equipment corrosion, and environmental pollution caused by hazardous acids. In addition, corrosive conditions require specific materials for the equipment, thus, increasing the capital investment and operating costs. This prompts research to invest and investigate heterogeneous solid or metal catalysts, that are easier to recover and more environmentally friendly [32]. Heterogeneous catalysts such as zeolites [58], acidic resins and polymers [59–61], metal oxides [62], heteropolyacids [63], have been tested, obtaining LA yields up to 70 mol%. These same classes of acid catalysts have also been studied to produce alkyl levulinate from C6 monosaccharides, the reaction mechanism being similar to that of its acid precursor.

Typical Brønsted-acid solids were deeply investigated; Xu et al. [64] reported the production of ethyl levulinate from glucose via zeolite; Kuo et al. [65], the synthesis of methyl levulinate via titanium oxide nanoparticles. On the other hand, several researchers have investigated the synergistic combination of Lewis and Brønsted catalysts. Indeed, starting from glucose, isomerization to fructose has been identified as a limiting step in the kinetics of biomass conversion to levulinates. Using dual-activity catalyst [66] or coupling of a Lewis acid catalyst, which acts on the isomerization, with a Brønsted catalyst, which is responsible for solvolysis, favors selectivity towards alkyl levulinate. Metal salts have been thoroughly investigated as they act as Lewis catalysts and are commonly stable, recyclable and inexpensive. Zhou et al. [66] studied the use of  $\text{Al}_2(\text{SO}_4)_3$  as a single-catalyst in the methanolysis of glucose. Achieving an ML yield of 64% at 160 °C, this catalyst was shown to provide Lewis and Brønsted sites via  $\text{Al}^{3+}$  ions [66]. This ion was also studied by Liu et al.[67], coupled to montmorillonite catalysts, resulting in a ML yield of 60%, with the possibility of recycling up to 5 times [67]. Metal oxides also exhibit Lewis acid activity; Heda et al. combined the action of zeolite H-USY and metal oxides, such as  $\text{TiO}_2$ ,  $\text{ZrO}_2$  and  $\text{SnO}_2$ , to synthesize EL from glucose [68]. They achieved an EL yield of 81 mol% using  $\text{SnO}_2$ , increasing the isomerization and glucose solubility rate in ethanol [68].

More control over kinetics and reaction rates allows higher monosaccharide concentrations to be handled, increasing the final concentration of levulinate products [68]. In "*high-gravity*" processes, the increase in initial monosaccharide and feedstock concentration, in order to increase the final product concentration, is related to an increase also in possible undesirable reactions, such as the production of the by-products humins [69].

Higher yields of LA and alkyl levulinate are obtained from the solvolysis of fructose. Liu et al.[70] reported a maximum yield of 84 mol% of ethyl levulinate, obtained by carbon nanotubes functionalized with sulfonic acid that catalyze the dehydration of fructose to ethyl levulinate [70]. Metal oxides have shown high catalytic activity and good thermal stability; Oprescu et al.[71] studied the production of

methyl levulinate from fructose, catalyzed by mixed  $\text{TiO}_2\text{-La}_2\text{O}_3$  oxides on solid- $\text{Fe}_3\text{O}_4$  nanoparticles. Conversion of fructose was complete, with a ML yield of 95%, and catalyst reusability showed a decrease of almost 10% after five cycles without any regeneration [71]. Xu et al. instead studied ML synthesis by sulfated montmorillonite ( $\text{SO}_4^{2-}/\text{MMT}$ ), reporting a 65% yield, but a 36% reduction in yield after the third cycle without regeneration, demonstrating sulfated solid catalysts suffer from reduced activity due to the easy loss of sulfate groups [72]. Acid ion exchange resins were also found to be very active, but catalyst regeneration is necessary to preserve their activity. Gel-type and macroreticular PS-DVB sulfonic resins were tested by Ramirez et al. [73] in the butanolysis of fructose, achieving good yields under moderate temperature conditions, compared to other catalysts. Gel-type resins were the most effective in terms of yield at BL (73.4 %), due to their higher swelling capacity and density of acid sites. The yield decreased by 22% after 3 cycles, due to both the loss of active sites and the deposition of polymer by-products (solid humins) during the reaction [73].

Few data are reported in the literature for the conversion of pentose sugars such as xylose, and on the application of solid catalysts; due to the more complex route involving the hydrogenation of the furan intermediate.

As with glucose, some studies have tested metal salts, such as metal chlorides, particularly  $\text{FeCl}_3$ , with excellent results in converting xylose. Wang et al. reported a maximum LA yield of 68 mol%, using  $\text{FeCl}_3$  together with  $\text{NaCl}$ , and lower yields with the catalytic action of  $\text{CuCl}_2$ ,  $\text{AlCl}_3$  and  $\text{CrCl}_3$  [74]. Zeolites have also been used as heterogeneous catalysts in xylose dehydration with an LA yield of 31 mol% [75]. To increase the yield to levulinic acid, new strategies involve the use of biphasic systems using alkylphenolic solvents. This strategy has proven to be efficient, as the organic solvent can play the role of the electrophile, transforming furfural into 5-HMF by electrophilic substitution, avoiding the hydrogenation step to furfuryl-alcohol. Hu and co-workers investigated the production of levulinic acid, methyl levulinate and ethyl levulinate via biphasic system; dimethoxymethane DMM-water and DMM-alcohol systems, reporting levulinate yields of up to 50 per cent using xylose as a starting substrate [76]. Other commercial catalysts, such as zeolites and ion-exchange resins, have been tested but with significantly lower yields than hexose sugars; Hu et al. [76] tested the use of Amberlyst-70 and reported yields for ML of 41.6 mol% and for EL of 21.8 mol%.



Table 1: Production of levulinic acid from sugar monomers using various catalytic systems. Adapted from [1].

Feedstock	Catalyst	Temperature	Time	Yield	Ref.		
Glucose	Mineral acids	H <sub>2</sub> SO <sub>4</sub>	140 °C	2 h	38 %	[77]	
			170 °C	2 h	34 %	[47]	
	Organic acid	TFA	180 °C	1 h	35 %	[51]	
	Mineral acid	CrCl <sub>3</sub> ,HCl	140 °C	6 h	46 %	[54]	
	Zeolite	CrCl <sub>3</sub> , HY	145.2 °C	2.45 h	55.2 %	[78]	
			Cr/HZSM-5	180 °C	3 h	64.4 %	[58]
	Graphene oxide	GO-SO <sub>3</sub> H	200 °C	2 h	74 %	[79]	
	Ion exchange resins	Amberlyst-36TM	140 °C	3 h	52.3 %	[59]	
Sn-Beta,Amberlyst-15			140 °C	12 h	45 %	[60]	
Fructose	Organic acid	TFA	180 °C	1 h	45 %	[51]	
			PTSA	88 °C	8.33 h	16 %	[48]
	Mineral acid	HCl	140 °C Water/Methanol	1.33 h	72 %	[52]	
				NaCl, HCl	88 °C	8.33 h	34 %
	Ion exchange resins	Amberlyst XN	100 °C	9 h	16 %	[61]	
	Zeolite	LZY	140 °C	15 h	43.2 %	[80]	
Xylose	Mineral acid	H <sub>2</sub> SO <sub>4</sub>	200 °C	0.13 h	64.4 %	[50]	
	Organic acid	Methanesulfonic acid (MSA)	180 °C	0.25 h	64.7 %	[50]	
	Metal salts	FeCl <sub>3</sub> / FeCl <sub>3</sub> +NaCl	180 °C	2 h	48.5/68 %	[81]	
			CuCl <sub>2</sub> ·2H <sub>2</sub> O	180 °C	2 h	34 %	[81]
			CrCl <sub>3</sub> ·6H <sub>2</sub> O	180 °C	2 h	25 %	[81]
			AlCl <sub>3</sub> ·6H <sub>2</sub> O	180 °C	2 h	26 %	[81]
	Zeolite	AZY0.25	170 °C	3 h	30.4 %	[75]	

Table 2: Production of levulinate esters from sugar monomers using various catalytic systems. Adapted from [1].

Feedstock	Catalyst	Temperture <sup>a</sup>	Time	Yield <sup>b</sup>	Cat. reuse <sup>c</sup>	Ref.	
Glucose	Aluminium sulfate	Al <sub>2</sub> (SO <sub>4</sub> ) <sub>3</sub>	160 °C	2.5 h	64 % (ML)	~64 % - 5 runs	[66]
	Sulfated metal oxides	SO <sub>4</sub> <sup>2-</sup> /TiO <sub>2</sub>	200 °C	2 h	33.2 % (ML)	20 % - 7 runs	[53]
	Montmorillonites	SO <sub>4</sub> <sup>2-</sup> /MMT	200 °C	4 h	48 % (ML)	-	[72]
		Al <sup>3+</sup> /MMT	220 °C	6 h	60 % (ML)	~60 % - 5 runs	[67]
	Zeolite	Sn-Al-β	160 °C	5 h	43 % (ML)	39 % - 5 runs	[74]
		USY	180 °C	3 h	45 % (EL)	~35 % - 6 runs	[64]
		H-USY, SnO <sub>2</sub>	180 °C	3 h	81 % (EL)	-	[68]
	Ionic liquids	NEt <sub>3</sub> B-SO <sub>3</sub> H	140 °C	24 h	6 % (EL)	-	[82]
Nanoparticles	Nano-TiO <sub>2</sub>	175 °C	9 h	61 % (ML)	-	[65]	
Fructose	Mineral acid	H <sub>2</sub> SO <sub>4</sub>	120 °C	30 h	56 % (EL)	-	[55]
	Zeolite	H-USY	160 °C	20 h	51 % (ML)	45 % - 5 runs	[83]
			160 °C	20 h	40 % (EL)	~40 % - 5 runs	[83]
	Sulfonic acid func. SBA-15	SO <sub>3</sub> H-SBA-15	140 °C	24 h	57 % (EL)	57 % - 3 runs	[84]
	Supported phosphotung. acid	HPW/H-ZSM-5	160 °C	2 h	43.1 % (EL)	25 % - 4 runs	[85]
	Aluminium sulfated	Al <sub>2</sub> (SO <sub>4</sub> ) <sub>3</sub>	160 °C	2.5 h	49 % (ML)	-	[66]
	Sulfated metal oxides	SO <sub>4</sub> <sup>2-</sup> /MMT	200 °C	4 h	65 % (ML)	-	[72]
		SO <sub>4</sub> <sup>2-</sup> /TiO <sub>2</sub>	200 °C	2 h	59 % (ML)	20 % - 7 runs	[53]
		SO <sub>4</sub> <sup>2-</sup> /TiO <sub>2</sub> -ZrO <sub>2</sub>	200 °C	1 h	71 % (ML)	30 % - 5 runs	[86]
		SO <sub>4</sub> <sup>2-</sup> /TiO <sub>2</sub> -La <sub>2</sub> O <sub>3</sub>	160 °C	3 h	95 % (ML)	86 % - 5 runs	[71]
	Grafted carbon nanotubes	CNT-PSSA	120 °C	24 h	69 % (ML)	-	[70]
			120 °C	24 h	84 % (EL)	69 % - 5 runs	[70]
			120 °C	24 h	86 % (PL)	-	[70]
			120 °C	24 h	87 % (BL)	-	[70]
	Ion exchange resins	Amberlyst-15	120 °C	24 h	73 % (EL)	-	[70]
			120 °C	24 h	89 % (BL)	-	[70]
Dowex 50Wx2		120 °C	8 h	73.4 % (BL)	51 % - 3 runs	[73]	
Silicotung. based	SnSiW-423	150 °C	2 h	70 % (EL)	~70 % - 7 runs	[87]	
	SnSiW-423	150 °C	2 h	66 % (BL)	-	[87]	
Nanoparticles	Nano-TiO <sub>2</sub>	175 °C	1 h	80 % (ML)	40 % - 5 runs	[65]	

Xylose	Ion exchange resins	Amberlyst 70	150 °C	6 h	41.6 % (ML)	-	[76]
			160 °C	2 h	21.8 % (EL)	-	[76]
	Mesoporous zirconium silicate	KITZ20	200 °C	5 h	87.7 % (BL)	79.8 % - 4 runs	[88]
	Zeolite	Modified- H $\beta$	160 °C 1,3,5-trioxane	18 h	50.4 % (ML)	~50 % - 5 runs	[89]
<sup>a</sup> using water as solvent, unless otherwise specified. <sup>b</sup> Methyl (ML), ethyl (EL), propyl (PL), butyl (BL) levulinate. <sup>c</sup> yield after N reuse cycles tested.							

### 1.3.3 Direct production of Levulinates from cellulose, hemicellulose and biomass

Compared to the use of pure monomers, such as fructose, glucose and xylose, and other precursors such as furfural and 5-HMF, the use of raw lignocellulosic substrates can provide an economical and promising alternative for the sustainability of levulinates production on an industrial scale, reducing waste disposal, and enhancing the valorization of local resources, increasing the development of economic initiatives in rural sectors. However, to date, the processing of simple monosaccharides offers higher product yields [90].

The complexity of the conversion process is often due to the variable composition of the raw material, which often results in mixtures of the simplest sugars (both hexoses and pentoses). Low-cost raw lignocellulosic sources should be privileged, such as fast-growing grasses and trees: switchgrass, giant reed, miscanthus, poplar; but also low-value municipal and industrial wastes: wheat straw, sugarcane bagasse, rice husk, corn stover, sawdust, pulp sludge, olive tree pruning, fruit peels [90–92]. The complexity and heterogeneity of these substrates require pre-treatment steps to improve subsequent yields and reaction rates.

Mineral acids have been used extensively and are still used today on both a laboratory and industrial scale (see Biofine [93], GFBiochemicals [94,95], Segetis [96,97], etc.) in the production of levulinic acid and esters from crude biomass, due to their high efficiency and low cost. The most commonly used mineral acid catalysts are H<sub>2</sub>SO<sub>4</sub> and HCl. The reactivity of the catalyst is strongly correlated to the nature and concentration of the initial raw material. For example, HCl is particularly suitable for converting biomass with a high calcium content, such as paper and tobacco, due to the tendency of H<sub>2</sub>SO<sub>4</sub> to form precipitant CaSO<sub>4</sub>, which can lead to reactor clogging [98].

Significant yields of levulinic acid have been obtained from the use of these acids in various lignocellulosic raw materials: pre-treated rice husks were used by Bevilaqua et al. [99] at 170 °C for 1 h, achieving LA yields of 59.4 and 45.7 wt% for HCl and H<sub>2</sub>SO<sub>4</sub> respectively [100]; paper sludge resulted in LA yields of 31.4 wt% and 15.4 wt% at 200 °C for 1 h under the action of dilute HCl and concentrated H<sub>2</sub>SO<sub>4</sub> in studies by Raspolli Galletti et al. [98]; wheat straw is another promising raw material, analyzed by Chang et al. [100] who reported yields around 20 wt% at 200 °C for both catalysts

[100]; the liquefaction of bagasse and paddy rice straw was tested with HCl at 220 °C by Yan et al. who reported LA yields of 22.8 and 23.7 wt% [101]; and fast-growing plants such as giant reed producing an LA yield of 24 wt% at 190 °C for 1 h [102].

Polar aprotic solvents, such as tetrahydrofuran (THF),  $\gamma$ -valerolactone (GVL), dimethyl sulfoxide (DMSO), are able to stabilize reactive intermediates. Wettstein et al.[103] investigated the deconstruction of cellulose in a biphasic system (water-  $\gamma$ -valerolactone) using HCl and NaCl, obtaining a yield of 51.6% h [103]. They emphasized GVL's ability to solubilize the components resulting from biomass deconstruction [103]. The effect of GVL was also investigated in the conversion of hemicellulose in the presence of sulfuric acid by Mellmer et al. [44], in which they obtained an increase in reaction rates and product selectivity in presence of GVL [44].

In the production of alkyl levulinate, mineral acids have been used extensively. Feng et al.[104] investigated the methanolysis of bio-renewable raw materials, such as bamboo and maize starch, in the presence of sulfuric acid in subcritical methanol, reporting a methyl levulinate (ML) yield of 27.7 wt% at 200 °C for 1 h. Methyl levulinate was also synthesized using wood waste, bagasse and wheat straw, as well as waste sources such as paper sludge; the latter substrate resulted in an overall ML yield of 27.7 wt% under mineral acid conditions at 220 °C [56].

Sulfuric acid was also very active in the degradation of cellulose and more complex biomass matrices in the presence of ethanol, giving molar yields of ethyl levulinate up to 60 mol% [105]. Chang et al. [106] valorized wheat straw, a cheap and widely available cellulose-rich substrate, efficiently converted to ethyl levulinate under the action of sulfuric acid with a yield of 17.9 wt% [106]. Paper pulp, wood shavings and field grass produced comparable EL results, with 25.9, 16.6 and 13.8 wt% yields, respectively [107]. Considering higher alkyl groups, such as the butyl group; Démolis et al. investigated the butanolysis of cellulose yielding 50 mol% with sulfuric acid [35]. While yields of up to 40 mol% were obtained using Eucalyptus wood [69] and rice straw [108].

Compared to homogeneous catalysis, yields tend to be lower when introducing solid catalysts; this can be attributed to a more difficult solid-solid interaction between catalyst and substrate and potential deactivation issues due to the deposition of solid by-products, such as humins and lignin-derived residues [90,92].

Commercially available heterogeneous catalysts tested in the production of levulinic acid and esters include zeolites, sulfated metal oxides, metal oxides [109], solid superacid [110] and ion exchange resins [111].

Peng et al.[112] studied the conversion of cellulose to levulinic acid, catalyzed by different metal chlorides, as metal salts, showing high catalytic activity and both types of acidity. Among them,  $\text{CrCl}_3$  was quite effective with an LA yield of 67% in 3 h [112].  $\text{CrCl}_3$  was also tested with  $\text{H}_2\text{SO}_4$  to produce levulinic acid from potato peel waste, reporting an LA yield of 49% [113]. Aluminum phosphate ( $\text{Al}_2(\text{SO}_4)_3$ ) was also tested, yielding a high production of alkyl levulinate: 52 wt% ML yield at 200 °C for 6 h using conifer bark as substrate [111], EL 36.4 wt% yield using cassava for 6 h at 200 °C [114].

Zeolites can also potentially be used to convert cellulose and raw lignocellulosic biomass. For instance, the hierarchical zeolite Mordenite (H-MOR) was synthesized and tested by Velaga and co-workers, yielding promising results in the production of levulinic acid: 56% yield for 3 h using cellulose, and an improved yield of 61% using bamboo sawdust as a starting substrate [115]. Zeolite HY was selected, due to its high catalytic reactivity as a Brønsted acid and with the addition of CrCl<sub>3</sub>, to obtain a hybrid catalyst and to catalyze the production of levulinic acid from empty fruit bunches and kenaf with a yield of 29.2 and 22.7 wt%, respectively [78]. The zirconia-zeolite hybrid (ZrY6), bi-functionalized with zirconia, showed high efficiency in the production of methyl levulinate, leading to ML molar yields of 53% from starch and 27% from cellulose at 180 °C [116]. Research has investigated the acidic solvolysis of lignocellulosic biomass catalyzed by ion exchange resins, such as Dowex and Amberlyst. These insoluble polymers can exchange specific ions in the reaction mixture to convert the initial substrates. Alonso et al.[117] reported the conversion of cellulose to levulinic acid on Amberlyst 70, achieving a high yield of 69% [117]; while Amberlyst 36 was tested in production from sugar beet molasses, achieving an LA yield of 78 mol% [59].

Due to steric problems in the interaction between catalyst particles and biomass and resistance to material transfer, resulting in low yields, there are not many studies on their use in the conversion of biomass to levulic esters, whereas they have been extensively tested in the solvolysis of simple sugars [73]. Heterogeneous catalysts can provide an efficient and sustainable route; moreover, the possibility of fine-tuning and functionalizing them improves process versatility and efficiency, especially in biomass cascade processes.

Table 3: Production of levulinate esters from cellulose and raw biomass using various catalytic systems. Adapted from [1].

Catalyst	Substrate	Temperature <sup>a</sup>	Time	Yield <sup>b</sup>	Catalyst reuse <sup>c</sup>	Ref.
HCl	Pretreated rice husks	170 °C	1 h	59.4 % (LA)	-	[99]
	Paper sludge	200 °C	1 h	31.4 % (LA)	-	[98]
	Wheat straw	200 °C	1 h	20 % (LA)	-	[100]
	Bagasse	220 °C	0.75 h	22.8 % (LA)	-	[101]
	Paddy straw	220 °C	0.75 h	23.7 % (LA)	-	[101]
	Giant reed	190 °C	1 h	24 % (LA)	-	[102]
	Poplar sawdust	200 °C	1 h	21.3 % (LA)	-	[98]
	Olive tree pruning	200 °C	1 h	18.6 % (LA)	-	[98]
	Cellulose	155 °C GVL/Water	1.5 h	51.6 % (LA)	-	[103]
H <sub>2</sub> SO <sub>4</sub>	Pretreated rice husks	170 °C	1 h	45.7 % (LA)	-	[99]
	Paper sludge	200 °C	1 h	15.4 % (LA)	-	[98]
	Wheat straw	200 °C	1 h	20 % (LA)	-	[100]
	Cellulose	150 °C	2 h	43 % (LA)	-	[77]
	Liquified bamboo	200 °C	1 h	27.7 % (ML)	-	[104]

	Corn starch	180 °C	2 h	48.7 % (ML)	-	[104]
	Cellulose	200 °C	2 h	23.9 % (ML)	-	[106]
	Wheat straw	183 °C	0.6 h	17.9 % (EL)	-	[106]
	Paper pulp	190 °C	1.7 h	25.9 % (EL)	-	[107]
	Wood chips	190 °C	1.7 h	16.6 % (EL)	-	[107]
	Switch grass	190 °C	1.7 h	13.8 % (EL)	-	[107]
	Bamboo	180 °C	3 h	53.7 % (EL)	-	[105]
	Cellulose	200 °C	0.5 h	50 % (BL)	-	[118]
H <sub>2</sub> SO <sub>4</sub> + CrCl <sub>3</sub>	Potato peel	180 °C	0.25 h	49 % (LA)	42 % - 3 runs	[113]
H <sub>3</sub> PO <sub>4</sub>	Cigarette butts	200 °C	6 h	49.6 % (LA)	-	[119]
Al <sub>2</sub> (SO <sub>4</sub> ) <sub>3</sub>	Softwood bark	200 °C	6 h	62 % (ML)	10 % - 3 runs	[111]
	Cassava	200 °C Ethanol/Water	6 h	47.05 % (EL)	5 % - 2 runs	[114]
	Bagasse	180 °C	0.6 h	65.1 % (ML)	-	[120]
	Poplar powder	180 °C	0.6 h	62.7 % (ML)	-	[120]
	Bamboo powder	180 °C	0.7 h	64.2 % (ML)	-	[120]
	Cellulose	180 °C	0.7 h	70.6 % (ML)	65.3 % - 5 runs	[120]
		180 °C	0.9 h	70.1 % (EL)	-	[120]
		180 °C	1.25 h	53.7 % (iPL)	-	[120]
180 °C		1.25 h	63.1 % (BL)	-	[120]	
Fe <sub>2</sub> (SO <sub>4</sub> ) <sub>3</sub>	Cellulose	220 °C	3 h	30.5 % (BL)	-	[121]
H-MOR	Cellulose	180 °C	2.5 h	56 % (LA)	-	[115]
	Bamboo sawdust	180 °C	4 h	61 % (LA)	-	[115]
HY+ CrCl <sub>3</sub>	Empty fruit bunch	145.2 °C	2 h	29.2 % (LA)	-	[78]
	Kenaf	145.2 °C	2 h	22.7 % (LA)	-	[78]
	Starch	180 °C	3 h	53 % (ML)	-	[122]
Micro-meso acidic H-USY	Wheat straw	200 °C	12 h	24.5 % (EL)	-	[123]
ZrO <sub>2</sub>	Cellulose	180 °C	3 h	53.9 % (LA)	~ 53 % - 3 runs	[124]
SBA-SO <sub>3</sub> H	Cotton straw	180 °C	6 h	18 % (LA)	-	[125]
Amberlyst 70	Cellulose	160 °C GVL/Water	16 h	69 % (LA)	28 % - 4 runs	[117]
Amberlyst 36	Beet molasses	140 °C	3 h	78 % (LA)	18 % - 5 runs	[59]

## 1.4 $\gamma$ -Valerolactone: Synthesis and applications

In addition to the above-mentioned applications, alkyl levulinates and levulinic acid are platform molecules for chemical transformations. Among the most investigated reactions in the literature involving alkyl levulinate is the conversion to  $\gamma$ -valerolactone (GVL). This molecule is a cyclic ester with a high boiling ( $\sim 207$  °C) and a low melting point ( $-31$  °C) [126]. Therefore, at ambient conditions, it is a liquid, which is colorless and of low viscosity [126].

The high polarity of GVL ensures its total miscibility with water. It has a low volatility, which allows its flammability risk to be neglected under normal conditions. However, since its vapor pressure, which is about 32 Pa (at 20 °C), slightly exceeds the threshold of 10 Pa, it is classified as a volatile organic compound (VOC) [127]. In addition, it is highly stable, as it does not decompose up to 150 °C in the absence of water [128], and it hydrolyses slightly at acid pH values [36,126,128].

These properties, together with its relatively low vapor pressure, even at high temperatures (3.5 kPa at 80 °C) [36], make it a relatively safe and promising solvent biomass-derived for large-scale uses, and several studies have praised its characteristics [127]. In the field of GVL conversion, several studies, as mentioned above, consider its use to facilitate the solubilization of intermediates and components of lignocellulosic biomass, such as sugar monomers and humins [44,117]. As aprotic polar solvent, its use increases levulinic acid and alkyl levulinate yields by stabilizing reaction intermediates and reducing side degradation reaction in homogeneous and heterogeneous catalysis [44,129]. Horváth proposed GVL as a solvent for the production of GVL itself from fructose [130]. Capecchi et al. [131] investigated its use as solvent for the hydrogenation of butyl levulinate. The major advantage lies in the fact that separation of the product from the solvent, GVL, is not required.

In addition, its properties have been candidate by several studies as a potential fuel additive, demonstrating properties similar to ethanol [36,127], which is widely used in the fuel sector today, precursors of other value-added chemicals as methyltetrahydrofuran (MeTHF) and bio-butene [28], and its characteristic sweetish odor also determines its current main application as an ingredient for perfumes or food additive [126,127].

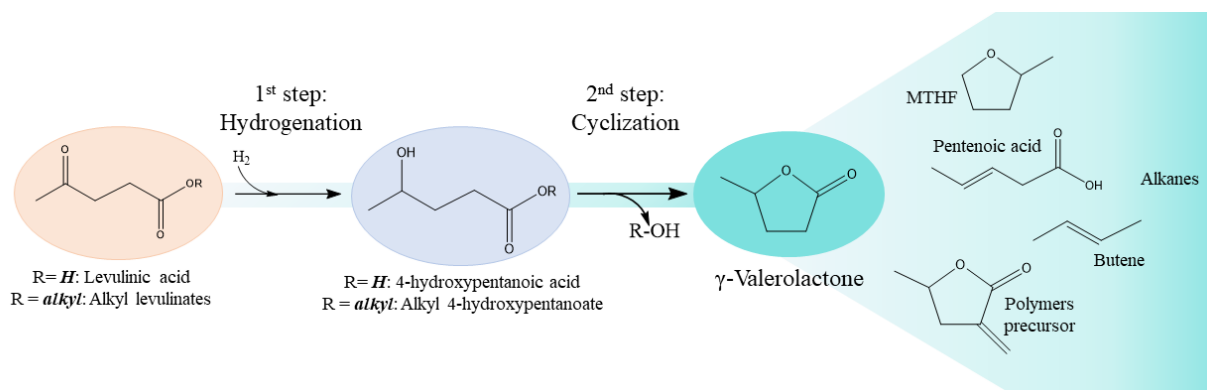


Fig. 5: Main pathway for GVL production by hydrogenation and its potential applications

The main route for the synthesis of GVL is by hydrogenating levulinic acid or alkyl levulinate on a metal catalyst; the mechanism occurs considering a two-steps reaction, as shown in Fig. 5: Main pathway for GVL production by hydrogenation and its potential applications. Firstly, the carbonyl group of AL or LA is hydrogenated. During the second step, the hydroxyl group of the intermediate (4-hydroxypentanoic acid for LA and alkyl-4-hydroxypentanoate for alkyl levulinates) reacts with the ester group leading to a cyclization. The main route of hydrogenation presented in literature consider: direct hydrogenation through the use of molecular H<sub>2</sub>-gas; hydrogen transfer by *in situ* decomposition of acids such as formic acid; catalytic transfer hydrogenation using alcohol as in the Meerwein–Ponndorf–Verley (MPV) reaction [19].

The production of GVL from levulinic acid has been extensively studied in the literature, however, several studies have focused recently on the synthesis from alkyl levulinate, and this is due to a number of advantages. For example, using ester would limit metal leaching from the catalyst caused by the carboxylic function of levulinic acid [35]. Among the metal catalysts investigated, noble metals were found to be the most efficient in hydrogen transfer. In particular, ruthenium is the metal that has shown the highest selectivity, and, therefore, the most studied in terms of Ru-catalyst support, such as carbon, TiO<sub>2</sub>, zeolites, etc. Catalysis using other metals, such as palladium or platinum, was found to have lower selectivity and also resulted in undesirable by-products [132,133]. Although there are some examples with homogeneous catalysts [134,135], most studies concern solid catalysts.

Among the different production routes, conventional hydrogenation with external molecular hydrogen is the most efficient and common route to reduce alkyl levulinate to GVL, in terms of yield and atomic economy, without the necessary production of by-products. Some research has pointed out some disadvantages of this route [35,136,137]; such as the safety concern due to the use of high-pressure hydrogen, and the negative environmental impact of the use of hydrogen, obtained mainly from fossil sources; however, the current expansion of green hydrogen, with very low impact, obtained through the use of renewable energy sources, allows the emission effects to be neglected.

Hydrogenation by catalytic transfer due to the in-situ decomposition of formic acid is particularly appropriate where levulinic acid is considered as a reagent, obtained from biomass-derivatives, and thus produced in an equimolar ratio with FA. However, in addition to the high acidity effect that can lead to leaching of the metal catalyst, the utilization of FA entails some drawbacks, such as the requirement of precious metal catalysts, homogeneous catalysts, and/or harsh reaction conditions such as high temperature [138,139]. Other hydrogen donors are alcohols through the use of the MPV reaction; the main advantage is the use of non-noble metal catalysts. However, they require high-temperature conditions, and the reaction produces the corresponding alkyl-ketone, as by-product together with GVL, increasing the complexity of separation and purification steps [51,140].

In terms of kinetics, the hydrogenation step can be modelled using Langmuir-Hinshelwood model with competitive adsorption of LA/ALs and GVL on the metal site of catalyst; the second step of cyclization can be modelled as an equilibrium reaction that occurs in the bulk liquid, catalyzed by protons, and



it represents the rate determination step and controls the overall reaction rate [141]. To enhance the kinetics, Delgado et al. proposed to combine the use of Ru/C to catalyze the hydrogenation through molecular hydrogen of butyl levulinate, together with Amberlite IR-120 to enhance the kinetics of cyclization [141].

Table 4: Production of GVL from levulinic acid and alkyl levulinates using various catalytic systems

Catalyst	Condition T(°C) / P (bar)	Reagent	Solvent	Time (h)	Yield (mol%)	Ref.
<b>- Molecular hydrogen-gas</b>						
Ni/HAP	70 °C / 5 bar	LA	Water	4	65	[142]
Pt/HAP	70 °C / 5 bar	LA	Water	4	88	[142]
Ru/HAP	70 °C / 5 bar	LA	Water	4	99	[142]
Ru/C	130 °C / 12 bar	LA	Methanol	2.4	84.4	[133]
Ru/C	130 °C / 12 bar	BL	Methanol	2.4	75.1	[133]
Ru/C	100 °C / 20 bar	BL	GVL	20	87	[141]
Ru/TiO <sub>2</sub>	200 °C / 40 bar	LA	Dioxane	4	92	[143]
Ru/ZSM-5	200 °C / 40 bar	LA	Dioxane	4	50	[143]
Cu/ZrO <sub>2</sub>	200 °C / 35 bar	LA	Water	5	100	[132]
Ni-MoO <sub>x</sub> /C	140 °C / 8 bar	LA	-	5	97	[144]
<b>- Formic acid as H-donator</b>						
Ru/C + Pd/C	150 °C / 35 bar	BL	Water	2	89	[145]
Ru-P/SiO <sub>2</sub>	150 °C	LA	Water	12	96	[146]
Cu/ZrO <sub>2</sub>	200 °C	LA	Water	5	100	[147]
Ru <sub>3</sub> (CO) <sub>12</sub>	130 °C	LA	Water	24	100	[148]
Ag-Ni/ZrO <sub>2</sub>	220 °C	LA	Water	5	99	[132]
Au/ZrO <sub>2</sub> -VS	150 °C	LA	Water	6	99	[149]
<b>- Alcohol as H-donator</b>						
ZrO <sub>2</sub>	150 °C / 21 bar	BL	2-Butanol	16	85	[140]
ZrO <sub>2</sub>	150 °C / 21 bar	LA	2-Butanol	16	22	[140]
Al <sub>2</sub> O <sub>3</sub> - ZrO <sub>2</sub>	220 °C	EL	2-Propanol	4	83	[150]
Zr-HBA	150 °C	EL	2-Butanol	4	96	[151]
ZrO <sub>2</sub> /SBA-15	150 °C	ML	2-Propanol	3	91	[139]

## 1.5 Integration of renewable energy sources (RESs)

### 1.5.1 Wind and solar energy

As mentioned above, the contribution to energy demand from renewable sources is growing rapidly, although still under the shadow of the fossil fuel contribution. Renewable sources, such as sunlight, wind, ocean tides, waves, biomass and geothermal energy, can be naturally replenished and directly or indirectly generate energy that can be used for power and heat production [152,153]. Among the various renewable energy sources, wind and solar power generation plants are increasingly attracting investment as they can provide substantial amounts of energy, thanks to increasingly efficient systems, and are cost-competitive [154].

According to the International Energy Agency, global additions of renewable energy capacity are expected to increase by one-third in 2023 in terms of solar and wind power, as growing political momentum, rising fossil fuel prices and energy security concerns drive their deployment [154,155]. This increase in capacity is notably driven by the growing installed capacity of solar photovoltaics (PV) systems, both large-scale utilities and smaller distribution systems, which account for about two-thirds of the expected increase in global renewable capacity [155]. In particular, photovoltaic solar power generation recorded a record growth of +26 % (270 TWh) in 2022, for a total of 1300 TWh [155]; recording the highest generation growth in absolute terms and surpassing wind power for the first time in RES history. The high rate of installation of PV technologies is also due to the growth of distributed solar photovoltaics, such as use on the roofs of buildings, which allows the production of renewable energy with easy installation even in urban settings. Among the PV technologies on the market, crystalline polysilicon remains the dominant technology for photovoltaic modules, with a market share of more than 97 % [155,156]. Different types of wafers and cells can be used, varying the efficiency of the panel. Although research has made considerable progress on these technologies, most commercial panels have an efficiency of between 15 % and 20 % [156,157].

Compared to solar technologies, wind potential conversion technologies, such as wind turbines (WTs), have much higher efficiency values, between 30-45 % for onshore wind power plants and around 50% for off-shore plants, where efficiency is expressed in terms of a '*capacity factor*' that indicates its average power output divided by its maximum power capability; this makes wind energy one of the most efficient forms of renewable electricity production [158–160].

WTs technologies convert the kinetic energy of moving air into electricity. In modern wind turbines, the wind rotates the rotor blades, which convert kinetic energy into rotational energy, which is then transferred from a shaft to the generator, thus producing electricity; with average hub heights of 100 m for on-shore turbines and over 150 m for off-shore systems [161].

In 2022, electricity production from wind power increased by 14 % (265 TWh) to over 2100 TWh [162]. Wind power generation is driven by on-shore plants, which account for 93 % of globally installed

capacity, and is estimated at 900 GW in 2022 [162]. Onshore wind is a mature and proven technology with a large global supply chain. In recent years, onshore wind has evolved to maximize the electricity produced per megawatt of installed capacity by increasing the size of the devices. In fact, wind turbines have become larger, with greater hub heights and larger rotor diameters [162]. However, the maximum height of onshore wind turbines is often limited for environmental and public acceptance reasons, thus limiting their capacity [163]. Offshore wind also has a high potential (capacity in 2022 of 66 GW), and is expected to grow in the coming years; in fact, the installation of turbines at sea allows stronger winds to be exploited, and unlike on-shore devices, without restrictions on turbine size, but with higher installation and maintenance costs [162].

Wind turbines are devices that generate electricity with a negligible impact compared to fossil energy sources, considering that the carbon footprint of a turbine in its life-cycle time is around 10 g-CO<sub>2</sub>eq./kWh (that of solar panels is 5 times higher, around 50 g-CO<sub>2</sub>eq./kWh)[164,165]. In addition, innovation in turbine technology has progressed together with innovation in terms of turbine recycling, and it is now possible to consider a high rate of recycling of decommissioned devices, up to 90%, considering their use in different material sectors [166].

The main disadvantage associated with renewable energies is their inherent variability, which therefore makes them unsteady energy sources and subject to fluctuations. One strategy to address this problem is the use of electrical energy storage systems to buffer energy demand and availability. On the other hand, another strategy considers the combination of two or more power systems, defined hybrid power systems (HPS). HPSs can meet the growing demand for energy by exploiting the complementarity of different sources, while reducing greenhouse gas (GHG) emissions in the case of fossil systems coupled with renewables. In addition to grid applications, HPSs can also help meet the energy demand of remote or isolated locations, where operating costs are too high due to the installation of long-distance plants [152,167,168].

On the other hand, in electrical energy systems, a buffer storage system is required to store energy for a medium/long duration and to give quick responses to power fluctuations. Among the main systems used are conventional batteries, such as lithium-ion and lead-acid batteries, and flow batteries, which have high efficiencies of up to 95 per cent, with short response times, in the order of milliseconds, but limited storage times, ranging from minutes to hours [14,169]. The main disadvantage of using such a storage system, coupled with renewable energy sources, is precisely the storage duration, where the seasonal availability of the renewable resource is limited for an extended period. Systems that allow a longer duration, in the order of even weeks, are chemical storage systems, involving the production of chemical energy carriers, in so-called Power-to-X system [169]. Among these, hydrogen is one of the most promising energy carriers, as it is a flexible vector that enables the storage and production of energy, with little or no environmental impact, for many sectors that currently use energy from fossil fuels.

## 1.5.2 Hydrogen

Hydrogen is currently considered the most promising low-carbon energy carrier and fuel; a key player in the green transition. This molecule is used for many applications, such as electricity generation and storage, transport, space heating, heavy industrial processes, and chemicals/fuels production [153]. In fact, as described above, hydrogen is an essential reagent in the conversion of lignocellulosic biomass, such as in the production of levulinic acid and alkyl levulinates from pentose sugars, and subsequent hydrogenation to GVL [36]. Nevertheless, more than as chemical reagent, hydrogen enables wide utilization and full market penetration of renewable energy sources, constituting a key complement to electricity for storing intermittent renewables [15], which is a major step towards greening of energy systems. In this context, some of the roles of hydrogen are [168,170]:

- Integration of large-scale renewable energy into existing energy infrastructure.
- Accessible, reliable, safe, clean and affordable energy for different sectors and geographical areas.
- Highly resilient energy systems.
- Integration with multi-generation systems to offer many valuable products with minimal losses.
- Cleaner transport thanks to fuel cells and hydrogen-powered internal combustion engines.
- Cleaner energy source for industry, residential applications, buildings, etc.
- Cleaner industrial raw material

The carbon footprint associated with hydrogen use comes from the raw material and production process (Fig. 6) [171]. Today, fossil fuels remain dominant in global hydrogen supply because production costs are strongly correlated to fossil fuel prices, which are still acceptable and cost-effective [16]. Of the various technologies, steam reforming of natural gas is the most widely used, along with coal gasification, both of which lead to the production of so-called 'grey' hydrogen [171]. Currently, the hydrogen market is still 92% fossil-based and therefore produces grey hydrogen, with a CO<sub>2</sub>-equivalent release between 1144-1291 Mt, corresponding to a range between 12-13.6 kg CO<sub>2</sub>eq. per kg-hydrogen produced [172]. With a market increasing demand for hydrogen by 3% in 2022 and an expectation of an increase of more than 60% in 2030 [172], different alternatives are needed in the hydrogen economy to reduce emissions; among them: low-carbon 'blue' hydrogen, obtained by steam reforming of natural gas and/or coal gasification, but integrating the production process with capture techniques and storage of the CO<sub>2</sub> produced (CCS systems); and above all 'green' hydrogen, which is the cleanest alternative with negligible emissions and is obtained by electrolysis of water fed by renewable energy sources [171].

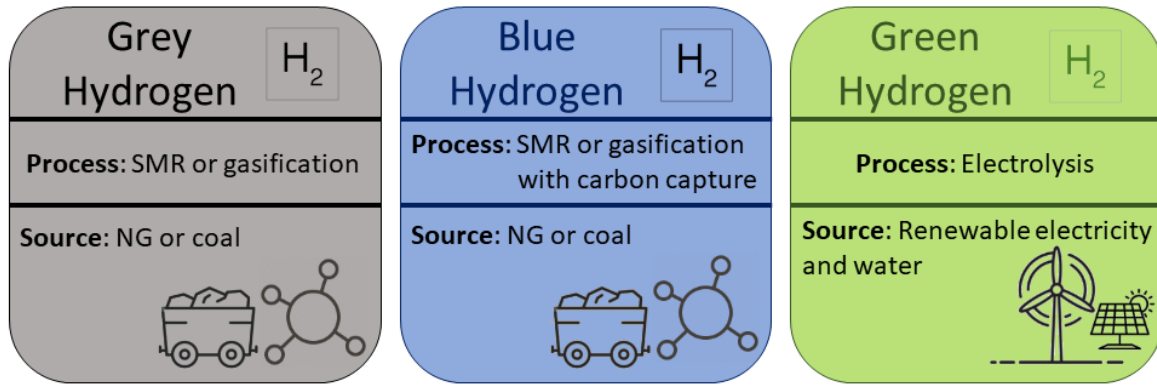


Fig. 6: Hydrogen colours based on process and raw materials

Several studies have analyzed blue and green hydrogen's competitiveness and complementarity. While Ueckerdt et al. [173] first showed that for green hydrogen to become competitive with blue hydrogen, a large share of low-cost renewable electricity is required to power the electrolyzers; on the other hand, Durakovic et al. [174] showed that the competitiveness of the blue alternative is strongly sensitive to the cost of natural gas. In particular, the price of natural gas in Europe increased considerably in 2022, with prices around 100 €/MWh in the first half of 2022, rising further in the second half of the year. If the price reached turn out to be firmly representative of future gas prices in Europe, blue hydrogen will probably not be an economical way to produce large quantities of hydrogen [174].

Consequently, although blue hydrogen may be more easily implemented as a first approach, the green alternative must be preferred in view of Europe's complete energy emancipation from the import of fossil fuels, as well as, of the complete decarbonization of the hard-to-abate sectors which use large quantity of hydrogen such as the refining sector, and metallurgy [3,15].

Hydrogen production by electrolysis of water is among the least emission-intensive production routes, as long as electricity from low-emission sources is considered.

The electrolysis of water is an electrochemical water splitting technique, in which one mole of water is split, using electricity, into one mole of hydrogen and half a mole of molecular oxygen. The basic reaction of water electrolysis is as follows (Eq. 1. 1):



Although in itself the production of hydrogen by electrolysis is emission-free, the impact in terms of emissions differs depending on the nature of the electricity involved in the process [175]. Green hydrogen has a negligible emission index due to the use of energy from renewable sources; in other cases, hydrogen can still be obtained by hydrolysis but have an emission impact due to the primary energy source (e.g., fossil or nuclear electricity) [171].

The electrolysis of water is currently a well-known and widely used technology in various industrial sectors and a continuous subject of research and development; starting from the first generation of

electrolytic cells continuous evolutions to maximize its energy efficiency, minimize its costs, up to today's industrialization of large-scale applications with capacities in the order of 100 GW [175–177]. Four types of water electrolysis technologies have been introduced, differing based on the electrolyte solution, operating conditions and ionic agents ( $\text{OH}^-$ ,  $\text{H}^+$ ,  $\text{O}_2^-$ ), such as Alkaline water electrolysis (AEL), Proton exchange membrane (PEM), Anion exchange membrane water electrolysis (AEM), and solid oxide electrolysis cell (SOEC) [175,178].

Among these technologies, AEL and PEM are already commercially available. Alkaline electrolyzers has a more mature technology with a long history of use in the chlor-alkali industry. However, for dedicated hydrogen production, both technologies are at the same level of technological readiness (TRL 9) [175,178,179].

Alkaline water electrolysis is the most established technology for the industrial production of hydrogen up to multi-megawatts in commercial applications worldwide. It is applicable for large-scale applications, with low investment costs and a high system lifetime (around 90,000 hours) [180].

In the alkaline cell, the main components are the electrodes, diaphragms/separators, current collectors, separation plates (bipolar plates) and end plates, respectively. In general, the electrodes (cathode and anode) are coated with non-noble metals such as nickel, perforated stainless-steel diaphragms are coated with asbestos/zircon/nickel and used as separators in the stack. Nickel-coated stainless-steel separator plates are used as bipolar and end plates [175,178,181]. In the cell during the process of alkaline electrolysis, two moles of alkaline solution are reduced at the cathode to produce one mole of hydrogen ( $\text{H}_2$ ) and two moles of hydroxyl ions ( $\text{OH}^-$ ); the  $\text{H}_2$  produced can be discharged from the cathode surface while the remaining hydroxyl ions ( $\text{OH}^-$ ) are transferred under the influence of the electrical circuit between anode and cathode, through the porous separator to the anode side. Then at the anode, the hydroxyl ions ( $\text{OH}^-$ ) are discharged to produce 1/2 molecule of oxygen ( $\text{O}_2$ ) and 1 molecule of water ( $\text{H}_2\text{O}$ ) [175].

The main challenges associated with alkaline water electrolysis are the limited current density, typically due to the moderate mobility of  $\text{OH}^-$  ions, and the use of corrosive electrolytes (KOH). In addition, the diaphragms do not completely prevent the cross-over of the gases, resulting in a lower purity of hydrogen (99.9%) [180].

The PEM cell is designed to overcome the disadvantages associated with alkaline electrolysis. In this type of cell, it is the sulfonated polymer membrane that is used as the electrolyte; the ionic charge carriers are  $\text{H}^+$  and water, permeating through the proton-conducting membrane, providing the functionality of the electrochemical reaction [181,182]. In the PEM cell, water molecules are initially decomposed on the anodic side to generate oxygen ( $\text{O}_2$ ) and protons ( $\text{H}^+$ ) and electrons ( $\text{e}^-$ ). The oxygen produced is released from the anode side and the remaining protons move through the proton-exchange membrane to the cathode side, while the electrons travel to the cathode through an outer circuit. At the cathode, the protons and electrons recombine to produce  $\text{H}_2$  gas. The main components of the PEM cell, besides the gas diffusion layer, separator plates (bipolar plates) and terminal plates, include the electrodes and

membrane. Among the best-known membranes is Nafion<sup>®</sup>, which has high proton conductivity, current density, mechanical strength, and chemical stability. Noble metals such as platinum (Pt) and iridium (Ir) are used for the anode and cathode electrodes, and together with other specific components; this makes the cell cost quite high [182,183].

Compared to alkaline electrolysis, PEM water electrolysis has faster kinetics due to the highly active metal surface area of the electrodes and the lower pH of the electrolyte. In addition, the PEM cell is safer due to the absence of caustic electrolytes and its smaller footprint. On the other hand, it has lower stability (around 60,000 hours of lifetime)[180], and the main obstacle is associated with the high cost of the components, i.e. the electrode materials, current collectors and bipolar plates [175].

Although for both types of electrolyzers, further innovations have reduced their investment cost, the cost disparity in favor of the alkaline electrolyzer means that it is currently favored for large-scale applications; nevertheless, there are projects in the future investment outlook of several countries considering both types [180].

*Table 5: Main advantages and disadvantages of alkaline electrolyzer and PEM systems*

<b>Electrolyzer</b>	<b>Advantages</b>	<b>Disadvantages</b>
Alkaline electrolyzer	<ul style="list-style-type: none"> <li>• Proven technology</li> <li>• Marketed for industrial applications</li> <li>• Noble metal-free electrocatalysts</li> <li>• Relatively low cost</li> <li>• Long-term stability</li> </ul>	<ul style="list-style-type: none"> <li>• Limited current density</li> <li>• Highly concentrated electrolyte liquid</li> <li>• Gas crossover</li> </ul>
PEM electrolyzer	<ul style="list-style-type: none"> <li>• Commercialized technology</li> <li>• Rapid response</li> <li>• Operates at higher current densities</li> <li>• High gas purity</li> <li>• Compact system layout</li> </ul>	<ul style="list-style-type: none"> <li>• Cost of cell components</li> <li>• Noble-Metal Electrocatalysts</li> </ul>

In spite of promising global project announcements, the increase in installed capacity is slowly coming to 130 MW in 2022, with a total installed capacity of about 690 MW [179]. Based on the prospectus of projects under development and expected commissioning dates, the world's electrolysis capacity could reach almost 3 GW by the end of 2023, increasing total capacity by more than four times compared to 2022. Furthermore, if all projects currently in the pipeline were realized, global electrolysis capacity could reach 170-365 GW by 2030. In this panorama, Europe would be in the lead with almost half of the total capacity [179].

In the growing market of renewable energy sources, green hydrogen production systems by means of water electrolysis are positioned as integrative systems that allow optimal management of the notoriously fluctuating power trends from renewable sources, as electrolysis cell modules can be combined to handle high power peaks, thus making the power supply from RES to the grid/end user more flexible. In this way, the integrated system can provide constant power to the final user, as it is able to absorb excess power by converting it into hydrogen via the electrolyzers, and to provide power in phases of negative fluctuations by using the stored hydrogen carrier.

In this sense, power-to-hydrogen systems with hydrogen electrical energy storage (HydEES) can be combined with hydrogen-to-power systems [184].

Hydrogen can be converted into electricity and heat through the use of fuel cell (FC) systems. A fuel cell is a device for converting the energy of a chemical reaction into electricity, in this case, hydrogen combustion using oxygen/air as an oxidant [184].

The most common type of fuel cell is the proton exchange membrane cell (PEMFC), also known as the polymer electrolyte membrane cell, and whose principle of operation is similar to that of the PEM electrolysis cell by using a solid polymer electrolyte membrane to separate the anode from the cathode; the difference being that in this case hydrogen and oxygen react to produce electricity and water [184]. Of the different technologies currently available, the PEMFC was the most installed worldwide in 2021, followed by the solid-oxide fuel cell (SOFC) technology [184]. Compared to traditional power generation technologies, fuel cells have several advantages such as high efficiency, in some cases up to 60 per-cent, no emissions during operation, very quiet and no moving parts, making them ideal for use in vehicles, buildings and other applications where low noise and small footprint are required [185–187].

In addition, the rapid response and start-up time makes PEMFC technologies widely deployed from smaller scales such as automotive to hydrogen vehicle operation, to larger scale systems where hydrogen can provide power from 1 MW to 10 GW, thanks also to their modularity and ability to provide highly reliable power [15].

In the context of the production and use of hydrogen for energy production, the storage system is a key element for a reliable and rapid supply of hydrogen to fuel cell system, and a connecting element between the latter and the upstream power-to-hydrogen system, as shown in Fig. 7. At present, the main hydrogen storage technologies include physical storage, as compressed gas or cryogenic liquid; or chemical storage through metal hydride. Given its technological maturity, high reliability, acceptable efficiency and cost-effectiveness, hydrogen storage in the form of compressed gas is the most popular form for both automotive and large-scale storage [188]. Depending on the end application, the most appropriate storage conditions may vary. Metal pressure storage vessels can be divided into: cylindrical pressure vessels Type I, and Type II which involves reinforcement with a resin fiber composite. Then



there are the pressure vessels based on fully composite materials and these are the Type III and Type IV [188].

In contrast to the automotive sector where high storage pressures of around 70 MPa are required (only possible with type III and IV tanks [189,190]), for large-scale stationary storage and industrial applications, hydrogen is typically not stored for pressures above 20 MPa. This results in large storage volumes and thus high costs, but lower operating costs when compressing large quantities of hydrogen. Under such operating conditions, type I metal cylinders are preferable as they have a low mass storage efficiency (about 1 wt% of hydrogen stored) but lower costs [189].

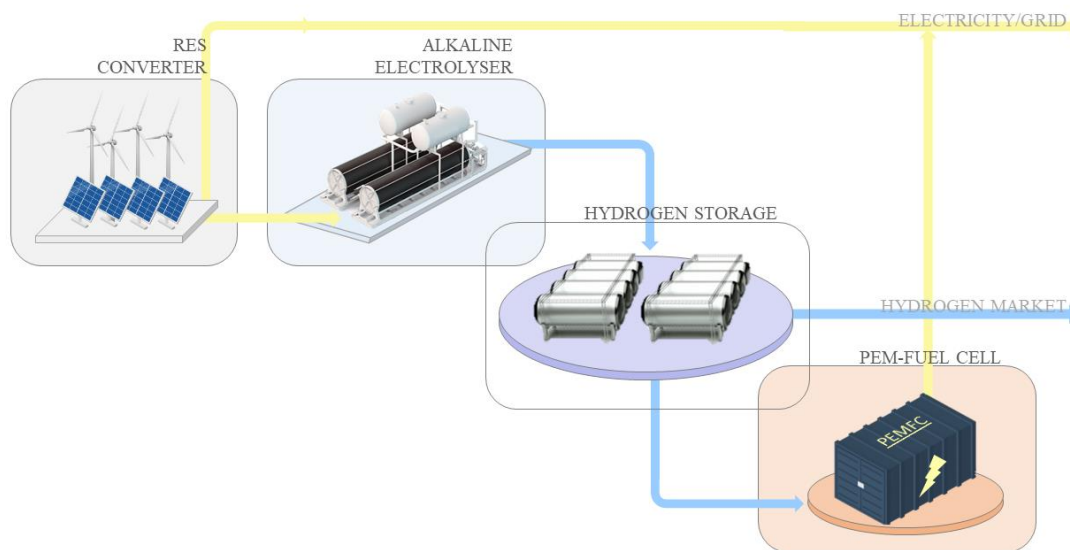


Fig. 7: Figurative representation of a hydrogen energy storage system (HydESS).

Numerous hydrogen energy storage projects have been initiated worldwide, demonstrating the potential of its wide industrial use. For example, Norsk Hydro and Enercon on the Norwegian island of Utsira installed a system to supply energy to the grid and residential areas, consisting of a 600 kW Enercon wind turbine, an alkaline electrolyzer with a production rate of 10 Nm<sup>3</sup>/h at 12 bar, a hydrogen compressor for hydrogen up to 200 bar, and a proton exchange membrane (PEM) fuel cell [191].

Another example is Hawaii's Hydrogen Power Park (HPP) in Kahua Ranch. The plant uses wind turbines and a photovoltaic system to produce wind and solar energy, which is partly converted into hydrogen by means of a PEM electrolysis cell and converted back into electrical power by means of a fuel cell in the low-power phase [192]. In Germany, the power-to-gas (PtG) plant 'Energiepark Mainz' was built to support the local power grid and to carry out large-scale research of PEM electrolyzers.

The plant is connected to an 8 MW wind farm and uses excess wind energy to produce hydrogen gas. Three PEM electrolyzers are installed, with a peak output of 6 MW, and a hydrogen production of 1000 Nm<sup>3</sup>/h, which is then compressed to 225 bar [193].

The plant use hydrogen as additive in the natural gas grid, as a reagent in the chemical industry or sold to hydrogen filling stations, and not to produce electricity in a fuel cell [193].

Other projects use hydrogen as an energy carrier to solve the problem of mismatching between demand and system load; for instance, in data management infrastructures such as the Datazero project [194]. Overall, based on data reported by the European Clean Hydrogen Alliance [195], more than 840 projects involving hydrogen-systems are active and many will be operational by the end of 2025, encompassing all stages of the hydrogen value chain, including hydrogen production, transmission and distribution, industrial applications in sectors such as chemicals, refining, steel or transport [195].

## **1.6 Process Design and Sustainable Development**

When designing a new process, the flow of research thinking-action considers essential steps such as: problem definition, solution synthesis and subsequent solution analysis [196]. In terms of the life cycle of a chemical process, these steps are reflected in a first essential phase, known as the synthesis of the chemical route or process synthesis, and corresponding to the development of the optimal chemical pathway for the process. This first stage is then followed by the conceptual process design step, where heuristic selection of unit operations and recycling structures are applied, and the process development step in which reaction kinetics, physical data, and properties are used to evaluate the performance of the scheme [196,197]. Although differentiated, these steps are sometimes performed simultaneously in the design of a new process.

The objective of process synthesis should be to find the best processing path, among numerous alternatives. Process synthesis is usually performed through different classes of methods: rule-based heuristic methods, which are defined based on process knowledge and know-how; mathematical programming-based methods, in which the best flow alternative is determined by optimizing the superstructure network; or hybrid methods using process insights, know-how, rules and mathematical programming [197]. To design a sustainable process, the evaluation of potential solutions in the early process design stage must be performed under a multi-criteria metric that considers different perspectives of sustainability, i.e., designing with sustainability goals and constraints [196,197]. In this context, the concept of “process intensification” is often applied, when, by definition, new equipment developments and techniques are implemented and, compared to those commonly used, they are expected to lead improvements in the process, substantially reducing the ratio of equipment size to production capacity, energy consumption or waste generation and, leading to more economical and sustainable technologies [198].

Among the first constraints applied in process design for sustainable development, there is the environmental sustainability perspective, through the application of green chemistry principles. In this case, the term eco-design (ecological design, also called green design or environmentally conscious design) is often used [199]. By applying these principles, the process synthesis and conceptual design phases are directed towards more environmentally conscious choices: use of renewable feedstock; benign solvents; design for energy efficiency, etc.[200][I]

In the field of eco-design process for the exploitation of renewable raw materials, such as lignocellulosic biomass, several investigations on process design and intensification have been presented in the literature, showing a wide range of alternative technologies for the production of high-value-added molecules [201–203]. For the production of the alkyl levulinates, the technology literature applied is not fully explored, and there is a lack of in-depth studies on the conceptual design of processes for the production of such molecules from precursor molecules such as sugars, and from raw biomass; especially for major alkyl groups such as butyl levulinate.

From an energy perspective, the optimization of sustainable process schemes, such as potential biomass biorefinery systems, can be further developed through the integration of renewable energy sources, such as wind and solar energy, and through the use of chemical storage systems, such as hydrogen (HyESS). Studies in the literature on the application of HyESS systems show that optimization of design and operation is crucial for the efficient and economical use of these systems [204].

Several studies, including in the field of hybrid renewable energy systems, define mathematical optimization methods, mainly based on mixed integer linear programming (MILP), that are deterministic in nature and can effectively capture the characteristics of a system with reasonable computational complexity [204]. An example is the work of Gabrielli et al. [205,206] in which a MILP system is used to optimize batteries and hydrogen storage systems considering a time horizon of one year with hourly resolution. Other investigations have instead considered the use of heuristic optimization methods in the design and operational control of electrical storage systems to reduce the cost of renewable electricity storage, such as minimizing the daily operating cost, net present cost, levelized cost of energy and total cost of operation [207–210]. Typically, optimization analyses, in addition to economic objectives, may also include other technological objectives, such as improving the efficiency and reliability of the storage system, and environmental objectives such as reducing emissions, often expressed in terms of their potential effect on global warming [204].

Minimization objective functions are therefore defined by potentially considering one to several objectives, and above all by considering realistic constraints related to the various technologies adopted in the system. Design constraints for hydrogen systems should consider realistic operational constraints related to hydrogen production and storage, electrolyzer and fuel cell capacities with respect to maximum achievable hydrogen charge and discharge rates, and storage size.

Furthermore, as renewable energy sources are site-specific, the size and type of technologies installed has to respond to restrictions related to the availability of local resources and their seasonal effects; this is also one of the main reasons why investigations on the optimization of electrical-storage systems based on renewable energy sources are typically linked to case studies with territorial specificities.

Process design defines a multi-objective problem and its optimization aims at finding a set of possible solutions for that given input system, considering specific restrictions.

Including the design of the energy system, the preliminary process design will define a set of different alternatives for the overall configuration. Based on specific perspectives and constraints, the evaluation of the optimal configuration can be performed through the use of various sustainability assessment tools.

### **1.6.1 Sustainability assessment**

The system of alternative solutions for the process design of a process can be analyzed by means of a sustainability assessment, considering the various possible drivers associated with the system under study, and then define an optimal solution that best meets the various criteria under consideration. In this sense, the optimal design phase of a process constitutes a necessary initial step in evaluating the possible technological alternatives for a given system, which can then be assessed from different sustainability perspectives [211].

According to Ness et al. [212], “The purpose of sustainability assessment is to provide decision-makers with an evaluation of global to local integrated nature–society systems in short- and long-term perspectives in order to assist them to determine which actions should or should not be taken in an attempt to make society sustainable”. Sustainability is a broad approach that takes the inter-relationship between social science, environmental science and technological innovation, through the economic, environmental, and social pillars [213]. A two-step approach to measuring sustainability was proposed by Warhurst et al. [214], considering the assessment of sustainable development indicators (SDIs) individually for each of the areas assessed and the assessment of the overall improvement achieved toward sustainable development by aggregating the individual areas against their respective dimensions. Over the years, different indicators have been proposed for each of the pillars as a result of the various sustainability methodologies and perspectives defined, such as Life-cycle assessment (LCA), Socioeconomic impact assessment, Strategic environmental assessment, Cost-benefit analysis, etc. [213]. From the individual indices considered and evaluated, it is then possible to define an aggregated index; the weighting system and the method used in aggregating the component scores plays a predominant role in the development of the integrated index. Depending on various approaches, it is possible to define weights for each index and once the weights have been assigned to each indicator and transformed into component scores, these scores are aggregated into a composite index. The various choices of the method used for weighting and aggregation depend on the objective, nature, scope, type of indicators, etc. [215]. Sustainability assessment is very often associated and integrated with Multi Criteria Decision Analysis (MCDA) methods [216]. MCDA methods make it possible to evaluate alternatives according to different criteria and perspectives and to obtain a final ranking of alternatives [217]. These methods can be classified as conventional and fuzzy; whereas conventional MCDA methods do not deal with uncertainty, fuzzy MCDA methods deal with uncertainty, and subjectivity of decision-makers or domain experts. Depending on the approach used, the most commonly applied fuzzy MCDA methods are the Analytical Hierarchy Process (AHP), a pairwise comparison method [218], and

the PROMETHEE technique (Preference Ranking Organisation METHod for Enrichment Evaluations), an outranking method [219].

Conceptualizing sustainable development as a decision-making strategy makes it possible to actually 'use' it, turning sustainability and its power as a 'guide to action' into an 'action-generating' concept [216]. On the implementation of sustainable process development and hydrogen systems, several investigations on the sustainability assessment of different technologies have been carried out, considering the use of specific indices, and in some cases the assessment of an aggregated index based on different decision-making perspectives [170,211,220–223].

## 1.7 Objectives and Outline of the thesis

The literature surveyed and the research context presented agree on the view of lignocellulosic biomass as a valuable renewable resource, which, together with other forms of renewable energy, can be exploited to reduce the impact of anthropogenic activities as a source of bio-carbon for the production of high added-value molecules, applicable in various industrial sectors, and as a source of bio-energy. Although scientific research is continuously focused on progress in integrating renewable sources into today's industrial economy that is still heavily dependent on fossil sources, most of the promising results are still limited to academic studies, without bridging the gap between the academic and industrial scales, due to issues related to process efficiency, process economics and more generally related to process sustainability, not merely technological and economic, but also environmental and social sustainability. The key question in evaluating a new process, and currently in evaluating of new processes using renewable energy sources and materials, is: Is the process sustainable?

This question is also the thread running through the research of this thesis, which focuses on evaluating a sustainable way of exploiting second-generation biomass towards promising molecules, integrating the use of other renewable energy sources.

In the wide panorama of possible bio-platform molecules derived from lignocellulosic biomass, particular attention has been paid to alkyl levulinate, esters of levulinic acid, praised in the literature for their potential as bio-additives for traditional fuels and as bio-fuels. Among these, butyl levulinate has shown exceptional properties and benefits in improving combustion efficiency and reducing emissions, applied as a bio-additive.

Compared to its minor ester counterparts, such as methyl and ethyl levulinate, the literature on butyl levulinate is less extensive, and mainly focused on the evaluation of the catalyst, while other key aspects in the production of this molecule have not been investigated in depth, such as the effect of the solvent, which in the context of the conversion of biomass and its precursors, such as monosaccharides, plays an essential role in controlling and limiting the onset of degradation reactions. The choice of catalyst and solvent system has an important effect on the reaction mechanism and kinetics, and although some kinetic models have been proposed for conversion from precursor molecules, the current literature is lacking in kinetic modeling in the production of butyl levulinate from primary complex molecules, such as biomass-derived monosaccharides.

For these reasons, the first part of this thesis is devoted to the experimental investigation of two key perspectives in butyl levulinate production via acid-solvolysis, analyzed in Chapters 2, 3 and 4:

- In Chapter 2, the evaluation of the optimal process conditions to favor its production, specifically investigating the efficiency in the choice of heterogeneous catalyst and solvent system.

- In Chapters 3 and 4, the kinetic modeling for the production of BL from the 5-HMF precursor, and the fructose platform molecule, including essential aspects such as degradation to humins and the dissolution kinetics of fructose, which plays a limiting role especially in the application of *High-Gravity* conversions.

Through the literature presented in Chapter 1, the possibility of transforming butyl levulinate, by means of hydrogen integration, to  $\gamma$ -valerolactone (GVL) was also highlighted, describing the considerable implications this molecule may have for highly impactful industries such as solvents, additives, fine chemicals, and heavy aviation fuels, being a precursor for the production of bio-jet fuel. Furthermore, produced by the hydrogenation of butyl levulinate, the production of this molecule also opens up an outlet for integrating green hydrogen, the primary player in the green transition, into the lignocellulosic biomass biorefinery system.

Having thus defined the optimal process conditions and kinetic modeling of BL production from fructose, which are fundamental building blocks for the evaluation of a possible process scheme, Chapter 5 extends the exploitation of fructose from biomass to include the step of hydrogenation of butyl levulinate to GVL and answer the sustainability analysis of this process.

This more methodological chapter consists of several parts:

- A first section aimed at evaluating a reference process scheme for the production of GVL from fructose, by production and hydrogenation of BL.
- A second section aimed at evaluating a systemic methodology for assessing the sustainability of the process, and applied more pragmatically to a case study in Normandy.

The analysis aims to assess the sustainability, from an economic, environmental, and social perspective, and by means of a methodology based on key performance indicators (KPIs), of different scenarios that consider the optimal design of a system that integrates, at different levels, renewable energy sources for the production of energy and hydrogen in the GVL production process. Site-specificity with a case study in Normandy was included by analyzing the actual availability on the territory of the potential of renewable sources.

Finally, Chapter 6 presents the conclusions that can be drawn from the research activities carried out and the results obtained, together with final recommendations and future perspectives.

# CHAPTER 2 - Optimization of process conditions for the solvolysis of fructose to butyl levulinate: effect of catalyst and solvent

Part of this chapter is adapted from the post-print of the following article:

Di Menno Di Bucchianico, D.; Buvat, J.-C.; Mignot, M.; Casson Moreno, V.; Leveneur, S. Leveneur, Role of solvent in enhancing the production of butyl levulinate from fructose, *Fuel*, 2022, 318, 123703.

Further permissions related to the material excerpted should be directed to the ScienceDirect. Copyright © 2023 Elsevier B.V. or its licensors or contributors. ScienceDirect® is a registered trademark of Elsevier B.V.

## 2.1 Introduction

In the context of the conversion of lignocellulosic biomass derivatives, such as hexose monosaccharides, the experimental work of this thesis was focus on the production of butyl levulinate (BL); in particular, focusing on the reactivity of fructose under acidic conditions, which, due to its higher molecular reactivity, results in higher conversion rates with promising yields in alkyl levulinate, compared to other monosaccharides such as glucose; although, it is less abundant in nature [I].

The interest in this molecule is due to its promising properties as oxygenated additive for blending gasoline and diesel, and fuel quality enhancer. Furthermore, compared to the more common ethyl ester, BL was found to have a higher cetane number and lower calorific value (LHV), to remain in solution with diesel up to the point of fuel cloud point, and to be more compatible with elastomers, being less corrosive [42]. As explained in the introductory chapter, BL production can occur via solvolysis of hexose sugar monomers, catalyzed mainly by Brønsted acids [I]. Of these, traditional mineral acids are now gradually being replaced by heterogeneous acid catalysts, due to some drawbacks, such as corrosion of equipment, separation and neutralization costs and ecotoxic effects. Among solid catalysts, zeolites, ion exchange resins, metal oxides, nanomaterials, and numerous other solid catalysts have been tested to produce butyl levulinate from biomass-derived carbohydrates [I].

An et al.[224] studied the production of BL from the alcoholysis of various carbohydrates catalyzed by ferric sulfate, and obtained a yield of 62.8 % for a reaction temperature of 190°C .

Higher yields of alkyl levulinate from fructose were also confirmed by Liu et al.[70] using carbon materials functionalized with sulfonic acid. BL was produced with a yield of 78 mol% after 12 h and complete conversion of fructose.

Ramirez et al. evaluated the use of ion exchange resins for the direct conversion of fructose to BL by alcoholysis [73], emphasizing the catalytic efficiency of the resins for moderate temperatures, lower than those required by other catalysts.



In the solvolysis kinetics of monosaccharides, in addition to the catalyst, the solvent also plays a key role. To the best of our knowledge, there were not many studies on the crucial role of the solvent, which can influence reaction kinetics and product selectivity, sugar dissolution, polymerization and degradation. Sun et al. reported that the conversion of sugars and furans, particularly fructose and 5-(hydroxymethyl)furfural, changes in different solvents, depending on their polarity and protic or aprotic nature [225]. In particular, the solvent influences proton transfer in the reaction medium, which is a key point in the mechanism of alcoholysis [226]. Water is one of the main solvents used in the pre-treatment and conversion of lignocellulosic biomass derivatives, and monosaccharides have a high reactivity in water, which provides a good solvation environment, enabling high dissociation of Brønsted acids and high solubility of sugars [227]. On the other hand, high reactivity in aqueous systems results in higher instability of sugars and furan intermediates, making them more prone to secondary reactions, such as degradation to humins [225,228,229]. Greater control over the reactivity of the reaction system can be achieved through the use of polar organic solvents, including alcohols [228,229]. In fact, some studies have reported promising yields of alkyl levulinates by operating in excess of alcohol; Ramirez et al.[73] obtained a 73.4 mol% yield of butyl levulinate, Sun et al. [225] a 51.6 mol% yield in ethyl levulinate, both catalyzed by ion-exchange resins and in excess of alcohol. Excess-alcohol results in an important control of the conversion steps, proton transfer and limitation of the polymerization of sugars and furans [225,227]. Further benefits can be obtained from the use of aprotic polar co-solvents to reduce unwanted degradation reactions of intermediates [44,129]. Among these,  $\gamma$ -valerolactone (GVL) can be a valuable co-solvent in fructose solvolysis. Several patents propose GVL as a green alternative to classical hazardous solvents, as it can be produced from biomass via the hydrogenation of levulinic acid and alkyl levulinate [230]. Mellmer et al. [44] demonstrated the advantages of using polar aprotic solvents, such as GVL, for acid-catalyzed reactions. Capecchi et al. [131] reported the synthesis of GVL by hydrogenation of butyl levulinate, identifying an excess of GVL as the best solvent system. The effect of such a solvent on the solvolysis kinetics of monosaccharides such as fructose for producing alkyl levulinate has not yet been explored in the literature. Therefore, in this study, an in-depth investigation was conducted into the effect of the solvent, particularly of water and GVL as co-solvents in butanol-in-excess. Among heterogeneous acid catalysts, ion exchange resins were favored in this investigation; specifically, gel-type resins are identified in the literature as efficient catalysts at lower temperatures than solid inorganic catalysts such as zeolites. Among these, Amberlite IR-120 was chosen for its good stability, high proton capacity, accessibility and recyclability without a significant decrease in activity [231–233]. To the best of our knowledge the solvolysis of fructose to butyl levulinate was not reported over Amberlite IR120. Therefore, this investigation is devoted also to filling this gap.

The experimental investigation of the solvolysis of fructose to butyl levulinate:

- Optimization of heterogeneous catalysis kinetics of Amberlite IR-120 by evaluating external and internal mass transfer resistances; investigating the effect of mixing rotation speed and catalyst particle size distribution;

- Studying the effect of the solvent butanol and co-solvents water and GVL, considering:
  - The swelling of the catalyst in the solvents studied;
  - The kinetics of conversion of fructose to BL, including degradation reactions to humins;
  - The dissolution kinetics of fructose in solvent systems in the absence of water.

With the aim of defining the optimal reaction conditions to maximize the productivity of BL from biomass-derived fructose.

## 2.2 Experimental and Analytical set up

### 2.2.1 Chemicals

Fructose ( $\geq 99\%$  purity), 5-(hydroxymethyl)furfural (5-HMF, 99% purity), 5-(ethoxymethyl)furfural (5-EMF, 97% purity) and  $\gamma$ -valerolactone ( $\geq 99\%$  purity) were purchased from Sigma-Aldrich. 1-Butanol (BuOH,  $\geq 99,5\%$  purity), butyl levulinate (BL,  $\geq 98\%$  purity), acetonitrile (ACN,  $\geq 99,9\%$  purity), butyl formate (BF,  $\geq 97\%$  purity) and acetone ( $\geq 99,9\%$  purity) from VWR chemicals. Amberlite IR120 ( $H^+$  form, ion-exchange resin) commercial catalyst provided by Acros Organics. Nitrogen gas ( $N_2$  purity  $> 99,999\%$  vol%) from Linde. All chemicals were employed without further purification.

### 2.2.2 Analytical methods

Reaction samples were analyzed by combining gas and liquid chromatography. HPLC Agilent 1100 Series was employed to quantify fructose, equipped with a SUPELCO SIL LC-NH<sub>2</sub> column (250 mm x 4.6 mm x 5  $\mu$ m), a UV detector set at 191 nm, and by using a mixture of acetonitrile and ultrapure water (90:10 v/v %) as mobile phase, with a flow rate of 1 mL/min and constant column temperature of 30 °C. Reaction products, as 5-HMF, BL, 5-(butoxymethyl)furfural (5-BMF), LA, and BF, and solvent systems were detected by Bruker Scion 456-GC, equipped with a VF-1701ms Agilent column (60.0 m x 250  $\mu$ m x 0.25  $\mu$ m) and a flame ionization detector (FID). The injector and detector temperature were 250 °C and the oven temperature was programmed from 40 °C to 250 °C with 20 °C/min of ramp rate. All experimental quantifications were based on daily calibration curves with standard solutions of pure commercially available chemicals. 5-EMF was used as reference for the 5-BMF calibration curve due to its commercial unavailability. Each experimental sample was analyzed three times to estimate the error in the analytical method, regarding standard deviation.

Fructose conversion, butyl levulinate yield and catalyst loading were defined as follows:

$$\text{Fructose conversion (\%)} = \left(1 - \frac{\text{mole of fructose after the reaction}}{\text{initial mole of fructose}}\right) \cdot 100 \quad \text{Eq. 2. 1}$$

$$\text{BL yield (\%)} = \frac{\text{mole of BL after the reaction}}{\text{initial mole of fructose}} \cdot 100 \quad \text{Eq. 2. 2}$$

$$\text{Catalyst loading } (\omega_{\text{CAT}} \left(\frac{\text{g}}{\text{L}}\right)) = \frac{\text{mass of catalyst}}{\text{liquid volume}} \quad \text{Eq. 2. 3}$$

## 2.2.3 Experimental set-up

The solvolysis reactions were performed in a 300 mL stainless steel batch reactor (Parr Company) under isothermal and isobaric conditions (Fig. 8: Setup of the autoclave for solvolysis experiment). The reactor was equipped with an electric heating jacket, a cooling coil, and a thermocouple capable of detecting the reactor temperature and communicating with the temperature controller to ensure that the temperature remains constant at the set point. Constant pressure is ensured by the supply of inert gas (nitrogen) to the reactor. The inert gas is fed to an intermediate buffer tank from an external tank, and through a pressure gauge, the pressure of the gas entering the reactor is regulated. Equipped with a gas entrainment impeller (diameter 2.5 cm) with a hollow shaft, it ensures gas entry and uniform mixing of the reactant mixture.

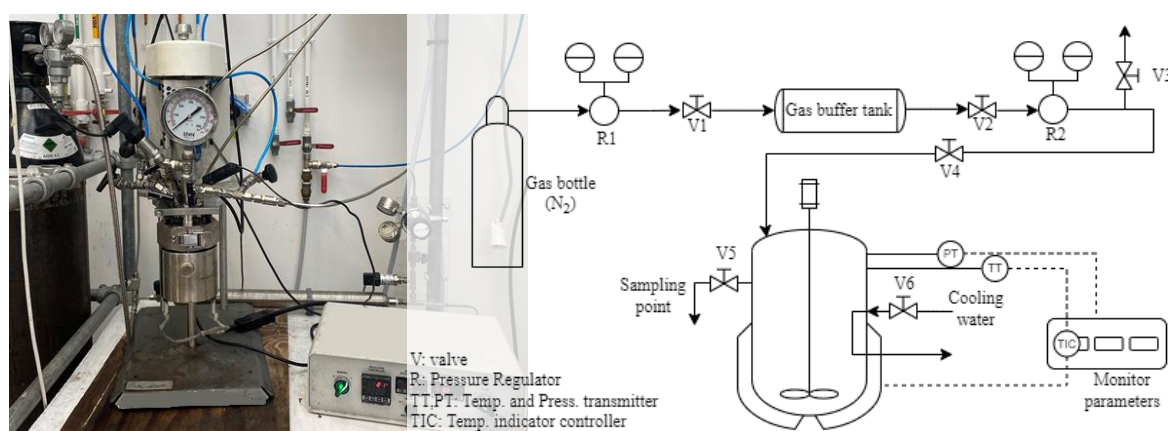


Fig. 8: Setup of the autoclave for solvolysis experiment

For each experiment, the reactor was loaded with 1.6 g fructose, 35 g/L catalyst (4.5 - 4.9 g catalyst) and a constant volume of solvent. The system was pressurized with nitrogen at 20 bars to limit the gas-liquid partition of the liquid phase. With the temperature and stirring set, the first sample was taken when the set temperature was reached (time zero). Subsequent samples were taken at 5 minutes, 30 minutes and then every hour up to 7 hours. In the investigation, the reaction temperature was set at 110 °C as the maximum temperature to maximize catalytic activity while operating below the catalyst degradation temperature. Indeed, the sulfonic groups, i.e. the active sites, of Amberlite IR-120 can leach when the temperature is above 120 °C.

Table 6: Properties of Amberlite IR-120 according to the manufacturer (Acros Organics).

AMBERLITE IR-120 (H-form)	
<b>Supplier</b>	Acros Organics
<b>Structure</b>	Styrene-divinylbenzene
<b>Resin type</b>	Gel-type
<b>Cross-linking (DVB%)</b>	8
<b>Moisture content (% mass)</b>	48-58
<b>Capacity by dry weight (m<sub>eq</sub>/g)</b>	4.4
<b>Native particle size range (µm)</b>	≥ 94 % (300 < d < 1180 µm)

Amberlite IR-120 is a cation exchange resin composed of a styrene-divinylbenzene sulfonate (PS-DVB) matrix with sulfonic acid functional groups. The catalyst is a gel-type resin with pearl-shaped particles, in which the PS-DVB copolymers result in a set of entangled chains with no spaces between them in the dry state. The degree of cross-linking (DVB%), related to the level of divinylbenzene, represents the tightness of the resin. Table 6 shows the properties of Amberlite IR-120 as purchased from the supplier. Amberlite IR-120 was pre-treated before its use, as described by Leveneur et al. [233]. The catalyst was washed through several cycles in distilled water and a final one in the main reaction solvent, butanol. After being filtered, the resin was dried in an atmospheric oven at 90 °C for 5 hours.

### 2.2.3.1 Mass transfer resistance investigation

The influences of external and internal mass transfer were studied, considering the effect of the rotational speed of the mechanical stirrer for the external transfer, and the catalyst particle size for the internal one [234]. To investigate the presence of internal mass transfer limitations, the particle size distribution (PSD) was analyzed using a standard sieve analysis; dividing the particles into “*high-PDS*”, for particles with diameter higher than 500  $\mu\text{m}$ , “*fine-PDS*” with diameter between 300-500  $\mu\text{m}$ , and “*very-fine-PDS*” for particles smaller than 300  $\mu\text{m}$ . For each PSD-category, an experiment was performed in the typical reacting conditions described above and setting the stirring speed to the optimum, determined from the external mass transfer limitations analysis. Indeed, influences on external mass transfer were investigated by considering the effect of the rotational speed of the mechanical stirrer, which varied between 500 and 1000 rpm, as shown in Table 7.

Table 7: Experimental matrix for external and internal mass transfer experiments

	Exp.	PSD	Stirrer (rpm)	Fructose (g)	Butanol (wt%)	Water (wt%)	$\omega_{\text{CAT}}$ (g/L)	T (°C)	time (h)	Inert gas
External	1MT	Fine	500	1.6	83	17	35	110	7	N <sub>2</sub> (20 bar)
	2MT	Fine	800	1.6	83	17	35	110	7	N <sub>2</sub> (20 bar)
	3MT	Fine	1000	1.6	83	17	35	110	7	N <sub>2</sub> (20 bar)
Internal	4MT	Fine	800	1.6	83	17	35	110	7	N <sub>2</sub> (20 bar)
	5MT	High	800	1.6	83	17	35	110	7	N <sub>2</sub> (20 bar)
	6MT	Native*	800	1.6	83	17	35	110	7	N <sub>2</sub> (20 bar)

\*indicated as “*Native*” the PSD of the catalyst as such by the supplier

### 2.2.3.2 Experimental investigation on the solvent effect

The solvent effect on the fructose solvolysis to butyl levulinate was investigated by considering three main solvent system, with all the other reaction parameters equal (temperature, initial fructose concentration and catalyst loading). Solvolysis experiments were performed in the presence of excess butanol, and considering the effects of water and GVL as co-solvents. As shown Table 8, the

experiments considered the solvent systems: pure butanol, butanol-water, butanol-water-GVL, and butanol-GVL.

Being characterized by a cross-linked styrene-divinylbenzene structure, the particles of Amberlite IR120 are subject to swelling, depending on the solvent. The swelling effect can affect reaction kinetics, so it was evaluated. Based on the procedure of Bodamer and Kunin [231,235], the degree of swelling was evaluated in each solvent system analyzed, in order to observe the behavior of the catalyst. The procedure considers adding a 20 mL volume of dry catalyst to a 100 mL graduated cylinder, and reading the initial volume to the nearest 0.5 mL. Then, the solvent was poured into the cylinder, up to full volume, without shaking or tapping. After 120 hours, the volume was read and the swelling percentage expressed as follows:

$$\%SW = \frac{\text{final volume } (V_{\text{final}}) - \text{initial volume } (V_{\text{initial}})}{\text{initial volume } (V_{\text{initial}})} \cdot 100 \quad \text{Eq. 2. 4}$$

Table 8: Experimental matrix for fructose solvolysis in different solvent systems (butanol, water and GVL).

	Exp.	T (°C)	Stirrer (rpm)	time (h)	Fructose (g)	Butanol (wt%)	Water (wt%)	GVL (wt%)	$\omega_{\text{CAT}}$ (g/L)	Inert gas
No GVL	1	110	800	7	1.6	83	17	0	35	N <sub>2</sub> (20 bar)
	2	110	800	7	1.6	91.5	8.5	0	35	N <sub>2</sub> (20 bar)
	3	110	800	7	1.6	96	4	0	35	N <sub>2</sub> (20 bar)
	4	110	800	7	1.6	100	0	0	35	N <sub>2</sub> (20 bar)
GVL	5	110	800	7	1.6	2.5	8.5	89	35	N <sub>2</sub> (20 bar)
	6	110	800	7	1.6	60.5	8.5	30	35	N <sub>2</sub> (20 bar)
	7	110	800	7	1.6	76.5	8.5	15	35	N <sub>2</sub> (20 bar)
	8	110	800	7	1.6	70	0	30	35	N <sub>2</sub> (20 bar)

### 2.2.3.3 Fructose dissolution investigation

A further aspect related to the effect of the solvent system is the dissolution rate of fructose. While fructose is highly soluble in water, it is not as soluble in alcohols such as butanol; therefore, the effect of GVL as co-solvent was evaluated with respect to the dissolution kinetics of fructose, in comparison to the pure butanol solvent. A modified experimental method was applied [236]; in this case, the known and constant mass quantity of fructose in the analysis (i.e., the specific fructose concentration of 11 g/L used in the solvolysis experiments) was added to a constant volume of solvent in the reactor system, mixed at the optimum rate, and at constant temperature and pressure of 20 bar for a sufficient period of time to determine the equilibrium of the system. In the literature, Engasser et al.[237] analyzed the

dissolution kinetics of monosaccharides and observed a rapid initial phase, in which approximately 40/50% of the maximum concentration was reached in less than 5 minutes. Therefore, a time interval of 30 minutes was conservatively assumed in this study as sufficient time to reach equilibrium at the set temperature. The system was tested under different temperature conditions, measuring the fructose concentration at each temperature. In particular, the dissolution kinetics of fructose was studied in pure butanol and in the butanol-GVL 70/30 wt% mixture.

## 2.3 Experimental results and discussion

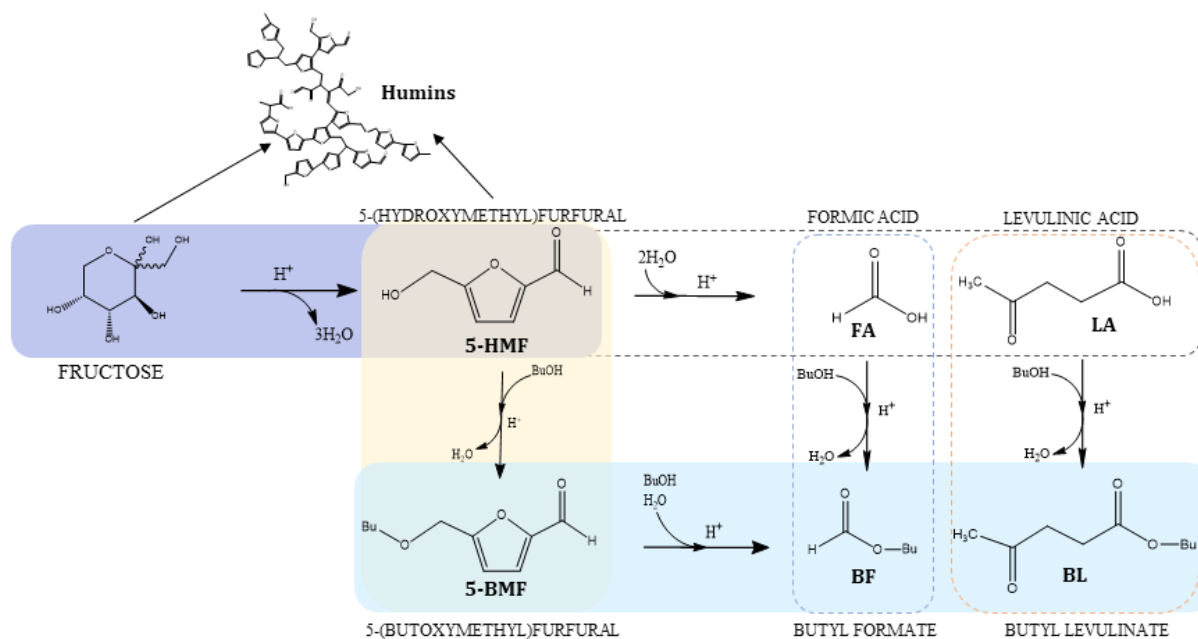


Fig. 9: Reaction steps for the fructose alcoholysis in acid-catalyzed system.

According to several articles, the reaction mechanism of the alcoholysis of fructose by butanol occurs according to Fig. 9 [I][35,73,214,215]. In the presence of acid catalyst, fructose is dehydrated to 5-HMF, the first reaction intermediate. In the predominantly alcoholic medium, in this case consisting of butanol, the 5-HMF can be rehydrated to levulinic acid and formic acid, then esterified to butyl levulinate and butyl formate or underwent an etherification reaction to 5-BMF, and then converted to BL and BF. Butyl formate is produced in an equimolar ratio and with similar kinetics to BL. Experimentally, levulinic acid was detected but always in very low concentrations, suggesting that the etherification step of 5-HMF to 5-BMF is favored over rehydration to LA and subsequent esterification. This is due to the low water concentration in the liquid phase, which is insufficient to favor 5-HMF rehydration rather than its etherification with butanol [I]. For this reason, the LA concentration trend was not considered in the subsequent discussion of the results. Furthermore, the reaction scheme also includes the inevitable production of humins from the secondary polymerization and condensation reactions of fructose and the furan intermediate 5-HMF. Some studies suggest a tendency for 5-BMF not to undergo degradation [238].

### 2.3.1 Mass transfer limitations effect

The influence of stirring speed on external matter transfer was evaluated in experiments 1MT, 2MT, and 3MT in Table 7 by varying the stirring speed from 500 to 1000 rpm. Fig. 10 shows the effect of stirring speed on the conversion kinetics of fructose, the intermediates 5-HMF and 5-BMF, and the final product BL. The concentration profiles show an increase in kinetics by increasing the speed from 500 rpm to

800 rpm. The kinetics of consumption of the intermediate 5-HMF, and production of 5-BMF and BL are increased, as well as the conversion of fructose. By further increasing the rotation to 1000 rpm, the kinetics are reduced, probably due to the occurrence of vortex effects that limit the transfer of matter; both the kinetics of fructose conversion and those of the intermediates and BL. It can therefore be concluded from the experiments that the optimum rotational speed that reduces the effect of resistance to external mass transfer is 800 rpm; consequently, it represents the rate set in all other solvolysis experiments in this system.

The external transfer resistance phenomena were evaluated conservatively considering the use of fine PSD, i.e., for the smallest catalyst particles.

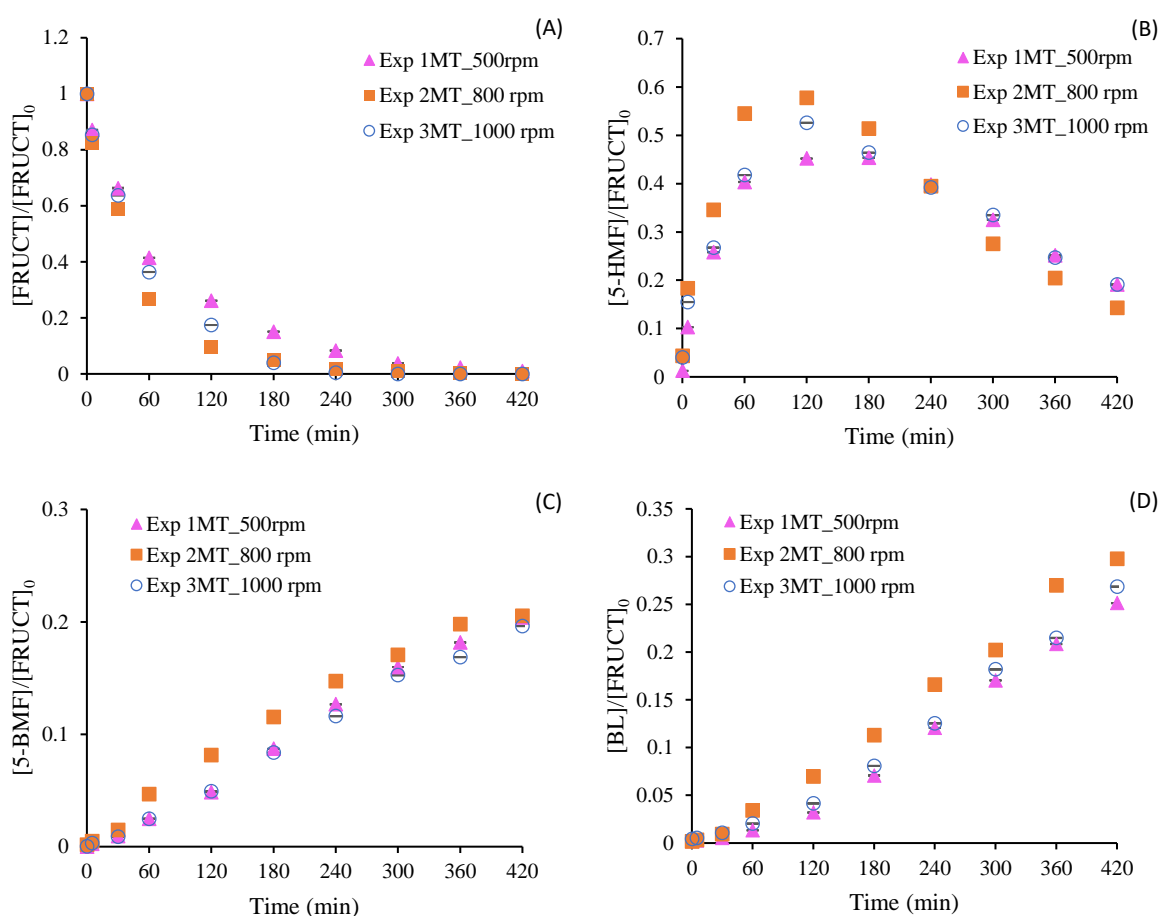


Fig. 10: Effect of the stirring rate on the concentrations (normalized with respect to the fructose concentration at time zero): (A) fructose, (B) 5-HMF, (C) BMF, and (D) BL.

The particle size distribution was analyzed using sieve analysis, showing a high percentage (around 84%) of particles with diameters greater than 500  $\mu\text{m}$  (High-PSD) and the remaining particles with diameters between 300 and 500  $\mu\text{m}$  (Fine-PSD). The effect of the different particles size distribution on kinetics was investigated in experiments 4MT, 5MT, and 6MT of Table 7, in which the two PSD were compared to the “Native” PSD of the commercial catalyst.



The comparison of the concentration profiles in Fig. 11 shows that the effect of the PSD of the catalyst on the solvolysis of fructose is negligible. In fact, it can be seen that under the operating conditions of this study, the PSD of the catalyst has a very negligible effect on the trend of fructose consumption (Fig. 11A), 5-HMF production (Fig. 11B), 5-BMF production (Fig. 11C) and BL production (Fig. 11D). Therefore, it can be assumed that the internal mass transfer resistances are negligible. Therefore, the native distribution was considered for the further investigations on solvent effect.

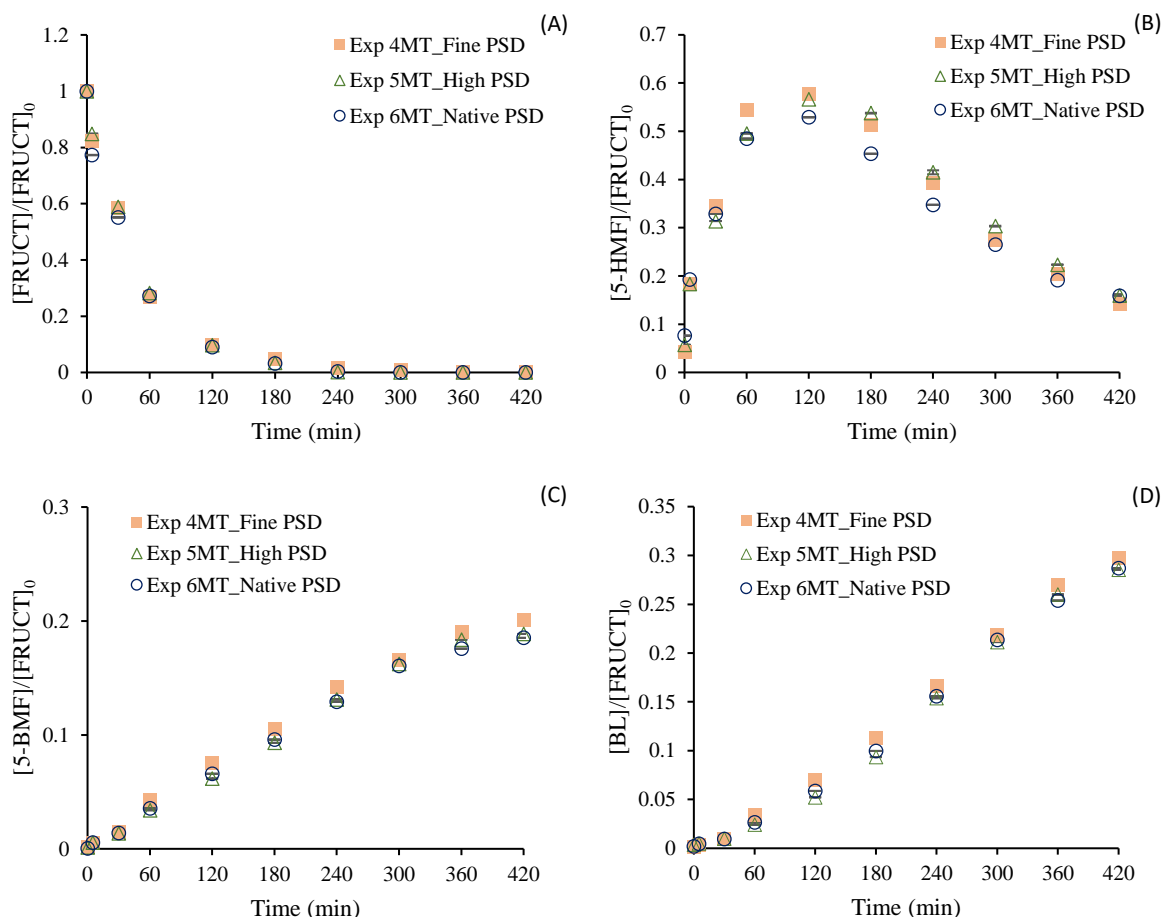


Fig. 11: Effect of catalyst PSD on the concentrations (normalized with respect to the fructose concentration at time zero): (A) fructose, (B) 5-HMF, (C) 5-BMF, and (D) BL

### 2.3.2 Solvent effect: kinetics and swelling effect

The effect of the solvent on the solvolysis of fructose to butyl levulinate was investigated by analyzing the influence on the reaction kinetics of the solvent system consisting of pure butanol, and the presence of water and/or GVL as co-solvents. The different solvent systems considered in Table 8 are:

- Pure butanol (Exp.4);
- Butanol-Water, with water content between 4 - 17 wt% (Exp.1-2-3);

- Butanol-Water-GVL, with water content fixed at 8.5 wt% and GVL between 15 - 89 wt% (Exp.5-6-7);
- Butanol-GVL, with GVL content at 30 wt% (Exp. 8).

### 2.3.2.1 Swelling effect

For all groups of solvent mixtures analyzed in this work, the swelling effect of the catalyst was evaluated and expressed in terms of the average percentage variation in the volume of catalyst, in contact with the solvent.

Table 9 shows that the swelling index of Amberlite IR120 exhibited similar behavior in the different solvents and mixtures tested: pure butanol, pure GVL, pure water, BuOH/GVL/water, BuOH/GVL and BuOH/water. In agreement with the literature data [57], water and butanol showed similar behavior in terms of swelling index, exceeding 100 % of the variation; on the other hand, GVL showed a slightly lower index (around 95 %), mainly due to its different solvent characteristics. Comparing the different mixtures, the swelling index is constant, all being the majority alcohol-aqueous phase.

Table 9: Results from swelling study of Amberlite IR-120 at room temperature.

<u>Solvent</u>		<u>V<sub>0</sub> (mL)</u>	<u>V<sub>fin</sub> (mL)</u>	<u>%SW</u>
BuOH	-	20	42	110±5
GVL	-	20	39	95±5
Water	-	20	42	110±5
BuOH/GVL/Water	53/30/17 %wt	20	42	110±5
BuOH/GVL	70/30 %wt	20	42	110±5
BuOH/Water	83/17 %wt	20	41	105±5

The results in pure water and in the binary alcohol-water mixture are in line to those obtained in the literature (approximately 100 % in water and 110 % in the ethanol-water mixture) [231,235]. The swelling effect in pure butanol is higher than that reported in the literature for ethanol (40 % obtained by Bodamer and Kunin [235], 70 % by Russo et al. [231]) and comparable to that obtained by Pérez-Màcia et al. [240] for 1-butanol, for which they reported a SW% index value greater than 85 % for alcohol contents above 50 v/v%. Adding GVL to the alcohol-water mixture does not affect the swelling capacity of the resin. Since the swelling parameter is therefore unchanged between the different solvent systems, it can be assumed that the effect of solvents on the kinetics catalyzed by Amberlite IR120 is independent by the swelling factor; furthermore, the analyses of the mass transfer resistances, preliminarily evaluated in the butanol-water solvent, and the results in terms of the optimum rotation speed and PSD are also valid in the other solvent systems considered.

### 2.3.2.2 Co-solvent effect: Water

The effect of water, as a co-solvent with butanol, on the fructose solvolysis kinetics was studied by considering the variation in water content (from 17 wt% to 0 wt%) in Exp.1, 2, 3, and 4 of Table 8.

Fig. 12 shows the concentration profiles of the different species over time: Fructose in Fig. 12A, 5-HMF in Fig. 12B, 5-BMF in Fig. 12C, and BL in Fig. 12D, normalized on the fructose initial loading.

The variation in water content influences the conversion kinetics of fructose but also its dissolution; the conversion kinetics of fructose results faster as the water content decreases, considering a complete conversion in the first 3h in the absence of water (Exp. 4), while for the other experiments starting at 4h and increasing as the water content increases. On the other hand, however, the water content affects the dissolution of fructose, which can no longer be considered instantaneous for water contents lower than 4%. For experiments 3 and 4, the normalized fructose concentration at time zero is not one, due to the

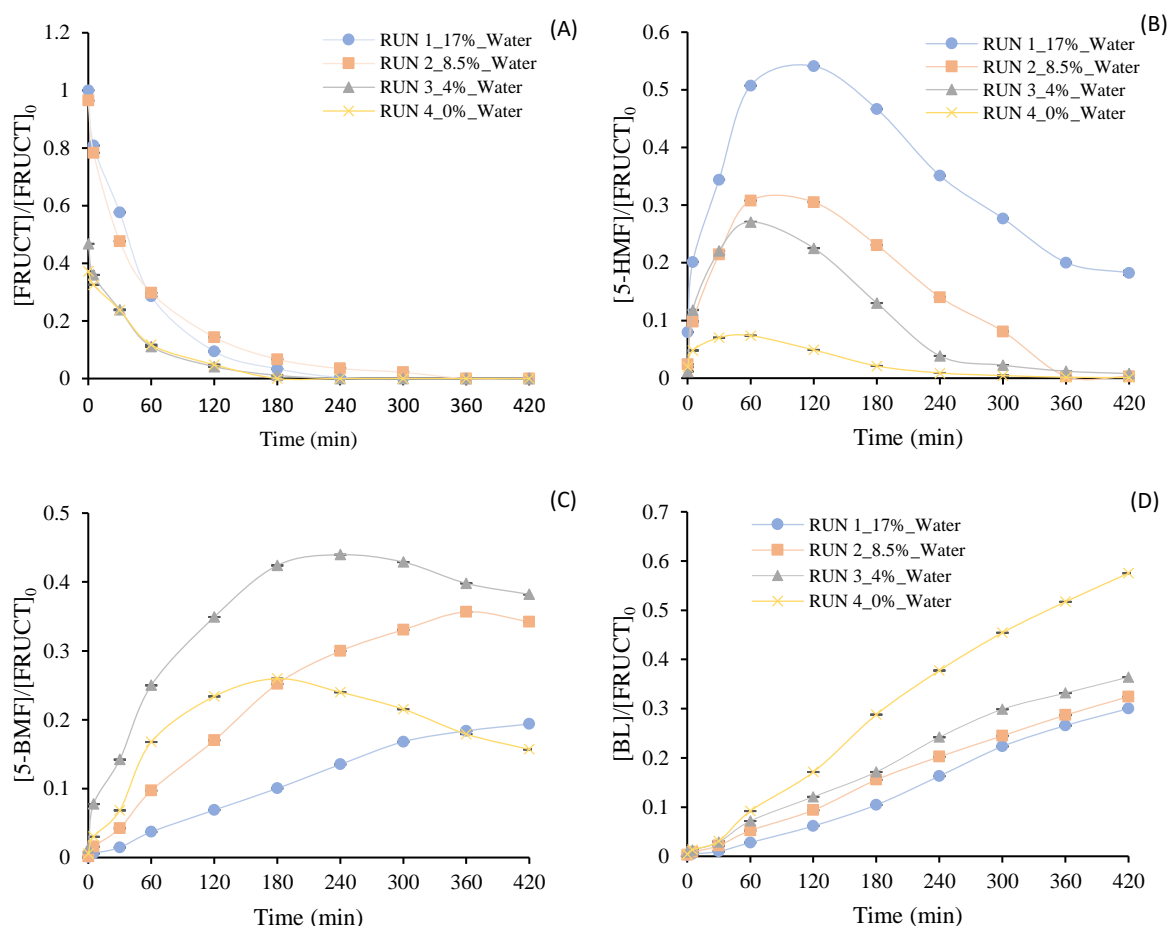


Fig. 12: Effect of water concentration on the concentrations (normalized with respect to the fructose concentration at time zero): (A) fructose, (B) 5-HMF, (C) 5-BMF, and (D) BL

slower dissolution of fructose in the solvent liquid-phase. Furthermore, secondary degradation reactions to humins also complicate fructose kinetics, and water might have a crucial influence on this aspect.

A clearer picture of the water content effect can be observed in the trend of the intermediate 5-HMF in Fig. 12B. The kinetics of 5-HMF production and consumption is faster in the absence of water (Run 4, Fig. 12B). In the presence of higher water content, 5-HMF selectivity tends to increase as higher water

concentrations are reached, and the conversion kinetics of 5-HMF to subsequent intermediates is slower. In fact, 5-HMF is still present after 7 hours for water content of 17 wt%. These effects are also reflected in the concentration trend of 5-BMF; by reducing the water concentration, the formation kinetics of this intermediate becomes faster, leading to a greater accumulation of the intermediate; this can be seen by comparing experiments 1, 2, 3, where the concentration profile of 5-BMF reaches its maximum concentration for the lower water content of 4 wt%. The kinetics changes in the absence of water; in fact, in this case, in addition to the production kinetics, the conversion kinetics of 5-BMF is also faster, resulting in less accumulation, and more conversion to BL, visible in Fig. 12D.

The production of BL is faster and higher as the water content decreases, corresponding to the major conversion of the intermediate 5-BMF, with an increased yield of 27.5% by reducing the water concentration from 17 wt% to zero.

In addition to slower kinetics, the lower yield of BL in the presence of water can be explained by highlighting the role of water in the degradation of fructose and 5-HMF to humins. On the basis of the overall mass balance, the water content is directly related to the moles of fructose unconverted in the main reaction species, and potentially degraded to humins, which amounts to approximately 22 mol% with the highest water content and decreases to 1.5 mol% in the absence of water.

These results confirm the role of water in affecting the stability of fructose in acidic condition, promoting secondary reactions with formation of by-product as humins [225,227,229]. In addition to the increased loss of fructose moles, the limited production of BL may also be influenced by the partial inhibition of the catalytic activity of exchange resins in the presence of water, as suggested by some research [241,242].

### **2.3.2.3 Co-solvents effect: GVL in presence of Water**

The addition of GVL as co-solvent was evaluated in the butanol-water mixture, considering a fixed average water content of 8.5 wt% and a GVL content between 15 - 89 wt% in Exp. 5,6 and 7, thus also considering the kinetics in excess of GVL. The water content of 8.5 wt% was considered to ensure a faster dissolution of fructose, neglecting its dissolution kinetics. In Fig. 13A, the fructose kinetics is affected by the presence of GVL; in systems with excess of butanol (Exp. 6 and 7), the increase in GVL content from 15 wt% to 30 wt% results in a slightly faster fructose conversion kinetics, comparable with the concentration profile in absence of GVL (Exp. 2). However, although the fructose conversion is comparable with Exp.2, the selectivity to the intermediates is not equivalent. Indeed, the GVL content

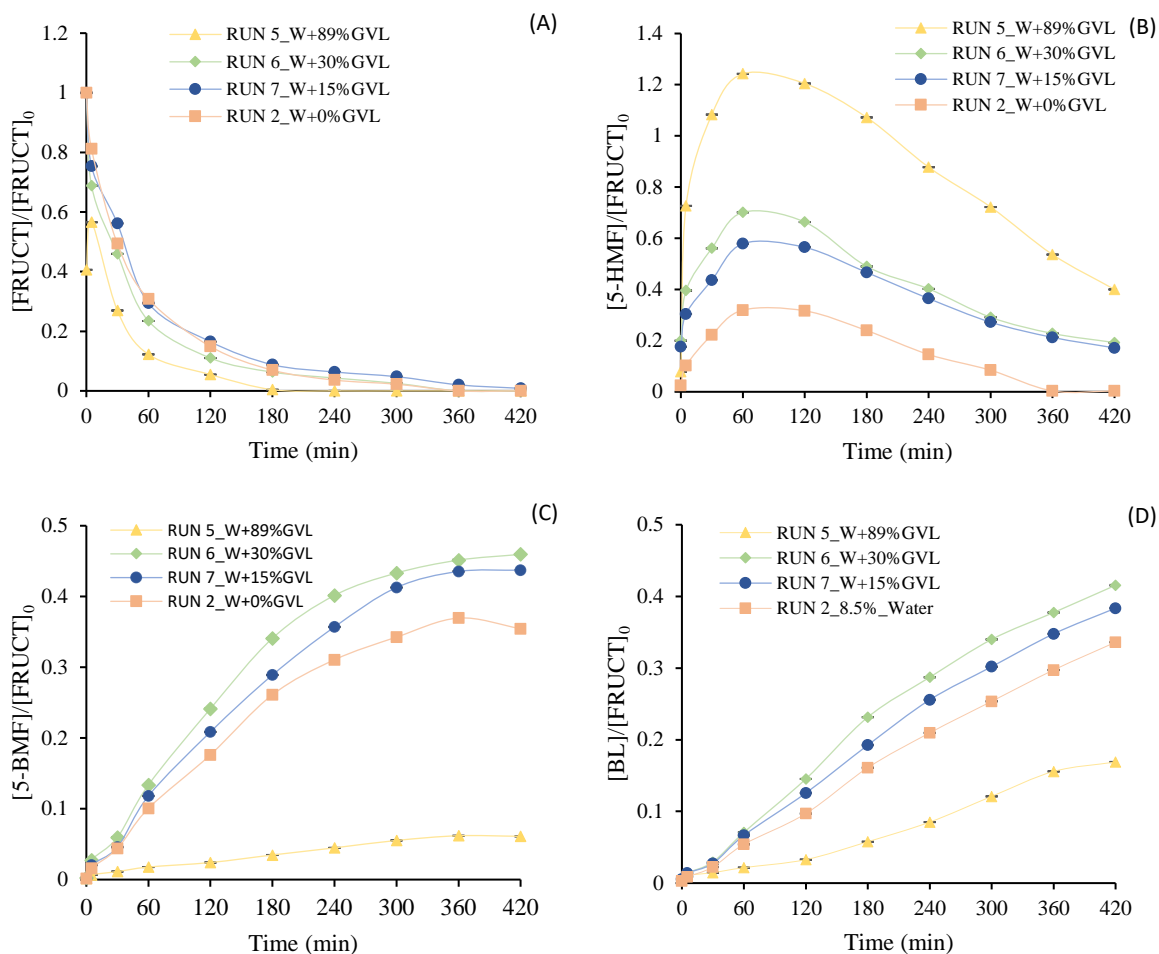


Fig. 13: Effect of GVL concentration on the concentrations (normalized with respect to the fructose concentration at time zero): (A) fructose, (B) 5-HMF, (C) 5-BMF, and (D) BL.

in Exp. 6 and 7 reveals a higher selectivity towards 5-HMF (Fig. 13B), for which the maximum concentration increases by increasing the GVL content, but also for the intermediate 5-BMF (Fig. 13C), and consequently enhancing the yield to the target product BL (Fig. 13D). The increase in yield of the final product, with simultaneously high concentrations of the intermediates and the same conversion of the main reagent, can be explained by considering an inhibition of secondary degradation reactions by GVL resulting in fructose being more available for conversion to BL. This effect is clearly more visible by increasing the GVL content, but the kinetics vary considerably for high concentrations of GVL as in Exp. 5. In this case, the selectivity to 5-HMF is maximized and the reduced butanol concentration leads to favor the rehydration step of 5-HMF to LA over the conversion to 5-BMF. The result is a reduced 5-BMF concentration and, a higher LA concentration in the reaction mixture. By showing slower BL production kinetics with a low yield for the same reaction time, it suggests that the esterification of LA is kinetically slower than the conversion of 5-BMF. The beneficial role of GVL in inhibiting secondary reactions and stabilizing reaction species can also be observed by evaluating the mass balance in terms of fructose moles, where the addition of GVL can result in up to 5% less fructose lost, compared to the butanol-water solvent. In terms of BL production and loss of fructose moles, the addition of 30 wt% GVL results as optimal.

### 2.3.2.4 Co-solvents effect: GVL in Butanol

Previous results showed that water does not improve butyl levulinate production, but rather plays a role in the degradation of fructose and potentially in the inhibition of the resin activity. For this reason, the effect of GVL was investigated in the absence of water in Experiment 8 of Table 8, considering the promising content of 30 wt%. Fig. 14A shows that the addition of GVL in 30 wt% results in a slower consumption of fructose than in pure butanol. This may be due to GVL's ability to limit unwanted degradation reactions towards humins, resulting in higher selectivity towards reaction intermediates such as 5-HMF and 5-BMF. In fact, the production of these intermediates is greater in the butanol-GVL system (Fig. 14B and C). In particular, the high production of 5-HMF means that the intermediate is not fully converted after 7 hours, whereas in pure butanol it quickly reaches complete conversion. As with fructose, this is determined by GVL's role in stabilizing the 5-HMF intermediate by preventing its degradation. This is also reflected in the reduction of the moles of fructose lost on the basis of the mass balance, which are approximately zero in the presence of GVL and more than 1 mol% in pure alcohol. This observation is in line with Fig. 14D, where the BL final yield increases in the presence of GVL, rather than in the presence of pure butanol. Although the increase in BL yield is about 3%, from 57.5% in pure butanol to 60.4% in butanol-GVL, the presence of GVL could result in higher yields even

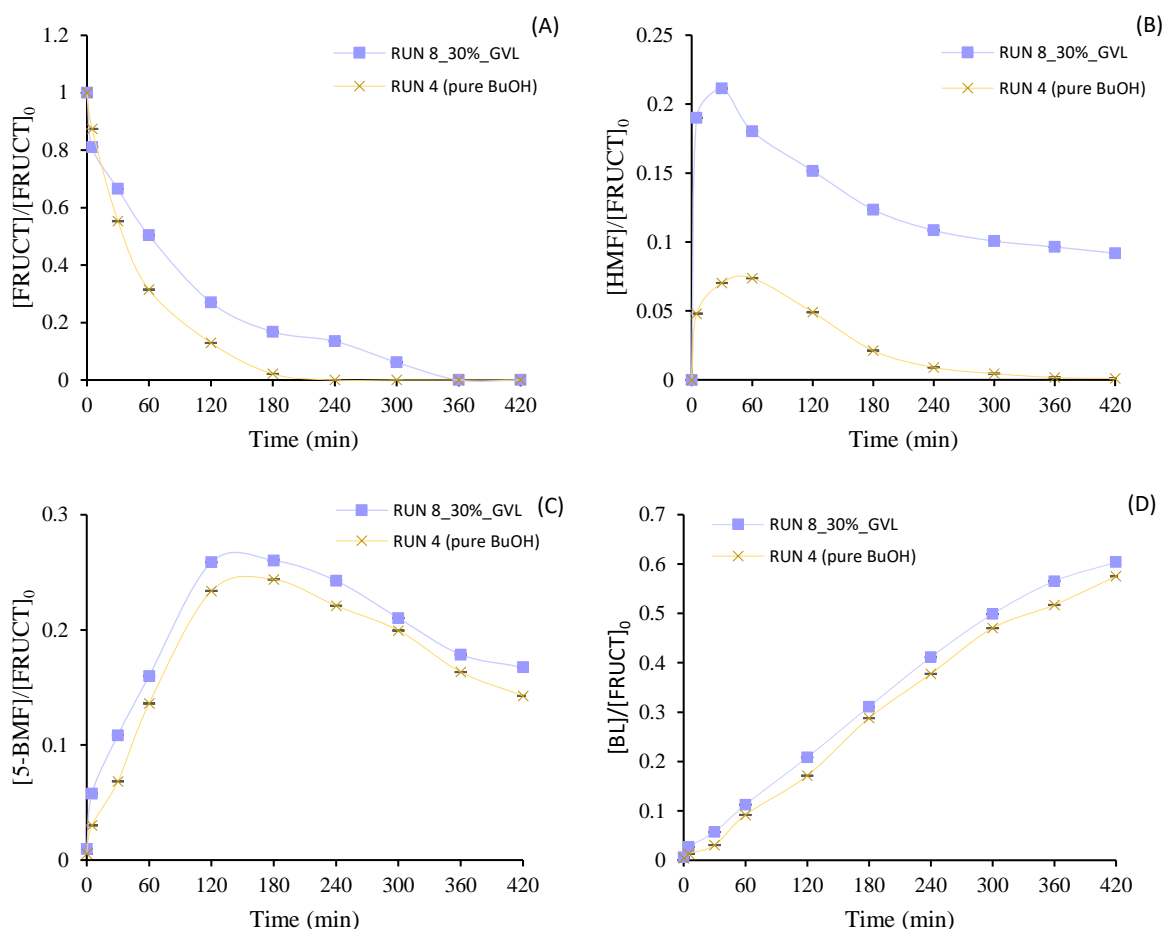


Fig. 14: Effect of BuOH/GVL concentration on the concentrations (normalized with respect to the fructose concentration at time zero): (A) fructose, (B) 5-HMF, (C) BMF, and (D) BL

considering longer reaction times, considering the high residual concentrations of the intermediates under the reaction conditions analyzed. Furthermore, the presence of GVL also brings benefits in terms of fructose dissolution, as shown in the following section.

### 2.3.2.5 Dissolution kinetics investigation

In the presence of water, even at low concentrations, fructose exhibits high solubility and the dissolution kinetics can be considered instantaneous. In the absence of water, dissolution is much slower due to the low solubility in the alcohol environment; for this reason, the dissolution of fructose was analyzed in pure butanol and in the solvent BuOH/GVL 70/30 wt%, according to the procedure described above.

In Fig. 15, dissolution of fructose is more rapid in the 70/30 wt% BuOH/GVL solvent at temperatures below 100°C. Both solvents result in complete dissolution at 100°C, but the dissolution kinetics in butanol are slower. The effect of the BuOH/GVL solution in promoting dissolution of fructose at temperatures below 100°C could be advantageous for catalysts suffering from thermal instability and for systems with high initial fructose concentration where the dissolution kinetics are not negligible (Fig. 15).

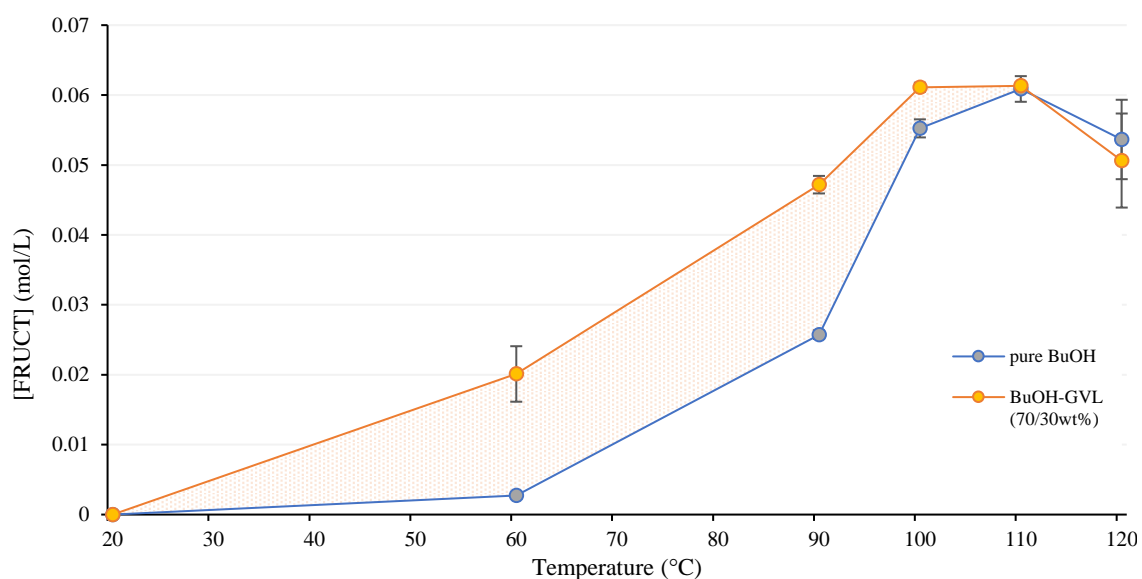


Fig. 15: Fructose dissolution in pure butanol and GVL/BuOH (30/70 wt%) solvents versus temperature

### 2.3.3 Comparison with literature

The results of this investigation are compared with some literature data on the solvolysis of fructose to butanol on different solid acid catalysts (Table 10). With the same degree of cross-linking (DVB%=8), since it has a direct effect on catalytic activity [73], the catalytic activity of Amberlite IR120 in this study was compared with some results obtained with Amberlyst 39 and Dowex 50Wx8. In the presence

of water, the BL yield obtained with Amberlite IR120 is slightly higher than the corresponding one obtained with Dowex 50Wx8 and Amberlyst 39, considering a higher catalyst loading but lower temperature and lower catalyst acid capacity (4.4 m<sub>eq</sub>/g versus 4.83 m<sub>eq</sub>/g of Dowex 50Wx8 and 4.82 m<sub>eq</sub>/g of Amberlyst 39, respectively [73]). The absence of water from the solvent system drastically affects BL production, increasing the yield to 57.5 % in pure butanol, compared to 30 % in the presence of 17 wt% water. This is due to the role of water in promoting secondary reactions of fructose and, secondly, its possible deactivation effect on the resin. The productivity obtained with Amberlite, expressed in terms of BL yield, is comparable with results in the literature for other solid acid catalysts. An et al. [224] obtained a BL yield of 62.8 % in the presence of Fe<sub>2</sub>(SO<sub>4</sub>)<sub>3</sub> at 190 °C; Kuo et al. [65] report a BL yield of 67 % using TiO<sub>2</sub> nanoparticles at 150 °C; Balakrishnan et al. [55] report lower yields, out of the average trend, using Dowex 50Wx8 resin, probably due to the high catalyst concentration.

By introducing GVL as co-solvent at 30 wt% with butanol, BL production was further improved with a yield of 60.4%. The presence of GVL also led to an increase in 5-HMF and 5-BMF selectivity and a drastic reduction in the fructose moles lost. GVL prevents the consumption of fructose and 5-HMF by secondary reactions, such as degradation to humins, and even higher BL yields could be achieved by increasing the reaction time. The use of GVL in the alcoholic medium also results in a faster dissolution of fructose.

Table 10: Comparison with literature data on fructose solvolysis to butyl levulinate.

Catalyst	T (°C)	t (h)	Fructose (g/L)	w <sub>CAT</sub> (g/L)	Solvent (wt%)		X <sub>fruct</sub> %	Y <sub>BL</sub> %	Ref.
Amberlite IR120	110	7	11	35	BuOH/GVL	70/30	100	<b>60.4</b>	This study
	110	7	11	35	BuOH	-	100	<b>57.5</b>	
	110	7	11	35	BuOH/Water	83/17	100	<b>30.0</b>	
Dowex 50Wx8	110	30	72	260	BuOH	-	97	<b>14.0</b>	[55]
	120	6	21	14.3	BuOH/Water	83/17	>99.5	<b>24.2</b>	[73]
Amberlyst 39	120	6	21	14.3	BuOH/Water	83/17	>99.5	<b>25.3</b>	
Fe <sub>2</sub> (SO <sub>4</sub> ) <sub>3</sub>	190	3	25	5	BuOH	-	>99	<b>62.8</b>	[224]
TiO <sub>2</sub>	150	1	20	5	BuOH	-	100	<b>67.0</b>	[65]
CNT-PSSA	120	12	12.5	5	BuOH	-	99	<b>78.0</b>	[70]



## 2.4 Conclusions

In this chapter, the solvolysis of fructose to butyl levulinate, on a commercial ion-exchange resin, such as Amberlite IR120, was studied, investigating the optimal process conditions, in terms of material transfer resistances and the effect of the solvent, evaluating the use of water and GVL as co-solvents together with butanol. The evaluation of external and internal matter transfer resistances showed that using a rotational speed of 800 rpm and the catalyst's native particle size distribution, fluid-solid mass transfer resistances can be excluded in the reacting system considered in this investigation.

In the subject of the solvent effect, the swelling behavior of the catalyst was studied and found to be independent of the nature of the solvents tested. The influence of water and the co-solvent GVL (polar aprotic) was studied on the kinetics of fructose, 5-HMF, 5-BMF and BL. The addition of water did not improve the kinetics of BL production, although it favored the rapid dissolution of fructose even at low temperatures. In addition, water was found to play a role in the kinetics of the secondary reaction to by-products such as humins, obtained from the degradation of fructose and 5-HMF and favored by high water contents in the system. By reducing the water content, the yield of BL increased from 30 mol% with 17 wt% of water to 57.5 mol% without water. Finally, the yield was further increased to 60.4 mol% with the addition of 30 wt% GVL in butanol. Furthermore, the BuOH/GVL mixture (70/30 wt%) was found to increase the dissolution of fructose, compared to pure butanol.

In general, the experimental investigation showed good performance of the ion-exchange resin (Amberlite IR-120) selected to catalyze the solvolysis of fructose to butyl levulinate, with a promising final BL yield, comparable to literature data, but under more moderate temperature conditions, significant in terms of energy savings. GVL in a content of 30 wt% was found to be a beneficial co-solvent with butanol, which is in excess, to enhance the fructose dissolution, inhibition of secondary degradation reaction, and the final yield to BL. These benefits make GVL also suitable as a co-solvent for high fructose systems, favoring faster dissolution and conversion kinetics.

This solvent system will therefore be employed for further kinetic studies, presented in the following chapters.

# CHAPTER 3 - Solvolysis of the platform molecule 5-Hydroxymethyl furfural (5-HMF) to butyl levulinate: kinetic modelling and model assessment

Part of this chapter is adapted from the post-print of the following article:

Di Menno Di Bucchianico, D.; Cipolla, A.; Buvat, J.-C.; Mignot, M.; Casson Moreno, V.; Leveueur, S. Kinetic study and model assessment for the n-butyl levulinate production from the alcoholysis of 5-HMF over Amberlite IR-120. *Ind. Eng. Chem. Res.* 2022, 61, 30, 10818–10836. Further permissions related to the material excerpted should be directed to the ACS Publications. Copyright © 2023 American Chemical Society.

## 3.1 Introduction

In the literature, the development of kinetic models for the alcoholysis of sugars to alkyl levulinate is still a matter of debate and development mainly due to the complexity of the reaction system and the effect of engineering parameters such as the solvent system; catalyst; reaction conditions; etc. on the kinetics and thermodynamics of the system. Indeed, in addition to the primary reaction steps, the occurrence of secondary and degradation reactions leading to the production of humins is a major and inevitable drawback of this conversion pathway, and the formation mechanism of this by-product is still under study. Most studies consider the rate of humins formation in a simplified manner as the difference between the rate of substrate decomposition and the rate of formation of the main products, without investigating in depth its kinetic rate of formation, which influences the process as a whole and its industrial applicability [243]. 5-Hydroxymethylfurfural (5-HMF) is one of the main direct precursor molecules in the formation of humins, as well as being a central intermediate in the solvolysis pathway of monosaccharides to alkyl levulinates, such as butyl levulinate. Starting with 5-HMF, it is possible to investigate the effect of kinetic parameters on the production of butyl levulinate and simultaneously on the degradation to humins. Although some studies have investigated the solvolysis of 5-HMF in the presence of methanol and ethanol for the production of methyl- and ethyl-levulinate [244–249], no experimental and kinetic

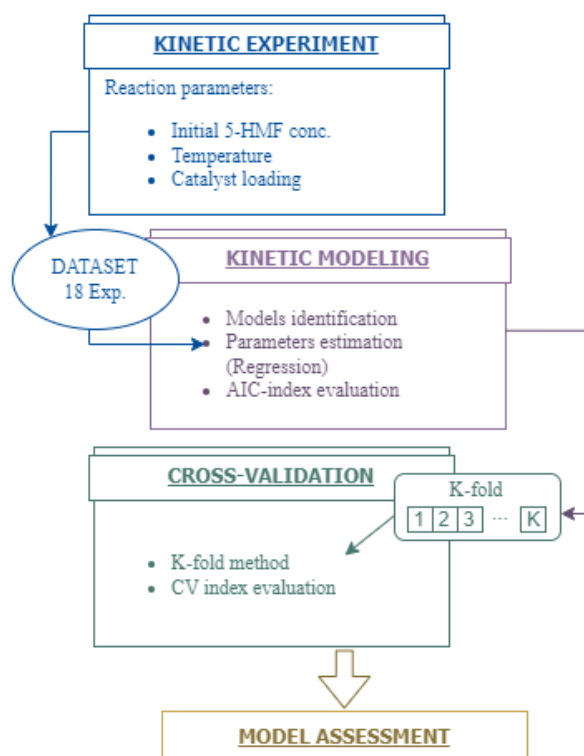


Fig. 16: Methodology adopted in Chapter 3

investigation were developed for the production of butyl levulinate from 5-HMF on a heterogeneous catalyst, and including the kinetics of humins formation.

To attain this objective, the research was organized involving the following steps as in Fig. 16:

- Experimental investigation of the solvolysis of 5-HMF in butanol-GVL as solvent and catalyzed by Amberlite IR-120; evaluating the effects of reaction parameters such as temperature, catalyst loading, and initial concentration of 5-HMF.
- Kinetic modelling step, involving:
  - the evaluation of different kinetic models including possible alternative reaction mechanisms and kinetics of humins formation.
  - regression phase using the dataset obtained through the kinetic experiments to estimate the kinetic parameters of the different models.
  - Evaluation of the Akaike information criterion (*AIC*) index.
- Validation stage:
  - Cross-validation through the K-fold method and evaluation of the  $CV_{(k)}$  indicator.
- Model assessment stage:
  - Based on the different indicators evaluated (*AIC*, *CV*, etc.) the best performing model is identified.

## 3.2 Experimental and Analytical set up

### 3.2.1 Chemicals

5-(hydroxymethyl)furfural (5-HMF, 99% purity), 5-(ethoxymethyl)furfural (EMF, 97% purity), levulinic acid (LA,  $\geq 97\%$  purity), formic acid (FA,  $\geq 95\%$  purity) and  $\gamma$ -valerolactone ( $\geq 99\%$  purity) were purchased from Sigma-Aldrich. 1-Butanol (BuOH,  $\geq 99.5\%$  purity), butyl levulinate (BL,  $\geq 98\%$  purity), butyl formate (BF,  $\geq 97\%$  purity) and acetone ( $\geq 99.9\%$  purity) from VWR chemicals. Amberlite IR120 H<sup>+</sup> form (ion-exchange resin, harmonic mean size: 0.620 to 0.830 mm) commercial catalyst was provided by Acros Organics. Nitrogen gas (N<sub>2</sub> purity > 99.999 vol%) came from Linde. All chemicals were employed without further purification.

### 3.2.2 Analytical methods

In the investigation of solvolysis by 5-HMF, the analytical method presented in section 2.2.2 Analytical methods can be reduced to the use of the gas chromatography apparatus alone, all chemical species of the system being compatible with a gas-phase analysis.

Therefore, diluted in acetone by a factor of 10, the samples are analyzed in the Bruker Scion 456-GC gas chromatograph, equipped with an Agilent VF-1701ms column and a flame ionization detector (FID), with the same characteristics, also in terms of programming the heating ramp, as described above. As previously mentioned, the analysis involves daily calibration curves using standard solutions of pure chemicals, and the corresponding ethyl ether 5-EMF was used as the standard for the calibration of 5-BMF. Each sample was analyzed three times.

### 3.2.3 Kinetic experiments set-up

As shown in Fig. 8: Setup of the autoclave for solvolysis experiment, the kinetic experiments were conducted in a 300 mL stainless steel Parr batch reactor equipped with an electric heating system and a central impeller to ensure uniform mixing of the reaction mixture. The system is supplied with nitrogen to pressurize to 20 bar and limit the gas-liquid partition of the liquid phase. As shown in Table 11, the experiments were conducted considering an initial mass loading of 5-HMF ranging from 1.6 to 7 g, and catalyst up to 15.3 g, with a fixed volume of butanol-GVL solvent phase at a ratio of 70:30 wt%. In addition to the solvolysis experiments of 5-HMF, many experiments (Experiments from 10 to 16 outlined in Table 11), on the esterification of levulinic acid and the levulinic acid-formic acid mixture (initial concentration range 0.05 - 0.5 mol/L) were carried out in the same reaction system. As previously shown by the studies on limiting phenomena to the transfer of matter with the catalytic system in question, although analyzed for the case of fructose solvation, the rotation speed was set at 800 rpm, to

limit the limiting phenomena to external and internal mass transfer, using the particle size distribution of the native catalyst. Amberlite IR120 was pre-treated as described above and fresh catalyst was used for each kinetic experiment (Table 11). The reusability of the catalyst was also tested by treating the used catalyst again, as described above, before reusing it in a second run. In the kinetic runs, the temperature parameter was set between 80 and 115 °C, without exceeding 120 °C, as the sulfonic active sites of Amberlite IR-120 can leach at higher temperatures. In all experiments, the initial load of 5-HMF (or LA, LA-FA mixture) is initially solubilized in the solvent phase and an initial sample taken at this stage to test the initial concentration then added to the reactor. Once the reactor was charged, the heating ramp of the system was recorded and several intermediate samples taken during this phase to monitor the catalytic action before the set point temperature was reached. Once the set point temperature was reached to study the kinetics isothermally, one sample is taken and subsequent samples at 5 minutes, 30 minutes and then hourly up to 7 hours.

Table 11: Experimental matrix

Exp.	Temp. °C	m 5-HMF <sub>0</sub> g	mLA <sub>0</sub> g	mFA <sub>0</sub> g	mBuOH <sub>0</sub> g	mGVL <sub>0</sub> g	[5-HMF] <sub>0</sub> mol.L <sup>-1</sup>	[LA] <sub>0</sub> mol.L <sup>-1</sup>	[FA] <sub>0</sub> mol.L <sup>-1</sup>	[GVL] <sub>0</sub> mol.L <sup>-1</sup>	[BuOH] <sub>0</sub> mol.L <sup>-1</sup>	m <sub>dried</sub> cat. g
1	110	1.6	0.00	0.0	85.2	36.5	0.08	0.00	0.00	2.40	7.57	4.9
2	100	1.6	0.00	0.0	85.2	36.5	0.08	0.00	0.0	2.40	7.57	4.9
3	90	1.6	0.00	0.0	85.2	36.5	0.08	0.00	0.00	2.40	7.57	4.9
4	110	7.0	0.00	0.0	85.2	36.5	0.31	0.00	0.00	2.31	7.27	8.0
5	100	3.0	0.00	0.0	85.2	36.5	0.16	0.00	0.00	2.38	7.49	9.2
6	100	3.0	0.00	0.0	85.2	36.5	0.15	0.00	0.00	2.38	7.49	4.9
7	80	3.0	0.00	0.0	85.2	36.5	0.15	0.00	0.00	2.38	7.49	4.9
8	85	7.0	0.00	0.0	85.2	36.5	0.32	0.00	0.00	2.31	7.27	8.0
9	105	3.0	0.00	0.0	85.2	36.5	0.14	0.0	0.00	2.38	7.49	10.0
10	80	0.0	8.13	0.0	80.9	34.7	0.00	0.51	0.00	2.28	7.17	4.0
11	95	0.0	8.13	0.0	80.9	34.7	0.00	0.51	0.00	2.28	7.17	4.0
12	110	0.0	8.13	0.0	80.9	34.7	0.00	0.51	0.00	2.28	7.17	3.0
13	80	0.0	1.64	0.63	84.0	36.0	0.00	0.10	0.09	2.39	7.53	2.0
14	110	0.0	1.63	0.64	84.0	36.0	0.00	0.10	0.09	2.39	7.53	2.0
15	95	0.0	1.00	0.40	84.5	36.3	0.00	0.06	0.06	2.40	7.57	6.0
16	100	0.0	1.63	0.64	84.0	36.0	0.00	0.12	0.09	2.39	7.53	8.0
17	100	5.0	0.00	0.0	85.2	36.5	0.28	0.00	0.00	2.34	7.37	15.3
18	115	3.0	0.00	0.0	85.2	36.5	0.17	0.00	0.00	2.37	7.49	10.0
19	100	3.0	0.00	0.0	85.2	36.5	0.17	0.00	0.00	2.37	7.49	1.0
20	100	3.0	0.00	0.0	85.2	36.5	0.17	0.00	0.00	2.37	7.49	0.0

### 3.3 Experimental results and discussion

The solvolysis of 5-HMF to n-butyl levulinate was investigated over a wide range of reaction parameters: temperature, catalyst loading, and initial furan concentrations. The effects of these parameters were analyzed by comparing the experimental results of several experiments as shown in the following figures. The concentration profile of the different main species over time were followed, with

the exception of formic acid (FA), normalized to the initial 5-HMF concentration,  $\left(\frac{[5-HMF]}{[5-HMF]_0}, \frac{[LA]}{[5-HMF]_0}, \frac{[5-BMF]}{[5-HMF]_0}, \frac{[BL]}{[5-HMF]_0}, \frac{[BF]}{[5-HMF]_0}\right)$ .

### 3.3.1 Effect of temperature

The effect of temperature on kinetics was investigated by comparing experiments 1, 2 and 3, in which the reaction temperature was varied from 90 to 110 °C under the same processing conditions. From Fig. 17, it is evident that the kinetics depend on the reaction temperature. As the temperature increases, the kinetics are faster, increasing 5-BMF production and consumption in BL and BF, which exhibit very similar kinetics (Fig. 17D-E). On the other hand, the production of the LA intermediate occurs at very low concentration values (Fig. 17B), due to the absence or reduced presence of water in the reaction medium, which therefore disfavors the hydration step of 5-HMF compared to the etherification reaction

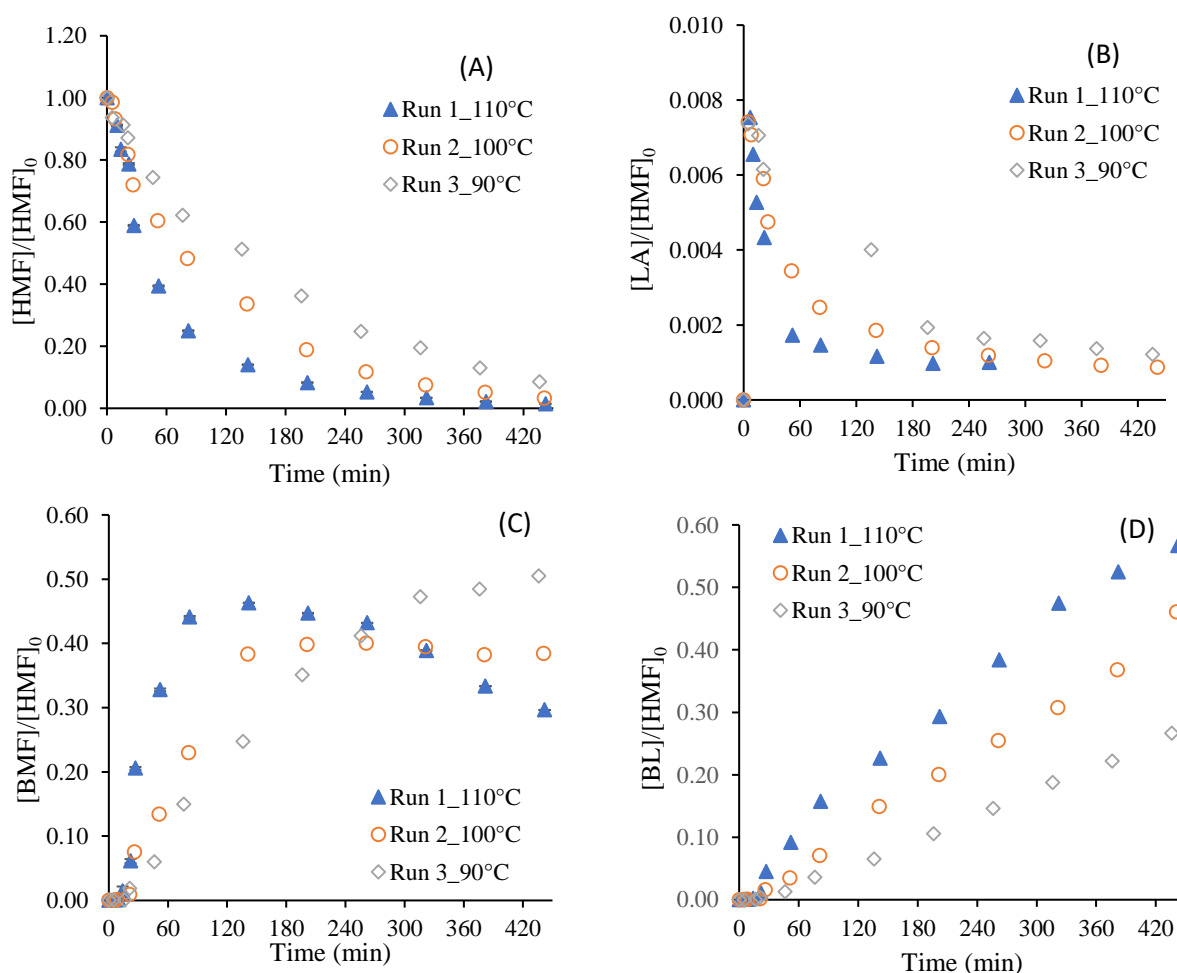


Fig. 17: Effect of temperature on the kinetics of 5-HMF solvolysis: (A) 5-HMF, (B) LA, (C) 5-BMF, (D) BL, (E) BF.

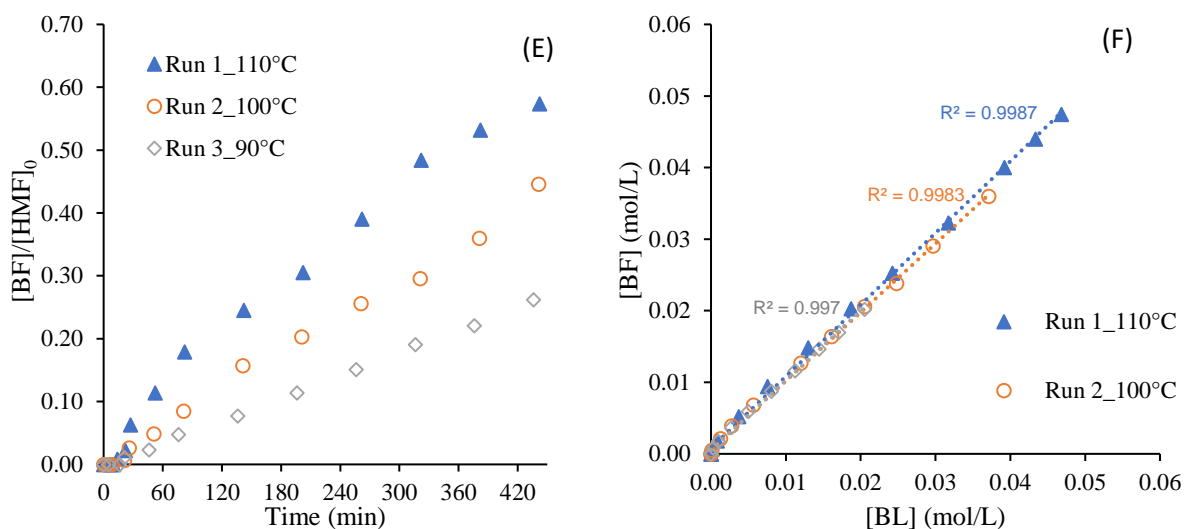


Fig. 17: Effect of temperature on the kinetics of 5-HMF solvolysis: (A) 5-HMF, (B) LA, (C) 5-BMF, (D) BL, (E) BF.

with butanol. Regarding degradation, the mass balance on the initial 5-HMF concentration shows a loss in moles of 5-HMF presumably at humins, which varies from 15 to 20% and is favored at higher temperatures.

### 3.3.2 Effect of catalyst loading

The effect of catalyst loading was evaluated by considering experiments 5, 6, 19 and 20. From Fig. 18, it can be seen that the increase up to 4.9 grams in catalyst loading results in an increase in the reaction kinetics in terms of 5-HMF conversion and BL production. The further increase in mass to 9.2 g, has no significant effect on the kinetics of the components.

Blank experiment 20 in the absence of catalyst shows that 5-HMF undergoes non-catalyzed degradation kinetics in the first hour of the reaction and then slows down. These two kinetic regimes could be linked to the production of humins and 5-BMF, which is detected albeit in reduced concentrations. This production could be initiated by a small amount of protons or by the production of LA, which although low is present in the initial phase of the reaction. Fig. 18 shows that protons catalyze each step of the reaction. Catalyst loading does not affect the equimolar production of the BL and BF, as shown in Fig. 18(F).

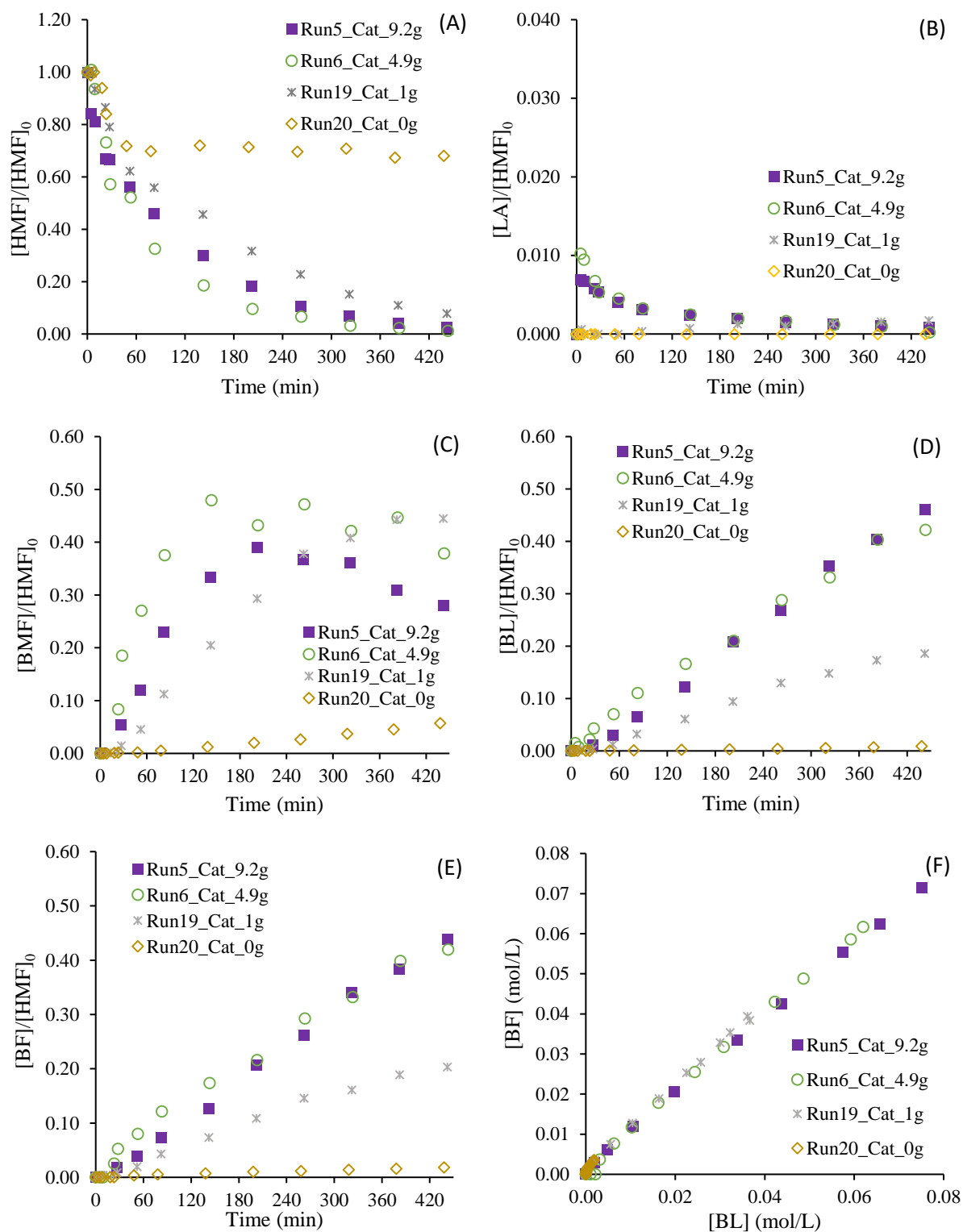


Fig. 18: Effect of catalyst loading on the kinetics of 5-HMF solvolysis: (A) 5-HMF, (B) LA, (C) 5-BMF, (D) BL, (E) BF

### 3.3.3 Effect of 5-HMF loading

The effect of 5-HMF loading was evaluated by comparing experiments 2, 5 and 17 in Fig. 19. In these experiments, the initial loading of 5-HMF was increased with the same temperature and catalytic



activity, expressed as  $n_{\text{HMF0}}/n_{\text{H}^+}$  molar ratio. Fig. 19A shows that the kinetics of 5-HMF consumption is slightly faster for high 5-HMF loading, i.e. experiment 17. Interestingly, this higher amount of 5-HMF leads to a higher production of LA (Fig. 19B), which is usually low; this result in terms of LA production can also be related to the reduced linearity/parity between BL and BF concentrations in Experiment 17 (Fig. 19E). Given the stoichiometry, at higher LA concentrations should correspond higher FA concentrations, but the volatility of the latter is higher than LA. Therefore, the lower concentration of FA in the liquid phase limits the esterification to BF, compared to BL from LA. The increase in 5-HMF loading also leads to an increase in 5-BMF concentration, and consequently to an increase in BL production. as in experiment 17. Also, for these experiments, the mass balance on the initial 5-HMF concentration shows a loss in moles of reactant, potentially due to a secondary degradation reaction at humins.

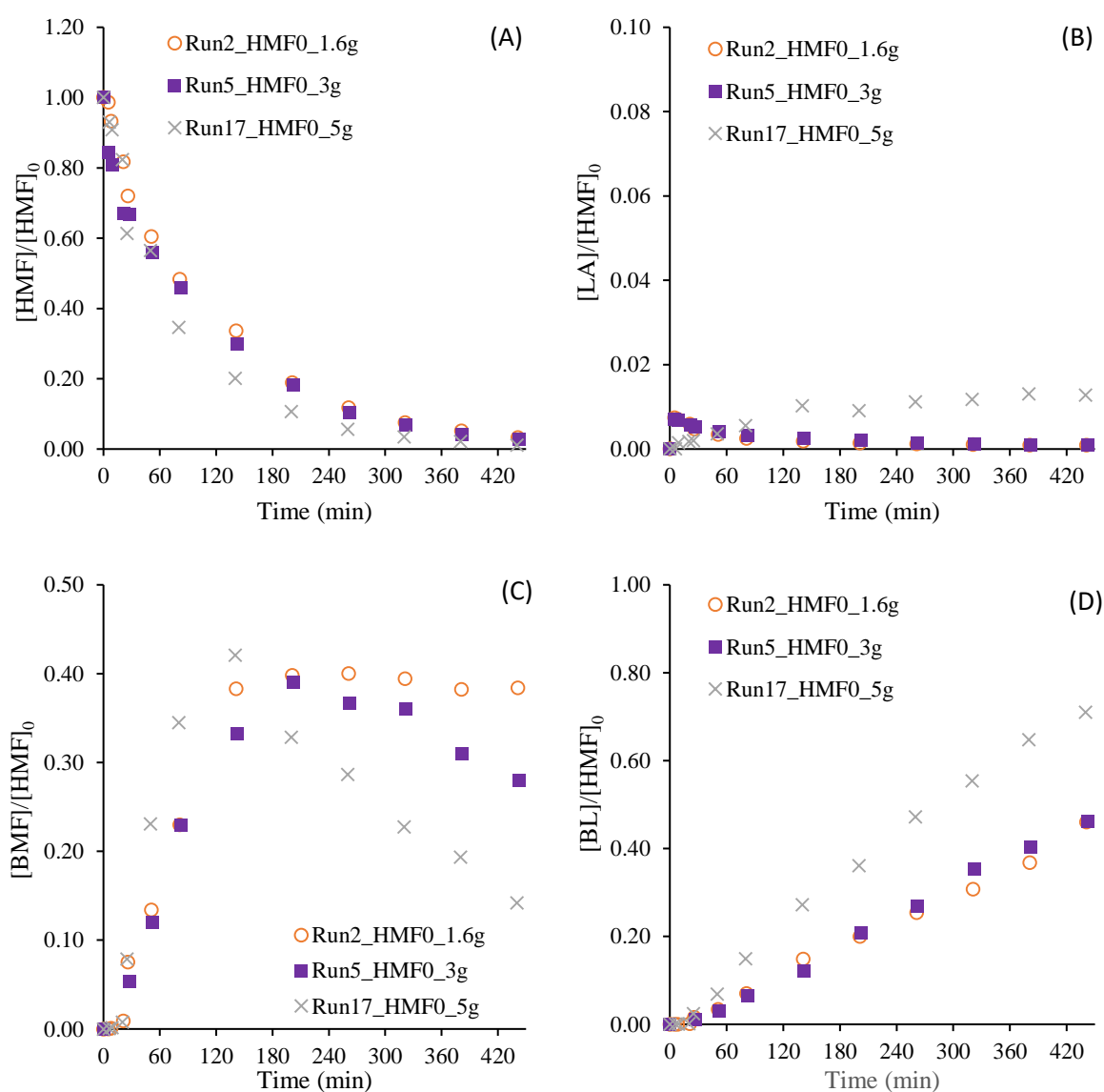


Fig. 19: Effect of 5-HMF loading on the kinetics of solvolysis: (A) 5-HMF, (B) LA, (C) 5-BMF, (D) BL, (E) BF

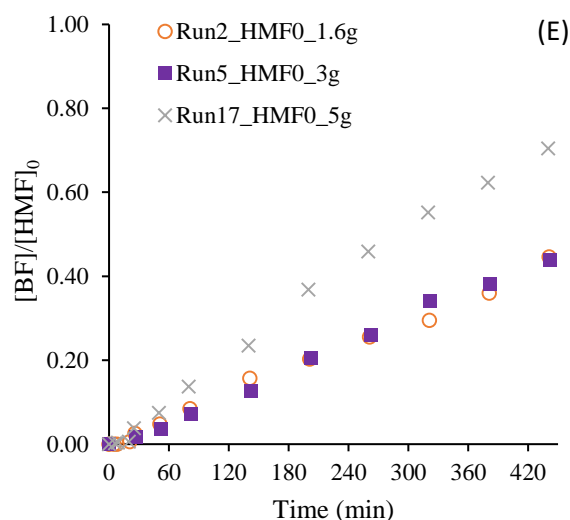


Fig. 19: Effect of 5-HMF loading on the kinetics of solvolysis: (A) 5-HMF, (B) LA, (C) 5-BMF, (D) BL, (E) BF.

### 3.3.4 LA and FA esterification results

From the hydrolysis step of 5-HMF, LA and FA intermediates are produced. As shown by the analysis of the concentrations resulting from the previous experiments, the concentrations of these two species are very low and difficult to trace. To gain further insight into the esterification step, some independent esterification experiments were carried out from LA and FA or mixture of the two in the butanol-GVL solvent system. The esterification step was then evaluated as the reaction parameters changed. In Fig. 20, the concentration trends are shown with varying temperature, and it can be seen that under these conditions the esterification reactions can be considered irreversible, with complete or nearly complete conversion of the initial reactants. The kinetics of FA esterification is faster than that of LA, and under these operating conditions, increasing the temperature does not significantly affect the rate of FA esterification, while it has a more noticeable effect on that of LA.

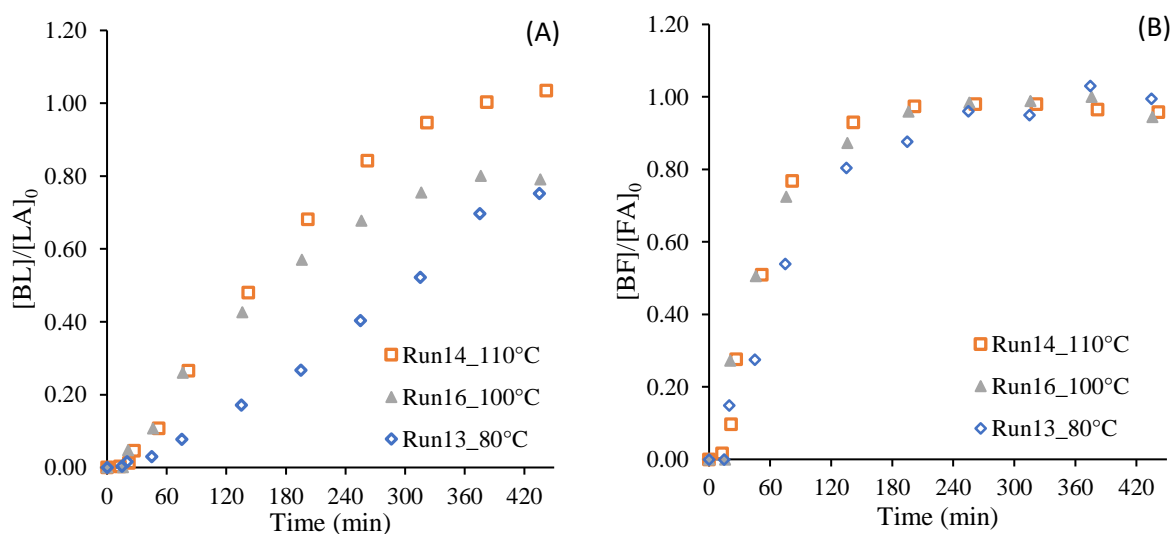


Fig. 20: Effect of temperature on LA and FA esterification kinetics.

### 3.3.5 Deactivation catalyst effect

The effect of possible catalyst deactivation was investigated by repeating an experiment under the same conditions but reusing the same catalyst. The catalyst used in experiment 6 was recovered by filtration from the reaction medium and retreated according to the catalyst treatment procedure described in the experimental set-up section. Fig. S1. 1 shows the kinetic profiles for each species in the two experiments. The evolutions of the normalized concentrations are very similar between the two experiments. The 5-BMF generation kinetics are slightly affected, in terms of maximum concentration. However, the production profile of the final BL product is similar for both experiments; thus, in the first approach, catalyst deactivation can be considered negligible.

### 3.3.6 Repeatability of kinetic experiments

To test the reliability of the experimental data, some experiments were repeated, such as experiments 1 and 6. For both experiments, it was observed that the concentration profiles are similar, with identical kinetics of reagent consumption and product production, as shown in Fig. S1. 2-3. The results thus demonstrate that the experimental procedure used in this study is reliable and repeatable, which is essential for estimating kinetic constants from experimental data.

## 3.4 Kinetic Modelling

The main mechanism of solvolysis of 5-HMF to levulinic acid and alkyl levulinate, and of monosaccharides in general, is still debated. The complexity of the investigation is increased by the presence of secondary degradation reactions to humins production, in which the hydroxyl group of 5-HMF plays an important role [73,250,251]. The solvent, especially GVL as an aprotic polar co-solvent,

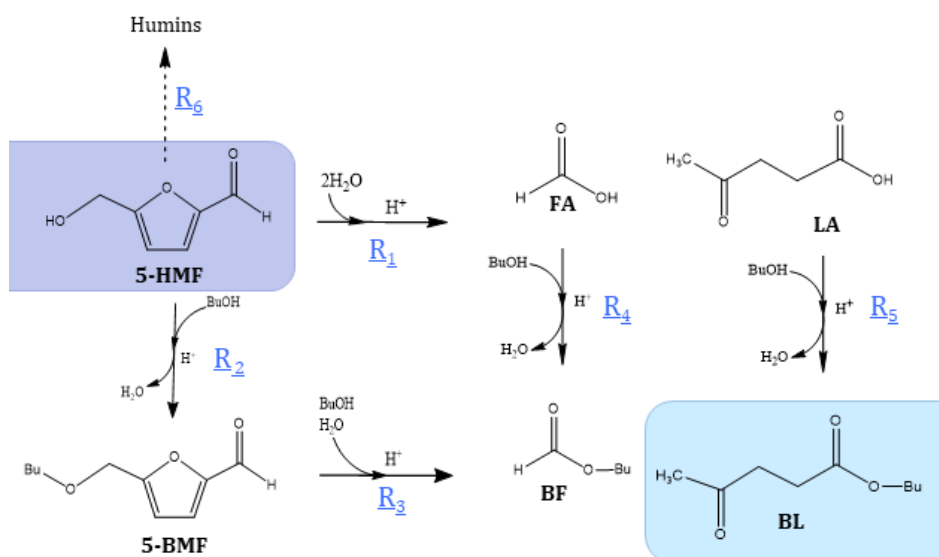


Fig. 21: Simplified 6-step reaction mechanism for the butanolysis of 5-HMF.

interferes with the kinetics and thermodynamics of this reaction system, and also with the physical effects of solubility of 5-HMF and monosaccharides as shown in the previous study, but also of humins which can therefore be solubilized in the reaction medium [252]. Online-analysis to trace the different intermediates of this reaction system is cumbersome, so some research groups have used DFT calculations to unravel some elementary steps and propose some reaction mechanisms [253–255].

In the work of Wang et al.[253], the mechanism of ethyl levulinate production was investigated in detail, outlining the potential presence of a kinetically limiting reaction intermediate on the alkyl levulinate production pathway from the 5-HMF ether intermediate; a similar analysis can be considered in parallel for the production of levulinic acid as also indicated by Nikbin et al. [254]. Based on this, with respect to the simplified reaction pathway shown in Fig. 21, we proposed another reaction scheme, illustrated in Fig. 22, in which the presence of an intermediate (named Int1) is assumed with a rate-determining step prior to the production of LA and BL, resulting from the release of formic acid and butyl formed and rearrangement of the cyclic structure of the furan molecules 5-HMF and 5-BMF, respectively.

Experimental analysis of the results shows that the esterification steps are irreversible, which is attributable to the reduced concentration of water in the reaction system. Likewise, the trend of almost complete consumption of 5-HMF and the absence of equilibrium states in the production of 5-BMF suggest that the etherification reaction is assumed to be irreversible.

Another possible secondary reaction suggested in the literature is the etherification of butanol to dibutyl ether in an acidic environment [256]; the low concentrations of this component, which is detected only in traces, allow this secondary reaction to be neglected.

For the production of humins from 5-HMF, some studies have expressed the reaction speed as a first-order function of the 5-HMF concentration. As the structure is complex, the production of humins is often indicated by a polymerization reaction system, and therefore the assumption of first-order kinetics may be incorrect. Consequently, second-order kinetics were also evaluated in this work.

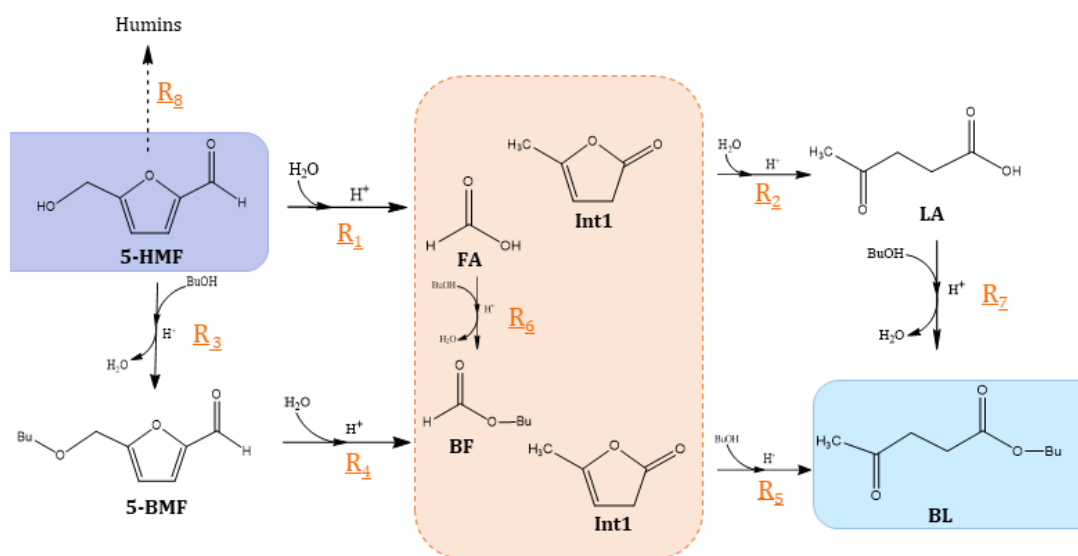


Fig. 22: 8-step reaction mechanism for the butanolysis of 5-HMF with Int1

All reaction steps were considered to be catalyzed by Amberlite IR-120 and the role of the protons of the resins was defined using a pseudo-homogeneous approach, in agreement with other kinetic studies that have shown good agreement with experimental data for ion exchange resins [257–259]. In other words, the protons of the sulfonic groups are considered to have a high degree of freedom. The adsorption and desorption phases on the sulfonic groups were not considered in the models developed. The acid catalytic effect due to LA was considered negligible due to the low concentration of LA. The proton concentration was calculated based on the acid capacity of Amberlite IR-120 [260].

$$[Prot.] = \frac{m_{dried\ catalyst} \cdot Capacity \left( \frac{mol\ of\ Proton}{m_{dried\ catalyst}} \right)}{V_{Reaction}} \quad Eq. 3. 1$$

The  $V_{Reaction}$  volume was evaluated by considering the total mass and the mixture density approximated by that of butanol at the corresponding temperature [261], and the effect of sampling was also taken into account.

### 3.4.1 Models

Based on the assumptions considered and the two reaction pathways proposed: the simplified pathway in Fig. 21 and the one with Int1 in Fig. 22; four models were developed based on the schemes and considering first- and second-order for the production rate of humins from 5-HMF.

#### 3.4.1.1 Model 1

The first model considers the simplified route shown in Fig. 21; the reaction rates of the individual steps are expressed as dependent on the first order of the concentration of 5-HMF, intermediates and butanol, and the production of humins is also expressed dependent on the first order. The reaction rates are indicated as follows:

$$R_1 = k_1 \cdot [5 - HMF] \cdot [Prot.] \quad Eq. 3. 2$$

$$R_2 = k_2 \cdot [5 - HMF] \cdot [BuOH] \cdot [Prot.] \quad Eq. 3. 3$$

$$R_3 = k_3 \cdot [5 - BMF] \cdot [BuOH] \cdot [Prot.] \quad Eq. 3. 4$$

$$R_4 = k_4 \cdot [LA] \cdot [BuOH] \cdot [Prot.] \quad Eq. 3. 5$$

$$R_5 = k_5 \cdot [FA] \cdot [BuOH] \cdot [Prot.] \quad Eq. 3. 6$$

$$R_6 = k_6 \cdot [5 - HMF] \cdot [Prot.] \quad Eq. 3. 7$$

The water concentration was not included directly in the expressions due to low concentrations and difficulties in quantification, which is why it was incorporated into the rate constant.

The batch reactor was assumed to be ideal, and therefore the material balances can be expressed as follows:

$$\frac{d[5 - HMF]}{dt} = -R_1 - R_2 - R_6 \quad \text{Eq. 3. 8}$$

$$\frac{d[5 - BMF]}{dt} = R_2 - R_3 \quad \text{Eq. 3. 9}$$

$$\frac{d[LA]}{dt} = R_1 - R_5 \quad \text{Eq. 3. 10}$$

$$\frac{d[BL]}{dt} = R_3 + R_5 \quad \text{Eq. 3. 11}$$

$$\frac{d[BuOH]}{dt} = -R_2 - R_3 - R_4 - R_5 \quad \text{Eq. 3. 12}$$

$$\frac{d[FA]}{dt} = R_1 - R_4 \quad \text{Eq. 3. 13}$$

$$\frac{d[BF]}{dt} = R_3 + R_4 \quad \text{Eq. 3. 14}$$

$$\frac{d[Humins]}{dt} = R_6 \quad \text{Eq. 3. 15}$$

### 3.4.1.2 Model 2

In model 2, humins formation was expressed with a second-order relation to the concentration of 5-HMF; compared to model 1, it differs only in the expression of  $R_6$ , and the material balance for 5-HMF is modified as follows:

$$R_6 = k_6 \cdot [5 - HMF]^2 \cdot [Prot.] \quad \text{Eq. 3. 16}$$

$$\frac{d[5 - HMF]}{dt} = -R_1 - R_2 - 2 \cdot R_6 \quad \text{Eq. 3. 17}$$

### 3.4.1.3 Model 3

In model 3, the more complex scheme considered in Fig. 22 is assumed; including *Int-1*, each phase has been considered as elementary, so the reaction rates can be expressed as follows:

$$R_1 = k_1 \cdot [5 - HMF] \cdot [Prot.] \quad \text{Eq. 3. 18}$$

$$R_2 = k_2 \cdot [INT1] \cdot [Prot.] \quad \text{Eq. 3. 19}$$

$$R_3 = k_3 \cdot [5 - HMF] \cdot [BuOH] \cdot [Prot.] \quad \text{Eq. 3. 20}$$

$$R_4 = k_4 \cdot [5 - BMF] \cdot [BuOH] \cdot [Prot.] \quad \text{Eq. 3. 21}$$

$$R_5 = k_5 \cdot [INT1] \cdot [BuOH] \cdot [Prot.] \quad \text{Eq. 3. 22}$$

$$R_6 = k_6 \cdot [FA] \cdot [BuOH] \cdot [Prot.] \quad \text{Eq. 3. 23}$$

$$R_7 = k_7 \cdot [LA] \cdot [BuOH] \cdot [Prot.] \quad \text{Eq. 3. 24}$$

$$R_8 = k_8 \cdot [5 - HMF] \cdot [Prot.] \quad \text{Eq. 3. 25}$$

The degradation of 5-HMF into humins was assumed to be of first order.

Material balances can be derived as:

$$\frac{d[5 - HMF]}{dt} = -R_1 - R_3 - R_8 \quad \text{Eq. 3. 26}$$

$$\frac{d[5 - BMF]}{dt} = R_3 - R_4 \quad \text{Eq. 3. 27}$$

$$\frac{d[INT1]}{dt} = R_1 - R_2 + R_4 - R_5 \quad \text{Eq. 3. 28}$$

$$\frac{d[LA]}{dt} = R_2 - R_7 \quad \text{Eq. 3. 29}$$

$$\frac{d[BL]}{dt} = R_5 + R_7 \quad \text{Eq. 3. 30}$$

$$\frac{d[BuOH]}{dt} = -R_3 - R_5 - R_6 - R_7 \quad \text{Eq. 3. 31}$$

$$\frac{d[FA]}{dt} = R_1 - R_6 \quad \text{Eq. 3. 32}$$

$$\frac{d[BF]}{dt} = R_4 + R_6 \quad \text{Eq. 3. 33}$$

$$\frac{d[Humins]}{dt} = R_8 \quad \text{Eq. 3. 34}$$

#### 3.4.1.4 Model 4

With respect to Model 3, Model 4 considers the R8 reaction to produce humins as second-order with respect to the concentration of 5-HMF and material balance for 5-HMF can be expressed as follows:

$$R_8 = k_8 \cdot [5 - HMF]^2 \cdot [Prot.] \quad \text{Eq. 3. 35}$$

$$\frac{d[5 - HMF]}{dt} = -R_1 - R_3 - 2 \cdot R_8 \quad \text{Eq. 3. 36}$$

## 3.5 Modelling results and discussion

### 3.5.1 Regression methods and strategy

The simulation and parameter estimation steps of the considered models were performed with the commercial software Athena Visual Studio [262,263].

The parameter estimation in the regression step was performed using the experimental concentrations of 5-HMF, LA, 5-BMF, BF and BL as observables, and a Bayesian framework approach was used, which is more suitable than the non-linear least-squares method for multi-response systems of this type

[264,265]. The approach considered requires the determination of the determinant criterion for the minimization of the objective function [265].

The ordinary differential equations (ODEs) from the material balances were integrated by the DDAPLUS solver, which is included in the software, based on a modified Newton algorithm [266].

The minimization of the objective function (OF), determination of the credibility intervals for each estimated parameter and calculation of the normalized covariance of the parameters were instead performed by the GREGPLUS subroutine, which uses successive quadratic programming to minimize OF, defined in Eq. 3. 37 [263,264].

$$OF = (a + b + 1) \cdot \ln|v| \quad \text{Eq. 3. 37}$$

where, b is the number of responses, a is the number of response events and  $|v|$  is the determinant of the response covariance matrix. Each element of the covariance matrix is defined as:

$$v_{ij} = \sum_{u=1}^n [C_{iu} - \hat{C}_{iu}] \cdot [C_{ju} - \hat{C}_{ju}] \quad \text{Eq. 3. 38}$$

with  $C_{iu}$  the experimental concentration and  $\hat{C}_{iu}$  the estimated value for response  $i$  and event  $u$ ;  $C_{ju}$  the experimental concentration and  $\hat{C}_{ju}$  the estimated value for response  $j$  and event  $u$ .

The interval estimates for each parameter is calculated from the final quadratic expansion of the OF and the uncertainty of the estimated parameters was evaluated by the maximum marginal posterior density (HPD) calculated by the GREGPLUS package [263].

A modified Arrhenius equation was applied to express the temperature dependence of rate constants. The strong correlation between the pre-exponential factor and activation energy in the Arrhenius equation can increase the confidence intervals, and thus the uncertainty. To reduce this effect, the linearization of the Arrhenius equation should be applied as indicated by Buzzi-Ferraris et al. [267] and used as follows to express rate constants:

$$k(T) = \exp \left[ \ln \left( k(T_{ref}) \right) + \frac{E_a}{R \cdot T_{ref}} \cdot \left( 1 - \frac{T_{ref}}{T} \right) \right] \quad \text{Eq. 3. 39}$$

where  $T_{ref}$  is the reference temperature, which was the median of the different reaction temperatures.

Estimated the parameters of each model and analyzed the fit of the models to the experimental data by comparing the sum of the squared-residuals (SSR) and the parity plot determinant coefficient ( $R^2$ ) for each species participating in the reaction, the evaluation of the models was expanded by introducing a further criterion: The Akaike information criterion (AIC) [268,269]; this parameter is defined as follows:

$$AIC = N^\circ \text{ of indep. events} \cdot \ln \left( \frac{SSR}{N^\circ \text{ of indep. events}} \right) + 2 \cdot N^\circ \text{ of estim. parameters} \quad \text{Eq. 3. 40}$$



This criterion not only depends on SSR and the number of independent events (i.e. experimental concentration data) but also takes into account the number of parameters estimated by the model. The lower the AIC value, the higher the quality and robustness of the model.

In the modelling strategy, the kinetic results obtained experimentally from the experiments in Table 11 were therefore used in the regression step to estimate the kinetic parameters, also including the esterification experiments of LA and FA, carried out under the same operating conditions as the solvation experiments of 5-HMF, given the low concentrations of the two acids and in order to estimate the esterification steps more accurately, as estimating their rate constants only from BL and BF could lead to some estimation bias.

Preliminarily, it was observed that experiments 19 and 20 (Table 11) could not be modelled correctly as they are carried out in the absence and reduced concentration of catalyst, respectively. The presence of a reduced number of active sites results in a modified mechanism, so the two experiments were discarded at the modelling stage.

### 3.5.2 Regression models results

In Table 12, the results of the assessment among the different considered models are summarized by considering the SSR, AIC index and  $R^2$  parameter.

Table 12: Summary of modelling results of SSR and determinant coefficient

	Model 1	Model 2	Model 3	Model 4
<b>Number of Parameters</b>	12	12	16	16
<b>SSR-5-HMF</b>	0.11	0.12	0.11	0.12
<b>SSR-5-BMF</b>	0.08	0.09	0.08	0.09
<b>SSR-LA</b>	0.09	0.10	0.08	0.08
<b>SSR-BL</b>	0.21	0.20	0.21	0.20
<b>SSR-BF</b>	0.03	0.03	0.03	0.03
<b>SSR-overall</b>	0.52	0.54	0.51	0.53
<b>AIC</b>	-23435	-23312	-23495	-23378
<b><math>R^2_{5-HMF}</math></b>	0.97	0.96	0.97	0.96
<b><math>R^2_{5-BMF}</math></b>	0.89	0.89	0.90	0.89
<b><math>R^2_{LA}</math></b>	0.99	0.99	0.99	0.99
<b><math>R^2_{BL}</math></b>	0.97	0.97	0.97	0.97
<b><math>R^2_{BF}</math></b>	0.98	0.98	0.98	0.98

All the models showed a good fitting of the experimental data with comparable results in terms of SRR for each compound considered; among them, Model 3 shows a better overall fit to the experimental data with the lowest SSR value. Even by comparing the values of the AIC index, Model 3 shows the lowest value, indicating the model's greater robustness compared to the others.

Finally, comparing the values of the parity plot coefficients for each compound, it is observed that Model 3 has the highest overall coefficients for all species (Fig. S1. 4). In general, coefficient values greater than 0.95 are observed for almost all compounds, with a slightly lower coefficient for 5-BMF.

Table 13 shows the values of the estimated constants and credibility intervals for Model 3, while for the other models they are given in Table S1. 1-2.

Furthermore, in Table S1. 3, the estimated activation energies are compared with some corresponding data from the literature. Although a rigorous comparison is not possible, as the estimation is strongly influenced by the proposed model and the reaction conditions (e.g., solvent system and catalyst), the activation energies obtained from some of the proposed models are compared with the corresponding energies determined from kinetic investigations in the presence of sulfuric acid or ion-exchange resins as the acid catalyst.

For models 1 and 2, the credibility intervals evaluated have low values, indicating that the values were well estimated. The credibility intervals are slightly wider for the kinetic constants estimated for the hydrolysis reaction of 5-HMF and the esterification of FA, which can be attributed to the low concentration of LA and the impossibility of monitoring the FA concentration. Similarly, for models 3 and 4, the credibility intervals are wider for conversion steps of Int1 to LA and FA and to BL and BF. These wider credibility intervals are related to the fact that the concentration of Int1 was not monitored.

Table 13: Summary of kinetic constants and activation energies for each reaction step

Reaction rates		k ((L <sup>2</sup> min)/mol <sup>2</sup> )	k ((L min)/mol)	HPD%	Ea (kJ/mol)	HPD%
<b>R<sub>1</sub></b>	5-HMF → Int1 + FA	-	0.006	1.42	20.29	36.6
<b>R<sub>2</sub></b>	Int1 → LA	-	0.008	62.8	60.9	>100
<b>R<sub>7</sub></b>	LA → BL	0.001	-	0.81	85.6	6.67
<b>R<sub>6</sub></b>	FA → BF	0.003	-	0.47	23.4	11.14
<b>R<sub>3</sub></b>	5-HMF → 5-BMF	0.028	-	12.3	53.8	81.3
<b>R<sub>4</sub></b>	5-BMF → Int1 + BF	-	0.022	1.36	7.19	64.29
<b>R<sub>5</sub></b>	Int1 → BL	0.006	-	0.31	33.14	4.55
<b>R<sub>8</sub></b>	5-HMF → Humins	-	0.006	1.57	17.93	41.23

The plots of residues for each compound and model showed values randomly distributed with respect to the experimental and estimated concentrations (Fig. S1. 5-6), indicating that the rate equations were well identified. Analyzing the correlation matrices for the estimated parameters in the different models, the binary correlation coefficients are less than 0.95, indicating that the parameters are not correlated with each other (Table S1. 4 for Model 3).

Below are some examples of comparisons between experimental data and simulation profiles of Model 3 (Fig. 23-Fig. 26). In general, Model 3 offers a reliable simulation of the system under varying process parameters; for high initial concentration as Experiment 8 (Fig. 23), and low initial concentration of 5-HMF in Experiment 3 (Fig. 24), the model presents a good fit of the experimental data for each species

in the system, and especially for the product of interested BL. In Fig. 24, the model also describes the system under low temperature conditions (90°C) and on the other hand also under the highest temperature conditions in Fig. 25, where furthermore the fast kinetics allow a high conversion rate of the 5-BMF intermediate as well, in addition to the complete conversion of the reagent..

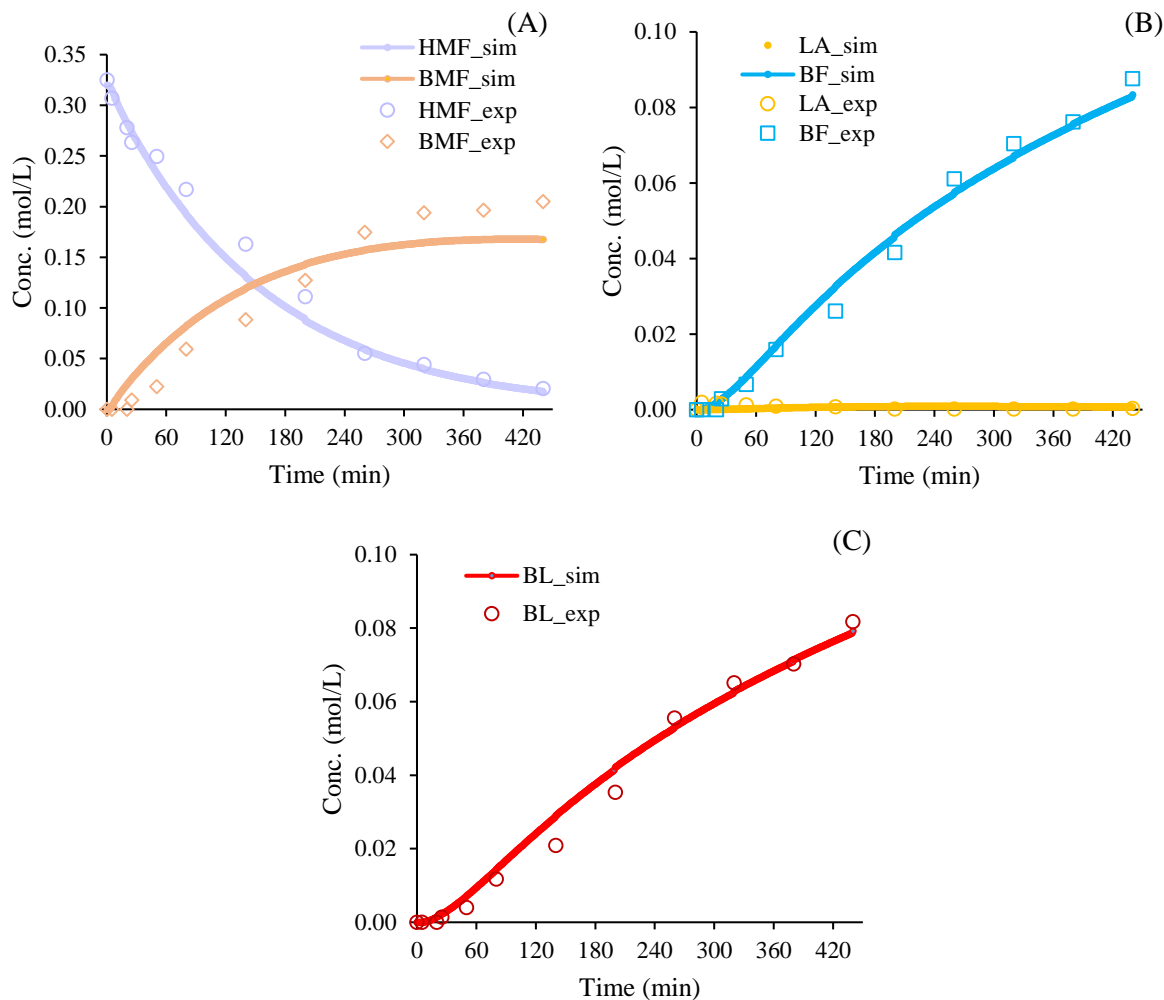
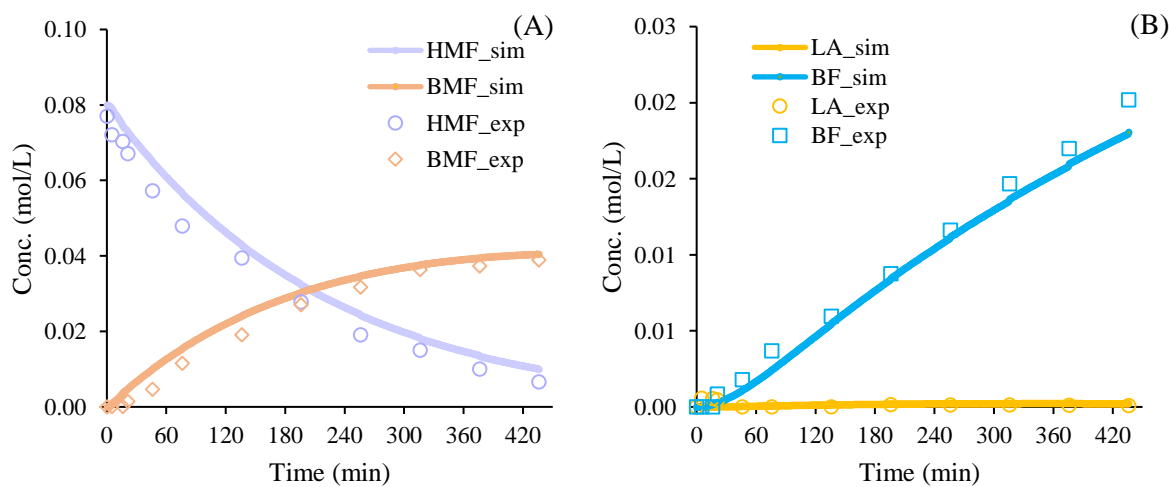


Fig. 23: Fit of Model 3 to experimental concentrations (Experiment 8); (A) 5-HMF, 5-BMF; (B) LA, BF; (C) BL



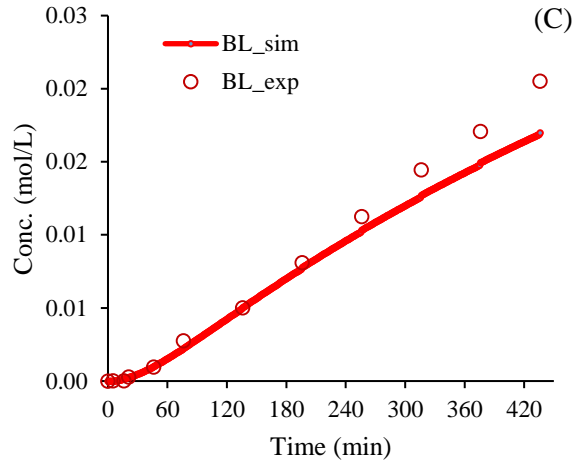


Fig. 24: Fit of Model 3 to experimental concentrations (Experiment 3); (A) 5-HMF, 5-BMF; (B) LA, BF; (C) BL

About the esterification reactions, the model has a slight uncertainty in estimating the concentration profile of BL, as in the simulation of Experiment 14 (Fig. 26), where the model slightly underestimates the experimental concentrations of BL and BF. Nevertheless, the esterification step is not the main route of BL production, and LA is generally present in very low concentrations.

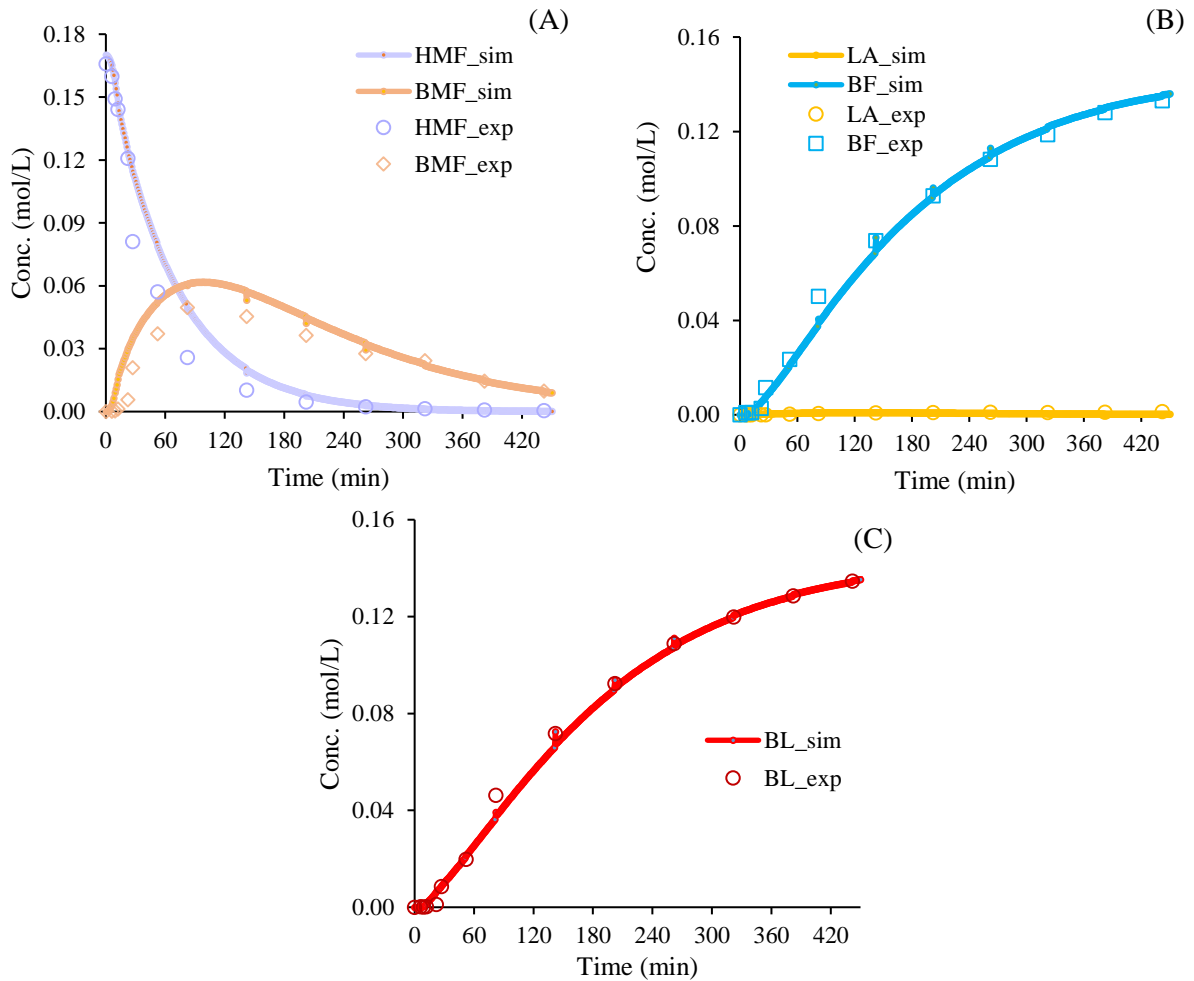


Fig. 25 Fit of Model 3 to experimental concentrations (Experiment 18); (A) 5-HMF, 5-BMF; (B) LA, BF; (C) BL

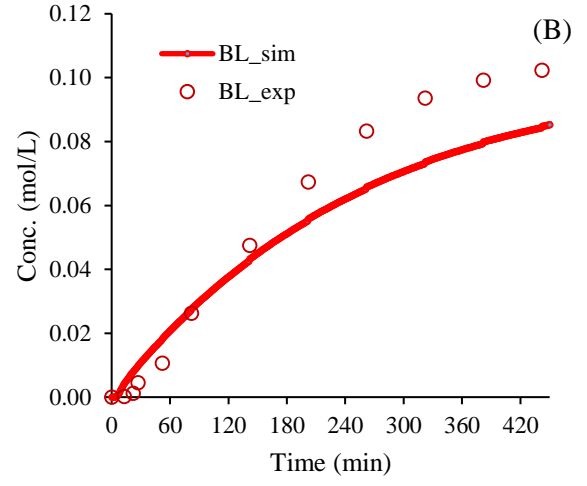
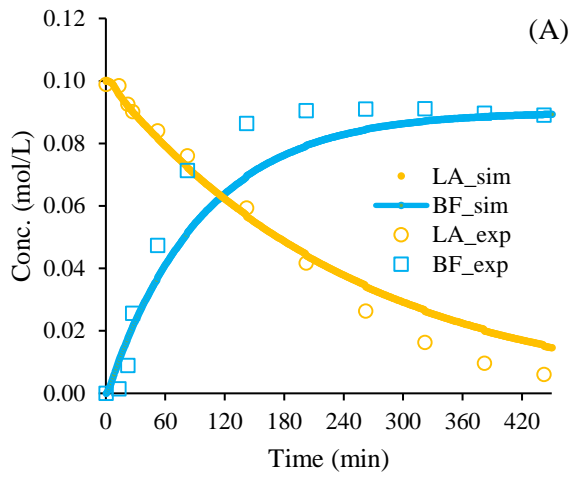


Fig. 26: Fit of Model 3 to experimental concentrations (Experiment 14)

### 3.5.3 Cross-Validation method and results

To finalize the evaluation of the different kinetic models, a validation phase is carried out, specifically a cross-validation by applying the K-fold method [270,271]. On the basis of this method, the 18 experiments used in the kinetic parameter estimation phase are randomly divided equally into 6 folds; in this case, the distribution is controlled to ensure that each fold contains at least one LA and FA esterification experiment, but no more than two. From the folds defined, the evaluation of 6 sets of folds is considered in which the training phase, i.e., regression is carried out on 5 folds and the test i.e., validation by means of the remaining fold, as the remaining fold changes, there are thus 6 different sets as shown in Table 14A-B.

Table 14: Distribution of experiments in 6 folds and evaluation of training and testing set of experiments

Fold	Experiment
<b>Fold 1</b>	12
	11
	5
<b>Fold 2</b>	6
	3
	10
<b>Fold 3</b>	7
	14
	8
<b>Fold 4</b>	16
	4
	17
<b>Fold 5</b>	1
	9
	13
<b>Fold 6</b>	15
	18
	2

(A)

Set	Training	Testing
<b>Set 1</b>	Folds 1-2-3-4-5	Fold 6
<b>Set 2</b>	Folds 6-1-2-3-4	Fold 5
<b>Set 3</b>	Folds 5-6-1-2-3	Fold 4
<b>Set 4</b>	Folds 4-5-6-1-2	Fold 3
<b>Set 5</b>	Folds 3-4-5-6-1	Fold 2
<b>Set 6</b>	Folds 2-3-4-5-6	Fold 1

(B)

For each set, the training folds were used to estimate the kinetic constants, such as  $\ln(k(T_{ref}))$  and  $\frac{E_a}{R \cdot T_{ref}}$ , for each model, and the remaining fold used for hold-out validation.

The prediction capability of each model is assessed through the index  $CV$  expressed as follows [271]:

$$CV_{(K)} = \frac{1}{K} \cdot \sum_{i=1}^K (Y_{i,experimental} - Y_{i,simulated})_i^2 \quad Eq. 3. 41$$

In this case,  $K=6$  and for each model, the square of the difference between the simulated value and the experimentally observed value of the validation experiment is evaluated for all fold sets, then summed

up and divided by the number of folds, thus giving an average representation of the system by the sets. The lower the value of this index, the greater the model's prediction capability.

Table 15: Results of CV index for cross-validation

	Model 1	Model 2	Model 3	Model 4
$CV_{(K)}$	0.130	0.144	0.126	0.248

The validation stage through the application of the K-fold method and the evaluation of the predictive capability index indicated Models 1 and 3 with the lowest index value as shown in Table 15; both models in which the degradation reaction of 5-HMF to humins is expressed through first-order kinetics with respect to the concentration of 5-HMF. Furthermore, Model 3, in which the kinetics consider a more complex reaction pathway with Int1, obtained the highest predictive capability, i.e., the lowest index value.

In general, models in which the humins formation step is expressed through second-order kinetics (Model 2 and 4) show high values of the comparison indices; higher *SSR* in the regression step, higher *AIC* index, and higher *CV*<sub>6</sub>, indicating a lower ability to describe and predict the reaction system behavior, as shown in Fig. 27 where each index has been internally normalized with respect to the maximum value. On the other hand, models 1 and 3 show lower index values; specifically, model 3 is the optimal model in terms of the indicators used in the assessment.

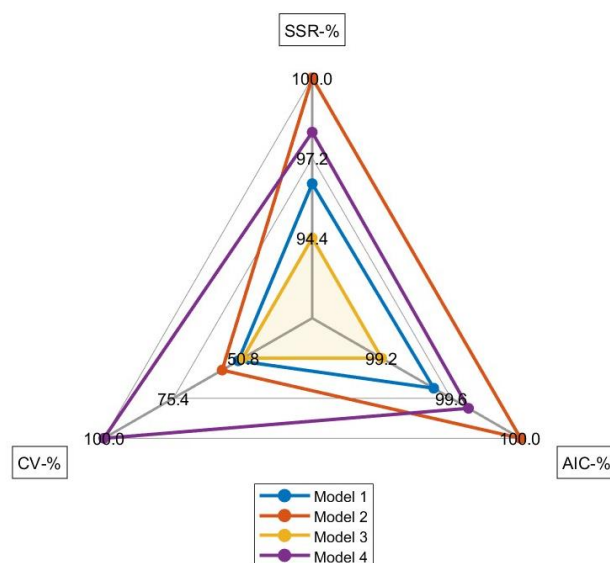


Fig. 27: overall graph of the 4 models against the 3 indices analyzed in the evaluation

### 3.6 Conclusions

In this chapter, the solvolysis reaction of 5-HMF to butyl levulinate was investigated in the organic phase with butanol as the main solvent and GVL as co-solvent, present at 30 wt%, and catalyzed by an ion exchange resin, Amberlite IR120. Preliminary observations showed experimentally that increasing the reaction temperature and catalyst loading increases the kinetics of all reaction steps. The intermediate esterification reactions of LA and FA were irreversible, as was the reaction of etherification of 5-HMF

to 5-BMF. In addition, the mass balance analysis revealed a loss in terms of 5-HMF moles, which can be attributed to the presence of secondary degradation reactions leading to the formation of humins.

The kinetics of the reaction system was analyzed, developing 4 different models, based on two main reaction paths: a more simplified one with 6 reaction steps; a second more complex one with the presence of an additional intermediate and 8 reaction steps. The models then consider two different orders to express the kinetics of secondary product formation, humins.

The proposed models were developed by estimating kinetic parameters and evaluated on the basis of probabilistic output and other determining criteria, such as the AIC criterion, and cross-validation steps using the K-fold method.

The evaluation showed that the system is best represented by models describing the formation of humins through a first-order reaction, and particularly among these, model 3, in which 8 reaction steps are considered was found to be the best performing model in terms of adherence to experimental data and predictive capacity of the reaction system. Model 3 is able to simulate the alcoholysis of 5-HMF for experiments with a 5-HMF load of 9.7 to 43.7 g/L, a dried Amberlite IR-120 load of 29.1 to 93.8 g/L and a reaction temperature of 80 to 115°C.

The developed and validated model constitutes a first in-depth analysis of the kinetics of acid solvolysis to alkyl levulinates, using platform molecules such as 5-HMF, and the starting point for extending the kinetic analysis to primary molecules such as sugar-monosaccharides and specifically to fructose as the starting molecule in this investigation for the production of butyl levulinate.



# CHAPTER 4 - In-depth kinetic modelling of butyl levulinate production from Fructose in High-Gravity condition

Part of this chapter is adapted from the post-print of the following article:

Di Menno Di Bucchianico, D.; Buvat, J.-C.; Mignot, M.; Casson Moreno, V.; Leveneur, S. Production of butyl levulinate from the solvolysis of high-gravity fructose over heterogeneous catalyst: In-depth kinetic modeling, *Chemical Engineering Journal*, 2023, 465, 142914.

Further permissions related to the material excerpted should be directed to the ScienceDirect. Copyright © 2023 Elsevier B.V. or its licensors or contributors. ScienceDirect® is a registered trademark of Elsevier B.V.

## 4.1 Introduction

The kinetic modelling of the solvolysis of 5-HMF to butyl levulinate was a first step towards a comprehensive kinetic analysis of the production of butyl levulinate from more complex biomass-derived platform molecules, such as monosaccharides. Among these, this analysis focused on the reactivity of fructose under acidic conditions, which due to its greater molecular instability, compared to other hexose monosaccharides such as glucose, results in higher conversion rates with promising yields to alkyl levulinate; although, this molecule is less abundant in nature.

The solvolysis of fructose to levulinic acid and alkyl levulinates has been investigated experimentally by several studies [65,66,70,72,73,84–87,272,273], but not as many investigations in the literature have explored the kinetics of the reaction system and defined suitable models for it. Indeed, most of the kinetic investigations have reported the conversion of fructose on homogeneous catalysts ( $\text{H}_2\text{SO}_4$ ,  $\text{HCl}$ , etc.) [238,274,275], and only a few have considered the use of heterogeneous catalysts [276]. Each case focusing on the kinetics of substitution of alkyl groups with reduced carbon number, such as methyl- for the production of methyl levulinate or ethyl- for EL, while there were no kinetic studies on major alkyl levulinates such as butyl levulinate.

Despite numerous advances in processes for the valorization of biomass and its derivatives such as monosaccharides, most of them are still limited to the academic level, without bridging the gap between laboratory and industrial scales, due to issues related to process efficiency, energy, waste minimization and product recovery [69]. New process optimization strategies should be implemented to reduce this gap; some of them point at increasing the concentration of the final product, as in the case of high gravity (HG) technologies [69,277,278]. In the high gravity approach, the initial load of feedstock is maximized, considering high initial substrate concentrations, to make the upgrading process industrially advantageous in terms of process economy and energy efficiency in the separation phase [69,279]. In fact, operating under high gravity conditions would result in higher concentrations of target products and thus lower separation costs and chemical consumption in the processing steps. However, higher concentrations can promote side reactions and the formation of undesirable by-products, as humins,

reducing target product yields and causing possible fouling and catalyst deactivation [280]. For these reasons, optimization of other process parameters is essential for high target product selectivity; such as the solvent system, as it can strongly influence the catalytic activity and selectivity of a target or intermediate product by protecting reactive functional groups from possible degradation reactions [44,129,228,281].

The solvent system defined so far in this study has shown benefits by using excess of butanol and the presence of GVL as co-solvent (30wt%); in terms of degradation of fructose to humins being reduced, potential effects of humins dissolution, increased selectivity towards BL, as well as faster dissolution of fructose in the alcoholic medium due to the presence of the green co-solvent GVL [II]. Consequently, it could play a key role in high-concentrated systems for the dissolution of fructose and other monosaccharides that generally exhibit reduced solubility in alcoholic solvents [II][237]. In the literature, a small number of studies have analyzed the dissolution kinetics of monosaccharides under dilution conditions [237], none of them integrating this kinetics into a scheme for the conversion of monosaccharides to high added-value molecules and especially under high concentration conditions.

Based on this overview, it can be concluded that the literature still lacks a detailed kinetic investigation of the conversion of fructose to butyl levulinate including the dissolution kinetics of the monosaccharide and the effect of high concentrations (HG conditions) of the latter on solvolysis kinetics.

The analysis developed in this chapter involves an experimental investigation of the solvolysis of fructose to butyl levulinate on Amberlite IR120 and in the butanol-GVL solvent system (70/30 wt%) considering high initial concentrations of fructose. In addition, the study involves the experimental analysis of the solubility of fructose in this specific solvent system so that in the second phase of the work an appropriate modelling of the solvolysis kinetics of fructose can be defined, including the dissolution kinetics of fructose and its degradation rates to humins.

Analyzing possible variations in the fructose conversion mechanism, several models are defined, developed in the regression phase for parameter estimation and subsequently validated using a hold-out validation approach. In modelling, 80% of the experiments were used for regression and parameter estimation, and the remaining 20% in the validation phase. Based then on the statistical output and the evaluation of the AIC index in the regression and validation phases, the most appropriate model is identified as shown in Fig. 28.

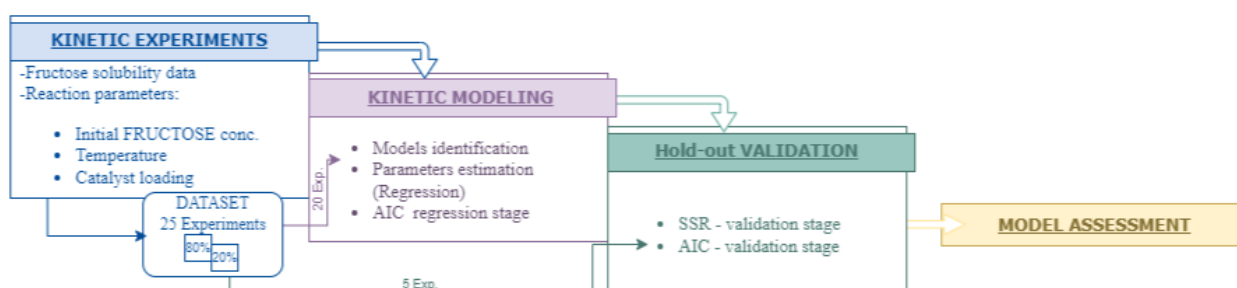


Fig. 28: Methodology approach used in Chapter 4

This analysis represents a deeper understanding of the kinetics of the fructose pathway to butyl levulinate, a promising biofuel and fuel additive, and thus a further step towards intensifying the conversion of sugar carbohydrates into high-value molecules and its scalability on a large scale.

## 4.2 Experimental and Analytical set up

### 4.2.1 Chemicals

Fructose ( $\geq 99\%$  purity), 5-(hydroxymethyl)furfural (5-HMF, 99% purity), 5-(ethoxymethyl)furfural (5-EMF, 97% purity) and  $\gamma$ -valerolactone ( $\geq 99\%$  purity) were purchased from Sigma-Aldrich. 1-Butanol (BuOH,  $\geq 99,5\%$  purity), butyl levulinate (BL,  $\geq 98\%$  purity), acetonitrile (ACN,  $\geq 99,9\%$  purity), butyl formate (BF,  $\geq 97\%$  purity) and acetone ( $\geq 99,9\%$  purity) from VWR chemicals. Amberlite IR120 ( $H^+$  form, ion-exchange resin) commercial catalyst provided by Acros Organics. Nitrogen gas ( $N_2$  purity  $> 99,999$  vol%) from Linde. All chemicals were employed without further purification.

### 4.2.2 Analytical methods

Extending the kinetic analysis on solvolysis to butyl levulinate from fructose, the analytical method applied follows that described in section 2.2.2 Analytical methods.

All reaction samples were analyzed by a combination of gas and liquid chromatography. The concentration of fructose was measured using an Agilent 1100 series HPLC equipped with a SUPELCOSIL LC-NH2 column, while the concentrations of reaction products, such as 5-HMF, LA, 5-(butoxymethyl)furfural (5-BMF), BL, BF and solvent systems (butanol and GVL) were analyzed with Bruker Scion 456-GC, equipped with an Agilent VF-1701ms column. Daily calibration curves were defined with standard solutions of pure commercial chemicals; Three injections were repeated for samples of each experiment in order to estimate the uncertainty, measured by the standard deviation, in the analytical measurement. The standard deviation resulted lower than 0.001 mol/L for each concentration determined.

Fructose conversion, products yields were defined as follows:

$$X_{FRUCT} (\%) = \left(1 - \frac{\text{mole of fructose after the reaction}}{\text{initial mole of fructose}}\right) \cdot 100 \quad \text{Eq. 4.1}$$

$$Y_i (\%) = \frac{\text{final mol of } i \text{ (} i = \text{BL, 5-HMF, 5-BMF, LA, BF)}}{\text{initial mole of fructose}} \cdot 100 \quad \text{Eq. 4.2}$$

### 4.2.3 Kinetic experiments set-up

The solvolysis experiments were performed in the same apparatus, described previously in Fig. 8: Setup of the autoclave for solvolysis experiment. With a volume of 300 mL, the stainless-steel batch reactor (Parr company) was used operating under isothermal and isobaric conditions; using nitrogen as inert gas to reach 20 bars, limiting the gas-liquid partition of the liquid volume. The presence of a gas entrainment impeller (diameter 2.5 cm) with a hollow shaft provided a uniform mixing of the mixture. As shown in

Table 16, the reactor was loaded with initial fructose mass varying between 1.6 and 28 g, catalyst mass up to 18.2 g. The solvent volume of butanol-GVL was kept constant among the experiments and by considering a fixed ratio of 70:30 wt%. The rotation speed was set to 800 rpm, since previous investigations on fructose solvolysis using the native particle size distribution of Amberlite IR120 ( $\geq 94\%$ , particle diameters between 300 and 1180  $\mu\text{m}$ ) in the same apparatus have shown the negligibility of external and internal mass transfer limitations. Amberlite IR120 was pre-treated as described above. In kinetic experiments, the temperature was varied between 80 and 115  $^{\circ}\text{C}$ , without exceeding 120  $^{\circ}\text{C}$ . Indeed, active sulfonic sites of the resins can leach and degrade for temperatures higher than 120 $^{\circ}\text{C}$ . During the heating phase, the temperature ramp of the system was recorded for each experiment and some samples were collected to monitor the kinetic reaction. Once the set temperature was reached, a sample was taken and the next ones at 5 min, 30 min, and then every hour for up to a maximum of 9 h. Table 16 shows the different initial conditions in the experiments to estimate the kinetic constants from different models, i.e. during the regression phase. To assess the reliability of the developed kinetic models, the models were validated using the hold-out method. The experiments shown in Table 17 were performed under average conditions, similar to those in Table 16, for the validation phase.

Table 16: Experimental matrix for kinetic solvolysis experiment from fructose to BL – Regression phase

Exp.	Temp. $^{\circ}\text{C}$	FRUCT <sub>0</sub>	[FRUCT] <sub>0</sub>	[FRUCT] <sub>0</sub>	[BuOH] <sub>0</sub>	[GVL] <sub>0</sub>	[LA] <sub>0</sub>	[FA] <sub>0</sub>	m <sub>dried cat.</sub> g
		g	g/L	mol/L					
1	110	14	100	0.56	6.9	2.2	-	-	11.8
2	90	21	150	0.83	6.5	2.1	-	-	13.2
3	100	14	100	0.56	6.9	2.2	-	-	11.8
4	110	28	200	1.11	6.2	2.0	-	-	11.8
5	110	21	150	0.83	6.5	2.1	-	-	8.9
6	110	14	100	0.56	6.9	2.2	-	-	5.9
7	115	14	100	0.56	6.9	2.2	-	-	11.8
8	110	14	100	0.56	6.9	2.2	-	-	17
9	105	21	150	0.83	6.5	2.1	-	-	13.2
10	110	1.6	11	0.06	7.6	2.4	-	-	4.9
11	100	1.6	11	0.06	7.6	2.4	-	-	4.9
12	90	1.6	11	0.06	7.6	2.4	-	-	4.9
13	110	4.5	32	0.18	7.4	2.3	-	-	13.7
14	110	15	107	0.59	6.8	2.2	-	-	13.7
15	80	28	200	1.11	6.2	2.0	-	-	17.3
16	95	17.5	125	0.69	6.7	2.1	-	-	9.8
17	95	17.5	125	0.69	6.7	2.1	0.29	-	9.8
18	95	17.5	125	0.69	6.7	2.1	-	0.25	9.8
19	105	24.5	175	0.97	6.7	2.1	-	-	18.2
20	105	24.5	175	0.97	6.4	2.0	0.22	0.24	18.2

Table 17: Experimental matrix for kinetic solvolysis experiment from fructose to BL – Validation phase

Exp.	Temp. °C	FRUCT <sub>0</sub> g	[FRUCT] <sub>0</sub> g/L	[FRUCT] <sub>0</sub>	[BuOH] <sub>0</sub>	[GVL] <sub>0</sub>	[LA] <sub>0</sub>	[FA] <sub>0</sub>	m <sub>dried cat.</sub> g
				mol/L					
V1	100	28	200	1.11	6.5	2.1	-	-	17.3
V2	100	3	20	0.12	6.5	2.1	-	-	4.9
V3	100	14	100	0.56	6.5	2.1	-	-	17
V4	85	17.5	125	0.69	6.8	2.2	-	-	14.7
V5	105	24.5	175	0.97	6.3	2.0	0.5	0.5	18.2

## 4.2.4 Solubility measurement

In order to investigate the kinetics of fructose dissolution in the selected solvent system. The solubility of fructose was measured, isothermally, in the solvent butanol/GVL (70/30 wt%), at different temperature values: 20, 40, 60, 80, 90, and 100 °C.

The measuring apparatus proposed consists of a glass round-bottomed flask sample (volume capacity of 250 ml) immersed in a silicone oil bath. The system is placed on a heating plate, equipped with a magnetic stirrer to ensure stirring of the bath and the fructose solution; a small magnetic stirring bar coated with polytetrafluoroethylene (PTFE) was inserted into the bath and the glass ampoule to ensure uniform temperature. In each measurement, the sample consists of an excess of fructose (200 g/L) suspended in the solvent at a fixed volume of 50 mL. The fructose was added to the solution once the system steadily reached the set-point temperature.

The flask was sealed with a silicone plug, which had two openings allowing the insertion of a temperature gauge and a sampling tube. Solubility measurements were carried out for more than 9 hours, sufficient to reach equilibrium and saturation of the solution, and during the measurement some samples were taken and analyzed, after filtration. Each measurement was repeated three times, as was the sample analysis. A schematic illustration of the proposed solubility measurement apparatus is shown in Fig. 29.

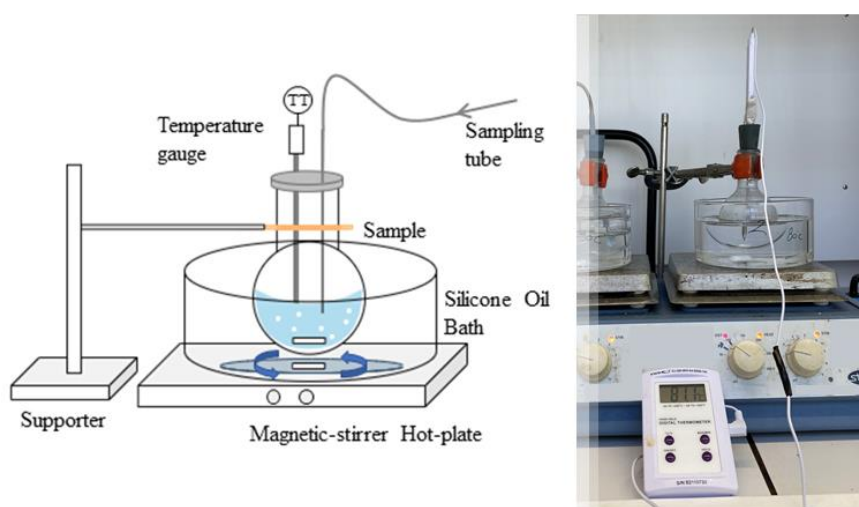


Fig. 29: Schematic illustration of an apparatus for solubility.

### 4.3 Experimental results and discussion

The solvolysis of fructose to n-butyl levulinate was studied in the butanol-GVL solvent system over a wide range of variation of reaction parameters: temperature, initial fructose concentrations and catalyst loading. The effect of these parameters was analyzed by comparing the experimental results of several experiments as shown in the following figures. The concentration profile of each main species (Fig. 9) over time were followed, with the exception of formic acid (FA), normalized to the initial fructose concentration,  $\left(\frac{[FRUCT]}{[FRUCT_0]}, \frac{[5-HMF]}{[FRUCT_0]}, \frac{[LA]}{[FRUCT_0]}, \frac{[5-BMF]}{[FRUCT_0]}, \frac{[BL]}{[FRUCT_0]}, \frac{[BF]}{[FRUCT_0]}\right)$ .

#### 4.3.1 Temperature effect

The effect of temperature on solvolysis kinetics was studied by comparing Experiments 1, 3 and 7 in which the temperature has been varied for the same initial load of fructose and catalyst (Fig. 30). Temperature influences the dissolution and conversion kinetics of fructose, increasing the conversion to intermediates and final products, BL and BF. The formation kinetics of butyl levulinate and formed butyl are very similar. From Fig. 30C it can be seen that the concentration of LA is an order of magnitude lower than that of the other intermediates; this result is also in line with the concentration trends obtained in the kinetic experiments of solvolysis of 5-HMF, suggesting the preferential pathway of 5-HMF to the 5-BMF intermediate in the presence of excess butanol. Above 100 °C, the kinetics are particularly rapid and consider total consumption of fructose and almost for 5-HMF, moderate levulinic acid production and conversion kinetics of 5-BMF to BL. The increase in temperature affects not only the conversion kinetics, but also the kinetics of degradation to humins, which in terms of loss of fructose moles, increases from 3.4% at 100°C to 5% at 115°C.

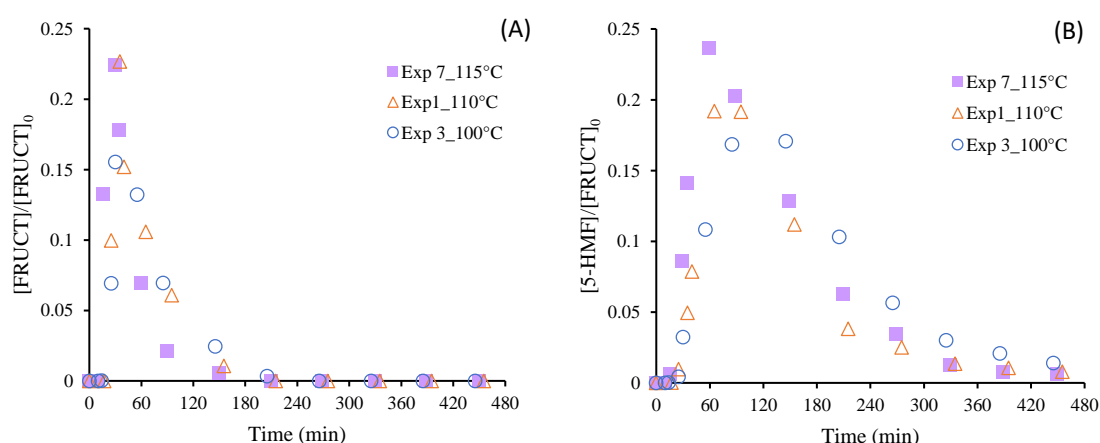


Fig. 30. Effect of temperature on normalized compounds trends on fructose initial concentration. Fructose (A), 5-HMF (B), LA (C), 5-BMF (D), BL (E), BF (F).

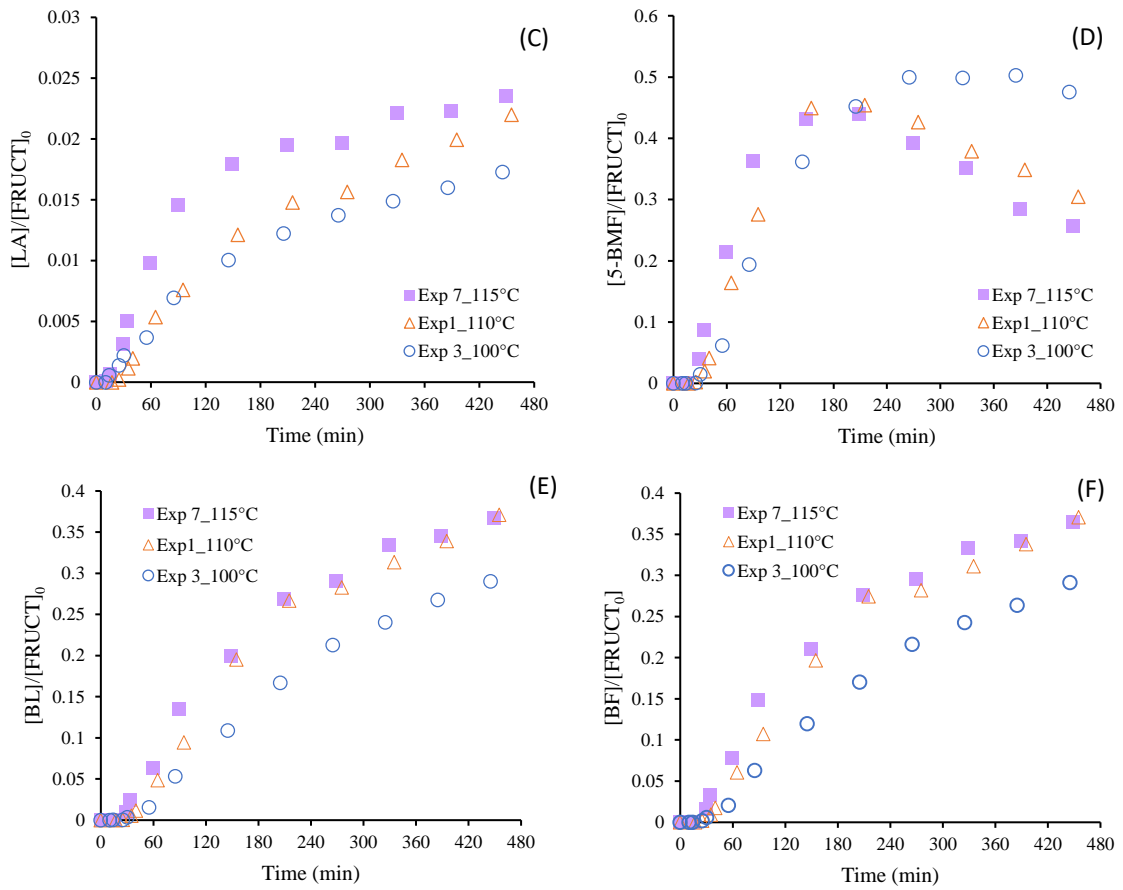


Fig. 30. Effect of temperature on normalized compounds trends on fructose initial concentration. Fructose (A), 5-HMF (B), LA (C), 5-BMF (D), BL (E), BF (F).



### 4.3.2 Catalyst loading

The effect of catalyst loading was assessed by comparing the results of experiments 1, 6 and 8 (Fig. 31). All other reaction conditions being equal, doubling the catalyst mass from 5.9 g to 11.8 g and then increasing it to 17 g results in a faster conversion of fructose; a lower maximum fructose concentration peak achieved in the higher catalyst loading is therefore observed due to the rapid conversion kinetics of fructose to 5-HMF. The formation and consumption kinetics of the intermediates, 5-HMF and 5-BMF, are also affected. For levulinic acid, although at lower concentrations, there is a distinct increase

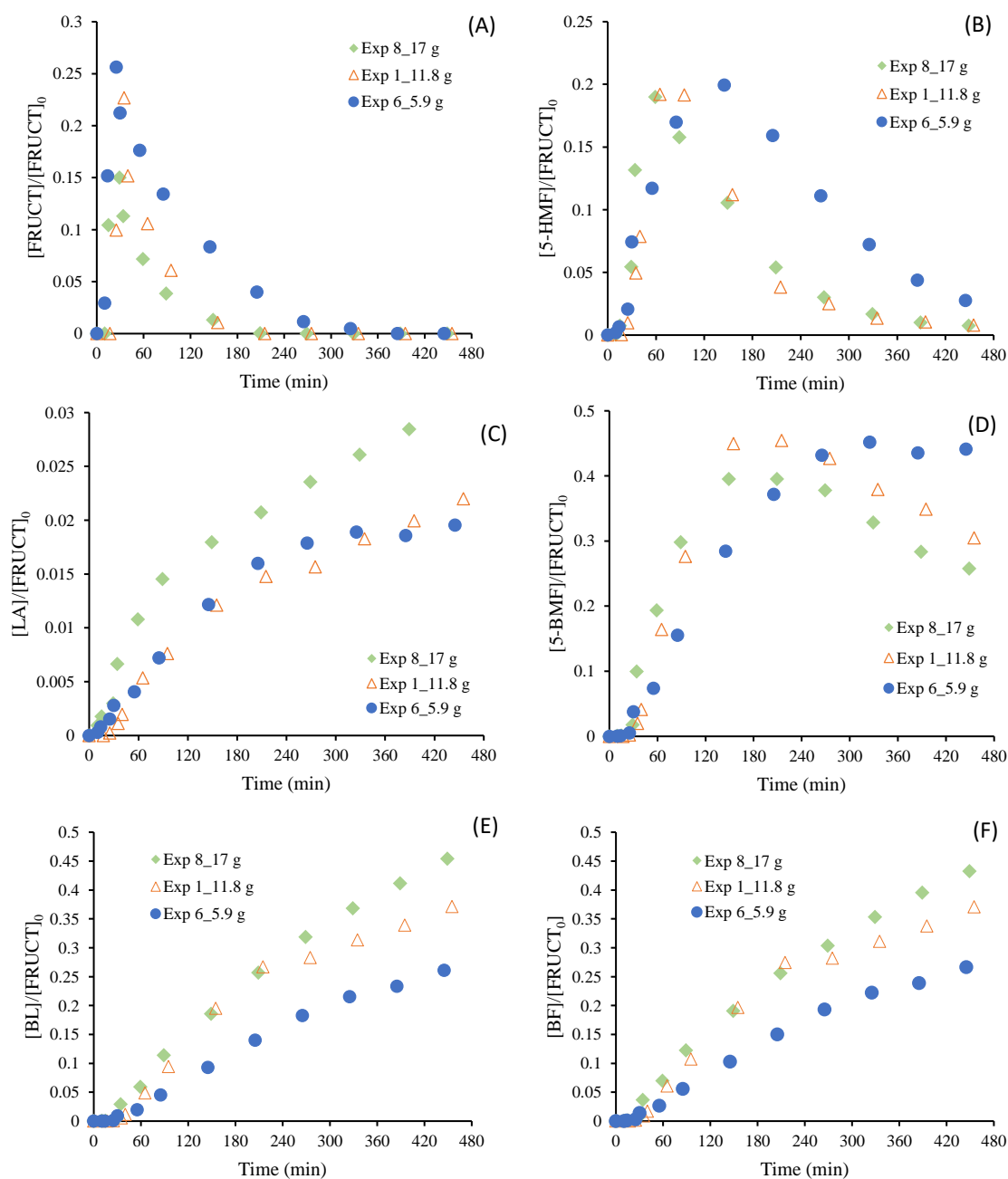


Fig. 31. Effect of catalyst loadings on normalized compounds trends on fructose initial concentration. Fructose (A), 5-HMF (B), LA (C), 5-BMF (D), BL (E), BF (F)

in concentration for higher catalyst loadings. With similar kinetic profiles, the production of BL and BF were enhanced, considering an increase in the final yields from 26-27 up to 43-45 mol%.

### 4.3.3 Deactivation catalyst effect

Some investigations were carried out to highlight possible deactivation effects of the catalyst; therefore, experiment V4 was repeated, reusing the catalyst used in a previous run. The catalyst from Experiment V4 was recovered from the reaction medium by filtration and was retreated according to the catalyst

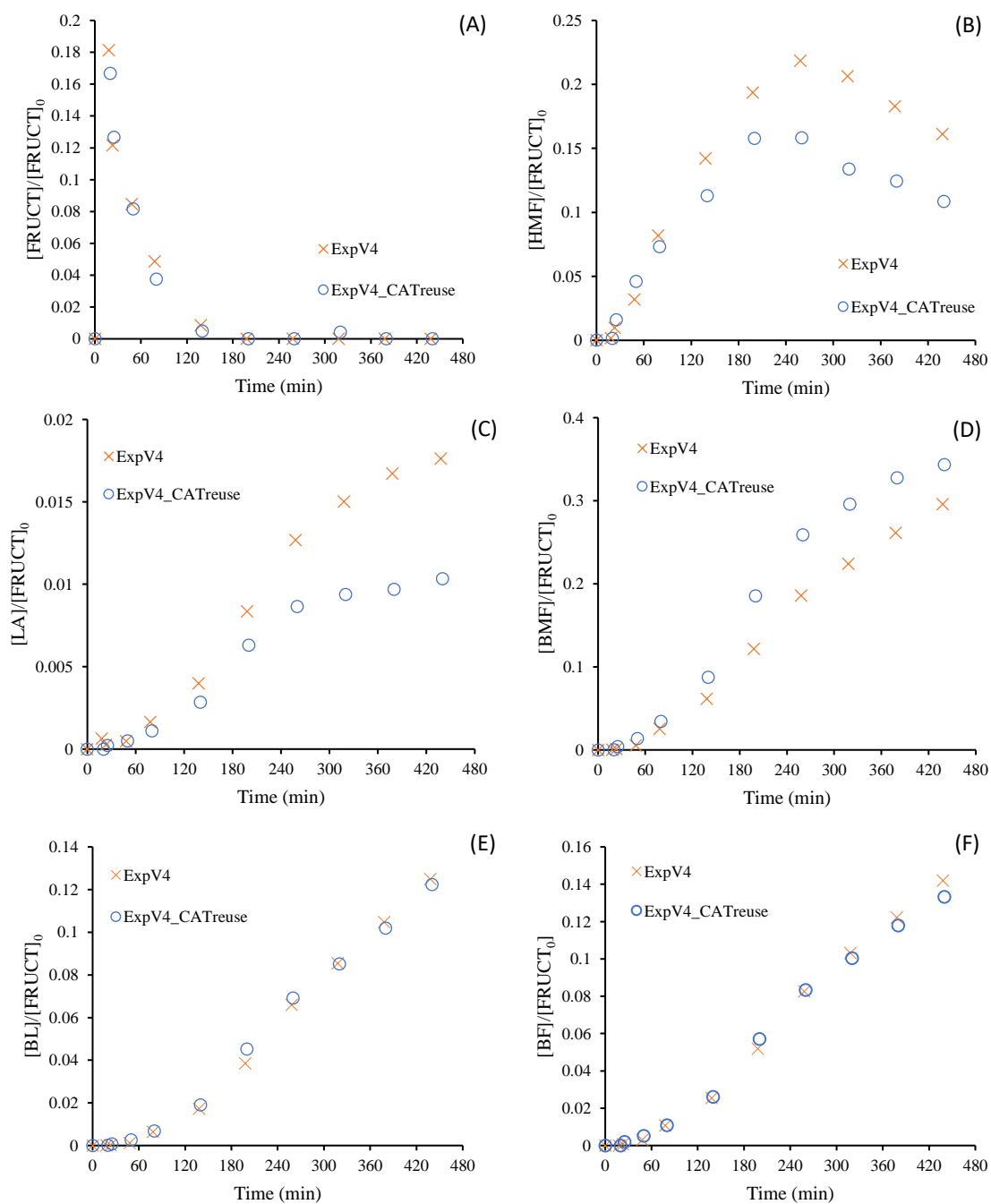


Fig. 32. Effect of catalyst deactivation on normalized compounds trends on fructose initial concentration. Fructose (A), 5-HMF (B), LA (C), 5-BMF (D), BL (E), BF (F).

preparation procedure. As shown in Fig. 32, the catalyst exhibits virtually unchanged activity, although it has changed in colour and morphology. The time course of the concentration of the end products, BL and BF, remained unchanged from Experiment V4, as did the fructose consumption kinetics. For the intermediates, the concentration profiles varied slightly; the consumption kinetics of 5-HMF is slightly faster in the repeated experiment, resulting in a slightly higher production of 5-BMF, LA and a higher degradation to humins, considering the mass loss of fructose from the total mass balance, which increases by 3% with the reused catalyst. The increase in humins production is also in line with the study by Ramirez et al.[73] which shows an increase in humins degradation in the first reuse cycle. However, the unaltered kinetics of BL production allows the catalyst deactivation in the first approach to be considered negligible.

### 4.3.4 Fructose initial loading

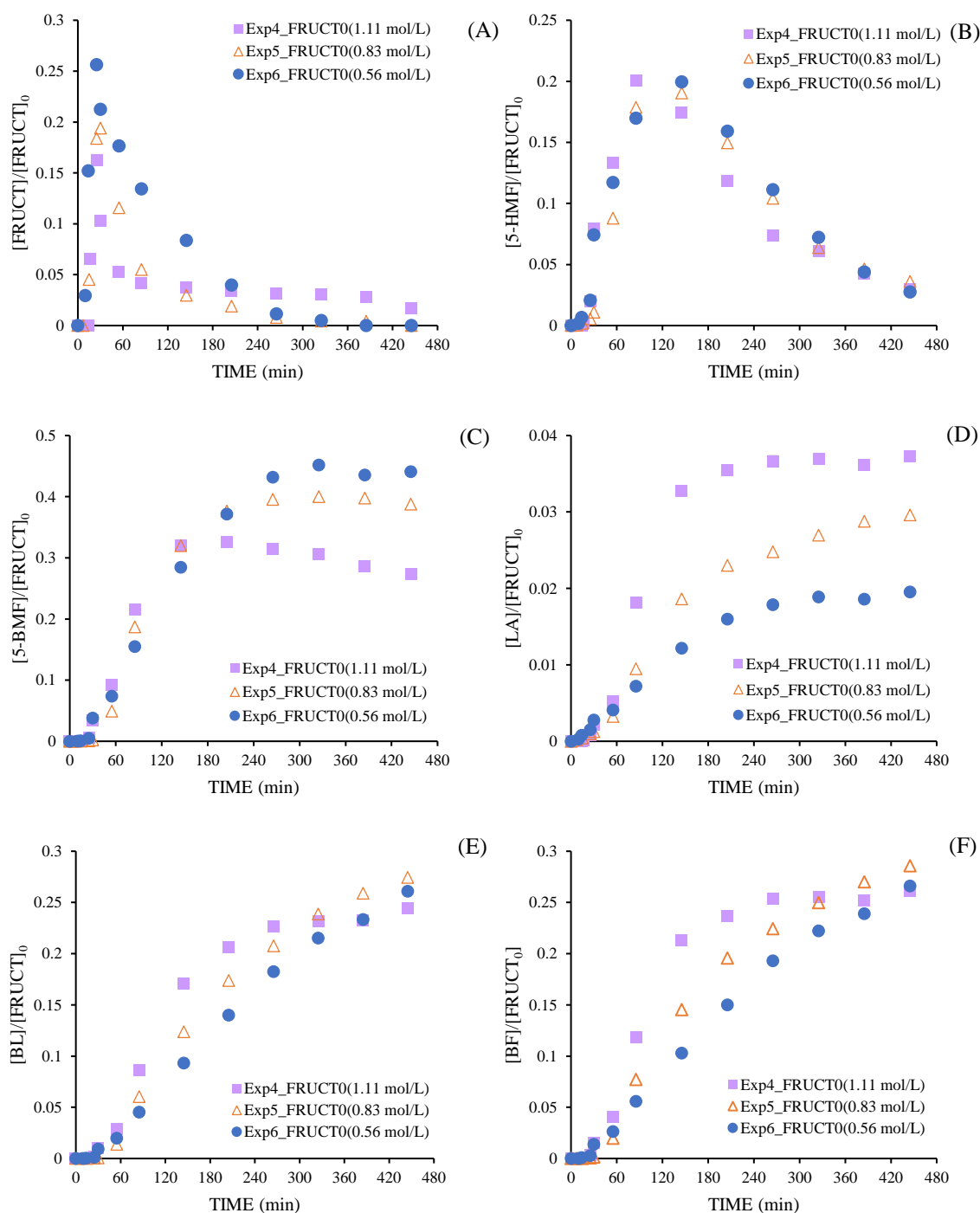


Fig. 33. Effect of fructose initial loadings on normalized compounds trends on fructose initial concentration. Fructose (A), 5-HMF (B), 5-BMF (C), LA (D), BL (E), BF (F).

In experiments 4, 5, and 6, the effect of the initial fructose concentration was compared with different initial fructose loadings (0.56, 0.83 and 1.11 mol/L), at the same temperature (110 °C) and catalytic activity, expressed in terms of the molar ratio between the equivalent moles of H<sup>+</sup> and fructose (ratio 0.3). As shown in Fig. 33, increasing the initial fructose concentration clearly affects the second intermediates: LA and 5-BMF. The production of LA is higher in Experiment 4 than in the other experiments, mainly due to the higher concentration of water in the reaction medium, produced by the

fructose dehydration step and which becomes available to the rehydration of 5-HMF. This then influences the profiles of 5-BMF, which exhibit similar formation kinetics in the first 3 hours, then the trend for Experiment 4 presents a slower consumption and conversion step to BL and BF, for which Experiment 4 appears to achieve lower final yields. The lower selectivity at BL can be attributed to the higher degradation to humins as a direct consequence of the increase in fructose concentration. Although Experiments 5 and 6 are characterized by a similar loss in terms of moles of fructose, 13% and 11% respectively, this value increases to 20.6% in Experiment 4. Therefore, higher concentrations of fructose must also be managed by carefully tuning the other reaction parameters in order to maximize selectivity towards BL.

### 4.3.5 Solubility measurement

Solubility concentration profiles are shown in Fig. 34 at 20 °C, 40 °C, 60 °C, 80 °C and 90 °C. In agreement with our previous results on the instantaneous dissolution of fructose (Fig. 15), the dissolution kinetics show a first phase of rapid dissolution, lasting between 10 and 30 minutes, in which more than 50 % of the maximum fructose solubility is reached, depending on the temperature. Then, a second, considerably slower phase in which saturated concentration is reached. The kinetics are strongly influenced by temperature in both phases. The effects of thermal degradation are more predominant from 100 °C. The values of the saturated fructose concentrations are used in the kinetic modelling step to consider the dissolution kinetics (Table 18).

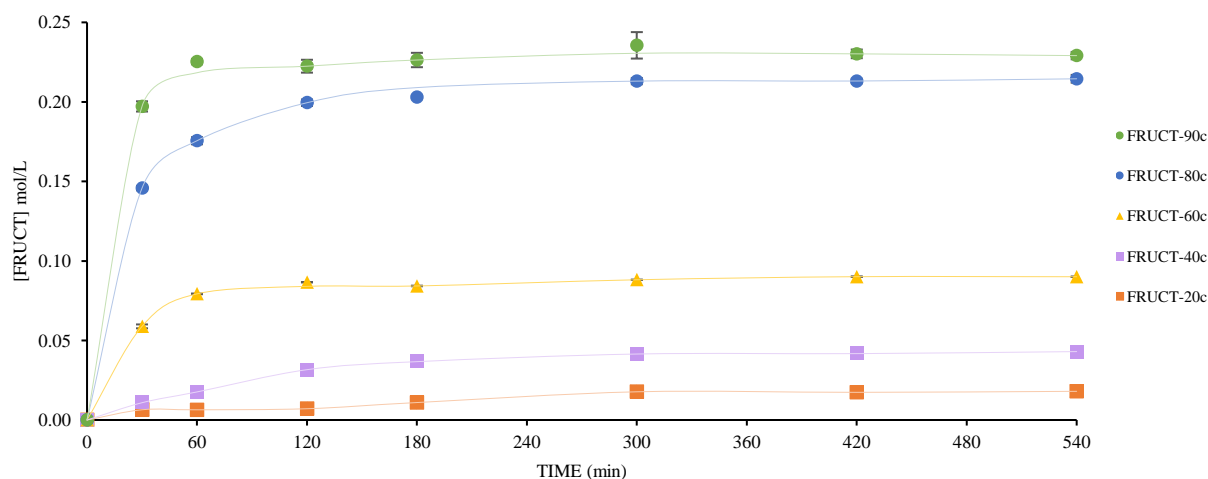


Fig. 34. Variation of dissolved fructose concentration over time during the dissolution of solid fructose in butanol/GVL at different temperatures, and for an initial solid fructose content of 200 g/L.

Table 18: Saturation molar concentration of fructose in isothermal conditions at different temperatures.

	Temperature (°C)				
	20	40	60	80	90
[FRUCT] <sub>SAT</sub> (mol/L)	0.018±0.001	0.043±0.001	0.09±0.001	0.215±0.002	0.230±0.001

### 4.3.6 Repeatability

In order to assess the repeatability of the experimental procedure used and the accuracy of the experimental data to be used in the kinetic modelling, some experiments were repeated: Experiments 4 and 5. In both experiments (Fig. 35, Fig. 36), considering an average standard deviation of the order of  $10^{-2}$  mol/L, the concentration trends in the repeated experiments are very similar to those in the original experiments, demonstrating the repeatability of the experimental data.

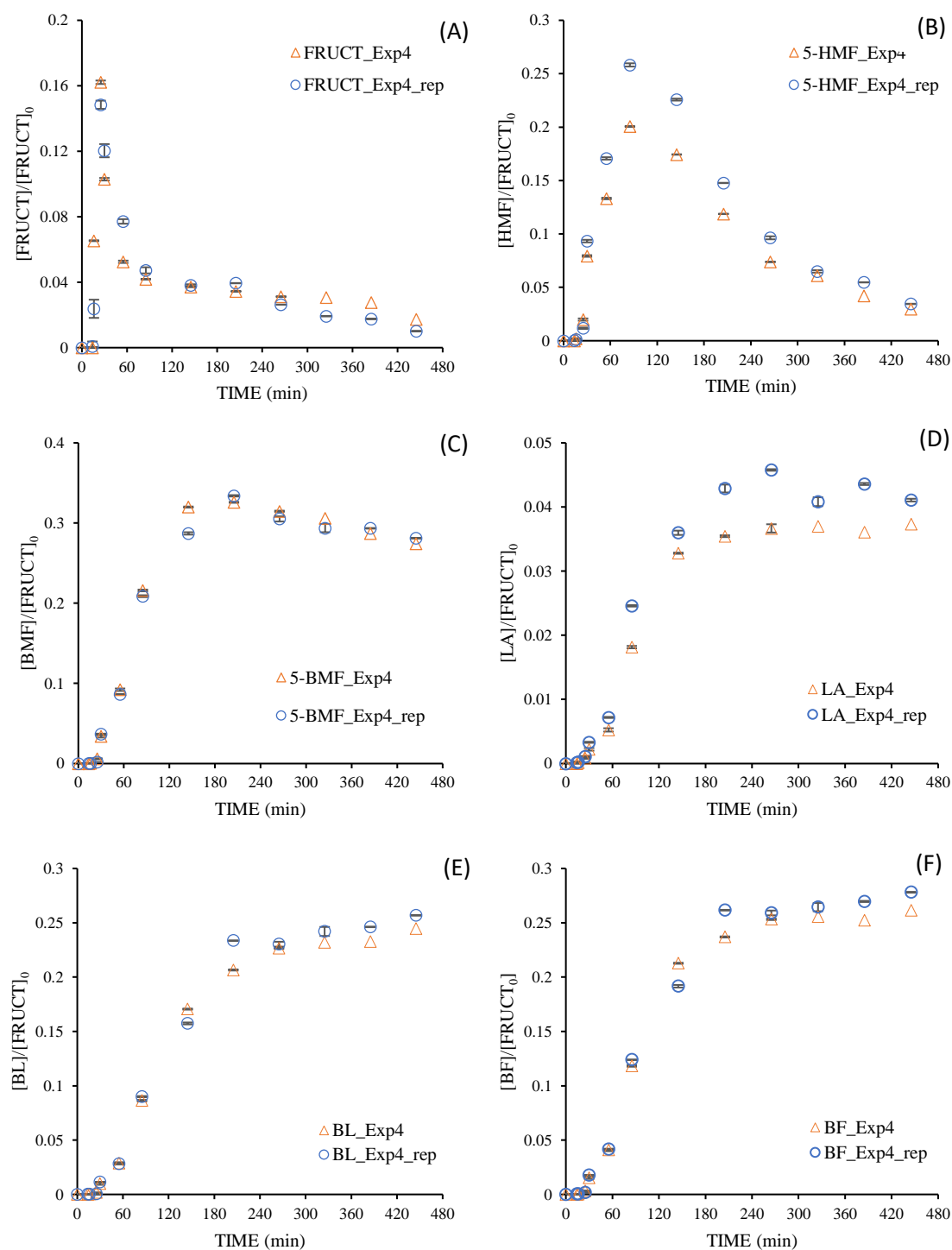


Fig. 35: Repeating experiment 4. Fructose (A), 5-HMF (B), 5-BMF (C), LA (D), BL (E), BF (F)

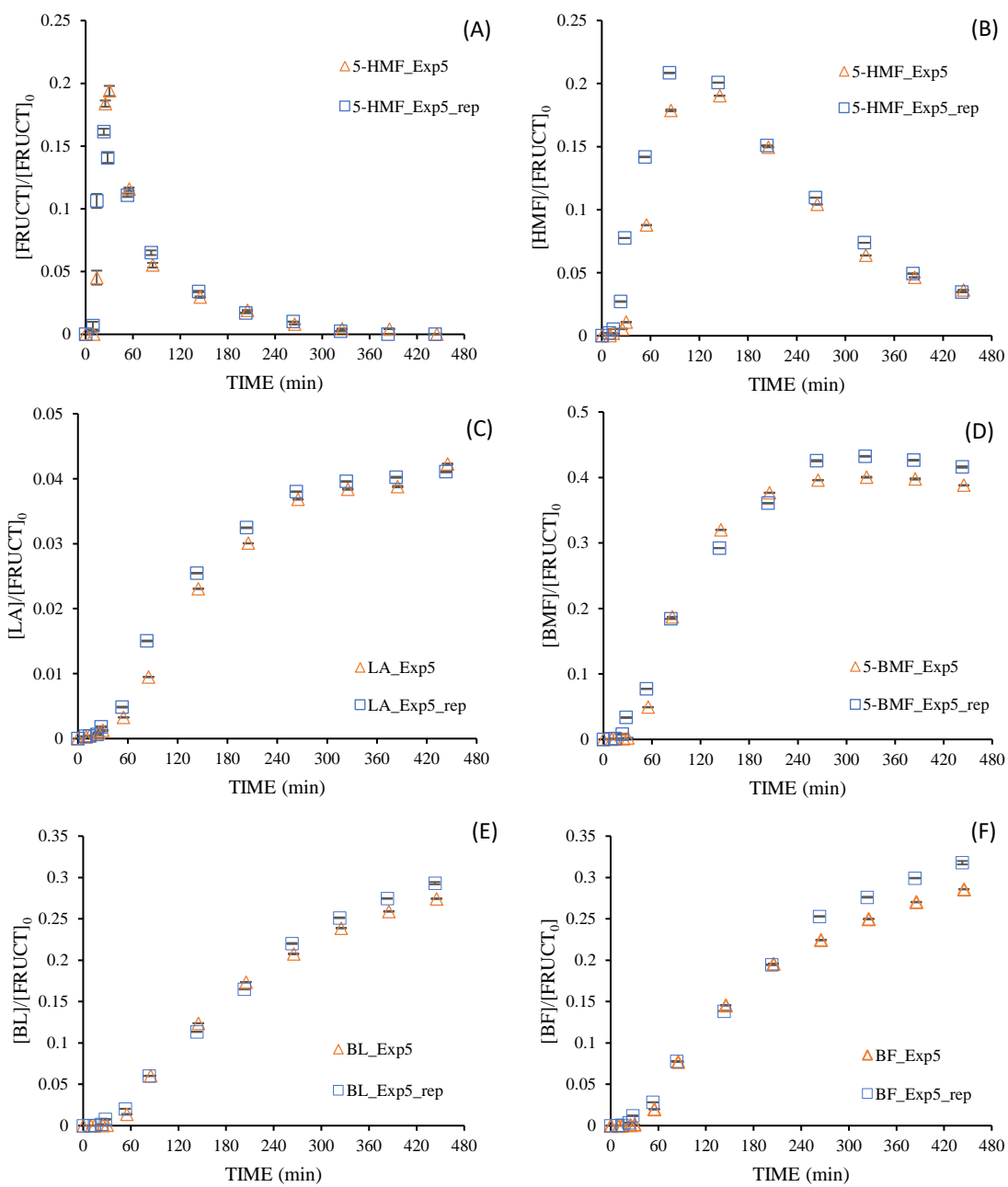


Fig. 36: Repeating experiment 5. Fructose (A), 5-HMF (B), 5-BMF (C), LA (D), BL (E), BF (F)

## 4.4 Kinetic Modelling

Based on the kinetic modelling of the solvolysis of 5-HMF previously developed, the main reaction scheme from Fructose solvolysis may include, together with the intermediates and products already indicated, an additional reaction intermediate, named Int1, in the conversion of the 5-HMF to LA and in the corresponding BL production from 5-BMF (Fig. 22). In this case, the complexity of the reaction scheme further increased by the degradation of fructose and 5-HMF to humins, by the dissolution kinetics of fructose in high-gravity condition, and the possible presence of intermediate rate-determining steps in the fructose dehydration to the 5-HMF. In order to include the fructose dissolution kinetics, a macroscopic dissolution approach, as described in the article of Joiner et al. [282], was applied, where the dissolution rate is considered proportional to the difference between the saturated solute concentration and its concentration in the bulk liquid phase. Thus, the rate of dissolution was expressed as follows:

$$r_d = k_d \cdot ([Fruct]_{Liq}^{Saturation} - [Fruct]_{Liq}) \quad Eq. 4. 3$$

where,  $k_d$  is the macroscopic rate of dissolution,  $[Fruct]_{Liq}^{Saturation}$  is the saturation concentration of fructose at the temperature T and  $[Fruct]_{Liq}$  is the fructose concentration in the bulk liquid phase. Besides the dissolution kinetics, a deeper investigation on fructose dehydration step should be considered, by the fact D-fructose can undergo to partial isomerization, from a mixture of  $\alpha/\beta$ -D-fructopyranose, to  $\alpha/\beta$ -D-fructofuranose. Some investigations [238,283,284] have pointed to the structure of fructofuranose as the main tautomer responsible for the formation of 5-HMF in aqueous systems. On the other hand, a different mechanism might occur in organic-media involving the fructose alkylation in presence of alcohol solvent [35,285]. Several studies [35,70,286] have demonstrated the formation of alkyl-fructosides as alkylation products of fructose under acid-condition, and then the possibility for the latter to be dehydrated to the corresponding 5-HMF-ether (in this case 5-BMF) [238]. In this investigation, working in a butanol-GVL solvent system, the formation of the isomerization intermediate D-fructofuranose and the alkylation product butyl-fructoside were considered in the reaction mechanism as alternative routes in the transformation of fructose. As shown in Fig. 37, the overall mechanism considers the inclusion in the initial reaction scheme of the additional alternative transformation pathways of the primary reagent Fructose: single-step dehydration to 5-HMF; isomerization to D-Fructofuranose and dehydration to 5-HMF; alkylation to Butyl-fructoside and dehydration to 5-BMF.

The kinetic modeling did not include the possible secondary reaction of butanol dehydration to di-butylether under acidic conditions, since no considerable concentrations of the species were found. On the other hand, an intermediate derived from the opening of the cyclic structure of GVL has been identified as butyl-4-hydroxyvalerate (BHP), and its formation has been considered as an equilibrium-



catalyzed reaction. Based on the experimental results, the esterification steps and the etherification of 5-HMF to 5-BMF are assumed as irreversible.

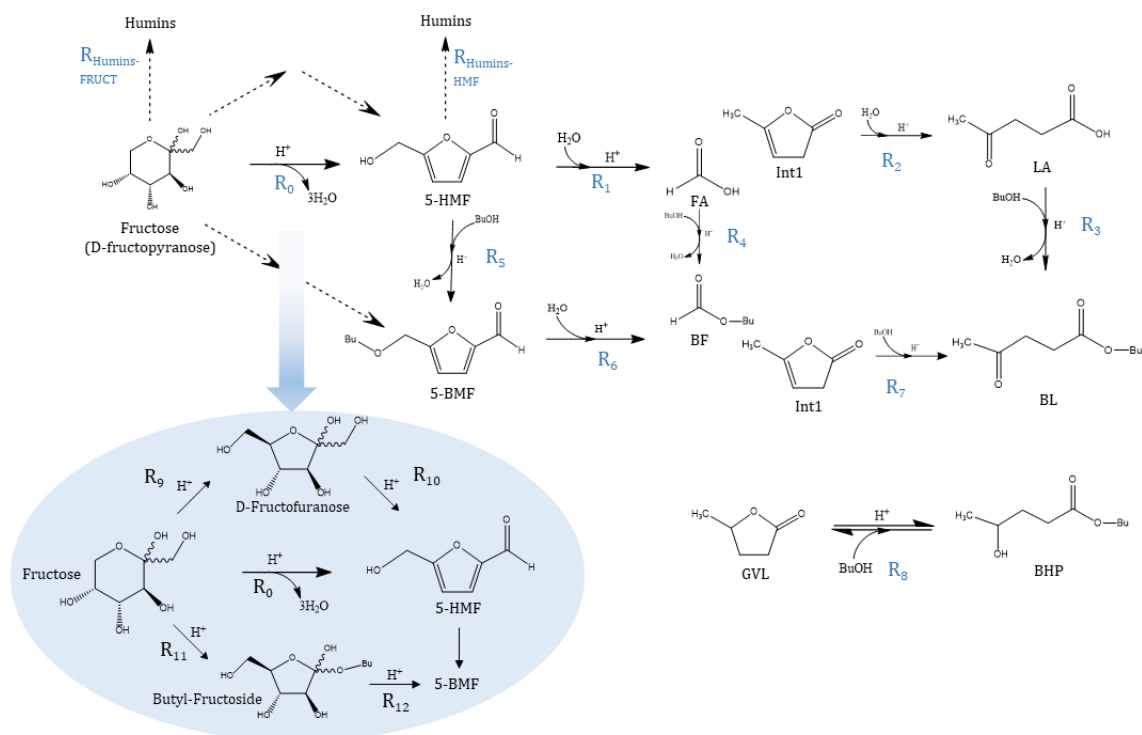


Fig. 37. Main reaction mechanism for Fructose solvolysis to butyl levulinate, including the intermediate species Int1, and focus on the dehydration step of fructose.

To express the catalytic activity of the resins, a pseudo-homogeneous (PH) approach was used, i.e., protons have been considered with a high degree of freedom in the reaction medium and without considering catalytic phenomena of absorption and desorption on the catalyst surface. Several kinetic investigations [257,287–291] have shown good agreement with experimental data using PH models for reactions catalyzed by ion-exchange resins, especially in a highly polar medium, as butanol/GVL in this work [259,291]. In the investigation, the proton concentration was expressed based on the acid capacity of the resin as in Eq. 4. 4.

$$[Prot.] = \frac{m_{driedCat} \cdot Capacity \left( \frac{[H^+]}{m_{driedCat}} \right)}{V_{Reaction}} \quad Eq. 4. 4$$

The reaction volume ( $V_{Reaction}$ ) was evaluated based on the total mass ratio to the butanol density at the corresponding temperature [261], and the volume was assumed constant, as the volume taken through the samples results in a variation of less than 10 % and, therefore negligible.

The reaction rates are supposed to be first order with respect to the concentrations of fructose, fructose-derived species, butanol, and acidic protons; while they are independent of water concentrations. The quantification of water was not possible due to its low amount in the reaction medium. Furthermore, the humins production rates are also expressed as first order with respect to the concentration of fructose

and 5-HMF, as shown in the previous study for solvolysis of 5-HMF and also assumed in this case for fructose. Reaction rates were expressed as follows:

$$R_0 = k_0 \cdot [\text{Fructose}]_{\text{Liq}} \cdot [\text{Prot.}] \quad \text{Eq. 4. 5}$$

$$R_1 = k_1 \cdot [\text{HMF}] \cdot [\text{Prot.}] \quad \text{Eq. 4. 6}$$

$$R_2 = k_2 \cdot [\text{INT1}] \cdot [\text{Prot.}] \quad \text{Eq. 4. 7}$$

$$R_3 = k_3 \cdot [\text{LA}] \cdot [\text{BuOH}] \cdot [\text{Prot.}] \quad \text{Eq. 4. 8}$$

$$R_4 = k_4 \cdot [\text{FA}] \cdot [\text{BuOH}] \cdot [\text{Prot.}] \quad \text{Eq. 4. 9}$$

$$R_5 = k_5 \cdot [\text{HMF}] \cdot [\text{BuOH}] \cdot [\text{Prot.}] \quad \text{Eq. 4. 10}$$

$$R_6 = k_6 \cdot [\text{BMF}] \cdot [\text{BuOH}] \cdot [\text{Prot.}] \quad \text{Eq. 4. 11}$$

$$R_7 = k_7 \cdot [\text{INT1}] \cdot [\text{BuOH}] \cdot [\text{Prot.}] \quad \text{Eq. 4. 12}$$

$$R_8 = k_8 \cdot [\text{Prot.}] \cdot \left( [\text{GVL}] \cdot [\text{BuOH}] - \frac{1}{K_8} \cdot [\text{BHP}] \right) \quad \text{Eq. 4. 13}$$

$$R_{\text{Humins-Fructose}} = k_{\text{Humins-Fructose}} \cdot [\text{Fructose}]_{\text{Liq}} \cdot [\text{Prot.}] \quad \text{Eq. 4. 14}$$

$$R_{\text{Humins-HMF}} = k_{\text{Humins-HMF}} \cdot [\text{HMF}] \cdot [\text{Prot.}] \quad \text{Eq. 4. 15}$$

$$R_9 = k_9 \cdot [\text{Fructose}]_{\text{Liq}} \cdot [\text{Prot.}] \quad \text{Eq. 4. 16}$$

$$R_{10} = k_{10} \cdot [\text{FRUCTfur}] \cdot [\text{Prot.}] \quad \text{Eq. 4. 17}$$

$$R_{11} = k_{11} \cdot [\text{Prot.}] \cdot \left( [\text{Fructose}]_{\text{Liq}} \cdot [\text{BuOH}] - \frac{1}{K_{11}} \cdot [\text{ButylFRUCT}] \right) \quad \text{Eq. 4. 18}$$

$$R_{12} = k_{12} \cdot [\text{ButylFRUCT}] \cdot [\text{Prot.}] \quad \text{Eq. 4. 19}$$

#### 4.4.1 Models

In this section, the different reaction pathways assumed in the investigation are described by considering three different model as shown in Fig. 38; in addition to the single-step dehydration of fructose ( $R_0$ ), the

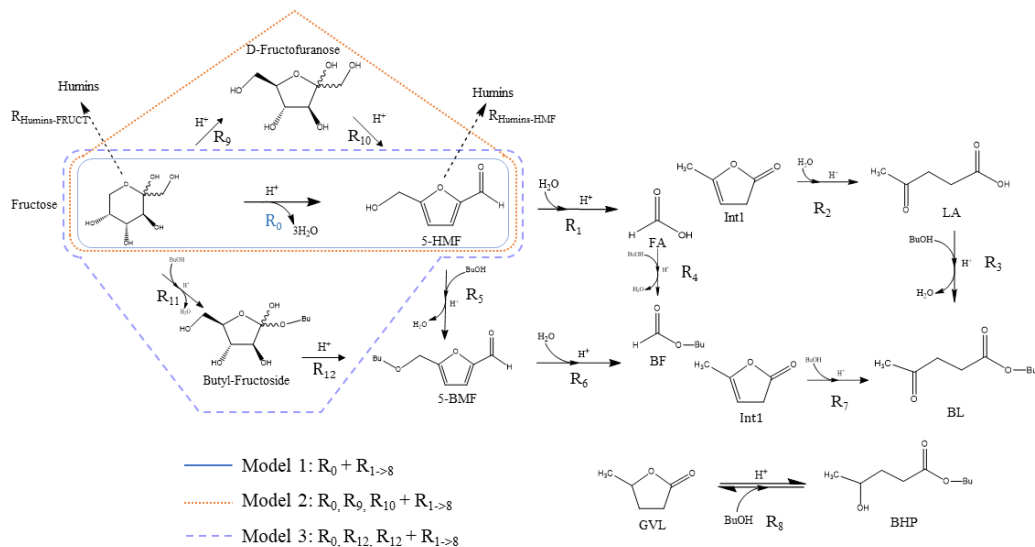


Fig. 38: Focus on fructose conversion step: single-step fructose dehydration in Model 1; isomerization to fructofuranose in Model 2; alkylation to butylfructoside in Model 3

presence of the isomerization intermediate and the alkylation intermediate product are also considered. The reactor is assumed as an ideal batch reactor.

#### 4.4.1.1 Model 1

Model 1 considers the fructose dehydration step to 5-HMF as a single step. It includes the reaction steps with reaction rates  $R_{0 \rightarrow 8}$  and the degradation steps:  $R_{Humins-Fructose}$ ,  $R_{Humins-HMF}$ .

$$\frac{d[Fructose]_{Liq}}{dt} = -R_0 - R_{Humins-Fructose} + r_d - \frac{[Fructose]_{Liq}}{V_{Liq}} \cdot \left( \frac{V_{Liq} \cdot r_d \cdot M_{Fructose}}{\rho_{BuOH}} \right) \quad Eq. 4. 20$$

$$\frac{d[HMF]}{dt} = R_0 - R_1 - R_5 - R_{Humins-HMF} - \frac{[HMF]}{V_{Liq}} \cdot \left( \frac{V_{Liq} \cdot r_d \cdot M_{Fructose}}{\rho_{BuOH}} \right) \quad Eq. 4. 21$$

$$\frac{d[BMF]}{dt} = R_5 - R_6 - \frac{[BMF]}{V_{Liq}} \cdot \left( \frac{V_{Liq} \cdot r_d \cdot M_{Fructose}}{\rho_{BuOH}} \right) \quad Eq. 4. 22$$

$$\frac{d[LA]}{dt} = R_2 - R_3 - \frac{[LA]}{V_{Liq}} \cdot \left( \frac{V_{Liq} \cdot r_d \cdot M_{Fructose}}{\rho_{BuOH}} \right) \quad Eq. 4. 23$$

$$\frac{d[BL]}{dt} = R_3 + R_7 - \frac{[BL]}{V_{Liq}} \cdot \left( \frac{V_{Liq} \cdot r_d \cdot M_{Fructose}}{\rho_{BuOH}} \right) \quad Eq. 4. 24$$

$$\frac{d[BF]}{dt} = R_4 + R_6 - \frac{[BF]}{V_{Liq}} \cdot \left( \frac{V_{Liq} \cdot r_d \cdot M_{Fructose}}{\rho_{BuOH}} \right) \quad Eq. 4. 25$$

$$\frac{d[BHP]}{dt} = R_8 - \frac{[BHP]}{V_{Liq}} \cdot \left( \frac{V_{Liq} \cdot r_d \cdot M_{Fructose}}{\rho_{BuOH}} \right) \quad Eq. 4. 26$$

$$\frac{d[FA]}{dt} = R_1 - R_4 - \frac{[FA]}{V_{Liq}} \cdot \left( \frac{V_{Liq} \cdot r_d \cdot M_{Fructose}}{\rho_{BuOH}} \right) \quad Eq. 4. 27$$

$$\frac{d[BuOH]}{dt} = -R_3 - R_4 - R_5 - R_7 - R_8 - \frac{[BuOH]}{V_{Liq}} \cdot \left( \frac{V_{Liq} \cdot r_d \cdot M_{Fructose}}{\rho_{BuOH}} \right) \quad Eq. 4. 28$$

$$\frac{d[Humins]}{dt} = R_{Humins-HMF} + R_{Humins-Fructose} - \frac{[Humins]}{V_{Liq}} \cdot \left( \frac{V_{Liq} \cdot r_d \cdot M_{Fructose}}{\rho_{BuOH}} \right) \quad Eq. 4. 29$$

$$\frac{d[INT1]}{dt} = R_1 - R_2 + R_6 - R_7 - \frac{[INT1]}{V_{Liq}} \cdot \left( \frac{V_{Liq} \cdot r_d \cdot M_{Fructose}}{\rho_{BuOH}} \right) \quad Eq. 4. 30$$

$$\frac{d[GVL]}{dt} = -R_8 - \frac{[GVL]}{V_{Liq}} \cdot \left( \frac{V_{Liq} \cdot r_d \cdot M_{Fructose}}{\rho_{BuOH}} \right) \quad Eq. 4. 31$$

$$\frac{dm_{Fructose}}{dt} = -V_{Liq} \cdot r_d \cdot M_{Fructose} \quad Eq. 4. 32$$

$$\frac{dm_{Liq}}{dt} = V_{Liq} \cdot r_d \cdot M_{Fructose} \quad Eq. 4. 33$$

#### 4.4.1.2 Model 2

Model 2 includes in the reaction pathway the isomerization step to D-fructofuranose (*FRUCTfur*) and its dehydration to 5-HMF. Reaction rates are:  $R_0$  (Eq. 4. 34),  $R_9$  (Eq. 4. 35) for the isomerization step,  $R_{10}$  (Eq. 4. 36) for dehydration. The introduction of the isomerization step changes the material balances of fructose and 5-HMF compared to model 1. The other material balances remain unchanged.

$$\frac{d[\text{Fructose}]_{\text{Liq}}}{dt} = -R_0 - R_9 - R_{\text{Humins-Fructose}} + r_d - \frac{[\text{Fructose}]_{\text{Liq}}}{V_{\text{Liq}}} \cdot \left( \frac{V_{\text{Liq}} \cdot r_d \cdot M_{\text{Fructose}}}{\rho_{\text{BuOH}}} \right) \quad \text{Eq. 4. 37}$$

$$\frac{d[\text{HMF}]}{dt} = R_0 + R_{10} - R_1 - R_5 - R_{\text{Humins-HMF}} - \frac{[\text{HMF}]}{V_{\text{Liq}}} \cdot \left( \frac{V_{\text{Liq}} \cdot r_d \cdot M_{\text{Fructose}}}{\rho_{\text{BuOH}}} \right) \quad \text{Eq. 4. 38}$$

$$\frac{d[\text{FRUCTfur}]}{dt} = R_9 - R_{10} - \frac{[\text{FRUCTfur}]}{V_{\text{Liq}}} \cdot \left( \frac{V_{\text{Liq}} \cdot r_d \cdot M_{\text{Fructose}}}{\rho_{\text{BuOH}}} \right) \quad \text{Eq. 4. 39}$$

#### 4.4.1.3 Model 3

Model 3, on the other hand, considers the substitution of the butyl functional group for fructose, resulting in Butyl-fructoside (*ButylFRUCT*), which is then dehydrated to 5-BMF. Considering the reaction rates  $R_0$  (Eq. 4. 40),  $R_{11}$  (Eq. 4. 41), and  $R_{12}$  (Eq. 4. 42), material balances of fructose, 5-BMF and butanol changed as follows:

$$\frac{d[\text{Fructose}]_{\text{Liq}}}{dt} = -R_0 - R_{11} - R_{\text{Humins-Fructose}} + r_d - \frac{[\text{Fructose}]_{\text{Liq}}}{V_{\text{Liq}}} \cdot \left( \frac{V_{\text{Liq}} \cdot r_d \cdot M_{\text{Fructose}}}{\rho_{\text{BuOH}}} \right) \quad \text{Eq. 4. 43}$$

$$\frac{d[\text{BMF}]}{dt} = R_{12} + R_5 - R_6 - \frac{[\text{BMF}]}{V_{\text{Liq}}} \cdot \left( \frac{V_{\text{Liq}} \cdot r_d \cdot M_{\text{Fructose}}}{\rho_{\text{BuOH}}} \right) \quad \text{Eq. 4. 44}$$

$$\frac{d[\text{BuOH}]}{dt} = -R_3 - R_4 - R_5 - R_7 - R_8 - R_{11} - \frac{[\text{BuOH}]}{V_{\text{Liq}}} \cdot \left( \frac{V_{\text{Liq}} \cdot r_d \cdot M_{\text{Fructose}}}{\rho_{\text{BuOH}}} \right) \quad \text{Eq. 4. 45}$$

$$\frac{d[\text{ButylFRUCT}]}{dt} = R_{11} - R_{12} - \frac{[\text{ButylFRUCT}]}{V_{\text{Liq}}} \cdot \left( \frac{V_{\text{Liq}} \cdot r_d \cdot M_{\text{Fructose}}}{\rho_{\text{BuOH}}} \right) \quad \text{Eq. 4. 46}$$

## 4.5 Modelling results and discussion

### 4.5.1 Training phase

As with the previous modelling, the commercial software Athena Visual Studio was used to estimate model parameters via regression [262,263]. A Bayesian framework was used for the regression, which is more suitable for the estimation of multiple-response parameters, as in the case of this system [264,292].

The DDAPLUS solver implemented in the Athena software allows the integration of ODEs derived from mass balances, using a modified Newton algorithm [266]. In the estimation, the experimental concentrations of fructose, 5-HMF, LA, 5-BMF, BL, BF and BHP were used as observable data. The temperature dependence of rate constants is expressed by a modified Arrhenius equation [267].

The GREGPLUS subroutine of the software was used to minimize the objective function, determine the credibility intervals for each estimated parameter and obtain the normalized covariance matrix of the parameters. GREGPLUS package defines the uncertainty of the estimated parameters evaluated by the 95% marginal highest posterior density (HPD).

Also, in this case, the selection of the best model was guided not only by the evaluation of the SSRs but also by Akaike's information criterion parameter (AIC); depending on the (SSR)\_Reg and the number

of estimated parameters, the lower is the AIC, the higher is the reliability and stability of the model. According to the AIC, the most suitable model can explain most of the variation using the smallest possible number of independent variables [269].

#### 4.5.2 Model estimation results

Once the parameters of the considered models have been estimated, the comparison of the models is shown in Table 19 on the basis of the sum of square residuals ( $SSR$ )<sub>Reg</sub> and Akaike Information Criterion (AIC)<sub>Reg</sub>. According to the results, Model 1 presents the lowest AIC value, i.e. the most reliable model, as a direct consequence of the minor number of parameters and an overall SSR comparable to the other models. In terms of each species, Model 1 shows the best fitting on the experimental data for BL and BF, with the lowest value of SSR for both compounds. On the other hand, by increasing the complexity of reaction steps with Model 2 and Model 3, the regression shows a better fitting for the intermediates such as 5-HMF, LA and 5-BMF. However, the AIC index for models 2 and 3 is lower than for model 1, indicating that the increase in complexity of models 2 and 3, i.e. number of parameters, does not coincide with a significant increase in model robustness. The analysis indicates model 1 as the best to represent the solvolysis of high fructose in BL.

Table 19: Regression results for Model 1, Model 2, and Model 3

	<b>MODEL 1</b>	<b>MODEL 2</b>	<b>MODEL 3</b>
<b>Number of parameters</b>	23	27	28
<b>Independent events (IE)</b>	266	266	266
<b>SSR-FRUCT</b>	0.0693	0.0672	0.0667
<b>SSR-5-HMF</b>	0.3276	0.2010	0.1991
<b>SSR-5-BMF</b>	0.6868	0.9629	0.6470
<b>SSR-LA</b>	0.0075	0.1036	0.0074
<b>SSR-BL</b>	0.1934	0.2508	0.2428
<b>SSR-BF</b>	0.3360	0.4446	0.4235
<b>SSR-BHP</b>	2.5709	2.5011	2.5811
<b>SSR_all</b>	4.1916	4.5310	4.1577
<b>AIC</b>	-1060.9	-1029.3	-1049.5

All three models gave a comparable response for fructose in terms of SSR. The parity diagrams of the models show for fructose a value of the coefficient of determination around 0.9, as shown in Fig. S2.1, which is lower than the other species for which it is higher than 0.90 (for BL around 0.97).

Furthermore, plotting the residuals against the experimental and estimated concentrations (Fig. S2.2- Fig. S2.3) the absence of correlations and a random distribution indicate that the rate equations are well identified.

Table 20: Estimated parameters at  $T_{ref}=368\text{ K}$  and statistical data for Model 1

Reaction rates		k ((L <sup>2</sup> min)/mol <sup>2</sup> )	k ((L min)/mol)	HPD%	Ea (kJ/mol)	HPD%
<b>R<sub>0</sub></b>	FRUCT → 5-HMF	-	0.1219	0.0	46.07	2.96
<b>R<sub>1</sub></b>	5-HMF → Int1 + FA	-	0.0118	0.71	65.38	4.0
<b>R<sub>2</sub></b>	Int1 → LA	-	17.310	93.33	43.46	-
<b>R<sub>3</sub></b>	LA → BL	0.0012	-	1.36	3.06	-
<b>R<sub>4</sub></b>	FA → BF	4.2000	-	3.88	82.68	7.06
<b>R<sub>5</sub></b>	5-HMF → 5-BMF	0.0100	-	0.45	58.24	3.73
<b>R<sub>6</sub></b>	5-BMF → Int1 + BF	-	0.0004	1.19	65.29	10.24
<b>R<sub>7</sub></b>	Int1 → BL	18.250	-	91.52	60.73	4.61
<b>R<sub>8</sub></b>	GVL → BHP	0.0007	-	0.8	17.32	29.23
<b>R<sub>Humins-</sub></b>	FRUCT → Humins	-	0.0141	2.54	40.53	24.06
<b>R<sub>Humins-5-HMF</sub></b>	5-HMF → Humins	-	0.0000	-	24.44	-

Examining the parameters estimated for Model 1 and shown in Table 20, the parameters were estimated with a low HPD and the activation energy values are comparable to those found in the literature, although slightly lower in some cases. For the first reaction step, the dehydration of fructose to 5-HMF ( $R_0$ ), Qi et al. [293] reported a value of 60.4 kJ/mol using an ion-exchange resin in acetone/DMSO solvent (70/30 w/w); while Carniti et al.[294] 65.8 kJ/mol in aqueous solution. In this case, the lower value obtained in Model 1 can be attributed to the effect of GVL as an aprotic solvent; in fact, as demonstrated by Ma et al. for the corresponding dehydration of glucose [295], the presence of GVL tends to reduce the activation energy of the dehydration reaction.

For the subsequent rehydration of 5-HMF ( $R_1$ ), the average value in the literature attests the activation energy to over 90 kJ/mol [296] in aqueous solution and considering the use of a homogeneous acid catalyst. On the other hand, in the presence of polar aprotic co-solvents and heterogeneous catalyst, the value is reduced to 64 kJ/mol as indicated by the work of Moreau et al.[276] and close to the value estimated in this work of 65.4 kJ/mol. For the conversion to 5-BMF by etherification, the activation energy value obtained is in line with that estimated in the modelling proceeding from 5-HMF with a value of 53.8 kJ/mol [III]. Complexities were encountered in the evaluation of the kinetic parameters of levulinic acid esterification due to low concentrations and reduced kinetics, and in the estimation of the kinetic parameters for the degradation of 5-HMF to humins, which was cumbersome in each model, probably due to the predominant contribution of fructose to the formation of humins compared to the corresponding furan intermediate. The formation of humins from fructose was estimated with an activation energy in line with average values in the literature (18-55 kJ/mol) [243], which is lower when compared to some work in the aqueous phase [253], due to the presence of GVL.

Comparing the performance of the model with experimental concentration data, it can be observed that it is able to estimate the concentration trends of intermediates, final products and the kinetics of simultaneous dissolution and solvolysis of fructose over a wide range of initial fructose concentrations. Fig. 39 and Fig. 40 show the fit of Model 1 to Experiments 1, 13, 14 and 17 (Table 16). In Fig. 39, the

experimental concentrations of Exp. 1 are compared with Model 1, which shows trends that adhere to the experimental results. Even perturbing the initial fructose load from a concentration of 0.18 mol/L to a high concentration of 0.59 mol/L, in Exp. 13 and 14, as shown in Fig. 40. In general, a better fit is observed for all species, particularly at high concentrations. The model was also compared with the results of Experiment 17 where the effect due to the addition of levulinic acid in the reaction system is considered. The results show slow esterification kinetics, hence the limitation in the determination of its kinetic parameters; the 5-BMF conversion pathway prevails in the butyl levulinate formation mechanism.

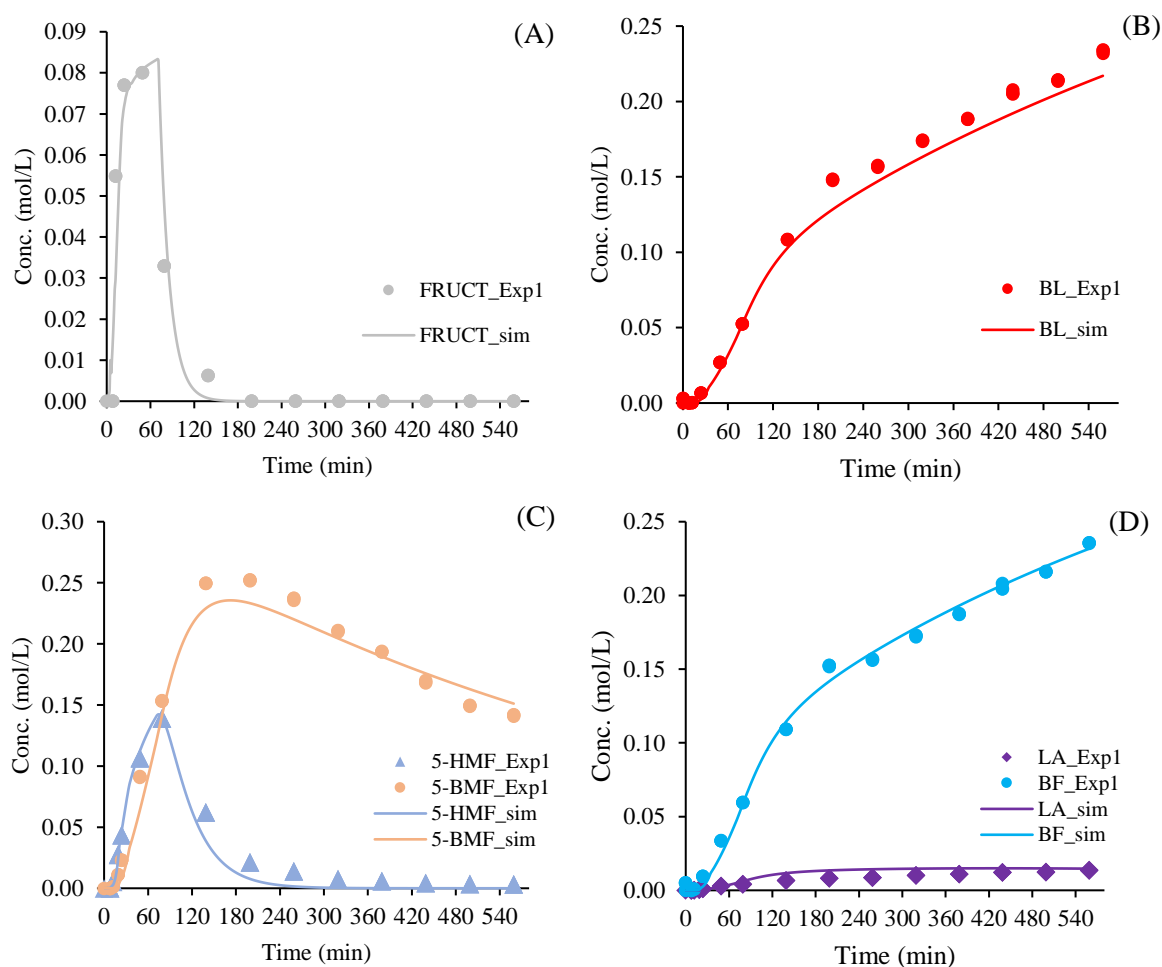


Fig. 39. Fit of model 1 to experimental concentration of Exp. 1, Fructose (A); BL (B), 5-HMF,5-BMF (C); LA, BF (D).

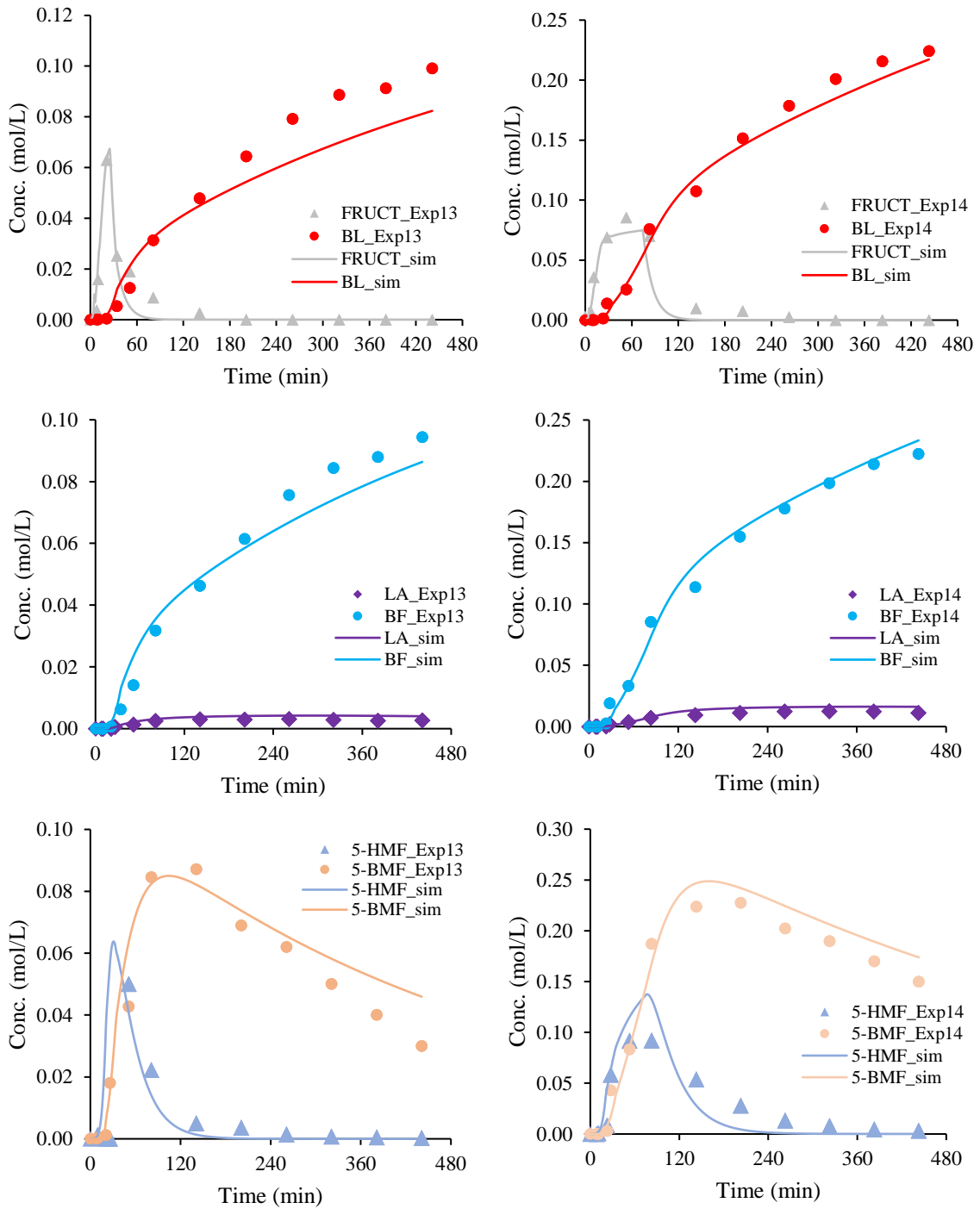


Fig. 40. Fit of model 1 to the experimental concentration of fructose and BL in Exp. 13, and Exp. 14. Fructose, BL (A-B); LA, BF (C-D); 5-HMF, 5-BMF (E-F).

### 4.5.3 Models validation results

The robustness of the developed models was assessed by means of a hold-out validation method, comparing the models with the independent experiments in Table 17, i.e., not included in the regression step. Using the Athena software, the models were simulated under the same experimental conditions as



the V1-V5 experiments (Table 17), and compared in terms of the  $SSR_{val}$  and  $AIC_{val}$  parameters, as shown in the table. From the values obtained, Model 1 is globally the most robust in terms of  $(SSR)_{val}$  and  $AIC_{val}$ .

Table 21: Summary of validation stage results.  $SSR_{val}$  and  $AIC_{val}$

	MODEL 1	MODEL 2	MODEL 3
<b>Independent events (IE)</b>	60	60	60
<b>SSR_FRUCT</b>	0.153	0.156	0.158
<b>SSR_5-HMF</b>	0.488	0.353	0.372
<b>SSR_5-BMF</b>	0.848	0.938	1.041
<b>SSR_LA</b>	0.003	0.003	0.004
<b>SSR_BL</b>	0.152	0.174	0.159
<b>SSR_BF</b>	0.262	0.294	0.273
<b>SSR_all</b>	1.907	1.919	2.006
<b><math>AIC_{val}</math></b>	-161.0	-152.6	-147.9

As shown in Fig. 41, overall in terms of SSR, model 1 results in the best modeling for the end products BL, BF, and the intermediates 5-BMH and LA, while the SSR value for 5-HMF is slightly higher than that of the other two models in both regression and validation. The good overall fit to the experimental data results in a higher value of the AIC parameter for this model in both regression and validation phases.

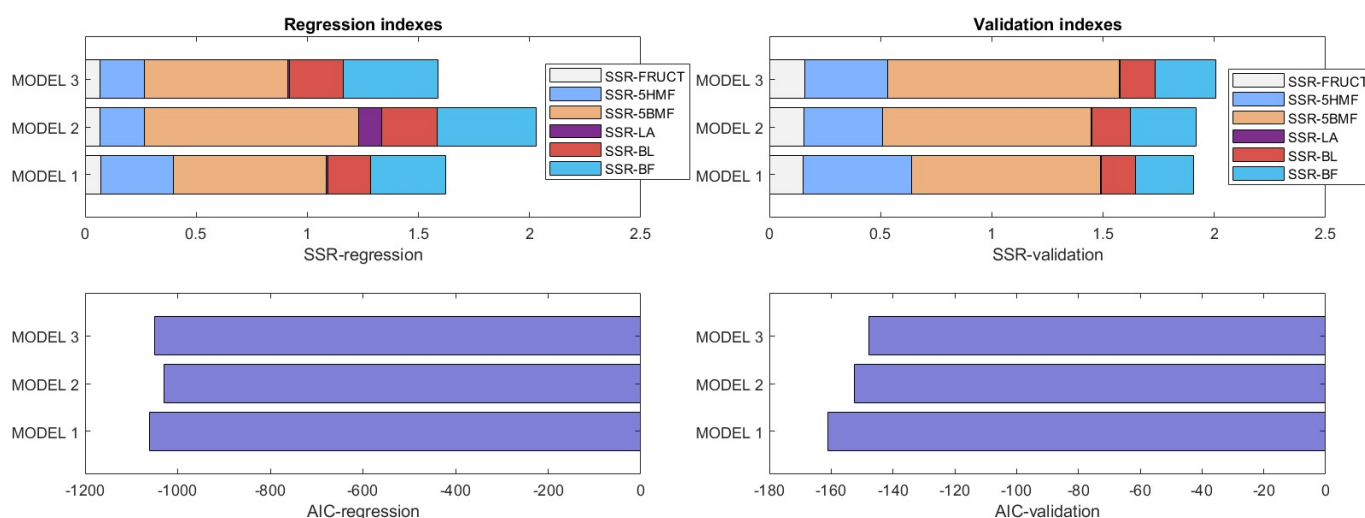


Fig. 41: Overall assessment among models respect with SSR and AIC indexes in regression and validation phases

#### 4.5.4 Tuning of process conditions

Validated over a wide range of process parameters: temperature (80-115 °C), initial fructose concentration (11-200 g/L) and catalyst loading (35-130 g/L), the developed model can simulate controlled process parameters to achieve optimal BL product yield. Table 22 shows examples of the simulation of the reaction system with Model 1 under varying reaction parameters with respect to the

conditions of Experiments 1, 8, 9, 13 and 19. In general, by increasing the reaction time and catalyst loading, the concentrations of the species are simulated until a final BL yield of 70.8% is obtained for an initial fructose concentration of 30 g/L. For higher initial concentrations, the final yield of the product of interest tends to decrease but can be maximized, as in experiment 8 to 64.8%, considering an optimum between the process parameters also based on techno-economic analyses. Fig. 42 shows the simulation of the concentration profiles of experiment 1 with a reaction time of 24 h.

Table 22: Simulation through Model 1 of the solvolysis system at different conditions.

Experiment	[FRUCT] <sub>0</sub> (g/L)	[FRUCT] <sub>0</sub> (mol/L)	T (°C)	Cat. (g/L)	time <sub>REAC</sub> (h)	X <sub>FRUCT</sub> (mol%)	Y <sub>INTER</sub> (mol%)	Y <sub>BL</sub> (mol%)	
<b>1</b>	100	0.56	110	84.3	9	100	28.6	42.0	Exp.
			110	84.3	24	100	11.1	<b>58.1</b>	<b>Sim.</b>
			115	84.3	9	100	22.9	<b>46.0</b>	<b>Sim.</b>
			110	130	9	100	19.4	<b>49.6</b>	<b>Sim.</b>
<b>8</b>	100	0.56	110	121	8	100	25.9	46.5	Exp.
			115	121	8	100	19.7	<b>49.1</b>	<b>Sim.</b>
			110	121	24	100	5.5	<b>64.8</b>	<b>Sim.</b>
<b>9</b>	150	0.83	115	94.3	8	100	26.8	36.2	Exp.
			115	130	8	100	21.4	<b>44.0</b>	<b>Sim.</b>
			115	94.3	24	100	8.8	<b>56.9</b>	<b>Sim.</b>
<b>13</b>	30	0.17	110	97.8	7	100	11.3	55.5	Exp.
			115	97.8	7	100	11.3	<b>55.1</b>	<b>Sim.</b>
			110	97.8	24	100	3.2	<b>70.9</b>	<b>Sim.</b>
<b>19</b>	175	0.97	105	130	8	100	33.7	31.2	Exp.
			115	130	8	100	23.3	<b>40.5</b>	<b>Sim.</b>
			105	130	24	100	13.1	<b>52.3</b>	<b>Sim.</b>

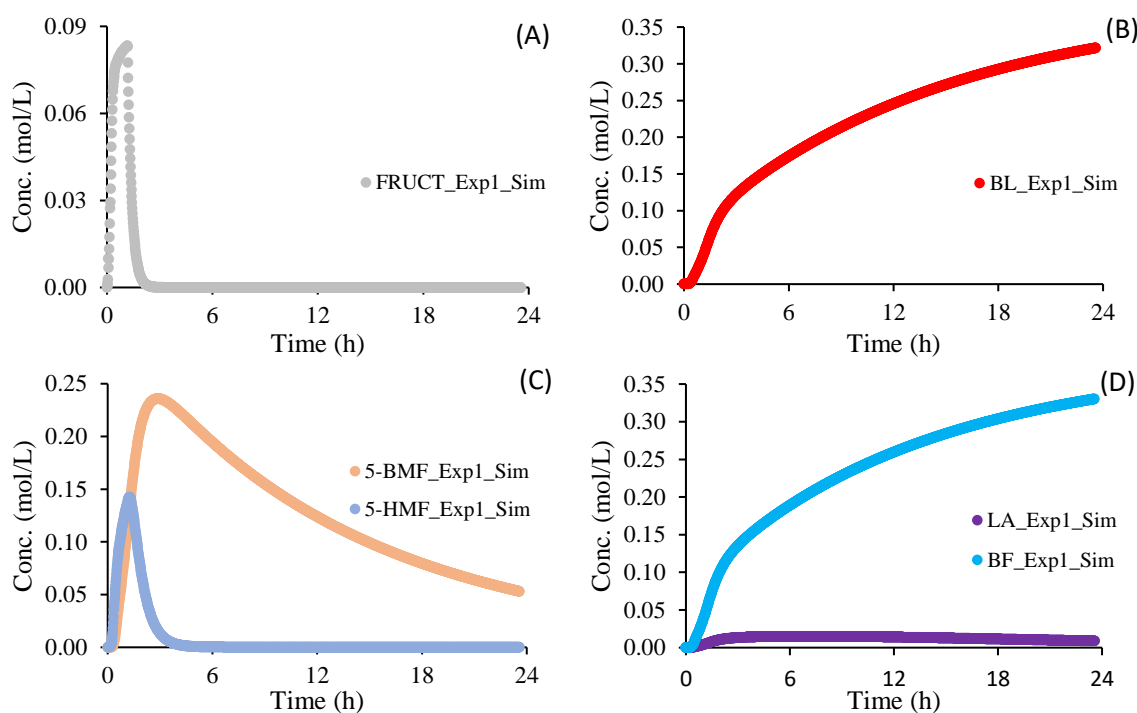


Fig. 42. Simulation of the reaction conditions of experiment 1 with a reaction time of 24h. Simulation of fructose conc. (A); BL (B); 5-HMF, 5-BMF (C); LA, BF (D).

## 4.6 Conclusions

In this chapter, the solvolysis of fructose to butyl levulinate, a promising biofuel and bio-additive, was investigated in depth, experimentally and in terms of kinetic modelling, under the previously defined process conditions; i.e., using the solvent butanol/GVL and on solid acid catalyst. Amberlite IR120 ion exchange resin was identified as an efficient catalyst in the acid solvolysis of fructose under a wide range of experimental conditions and at high initial fructose concentrations (up to 200 g/L), following the high gravity approach. The use of high initial concentrations of fructose in the HG approach and the effects of these concentrations on the kinetics of fructose degradation and dissolution were studied and included in the global kinetic modelling of solvolysis, for which three different kinetic models were proposed, including possible intermediates of fructose isomerization and alkylation. The assessment of the models indicated model 1 as the most reliable model, in which the fructose dehydration step was expressed as a single rate-determining step, excluding possible intermediates. The model was validated by holdout method (using an 80/20% ratio of kinetic experiments for the regression and validation step) and is able to reliably simulate the kinetics of simultaneous fructose dissolution and conversion kinetics to butyl levulinate over a wide range of initial fructose concentrations, from 11 to 200 g/L, reaction temperature (80-115 °C) and dry catalyst loading (35-130 g/L), with final BL yields exceeding 70%. This investigation provides a reliable model to describe and predict the kinetics of solvolysis with initial substrate concentrations on a larger scale, closer to industrial scale, opening a reliable route for the conversion of highly concentrated biomass-derived sugars into oxygenated liquid fuels and versatile chemicals.

# CHAPTER 5 - Sustainability assessment of $\gamma$ -valerolactone production from fructose

## 5.1 Introduction

In the development of a chemical process, kinetic and thermodynamic knowledge plays a key role in the optimization of process parameters that make the process economically, environmentally and socially sustainable.

Developed a robust and reliable kinetic model for the fructose solvolysis to n-butyl levulinate in High-Gravity conditions and defined the optimal process conditions in terms of solvent and catalyst system, these tools can be applied to develop and simulate a process scheme for the BL production from the biomass-derived fructose, and the further transformation to  $\gamma$ -valerolactone (GVL) by using kinetic models reported in the literature [141].

Although known for several decades as an excellent solvent and precursor to numerous products in various sectors (biofuels, pharmaceuticals, food ingredients)[19,127,297], and praised by numerous articles as very environmentally friendly and versatile, GVL has never reached the level of a large-scale industrial product [127]. One main reason can be found in the high production costs, which have recently diminished thanks to improvements in the production of levulinic acid and its derivatives [19], but also on the other hand, the lack of regulated data on its toxicity and biodegradability has limited its diffusion [127].

Many of the recent investigations into the GVL production process in terms of process simulation and sustainability analysis consider the direct production from platform molecules as levulinic acid [298], or ethyl levulinate [297], without including the production steps of the latter or where these are taken into account the sustainability analysis is limited to the economic pillar without considering the further environmental and safety impacts of the process [299,300]. Moreover, none of them considers the possibility of integrating the exploitation of renewable energy sources into the GVL biorefinery for the production of energy and hydrogen. In fact, GVL production through the use of molecular hydrogen is still the common production route in terms of atom economy. In the view of Europe's targets of carbon neutrality, reduction of emissions from hard-to-abate sectors, and dependence on fossil energy sources [301], the integration of alternative and renewable energy sources is a key step to reduce the impact of chemical processes, even those conceived as 'green' due to the use of renewable raw materials such as biomass, and can also induce market diversification of the industrial initiative through the production of electricity and value-added products such as green-hydrogen, produced from water electrolysis. The green-hydrogen market has seen rapid growth in recent years due to reduced investment costs and increased efficiency of electrolysis cell technologies, together with the rise in its market drivers in

chemical and energy sectors as chemical reagent and energy vector for transportation, energy storage and back-up system [180]. Indeed, EU policy strongly supports the implementation of a hydrogen-based energy system as one of the key instruments to realize the European Green Deal. Furthermore, it aims to limit European dependence on hydrocarbons and contribute to the EU's economic growth as a leader in renewable technologies and the hydrogen market [302].

In this context, the main aim of the analysis presented in this chapter is to develop a process scheme for the production of GVL via the pathway of hydrogenation of butyl levulinate by fructose solvolysis, still unexplored in the literature, and to assess the process based on the pillars of sustainability: economic, environmental, and inherent safety. The investigation also considers the potential integration of renewable sources for energy and hydrogen production (PtX-system, presented in section 1.5.2 Hydrogen) that are site-specific, strongly dependent on the territory and its resources. For this reason, the analysis is applied to a real case study in the Normandy region to assess the potential of its renewable resources.

The main purposes can be summarized in the following order (Fig. 43):

- Development of the process scheme for the production of GVL from fructose, in line with the principle of “green-chemistry”, i.e., Atomic economy, Design Safer Chemicals, Benign Solvents & Auxiliaries, Design for Energy Efficiency; Catalysis; etc.
- Development of renewable energy system integration for power and hydrogen production.
  - Evaluation of site-specific renewable resource potential with case study in Normandy.
- Sustainability assessment of possible integrated bio-refinery configurations based on the pillars:
  - Economic
  - Environmental
  - Social (Inherent safety)

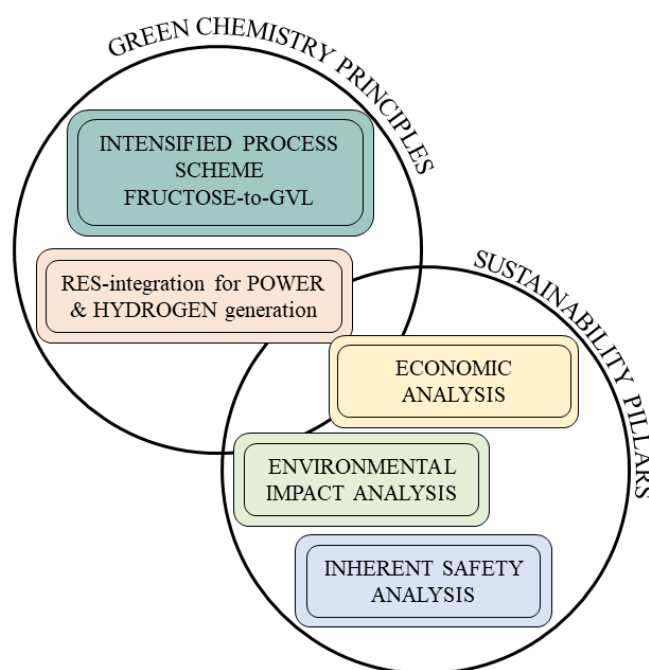


Fig. 43: Main aspects of the investigation in Chapter 5

## 5.2 Methodology

As shown in Fig. 44, The methodology introduced and applied for the sustainability analysis of the GVL production process integrated with renewable energy sources can be schematized through the following steps:

- **PHASE-1:** the availability of site-specific renewable resources is assessed, with specific reference to the Normandy region as a case study. This section then defines the regional and local renewable resource potential, focusing on the availability of unexploited waste lignocellulosic biomass and wind energy:
  - The availability of LCB is assessed on the basis of literature data, regional and national reports on the annual census of this resource and its possible future potential.
  - The availability of wind energy is assessed through the analysis of wind data at the defined location using databases and forecast data reanalysis systems. The potential of the wind resource is then complemented by the evaluation of the most suitable conversion device to convert wind energy into electricity, i.e. the most suitable wind turbine in terms of capacity and performance characteristics is evaluated.
  
- **PHASE-2:** In this phase, the technological design of the biomass valorization process:
  - An essential first step is the conceptual design of the process for the production of  $\gamma$ -valerolactone from biomass-derived fructose via butyl levulinate. In this step, the overall design involves the use of solvolysis technology, under the optimal process conditions and kinetic modeling defined by the previous results described in this thesis, integrated with the hydrogenation reaction step based on literature research, in terms of catalyst, process conditions and kinetics.
  - The following step involves process simulation, through the use of a simulation software and the evaluation of a thermodynamic model to describe reacting species and mixture properties; and subsequent optimization to define an intensified process scheme. This phase involves the evaluation and implementation of material recovery (i.e., solvent recovery) and heat/power stages in the system.
  - From the optimized process scheme, the process energy analysis is defined, evaluating the energy demands in terms of electrical/heat power.
  
- **PHASE-3:** In this phase, the energy system integrated with the process scheme is evaluated. Starting from a conventional configuration in which energy/hydrogen demands are provided by the grid/supplier, different energy configurations were defined with or without the integration of renewable resources into the system; if the system is integrated with renewable energy sources, three main systems were evaluated: exclusive use of wind energy for the fully electrified configuration;

use of wind energy for electrical power demand and use of biomass for thermal energy generation; only use of biomass for thermal power generation.

- For each scenario, the configuration design is defined by evaluating the appropriate technological elements required. For systems involving the generation of renewable electricity from wind, an optimal design procedure of the wind farm and hydrogen production and storage system has been defined and optimized, based on specific design elements.
- **PHASE-4:** Finally, for each scenario defined on the basis of the energy system, the sustainability analysis includes the evaluation of the configuration performance on the basis of key performance indices (KPIs), with respect to the economic, environmental and social perspective. The individual sub-indices are analyzed and aggregated, according to specific methods, in order to define an overall aggregate sustainability index for each scenario and compare them.

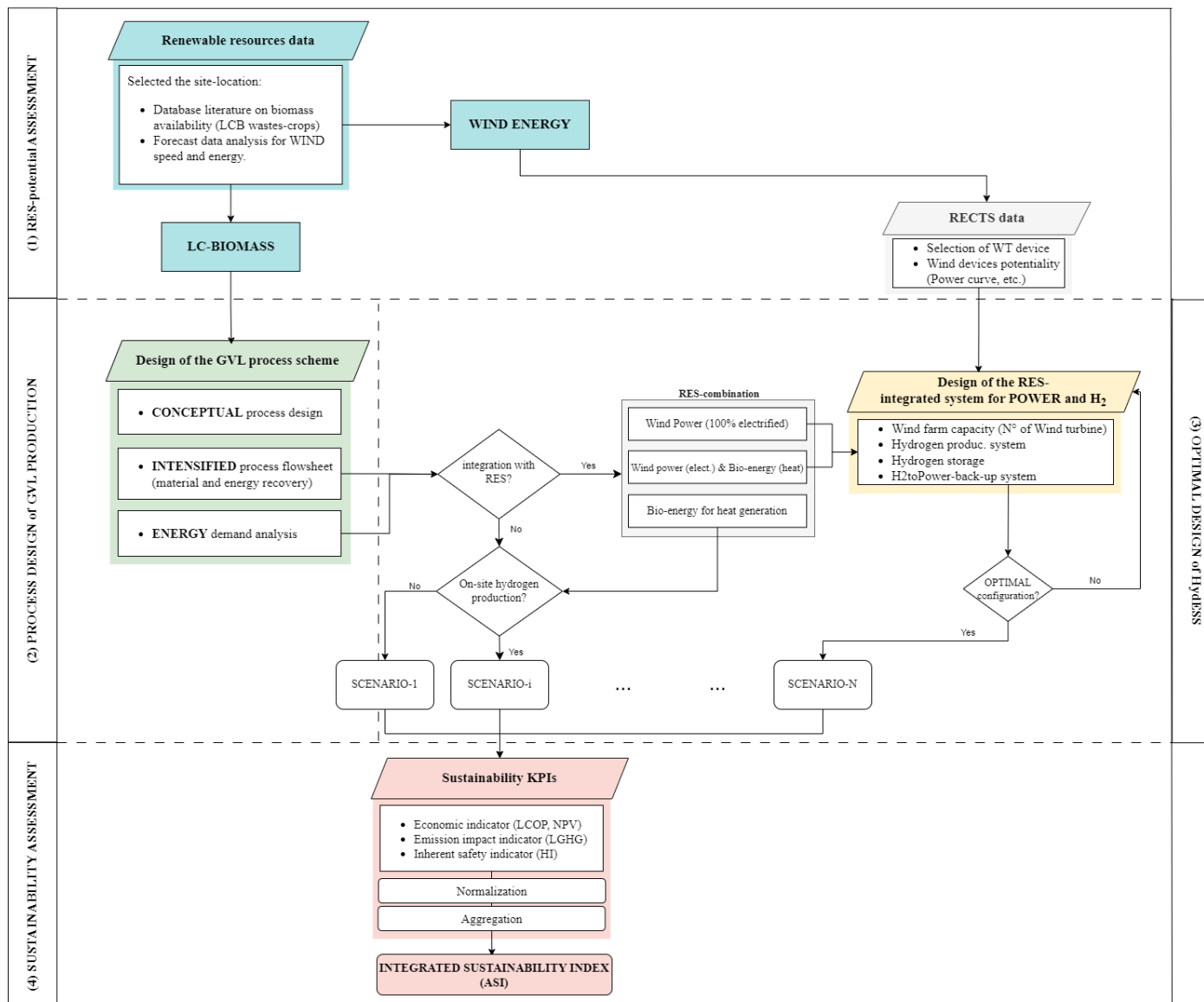


Fig. 44: Flow chart of the proposed methodology for the conceptual design of the GVL process integrated with hybrid energy systems based on renewable sources and sustainability assessment



## 5.2.1 Assessing site-specific renewable energy sources

### 5.2.1.1: Lignocellulosic biomass availability

With 70% of the territory covered by agricultural land and 14% by forests, the Normandy region shows a high potential for lignocellulosic biomass resources regarding wastes and specific crops, generally classified in three categories: agricultural biomass, forestry biomass, and municipal wastes. In the agricultural sector, besides the food crops such as cereals and oilseeds, part of the regional territory is dedicated to the cultivation of fiber flax, of which the region is the leading producer nationally and in Europe, with a production of 470200 tons in 2020 (63% of the national production) [303]. From the fiber production process, flax shives are the mainly residue wastes that cause of quality defects in the fiber transformation processes and represent around 50 % in weight of retted flax stems [304]. The high cellulose content ,approximately 65-85% of the composition, make the flax shives a promising and abundant raw material candidate for the valorization to value-added chemicals as GVL [304,305]. From the forestry sector, the main wood products and wastes by-products come from oak and beech trees [306], which are the most abundant species and both have a cellulose and hemicellulose content around 22-50% and 17-30%, respectively [307,308]. In addition, the interest in specific rapid-growing crops is increasing at regional and national levels as for miscanthus and hemp, with a constant growth rate in cultivation of around 10% per year and with production volumes over 50,000 – 60,000 tons in 2019 [309]; besides to the content in cellulose and hemicellulose, these species shows also capacity of phytoremediation, improving the physicochemical properties of the soil and prevention of soil erosion, together with a rapid cultivation [310,311]. Besides specific crops, LCB wastes and residues from the region's agricultural, industrial and municipal sector constitute an abundant and great resource of sugar monomers, currently under-exploited. Nowadays, only the 10% of bio-wastes are valorized in France by methanation and composting, then 60% of wastes are landfilled with a cost around 60-100 €/t and the remaining 30% are burned with a cost of 70-120 €/t; costs are expected to increase over time [312,313].

At the regional level, the amount of collected lignocellulosic biomass wastes is over 400 kilo-tons for year, with 133 kg per capita per year whereas the national average is 79 kg/per capita ·y [314]. The rate observed for material recovery in Normandy is around 46%, which remains below the targets set by the French Law on Energy and Green Transition (LTECV), and, therefore further exploitable [314]. The high availability of resources makes Normandy a promising candidate for further development into bio-chemicals and a potential location for the process site can be selected in the Seine-Maritime department; in fact, this department holds the highest percentage of lignocellulosic biomass waste (34% of the regional total [315]) thanks also to an extensive and advanced agricultural network; in fact, Seine-Maritime also holds 50% of the regional surface area cultivated with flax (42519 ha out of 85256

regional ha). In addition to the departmental biomass availability, which reduces the time and logistical costs of biomass supply, the department has a strong industrial profile with high investment in wind energy, a symptom of its wind potential and, recently, in green hydrogen production development [316,317]. Excluding areas of the department near natural parks and protected areas typically concentrated along the course of the Seine River [318], the choice for a potential industrial site fell on the “*Alabaster Coast*”, an area near the Normandy coast with particular industrial potential and included in the 124 national high industrial development zones by the French government [319]. The location of the site selected in this study is indicated by the area indicated in Fig. 45.

The average yields in literature for the production of sugar monomers such as glucose and xylose from biomass are around 25 wt% [320,321], around 11-15 wt% for fructose through glucose isomerization and up to 24 wt% for high-concentrated fructose syrup from waste biomass [322,323]. Considering a biomass cellulose content around 50 wt%, the potential production of fructose from the amount of waste biomass not exploited in Normandy is over 30 kt/y, fulfilling the demand for different production sizes of GVL. The production size of 2 kt/y of GVL is considered a reference production size, as it is defined on the basis of the production size of levulinic acid by GFBiochemicals, the only company currently producing levulinic acid and derivatives such as alkyl levulinate directly from biomass on a commercial scale [324].

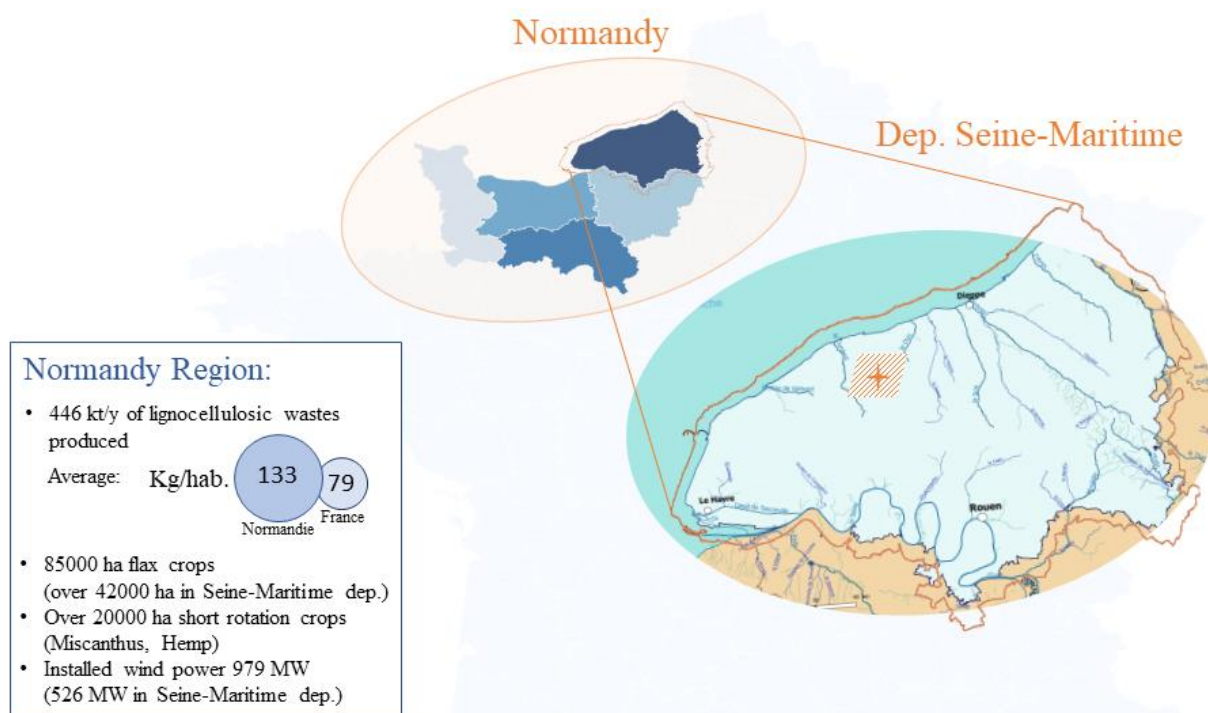


Fig. 45: Potential site location in the Seine-Maritime department (Normandy) and summarized potential biomass info and wind exploitation in the region.

### 5.2.1.2: Wind data analysis and characteristic parameters

With an installed capacity of 526 MW wind farms out of a total of 979 MW in the region by 2022 [325], the Department of Seine-Maritime has a high exploitable wind potential. Once the location site has been selected, the wind potential of the site can be assessed by analyzing wind speed trends and seasonal effects; this can be done by using climate forecasting tools that allow to analyze the wind data in a specific site and for different time periods. Among them, the European ERA5 is a tool implemented by ECMWF (European Centre for Medium-Range Weather Forecasts) and available from the Copernicus Climate Change Service [326]; it provides hourly data of several terrestrial and sea-state weather variables from 1979 to 2-3 months before the present, on regular latitude-longitude grids  $0.25^\circ \times 0.25^\circ$ . Horizontal and vertical wind speeds can be evaluated hourly at a height of 10-100m in the location site and for longer periods in order to assess possible seasonal effects and the characteristic parameters of the wind potential. In literature, the wind speed distribution is traditionally described by the Weibull distribution, characterized by dimensionless shape parameter  $k$  (dimensionless) and the scale parameter  $c$  in m/s, and several parameters can be empirically evaluated, based on the distribution characteristics, in order to evaluate the wind energy potential and the specificity of the location [327–331].

$$f(v) = \left(\frac{k}{c}\right) \left(\frac{v}{c}\right)^{k-1} \exp\left[-\left(\frac{v}{c}\right)^k\right] \quad (v > 0, c > 0) \quad \text{Eq. 5. 1}$$

In case of values of  $k$  smaller than 1.5, the wind is variable and gusty in the site, then it is moderate and steady for values higher than 2 [332]. Knowing the distribution parameters, the wind power density ( $WPD$ ) can be evaluated as key parameter that reflects how energetic the wind is and defined as follows [330]:

$$WPD = \frac{P}{A} = \int_0^{\infty} \frac{1}{2} \rho v^3 f(v) dv = \frac{1}{2} \rho c^3 \Gamma\left(1 + \frac{3}{k}\right) \quad \text{Eq. 5. 2}$$

Where  $\rho$  is the density of the ambient air, generally estimated at  $1.225 \text{ kg/m}^3$  at  $15^\circ\text{C}$ .

The analysis of the wind speed distribution is fundamental for choosing the most adaptable wind turbine technology. Among the parameters specific to each turbine, key characteristics of the selected turbine are: the wind cut-in ( $v_c$ ) which represents the wind speed (in m/s) at which the turbine blades begin to turn, generating energy; wind cut-off ( $v_f$ ) the maximum wind speed (in m/s) at which the turbines stop for safety reasons; and rated wind speed ( $v_r$ ) the wind speed corresponding to reaching the turbine's rated power. The analysis of the specific characteristics of turbines can be combined with the evaluation of empirical parameters that guide the choice of device, such as the most probable wind speed ( $v_{mp}$ ) and the wind speed carrying the maximum energy ( $v_{max-E}$ ); as the first is close to the mean value of the distribution and the second should be closely related to the rated wind speed of the selected wind turbine in order to have an efficient system [327].

$$v_{mp} = c \cdot \left(1 - \frac{1}{k}\right)^{1/k} \quad v_{max-E} = c \cdot \left(1 + \frac{2}{k}\right)^{1/k} \quad Eq. 5.3$$

Once a device has been selected on the basis of its operating specifications, adapted to the wind distribution and territory, the capacity factor ( $CF$ ) and the probability of site-specific operation ( $P$ ) of the wind farm can be assessed [327,330]. The capacity factor represents the ratio between actual energy production and the maximum possible, while the second parameter indicates the probability that the turbine is in operation at the location considered:

$$CF = \frac{\exp\left[-\left(\frac{v_c}{c}\right)^k\right] - \exp\left[-\left(\frac{v_r}{c}\right)^k\right]}{\left(\frac{v_r}{c}\right)^k - \left(\frac{v_c}{c}\right)^k} - \exp\left[-\left(\frac{v_f}{c}\right)^k\right] \quad Eq. 5.4$$

$$P(v_c < v < v_f) = \exp\left[-\left(\frac{v_c}{c}\right)^k\right] - \exp\left[-\left(\frac{v_f}{c}\right)^k\right] \quad Eq. 5.5$$

### 5.2.1.3: Wind potential assessment

In this investigation, the wind data analysis in the selected site was carried out by considering a period of 10 years (2011-2021) in order to assess the potentiality and seasonal effects of the wind and at a height of 100m, assuming it as a typical hub-height for an on-shore wind device. Comparing the distribution of data during this decade, 2018 was chosen as the reference year, as in terms of average speeds and power density it is the closest to the annual and seasonal median values over the entire decade (power density ( $W/m^2$ ) in 2018 of 254.2 in Spring, 145.6 in Summer, 299.7 in Autumn, 556.8 in Winter, 314 in the year, comparable with average values in Fig. 46 and data in Table S3. 2) [333].

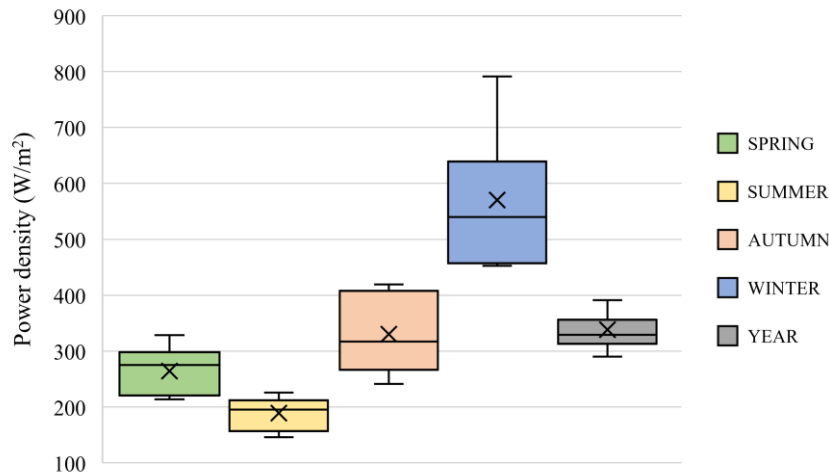


Fig. 46: Box plots of the annual and seasonal available wind power density in the location site (years 2011–2021).

Knowing the real-forecast wind data, the maximum likelihood method (MLM)[329] was used to estimate the distribution parameters  $c$  and  $k$ , from real data fitting, using the Weibull distribution (“WeibullDistribution” function [334]) implemented on MATLAB-R2023a [335].

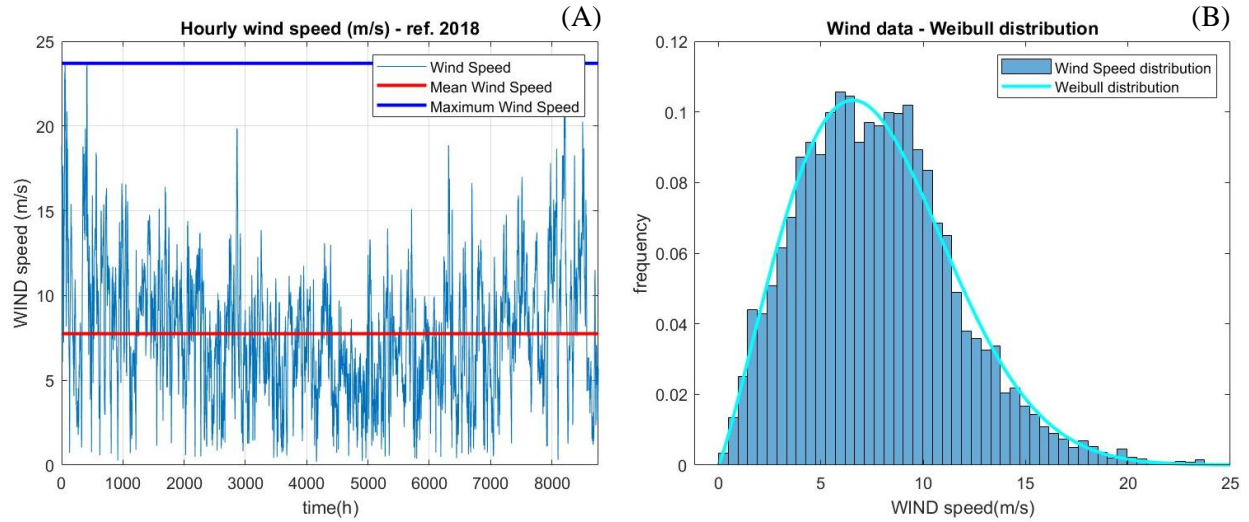


Fig. 47: (A) Punctual values of wind speed data at the selected site in 2018; (B) Wind data according to Weibull distribution

Table 23: Characteristic data of wind distribution and power at the site considered

Wind distribution characteristics	
$k$	2.16
$c$ (m/s)	8.75
$v_{mean}$ (m/s)	7.75
$v_{MAX}$ (m/s)	23.7
$v_{mp}$ (m/s)	6.56
$v_{E-max}$ (m/s)	11.85
$WPD$ (W/m <sup>2</sup> )	506.23

The wind analysis in this site shows a  $k$  value of 2.16, corresponding steady and moderate wind type, and a scale  $c$  value of 8.75 m/s. In terms of mean wind speed (7.75 m/s) and most-probable value (6.56 m/s) at 100 m, the wind-site can be exploited by using a turbine of the class IEC III [336].

Based on these parameters, government guidelines and the average power of turbines installed in the region [325,337], the selected turbine is V110-2.0 MW from Vestas [338], with a cut-in of 3 m/s, cut-off of 20 m/s and a rated wind speed of 11.5 m/s. A rated wind speed close to  $v_{max-E}$  allows nominal energy production to be maximized with this device. Other properties of the wind turbine are reported in Table 24.

Table 24: Characteristics of the selected wind turbine V110-2.0 MW Vestas

<b>V110-2.0 Vestas [338]</b>	
<b>Operating Data</b>	
Rated power	2000 kW
Rated wind speed	11.5 m/s
Cut-in wind speed	3 m/s
Cut-out wind speed	21 m/s
Wind Class	IEC IIIA
<b>Rotor</b>	
Diameter	110 m
Swept area	9503 m <sup>2</sup>
<b>Tower</b>	
Hub height	95 m

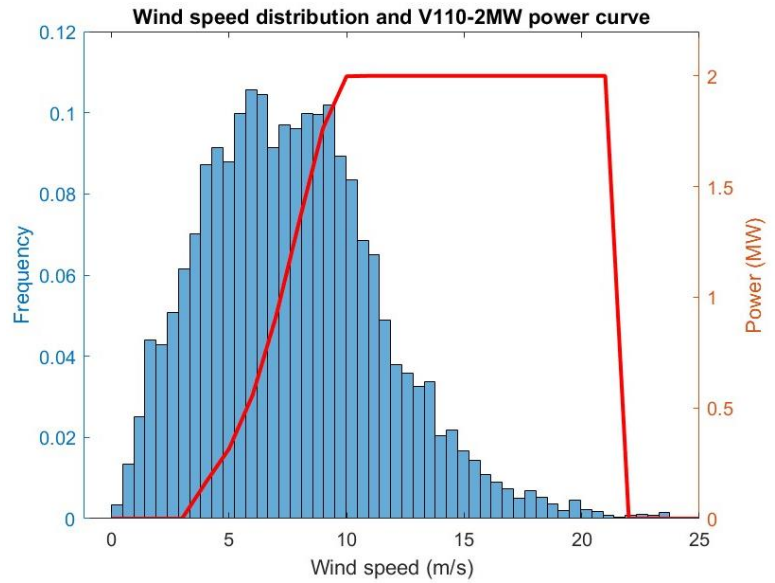


Fig. 48: Overlay between wind speed frequency data and turbine device power curve

The capacity factor of turbine technology in this location is 45.2 %; it represents the ratio of predicted actual energy output to the maximum possible and it is in line with the average 30-45% reported in the literature for onshore wind turbine technology in 2022 [339]. The probability of operativity of the turbine with the wind distribution is over 90%. Knowing the WT's characteristics and power curve (Fig. 48), the wind potentiality can be coupled with the device to evaluate the hourly-power produced. The size of the wind farm, in terms of the number of wind turbine units, is then evaluated according to the demand for electricity from the process.

## 5.2.2 Conceptual design of the chemical process

The conceptual process scheme presented in this work consists in a combination of two process steps in series in which the production of GVL is obtained by hydrogenation of butyl levulinate as precursor, and the production of the latter via acid solvolysis of biomass-derived fructose. The scheme does not include preliminary biomass pre-treatment stages for the fructose production, considering the feeding of biomass-derived fructose to the process as raw material provided off-site. The first reaction stage considers the solvolysis of fructose to n-butyl levulinate on the basis of the optimal reaction conditions determined experimentally and discussed in the previous chapters; the reaction is then catalyzed by the acid ion exchange resin, Amberlite IR120, and the solvent system defined is butanol-GVL (70/30 wt% ratio). The experimental results presented in the previous chapters showed the high efficiency of this solid acid catalyst under moderate temperature conditions and the advantages of using GVL as a co-solvent in terms of dissolving fructose and inhibiting the degradation of sugar and intermediates into humins. Furthermore, a robust kinetic modeling was presented in the previous chapter, considering the effect of high fructose concentration. The model in particular was used to simulate potential process conditions; in this case, conditions of 110 °C, 20 bar, feeding an initial fructose concentration of 100 g/L, and with a catalyst loading of 130 g/L were considered in the process design. In these conditions, the model considers a molar yield in BL of 78 %, for a residence time of 24 h, with a remaining share of convertible intermediates. A complete conversion of the intermediates 5-HMF, and 5-BMF to BL is considered, while LA and FA are not fully converted due to slower kinetics. By considering the reaction kinetics, the mixture of products exiting the reactor consists of the main product, butyl levulinate, as well as secondary products, such as butyl formate and water, content of intermediates, such as levulinic acid and formic acid, together with solvents and the degradation product, humins.

Consequently, the reaction stage is followed by a separation unit to isolate and convey butyl levulinate, levulinic acid and GVL to the second reaction stage: hydrogenation.

The GVL production is carried out by hydrogenating butyl levulinate, and levulinic acid in minor concentration, with H<sub>2</sub>-gas over heterogeneous catalyst. Even though the production of GVL can occur also by using a hydrogen-donor as alcohols or degraded acids as formic acid, the use of molecular hydrogen is still the most common route in terms of atom economy. Delgado et al. [257] elucidated the kinetics of hydrogenation of butyl levulinate over ruthenium on activated carbon (Ru/C) and in GVL-solvent system. The reaction path considers the initial hydrogenation step to the intermediate BHP for butyl levulinate and HPA for levulinic acid, and the subsequent cyclization of the latter to GVL. The kinetics of this system show the complete conversion of the butyl levulinate, levulinic acid and for the instable intermediate HPA, but not that of BHP, whose cyclization kinetics reach the equilibrium and consequently it is present in the products stream. An 80% conversion of BHP to GVL was considered in the design, based on the average reaction conditions of 150 °C, 20 bar given in the literature,

considering a catalyst load of 1.7 g/L [131,141]. After the reaction step, a train of separation unit is therefore necessary to remove the by-products, such as water and butanol, and isolate the reaction intermediate BHP that can be recycled back to the reactor and a further unit may be needed to obtain the market purity specifications for GVL ( $\geq 99\%$  wt) [299]. Given the difference in boiling point temperatures and the high degradation temperatures for these components, distillation results a suitable unit operation. The final stream of GVL product at the desired concentration is then partially recycled into the solvolysis reaction block, as part of the solvent system.

The fraction of light components, resulting from the separation steps of each reaction block, consists mainly of butanol, water, butyl formate and some traces of formic acid. The resulting stream is sent to further separation stages to first remove the water content and then the traces of butyl formed are treated. Separation of butyl formate from butanol by distillation would require a column train and expenditure of energy, due to the reduced driving force in terms of similar relative volatility between the components. For this reason, a separation by reaction decomposition of BF into butanol and carbon monoxide over a metal oxide catalyst was considered on the basis of established patented technologies [340,341], and the regenerated butanol solvent sent back to the solvolysis process block, as shown in Fig. 49.

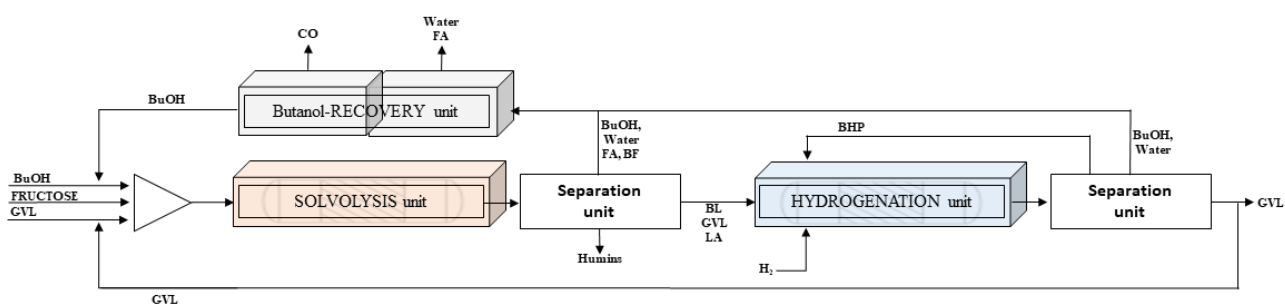


Fig. 49: Block diagram of the conceptual design of the GVL production process from fructose.



### 5.2.3 Process modelling for an intensified process flowsheet

Defined the basis of the conceptual process scheme, process units were simulated by using a process simulator: Aspen Hysys from Aspen Technology [342]. The sequential modular approach is used to build the flowsheet by linking multiple process units, auxiliary units, components, stream and selecting the suitable thermodynamic methods and units of measurement. Defined an initial reference process scheme, the intensified process scheme is then evaluated at the steady-state condition, optimizing and integrating the process in terms of material recovery (i.e. recycling reactants and solvents to the reaction units and purging undesirable compounds) and/or heat and power recovery (i.e. high-temperature streams may be used to heat and/or vaporize cold streams in the process and vice versa). The simulation considers a final production size of GVL of 2 kt/y with a purity >99.9% with an overall fructose-to-GVL yield of 50.5 wt%; then further production sizes were implemented. For the thermodynamic model choice, the equation of state Benedict-Webb-Rubin-Lee-Startling was selected in the simulation for the component properties estimation and phases equilibrium data, particularly suitable for the simulation of the hydrogenation step [299,343] and for the description of this component system, in particular in presence of butyl levulinate, butanol and GVL as shown by the work of Ariba et al. [261]. The physicochemical properties of most components are present in Aspen Hysys database, except for fructose, butyl levulinate, BHP and humins. For these components, literature data for properties were implemented in the simulation [43,127]. A preliminary process flow diagram for the production of GVL from fructose is shown in Fig. 50.

Beside the process units, the utility units were simulated; steam generation at high pressure (45 bar, 250°C) is supplied by boilers powered by electricity or by fuel combustion (natural gas or biomass) depending on the different energy scenarios. Boiler efficiency (LHV – lower heating value – basis) is 87.7 % for natural gas-user, 89.9 % for biomass-user system and 100 % for the electrical one. Cooling water is supplied to the system at 30°C and returns to the cooling tower at 40°C with the air flow demand determined by simulation in order to cooled down the water, while energy demand is based on literature data from datasheets on commercially available technologies [344]; chilled water is provided at 5°C, through a propane refrigeration loop.

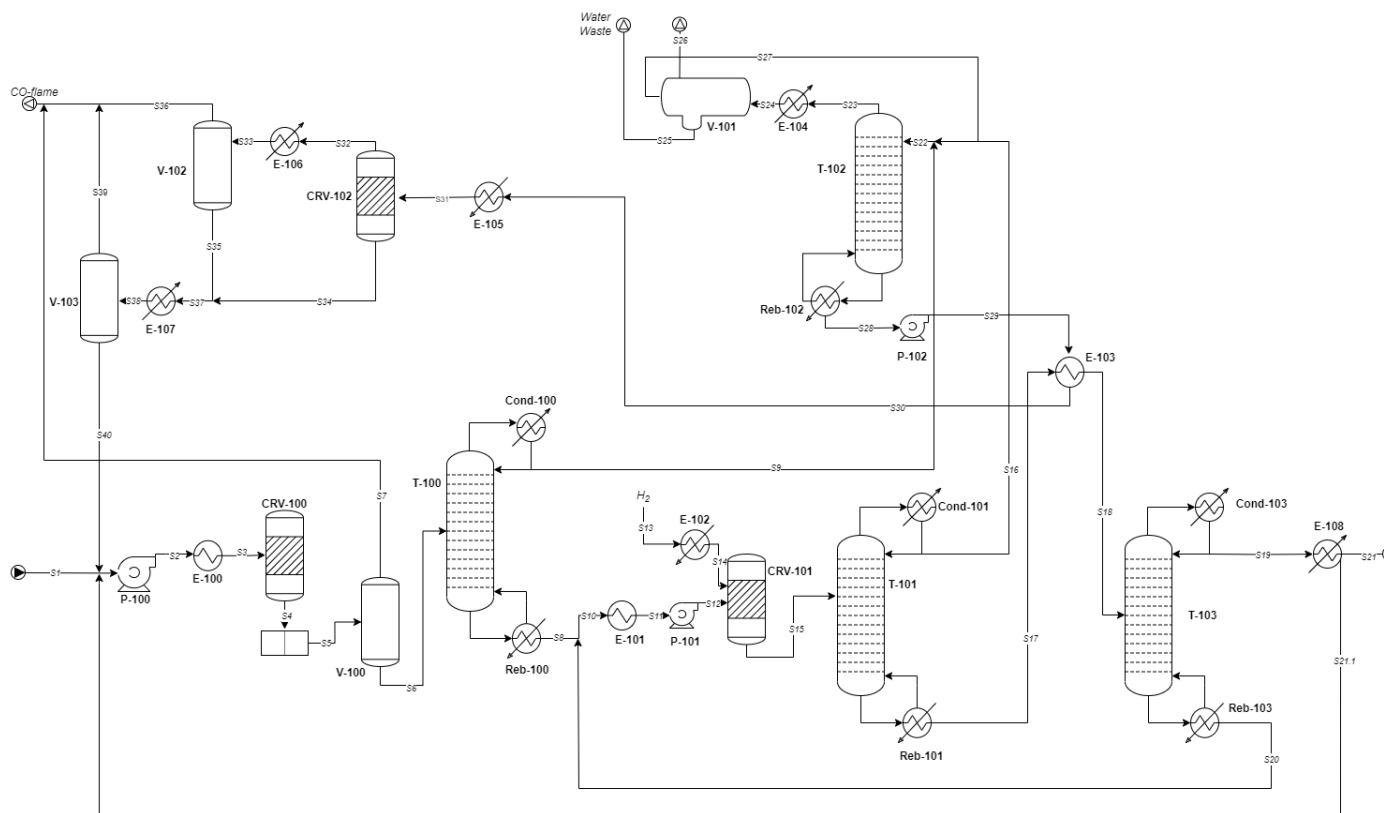


Fig. 50: Preliminary Process Flow Diagram for GVL-production from fructose

Table 25: Equipment flowsheet legend

<b>Equipment legend:</b>		
<b>Reactor CRV:</b> CRV-100; CRV-101; CRV-102	<b>Heat&amp;Exchanger E:</b> E-100-108	<b>Pumps P:</b> P-100; P-101; P-102
<b>Separator V:</b> V-100; V-101; V-102; V-103	<b>Col. Condenser Cond.:</b> Cond-100; Cond-101; Cond-103	
<b>Distillation columns T:</b> T-100; T-101; T-102; T-103	<b>Col. Reboiler Reb.:</b> Reb-100; Reb-101; Reb-103	

### 5.2.3.1 Solvolysis Fructose to n-butyl levulinate

In the solvolysis section, as shown in Fig. 51, a pre-mixed stream of fructose and butanol was mixed with a stream of pure GVL in order to achieve the request solvent ratio 30/70 wt% of GVL/butanol and a fructose concentration of 100 g/L. The stream is sent to a volumetric pump and a heater exchange to be conditioned to the specific reaction condition of pressure 20 bar and temperature 110°C. The reactor (CRV-100) was simulated based on the known kinetics mentioned above and final yields, catalyzed by Amberlite IR120 (catalyst loading 130 g/L); considering the full conversion of fructose, and intermediates 5-HMF and 5-BMF. The presence of degradation besides reactions leads to the presence of humins, typically in insoluble or partial soluble form (with a maximum yield to it of 10 mol%), and content of levulinic and formic acids in the final product stream are present due to the slower esterification kinetics compared to the conversion of 5-BMF. The virtual process operator, named “*splitter*” in the software, was used to simulate the separation of humins from the product stream, usually obtained by filtration in case of solid by-products. Before being treated in a distillation column, the stream is fed to a separator (V-100) for the removal of solubilized CO during the butanol solvent regeneration phase. The product stream, with a composition in butyl levulinate of 11.8 wt%, is sent to a distillation column (T-100). In this separation unit, the heavier components are isolated in the bottom stream with a composition around 77 wt% of GVL, 22 wt% of BL and >1 wt% of levulinic acid, and then conveyed to the hydrogenation stage.

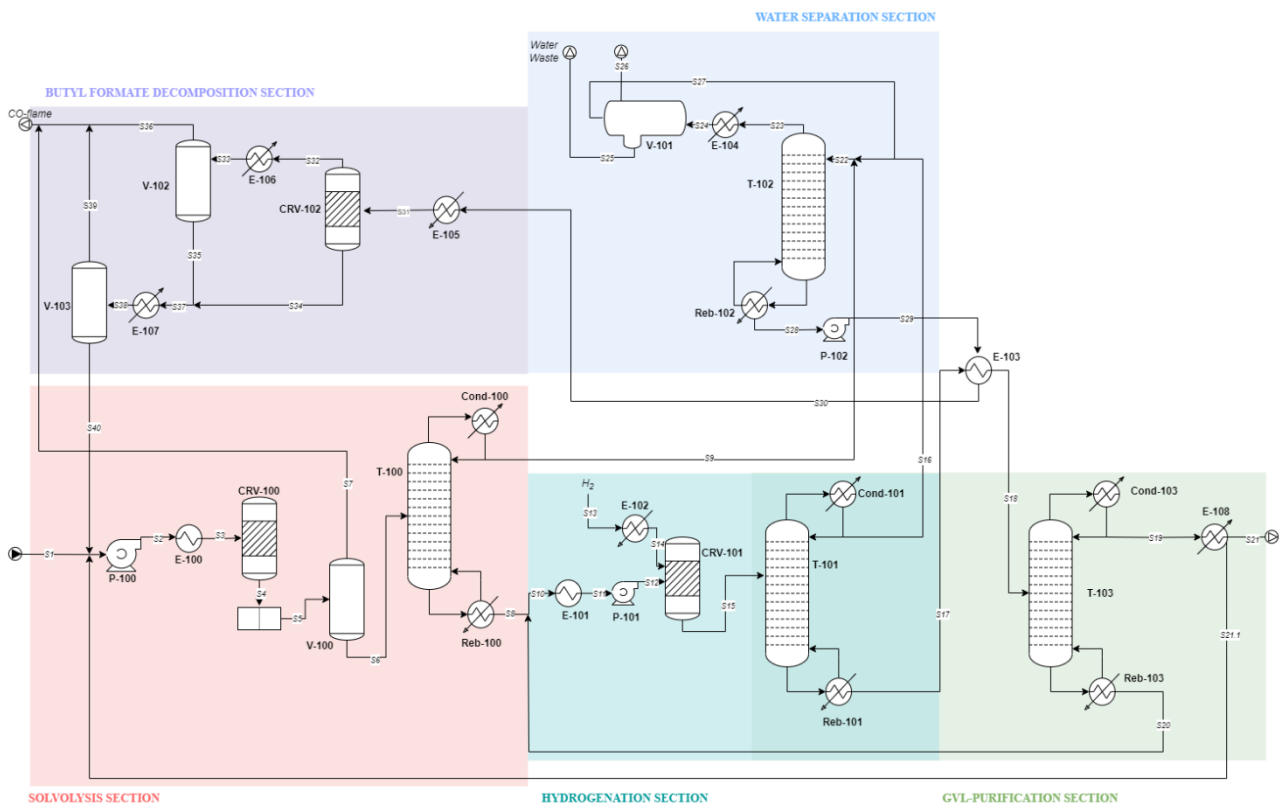


Fig. 51 Preliminary process flow diagram for the production of GVL from fructose highlighting the different process sections

### 5.2.3.2 Hydrogenation of n-butyl levulinate to $\gamma$ -valerolactone

The stream resulting from the solvolysis block is fed to the hydrogenation reactor (CRV-101), in the process specification at 150 °C and 20 bar (Fig. 51). A stream of hydrogen gas is fed to the reactor with a molar flow to ensure complete stoichiometric conversion to the hydrogenation intermediate BHP and HPA, corresponding to 5 kg/h for the considered production size of 2 kt/y of GVL. Given the kinetics of the cyclisation step, the conversion of BHP to GVL is not complete (around 80%), so the output stream to the reactor will see a BHP content of 7.6 wt% and around 77 wt% of GVL, together with butanol and water as secondary products. The reactor is followed by a train of two distillation columns: T-101 separates the light phase consisting of butanol and water, obtained as head products and sent to the butanol purification block, from the bottom products such as GVL and BHP. The bottom stream is used as hot stream for heat recovery in the E-103 heat exchanger (stream temperature 236 °C), before being sent to the second column T-103. In the second column, the stream is processed to achieve the required purity specifications for GVL, obtained as a top product with a purity >99.9 wt% while the bottom stream with a content >99.4 wt% in BHP is recycled to the reactor. The final stream of GVL is cooled down and partially recycled to the solvolysis block.

### 5.2.3.3 Water separation and butyl formate decomposition

Butanol, butyl formate and water form a minimum-boiling heterogeneous ternary azeotrope, thus separation by distillation is carried out producing anhydrous butanol-butyl formate mixture as a bottom product with a content in butyl formate less than 10 wt%, and butanol-butylformate-water azeotrope as top stream product. After condensation, the azeotropic distillate is sent to a decanter (V-101) in which aqueous-organic phase are separated. While the aqueous phase (water content over 93 wt%) is sent to wastewater treatment, the organic phase is fed back to the column. For the binary mixture butanol-BF, separation by distillation would be particularly cost and energy-intensive due to the reduced driving force (reduced relative volatility); thus, the stream is preconditioned and fed to a catalytic reactor to decompose the butyl formate over heterogeneous catalyst. Metal oxides are particularly efficient in decomposing formic esters into carbon monoxide and alcohol as shown from some patents [340,341]; considering a fixed-bed reactor with DHT-4A/Alumina (over 50 wt%) and specific process condition (190 °C and 20 bar) butyl formate is converted in CO-gas and butanol with a full conversion. In the process simulation, the reactor was considered as a conversion reactor. By cooling down the gas product stream, part of vaporized butanol is condensates and conveyed to the liquid product stream through a gas-liquid separator. The final butanol stream (>99.5 wt%) is cooled down and then recycled as feed solvent to the solvolysis block. The CO gas streams from the reactor and the separators are conveyed and sent to flame. A back-up butanol stream is considered in order to adjust the concentration specs at the reactor feed.

## 5.2.4 Energy analysis

Based on a GVL production of 2 kt/y, the electrical and thermal power requirements were evaluated on the basis of heat and power streams. Considering the electrical items, such as the process pumps, the propane circuit compressor for chilled water and the cooling tower fans, the electrical power required is 1.38 MW, to which is added the thermal power required by the boiler for steam generation, amounting to 1.89 MW. For higher production capacities, the estimated electricity and heat demands are 1.85 MWh and 3.99 MWh for 4 kt/y of GVL, and 3.84 and 9.65 MWh for 10 kt/y, respectively. The demand for heat for steam production can be achieved by combustion of fuel (mainly natural gas), biomass not intended for chemical valorization and other waste by-products (as solid humins), or by electricity, defining different energy scenarios. Beside the natural gas, the use lignocellulosic biomass as bioenergy source was evaluated in this context in terms of availability and heat capacity. Considering an average higher heating value (HHV) of 19 MJ/Kg [345] and the efficiency of the boiler (89.9%), the energy demand can be covered by 3.4 kt/y of wasted biomass; the amount of biomass destined to the energy production can be further reduced to around 3 kt/y including the by-product humins as energy source since it presents a valuable heating value estimated around 19.5 MJ/Kg [346]. For a production size of 4 kt/y, the amount of biomass required, net of the amount of humins, is 5.5 kt/y, while it is 10.4 kt/y for a GVL production size of 10 kt/y. The biomass demand of the largest plant, including chemical and heating valorization, starts to be burdensome, even still within the limits of availability in the region. For this reason, to consider a self-sustained regional scheme for biomass supply, further analyses focus on the small and medium-sized production size of GVL, i.e. 2 and 4 kt/y.

Besides natural-gas and biomass-system, the comparison with a potential fully electrified configuration, i.e. with an electric boiler for steam production, was included in the further analyses due to the specificities of the French electricity grid, which through an energy contribution from nuclear power of over 40% in 2022, is able to provide electricity with costs and CO<sub>2</sub>eq. emissions below the European average and in competition with other energy sources [2,347]. For electrical supply to the plant, the supply of electricity from the grid was compared to the on-site production of electricity from renewable energy sources, specifically wind power.

## 5.2.5 Integrating renewable energies into the GVL biorefinery

Having defined the process scheme for the production of GVL from fructose derived from LCB biomass and considered its energy requirements, the other main objective of this work is to also consider the integration of renewable wind energy into the GVL biorefinery in terms of electricity but also hydrogen supply. In fact, wind energy can be further exploited to integrate in the GVL process the on-site production of green hydrogen for the hydrogenation step via water electrolysis. The integration of renewable energy in the continuous production flowsheet requires the installation of back-up system in

order to deal with the positive and negative fluctuation of the energy source; thus, the integrated-scheme considers also the presence of a hydrogen fuel-cell, back-up battery system and hydrogen buffer storage.

### 5.2.5.1 Alkaline electrolyzer (AEL)

Of the currently available technologies, the alkaline electrolyzer (AEL) is the most mature (TRL 9) and widely used technology in the industry [179,348], accounting for almost two-thirds of the world's electrolyzer production capacity, and followed by the proton exchange membrane electrolyzer (PEM) for one-fifth of capacity [179,348]. Like the alkaline electrolyzer, PEM is already commercial, with a TRL of 9, while other technologies such as solid oxide electrolyzer cell (SOEC) and anion exchange membrane (AEM) are still under development with TRLs of 7 and 6, respectively [179]. Although PEM technology has higher efficiency, current density and output pressure, the main disadvantages limiting its large-scale application use compared with AEL is the high cost of components (Nafion membrane, titanium bipolar plates and metal catalysts) and shorter lifetime [349,350]. The AEL technology considers the water electrolysis into hydrogen and oxygen in a stack operating at approximately 70-90 °C and at a maximum of 30 bar, with an alkaline electrolyte (NaOH or KOH) in concentration 20-40 wt% [351]. The main elements of the stack are the membrane for the transport of OH<sup>-</sup> ions, separation of product gasses (H<sub>2</sub> and O<sub>2</sub>) and electrical insulation of electrodes; electrodes (cathode and anode) coated with non-noble metals like Nickel; gaskets and seals to prevent possible gas leaks; and bipolar plates to separate each cell in a stack but providing electrical conduction between them [183]. In addition to the stack, the electrolyzer module has other elements required to achieve the requested hydrogen purity, as shown in Fig. 52. The two gaseous product streams are sent separately to a gas separator to recover and recirculate the lye solution to the cell block, after being cooled. The hydrogen stream is then conveyed into a scrubber before being stored in a buffer tank to remove residual traces of electrolyte, cool the hydrogen and feed make-up water for the alkaline solution. From the buffer tank, the hydrogen produced is compressed to the desired pressure and treated in a deoxidizer to reduce its oxygen content ( $\leq 0.2\%$ ) by a catalytic reaction and in a desiccator, before being stored [348]. Alkaline technologies are widely implemented in industry for large-scale hydrogen production with possible energy capacity of more than 100 MW by coupling different alkaline modules. Based on commercial data sheets, alkaline

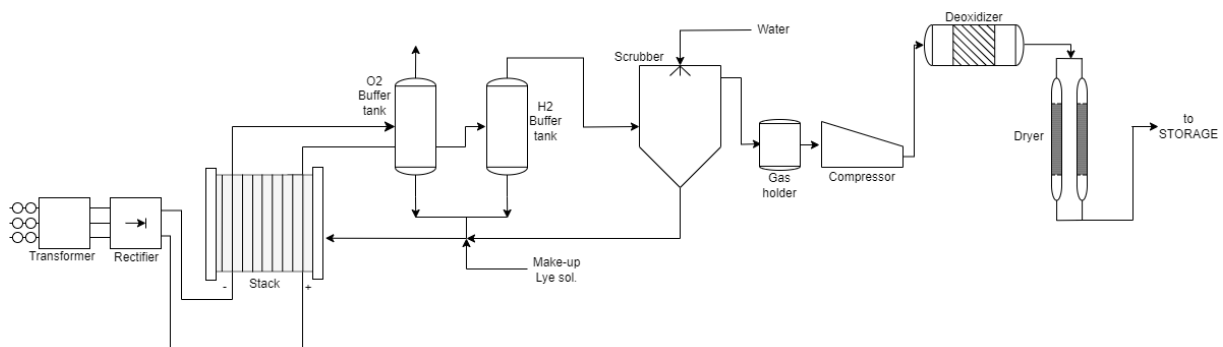


Fig. 52 Typical system design and balance of plant for an alkaline electrolyzer

electrolyzer modules can provide production rates from 4.5 to 45 kg/h with a DC power consumption of between 42.2 and 51 kWh/kg of hydrogen [351]. Table 26 reports the specification used in this investigation for single-unit and AELs-module production. For large stacks (>1MW), the capital cost is estimated to \$270/kW and to 500-1000\$/kW for the entire system, including the balance of stacks, power plant rectifiers, the hydrogen purification system, water supply and purification, cooling and commissioning costs for capacity higher than 10 MW, with an operating lifetime of 60,000-80,000 h [180,352]. Depending on the size of the wind farm, related to the renewable energy demand for the plant, the electrolyzer cell modules are sized to absorb the maximum energy peaks in the favorable seasons and convert it into hydrogen, the capacity of the AEL modules ranges from 0.5 to 70 MW in this investigation, considering an average investment cost of \$750/kW, and an operating cost of 2% of capital cost [180]. Considering a stack-lifetime of 75000 h (corresponding to 9 years for a plant working at 95%/annual), the stack replacement cost considered is \$340/kW [352]. Gaps in cost and performance are expected to drop over time, considering a predicted total cost of the AEL system at less than \$200/kW in 2050 [180].

Table 26: Datasheet specification Alkaline electrolyzer

<b>Alkaline Electrolyzer (AEL)</b>	
Capacity Range per Unit	4.5 – 43.5 kg/h
Efficiency	42.2 – 48.9 kWh/Kg
Operating Temperature	80 °C
Operating Pressure	30 bar
Hydrogen purity	99.99-99.999%
O <sub>2</sub> -content	≤ 2 ppm vol.
Electrolyte sol.	Aq.-KOH (25 wt%)
Water Consumption	7.8 kg <sub>H2O</sub> /kg <sub>H2</sub>
Dim. Footprint	~150-225 m <sup>2</sup>
Lifetime stack	< 90,000 h
Lifetime AEL system	20 – 30 y

### 5.2.5.2 Hydrogen Storage

The storage system is a crucial part in integrating the renewable hydrogen in the production plant since it is generally design in order to balance the demand of it as reagent for the process and its use for backup purpose. In this case, given the large volumes and the demand for hydrogen in the gas phase for the hydrogenation step, storage of hydrogen in the compressed gas phase is the most suitable [189]. Beside the possible storage in underground salt cavities, the most promising option for large-scale stationary storage is the storage bullets (Type I), in which hydrogen can be stored with maximum pressure of

approximately 150-200 bar (corresponding to 14-15 kg/m<sup>3</sup>) [189,353]. Type I is an all-metal tank, usually made of steel, capable of storing only about 1 % hydrogen by weight and, therefore, only used for stationary use. As gas compressed, hydrogen can be stored also in racks of vertical bottles (or horizontal tubes) up to several tons of hydrogen and under higher pressure 200-300 bar; the main problematic aspect of this type of configuration is its large footprint on the ground and the potential for domino effects in case of accident [354]. Given their greater technological maturity and the possibility of mitigating the domino effect by burying them, bullet tanks are considered for storing hydrogen at 200 bar in gas-compressed form in this investigation. In addition to the type of storage, the compression of hydrogen in this case from 30 bar (output pressure at the electrolyzer) to 200 bar is achieved by using a multi-stage compressor (reciprocating or rotary compressor can be used for stationary hydrogen storage) [355]. Literature data estimate the energy consumption to 2-7 kWh/kg of hydrogen for compression to high pressure (350-700 bar) depending on the type of compressor, considering that the theoretical energy required to compress hydrogen isothermally from 20 bar to 350 bar is 1.05 kWh/Kg and 1.35 kWh/kg for 700 bar [356]; by working in a range of pressure 150-200 bar we assumed an average consumption of 1.5 kWh/kg (considering an adiabatic efficiency for the compressor of 50-60 %) in this work. Data for compressor cost are scarce in literature; a price of \$M 0.086 USD/ton is reported based on the work of Wang et al. [167,357]. The capital investment for stationary storage tanks, operating in a pressure range of 50 to 200 bar, ranges from \$800 to \$850/kg of hydrogen, costs referred to 2014, down to \$700/kg, as indicated by the Department of Energy (DOE) and with further potential reductions [187,357]. In this analysis, a capital cost of \$786/kg was considered for the storage unit, which includes the tank and compressor, plus the operating and maintenance costs of the hydrogen storage and compression plant.

### **5.2.5.3 Hydrogen Fuel Cell**

The presence of a fuel cell as a backup system is essential in hydrogen energy storage systems (HydESS), as the fuel cell can supply the energy demand of the process during periods of low wind potential by burning the excess hydrogen produced by wind energy peaks, rendering the system energetically self-sufficient. Similarly, to an electrolyzer, the main fuel cell element is a stack with electrodes in which hydrogen is fed to the anode where the ionization occurs realizing ions H<sup>+</sup> and oxygen (generally air) is supplied at the cathode producing negative ions; the reaction generates water and electricity and it is generally facilitated by using catalyst as carbon material coated with platinum [358,359]. Depending on the electrolyte and the catalyst, different type of fuel cell technologies can be considered; among them, the Proton Exchange Membrane fuel cell (PEMFC) is the most extensively used technology, employed in numerous fields, as backup power, portable power and distribution generation for both stationary and automotive use [186,358]. Compared to other type of cell, PEM technology presents high-power density, rapid start-up, and high efficiency (50–60 %) at low operating



temperature, typically 80-100 °C while the main challenge remains related to the high cost of the catalyst [186,358]. Depending on the end use, i.e. power demand, different sized stationary fuel cells are used, and the investment cost for large-scale installations (0.4-30 MW) is between 2,000 and 3,000 EUR/kW, with target prices expected to drop to 1,200-1,750 EUR/kW in 2030 [358,360]. Depending on the size of GVL plant considered and the electricity demand (i.e. type of boiler installed for steam generation), this study considers fuel cell modules with power capacities between 1.7 to 6.7 MW, operating lifetime of 40,000 h [358], and an average capital cost of \$2,200/kW. Operating costs are estimated around 1.5% of the Capex investment and with stack replacement costs of \$1,100-1,200/kW (i.e. about 50% of the capital cost) [361,362]. Average data specification for PEMFC, reported in Table 27.

Table 27: Average data specification of PEMFC from literature

<b>Polymer Electrolyte Membrane (PEMFC)</b>	
Efficiency	45 – 60 %
Operating Temperature	70 °C
Operating Pressure	3-4 bar
Lifetime stack	< 50,000 h
Lifetime FC system	~20 y

## 5.2.6 Description of the scenarios analyzed

Once the flowsheet of the process for the production of GVL from biomass-derived fructose has been defined, different scenarios can be distinguished on the basis of energy and hydrogen demand and the in-site or off-site supply of it to the plant, through the integration of renewable energy sources. Represented in Fig. 53, a baseline scenario (Scenario 1) was defined considering for the two GVL production sizes under examination (2 and 4 kt/y) the off-site supply in terms of electricity demand from the grid, natural gas demand to the boiler for steam generation, and hydrogen from an external supplier; Scenario 2 considers the heat demand at the boiler provided by biomass, instead of natural gas as in Scenario 1, and the supply of electricity and hydrogen off-site; Scenario 3 involves the off-site supply of natural gas for the boiler's heat and electricity needs, part of the electricity is however used in this case for the on-site production of hydrogen; Scenario 4 considers the off-site supply of biomass to the boiler and of electricity, with the production in-site of hydrogen; Scenario 5 similar to the previous two considers in-site hydrogen production but a fully electrified configuration (equipped with electrical boiler), with off-grid electricity supply; Scenario 6 considers a fully electrified configuration in which electricity is produced from wind power, by means of in-site wind turbines, and used to also produce in-site hydrogen for hydrogenation and as an energy carrier in fuel cell back-up systems; finally, Scenario 7 still considers the integration of wind energy for electricity and hydrogen production in-site but it

considers also the use of supplied biomass for bio-energy in the boiler. Each scenario includes a specific hydrogen storage system, both for hydrogen supplied off-site and for hydrogen produced on-site, as indicated in Table 28; in cases where hydrogen is used only as a chemical reagent (Scenarios from 1 to 5), the storage system is sized to handle the required flow of hydrogen for 24 hours in the case of on-site production or for 7 days for hydrogen supplied off-site. For scenarios 6 and 7, the storage is specifically sized and described later.

Clearly enough, the differences in terms of power source, power to the boiler and hydrogen supply to the system affect the economics, environmental impact and safety aspect associated with the entire biomass-to-GVL process system.

Table 28: Summary of scenarios defined according to electrical, thermal power and hydrogen supply.

	ELECTRICAL power	HEAT power	HYDROGEN
<b>SCENARIO 1</b>	POWER GRID	Natural gas-BOILER	SUPPLIED (off-site)
<b>SCENARIO 2</b>	POWER GRID	Biomass-BOILER	SUPPLIED (off-site)
<b>SCENARIO 3</b>	POWER GRID	Natural gas-BOILER	Water ELECTROLYSIS
<b>SCENARIO 4</b>	POWER GRID	Biomass-BOILER	Water ELECTROLYSIS
<b>SCENARIO 5</b>	POWER GRID	Electric-BOILER	Water ELECTROLYSIS
<b>SCENARIO 6</b>	WIND TURBINES	Electric-BOILER	Water ELECTROLYSIS
<b>SCENARIO 7</b>	WIND TURBINES	Biomass-BOILER	Water ELECTROLYSIS

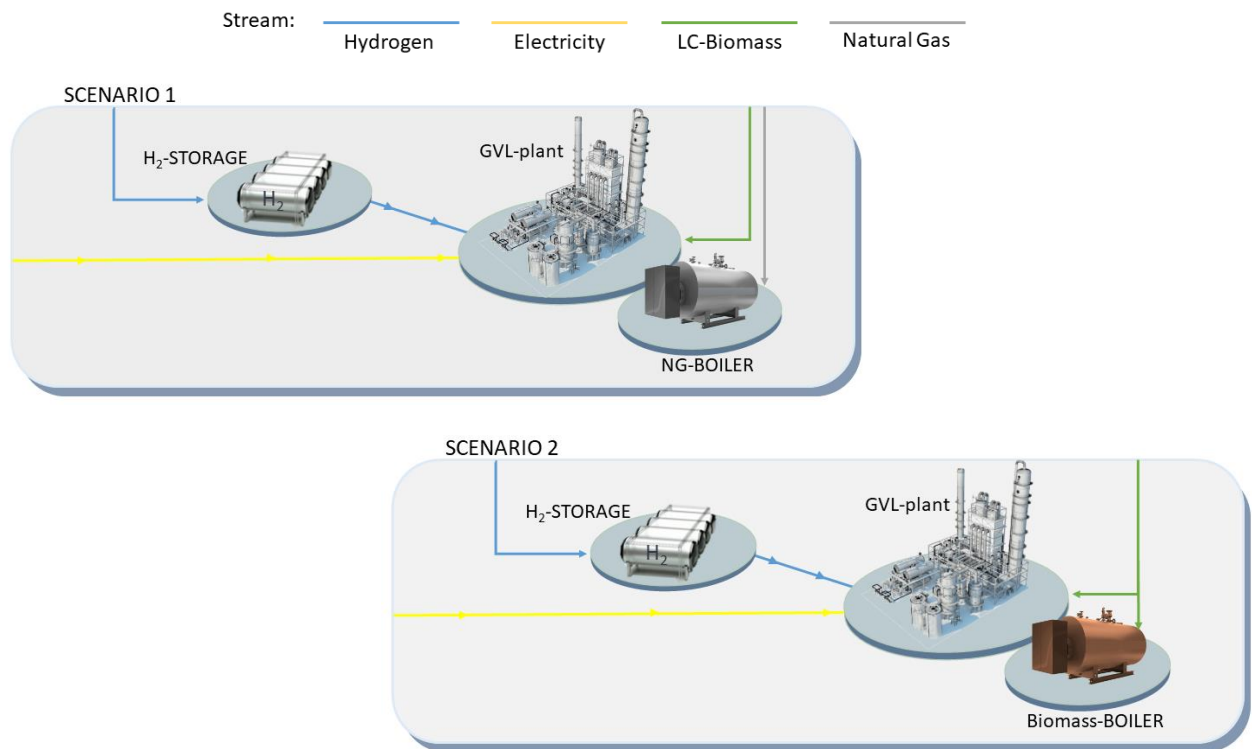


Fig. 53: Figurative representation of scenarios including process sections and energy and material supply streams

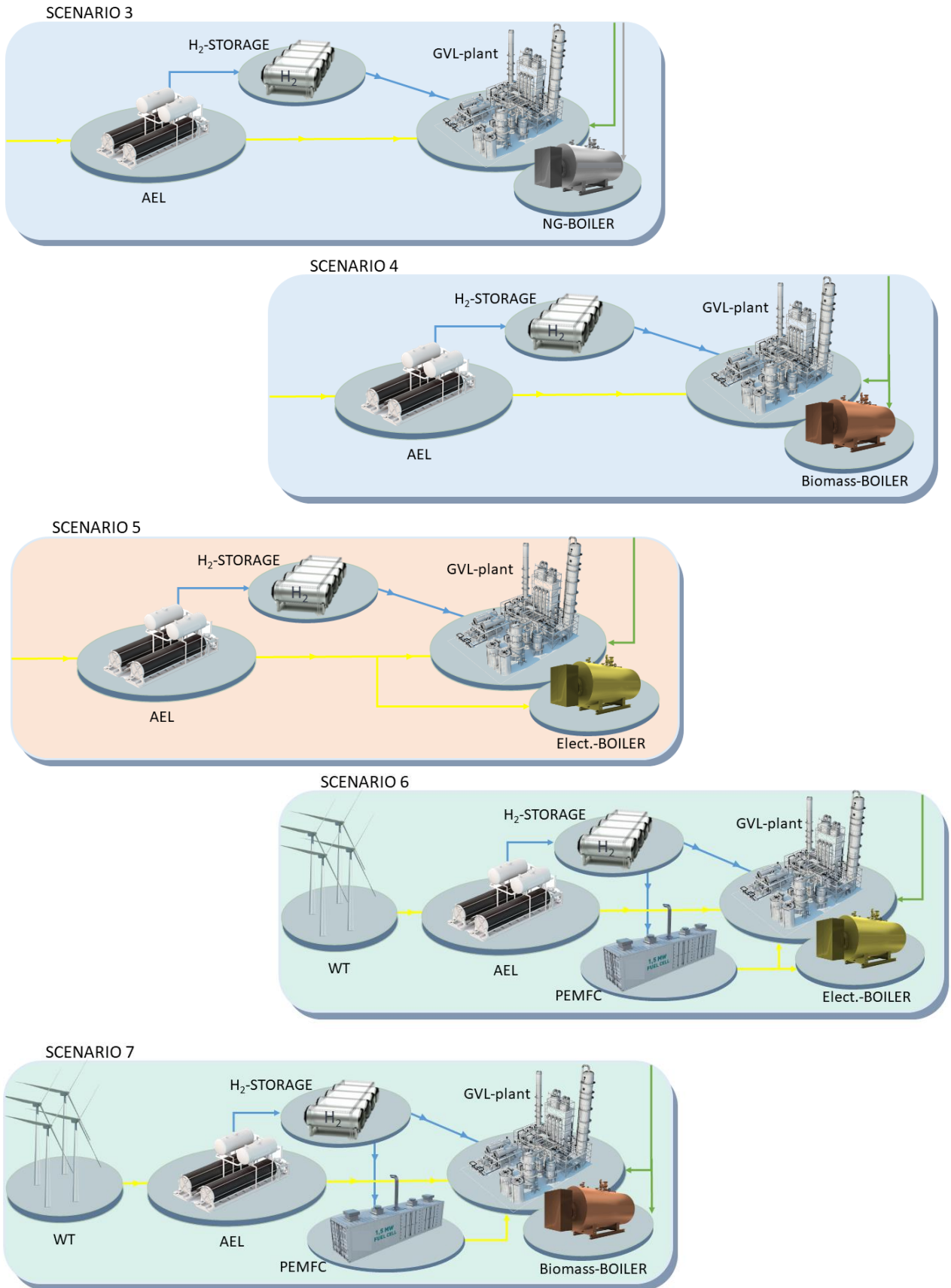


Fig. 53 Figurative representation of scenarios including process sections and energy and material supply streams

## 5.2.7 Conceptual design of the integration system for electricity and hydrogen from RES

For the scenarios in which the wind potential, through the use of wind turbines, is exploited in order to integrate the production of renewable electricity and hydrogen, a methodology was developed in order to design the optimal energy-hydrogen-system in terms of the size of the wind farm, electrolysis modules, fuel cells and hydrogen storage to sustain the demand of electricity and hydrogen of the biorefinery process to GVL. Defined the process to be integrated, its energy demands and the potentiality of RES in the site, together with the optimal renewable-energy converter technology (i.e., WT), the design of the RES-system is strongly dependent on the number of WTs, directly related to the power-generation, and the size of the hydrogen storage, related to the hydrogen back-up system. Due to the seasonality of wind potential, the storage system must be dimensioned to stack enough hydrogen as reserve energy carrier to cover the hydrogen demand for the process and the negative net power phases. The optimal system design is evaluated by defining an objective function dependent on the number of WTs and the hydrogen storage inventory, and which has as its output variable to be minimized, the technology variable indicating the percentage of the required electricity supplied from the grid. The variable will have a non-zero value if the designed configuration, in terms of wind farm and hydrogen storage system, is unable to meet the energy demand of the process, i.e. the system is not energetically self-sufficient and must therefore draw from the grid. This variable can also be expressed in terms of the time interval over the annual working hours, net of plant shutdown hours, in which hydrogen storage does not satisfy energy demand, as shown in the expression (Eq. 5. 6):

$$t_{ENERGY-GRID}(\%h/h) = \frac{\sum_i t_i [Acc_{H2,i} < 0] - t_{PlantShutdown-hours/y}}{t_{Working-hours/y}} \cdot 100 \quad Eq. 5. 6$$

Where the variable  $Acc_{H2,i}$  indicates the hourly value of hydrogen accumulation in the storage system, and depending on the production-demand flows of hydrogen during the operation of the plant.

Assuming that shutdown and maintenance times are scheduled during the negative power phases, the objective function determines for each storage size the minimum number of turbines that results in a value of the variable less than or equal to zero, i.e. that has insufficient hydrogen storage for a number of annual hours less than or equal to the number of plant shutdown hours.

As shown in Fig. 54, in the design of the integrated system, the storage and wind plant sizes are iteratively varied in order to find the best combination that minimize the objective function. Defined a suitable range of variation for the storage size, accounted from 2000 tons up to 15000 tons of hydrogen; for each storage-size, the number of WTs can range from 0, extreme condition in which the plant is grid-dependent, to 35, maximum number of devices considering a land-constrain. The maximum number of WTs was evaluated by considering a reasonable area for wind farm installation of 5 km<sup>2</sup> and the main

inter distance between devices of 5 times the rotor diameter to optimize the placement of WTs [363]. Fixed the storage size, for each number of WTs the power output is evaluated based on the power curve of the WT and the number of devices, and deducted from the power demand which is hourly constant. Consequently, in case of positive net power, the surplus of output power is fed to the AEL modules and converted in “*positive*” mass flow of hydrogen ( $H_2^+$ ) by using a linear correlation based on the specification capacity of the AEL module (i.e. efficiency rate) and assuming a production capacity dynamic range of 100 % of the flow range; on the other hand, for negative net power this value is converted in terms of “*negative*” mass flow of hydrogen ( $H_2^-$ ) based on its LHV and the efficiency of the PEMFC. Based on the hydrogen mass flow, the variable accumulation is defined by the sum of the positive and negative hydrogen flows. Given the wind potential seasonality, wind data analysis for power generation are considered starting from the winter season (December-February) in which higher wind speeds determine higher power surplus-production, i.e. “*positive*” hydrogen mass flows, and an increasing average trend of the accumulation variable. The level of hydrogen storage therefore fluctuates to the extent of the positive and negative hydrogen flows, but the maximum storage value is given by the set storage size. Therefore, once the maximum storage capacity has been reached, the additional positive hydrogen flows are accounted for as outflows from the storage system and as a potential market product that together with the GVL contributes to the initiative's income. Consequently, the capacity for

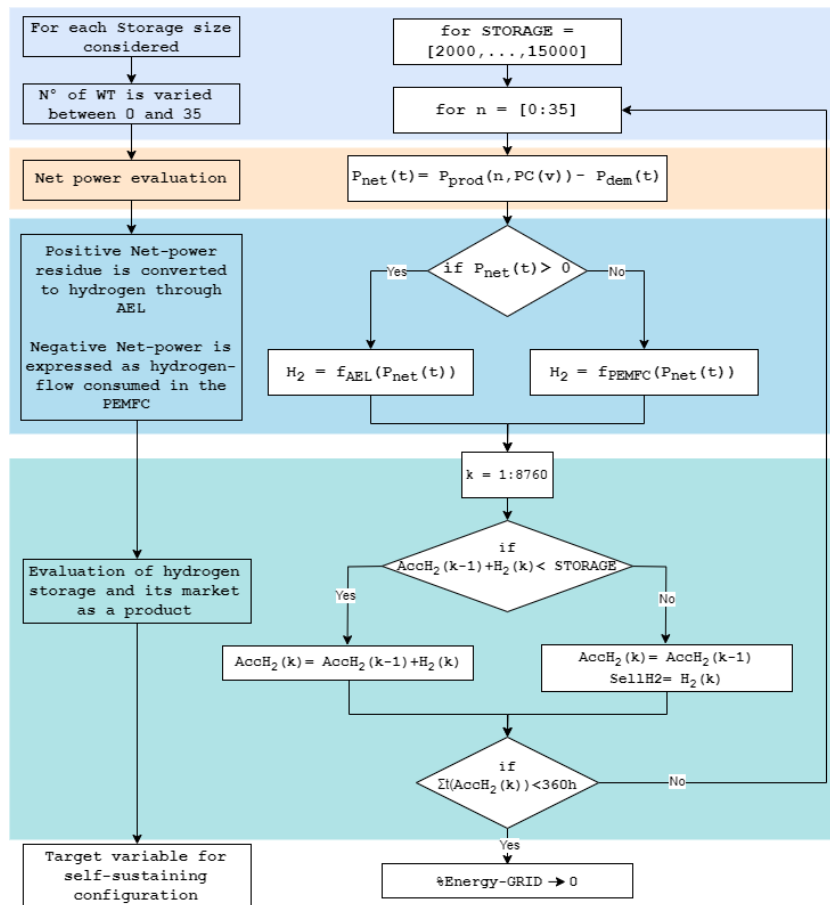


Fig. 54: Flow chart of the optimal design algorithm for the wind farm-hydrogen energy storage configuration, minimising the objective function represented by the parameter %Energy-grid.

the AELs modules is designed by considering the maximum surplus-output power absorbed, plus the power demand for hydrogen reagent production, and for the FCs modules by considering the power demand of the process.

For each storage size considered, the objective function iterates on the number of WTs up to find the minimum one which minimize to zero the share of power needed from the grid for each hydrogen storage size, and determine the size capacity of AEL and FC modules.

For each process size (2 and 4 kt/y), the combinations of storage and wind plant size are then assessed through the sustainability indicators, primarily through the economic ones to highlight the effects of the system sizes on the profitability of the initiative.

## 5.2.8 Sustainability Assessment and Key Performance Indicators (KPIs)

Once the optimized process scheme and the different scenarios considered have been defined, the sustainability assessment is carried out by means of KPIs representing scenarios economics, environmental impacts and process safety.

### 5.2.8.1 Economic KPIs

The economic analysis of the scenarios was based on two main economic KPIs: the levelized cost of product (*LCOP*) and the Net Present Value (*NPV*). The Levelized cost of product represents the averaged production cost of the product per unit over the lifetime of the production scheme and it is defined as follows:

$$LCOP \left[ \frac{\text{€}}{\text{Kg}} \right] = \frac{CAPEX + \sum_n^N \frac{OPEX}{(1+r)^n}}{\sum_n^N \frac{P_i}{(1+r)^n}} \quad \text{Eq. 5.7}$$

Where CAPEX and OPEX are the capital investment and annual operating costs, discounted by the discount rate  $r$  referred to the  $n$ -th year;  $N$  is the lifetime of the plant;  $P_i$  is the annual production of the product  $i$ -th in term kg/y. While, given the definition of LCOP, the most profitable scenarios consider lower production costs per unit of output, the NPV indicator allows us to define the profit value generated by an initiative over its lifetime and, therefore, the objective is to consider the scenario that maximizes it. By definition, NPV is expressed as follows:

$$NPV[\text{€}] = \sum_n^N \frac{F_n}{(1+r)^n} - I \quad \text{with } F_n = [\text{Revenue}_n - \text{OPEX} - \text{Deprec}] \cdot (1 - \text{Tax}) + \text{Deprec} \quad \text{Eq. 5.8}$$

Where  $F_n$  is the cash flow (€/y) generated by the scheme in  $n$ -th year, discounted with the rate  $r$ ; while  $I$  (€) is the initial capital investment. The Cash Flow  $n$ -th is calculated on the basis of the net profit before taxation, given by  $n$ -th revenue reduced by annual operating expenses (OPEX) and depreciation, which multiplied by the taxation rate generates the net profit after taxation in the  $n$ -th year, and to which is added back the share of depreciation. The depreciation is a non-cash charge reported as an expense in order to reduce income for taxation purposes; in this case, the depreciation is evaluated by the straight-line method and annually fixed to 4% of the fixed capital investment (FCI) [364]. The discount rate is assumed to be 8 %, as average value for biomass-application processes and new energy installations [365,366]. The value of discount rates for new technologies is subject to a certain degree of uncertainty due to the perception of risk associated with the investment and dependent on the level of maturity of the technology. While the perceived risk associated with on-shore wind energy is generally low, making the discount rate between 7 and 10 %, referred to 2011 data [367], and between 5.50 - 6.75 % in 2018 [368], that associated with the use of biomass (for bio-energy uses) and hydrogen technologies is

relatively higher, with a range of 9 -13 % for biomass [367]. Based on that, several techno-analysis and economic reports considers a value of 8 % as a real good compromise value of discount rate for new technologies [180,365,366,369,370]. The Internal Rate of Return (IRR) is also evaluated to determine the attractiveness of the investment; the IRR is the value of the discount rate corresponding to a cumulative NPV-zero at the end of the plant's life, therefore it represents the highest  $r$ -value that justifies the investment.

The economic analysis is conducted considering a plant lifetime of 25 years, with a construction period of 2-years, assuming the FCI spent over the construction period with 80% and 20%, first (year 1) and second year (year 0), respectively. The plant operates in continuous for 8400/y, considering two weeks per year of annual shutdown and maintenance. The fixed capital investment for the GVL-production unit operations, as described in the intensified flowsheet, is estimated by the use of Aspen Process Economic Analyzer (APEA) [371]. After a preliminary design, the software is used to determine the equipment and installation cost for each process equipment (heat exchangers, columns, agitated-reactors, separators, etc.), excluding equipment for utility fluids for which costs are based on supplier or literature data. Cost adjustments to €<sub>2022</sub> were performed by considering currency conversion rates, CEPCI values (CEPCI<sub>2022</sub> 816.5 [372]) and Location factor ( $L_i$ ) of 1.13 for France-site, considering the baseline reference location in US, Gulf Coast region [364]. The capital cost is determined including the Direct Costs: equipment and setting, piping, civil and structural cost, instrumentation and controls, electrical equipment and materials, insulation, paint; Indirect Field Costs: engineering and supervision, commissioning, construction expenses - fringe benefits, burdens, insurance, scaffolding, equipment rental, field services, temporary constructions, etc.; Indirect Non-Field Costs: taxes and permits, engineering, contingency, general and administrative expenses [373,374]. Depending on the type of scenario, the fixed costs are also added to the costs of purchasing and installing wind turbines, electrolysis cells, fuel cells and hydrogen storage.

The Total Capital Investment (TCI) is defined by summing to the fixed capital investment (FCI), the Working capital (WC), which represents the additional expenditure required to start up the plant and run it until it starts producing income, generally estimated as two months of operating costs [364], and Start-up Capital (STC) assumed as 8 % of FCI (typical range 8-10%) and it considers modifications and changes frequently made after the construction plant in order to maximize the operativity of the plant [375]. In some scenarios, the total capital invested is reduced through the application of special state incentives as part of the decarbonization plan for industry and investment in renewable energy and green hydrogen implemented by the current French government through the “*France 2030*” investment plan [376]. In the document on project calls for investments in the renewable energy sector, state incentives are presented and can be granted on new investments to integrate the use of renewable energies (use of wind turbines, biomass, hydrogen, etc.) (“*France 2030 – AAP AIDE A L’INVESTISSEMENT DE L’OFFRE INDUSTRIELLE DES ENERGIES RENOUVELABLES*”) [377]; specifically, the expenses eligible for incentives are those related to investment in new equipment, and are set at 35 % for industry



with annual business turnover lower than 10 M€ per year, 25 % under 50 M€ per year, and 15 % for over business. Therefore, the analysis for Scenario 6 and 7 includes also the incentives, evaluated on the basis of the installation cost of the equipment.

The annual operating cost (OPEX) is defined by the sum of the variable operating expenses (VOE), fixed operating expenses (FOE) and general operating expenses (GOE); annual variable quote of expenses accounts the cost of raw materials, utilities (heating and cooling systems), catalysts, make-up, wastewater treatments and waste disposal. Fixed expenses consider the annual cost of operating labor, estimated considering 4 operators per shift, one for each process section (solvolysis section; hydrogenation section; solvent regeneration section; hydrogen production section), 5 shifts, and with remuneration of 32€ per hour, referred to France labor cost in 2022 [378]; maintenance, generally considered as 3% FCI except for some specific equipment; operating supplies; patents and royalties; overheads (plant and payroll); local taxes; insurance. Then, the general expenses also add the cost of administration, distribution, and selling.

In the raw material cost evaluation, the cost of fructose supply is considered by reporting the literature cost for fructose derived from waste biomass; with a view to considering a continuous value chain from raw biomass to GVL, even though the fructose production step was not included in this technology design. In the absence of data from the literature on costs related to the production of pure fructose from LCB biomass, a cost of US\$747/ton was assumed from the work of Kwan et al.[323] related to the production of a high concentration fructose syrup obtained from waste biomass. This cost item is, however, indirectly discounted by the avoided cost of disposal of biomass needed to produce fructose, which averages 76.5 €/ton (considering disposal by incineration and burial). Therefore, the avoided-cost of disposal index is shown with a negative sign in the cost item related to waste disposal. For the price of hydrogen and GVL, a market range, updated to 2022, was reported so as to later evaluate market-consistent minimum sales prices in the analysis. Specifically, for GVL, the most up-to-date price range in the literature considers a price between \$1.25 and \$3.88/kg carried forward to 2019; this range was updated by changing the upper price limit through CEPCI<sub>2022</sub>, resulting in an increase to \$5.25/kg. For hydrogen, on the other hand, the cost of production by steam reforming fluctuated between €1.4-1.8/kg reported in 2020; the rise in the cost of natural gas in 2021-2022 led to a hike in the cost of hydrogen production to €4.8/kg at the end of 2021. Considering the current costs of hydrogen transport and distribution, such as through fueling stations, the final cost may rise further by 50-60%. For these reasons, the cost of hydrogen is in the range of 4.8-7.65 €/kg in this analysis, as shown in Table 30.

Table 29: Cost assumptions for specific process items

Cost item in FCI		Ref.
Wind Turbine		
• <b>Installed equip. cost</b>	\$1500/kW	[379]
• <b>Operating cost</b>	\$43/kW·y	
Alkaline Electrolyzer (AEL)		
• <b>Installed equip. cost</b>	\$750/kW	[180,352]
• <b>Operating cost</b>	\$15/kW·y (2% of Equip. cost)	
• <b>Stack replacement cost</b>	\$340/kW	
PEM Fuel Cell (PEMFC)		
• <b>Installed equip. cost</b>	\$2200/kW	[358]
• <b>Operating and maintenance cost</b>	\$33/kW·y (1.5% of Equip. Cost)	
• <b>Stack replacement cost</b>	\$1100/kW	
Storage and Compression Hydrogen system		
• <b>Installed equip. cost</b>	\$786/kgH <sub>2</sub>	[167,357]
• <b>Operating cost</b>	\$24/kgH <sub>2</sub> ·y	
Stand-by Battery		
• <b>Installed equip. cost</b>	\$1200/kW	[380]
• <b>Operating cost</b>	3% of capital equip. investment	

Table 30: Cost assumptions for chemicals, catalysts, and utility.

Cost raw materials and catalyst		Ref.
<b>Chemicals</b>		
• Fructose	\$747/t	[323]
• Butanol	\$1205/t	[381]
• GVL	\$1.25-5.25/kg	[382]
• Hydrogen	\$5.05-8.05/kg	[383,384]
<b>Catalyst:</b>		
• Amberlite IR-120 (H-form)	\$63/kg	[385,386]
• Ru/C	\$5.7/g	[387]
• Alumina	\$25/kg	[388]
• DHT-4A	\$8/kg	[389]
<b>Utilities:</b>		
• <b>Electricity</b>	0.127 €/kWh	[390]
• <b>Natural-gas</b>	0.073 €/kWh	[391]

• <b>Biomass</b>	0.027 €/kWh	[392]
<b>Other utilities</b>		
• Chilled water	\$0.08/m <sup>3</sup>	[364]
• Cooling water (Tower water)	\$0.03/m <sup>3</sup>	
• Steam	\$0.0145/kg	
• Refrigerant fluid (Propane)	1%-Capex Refr.system	

Table 31: Assumptions employed in economic indicators analysis.

<b>Evaluation year</b>	<b>2022</b>	<b>Ref.</b>
Plant lifetime	25 years	[393]
Construction period	3 years	[393]
Working capital	7/8 weeks of operating costs	[364]
Start-up capital	8% of fixed capital investment	[375]
Discount rate	8%	[365,366]
Taxation	20%	[299]
<b>Operating Expenses</b>		
Waste disposal	\$1.5/ton	[364]
N° operator/shift	4 operators per shift	[393]
Labor cost	32€/h – 2080 h/y	[378]
Maintenance	3% of FCI	[375]
Operating supplies	15 % of maintenance cost	[375]
Patents and Royalties	1 % of total operating expenses	[375]
Overheads	10 % of sum of labor and maintenance costs	[364]
Local taxes	1 % of FCI	[375]
Insurance	1 % of FCI	[375]
Administration	25 % of labor cost	[375]
Distribution and Selling	5 % of operating expenses	[375]

### 5.2.8.2 Environmental impact KPIs

Currently, the decarbonization of hard-to-abate industrial sectors and the reduction of the fossil contribution in the energy mix is high on the agenda of the investment plan in France, and in Europe in general, in view of the carbon-neutrality targets and because the most critical environmental concern identified for these sectors is their contribution to global warming from greenhouse gas (GHG) emissions. In this context, the sustainable exploitation of renewable resources and the market

introduction of biorefineries and integrated bioenergy systems represent the main challenge and, although they are perceived as having a positive effect on the environment, the assessment of other parameters, besides greenhouse gas emissions, such as resource depletion, ecotoxicity, and land use, is necessary [12,394]. However, these effects are less critical since the biomass resource considered in this study for bio-conversion and bio-energy is residual waste and difficult to evaluate at the current level of analysis [365]. On the other hand, the environmental impact analysis that is carried out in this investigation is a comparative assessment among the scenarios considered, i.e. related to the integration of fossil and/or renewable resources for energy and hydrogen production in the GVL process, of which the impact of the biomass conversion process itself is constant among all scenarios and therefore not considered in the analysis. Furthermore, as indicates in the works of Steinmann et al. [395] and Huijbregts et al.[396], fossil greenhouse gas indicators also provide insight into other environmental impact categories (e.g. resource depletion, acidification), since they are all roughly proportional to the energy demand of the system. The effect of greenhouse gas emissions is based on the global warming potential (GWP) and quantified in terms of tons of CO<sub>2</sub> equivalents. The levelized greenhouse gas emission (*LGHG*) was adopted as key environmental indicator and defined as follows:

$$LGHG \left[ \frac{t - CO_{2,eq}}{t_{PROD}} \right] = \frac{\sum_1^j GHG_{tot,j}}{P_i} \quad Eq. 5. 9$$

$$GHG_{tot,j} = GHG_{fossil,j} + GHG_{biogenic,j} = \sum_{i=1}^n f_{fossil} \cdot F_i + \sum_{k=1}^m f_{biogenic} \cdot F_k \quad Eq. 5. 10$$

This indicator represents the emission-CO<sub>2</sub>eq per unit of product, through  $P_i$  that indicates the hourly production of the  $i$ -th product, expressed in tons/h. At the numerator, the sum of the emissions of the  $j$ -units, expressed as sum of the fossil and biogenic carbon contributions. Each contribution is estimated by an emission factor  $f$ , representing the CO<sub>2</sub> equivalents emitted per unit product, and the quantity of product  $F$ . The biogenic carbon contribution is accounted, separately from the fossil one, in order to quantify the effect of combustion or decomposition of biologically-based material, i.e. LCB biomass, in the scenarios in which it is used as bio-energy source. Biomass is generally indicated as a carbon-neutral source due to the fact that the amount of carbon emission during its combustion is almost compensated by the same amount of carbon fixed through photosynthesis during its growing phase; in this case, no CO<sub>2</sub> compensation effect is considered since the biomass, during its growth phase, is outside the system boundaries of the analysis. All emission factors are reported in Table 32. The electricity emission index is based on the emissions of the French electricity grid in 2022 [347], as it directly depends on the country's energy mix, while for the other factors, databases, commercial documents and data from literature are used. The biogenic carbon footprint of biomass for energy use is derived from the work of Cherubini et al.[397] in which a range of 5-20 gCO<sub>2</sub>eq/MJ of greenhouse gas emissions from biomass for heat generation is given. The value of 0.18 GWP, i.e. 3.41·10<sup>-5</sup> tonCO<sub>2</sub>eq/kWh, is used considering the effect of a biomass with a 30-year crop cycle rotation [398,399].

The carbon footprint of equipment and systems that differ between scenarios were taken into account; the carbon footprint of turbines for kWh of renewable electricity produced is derived from the manufacturer's own turbine life-cycle analysis [400], while the effect of AEL and FC from literature data [401,402]. For hydrogen storage, the effect of carbon expressed per kg-H<sub>2</sub> stored is derived from the work of Bhandari et al.[351] and accounts for 18% of the GWP of wind electrolysis.

Table 32: Emission factor for environmental impact analysis

Source	Emission factor		Ref.
	ton-CO <sub>2</sub> eq/kWh	ton-CO <sub>2</sub> eq/kg-H <sub>2</sub>	
Electricity	$8.40 \cdot 10^{-5}$	$1.68 \cdot 10^{-3}$	[347]
Natural gas (Fuel)	$1.81 \cdot 10^{-4}$	$3.62 \cdot 10^{-3}$	[403]
Biomass (Fuel)	$3.41 \cdot 10^{-5}$	$6.60 \cdot 10^{-3}$	[397]
Hydrogen	$4.95 \cdot 10^{-4}$	$9.89 \cdot 10^{-3}$	[404]
Wind turbine	$7.00 \cdot 10^{-6}$	$1.40 \cdot 10^{-4}$	[400]
Alkaline electrolyzer	$2.00 \cdot 10^{-6}$	$4.00 \cdot 10^{-5}$	[401]
Fuel cell	$1.72 \cdot 10^{-5}$	$3.44 \cdot 10^{-4}$	[402]
Storage tank	$1.98 \cdot 10^{-6}$	$3.95 \cdot 10^{-5}$	[351]

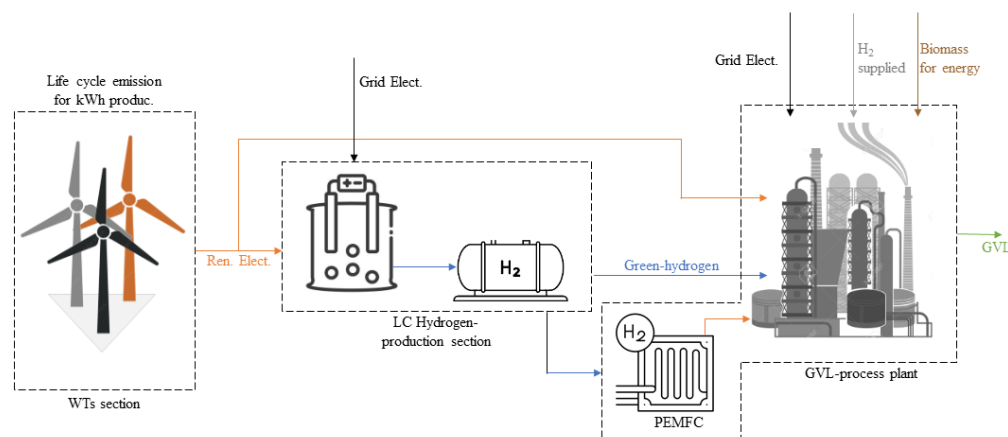


Fig. 55: System boundary for emission contributions for each process section.

The calculation of the defined index was evaluated by allocating the emission contributions for each product of the different sections of the configuration: GVL, hydrogen and electricity (Fig. 55). Depending on the scenario assessed, different contributions to emissions are accounted for, depending on whether the product is supplied externally or produced on-site. When comparing scenarios, on-site production of electricity and/or hydrogen also considers the contribution given by the life cycle of the equipment involved. As the process scheme for producing GVL from fructose is common to all scenarios, its contribution is not accounted for in the comparative analysis.

### 5.2.8.3 Inherent Safety KPIs

The sustainability assessment cannot disregard the safety analysis as social pillar of sustainability and related also to the societal acceptability of new process technologies. Biorefining processes involving biomass or renewable energy resources are generally perceived as safer, or even risk-free, than traditional processes involving oil derivatives, although they present specific criticalities. Casson Moreno et al.[405] highlighted the increase in the number of serious accidents in the bioenergy sector and in the feedstock supply chain, emphasizing the importance of increasing risk awareness in the bioenergy and biorefinery sector [405,406]. In this context, inherent safety (IS) is becoming a widespread tool in process risk management for new technologies, especially for risk assessment in early process and plant design stages. Recent works apply IS principles to new bio-technologies such as biogas production [407], bio-diesel production [223], and hybrid-energy system with renewable energy integration, presenting assessment tools based inherent safety drivers. The concept of the inherent safety consists in reduce, or possibly eliminate, the hazard associated to a specific process during its design and operation, by minimizing the quantities of hazardous chemicals, or substituting them with less hazardous ones, by mitigating the process conditions and simplifying the process design reducing possibilities of failures. To assure systemic tools for assessing the inherent safety of new technologies, specific metrics based on Key Performance Indicators (KPIs) have been developed, such as the one proposed by Tugnoli et al. [408], initially conceived for the hydrogen-energy system and then further developed; as in the work of Scarponi et al. where the set of KPIs was extended to include hazard-specificity in terms of flammability and toxicity for biogas production inherent safety [407]. The based-methodology IS-KPIs is therefore a generally valid and applicable metric for evaluating the inherent safety of any technological processes and comparing them at a preliminary design stage.

The set of KPIs proposed by Scarponi et al. [407] are applied in this investigation to evaluated the inherent safety of the production process of GVL from fructose, including the hydrogen-based and wind energy integrated system.

Defined the reference process scheme as preliminary stage (STEP 0), the IS-KPIs methodology considers the identification of the critical operation units (PUs) (STEP 1), i.e major hazard equipment (MHE). For each PU, a set of credible loss of containment (LOCs) is assigned (STEP 2) based on the process unit inventory (PUI), expressed in  $m^3$  and the maximum flow rate  $\dot{V}_i$  ( $m^3/s$ ) of the  $i$ -th inlet or outlet stream to the unit considered.

$$PUI > \max(\dot{V}_i) \cdot 180s \quad Eq. 5. 11$$

In case the expression (Eq. 5. 11) is verified, the PU inventory is identified as the most critical hazard factor and Type 1, 2 and 3 LOCs are assigned. On the contrary, if the maximum volumetric flow rate at the unit for a time of 3 minutes is greater, the criticality is associated with the flow rates and not with the inventory, and LOC Type 4 and 5 are assigned. Loss of Containment are defined according to Purple

Book [409] as follows: LOC1: small leak, continuous release from a 10 mm equivalent diameter hole; LOC2: catastrophic rupture, release of the entire inventory in 600 s; LOC3: catastrophic rupture, instantaneous release of the entire inventory; LOC4: pipe leak, continuous release from a hole having 10% of pipe diameter; LOC5: pipe rupture, continuous release from the full-bore pipe. A credit factor ( $C_j$ ) is assigned to each type of LOCs (STEP 3), representative of the expected probability of occurrence and expressed as yearly frequencies. Frequencies are derived from literature (“Purple Book”) [409] based on baseline values for equipment failures. For each LOCs, a set of reference scenario are considered by means of event tree (STEP 4), considering the approach proposed in the Methodology for the Identification of Major Accident Hazards [410]. The methodology considers then the estimation of damage distances  $d_{i,j,k}$  (DDs) for each reference i-th scenarios identified, referred to the j-th LOCs and for the k-th PU (STEP 5) based on the models reported in the “Yellow book” [411]. Damage distances represent the maximum distance at which the effect of the considered scenario corresponds to a specific threshold value, reported in Table 33, which is specific for each dangerous consequence (i.e. exposure to irradiation, overpressure, toxic concentration) considering human targets [407,408], and target equipment, specifically atmospheric and pressurized.

Table 33: Threshold Values assumed for the evaluation of damage distances

Dangerous Phenomena	Threshold value for human target	Threshold value for Equipment (Domino effect)
Pool-fire	7 kW/m <sup>2</sup>	15 - 50 kW/m <sup>2</sup>
Jet-fire	7 kW/m <sup>2</sup>	15 - 50 kW/m <sup>2</sup>
Fireball	7 kW/m <sup>2</sup>	n.a.
Flash-fire	½ LFL	n.a.
Physical explosion	14 kPa	16 - 22 kPa
Vapor cloud explosion	14 kPa	16 - 22 kPa
Toxic exposure	IDLH	n.a.

Based on the DD calculated, the set of IS-KPI is determined considering different indexes as reported in Table 34. Where the  $UPI_i$  (Unit Potential hazard index – m<sup>2</sup>) represents the maximum impact area considering the worst-case scenarios associated to the i-th PU, since it is defined as the maximum among the squares of the damage distances  $h_{i,j,k}$  for the LOCs assigned for the i-th PU. The index  $UHI_i$  (Unit Inherent hazard index – m<sup>2</sup>/y) accounts also the probability of the scenarios, considering the sum of the squares of the damage distances, each multiplied by the specific credit factor. In order to account separately toxic- and flammability-hazard, the unit flammability hazard index  $UFHI_i$  and the unit toxic hazard index  $UTHI_i$  are defined; by considering in the first one only damage distances  $f_{i,j,k}$  from fire and explosion scenarios, and in the second one the damage distances  $t_{i,j,k}$  for toxic cloud scenarios. In case, the inherent safety analysis is extended to the overall process scheme, overall IS-KPIs may be

evaluated by considering, for all the process units of the scheme, the sum of  $UPI_i$  for the Overall Potential Hazard Index ( $PI$ ), the sum of  $UHI_i$  for the Overall Inherent Hazard Index ( $HI$ ), the sum of  $UFHI_i$  for the Overall Flammability Inherent Hazard Index ( $FHI$ ), and the sum of  $UTHI_i$  for the Overall Toxicity Inherent Hazard Index ( $THI$ ).

Table 34: Inherent Safety Key Performance Indicators (KPIs)

Indicators		
$UPI_i$ – Unit potential hazard index ( $m^2$ )	$UPI_i = \max_j(h_{i,j}^2)$	Eq. 5. 12
$UHI_i$ – Unit inherent hazard index ( $m^2/y$ )	$UHI_i = \sum_j C_{f,i,j} \cdot h_{i,j}^2$	Eq. 5. 13
$UFHI_i$ – Unit flammable inherent hazard index ( $m^2/y$ )	$UFHI_i = \sum_j C_{f,i,j} \cdot f_{i,j}^2$	Eq. 5. 14
$UTHI_i$ – Unit toxic inherent hazard index ( $m^2/y$ )	$UTHI_i = \sum_j C_{f,i,j} \cdot t_{i,j}^2$	Eq. 5. 15
$PI$ – Overall potential hazard index ( $m^2$ )	$PI = \sum_i UPI_i$	Eq. 5. 16
$HI$ – Overall inherent hazard index ( $m^2/y$ )	$HI = \sum_i UHI_i$	Eq. 5. 17
$FHI$ – Overall flammable inherent hazard index ( $m^2/y$ )	$FHI = \sum_i UFHI_i$	Eq. 5. 18
$THI$ – Overall toxic inherent hazard index ( $m^2/y$ )	$THI = \sum_i UTHI_i$	Eq. 5. 19

On the basis of the indices presented, the different scenarios were conservatively evaluated by considering the reference process scheme with the largest production size (4 kt/y of GVL), given the largest inventory of substances compared with the smallest process size at equal process conditions. In particular, the inherent safety analysis is carried out by segmenting the overall process in the GVL-production section, common to all the scenarios, and the plant section dedicated to the production, managing and storage of hydrogen that is the diversifying element among the scenarios considered. In terms of potential hazardous substances, butanol, GVL, and hydrogen are the substances present in larger inventories in both process sections; the presence of hydrogen in the GVL-production section is mainly limited to the hydrogenation reactor. Although pre-registered since 2010, GVL is missing REACH registration [127], and flammability and toxic data still unknown or insufficient making unfeasible the application of the methodology to assess the damage distances for this component. For this reason, certain assumptions have been made for the sake of simplicity, given in some scenarios more conservative results: butanol is assumed as reference substance in the inventory of process units, considering the only inventory of butanol for the calculation of damage distances from flammability and toxicity scenarios for process units where butanol is the only component or in mixture with non-hazardous components; instead for process units in which butanol is in mixture with other substances with unknown hazard properties but potentially flammable, as GVL, BL, and BF, the overall inventory



is used for flammability-derived scenario, assuming the flammability properties of butanol for the overall mixture, and the inventory of butanol only is used to evaluate toxic-damage-distances. Since butanol is therefore considered the reference component in the analysis, process units without butanol are not classified as major hazard equipment and not accounted in the methodology. Instead, the analysis refers to the hydrogen inventory for the process units used to produce and handle it and the hydrogenation reactor in which the hydrogen occupies the gas volume and is partially solubilized in the liquid phase. Fig. 56 shows the main process units considered in the analysis, whose hazard is associated with butanol (except for the CRV-101 reactor whose criticality is associated with the presence of hydrogen in the reactor gas phase).

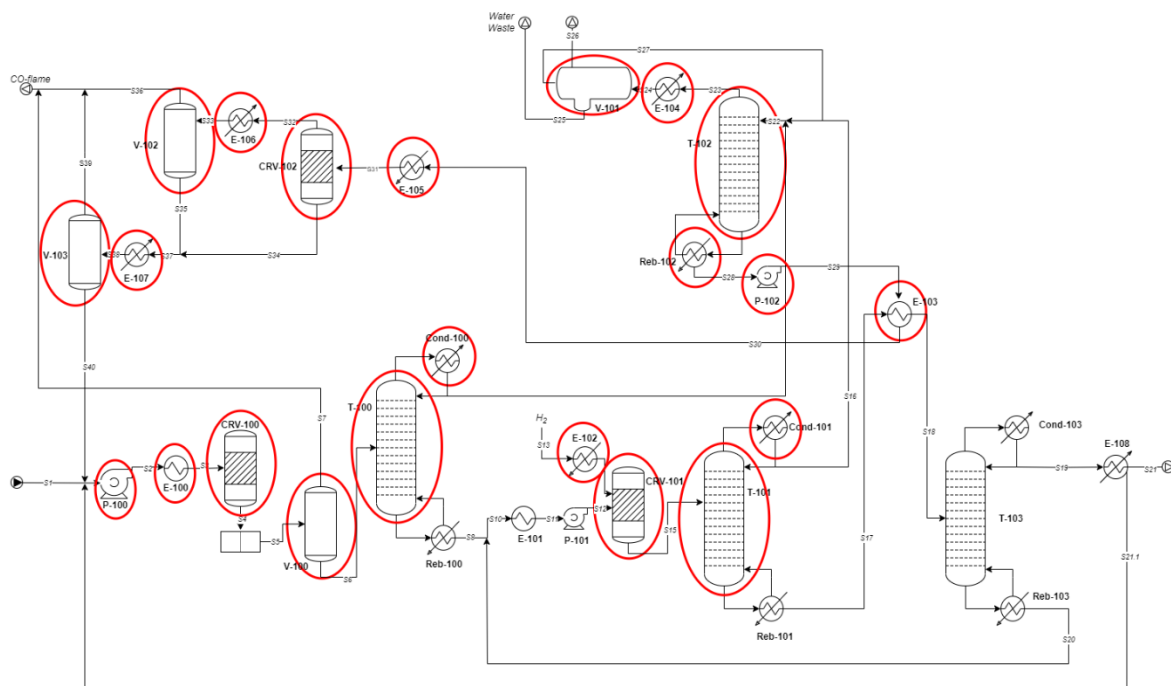


Fig. 56: The critical Pus-MHE highlighted in the simplified diagram of the GVL production process.

In the hydrogen production and management section, the criticality due to the hazardous nature of hydrogen is mainly highlighted in the alkaline stack and the associated buffer tank, the fuel cell stack, and the compression system and storage tanks, considering the different storage sizes per type of scenario.

**5.2.8.4 Overall Sustainability Index: Normalization, Weighting and Aggregation**

The sustainability analysis, through the indices defined above according to the pillars: economic, environmental, social, can be further developed by means of a multi-criteria decision analysis (MCDA), which on the basis of a decision-making process allows the evaluation of weighting factors specific to each index and necessary for aggregation into an overall index, allowing a clearer reading of the assessment.

The index weighting and aggregation phases are preceded by a normalization step. In fact, the normalization of sustainability indices is a necessary precursor stage in multi-criteria decision analysis, as shown in Fig. 57. The normalization phase allows a sustainability indicator to be transformed into a non-dimensional value between zero and one through comparison with a sustainable reference level [412–414]. Among the different normalization methods, such as ratio normalization, Z-score normalization, unit equivalence normalization, and target normalization to the interval [0,1] [415], an internal normalization was performed in this analysis by considering for each type of index the maximum among the compared scenarios as the reference target value [416].

The non-dimensional sub-indicators ( $X_{i,j}$ ) of sustainability for the three perspectives, ranging between zero and one, are determined by comparing the absolute sustainability sub-indicators ( $Y_{i,j}$ ) with the target values ( $Y_{i,j,T}$ ) that correspond to the maximum values of the sub-indicators between scenarios. A non-dimensional sub-indicator is calculated, as follows:

$$X_{i,j} = \frac{Y_{i,j}}{Y_{i,j,T}}, \quad \text{where } Y_{i,j,T} = \max(Y_i)_j \tag{Eq. 5. 20}$$

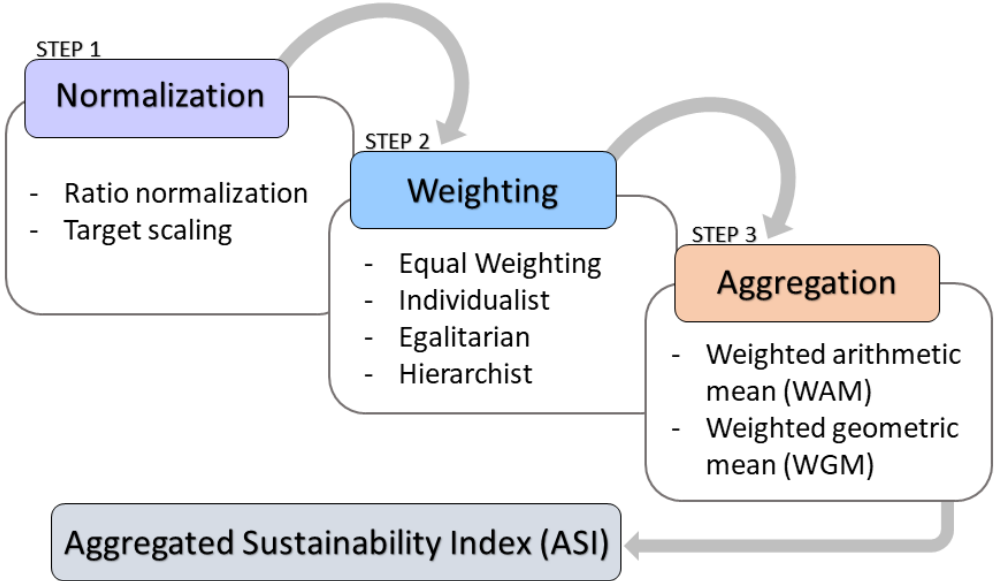


Fig. 57: Illustration of the different stages of the sustainability index analysis.

Following normalisation is the weighting phase; the weighting is typically performed using the Analytic Hierarchy Process method (AHP) [218]. Given a set of alternatives to compare, the AHP uses pairwise comparisons to evaluate the performance of the alternatives on the indicators (scoring) and between the indicators themselves (weighting). The evaluation of the weights is carried out on the basis of priority coefficients, with respect to time-space-receptor dimensions, and for different profiles of decision-makers or stakeholders [218,220]. To consider potentially different priorities, three different theoretical stakeholder profiles, as defined by Cultural Theory (CT), are usually considered in practical applications: Individualist, Hierarchist, and Egalitarian [221,412,417,418].

In the CT, the different stakeholder profiles are identified through two different positions (high or low priority) on the 'grid' scale in one dimension and on the 'group' scale in the other dimension, also interpretable as "ecosystem" receptor the first and "humans" the second. In fact, the grid dimension represents the structures of society, such as legislation, rules and regulations, while the other dimension represents the emphasis on relationships with others [417].

The individualist perspective is oriented towards self-seeking and is not interested in inter- and intragenerational equity. Therefore, indicators are evaluated from a local and short-term perspective. The individualist view of nature is one of resilient and abundant nature, which results in a concern for human over ecosystem receptors [417,418].

In contrast, the egalitarian perspective is concerned with inter- and intra-generational equity, showing a long-term and global perspective. The egalitarian view of nature as fragile leads to concern for ecosystem receptors [417,418].

More moderate, and preferable, is the hierarchical perspective that believes nature and natural resources can be managed within certain limits. It considers both the ecosystem and human receptor and leads to a balanced approach to decision-making, based on negotiation and compromise [417,418].

Based on the definitions of each of the three stakeholder profiles, they can be considered to have

different priorities with respect to the dimensions of sustainability, as shown in Table 35 and Fig. 58; and it is therefore possible to assign a specific weight value to the sustainability dimension according to the priority considered by the social profile. As suggested by Ekener et al.[417], applied to a sustainability analysis for bio-fuels production, a weighting factor of 0.6 for the 1<sup>st</sup> dimension prioritized, 0.28 for the 2<sup>nd</sup> one, and 0.12 for the 3<sup>rd</sup>, respectively, can be assigned to the economic, environmental, and social dimension depending on the social profiles considered [412,417].

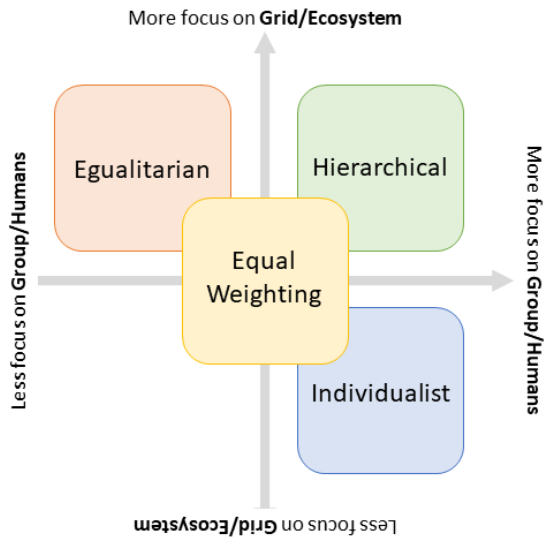


Fig. 58: Profile schematisation of stakeholders in CT

Table 35: Description of the different stakeholder profiles and corresponding priority among the sustainability perspectives used in this study.

	<b>Individualist</b>	<b>Egalitarian</b>	<b>Hierarchist</b>
<b>Group (Human)</b>	Weak	Strong	Strong
<b>Grid (Ecosystem)</b>	Strong	Weak	Strong
<b>Receptor</b>	Human	Ecosystem	Human/Ecosystem
<b>Nature view</b>	<i>Stable and strong</i>	<i>Fragile and unstable</i>	<i>In equilibrium</i>
<b>Priority 1</b>	Social	Environmental	Environmental
<b>Priority 2</b>	Economic	Economic	Economic/Social
<b>Priority 3</b>	Environmental	Social	-

With respect to the indices presented in this analysis, the sustainability perspectives on GVL production are thus represented by the LCOP index for the economic pillar, LGHG for the environmental pillar, and HI for the social pillar, as shown in Table 36. The prioritization for the economic, environmental and social perspectives was defined by asserting the environmental perspective in the ecosystem dimension/receptor, while the economic-social perspectives related to the human dimension/receptor; for this reason, in the "Hierarchical" profile where the receptors are both the ecosystem and humans, the weight was not assigned with the three factors indicated above but half was given to the environmental index and the other half equally divided between the economic and inherent safety index.

Table 36: Weighting coefficients for the different stakeholder profiles considered.

	<b>Individualist</b>	<b>Egalitarian</b>	<b>Hierarchist</b>	<b>Equal Weighting</b>
<b>LCOP</b>	0.28	0.28	0.25	0.33
<b>LGHG</b>	0.12	0.60	0.50	0.33
<b>HI</b>	0.60	0.12	0.25	0.33

In addition to these profiles, there is also the equal-weighting method, in which weighting factors are assigned equally among the indices. In some analyses, the panel method is also added, in which a panel of experts and stakeholders is consulted to assign and distribute the weighting factors [221,412].

Comprehensive sustainability is assessed through an Aggregated Sustainability Index (ASI) determined by aggregating the category indicators and their respective weights using linear or geometric aggregation techniques. This leads to

$$ASI_i = \sum_{j=1}^n X_{i,j} \cdot w_j \text{ or } \prod_{j=1}^n X_{i,j}^{w_j} \quad \text{where } \sum_j w_j = 1 \quad \text{Eq. 5. 21}$$

where  $n$  represents the number of categories in an evaluation and  $w_j$  represents the weight associated with category- $j$ . The sum of the inter-category weights is equal to one regardless of the aggregation procedure. With the linear aggregation method, there is perfect substitutability and compensability between all sub-indices. This means that in the aggregation, low values of some sub-indices are compensated by high values of other sub-indices. The arithmetic method is independent of extreme differences between the values of two sub-indices, so if the distance between pairs of indices is different but the mean value of the range is the same, the values of the aggregated indices of the two pairs are equal. Unlike the arithmetic method, the geometric method does not create perfect compensability between the values of the sub-indices of the indicators; a low value of one sub-index is not compensated by that of other high sub-indices in a linear manner, and this is because the geometric method considers the differences between values of the sub-indices when aggregating the indicators. Therefore, if the difference in sub-index values is important, the geometric method can be more appropriate [413,414].

## 5.3 Results and discussion

### 5.3.1 Results of the conceptual design of the process and RES system

For Scenarios 6 and 7, in which the generation of electricity and hydrogen takes place in-site with the integration of renewable wind potential, the methodology for conceptual design of RES system is applied to determine the size of wind turbine plant, hydrogen storage, and consequently electrolyzes modules and fuel cells, optimal for the plant's stand-alone operation, i.e. with zero electricity demand to the grid.

Matlab-R2023a [335] was used to systematically solve the objective function by iteratively varying the size for hydrogen storage and the number of wind devices in specific ranges, to minimize the variable % energy-grid; the conceptual design was performed for both production plant sizes considered and for both scenarios.

In addition to the wind power potential assessed through forecast data at the selected location and coupled with the power curve of the selected converter, the power demand for each plant size considered is a key input parameter in the methodology, as it is necessary for the evaluation of the wind turbine number and back-up system size. For the production size of 2 kt/y of GVL, the energy demand, considering the contribution of electrical demand and the energy demand from the steam-generation boiler separately, are 1.7 and 1.89 MWh, respectively. The energy demand to the boiler is then converted in full electricity in the scenarios in which an electrical boiler is employed (Scenario 6).

Fig. 59 shows the trends in the variation of the %Energy-Grid variable with increasing number of turbines in each storage size category; the smallest storage size is unable to independently manage the back-up of the system with a number of turbines below 35, for which number of devices still requires 3.99 % energy from the grid. The minimum number of turbines for this size is 63, thus not fulfilling the land constraint considered in the analysis. For larger storage sizes, the objective function is able to find a first minimum of the output variable for turbine number values below the maximum extreme; 19, 13, 12, and 11 are the minimum number of WTs for sustaining the energy demand in Scenario 6 for storage size categories of 5, 7.5, 10, and 15 tons of H<sub>2</sub>, respectively (Fig. 59-Table 37). The trends show that as the storage size increases, the minimum number of turbines decreases due to the greater storage capacity and thus the better response to the hydrogen flows produced and the hydrogen flows required for the back-up system in the low wind phases. For each combination of storage and wind farm size, the size of AEL-cell-modules and PEM-fuel-cell-modules are designed. Whereas the FCs sizes depends only on the maximum power demand of the process and, therefore, independent from the number of WTs and storage size, the capacity of AELs is defined by the maximum power absorbed during positive wind power phases and therefore the size of these modules increases as the number of wind devices installed increases and decreases as the storage size increases.

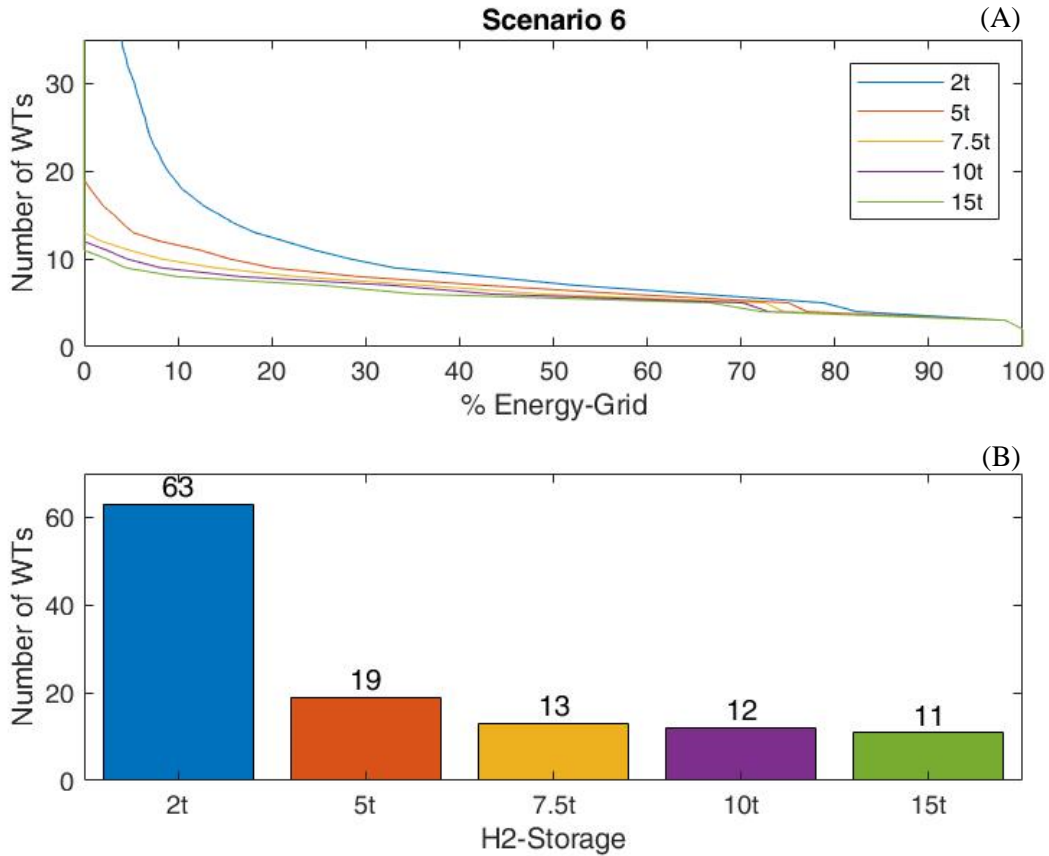


Fig. 59: Optimal configuration design Scenario 6 - 2kty (A) variation of %Energy-Grid parameter as the number of WT's varies for different storage sizes (B) minimum number of WT's minimising the target term for each storage size

Table 37: Equipment Design Configuration for Scenario 6 – Production size 2 kt/y

Scenario 6 – Production GVL size 2 kt/y					
Storage Capacity (t)	2	5	7.5	10	15
N° WT <sub>MIN</sub>	63*	19	13	12	11
AEL (MW)	123	35	23	21	19
FC (MW)	3.6	3.6	3.6	3.6	3.6

Compared to the results of Scenario 6, the decrease in total electricity demand from 3.6 MW to 1.89 MW in the Scenario 7, due to the production of heat for steam production from biomass consumed, results in a clear reduction in the minimum number of WT for the storage category (Fig. 60). In fact, for this scenario, the smallest capacity size has already a lower minimum number of turbines than the upper limit, specifically 11 devices are sufficient for self-sustainability of the system with a storage capacity of 2 tons of hydrogen as shown in Table 38. Increasing the storage capacity, the number of required WT's decreases, up to a minimum number of 4 turbines for the biggest hydrogen capacity. Reducing the potential of number of wind devices directly affects the capacities of the AEL system, which are lower in this case due to the reduction of power surplus phases, from a capacity range of 19-123 MW in

Scenario 6 to 6.9-20.9 MW in Scenario 7; while the size of FC modules is reduced as result of the reduced demand of power by the process scheme.

Table 38: Equipment Design Configuration for Scenario 7 – Production size 2 kt/y

Scenario 7 – Production GVL size 2 kt/y					
Storage Capacity (t)	2	5	7.5	10	15
N° WT <sub>MIN</sub>	11	6	5	5	4
AEL (MW)	20.9	10.9	8.9	8.9	6.9
FC (MW)	1.7	1.7	1.7	1.7	1.7

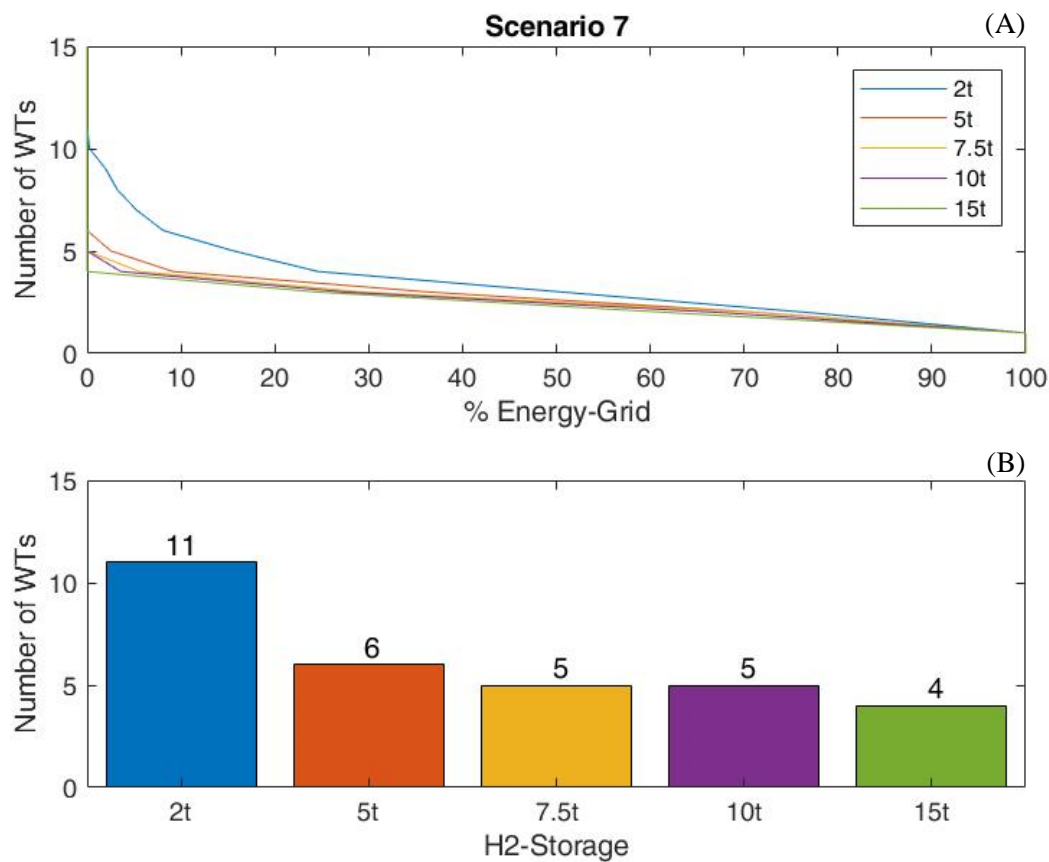


Fig. 60: Optimal configuration design Scenario 7 - 2kty (A) variation of %Energy-Grid parameter as the number of WT's varies for different storage sizes (B) minimum number of WT's minimising the target term for each storage size

The conceptual design of the integrated RES system has been performed for the production size of 4 kt/y as well. Given the higher capacity of the plant, and consequently the higher energy demand estimated at 6.73 MWh for Scenario 6 and 2.73 MWh for Scenario 7, where the energy to the boiler is 3.99 MWh obtained using biomass, the results of the methodology in terms of number of wind turbine revealed an increased range of variations for the minimum number of WT for the same storage capacities considered. For Scenario 6, storage capacities of less than 10t are not suitable to support the energy demand with a wind farm with less than 35 WT; specifically, a minimum number of turbines of 73, 71,



and 44 were obtained for 2, 5, and 7.5 tons capacity, while the system can operate within the land restrictions for 10- and 15-tons storage (Fig. 61A,B-Table 39). Reducing the power demand as in Scenario 7, the number of requested WTs drastically fell down, considering already with the littlest storage size a suitable number of 23 wind turbines, as well as, the capacities of AEL modules which are size up to 140 MW for Scenario 6 and ranged between 12 and 44 for Scenario 7 (Fig. 61A',B'-Table 39).

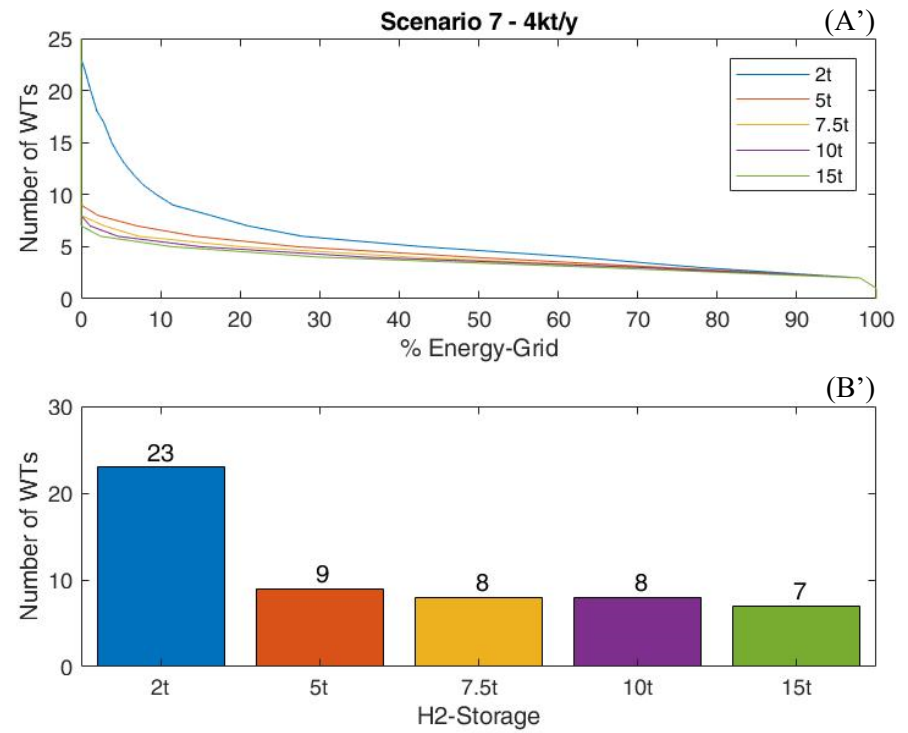
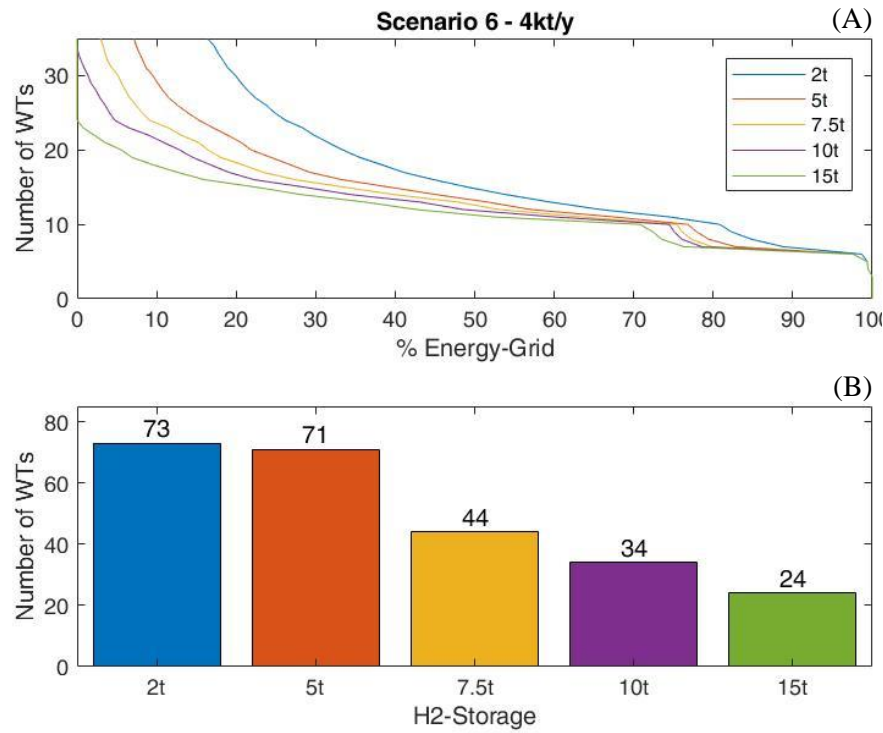


Fig. 61: Optimal configuration design Scenario 6 and 7 - 4kt/y (A-A') variation of %Energy-Grid parameter as the number of WT's varies for different storage sizes (B-B') minimum number of WT's minimising the target term for each storage size

Table 39: Equipment Design Configuration for Scenario 6 and 7 – Production size 4 kt/y

	Scenario 6 – Production GVL size 4 kt/y					Scenario 7 – Production GVL size 4 kt/y				
Storage Capacity (t)	2	5	7.5	10	15	2	5	7.5	10	15
N° WT <sub>MIN</sub>	73	71	44	34	24	23	9	8	8	7
AEL (MW)	140	136	82	62	41.9	44.2	16.2	14.2	14.2	12.2
FC (MW)	6.73	6.73	6.73	6.73	6.73	2.73	2.73	2.73	2.73	2.73

The methodology applied for the conceptual design of integrated systems evaluated the optimal size configurations for the different equipment in Scenarios 6 and 7. Specifically, the methodology has indicated the need for a minimum storage of 5 tons with at least 19 turbines for the GVL-process size of 2 kt/y, and 10 tons as minimum storage needed with 34 turbines for the 4 kt/y scheme size for Scenario 6. In evaluating the configurations for Scenario 7, the methodology evidenced the suitability for process energy self-sustainment purposes for both process sizes of the smallest storage capacity among those considered in the analysis: 2 tons, coupled with 11 and 23 turbines, respectively.

For the purpose of the conceptual design, the criterion of energy self-sustain was primarily considered; the evaluation of the optimal configurations and the effect of key system elements, such as storage size and number of turbines, will be further analyzed by evaluating the other indices in this analysis, and especially in light of the economic indicators.

### **5.3.2 Results of the economic analysis**

The economic analysis was carried out on the scenarios described and based on the indicators presented above. Specifically, the LCOP indicator was used to compare the cost investment for units produced of GVL and, secondary of H<sub>2</sub> and electricity among the scenarios when they are produced on-site. The cost items for the individual equipment in terms of capital and related operating costs have been allocated appropriately to the different plant sections for the evaluation of the different levelized costs: energy production section, when it is produced on-site from wind energy, in which installation costs and O&M costs of wind turbines are allocated; hydrogen production section with installation and operating costs of AELs module and the storage quota related to the excess of hydrogen sold as market product. The remaining quota of storage capacity, i.e. the cost of the storage item related to hydrogen stored as a reagent and back-up fuel, is charged to GVL's investment, together with the capital and operating investment of the plant, and the costs related to the back-up fuel cell. On the other hand, the indicator NPV was employed instead as a metric indicator to assess and compare the economic profitability of the different cases over a time period of 10 years, i.e., considering the value of NPV to 10 years of plant operation as a reference year [365].

Besides the technological efficiency parameter, expressed in terms of percentage of energy from the grid, the conceptual design of the optimal configuration for Scenarios 6 and 7 can be further developed considering the effect of variation in storage size and number of turbines on the economic indices.

#### **5.3.2.1 Results of preliminary design and cost estimation of GVL-process scheme**

The preliminary design and capital cost estimation for all the process units were performed by Aspen Process Economic Analyser (APEA)[371] for both production plant sizes; default design procedures are implemented in the software in order to define a preliminary design for all the equipment in the process

scheme, such as heat exchangers, distillation columns, condensers, reboilers, pumps, separation vessels and reactors. For utility-equipment, the sizing and cost-evaluation was based on commercial datasheets and literature data.

Table 40: Preliminary results economic evaluation: capital cost of the GVL scheme for production sizes 2 and 4 kt/y

	SIZE-2kt/y		SIZE-4kt/y	
	Equip. Cost (\$ <sub>2018</sub> )	Install. Cost (\$ <sub>2018</sub> )	Equip. Cost (\$ <sub>2018</sub> )	Install. Cost (\$ <sub>2018</sub> )
Reactors	$1.81 \cdot 10^5$	$6.23 \cdot 10^5$	$2.35 \cdot 10^5$	$6.91 \cdot 10^5$
Heat Exchangers	$9.95 \cdot 10^4$	$6.11 \cdot 10^5$	$1.40 \cdot 10^5$	$7.43 \cdot 10^5$
Dist. Columns	$7.44 \cdot 10^5$	$2.27 \cdot 10^6$	$1.28 \cdot 10^6$	$2.99 \cdot 10^6$
Separat. vessels	$7.22 \cdot 10^4$	$4.53 \cdot 10^5$	$7.48 \cdot 10^4$	$4.57 \cdot 10^5$
Pumps	$1.04 \cdot 10^5$	$1.97 \cdot 10^5$	$1.06 \cdot 10^5$	$2.05 \cdot 10^5$
Total Equip. Cost	$1.20 \cdot 10^6$	$4.16 \cdot 10^6$	$1.83 \cdot 10^6$	$5.08 \cdot 10^6$
Including:				
<ul style="list-style-type: none"> <li>• Instrumentation (2-8%-TCC)</li> <li>• Piping (3-20%-TCC)</li> <li>• Electrical system (2-10%-TCC)</li> <li>• Building (3-18%-TCC)</li> <li>• Yard improv. (2-5%)</li> <li>• Services (8-20%-TCC)</li> <li>• Land (1-2%-TCC)</li> <li>• Engineering (4-21%-TCC)</li> <li>• Construction (4-16%-TCC)</li> <li>• Contractor's fees (2-6%-TCC)</li> <li>• Contingency (5-15%-TCC)</li> </ul>				
Total Capital Cost-TCC		$10.6 \cdot 10^6$		$12 \cdot 10^6$
Total Capital Cost-TCC (€-2022)		$15.5 \cdot 10^6$		$17.4 \cdot 10^6$

In addition to the purchase and installation cost of the equipment, the software includes various direct and indirect cost items. The overall value of the total capital invested is consistent with the percentage ranges of the individual cost items in relation to the total cost reported by Peters et al. [375].

Increasing production capacity from 2 to 4 kt/y results in an increase of less than 20 per-cent in invested capital, while raw material and catalyst expenses tend to double, as shown in Table 40 and Table 41.

Table 41: Preliminary results economic evaluation: partial OPEX cost of the GVL scheme for production sizes 2 and 4 kt/y

	SIZE-2kt/y	SIZE-4kt/y
<b>Raw Materials (€/y)</b>		
Fructose	$2.96 \cdot 10^6$	$5.86 \cdot 10^6$
Butanol	$2.50 \cdot 10^5$	$5.97 \cdot 10^5$
GVL	$1.50 \cdot 10^5$	$3.00 \cdot 10^5$
<b>Catalyst (€/y)</b>		
Amberlite IR120	$4.86 \cdot 10^3$	$9.28 \cdot 10^3$
Ru/C	$4.33 \cdot 10^3$	$8.66 \cdot 10^3$
Alumina/DHT-4A	$6.11 \cdot 10^2$	$1.06 \cdot 10^3$
Total	$3.37 \cdot 10^6$	$6.78 \cdot 10^6$

At steady-state, the cost of solvents and reagents that are recycled in the process scheme, such as butanol, is defined by considering the make-up cost and a start-up cost corresponding to the nominal flow rate for a 48-hours duration time, the same for evaluating an initial cost for GVL as a solvent to the system. For the catalyst, on the other hand, 10% of the catalyst is renewed every 6 months at a cost equivalent to 20% of its original value [299]. Hydrogen will be considered in the raw material evaluation later as its cost item depends on in-situ production or external supply and thus on the different configurations considered in the analysis. Depending on the different scenarios considered, the analysis of fixed capital investment will include different cost elements due to the different configurations.

### 5.3.2.2 Effect of parameters: wind farm size and storage system on economic indicators

Among all the optimal configurations defined in the conceptual design phase for Scenarios 6 and 7, for each plant size, the use of different wind farm and storage sizes has effects on the unit cost of the product and the profitability of the initiative. For Scenario 6 considering the 2kt/y-GVL size, the LCOP was evaluated for different hydrogen storage capacities, excluding the 2t storage size, as it corresponds to a high number of WT (Table 42):

- The increase in storage capacity from 5 to 15 tons, with the corresponding reduction in terms of minimum wind turbines required, results in the increase of the levelized costs of hydrogen and GVL; with range of variation of levelized cost from 3.68 to 4.07 €/kg for GVL and from 3.72 to 4.80 €/kg for hydrogen. This is the result of a reduction in the flow of hydrogen sales and an increase in invested capital for higher storage sizes.
- Considering the maximum land use, the increase in the number of WTs, until the maximum limit of 35, positively affects the levelized costs of the products for the same size of storage. The maximization of the number of wind devices, and the subsequent high-power production in the power surplus phases, results in overproduction of hydrogen and a reduction in its unit production cost, which consequently affects the production cost of GVL.

Table 42: LCOP values for Scenario 6 – 2 kt/y GVL production size.

Scenario 6 – 2kt/y Storage Capacity (t)	%E-Grid = 0 WT	LCOP (€/kg)		Max Land WT	LCOP (€/kg)	
		GVL	H <sub>2</sub>		GVL	H <sub>2</sub>
2	>35	-	-	35	-	-
5	19	<b>3.68</b>	<b>3.72</b>	35	<b>3.59</b>	<b>3.51</b>
7.5	13	<b>3.83</b>	<b>4.14</b>	35	<b>3.61</b>	<b>3.56</b>
10	12	<b>3.91</b>	<b>4.36</b>	35	<b>3.61</b>	<b>3.62</b>
15	11	<b>4.07</b>	<b>4.80</b>	35	<b>3.63</b>	<b>3.73</b>

The effects on production costs resulting from variations of these technological parameter directly affect the profitability of the initiative, which is determined partly by the costs incurred but mainly by the revenue of the initiative. For this reason, the economic indicator NPV at 10 years (indicated as NPV10) was considered for each configuration. Assuming the value of NPV10 greater or equal to zero as if the payback time of the initiative is at most 10 years for it to be cost-effective, the minimum selling price ( $SP_{min}$ ) for GVL and H<sub>2</sub> were evaluated and compared with the actual market selling price.

Affected by LCOPs, the minimum selling prices are subject to increase as storage capacities increase. For the storage sizes of 7.5, 10 and 15 tons and their respective minimum turbines,  $SP_{MIN}$  for GVL and hydrogen are out of the market range, making the capacity of 5 tons the only suitable storage size in

terms of profitability with a minimum selling price of 4.19 and 6.95 €/kg for GVL and hydrogen, respectively. Increasing the number of wind devices for each storage size, the trend of minimum prices sees a lowering, especially for GVL as shown in Table 43. This is closely linked to the maximization of hydrogen production in configurations with a high number of turbines, and the shifting of the revenue picture from GVL to hydrogen as main market product of the initiative. As shown in Fig. 62a and Fig. 62b in which the values of NPV10 are displayed by varying the two selling prices for the configuration 5t-18WT and 5t-35WT, the green area indicating the positive values of the indicator tends to widen as the number of turbines increases, while when compared with Fig. 62c and Fig. 62d corresponding to the 7.5t-13WT and 7.5t-35WT configurations, the effect of increasing the storage size causes the area of positivity of the index to regress.

Table 43:  $SP_{min}$  values for Scenario 6 – 2 kt/y GVL production size.

Scenario 6 – 2kt/y Storage Capacity (t)	%E-Grid = 0 WT	SP <sub>MIN</sub> (€/kg)		Max Land WT	SP <sub>MIN</sub> (€/kg)	
		GVL	H <sub>2</sub>		GVL	H <sub>2</sub>
2	>35	-	-	35	-	-
5	19	<b>4.19</b>	<b>6.95</b>	35	<b>2.39</b>	<b>6.55</b>
7.5	13	<b>&gt;4.99</b>	<b>&gt;7.65</b>	35	<b>2.49</b>	<b>6.65</b>
10	12	<b>&gt;4.99</b>	<b>&gt;7.65</b>	35	<b>2.79</b>	<b>6.75</b>
15	11	<b>&gt;4.99</b>	<b>&gt;7.65</b>	35	<b>3.19</b>	<b>6.95</b>

The same trend in the variation of the LCOP indicator can also be seen for Scenario 7 with values of the index clearly lower than in Scenario 6 as shown in Table 44. In this case, the smallest storage size is also applicable to the system operation and with lower unit production cost values than for larger storage capacities; furthermore, the increase in the number of wind devices also leads to a reduction in the indicator for both GVL and hydrogen. This effect is particularly visible when comparing configurations with minimum number of turbines (Fig. 62a - Fig. 62c).

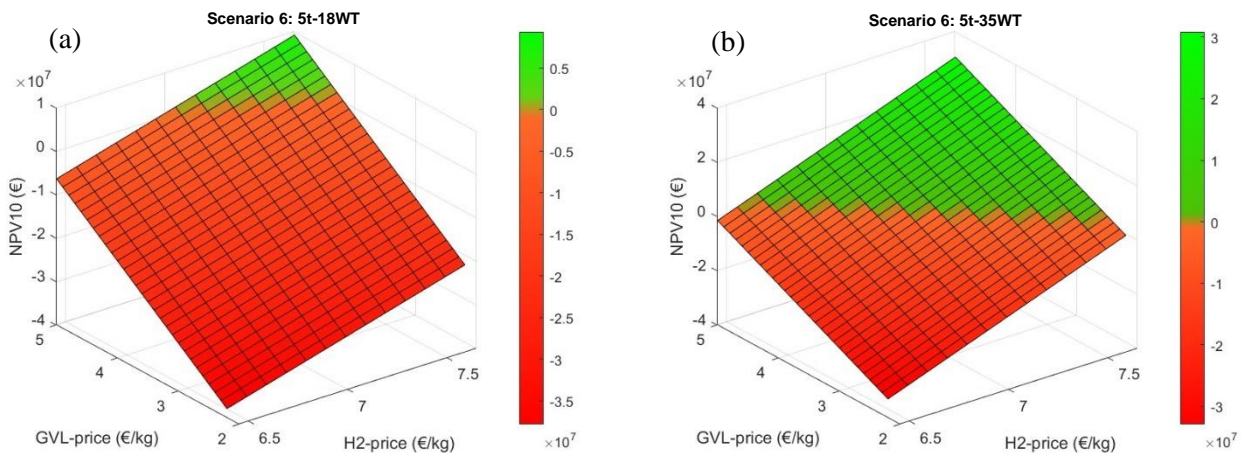


Fig. 62: NPV10 index value in Scenario 6 (expressed by colour) varying the price of GVL and hydrogen; (a) 5t-18WT, (b) 5t-35WT, (c) 7.5t-13WT (d) 7.5t-35WT.

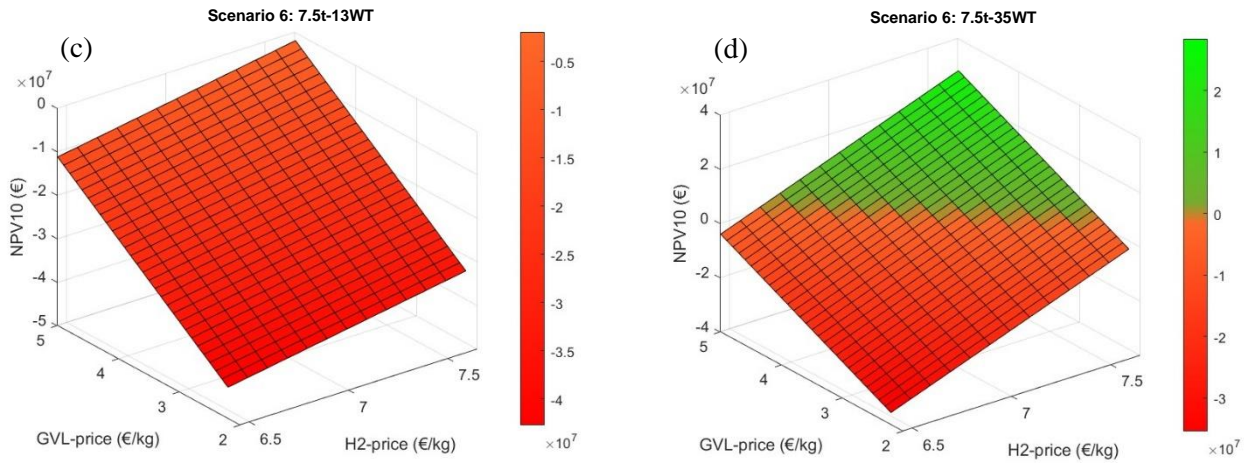


Fig. 62: NPV10 index value in Scenario 6 (expressed by colour) varying the price of GVL and hydrogen; (a) 5t-18WT, (b) 5t-35WT, (c) 7.5t-13WT (d) 7.5t-35WT.

Table 44: LCOP values for Scenario 7 – 2 kt/y GVL production size.

Scenario 7 – 2kt/y Storage Capacity (t)	%E-Grid = 0	LCOP (€/kg)		Max Land	LCOP (€/kg)	
	WT	GVL	H <sub>2</sub>	WT	GVL	H <sub>2</sub>
2	11	<b>3.06</b>	<b>4.01</b>	35	<b>2.99</b>	<b>3.42</b>
5	6	<b>3.20</b>	<b>4.65</b>	35	<b>3.00</b>	<b>3.48</b>
7.5	5	<b>3.33</b>	<b>5.27</b>	35	<b>3.00</b>	<b>3.54</b>
10	5	<b>3.39</b>	<b>5.61</b>	35	<b>3.01</b>	<b>3.59</b>
15	4	<b>3.61</b>	<b>6.91</b>	35	<b>3.02</b>	<b>3.70</b>

As for Scenario 6, the profitability analysis for Scenario 7 was expressed in terms of minimum selling price of the two main market products (Table 45). Although the sales prices of both products are subject to increases in this scenario as storage capacity increases, they show a different trend when the number of wind turbines changes. Specifically, while the selling price of GVL generally tends to decrease and for some capacity categories even considerably, the price of hydrogen is instead subject to an increase with the increase in the number of turbines to 35, and that only for the 2, 5 and 7.5-tons storage categories. The reason for these results can be explained mainly by considering the hydrogen flows for sale; due to the lower electricity demand in Scenario 7, the amount of energy available for surplus hydrogen production is higher than in Scenario 6 with the same number of wind turbines, leading to a higher production of hydrogen as a market product. Especially for smaller storage facilities, the hydrogen flows for sale are therefore high and form a predominant part of the initiative's revenue compared with that of GVL, which for this reason has very low selling prices. In Fig. 63, values of NPV10 over the same range of variation for GVL and hydrogen price at the same number of WTs and storage size are compared between the two scenarios, showing the largest area extension for positive indicator values in Scenario 7 compared to Scenario 6.



Generally, the results of both indicators show that the most cost-effective and profitable configurations consider a lower capital investment in storage capacity, using the smallest storage size suitable for the system operation, and by maximizing the wind power and hydrogen productivity increasing the number of the wind turbines.

Table 45:  $SP_{min}$  values for Scenario 7 – 2 kt/y GVL production size.

Scenario 7 – 2kt/y	%E-Grid = 0	SP <sub>MIN</sub> (€/kg)		Max Land	SP <sub>MIN</sub> (€/kg)	
		GVL	H <sub>2</sub>		WT	GVL
Storage Capacity (t)	WT	GVL	H <sub>2</sub>	WT	GVL	H <sub>2</sub>
2	11	<b>3.29</b>	<b>5.25</b>	35	<b>0.49</b>	<b>5.95</b>
5	6	<b>4.19</b>	<b>5.05</b>	35	<b>0.79</b>	<b>6.05</b>
7.5	5	<b>4.59</b>	<b>5.65</b>	35	<b>0.99</b>	<b>6.15</b>
10	5	<b>4.79</b>	<b>6.55</b>	35	<b>1.19</b>	<b>6.15</b>
15	4	<b>&gt;4.99</b>	<b>&gt;7.65</b>	35	<b>1.59</b>	<b>6.35</b>

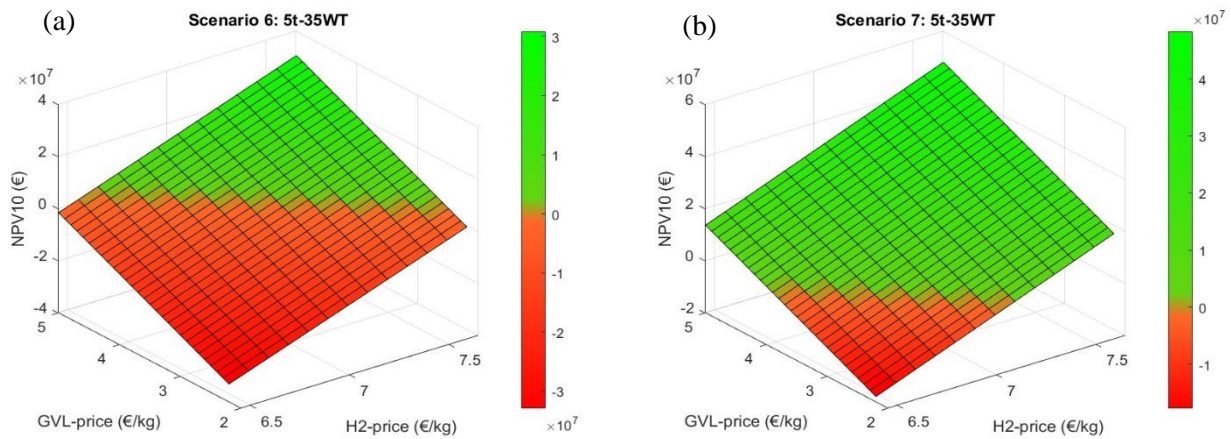


Fig. 63: Comparison NPV10 index value in Scenario 6 (a) and Scenario 7 (b) varying the price of GVL and hydrogen;

Table 46: LCOP values for Scenario 6 – 4 kt/y GVL production size.

Scenario 6 – 4kt/y	%E-Grid = 0	LCOP (€/kg)		Max Land	LCOP (€/kg)	
		GVL	H <sub>2</sub>		WT	GVL
Storage Capacity (t)	WT	GVL	H <sub>2</sub>	WT	GVL	H <sub>2</sub>
2	>35	-	-	35	-	-
5	>35	-	-	35	-	-
7.5	>35	-	-	35	-	-
10	34	<b>2.77</b>	<b>3.67</b>	35	<b>2.77</b>	<b>3.65</b>
15	24	<b>2.92</b>	<b>4.04</b>	35	<b>2.79</b>	<b>3.77</b>

Table 47:  $SP_{min}$  values for Scenario 6 – 4 kt/y GVL production size.

Scenario 6 – 4kt/y	%E-Grid = 0	SP <sub>MIN</sub> (€/kg)		Max Land	SP <sub>MIN</sub> (€/kg)	
		WT	GVL		H <sub>2</sub>	WT
Storage Capacity (t)						
2	>35	-	-	35	-	-
5	>35	-	-	35	-	-
7.5	>35	-	-	35	-	-
10	34	<b>3.09</b>	<b>5.75</b>	35	<b>2.99</b>	<b>5.75</b>
15	24	<b>3.89</b>	<b>5.85</b>	35	<b>3.19</b>	<b>5.95</b>

The effects of the increase in GVL's production capacity on economic indicators was analyzed by comparing the results obtained with the 2 kt/y size with the larger 4 kt/y size for both Scenarios 6 and 7. The increase in electricity demand due to the higher production capacity of the plant directly influences the capacity requirements of the wind turbine system and hydrogen storage, which are increased. As shown in Table 46, LCOP values were evaluated for the only storage sizes suitable for the plant's operation: 10 and 15 tons; compared to the corresponding results for size 2 kt/y in Table 42, LCOP values decreased as an effect of the higher throughput volumes, and the same effect is also seen for the minimum selling price values for both products, as shown in Table 47. A clear decreasing is observable also by considering the indicator values for Scenario 7 in Table 48 and Table 49. For this scenario, all storage capacities are suitable for the operation of the system at 4 kt/y of GVL production size, even the 2-tons storage size, which has the lowest LCOP for both products. Analyzing the sales prices in Table 49, in relation to indicator NPV10, it can be observed that for the different storage sizes, the increase in the number of turbines does not lead to a substantial reduction in prices, at least for hydrogen; this can again be traced back to hydrogen's main income support for large numbers of wind devices, but also in this case to the reduction in government incentives due to the increase in the initiative's annual turnover (i.e. exceeding the 50 million annual profit) and observable from Fig. 64 in which we observe the sharp decline in the value of NPV10 at a specific price range. For configurations with 35 turbines, the price of the GVL can be considerably reduced, even below the minimum market price; it has instead a price in the market range for configurations with minimum number of wind turbines where it is instead the GVL that mainly supports the initiative's income and this is reflected in the price of hydrogen, which is below the market price in this case, as can also be seen in Fig. 64c where the green area of positivity of NPV10 extends over the entire range of variation of the hydrogen price.

Table 48: LCOP values for Scenario 7 – 4 kt/y GVL production size.

Scenario 7 – 4kt/y	%E-Grid = 0	LCOP (€/kg)		Max Land	LCOP (€/kg)	
		WT	GVL		H <sub>2</sub>	WT
Storage Capacity (t)						
2	23	<b>2.09</b>	<b>3.49</b>	35	<b>2.08</b>	<b>3.41</b>
5	9	<b>2.19</b>	<b>4.18</b>	35	<b>2.08</b>	<b>3.47</b>
7.5	8	<b>2.25</b>	<b>4.58</b>	35	<b>2.09</b>	<b>3.53</b>
10	8	<b>2.28</b>	<b>4.86</b>	35	<b>2.09</b>	<b>3.58</b>
15	7	<b>2.41</b>	<b>5.75</b>	35	<b>2.10</b>	<b>3.70</b>

Table 49: SP<sub>min</sub> values for Scenario 7 – 4 kt/y GVL production size.

Scenario 7 – 4kt/y	%E-Grid = 0	SP <sub>MIN</sub> (€/kg)		Max Land	SP <sub>MIN</sub> (€/kg)	
		WT	GVL		H <sub>2</sub>	WT
Storage Capacity (t)						
2	23	<b>1.49</b>	<b>3.25</b>	35	<b>&lt;1.19</b>	<b>4.35</b>
5	9	<b>2.49</b>	<b>&lt;4.80</b>	35	<b>&lt;1.19</b>	<b>4.45</b>
7.5	8	<b>2.69</b>	<b>&lt;4.80</b>	35	<b>&lt;1.19</b>	<b>4.55</b>
10	8	<b>2.79</b>	<b>&lt;4.80</b>	35	<b>&lt;1.19</b>	<b>4.55</b>
15	7	<b>3.09</b>	<b>&lt;4.80</b>	35	<b>1.29</b>	<b>4.75</b>

The analysis of economic indicators between the two scenarios in which the GVL production plant is fully integrated with a renewable-based energy system, and for both production sizes considered in this investigation, revealed the effect on investment costs and profitability of the size of hydrogen storage and the number of turbines in the wind farm. In particular, the general trends of LCOP and NPV10 indicators on the basis of minimum prices show:

- The decrease of LCOP indicator values and the increase of NPV10 order of magnitude by increasing the plant production capacity from 2 kt/t to 4 kt/y of GVL-produced.
- The increase of LCOP indicator for both products (GVL and hydrogen) by increasing the hydrogen storage capacity, and affecting also the minimum selling price.
- The decrease in both LCOP and selling price indices as the number of turbines, i.e. wind farm size, increases from the minimum number to the maximum number of turbines; with exceptions in some cases for the selling price of hydrogen.

For these reasons, the comparison in the economic analysis with the other scenarios for each size were performed by considering for Scenarios 6 and 7 the minimum functional storage size for system operation and the maximum number of turbines. For the other scenarios (Scenario1-5), the equipment sizing is set by the process specifications, in terms of energy and hydrogen demand. The sizing details of individual elements for each scenario and size are given in the Table 50.

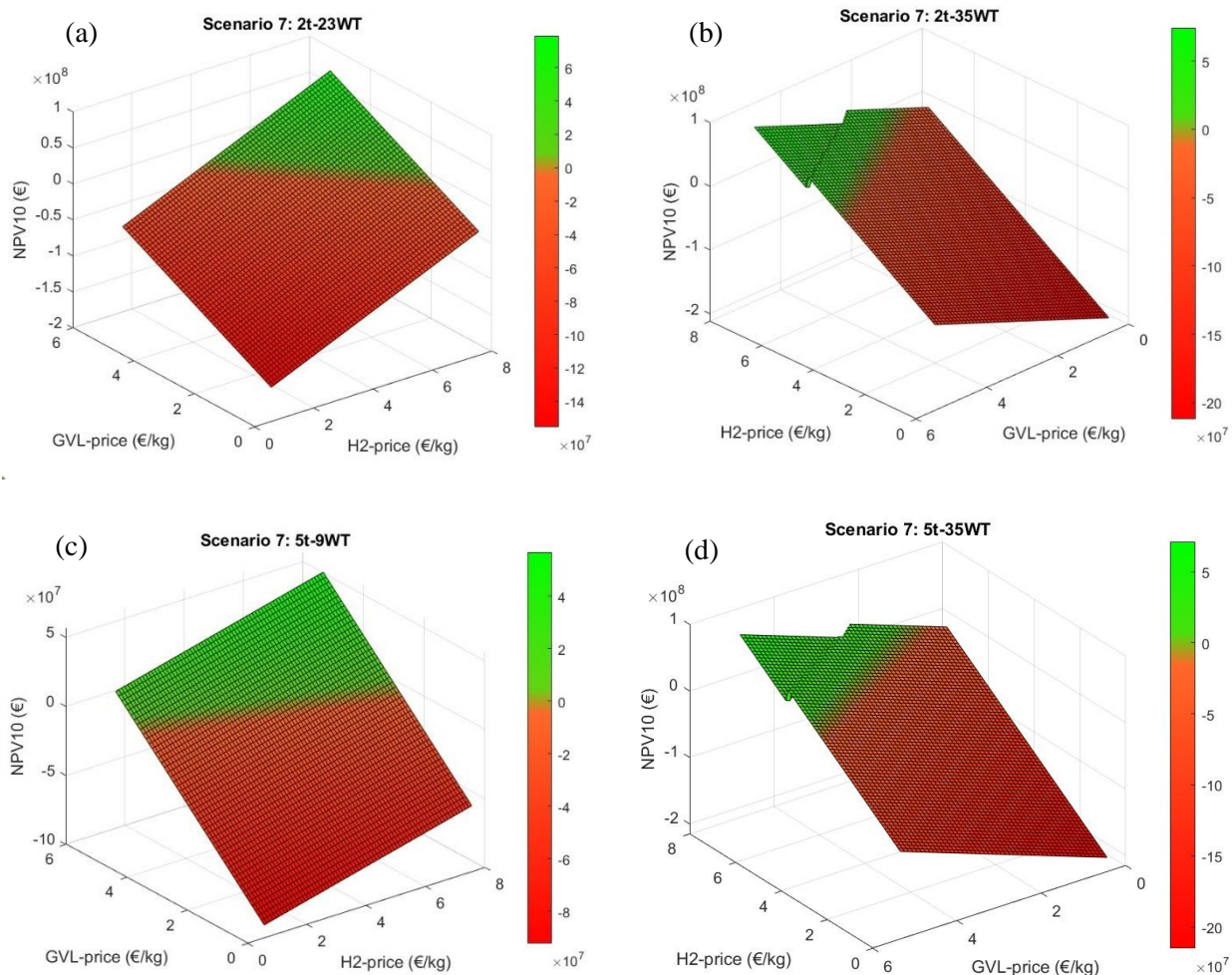


Fig. 64: NPV10 index value in Scenario 7-4kty (expressed by colour) varying the price of GVL and hydrogen; (a) 2t-23WT, (b) 2t-35WT, (c) 5t-9WT (d) 5t-35WT.

Table 50: Results of optimal system sizing of renewable energy integration, hydrogen production and storage for each scenario

Scenario	GVL-production Capacity (kt/y)	N° of Wind Turbine (WT)	Hydrogen storage capacity (Kg <sub>H2</sub> )	AEL module capacity (MW)	PEMFC module capacity (MW)
1	2	-	840 (60m <sup>3</sup> )	-	-
	4	-	1680 (120m <sup>3</sup> )	-	-
2	2	-	840 (60m <sup>3</sup> )	-	-
	4	-	1680 (120m <sup>3</sup> )	-	-
3	2	-	324 (25m <sup>3</sup> )	0.285	-
	4	-	650 (50m <sup>3</sup> )	0.570	-
4	2	-	324 (25m <sup>3</sup> )	0.285	-
	4	-	650 (50m <sup>3</sup> )	0.570	-

5	2	-	324 (25m <sup>3</sup> )	0.285	-
	4	-	650 (50m <sup>3</sup> )	0.570	-
6	2	35	5000 (400m <sup>3</sup> )	35	3.6
	4	35	10000 (750m <sup>3</sup> )	62	6.73
7	2	35	2000 (160m <sup>3</sup> )	20.9	1.7
	4	35	2000 (160m <sup>3</sup> )	44.2	2.73

### 5.3.2.3 Cost analysis and economic indicators: scenario comparison

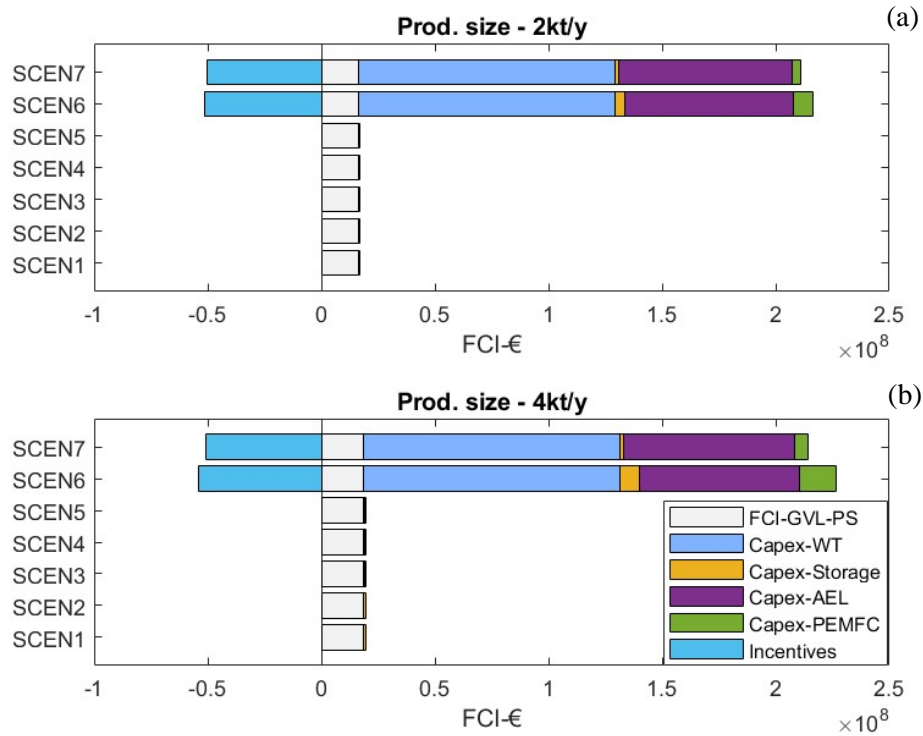


Fig. 65: Contributions of each item to the CAPEX of each scenario configuration; (a) 2 kt/y, (b) 4 kt/y

As shown in Fig. 65, the analysis of fixed capital investment (FCI) reveals the investment disparity among scenarios. While for Scenarios 1-5, the main investment contribution is made by the capital cost of the GVL production plant, in Scenarios 6 and 7 the largest investment is associated with the integrated system for electricity and hydrogen production from renewable sources. For these scenarios, the main cost-item is related to the investment in the wind farm with the cost of installation for wind turbines amounting to 112.8 M€. Scenario 6 presents the highest capital investment, compared to Scenario 7, in both production sizes. This is mainly due to the higher investment in Scenario 6 for hydrogen storage capacity and PEMFC modules, although the costs of AEL modules are higher in Scenario 7 for the same wind farm size. Investment in the exploitation of renewable energy sources allows Scenarios 6 and 7 to take advantages from government incentives. In Fig. 65, the maximum values of incentives are reported as negative values, corresponding to the 25 % of equipment installation costs; for initiative revenues higher than a threshold value of 50 M€/y, the incentive percentage is reduced to 15%.

Considering average market prices for GVL and hydrogen, €3.09 and €6.23/kg respectively, the earnings of the different configurations are shown in Fig. 66. It is clear that the profitability of Scenarios 6 and 7 depends on maximizing hydrogen production for both production sizes, which is the main source of earnings for these initiatives, with the sale of GVL constituting 16-17% of the profit for the smallest size and 28-32% for the largest size. Among these two scenarios, the lower demand in hydrogen storage

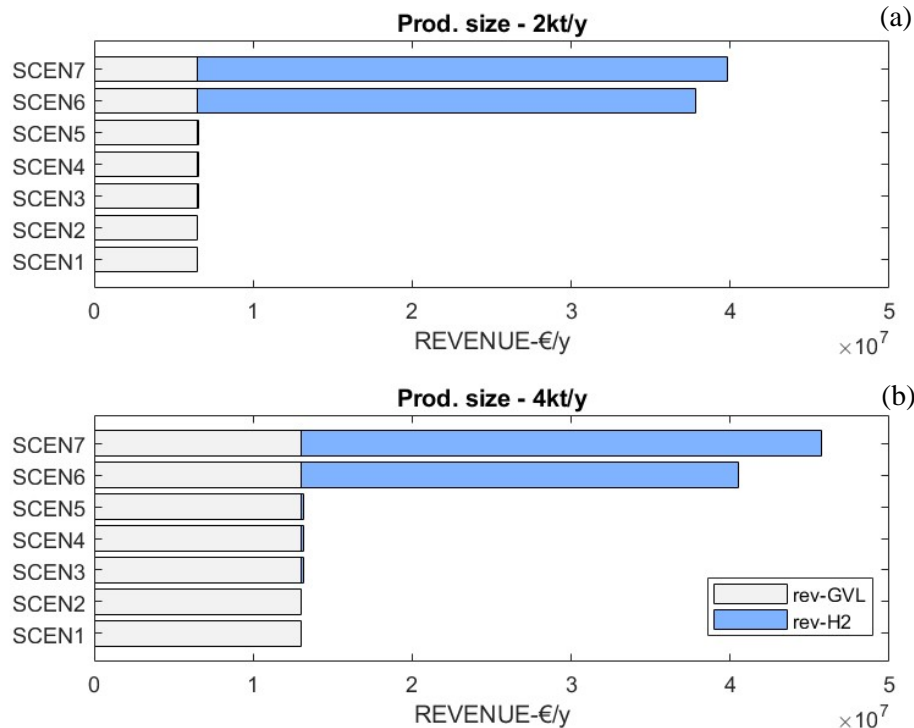


Fig. 66: Contribution of GVL and hydrogen sales to total revenue for each scenario; (a) 2kt/y, (b) 4 kt/y.

capacity in Scenario 7 leads to higher hydrogen selling for the same wind farm capacity. Between these two scenarios, the lower demand for hydrogen storage capacity in Scenario 7 leads to a higher sale of hydrogen for the same wind farm capacity; this increase is even more evident in the 4 kt/y-GVL production size where, while for Scenario 6 the demand for hydrogen in the back-up system and storage is doubled, for Scenario 7 it is comparable. On the other hand, for all the other scenarios the sale of the GVL constitutes the main source of income (98.9-100% of the total income); in Scenarios 3, 4 and 5, where hydrogen is produced on-site, the residual hydrogen (between process demand and alkaline module productivity) could eventually be sold.

In terms of operating costs (OPEX), the picture of OPEX-cost analysis changes between the two different production sizes, as shown in Fig. 67. For the GVL production size of 2 kt/y, Scenario 6 and 7 are still characterized by the highest operating expenses, caused mainly by the operating and maintenance costs of wind turbines and AEL modules, and to a lesser extent by storage and PEMFC. In terms of utility costs, Scenario 5 has the highest contribution due to the high consumption of electricity from the grid, being a fully electrified configuration; this consumption doubles by scaling up to the largest production size, making this scenario the one with the highest operating costs for size 4 kt/y, while Scenario 6 presents a negligible utility-cost in both production sizes. In general, configurations involving use of natural gas or electricity to fuel the boiler have a higher utility cost than the use of biomass, as between Scenarios 1 and 2 and 3 and 4. Comparing Scenarios 6 and 7, on-site, low-cost electricity generation results in a lower contribution than the use of biomass. In contrast, off-site

purchase of hydrogen leads to a higher feedstock cost contribution for Scenarios 1 and 2, compared to the other scenarios in which hydrogen is produced on-site.

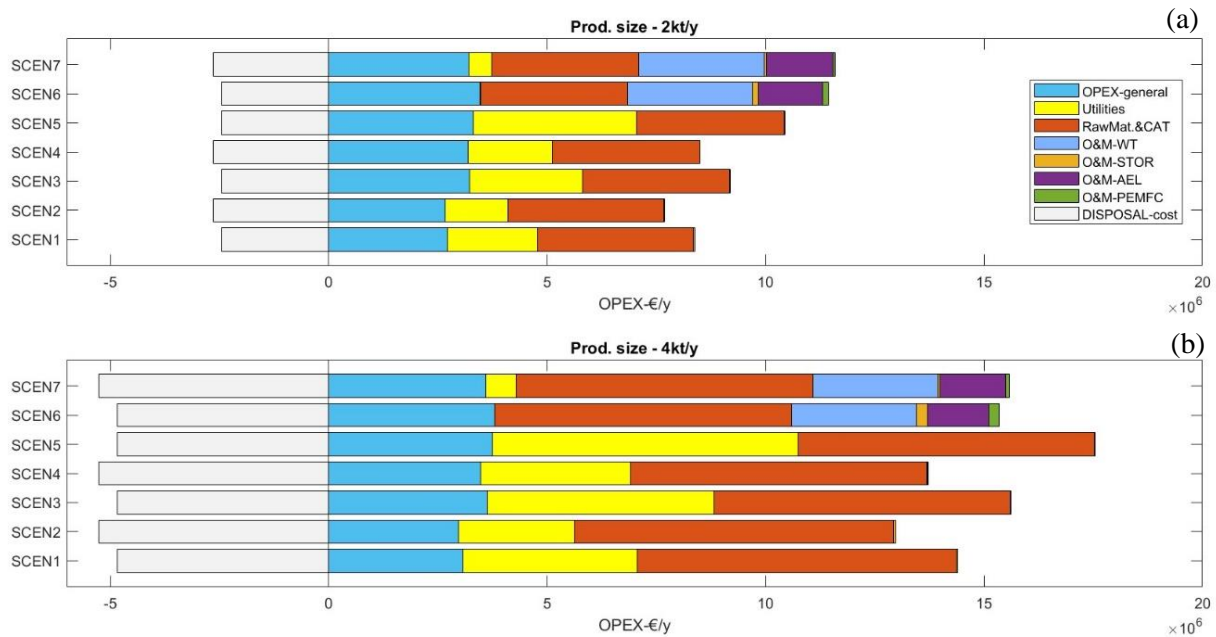


Fig. 67: Contributions of each item to the OPEX of each scenario configuration; (a) 2 kt/y, (b) 4 kt/y

In Fig. 67, the cost item listed as "OPEX-general" accounts for all other cost elements related to the labor and administrative management cost of the initiative; part of these costs is related to the fixed capital invested and, therefore, their contribution is higher in the higher FCI-scenarios, due to the assumptions made in the analysis. The operating costs of each scenario are considered net of the avoided cost of biomass disposal by transformation into fructose and/or energy for steam generation, and therefore higher in biomass-boiler configurations.

Analyzing the economic indicators among the different scenarios, it can be seen that the levelized cost of product and the minimum selling price of GVL are generally lower in all scenarios that exhibit a biomass boiler for steam generation, compared to the corresponding scenarios equipped with an electric or natural gas boiler instead, specifically, comparing Scenario 1-2, 3-4, and 6-7 in Fig. 68. The scenarios determine comparable values of the economic indicator for GVL, with the only exception of the Scenario 7 which obtains the lowest LCOP-GVL with 2.99 €/kg. On the other hand, the production costs for unit related to hydrogen are quite different among the scenarios. Excluding Scenario 1 and 2 in which hydrogen is provided off-site from a supplier and accounted as raw material for a minimum purchased cost of 4.8 €/kg, the highest-LCOP for hydrogen is obtained by Scenario 3,4 and 5, where the on-site hydrogen production is limited to the demand of the GVL-process, and produced by using electricity from the grid. Although this cost indicator is quite high, it does not strongly affect the GVL production cost for these scenarios, and that is because of the production asset of the configuration. For Scenarios 3, 4, and 5 (as well as for Scenarios 1 and 2), GVL is the main market product, with a share of the initiative's income from 98-99%, as only any hydrogen residues is destined for sale. This aspect is also



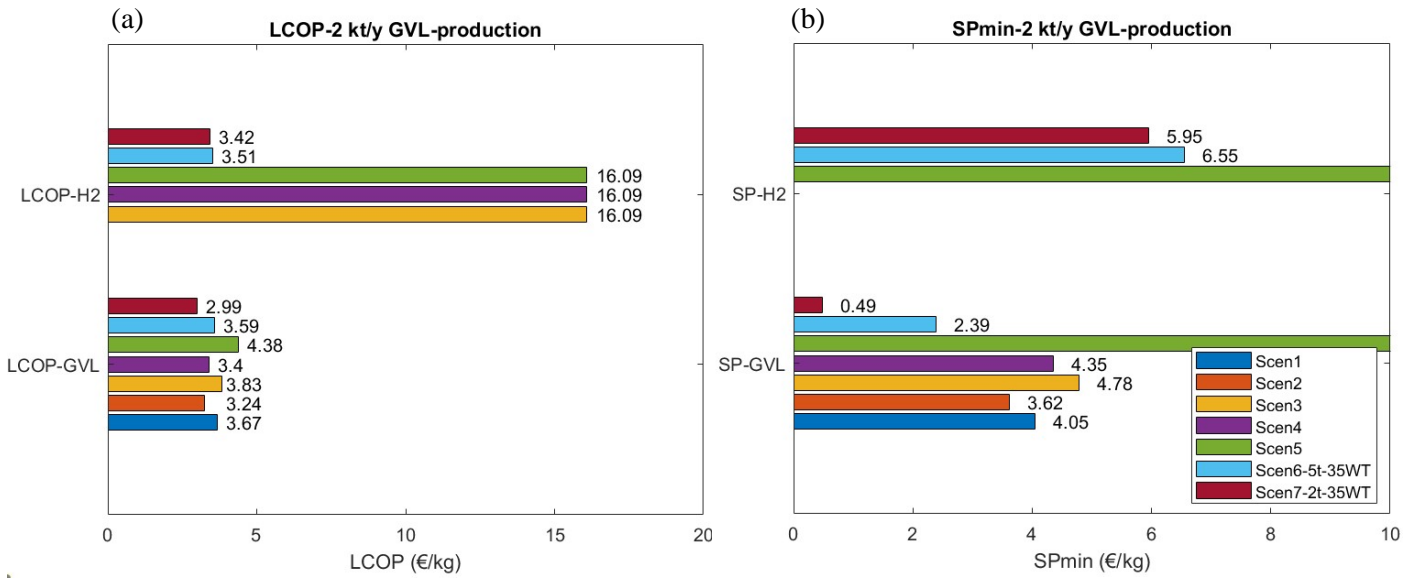


Fig. 68: LCOP GVL-H2(a) and SPmin GVL-H2 (b) values for each scenario and production size 2 kt/y

visible in Fig. 68b, where the minimum selling price of hydrogen for the Scenario 3 and 4 is around zero, since it does not affect the initiative profitability, and the selling of GVL is sufficient for the initiative to return of the investment before 10 years. Comparing the minimum selling-price values, the optimized configurations of Scenarios 6 and 7 have the lowest values for the sale of GVL with values of €2.39 and €0.49/kg, due to high hydrogen production, and followed by Scenarios 1 and 2 with values of 4.05 and 3.62 €/kg, respectively.

Among the scenarios, Scenario 5 which considers a configuration fully-electrified and supplied by the grid, present the highest values of production cost and minimum-selling price, even though, the cost of grid-electricity in France is very attractive, compared to the European average. It demonstrates the current inconvenience of fully electrified configurations for this size, without the use of supplementary fossil or renewable energy systems.

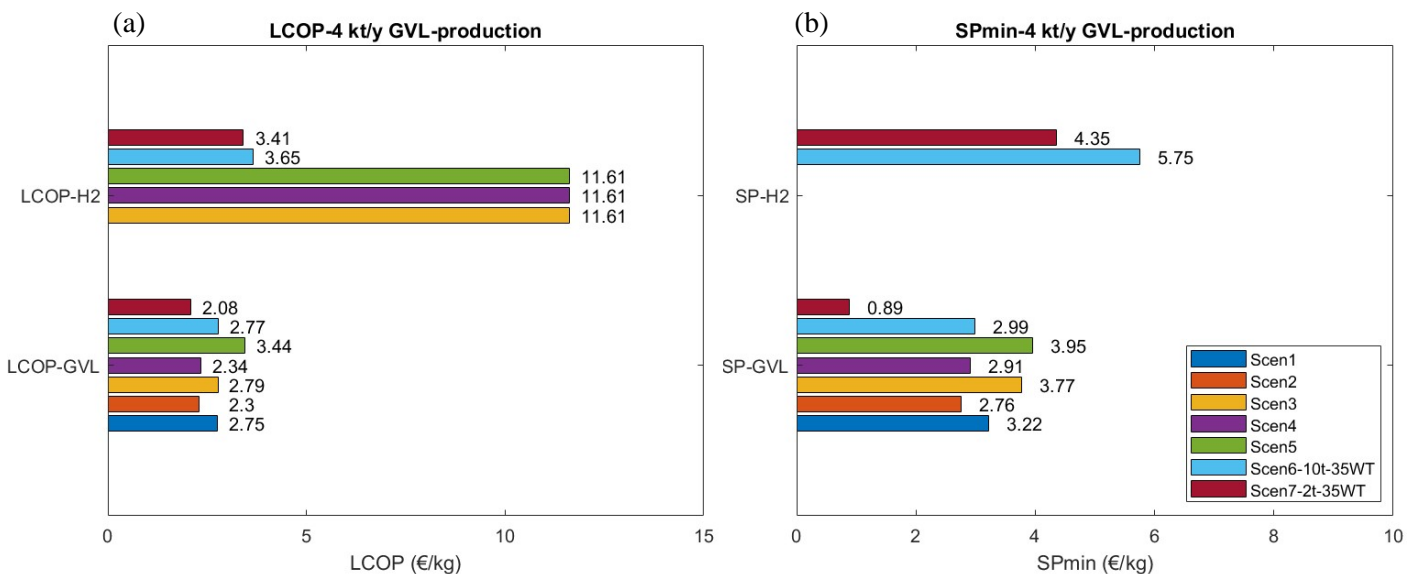


Fig. 69: LCOP GVL-H2(a) and SPmin GVL-H2 (b) values for each scenario and production size 4 kt/y

By increasing the plant production capacity to 4 kt/y of GVL (Fig. 69), Scenario 5 become more economically favorable with a reduction of GVL's LCOP from 4.38 to 3.44 €/kg, and a minimum selling price within the market range. This result therefore opens up the hypothesis that a configuration supplied entirely with electricity from the grid can be economically attractive but for larger production sizes. In any case, this scenario remains the one with the highest LCOP and selling prices also for this size. In general, the increase in GVL production led to a decrease in the unit cost of producing GVL for each scenario; Scenario 7 remains the one with the lowest index values, 2.08 €/kg for LCOP-GVL and 0.89 €/Kg for the lowest selling price, followed by Scenarios 2 and 4, both with biomass-fired boilers. In Scenario 6, where the configuration includes an electric-boiler, the LCOP value of the GVL is comparable to that of Scenarios 1 and 3 with a natural gas-fired boiler, but characterized by a lower minimum sales price value. Considering a selling price for GVL and hydrogen corresponding to the higher value among the scenarios, 3.95 €/kg for GVL and 5.75 €/kg for hydrogen, the trends of NPV over the lifetime of the plant (for size 4 kt/y) was plotted in Fig. 70. The comparison shows that for scenarios in which wind energy and the resulting integration energy system is not considered like Scenario 1-5, the initial capital investment is in the order of €20 million and the gain, purely based on the sale of the GVL alone, allows a return on investment within 10 years with a capital at the end of life in the order of €50 million, with Scenarios 2 and 4 in the top positions for revenue and payback time. On the other hand, the introduction of wind turbines and hydrogen energy-storage system in scenarios 6 and 7 leads to a surge in the initial capital investment, in the order of €200 million, and a change in the indicator's increase rate, driven in this case by a profit also related to hydrogen. Although the two scenarios resulted in a 10-12-year payback time with the prices considered, which is higher than the other scenarios, they have a higher NPV growth rate and consequently a clearly higher term-life capital,

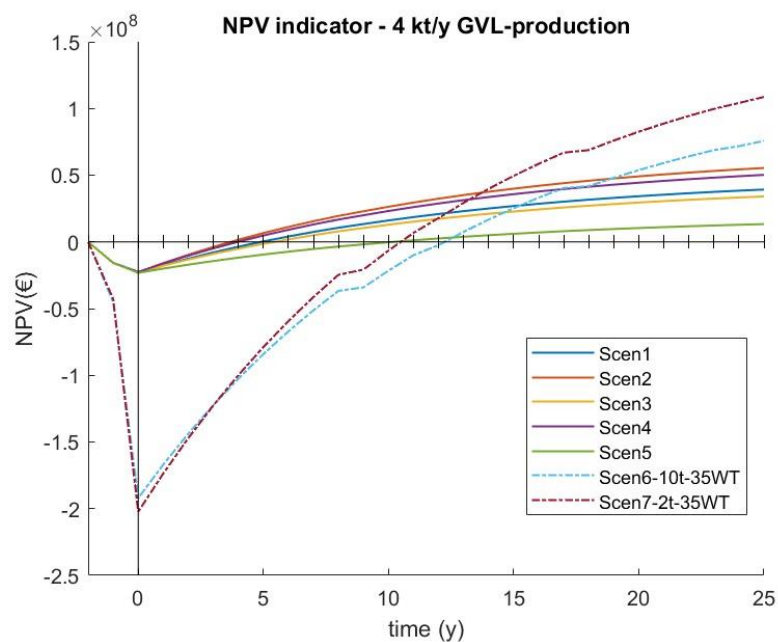


Fig. 70: NPV10 trend over 25 years, plant lifetime, for each scenario and relative to size 4 kt/y

in the order of €75-100 million. Depending on the size of the investment and the time required for return on investment, the choice of one scenario over another can be more specifically addressed.

### 5.3.2.4 Sensitivity analysis on the economic KPI

The robustness of the analysis was tested by performing a sensitivity analysis and a ranking among scenarios based on the indicator NPV10 established. Based on the Monte Carlo method, multiple key-variables are randomly varied in a range corresponding to  $\pm 20\%$  of the mean value and applied for the evaluation of the indicator for a number of  $10^5$ -iterations (Table 51). The variation of parameters was defined according to the uniform distributions, which conservatively for the analysis considers the same probability for all points of the interval.

Table 51: Variation of cost items with the major impact for sensitivity analysis

Independent Variables	Mean value	Range	
		-20%	+20%
CAPEX-PS <sub>GVL-2KTY</sub> (€-10 <sup>7</sup> )	1.63	1.30	1.96
OPEX- PS <sub>GVL-2KTY</sub> (€-10 <sup>6</sup> )	2.80	2.24	3.36
CAPEX-PS <sub>GVL-4KTY</sub> (€-10 <sup>7</sup> )	1.84	1.47	2.21
OPEX- PS <sub>GVL-4KTY</sub> (€-10 <sup>6</sup> )	3.81	3.05	4.57
WT-cost (€/kW)	1500	1200	1800
AEL-cost (€/kW)	1027	822	1232
PEMFC-cost (€/kW)	2200	1760	2640
H <sub>2</sub> -STORAGE-cost (€/kg)	786	629	943
GVL-price (€/kg)	3.09	1.19	4.99
H <sub>2</sub> -price (€/kg)	6.23	4.80	7.65
Electricity-Grid-cost (€/kWh)	0.127	0.102	0.152
NG-fuel-cost (€/kWh)	0.073	0.058	0.088
Biomass-fuel-cost (€/t)	0.125	0.100	0.150
Discount rate (%)	8	6	10

In the evaluation of the NPV10 indicator, based on the randomly varied variables, the cumulative probability was plotted for each scenario. As shown in Fig. 71a-b, Scenarios 6 and 7 show greater variability in the value of the indicator in both production sizes, compared to the other scenarios, which therefore have a flatter trend, with cumulative probability values tending to 1 for higher values of the economic index. Based on the iterations, different combinations of scenarios were defined according to the NPV10 indicator and a ranking on the basis of the probability of occurrence of each combination depicted in Fig. 72.

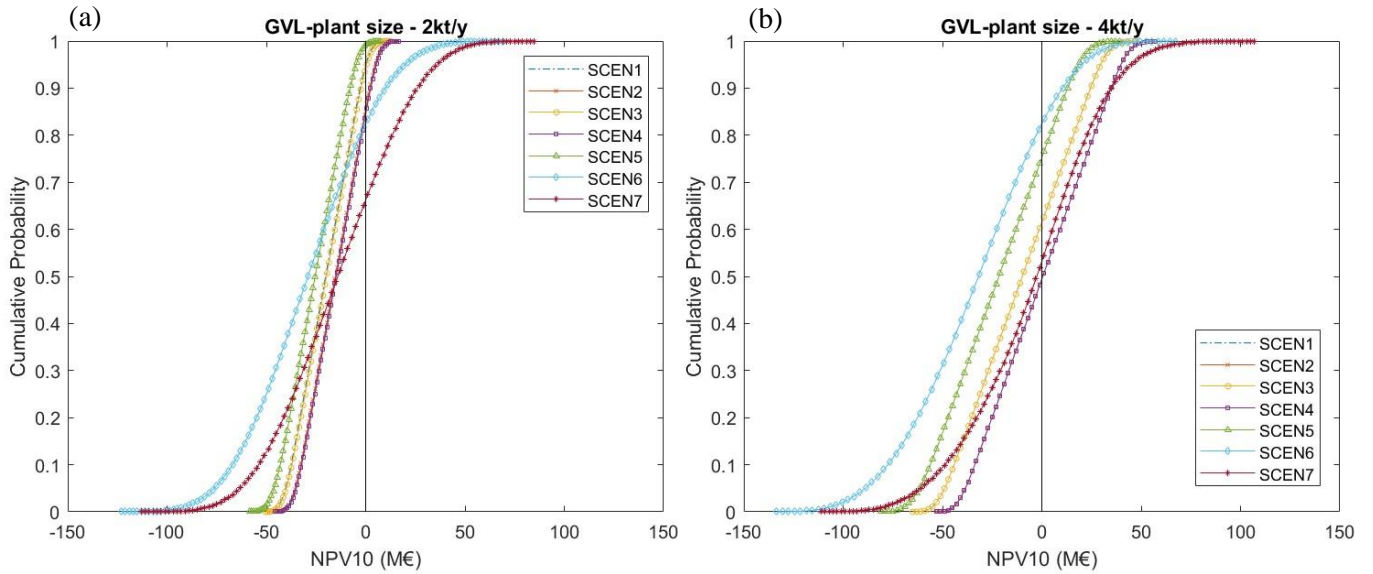


Fig. 71: Cumulative probability trends related to sensitivity analysis on the NPV10 index; (a) 2kt/y, (b) 4kt/y

Subsequently, the probability for each scenario to be the greatest in terms of NPV10 among all combinations was evaluated and reported in Fig. 73. For both production sizes, Scenario 7 was the most likely scenario in all combinations with the highest NPV10 value, with probabilities of 51% and 41% in size 2 kt/y and size 4 kt/y, respectively. Comparing the two sizes, Scenario 2 has a higher probability of occurrence as first scenario in the combinations in the 2 kt/y size with a probability of 48%, compared to a probability of 37% in the greater production size. Scenario 4 only appears to have a certain probability of occurrence as the first scenario from the plant size of 4 kt/y onwards, indicating that on-site hydrogen production via grid electricity is cost-effective on a large scale. This scenario is the one most frequently found in second position for both sizes, as shown in Fig. 74, and followed by scenario 6 in the 2 kt/y size and Scenario 2 in the 4 kt/y size.

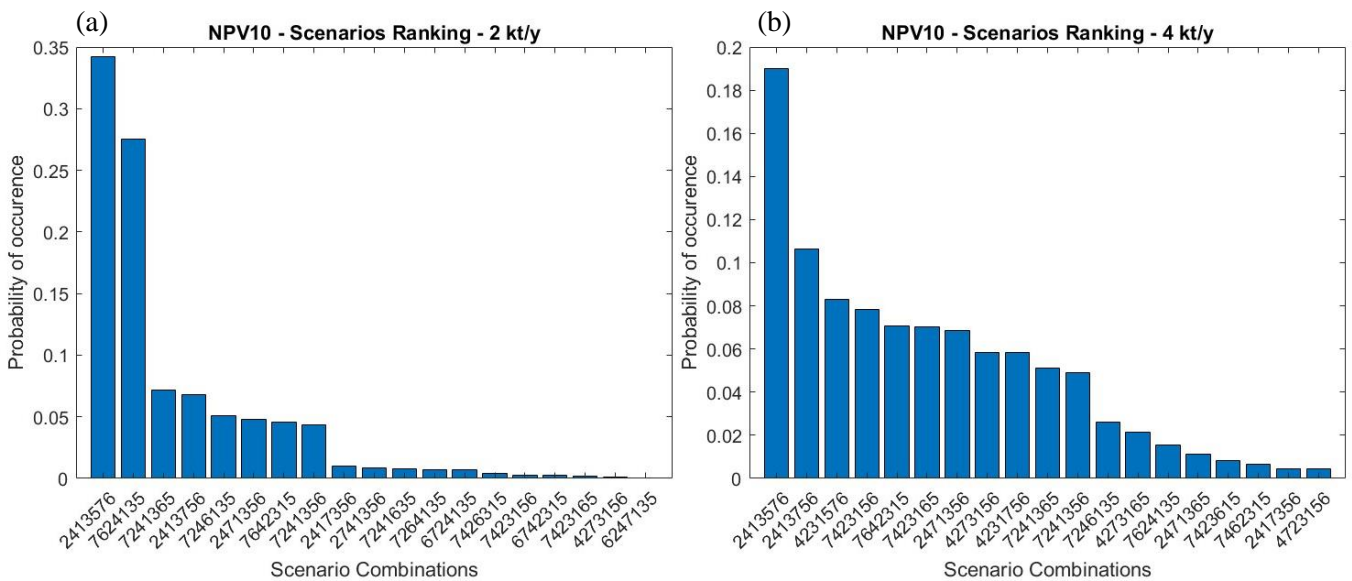


Fig. 72: Probability of occurrence of combinations of scenarios with respect to the NPV10 index value, i.e. the scenarios are in descending order of the index value in each combination; (a) 2 kt/y, (b) 4 kt/y.

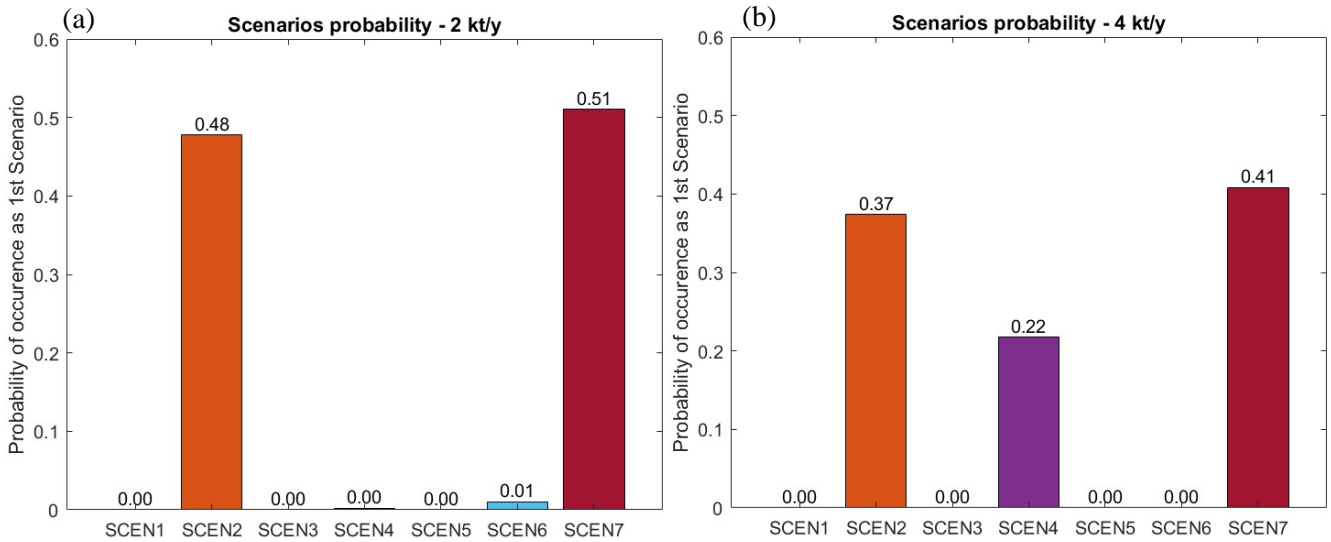


Fig. 73: Probability of occurrence of each scenario as a first scenario in terms of NPV10; (a) 2 kt/y; (b) 4 kt/y.

Generally, the rankings show that scenarios that exploit bio-energy, i.e., energy demand for steam production from biomass, have higher probability of a high NPV10 value, and thus, major profitability of the initiative. Among these, Scenario 7 is the most probable with higher value of the indicator, followed by Scenario 2.

An additional investigation of NPV10 was conducted also to highlight the cost items that most affect the final value of the indicator, i.e., the profitability of the initiative. Considering a  $\pm 5\%$  variation from the average value of the key-parameters considered in the sensitivity analysis, the variation in percentage of NPV10 was evaluated for each scenario. For Scenarios 1-5, the economic parameter with the greatest effect is the selling price of GVL, as shown in Fig. 75 for Scenarios 1 and 2, followed by the fixed and operating costs of the GVL plant with a different effect. The nonlinear trend of the NPV10 indicator with respect to the parameters considered leads to a different variation effect among the scenarios with

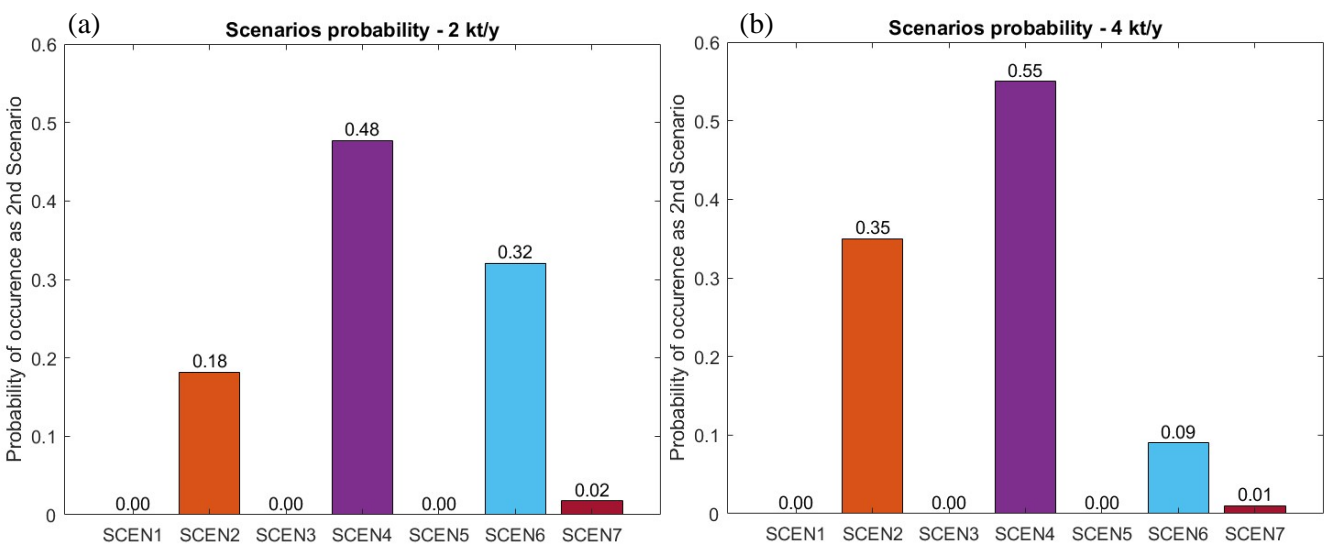


Fig. 74: Probability of occurrence of each scenario as second scenario in terms of NPV10; (a) 2 kt/y; (b) 4 kt/y.

higher variations in NPV10 indicator are resulted from Scenario 2 than from Scenario 1, and in general for biomass-boiler scenarios. As in Scenario 7 where the selling price of hydrogen is the most affecting parameter being the main market element of the configuration; and compared to Scenario 6, the influence of the hydrogen price is more prominent in Scenario 7 with a variation greater than 100 percent. As well as for Scenario 6, this item is followed by the cost of wind turbines, which strongly influences the two scenarios since it is one of the main items of fixed investment cost. According to different energy systems, the effect of electricity, natural gas and biomass as fuels affects the economic index differently.

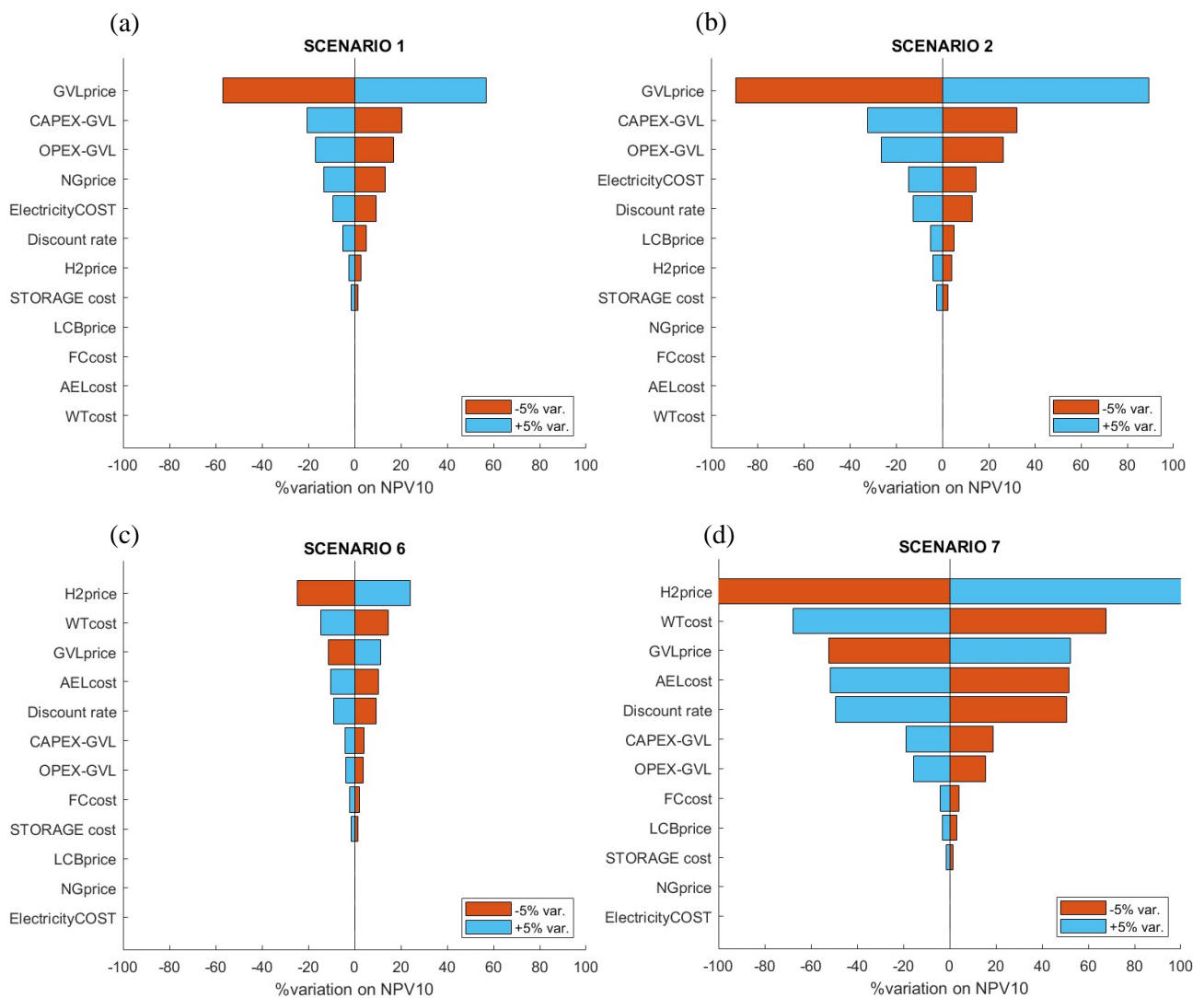


Fig. 75: Effect of the variation ( $\pm 5\%$ ) of the main cost items on the NPV10 index; (a) Scenario 1, (b) Scenario 2, (c) Scenario 6, (d) Scenario 7

### 5.3.3 Results of the environmental impacts analysis

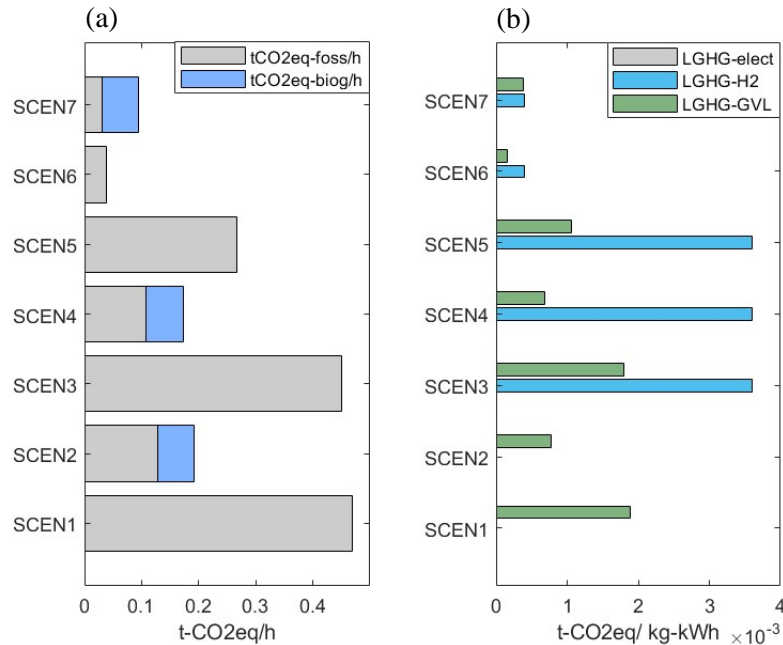


Fig. 76: (a) global emissions released per scenario (size 2 kt/y), considering fossil and biogenic contribution; (b) LGHG index for GVL, hydrogen and electricity per scenario and size 2kt/y.

The comparative environmental impact analysis was performed among the scenarios (Fig. 76), distinguishing between the impact in terms of CO<sub>2</sub> equivalents from fossil energy sources and those from bio-organic sources, such as biomass. Since the emissions associated with the use of biomass, as fuel, are dependent on the energy demand at the boiler, it is constant at 0.065 t/h of CO<sub>2</sub>eq.-biogenic between Scenarios 2, 4, and 7 for the same size of 2 kt/y-GVL production. On the other hand, the fossil contribution varies widely between configurations, with the highest emission in Scenario 1 with 0.47 t/h of CO<sub>2</sub>-eq-fossil, due mainly to contributions from the use of grid electricity and hydrogen supplied, and the lowest in Scenario 7 with 0.029 t/h in which emissions are related to the use of wind turbines and fuel cell for electricity generation and electrolyzes and storage modules for hydrogen production and handling, i.e. accounting the “cradle-to-grave” emission impacts of the different equipment. By considering the overall CO<sub>2</sub>-eq. emission impact, Scenario 6 is characterized by the lowest total amount of emission (0.0396 t/h), thanks to the on-site production of electricity and hydrogen from wind energy, and the absence of biogenic emissions. In general, among the other scenarios where electricity is supplied from the grid, lower emissions are observed for configurations with a biomass-boiler as in Scenarios 2 and 4, compared to the corresponding Scenarios 1 and 3 with a natural-gas-boiler or the fully-electrified Scenario 5. The overall emission estimations are then reflected in the evaluation of the levelized greenhouse-gases indicator (LGHG), considering in this case the only CO<sub>2</sub>eq. emission impact. For hydrogen production, the emission impact index for produced-unit, expressed in kg of hydrogen,

resulted higher for Scenario 3, 4, and 5, with a value of  $3.9 \cdot 10^{-3}$  t-CO<sub>2</sub>eq/kg due to the lower production size, compared to the Scenario 6 and 7 with an impact of  $3.97 \cdot 10^{-4}$  t-CO<sub>2</sub>eq/kg where instead the production is maximized; however, it is lower than the emission index related to the off-site supplied-hydrogen, estimated around  $9.89 \cdot 10^{-3}$  t-CO<sub>2</sub>eq/kg. Consequently, these results affect the emission index related to the production of GVL which has the lowest value in Scenario 6 with  $1.58 \cdot 10^{-4}$  t-CO<sub>2</sub>eq/kg of GVL and the highest in Scenario 1 with  $1.88 \cdot 10^{-3}$  t-CO<sub>2</sub>eq/kg. Considering Scenario 1 as baseline, the fully-electrified configuration, integrated with wind renewable energy system for electricity and hydrogen production as in Scenario 6, leads to a reduction of LGHG-GVL index by 92%, and a saving in annually CO<sub>2</sub>eq. emission of 3615 t/y. In Scenario 3, the production in-site of hydrogen by using an electrolyzer module, supplied with grid-electricity, determines a saving in emission of 156 tCO<sub>2</sub>eq/y, compared to the baseline scenario in which hydrogen is purchased. Comparing Scenarios 3,4, and 5 in Fig. 77.b, the effect in terms of emission savings of the different boiler-supply is evaluated; with a saving of 1697 t/y of CO<sub>2</sub>eq. by using an electrical boiler, and 2490 CO<sub>2</sub>eq.-t/y with a boiler supplied with biomass. Although the use biomass as fuel determines a generally reduction in emissions, compared to the use of NG and electricity, it has an emission impact factor greater than the electricity produced by

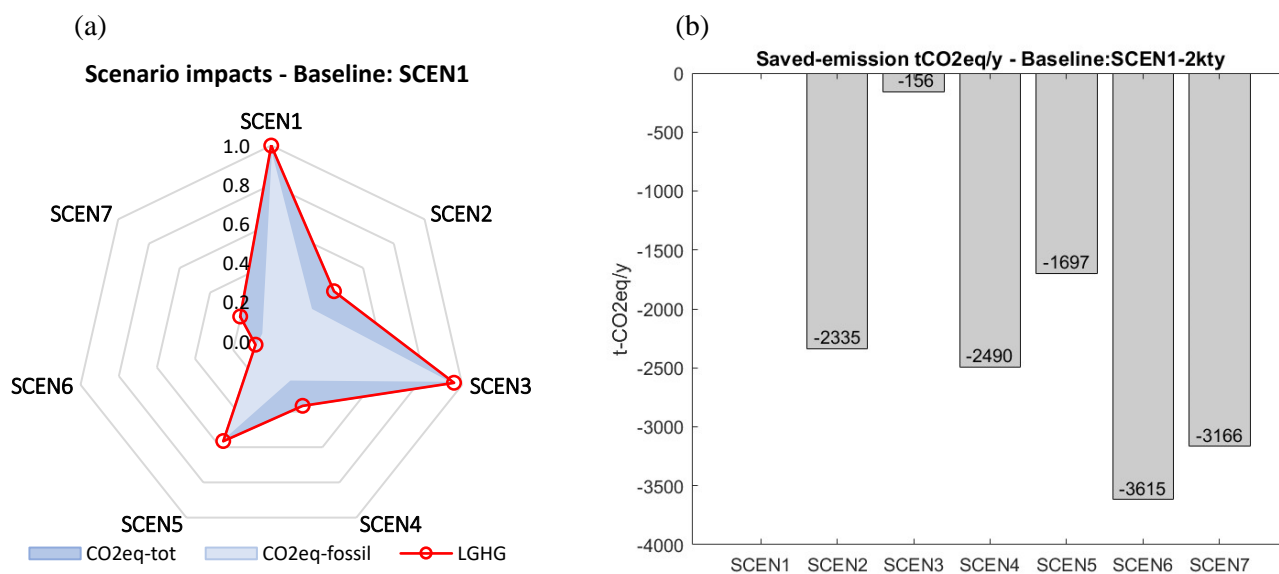


Fig. 77 (a) Radar plot indicating emission contribution and GVL-LGHG; (b) Emissions saved per scenario compared to scenario 1 baseline.

wind-energy which is related to the emission impact of the wind turbine devices, estimated to  $7 \cdot 10^{-6}$  t-CO<sub>2</sub>eq/kWh; thus, Scenario 7 presents a levelized emission factor higher than Scenario 6. The same ranking on the basis of the levelized impact index is also observed in the larger size of 4 kt/y of GVL. By doubling the production capacity, the annual emissions are almost double, with Scenario 1 being the most impactful in terms of emissions with 8220 t/y of CO<sub>2</sub>eq.-emissions, and Scenario 6 with the lowest emission amount of 638 t-CO<sub>2</sub>eq./y. In terms of LGHG indicator, the increase in GVL-production did not clearly affect the indicator which presents comparable values between the two sizes for each scenario, as emissions and production capacity both increase by about a factor of two; The index values



for both sizes are shown in Table 52; for size 4 kt/y the maximum index value for Scenario 1 slightly increased, while the minimum in Scenario 6 slightly decreased compared to the smaller size, as also shown in Fig. 78 where the indices are shown in ascending order of value.

Table 52: Summary from the indices evaluated for the two different sizes

	LGHG-electricity (t-CO <sub>2</sub> eq./kWh) 2 kt/y – 4kt/y	LGHG-H <sub>2</sub> (t-CO <sub>2</sub> eq./kg-H <sub>2</sub> ) 2 kt/y – 4kt/y	LGHG-GVL (t-CO <sub>2</sub> eq./kg-GVL) 2 kt/y – 4kt/y
SCEN-1	-	-	1.88-1.95·10 <sup>-3</sup>
SCEN-2	-	-	7.67-7.83·10 <sup>-4</sup>
SCEN-3	-	3.9·10 <sup>-3</sup>	1.80-1.86·10 <sup>-3</sup>
SCEN-4	-	3.9·10 <sup>-3</sup>	6.93-6.88·10 <sup>-4</sup>
SCEN-5	-	3.9·10 <sup>-3</sup>	1.07-1.09·10 <sup>-3</sup>
SCEN-6	7.0·10 <sup>-6</sup>	3.97-3.95·10 <sup>-4</sup>	1.58-1.52·10 <sup>-4</sup>
SCEN-7	7.0·10 <sup>-6</sup>	3.97-3.95·10 <sup>-4</sup>	3.71-3.56·10 <sup>-4</sup>

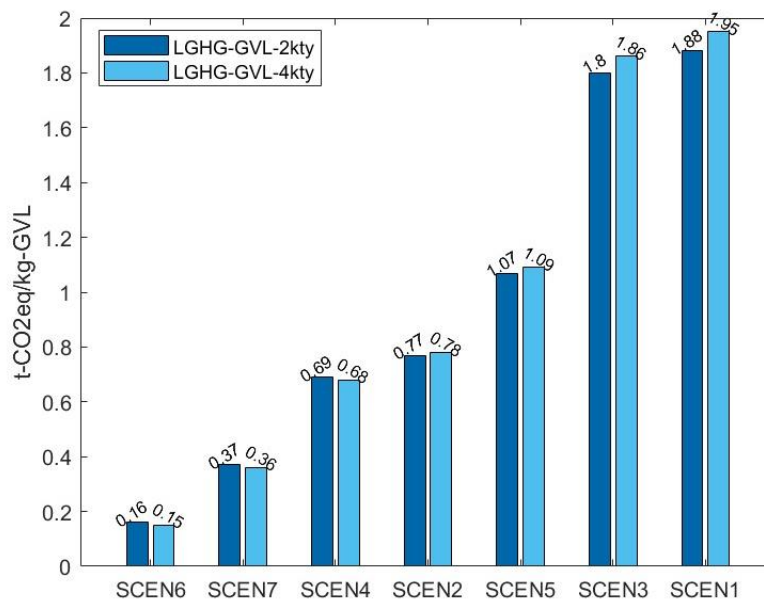


Fig. 78: Overall view of LGHG index related to GVL for size 2 and 4 kt/y

### 5.3.3.1 Sensitivity analysis on the environmental KPI

A sensitivity analysis was performed also to assess the robustness of the emission impact indicator, by selecting specific parameters. The analysis variables were defined by considering the possible variation in terms of demand or production of energy, electricity and hydrogen, i.e. variations in terms of efficiency of wind turbines, AEL modules, PEMFC modules, and GVL process scheme. As for the economic indicator, multiple key-variables are randomly varied in a range +/-20 % of the mean value, according to the uniform distribution, and the indicator evaluated over 10<sup>5</sup> iterations (Table 53).

Table 53: Variation of material and energy demand with the major impact on emissions for sensitivity analysis

Independent Variables	2 kt/y size	Range	4 kt/y size	Range
	Mean value	$\pm 20\%$	Mean value	$\pm 20\%$
Demand-Elect-GVL-PS (kWh)	938	710/1126	1893	1514/2272
Demand-Energy-Boiler-GVL-PS (kWh)	1892	1513/2270	3991	3193/4789
Demand-AEL-SINGLE-module (kW)	285	228/342	570	456/684
Electricity-Produced -WT (kWh-10 <sup>4</sup> )	3.81	3.05/4.57	3.81	3.05/4.57
Demand-H <sub>2</sub> -GVL-PS (kg/h)	5	4/6	10	8/12
Surplus-Prod.-H <sub>2</sub> -AEL (kg-10 <sup>6</sup> )	5.0	4/6	4.4	3.5/5.3
Consumed-H <sub>2</sub> -PEMFC (kg-10 <sup>5</sup> )	1.8	1.4/2.2	4	3.2/4.8

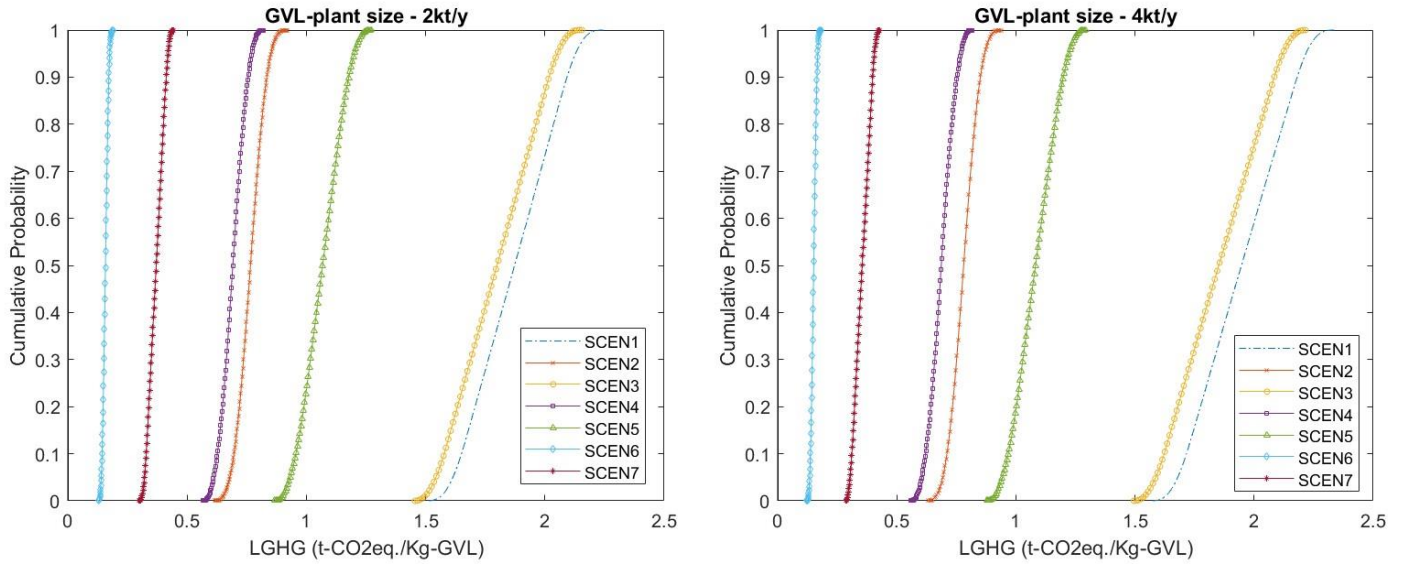


Fig. 79: Cumulative probability trends related to sensitivity analysis on the LGHG index; (a) 2kt/y, (b) 4kt/y

The analysis demonstrates the sensitiveness of the index for each scenario as the input parameters change; Scenarios 1 and 3 are subject to a greater variation in the index, visible by the elongated accumulated probability trend compared to the other scenarios. Fig. 79 shows that there is no overlap between the different trends for both production size, and that the ranking most probable among the scenario considers Scenario 6 as the first one, being characterized by the lowest index value, and Scenario 1 as the last one with the highest value of the LGHG index for GVL. In intermediate positions, scenarios equipped with biomass-boiler as Scenario 2,4, and 7 present value of the index globally lower than the corresponding scenarios with electrical and natural gas-boiler. The effect of the different variables on the index was also investigated punctually by considering a variation of  $\pm 5\%$  respect the mean value of the variables considered. In Fig. 80, the demand of energy to the reboiler is the variable which affects most the final value of the index for Scenario 1,3 and 5 with variation on the LGHG index

between 2-4%, i.e. for the scenarios in which the energy for steam production is supplied by using natural gas or grid-electricity.

For Scenarios 2 and 4, on the other hand, this variable result, in second rank, after the overall electricity demand of the process, due to the lower emission impact of biomass supplied to the boiler compared to the emission index of electricity from the grid. Among these scenarios, demand for hydrogen has a greater effect on the index for Scenarios 1 and 2 because it is supplied from an external customer site, compared to the other scenarios in which it is produced on-site, and a change in production output has a negligible result on the final index.

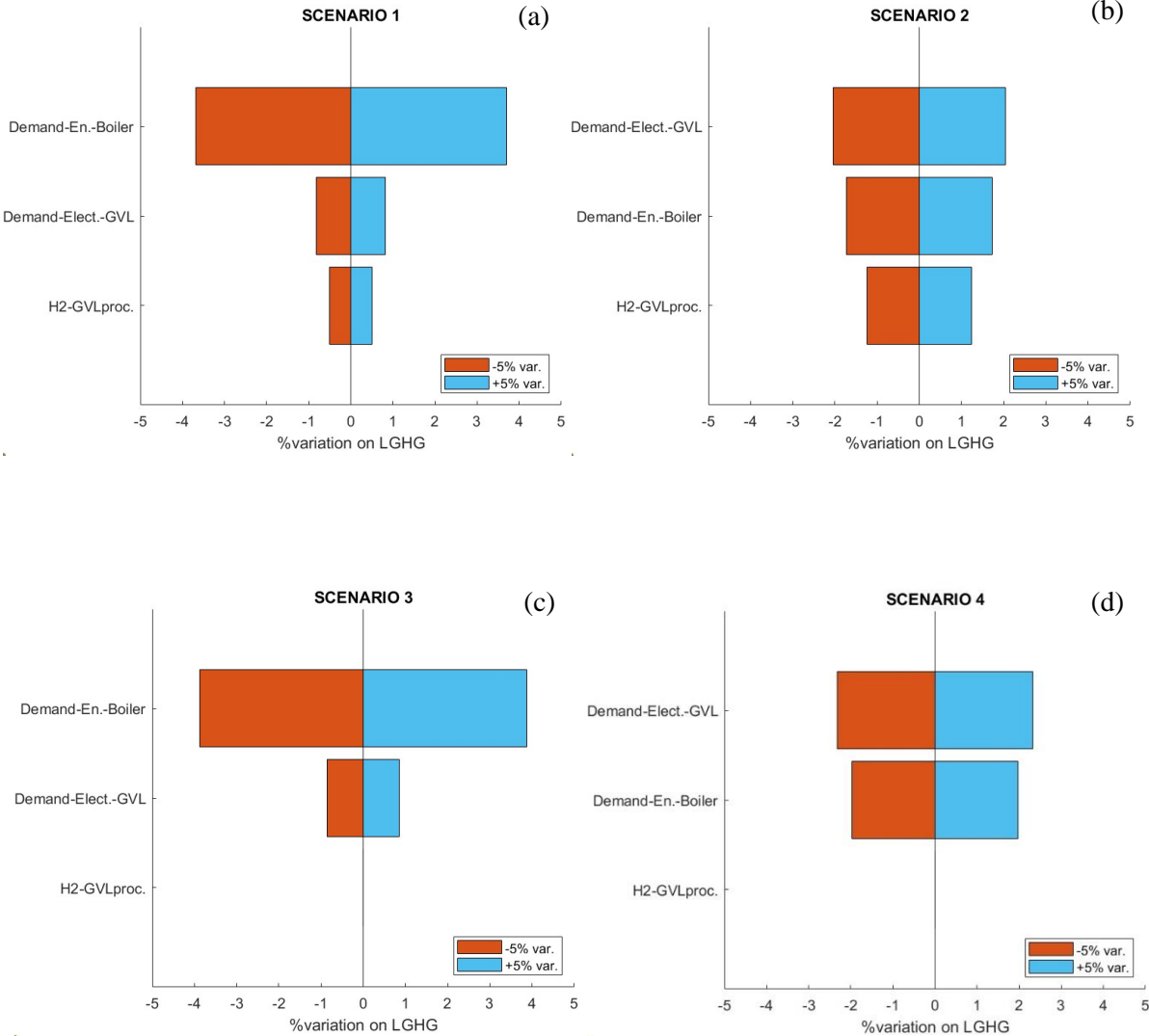


Fig. 79: Effect of the variation ( $\pm 5\%$ ) of the main energy-resource demand on the LGHG index; (a) Scenario 1, (b) Scenario 2, (c) Scenario 3, (d) Scenario 4

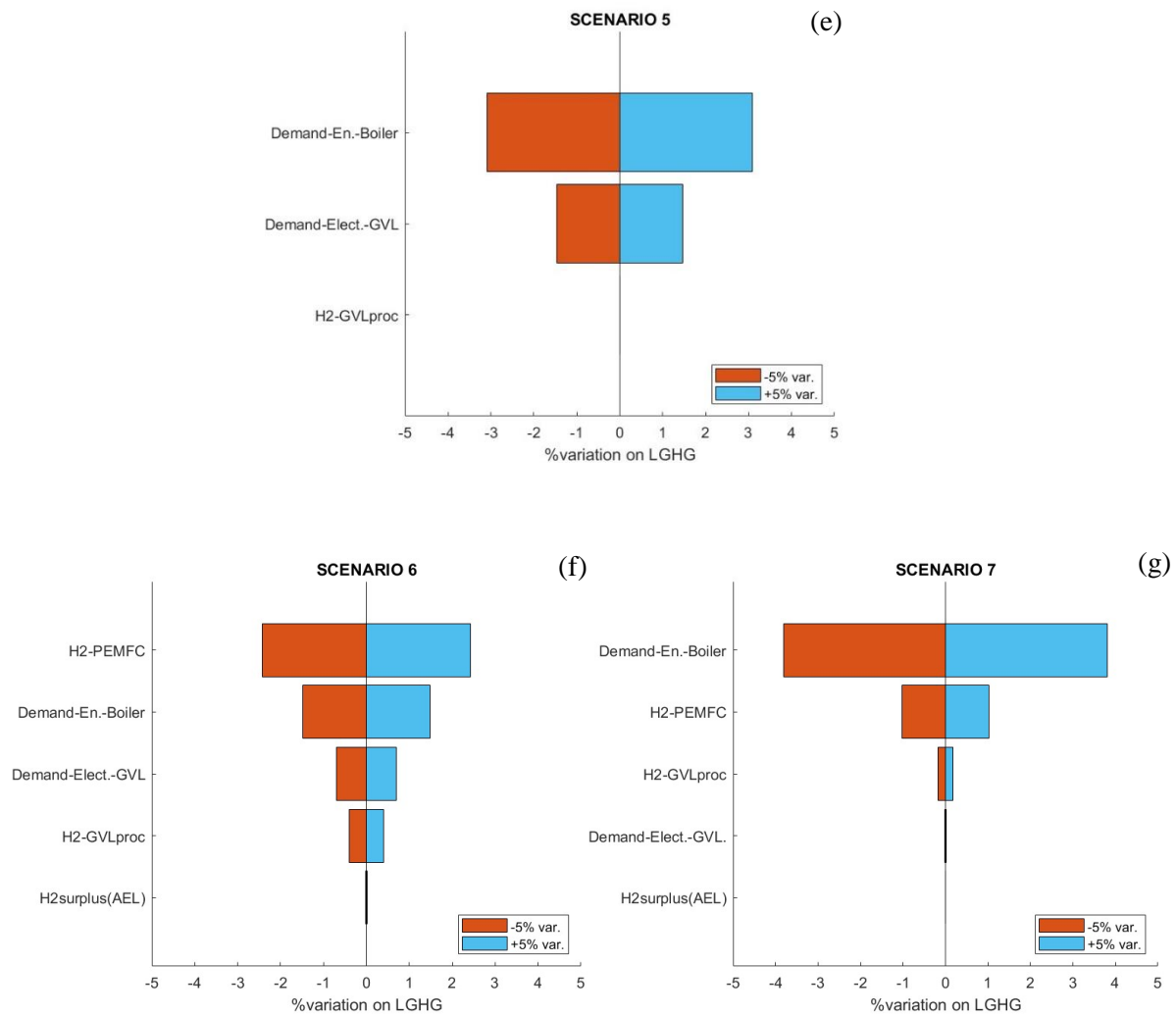


Fig. 80: Effect of the variation ( $\pm 5\%$ ) of the main energy-resource demand on the LGHG index; (e) Scenario 5, (f) Scenario 6, (g) Scenario 7

In Scenario 6, low-emission electricity from renewable sources means that the direct energy demand of the GVL process is not the variable that most influences the emission index, which in this case is most impacted by the contribution of the fuel cell modules (variation above 2% for a 5% variation in hydrogen demand at the cell), proportional to the hydrogen-fuel demands; less variation in the index is due to changes in the demands for electricity in the boiler and the process itself, as well as the demand for hydrogen for the reaction phase. In Scenario 7, on the other hand, the use of biomass for heat generation increased the emissions of the scenario, and in terms of energy demand at the boiler, it is the variable that affects the index the most, with a variation of the index around 3.8%; followed by the contribution of fuel cells causing a 1% variation.

### 5.3.4 Results of the Inherent safety analysis

In this section, the indices resulting from the inherent safety analysis of GVL's production size of 4 kt/y are presented; based on the criterion presented in Eq. 5. 11, a set of credible loss of containment (LOCs) and credit factor were associated to all critical process units. Known inventory and operating conditions of each process units (reported in Table S3. 3-6), the software PHAST v.8.4 [419] was used for the consequence evaluation and to calculate the damage distances, applying the reference environmental conditions of average wind speed of 1.5 m/s, Pasquill category F (i.e., night, air temperature of 25 °C with 70 % relative humidity and surface temperature of 10 °C). Based on the damage distances assessed, indices related to the GVL-process scheme were calculated and reported for each unit in Table 54.

Table 54: Summary of inherent safety indices covered for critical equipment in the GVL scheme for target human

	Process unit	LOC	$h_{i,jMAX}$ Scenario	UPI (m <sup>2</sup> )	UHI (m <sup>2</sup> /y)	UFHI (m <sup>2</sup> /y)	UTHI (m <sup>2</sup> /y)
Reactor (CRV)	CRV-100	1-2-3	PF	3.49E+03	3.77E-01	3.77E-01	6.80E-02
	CRV-101	1-2-3	FB	3.96E+02	4.15E-02	4.15E-02	0.00E+00
	CRV-102	1-2-3	FB	1.83E+04	4.81E-01	4.81E-01	3.45E-02
Heat- Exchanger (E)	E-100	4-5	FB	1.46E+04	8.21E+00	4.73E+00	8.07E+00
	E-102	4-5	EXP	1.78E+02	1.78E-03	1.78E-03	0.00E+00
	E-103	4-5	JF	2.09E+04	6.31E+00	4.02E+00	6.11E+00
	E-104	4-5	JF	4.64E+02	9.52E-02	9.52E-02	0.00E+00
	E-105	4-5	JF	1.97E+04	9.68E+00	7.16E+00	9.51E+00
	E-106	4-5	JF	1.87E+02	1.02E-01	1.02E-01	0.00E+00
	E-107	4-5	JF	2.57E+03	2.11E+00	2.11E+00	3.64E-01
	Cond-100	4-5	JF	1.99E+03	5.04E-01	5.04E-01	2.68E-03
	Cond-101	4-5	JF	3.00E+02	1.25E-01	1.25E-01	0.00E+00
	Reb-102	4-5	JF	1.58E+03	3.50E-01	3.50E-01	1.64E-03
Column (T)	T-100	1-2-3	FF	2.15E+02	1.07E-03	1.07E-03	3.53E-04
	T-101	1-2-3	FB	2.12E+02	1.06E-03	1.06E-03	3.40E-04
	T-102	1-2-3	FB	1.54E+02	7.68E-04	7.68E-04	4.32E-04
Separation Vessel (V)	V-100	1-2-3	TOX	8.19E+04	7.24E-02	3.60E-02	4.39E-02
	V-101	1-2-3	TOX	2.77E+03	1.97E-02	1.97E-02	1.55E-04
	V-102	1-2-3	PF	4.85E+03	1.19E-02	1.07E-02	3.14E-03
	V-103	1-2-3	PF	3.50E+03	1.24E-02	1.24E-02	3.23E-05
Pump (P)	P-100	4-5	PF	3.20E+03	2.72E-01	2.72E-01	1.78E-03
	P-102	4-5	TOX	8.93E+02	1.57E-01	1.38E-01	1.57E-01

Analyzing the main damage distances and their indices, the separation vessel V-100 is the most critical process unit in the process scheme defined in terms of maximum damage distance, i.e. through the UPI index, with a damage distance of 286 m. associated with the formation of a toxic cloud as accident scenario, from the catastrophic rupture with instantaneous release (LOC3) of the unit. Introducing the credit factors in the evaluation of the unit inherent index, the highest inherent safety index values are obtained from heat exchangers, such as E-100 and E-105, where the toxicity effect has a greater contribution in terms of damage distances; in fact, for these units, the UTHI index is higher than UFHI, as shown in Fig. 81.

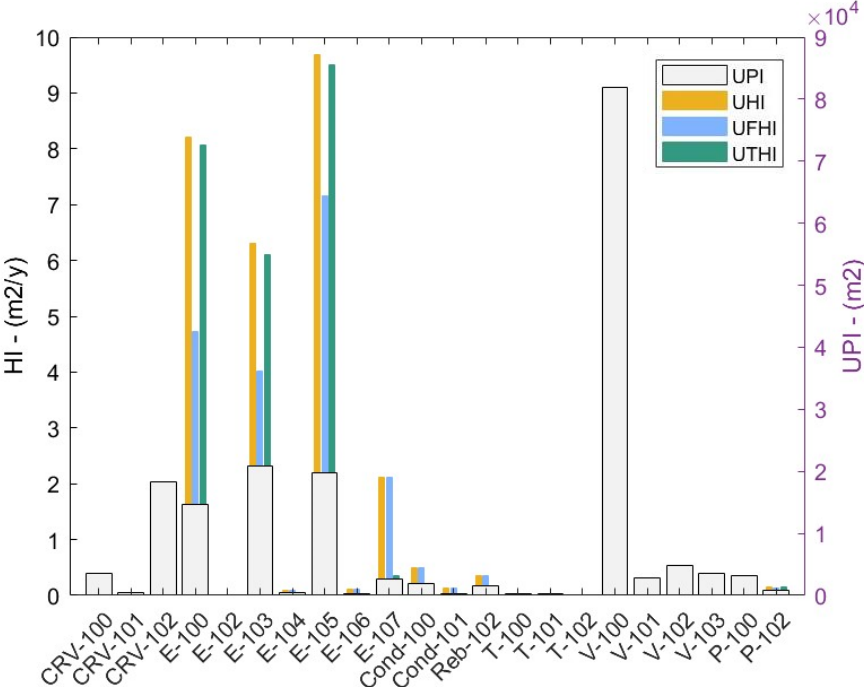


Fig. 81: Overall of safety indexes on the target human

Considering the contribution of each accident scenario for all process units as percentage of the overall

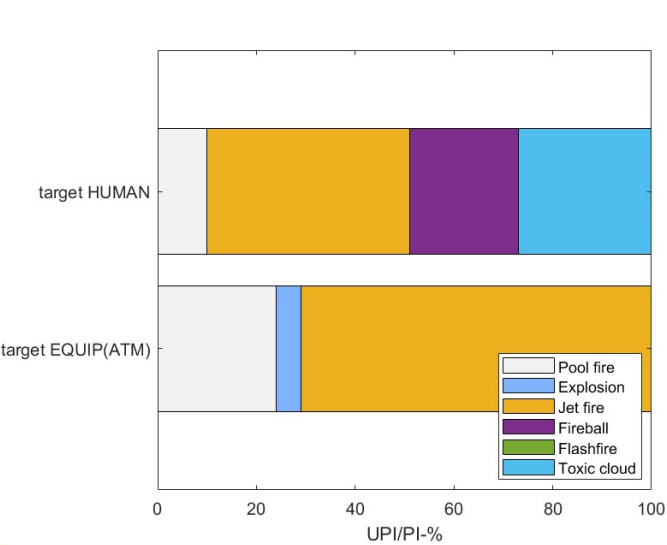


Fig. 82: Percentage contribution of the different accidental scenarios to the overall PI index

potential hazard index (PI), the scenarios with the major effect in terms of DDs respect to the target-humans in the GVL-process scheme are Jet-fire (41% of PI) and Toxic-cloud (27%), followed by Fireball (22%) and Pool-fire (10%), as shown in Fig. 82. Considering instead the analysis of damage distances related to the effect on equipment, and thus the possible occurrence of domino effects, Jet-fire is the scenario with the largest contribution (71%) to the overall index, followed by

Pool-fire (24%), and Explosion (5%) based on the results in Table 55. These indices are evaluated on the basis of DDs for effects on atmospheric and pressurized equipment. As they are not impacted by the effect of toxic concentrations, the inherent hazard index for equipment is not differentiated into flammability and toxicity indexes, thus only the UHI for each process unit is reported.

Table 55: Summary of inherent safety indices for PU in the GVL scheme for target <sup>a</sup>atmospheric, <sup>b</sup>pressurized equipment.

	Process unit	LOC	$h_{i,jMAX}$ Scenario	UPI <sup>a</sup> (m <sup>2</sup> )	UHI <sup>a</sup> (m <sup>2</sup> /y)	UPI <sup>b</sup> (m <sup>2</sup> )	UHI <sup>b</sup> (m <sup>2</sup> /y)
Reactor (CRV)	CRV-100	1-2-3	PF	2.42E+03	2.63E-01	1.42E+03	1.30E-01
	CRV-101	1-2-3	EXP	1.59E+02	1.59E-02	1.46E+02	1.46E-02
	CRV-102	1-2-3	PF	4.00E+03	3.16E-01	2.83E+03	1.92E-01
Heat- Exchanger (E)	E-100	4-5	JF	1.05E+04	4.09E+00	6.44E+03	2.28E+00
	E-102	4-5	JF	1.70E+02	1.70E-03	1.54E+02	1.54E-03
	E-103	4-5	JF	1.52E+04	2.97E+00	9.52E+03	2.27E+00
	E-104	4-5	JF	3.72E+02	3.72E-03	4.56E+01	4.56E-04
	E-105	4-5	PF	6.32E+02	6.32E+00	9.56E+03	1.80E+00
	E-106	4-5	JF	1.20E+02	1.20E-03	0.00E+00	0.00E+00
	E-107	4-5	JF	2.06E+03	1.20E+00	1.42E+03	3.62E-01
	Cond-100	4-5	JF	9.59E+02	9.59E-03	3.29E+02	3.29E-03
	Cond-101	4-5	JF	1.66E+03	1.66E-02	1.25E+03	1.25E-02
	Reb-102	4-5	JF	1.71E+02	1.71E-03	0.00E+00	0.00E+00
Column (T)	T-100	1-2-3	-	0.00E+00	0.00E+00	0.00E+00	0.00E+00
	T-101	1-2-3	-	0.00E+00	0.00E+00	0.00E+00	0.00E+00
	T-102	1-2-3	-	0.00E+00	0.00E+00	0.00E+00	0.00E+00
Separation Vessel (V)	V-100	1-2-3	EXP	2.94E+03	1.90E-02	2.85E+03	5.89E-03
	V-101	1-2-3	PF	7.99E+02	5.33E-03	1.64E+02	9.63E-04
	V-102	1-2-3	PF	1.32E+03	5.64E-03	2.74E+02	1.04E-03
	V-103	1-2-3	PF	1.87E+03	6.56E-03	4.09E+02	1.23E-03
Pump (P)	P-100	4-5	PF	2.13E+03	1.89E-01	9.14E+02	1.10E-01
	P-102	4-5	JF	5.35E+02	1.02E-01	3.87E+02	7.67E-02

Based on the threshold values for the effects on equipment (potential domino effect), the exchangers present the greatest criticality with greater damage distances associated with the jet-fire scenario; the high damage distances must also be considered in relation to the conservative assumption of assuming the entire inventory to be butanol-like and the model used to simulate LOC-5 in the software (“*Short-pipe model*”).

In the section of the process scheme section related to the production and storage of hydrogen, the most critical points were identified Table 56: AEL-module system, with the AEL-stack and hydrogen buffer tank, without considering additional auxiliary equipment such as the dryer and deoxidiser for which no inventory specifications are known and which may differ in different electrolysis systems; PEMFC stack; and storage system, including compressor and storage tanks. On the basis of the inventory criterion, the AEL and PEMFC stack were assimilated to 'pipe-systems' and analysed according to LOC type 4 and 5, and the credit factor assumed equivalent to that of pumps and compressors for leak and continuous release from pipe. Furthermore, AEL system with power capacity of 0.57MW, present in Scenario 3,4, and 5, is equipped with an individual gas-holder buffer tank of 3.8 m<sup>3</sup>; for higher nominal power capacity required as in Scenario 6 and 7, individual cells of 2.2MW power are organized in modules of up to 8 cells, connected to a common buffer tank of 100 m<sup>3</sup>. The resulting values of the indices for each type of process unit, evaluated considering the effect on human-target and atmospheric and pressurized equipment are reported in Table 56:

Table 56: Summary of inherent safety indices for PU in the H2 section for target human,<sup>a</sup>atmospheric, <sup>b</sup>pressurized equipment

	Process unit	LOC	$h_{i,jMAX}$ Scenario	UPI (m <sup>2</sup> )	UHI (m <sup>2</sup> /y)	UPI <sup>a</sup> (m <sup>2</sup> )	UHI <sup>a</sup> (m <sup>2</sup> /y)	UPI <sup>b</sup> (m <sup>2</sup> )	UHI <sup>b</sup> (m <sup>2</sup> /y)
AEL (0.57 MW)	Electrolyzer stack	4-5	EXP	1.81E+02	9.05E-02	0.00E+00	0.00E+00	0.00E+00	0.00E+00
	Gas-holder tank (3.8 m <sup>3</sup> )	1-2-3	FB/EXP	1.50E+03	4.77E-03	1.77E+02	1.77E-03	1.61E+02	1.61E-03
	Compressor	4-5	-	0.00E+00	0.00E+00	0.00E+00	0.00E+00	0.00E+00	0.00E+00
Modules AEL (2.2 MW)	Electrolyzer stack	4-5	EXP	1.88E+02	9.38E-02	1.77E+02	8.87E-02	1.60E+02	8.01E-02
	Gas-holder tank (100 m <sup>3</sup> )	1-2-3	FB/EXP	1.20E+04	1.07E-02	5.97E+03	5.43E-03	4.35E+03	4.40E-03
	Compressor	4-5	EXP	1.34E+03	3.98E-01	1.29E+03	3.17E-01	1.21E+03	2.94E-01
PEMFC	Stack mod. (2.7MW)	4-5	EXP	1.49E+02	4.15E-02	1.44E+02	1.44E-02	1.35E+02	1.35E-02
	Stack mod. (6.7MW)	4-5	EXP	1.86E+02	1.06E-01	1.77E+02	1.01E-01	1.60E+02	9.20E-02
Hydrogen storage tank	50 m <sup>3</sup>	1-2-3	FB/EXP	2.59E+04	5.32E-02	1.35E+04	3.44E-02	9.86E+03	3.03E-02
	120 m <sup>3</sup>	1-2-3	FB/EXP	4.33E+04	5.16E-02	2.34E+04	4.04E-02	1.71E+04	3.51E-02
	150 m <sup>3</sup>	1-2-3	FB/EXP	5.17E+04	6.95E-02	2.81E+04	4.48E-02	2.08E+04	3.86E-02
	250 m <sup>3</sup>	1-2-3	FB/EXP	7.12E+04	8.25E-02	3.98E+04	6.50E-02	2.95E+04	5.66E-02



Based on the resulting DDs, the hazard scenario with the most impact on the overall PI is Fireball on the human target, while it is Explosion for the effect on equipment. In general, the process units in the hydrogen section that cause the greatest damage distances, i.e. UPI, are the storage units, with the maximum value for the storage tank of 250 m<sup>3</sup>.

Considering for each different scenario the number of recurring process units, such as the AEL units for Scenarios 6 and 7, which are 29- and 31-2.2MW-units respectively, and the sum of the unit hazard indices of each process unit, the overall indices are given in Table 57:

Table 57: Summary global indices for each scenario and compared to human and equipment target

	PI (m <sup>2</sup> )	HI (m <sup>2</sup> /y)	FHI (m <sup>2</sup> /y)	THI (m <sup>2</sup> /y)	PI <sup>a-b</sup> (m <sup>2</sup> )	HI <sup>a-b</sup> (m <sup>2</sup> /y)
GVL-process (4kt/y)	1.82E+05	2.89E+01	2.06E+01	2.44E+01	4.80-3.81E+04	1.55-0.73E+01
SCEN 1	2.26E+05	2.90E+01	2.06E+01	2.44E+01	7.14-5.52E+04	1.56-0.73E+01
SCEN2	2.26E+05	2.90E+01	2.06E+01	2.44E+01	7.14-5.52E+04	1.56-0.73E+01
SCEN3	2.10E+05	2.91E+01	2.91E+01	2.44E+01	6.17-4.81E+04	1.56-0.73E+01
SCEN4	2.10E+05	2.91E+01	2.91E+01	2.44E+01	6.17-4.81E+04	1.56-0.73E+01
SCEN5	2.10E+05	2.91E+01	2.91E+01	2.44E+01	6.17-4.81E+04	1.56-0.73E+01
SCEN6	4.45E+05	3.26E+01	3.26E+01	2.44E+01	1.95-1.48E+05	1.87-1.02E+01
SCEN7	2.89E+05	3.26E+01	3.26E+01	2.44E+01	1.07-0.83E+05	1.87-1.01E+01

The overall indices obtained indicate Scenario 6 as the configuration with the highest value of the overall potential hazard (PI) and inherent hazard (HI) index, followed by Scenario 7; this is determined by the

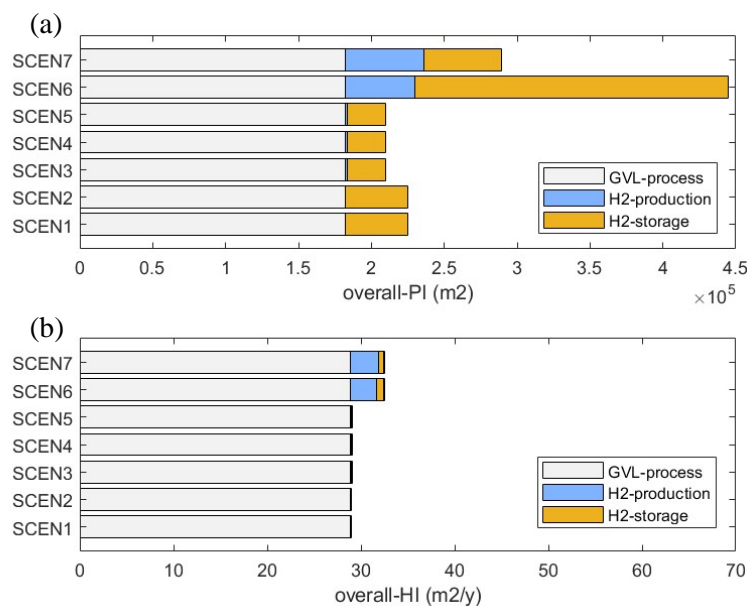


Fig. 83: Plot of the overall PI(a) and HI(b) indices for each scenario for target human, highlighting the contribution of the GVL production section, hydrogen production section, storage section.

Although characterized by a higher potential hazard index, Scenario 6 is roughly equivalent to Scenario 7 from the point of view of the inherent hazard index, and this is due to the reduced effect of the storage section on the overall HI index, compared to the GVL plant section, which is the main index contributor. As shown in Fig. 84, in which all scenarios are plotted with regard to scenario 6, which represents the baseline, Scenarios 1 and 2 and Scenarios 3,4 and 5 are equivalent to each other in terms of the HI index, with a reduction of 7% with respect to the baseline index with reference to the effect on human targets; this deviation is greater in the analysis on the equipment target where they show a difference with respect to the baseline index value of 11-18% depending on whether the effect on atmospheric or pressurized equipment is considered. In terms of UPI<sub>max</sub> and UHI<sub>max</sub> for target human, all scenarios present the same value as it is related to a common process unit in the GVL-production scheme, related to the PU V-100 and E-105, respectively. For the equipment target, the UHI<sub>max</sub> contribution is constant for all scenarios as it is still associated with the contribution of PU E-105, while the UPI<sub>max</sub> contribution varies between scenarios, and is related to the hydrogen storage PU for Scenarios 1,2,6 and 7, thus corresponding to the 130, 250, and 150 m<sup>3</sup> storage tanks, while for Scenarios 3,4, and 5 this index is given by the contribution of E-103 in the GVL section. Instead, the ranking between scenarios on the potential hazard index (PI) is defined by the maximum damage distances that within the different configurations are generally associated with the hydrogen storage process units, i.e. dependent on the stored hydrogen capacity; and therefore, Scenario 1 and 2 show higher values than Scenario 3, 4, and 5.

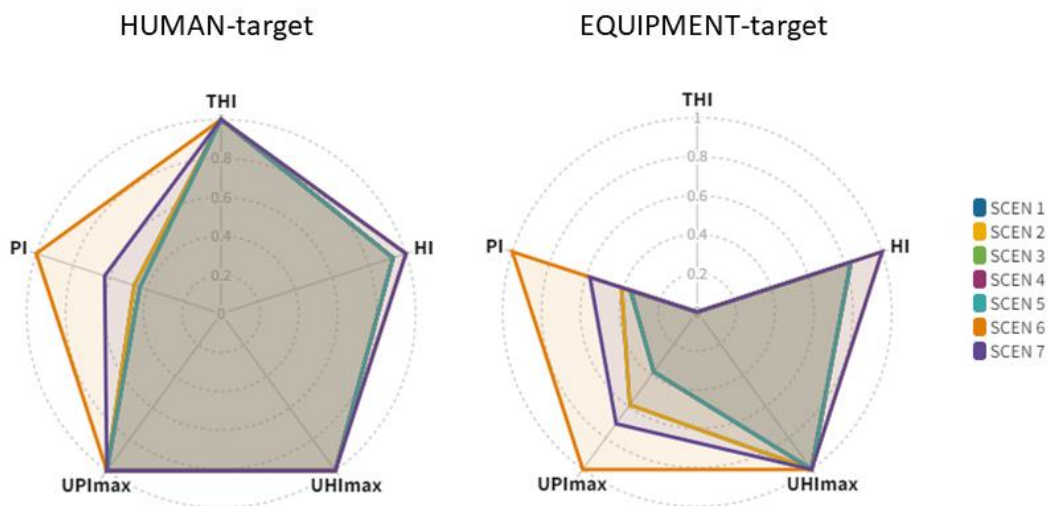


Fig. 84 Overall indices for human and equipment (atm) target per scenario

#### 5.3.4.1 Sensitivity analysis on the inherent safety KPI

Sensitivity analysis was conducted on the overall inherent safety index (HI) for each scenario considering the effect of variation of credit factors ( $C_j$ ) for each type of loss of containment per equipment type; The factors were varied by an order of magnitude, i.e.  $10^{\pm 1}$  (Table 58).

Table 58: Credit factor variation for sensitivity analysis

Type of Equipment	LOC	$C_f (10^{\pm 1})$
Reactor vessel	1	$1 \cdot 10^{-5} - 1 \cdot 10^{-3}$
	2	$5 \cdot 10^{-7} - 5 \cdot 10^{-5}$
	3	$5 \cdot 10^{-7} - 5 \cdot 10^{-5}$
Pressure vessel	1	$1 \cdot 10^{-6} - 1 \cdot 10^{-4}$
	2	$5 \cdot 10^{-8} - 5 \cdot 10^{-6}$
	3	$5 \cdot 10^{-8} - 5 \cdot 10^{-6}$
Heat&Exchanger	4	$1 \cdot 10^{-3} - 1 \cdot 10^{-1}$
	5	$1 \cdot 10^{-6} - 1 \cdot 10^{-5}$
Pump-Compressor	4	$5 \cdot 10^{-5} - 5 \cdot 10^{-3}$
	5	$1 \cdot 10^{-5} - 1 \cdot 10^{-3}$

The results of the analysis were reported in terms of the difference from Scenario 6, which was the scenario with the highest index in the previous discrete analysis. Scenarios 1-2 and 3-4-5 were condensed into a single profile with very similar index trends.

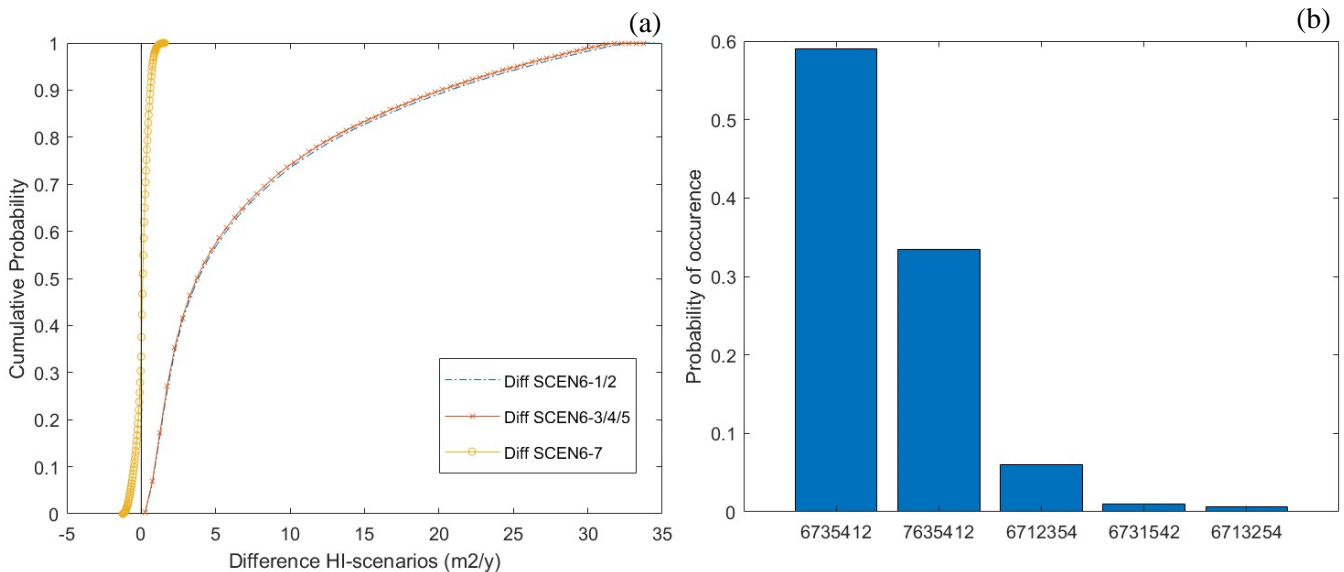


Fig. 85 (a) Cumulative probability trends related to sensitivity analysis on the difference of HI among scenarios, (b) Probability of occurrence of scenarios combinations with respect to the HI index value.

The analysis confirmed the previous ranking with Scenario 6 having the highest value of the intra-inherent safety index, as shown in Fig. 85a; in particular, Scenario 6 has a higher index value than Scenarios 1,2,3,4, and 5 in the variation considered. Compared to Scenario 7, the probability of Scenario 6 having higher index is 67% in the  $10^5$ -iterations, while Scenario 7 has a probability of occurrence as the first scenario with respect to this index of 33% (Fig. 85b). Scenarios 2 and 4, on the other hand, have an overall lower index, specifically Scenario 2 has a 93% probability of occurrence as the lowest index

scenario. The sensitivity analysis confirms the robustness of the analysis performed and the ranking defined with respect to the HI index.

### 5.3.5 Overall sustainability index analysis

In this section, the overall sustainability index was evaluated for each scenario. The method considers, first of all, the normalisation of the sub-indices, which in this case was carried out using an internal method with respect to the maximum value among the scenarios for each category, as shown in Table 59 where the absolute values of the indices for each scenario with respect to the three categories considered in the analysis and their respective normalized values are reported.

Table 59: Absolute and normalized (by internal normalization) values of global indices

	Absolute Indices			Normalized Indices		
	LCOP (€/kg)	LGHG (t-CO <sub>2</sub> eq/kg)	HI (m <sup>2</sup> /y)	LCOP	LGHG	HI
Scenario 1	2.75	2.0E-03	29.0	0.799	1.000	0.890
Scenario 2	2.30	7.8E-04	29.0	0.669	0.402	0.890
Scenario 3	2.79	1.9E-03	29.1	0.811	0.954	0.893
Scenario 4	2.34	6.9E-04	29.1	0.680	0.353	0.893
Scenario 5	3.44	1.1E-03	29.1	1.000	0.559	0.893
Scenario 6	2.77	1.5E-04	32.6	0.805	0.078	1.000
Scenario 7	2.08	3.6E-04	32.6	0.605	0.183	1.000

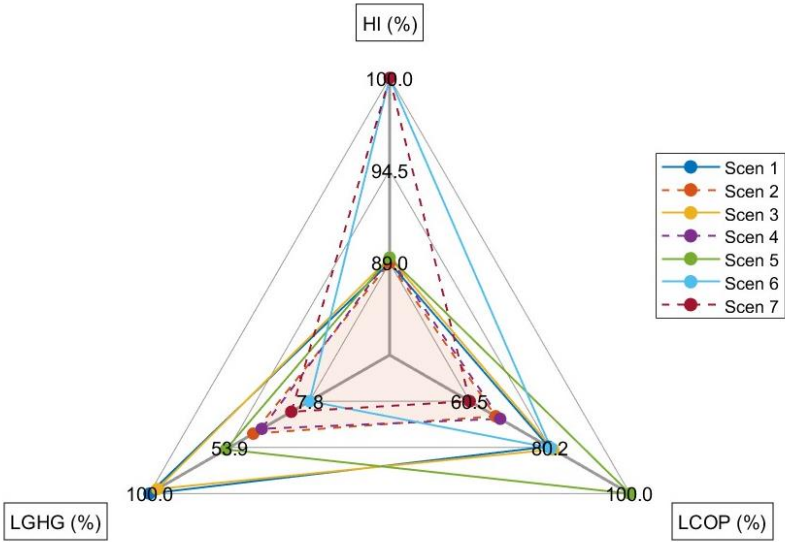


Fig. 86: Performance of scenarios relative to normalized indices, in percentage terms.

As can also be seen from Fig. 86, Scenarios 1 and 3 result as the most impactful initiatives from the point of view of emissions, and therefore of the environmental sustainability perspective, while Scenario

5 is characterized by the highest cost index, resulting as the scenario with the highest economic impact. Scenarios 6 and 7, on the other hand, are predominant considering the inherent risk effect with respect to the human receptor and, thus, from a social sustainability perspective. Overall, Scenarios 2 and 4 are those with average values with respect to the three sustainability categories investigated and, thus, with lower impact area. The evaluation of the overall index aggregating all sustainability categories depends on the weight factor of each category and on the type of aggregation method considered. The overall indices were aggregated according to the linear method for each scenario, as shown in Table 60.

Table 60: ASI for each scenario with linear aggregation (relative color scale for each profile/per column).

	ASI-Linear aggregation			
	Equal Weighting	Individualist	Egalitarian	Hierarchist
Scen 1	0.887	0.878	0.931	0.922
Scen 2	0.647	0.769	0.535	0.590
Scen 3	0.877	0.877	0.907	0.903
Scen 4	0.635	0.768	0.509	0.570
Scen 5	0.809	0.883	0.723	0.753
Scen 6	0.621	0.835	0.392	0.490
Scen 7	0.590	0.791	0.399	0.492

**Color scale:**

A compensatory analysis was deemed more appropriate for assessing the overall sustainability of the scenarios, which is why the aggregation was done according to the linear method (Eq. 5. 21). On the basis of the different stakeholder profiles and specific weights, the aggregation did not highlight a scenario first among all. However, Fig. 87 did globally indicate the higher sustainability of the scenarios integrated with wind renewable energy, i.e. Scenarios 6 and 7. In fact, in the equal-weighting mode, Scenario 7 emerged as the best scenario considering an equal priority of the indices considered,

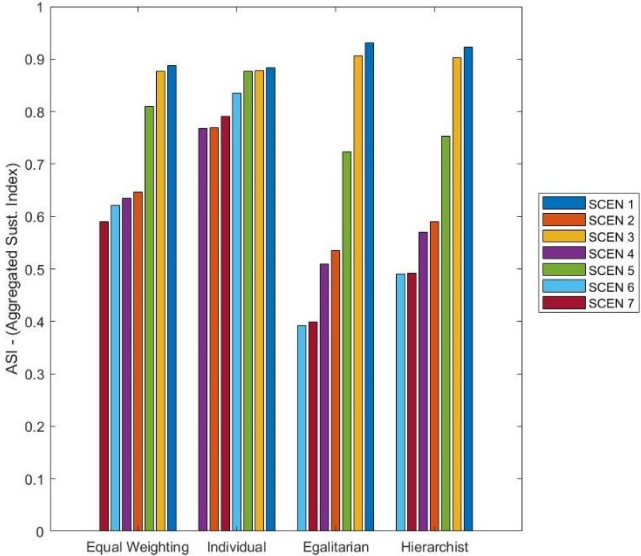


Fig. 87: Graph of aggregated indices according to the different stakeholder profiles considered

followed by Scenario 6; the egalitarian and hierarchical visions indicates Scenario 6 as the most sustainable in both cases, followed by Scenario 7. Solely, in the individualist view, it is Scenarios 4 and 2 that obtain a lower impact index, considering the higher priority assigned to the social perspective, with the inherent safety index being particularly penalising for Scenarios 6 and 7.

Scenarios 1, 3 and, to a lesser extent, Scenario 5 are characterized by the highest indices according to all weighting modes considered.

Overall, Scenarios 6 and 7 are the best performers in terms of sustainability, with Scenario 6 coming out on top in higher-priority ecosystem perspectives due to its reduced contribution in terms of emissions, and Scenario 7 coming out on top in the equally prioritized profile, and ahead of Scenario 6 in the individuality profile with high social priority.

## **5.4 Conclusions**

Having defined a potential process scheme for the production of GVL from biomass-derived fructose, the main objective of the analysis presented in this chapter was to assess the overall sustainability of the GVL process, particularly with respect to the integration of renewable energy sources for energy and hydrogen production.

The methodology used in the study was defined in three main sections: a first section focused on assessing the availability of site-specific renewable resources (availability of LCB biomass and wind energy), with reference to the Normandy region as a case study. The choice of a site-specific study is essential for the assessment of renewable resources that are territory-dependent. A second section focused on design and technology assessment in which the process scheme for the production of GVL was defined, evaluating the production size effect consistent with the availability of biomass on the territory and the energy and hydrogen demand of the process. Based on the integration of wind energy into the defined scheme, an optimal system design of the renewable energy conversion technology for the production of electrical power and green hydrogen was evaluated.

Depending on the level of integration or non-integration of wind energy and bio-energy, different scenarios were defined; starting from a base-line scenario, named Scenario 1, in which the demand for electrical power, thermal power and hydrogen is met through external supply (i.e. from the power grid, use of natural gas as a thermal source, and hydrogen supply from external supply), other configurations were then defined integrating the use of renewable energy sources for heat and power production; specifically biomass for thermal power production, and wind energy for electric power and hydrogen production.

Finally, a third section in which each scenario is subjected to a sustainability assessment by means of performance indices, with respect to the economic, environmental and social perspective. From the individual indices of each perspective, an overall aggregated sustainability index was evaluated by means of appropriate aggregation methods considering the sustainability analysis in a broader multi-criteria decision analysis method.

The sustainability analysis globally indicated the beneficial implications of integrating wind and biomass energy into GVL's production scheme.

From the perspective of economic and environmental sustainability, the use of bio-energy from biomass for the thermal power demand to the process (in Scenarios 2, 4) resulted in a clear reduction of the levelized cost of product (LCOP) and the equivalent emission index (LGHG) of the GVL compared to the corresponding Scenarios 1, 3 using natural gas as the thermal energy source and Scenario 5 having a fully electrified system. In the comparison of Scenarios 6 and 7, the effects of bio-energy are combined with the benefits of wind energy. Indeed, for the same technological configuration, the combination of both resources results in a lower cost index in Scenario 7, but the use of a configuration entirely supported by wind power results in a lower emission index in Scenario 6. Compared to the social perspective, expressed in terms of inherent safety, the technological complexity penalises Scenarios 6 and 7, mainly due to the criticality contributions determined by the hydrogen production, management and storage section. In general, the inherent safety analysis, expressed through the overall HI index, indicated that the greatest contribution is associated with the GVL production scheme in each scenario.

Overall, the global composite index assessment showed, considering different decision profiles adopted in the multi-criteria decision analysis method, the predominance of scenarios with full integration of renewable resources. In particular, Scenario 7 was the best in a fair-weighting perspective of the three indices associated with the three pillars of sustainability, while Scenario 6 was the lowest overall impact with respect to the two profiles adopted, resulting in the best ranking of the scenarios. The sustainability analysis results show the advantage of integrating the green hydrogen production asset from renewable energy sources into the defined GVL biomass biorefinery model. The overall sustainability of this integrated configuration derives from the beneficial synergy between the conversion of biomass into a high value-added product, and the conversion of the wind potential in terms of hydrogen, which in addition to meeting the demand of the process has a high market, and in terms of low-emission electrical power.

# CHAPTER 6 – Conclusions and perspectives

The main objective of the research work presented in this thesis is to analyze the sustainability, in a broad sense, of second-generation biomass exploitation from the perspective of a broader bio-economy vision, and thus in complementarity with the integration of renewable energy sources into the exploitation process.

Sustainability was investigated experimentally and methodologically, analyzing it with respect to pivotal technological, economic, environmental and social perspectives.

Chapters 2, 3, and 4 were devoted to the presentation of experimental results concerning the technological aspect of the valorization process. Having analyzed the literature in the field of the production of high-value-added molecules from lignocellulosic biomass and the potential industrial market for them, the technological investigation focused on research into the production of alkyl levulinate, specifically butyl levulinate and its transformation into  $\gamma$ -valerolactone. To make up for the gaps in the literature for the production of this molecule, the objectives set by these sections, also with a view to investigating the process on a larger scale, are the investigation of optimal process conditions and kinetic modelling from precursor molecules such as the monosaccharide fructose.

In Chapter 2, the solvolysis of fructose to butyl levulinate was investigated experimentally to assess the conditions that favor its final yield, in terms of choice of catalyst and solvent system.

The main results of this section showed the catalytic efficiency of the heterogeneous catalyst, Amberlite IR120 ion-exchange resin, compared with other results obtained in the literature with other solid and homogeneous catalysts; and evaluated the optimal kinetic conditions for limiting any resistance to matter transfer in the system.

The solvent system was investigated, highlighting the benefits of using  $\gamma$ -valerolactone as a co-solvent together with butanol; the presence of GVL, in addition to favoring a direct increase in butyl levulinate yield, has positive effects on the control of secondary degradation reactions, stabilizing the most active reaction intermediates, and favoring the dissolution kinetics of fructose, which is particularly important in high concentration systems.

The defined process conditions are reflected in the principles of green chemistry, defining a pathway for the conversion of biomass-derived fructose to BL by means of heterogeneous catalysis, subsidizing the disadvantages in terms of energy and material requirements of homogeneous catalysts requiring specific post-treatment, and promoting the use of a green solvent with pronounced sustainability, stability and non-toxicity characteristics, which is also the optimal reaction solvent in its own production by hydrogenation of butyl levulinate.



The results obtained were then used in Chapters 3 and 4, where the investigation was extended to the kinetic study of butyl levulinate production via solvolysis.

In Chapter 3, the kinetics of solvolysis of the 5-HMF intermediate was investigated in the butanol-GVL solvent system, with a focus on the reaction mechanisms and kinetics of the degradation product humins. The results showed that the system is well represented by models describing the formation of humins through a first-order reaction and, in particular, the model, in which the system was described with 8 reaction steps, was found to be the best performing model in terms of adherence to experimental data and predictive ability of the reaction system. The model developed and validated by means of a cross-validation method constitutes a first in-depth analysis of the kinetics of butyl levulinate acid solvolysis, using platform molecules such as 5-HMF, and the starting point for extending the kinetic analysis to fructose in Chapter 4.

In Chapter 4, the kinetic investigation was extended to fructose solvolysis, including an in-depth investigation of the mechanisms of fructose conversion, degradation of fructose to humins, and the kinetics of fructose dissolution in the solvent system considered. The kinetic analysis conducted under conditions of high initial fructose concentration ('High-gravity' approach), revealed the most robust model in which the first step of fructose conversion is represented by dehydration to 5-HMF as a single rate-determining step, excluding possible intermediates. The model was validated with the holdout method (using an 80/20% ratio of kinetic experiments for the regression and validation phase) and is able to simulate the system over a wide range of parameter variation, including the kinetics of fructose dissolution with final BL yields above 70%.

The kinetic analysis from fructose and 5-HMF provide robust results to describe and predict the kinetics of solvolysis, and in the case of the high-gravity approach with initial substrate concentrations on a larger scale, increasing the research landscape on the kinetics of converting bio-intermediates from biomass into high-value-added molecules.

These experimental results and the investigated solvolysis technology were then used in Chapter 5 to define the process scheme for producing of butyl levulinate from fructose and subsequent hydrogenation to  $\gamma$ -valerolactone. In addition to assessing the sustainability of the GVL production process, the analysis focused on integrating energy systems from renewable energy sources and hydrogen energy storage systems. The analysis showed that the process of producing GVL from biomass-derived fructose, through the production of BL, is a potentially sustainable process, especially considering its synergistic integration with the in-site hydrogen production asset and energy from renewable sources such as wind and biomass. The sustainability analysis was conducted with a specific methodology based on the real availability of renewable resources with territorial specificity in Normandy, as a case study, and the evaluation of specific performance indices with respect to economic, environmental and social perspectives.

Through the various results achieved, this research attempted to answer the initial question of the sustainability of biomass conversion with a focus on the production of butyl levulinate and GVL in the current context of the extreme need to accelerate the conversion of our economy towards a greener and more sustainable one, with hydrogen as a key player in the energy sector.

In view of future perspectives, the analysis presented can be extended by considering a broader chain in biomass conversion, including the production of alkyl levulinate from more complex systems, such as raw biomass, optimizing the pre-treatment steps and analyzing the kinetics. From a kinetic point of view, the use of non-noble metal catalysts for hydrogenation at GVL, and the use of different alkyl levulinates, in addition to butyl levulinate, can be investigated in depth, also assessing reactivity effects of the different alkyl structures. With possible application of DFT calculation methods for a further understanding of reaction pathways.

Consequently, the sustainability analysis can be extended over a broader picture from the biomass feedstock to the final product, as GVL, or further value-added molecules obtainable from it, as MeTHF, and bio-butene. In terms of renewable energy resources, other sources besides wind, such as solar, wave, can be evaluated for the design of hybrid energy systems. In terms of ASI and KPIs, multi-criteria decision analysis can be deepened by including additional indices with respect to environmental and social sustainability perspectives; other environmental impact indices can include footprint and land use, which can have a considerable impact especially in integrated systems with RES, and in the social sphere indices to include aspects of social awareness and acceptance.

# Appendix S1: Additional Data-Chapter 3

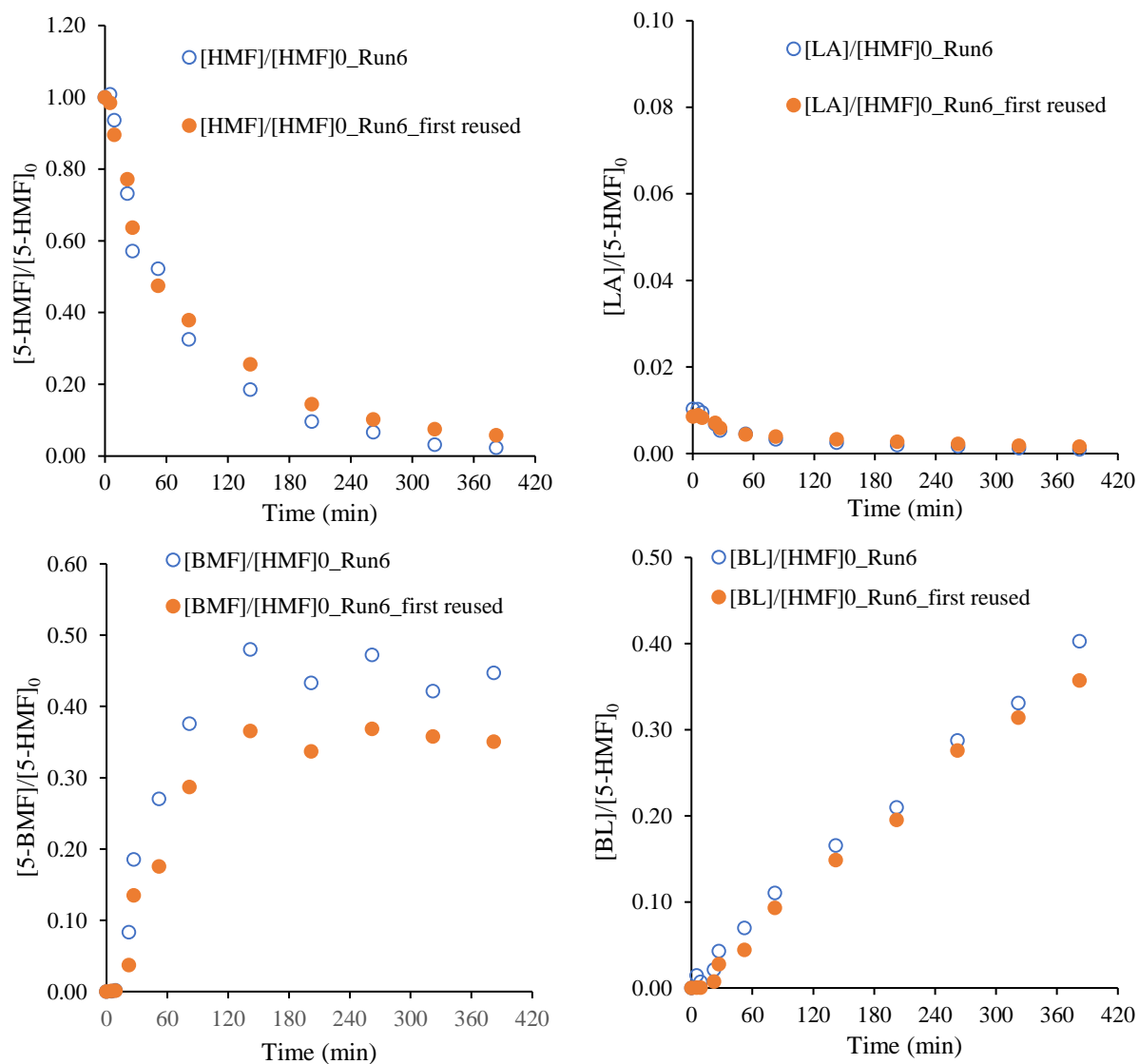


Fig. S1. 1: Reusability of the catalyst in Experiment 6.

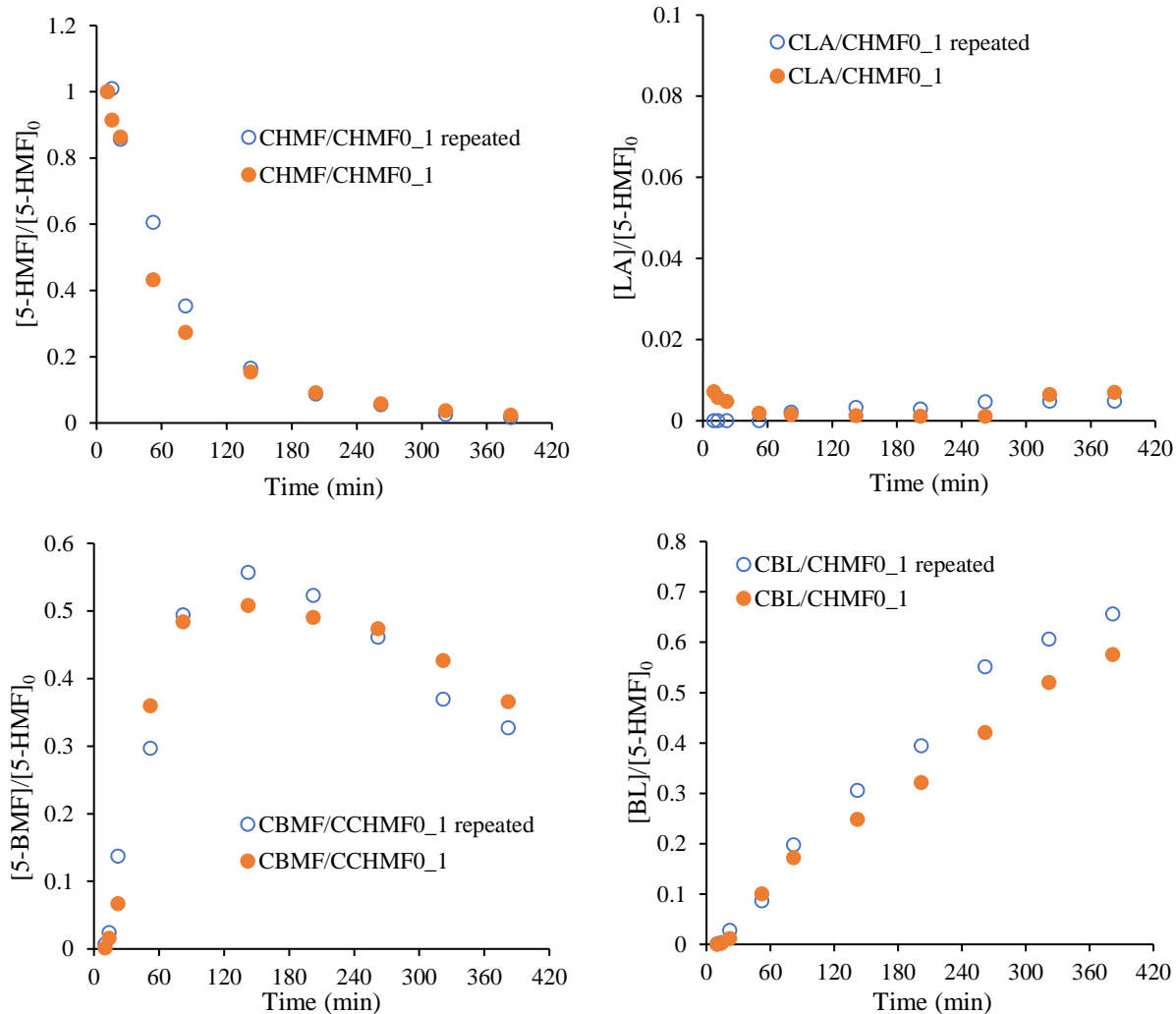


Fig. S1. 2: Repeatability by comparing Experiments 1 and 1-repeated

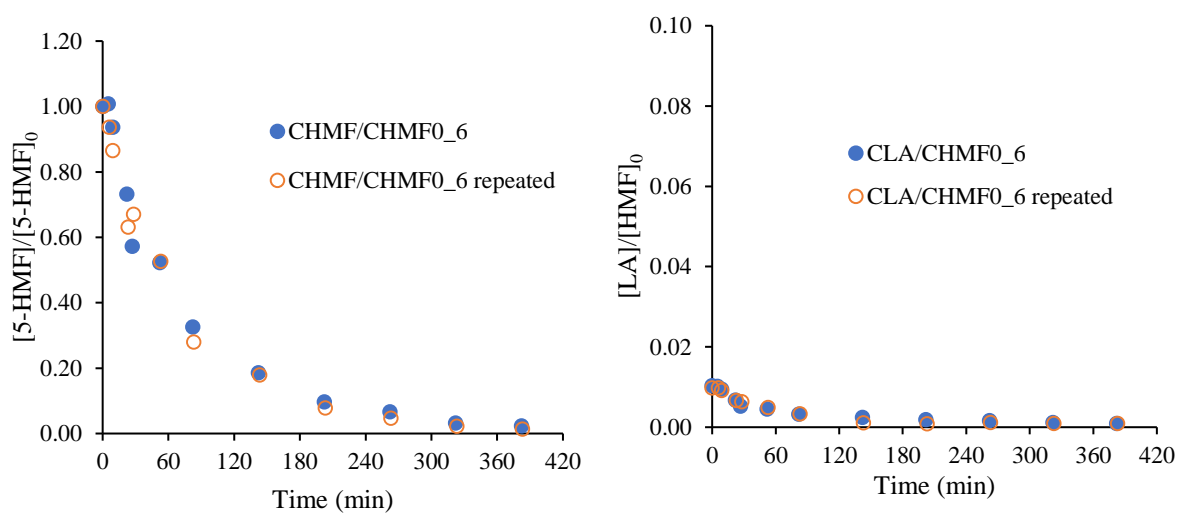


Fig. S1. 3: Repeatability by comparing Experiments 6 and 6-repeated.

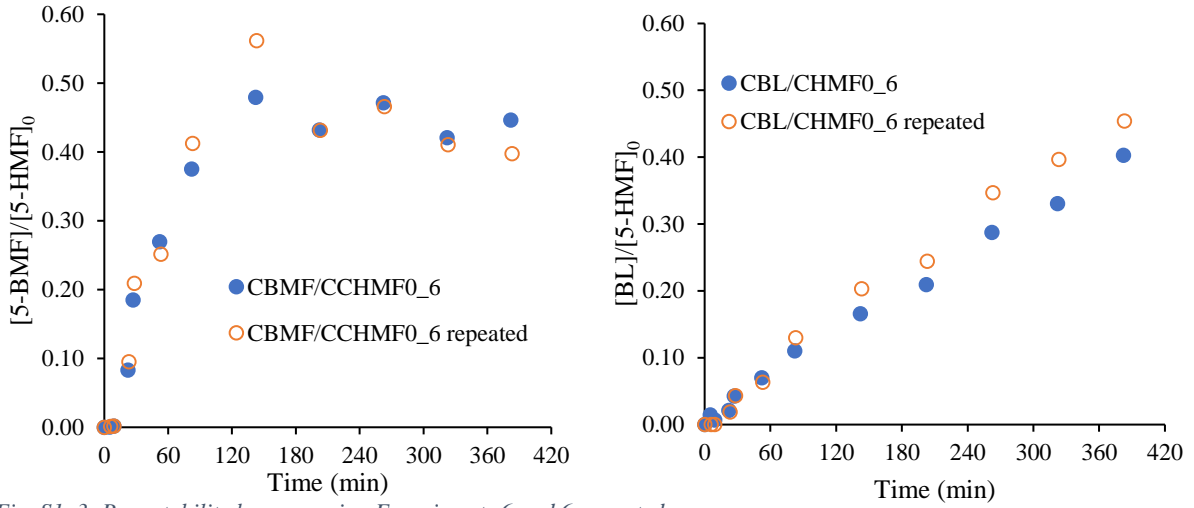


Fig. S1. 3: Repeatability by comparing Experiments 6 and 6-repeated.

Table S1. 1: Estimated values at  $T_{ref} = 368$  K and statistical data for Models 1 and 2.

	Model 1			Model 2		
	Estimates	HPD_%	Units	Estimates	HPD_%	Units
$\ln(k_1(T_{ref}))$	-5.21	1.52	L/mol/min	-5.14	1.42	L/mol/min
$\frac{E_{a1}}{R \cdot T_{ref}}$	4.23	61.06	-	5.48	43.72	-
$\ln(k_2(T_{ref}))$	-5.70	0.47	L <sup>2</sup> /mol <sup>2</sup> /min	-5.70	0.49	L <sup>2</sup> /mol <sup>2</sup> /min
$\frac{E_{a2}}{R \cdot T_{ref}}$	8.37	9.98	-	8.19	10.82	-
$\ln(k_3(T_{ref}))$	-7.18	0.86	L <sup>2</sup> /mol <sup>2</sup> /min	-7.22	0.88	L <sup>2</sup> /mol <sup>2</sup> /min
$\frac{E_{a3}}{R \cdot T_{ref}}$	28.49	6.55	-	29.07	6.86	-
$\ln(k_4(T_{ref}))$	-5.12	0.27	L <sup>2</sup> /mol <sup>2</sup> /min	-5.12	0.27	L <sup>2</sup> /mol <sup>2</sup> /min
$\frac{E_{a4}}{R \cdot T_{ref}}$	11.22	3.84	-	11.23	3.85	-
$\ln(k_6(T_{ref}))$	-5.12	1.68	L/mol/min	-3.99	2.59	L <sup>2</sup> /mol <sup>2</sup> /min
$\frac{E_{a6}}{R \cdot T_{ref}}$	6.27	40.93	-	13.75	22.86	-
$\ln(k_5(T_{ref}))$	-3.83	1.62	L <sup>2</sup> /mol <sup>2</sup> /min	-3.83	1.62	L <sup>2</sup> /mol <sup>2</sup> /min
$\frac{E_{a5}}{R \cdot T_{ref}}$	2.40	75.93	-	2.46	73.81	-

Table S1. 2: Estimated values at  $T_{ref} = 368$  K and statistical data for Models 3 and 4.

	Model 3			Model 4		
	Estimates	HPD_ %	Units	Estimates	HPD_ %	Units
$\ln(k_1(T_{ref}))$	-5.11	1.42	L/mol/min	-5.06	1.34	L/mol/min
$\frac{E_{a1}}{R \cdot T_{ref}}$	6.63	36.61	-	7.76	29.51	-
$\ln(k_2(T_{ref}))$	-4.83	62.79	L/mol/min	-4.96	64.77	L/mol/min
$\frac{E_{a2}}{R \cdot T_{ref}}$	19.91	>100%	-	25.12	>100%	-
$\ln(k_6(T_{ref}))$	-5.72	0.47	L <sup>2</sup> /mol <sup>2</sup> /min	-5.73	0.49	L <sup>2</sup> /mol <sup>2</sup> /min
$\frac{E_{a6}}{R \cdot T_{ref}}$	7.65	11.14	-	7.32	12.18	-
$\ln(k_7(T_{ref}))$	-7.23	0.81	L <sup>2</sup> /mol <sup>2</sup> /min	-7.27	0.81	L <sup>2</sup> /mol <sup>2</sup> /min
$\frac{E_{a7}}{R \cdot T_{ref}}$	27.97	6.67	-	28.35	6.89	-
$\ln(k_3(T_{ref}))$	-3.59	12.31	L <sup>2</sup> /mol <sup>2</sup> /min	-3.65	11.55	L <sup>2</sup> /mol <sup>2</sup> /min
$\frac{E_{a3}}{R \cdot T_{ref}}$	17.57	81.27	-	18.08	75.49	-
$\ln(k_4(T_{ref}))$	-3.81	1.36	L <sup>2</sup> /mol <sup>2</sup> /min	-3.81	1.37	L <sup>2</sup> /mol <sup>2</sup> /min
$\frac{E_{a4}}{R \cdot T_{ref}}$	2.35	64.29	-	2.42	62.83	-
$\ln(k_5(T_{ref}))$	-5.11	0.31	L <sup>2</sup> /mol <sup>2</sup> /min	-5.11	0.31	L <sup>2</sup> /mol <sup>2</sup> /min
$\frac{E_{a5}}{R \cdot T_{ref}}$	10.83	4.55	-	10.82	4.55	-
$\ln(k_8(T_{ref}))$	-5.17	1.57	L/mol/min	-4.07	2.59	L <sup>2</sup> /mol <sup>2</sup> /min
$\frac{E_{a8}}{R \cdot T_{ref}}$	5.86	41.23	-	14.14	22.50	-

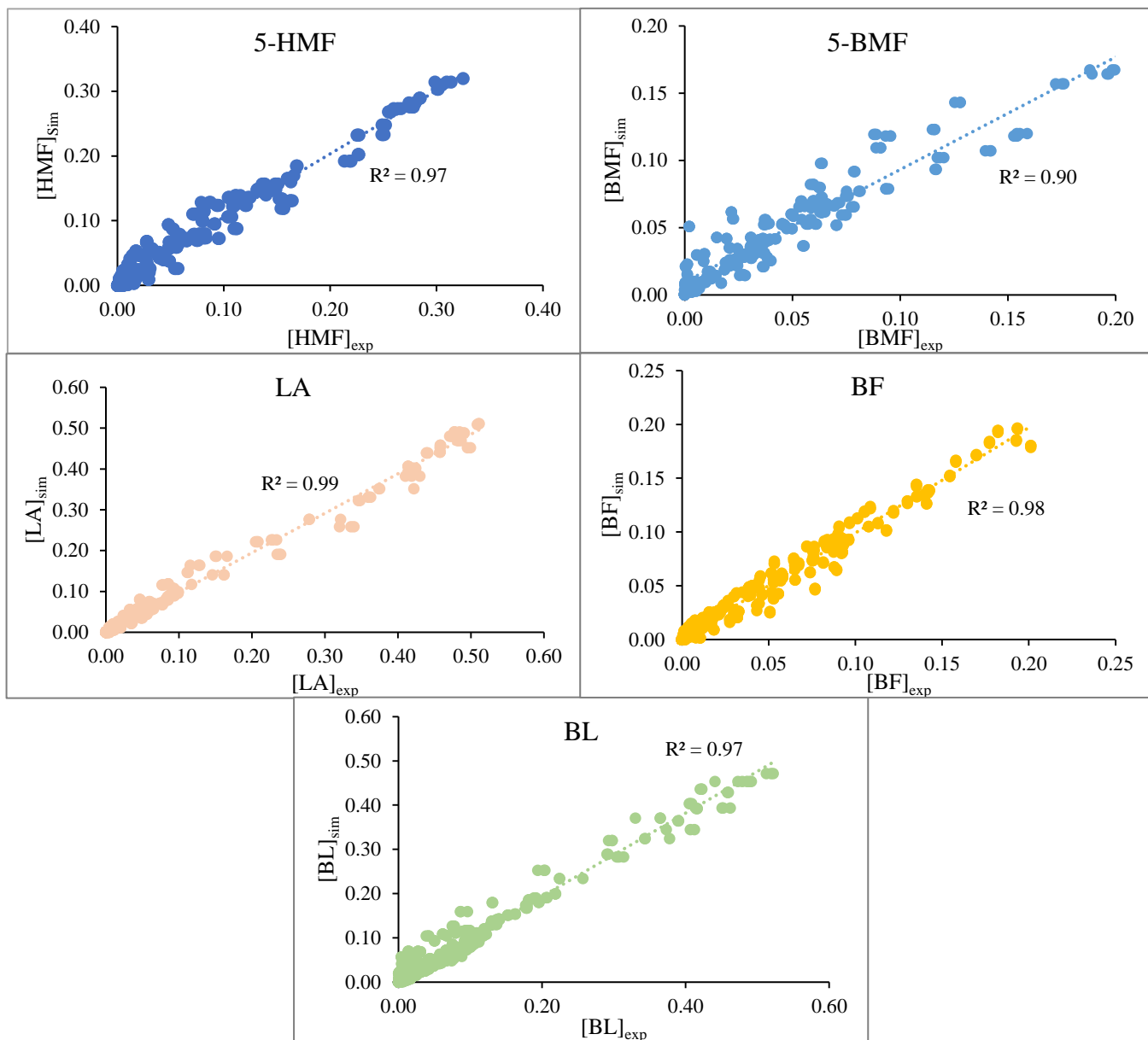


Fig. S1. 4: Parity plot for Model 3 (experimental versus simulated concentrations in mol/L).

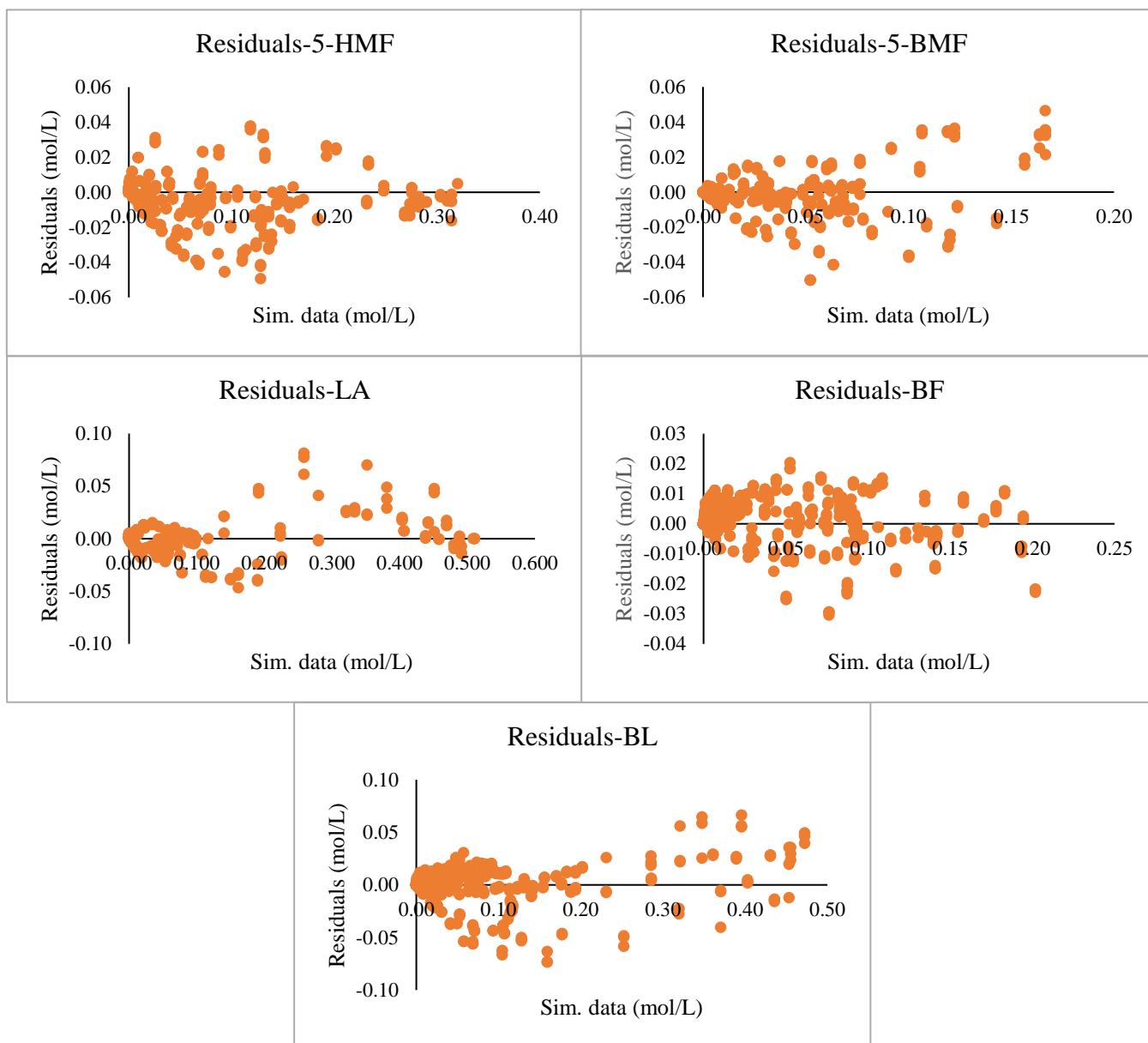
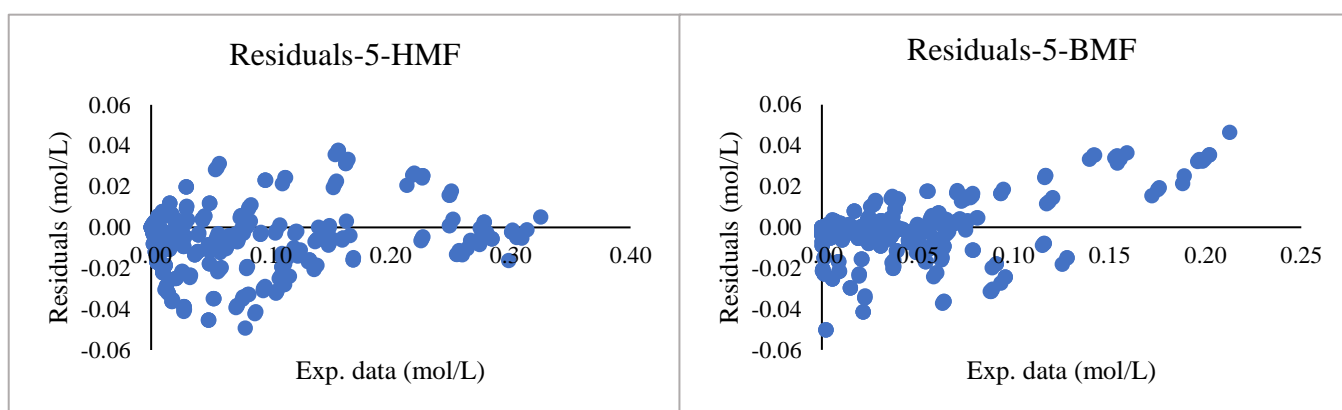


Fig. S1. 5: Plot of residuals versus simulated data for Model 1





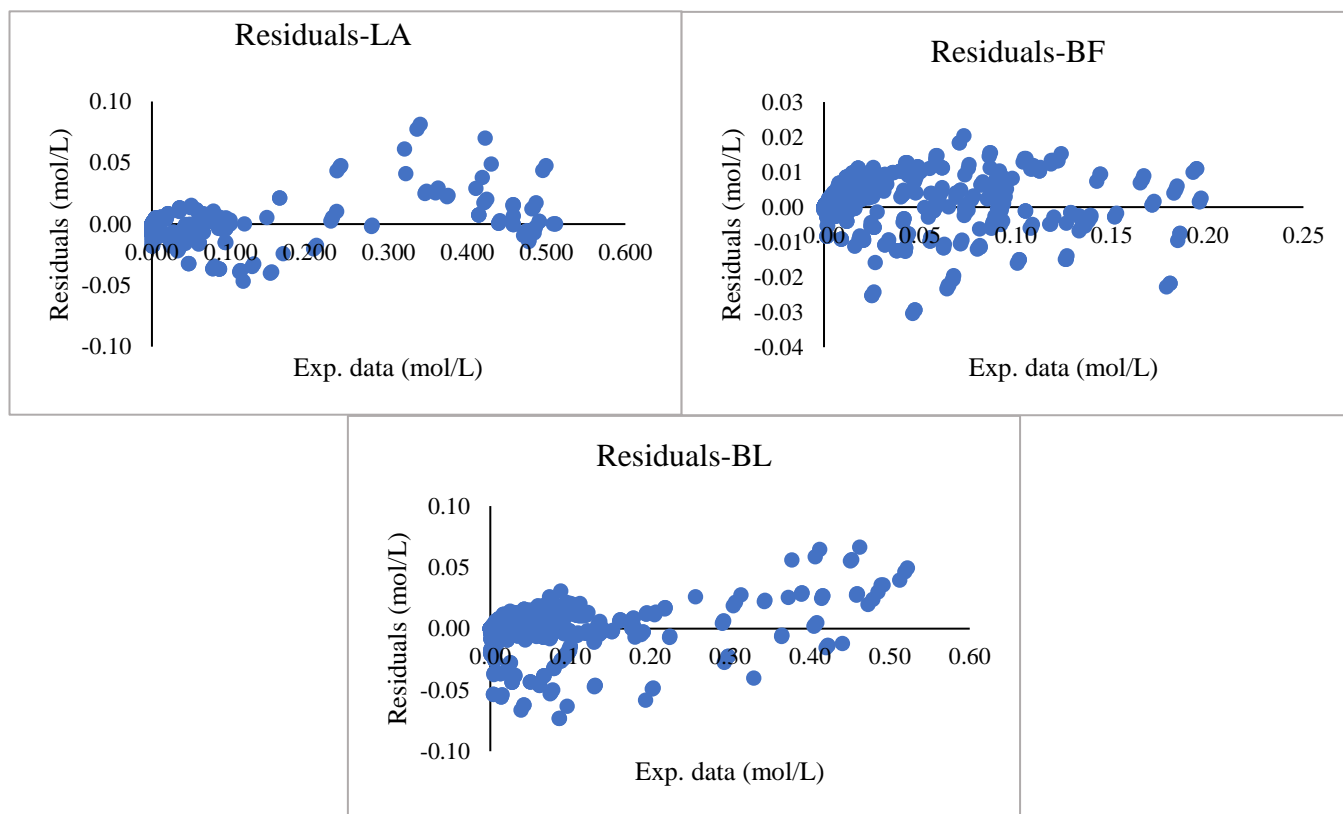


Fig. S1. 6: Plot of residuals versus experimented data for Model 1.

Table S1. 3: Comparison of activation energies estimated to the data literature.

Solvent	Catalyst	Reaction rate expression	$E_{att}$ (kJ/mol)	Ref.
<b>5-HMF hydrolysis to LA+FA</b>				
H <sub>2</sub> O	H <sub>2</sub> SO <sub>4</sub>	$R = 0.340 \exp \left[ -\frac{E_A}{R} \left( \frac{1}{T} - \frac{1}{413} \right) \right] [H^+]^{1.38} [HMF]^{0.88}$	110.5	[296]
H <sub>2</sub> O	H <sub>2</sub> SO <sub>4</sub>	$R = 2.4 \times 10^{11} \alpha_H [H_2SO_4] \exp \left[ -\frac{E_A}{R} \left( \frac{1}{T} - \frac{1}{413} \right) \right] [HMF]$	96.8	[296]
Butanol	Amberlite IR-120	<b>(Model 1)</b> $R = \exp \left[ \ln(k(T_{ref})) + \frac{E_a}{R \cdot T_{ref}} \cdot \left( 1 - \frac{T_{ref}}{T} \right) \right] [HMF][Prot]$	<b>12.94</b>	This work
<b>LA esterification</b>				
Butanol	Amberlyst -15	$R = A \exp \left[ -\frac{E_A}{RT} \right] [LA][BuOH]$	34.91	[420]
Butanol	Amberlyst -15	$R = A \exp \left[ -\frac{E_A}{RT} \right] K_{LA} K_{Bu} \frac{[LA][Bu] - \frac{1}{K} [BL][H_2O]}{(1 + K_{LA}[LA] + K_{Bu}[Bu] + K_{BL}[BL] + K_{H_2O}[H_2O])}$	39.89	[420]

Ethanol	H <sub>2</sub> SO <sub>4</sub>	$R = A \exp \left[ -\frac{E_A}{RT} \right] [LA][EtOH][H_2SO_4]$	54.28	[421]
Ethanol	Amberlite IR-120	$R = k_{eff} \exp \left[ -\frac{E_{ac}}{R} \cdot \left( \frac{1}{T} - \frac{1}{T_{ref}} \right) \right] \left( [LA][EtOH] - \frac{1}{K_{ea}} [H_2O][EL] \right)$	68.83	[231]
Butanol	Amberlite IR-120	<b>(Model 1)</b> $R = \exp \left[ \ln \left( k(T_{ref}) \right) + \frac{E_a}{R \cdot T_{ref}} \cdot \left( 1 - \frac{T_{ref}}{T} \right) \right] [LA][BuOH][Prot]$	<b>34.33</b>	This work
Butanol	Amberlite IR-120	<b>(Model 3)</b> $R = \exp \left[ \ln \left( k(T_{ref}) \right) + \frac{E_a}{R \cdot T_{ref}} \cdot \left( 1 - \frac{T_{ref}}{T} \right) \right] [LA][BuOH][Prot]$	<b>85.58</b>	This work
<b>FA esterification</b>				
Ethanol	H <sub>2</sub> SO <sub>4</sub>	$R = (5.25 \times 10^{-6}) \times \left( \frac{[EtOH]}{[FA]} \right)^{1.91} \times [H_2SO_4] \times \left( 10^{9.5 - \frac{3000}{T}} \right) ([EtOH]\alpha_F)^{2.64}$	13.70	[422]
Butanol	Amberlite IR-120	<b>(Model 1)</b> $R = \exp \left[ \ln \left( k(T_{ref}) \right) + \frac{E_a}{R \cdot T_{ref}} \cdot \left( 1 - \frac{T_{ref}}{T} \right) \right] [FA][BuOH][Prot]$	<b>7.34</b>	This work
Butanol	Amberlite IR-120	<b>(Model 3)</b> $R = \exp \left[ \ln \left( k(T_{ref}) \right) + \frac{E_a}{R \cdot T_{ref}} \cdot \left( 1 - \frac{T_{ref}}{T} \right) \right] [FA][BuOH][Prot]$	<b>23.41</b>	This work
<b>5-HMF etherification</b>				
Ethanol	Amberlyst -15	$R = A \exp \left[ -\frac{E_A}{RT} \right] [H^+][HMF D(R)A]$	107.6*	[423]
Butanol	Amberlyst -15	$R = A \exp \left[ -\frac{E_A}{RT} \right] [H^+][HMF D(R)A]$	110.1*	[423]
Butanol	Amberlite IR-120	<b>(Model 1)</b> $R = \exp \left[ \ln \left( k(T_{ref}) \right) + \frac{E_a}{R \cdot T_{ref}} \cdot \left( 1 - \frac{T_{ref}}{T} \right) \right] [HMF][BuOH][Prot]$	<b>25.61</b>	This work
Butanol	Amberlite IR-120	<b>(Model 3)</b> $R = \exp \left[ \ln \left( k(T_{ref}) \right) + \frac{E_a}{R \cdot T_{ref}} \cdot \left( 1 - \frac{T_{ref}}{T} \right) \right] [HMF][BuOH][Prot]$	<b>53.76</b>	This work

\*Sacia et al. 2014 have included different intermediates in the etherification pathway. Here the activation energies in ethanol and butanol for the intermediate step are reported.

Table SI. 4: Correlation matrix for Model 3.

	ln_k01	E1_Rg_Tr	ln_k02	E2_Rg_Tr	ln_k06	E6_Rg_Tr	ln_k07	E7_Rg_Tr	ln_k03	E3_Rg_Tr	ln_k04	E4_Rg_Tr	ln_k05	E5_Rg_Tr	ln_k08	E8_Rg_Tr
ln_k01	1.00															
E1_Rg_Tref	0.14	1.00														
ln_k02	-0.05	0.00	1.00													
E2_Rg_Tref	0.01	-0.04	-0.70	1.00												
ln_k06	0.12	-0.21	-0.02	0.02	1.00											
E6_Rg_Tref	-0.23	0.10	0.02	-0.02	-0.13	1.00										
ln_k07	-0.70	0.11	0.03	-0.01	0.07	0.10	1.00									
E7_Rg_Tref	0.17	-0.67	-0.01	0.03	0.00	-0.03	-0.65	1.00								
ln_k03	-0.18	-0.04	-0.09	0.12	0.00	0.03	0.14	-0.03	1.00							
E3_Rg_Tref	-0.04	-0.15	0.11	-0.05	0.02	0.00	-0.01	0.11	-0.19	1.00						
ln_k04	-0.12	-0.03	0.01	0.00	0.05	0.02	0.07	-0.02	0.08	0.01	1.00					
E4_Rg_Tref	-0.03	-0.09	0.00	0.01	0.02	0.05	0.01	0.04	0.01	0.07	-0.06	1.00				
ln_k05	0.00	0.00	0.01	0.00	0.00	0.00	0.00	0.00	0.00	0.00	0.01	0.00	1.00			
E5_Rg_Tref	0.00	0.00	-0.01	0.01	0.00	0.00	0.00	0.00	0.00	0.00	0.00	0.01	-0.02	1.00		
ln_k08	-0.07	-0.02	0.04	-0.03	0.17	0.07	0.28	-0.13	0.06	-0.01	0.05	-0.01	0.00	0.00	1.00	
E8_Rg_Tref	0.01	-0.07	-0.02	0.04	0.05	0.19	-0.14	0.27	-0.02	0.04	-0.02	0.04	0.00	0.00	-0.52	1.00

# Appendix S2: Additional Data-Chapter 4

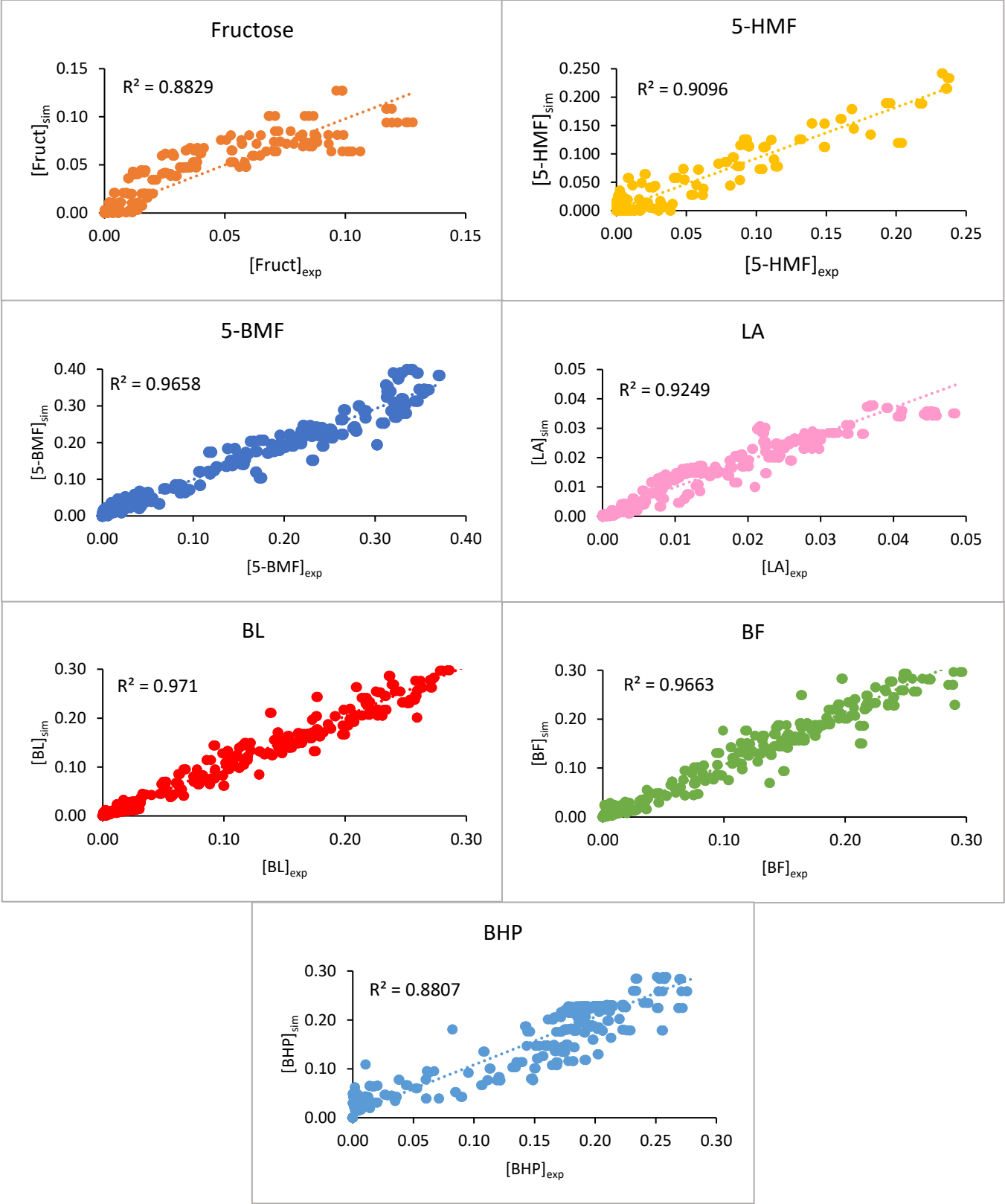


Fig. S2.1: Parity plot for Model 1 (experimental versus simulated concentrations in mol/L)

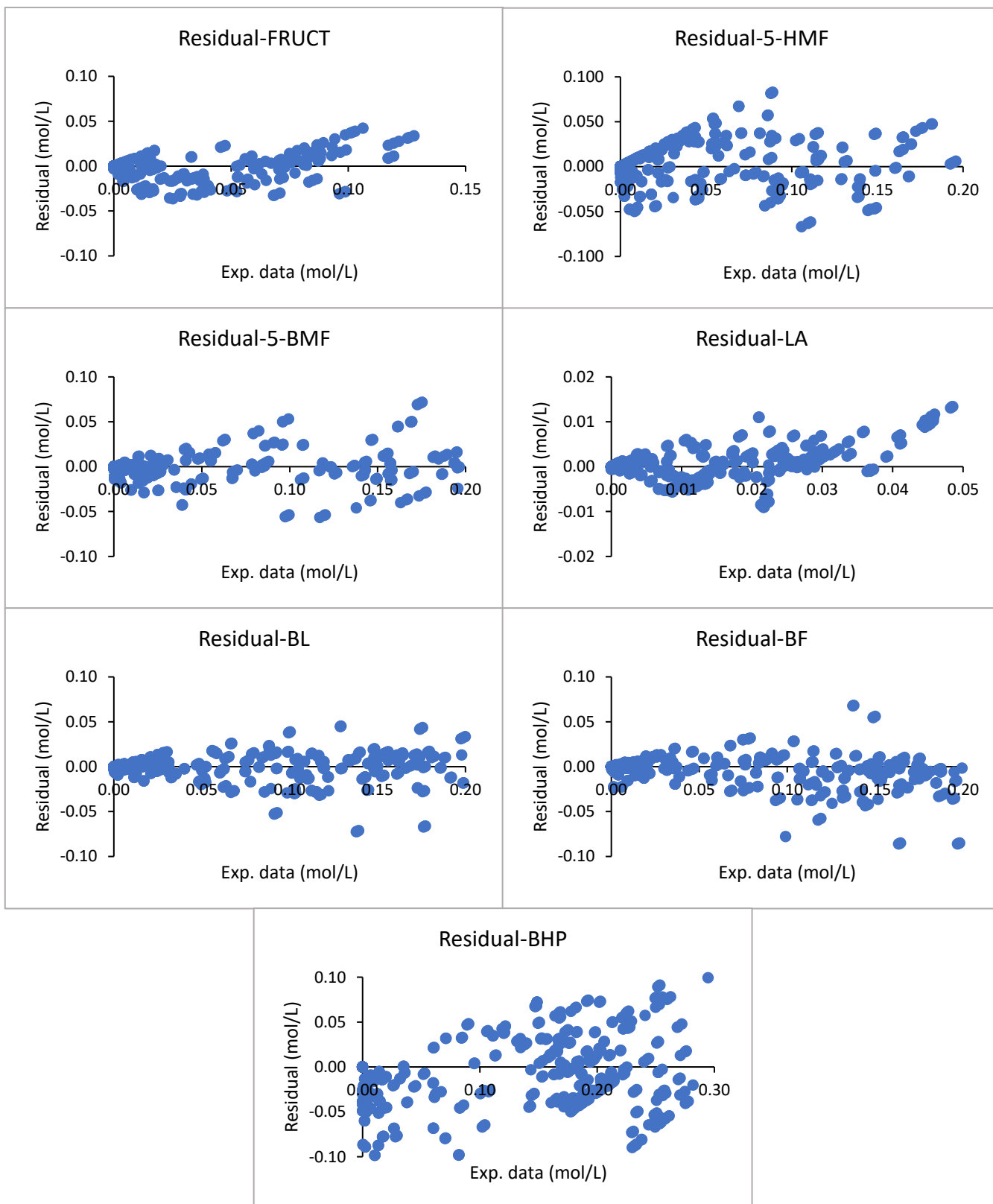


Fig. S2.2: Plot of residuals versus experimental data for Model 1

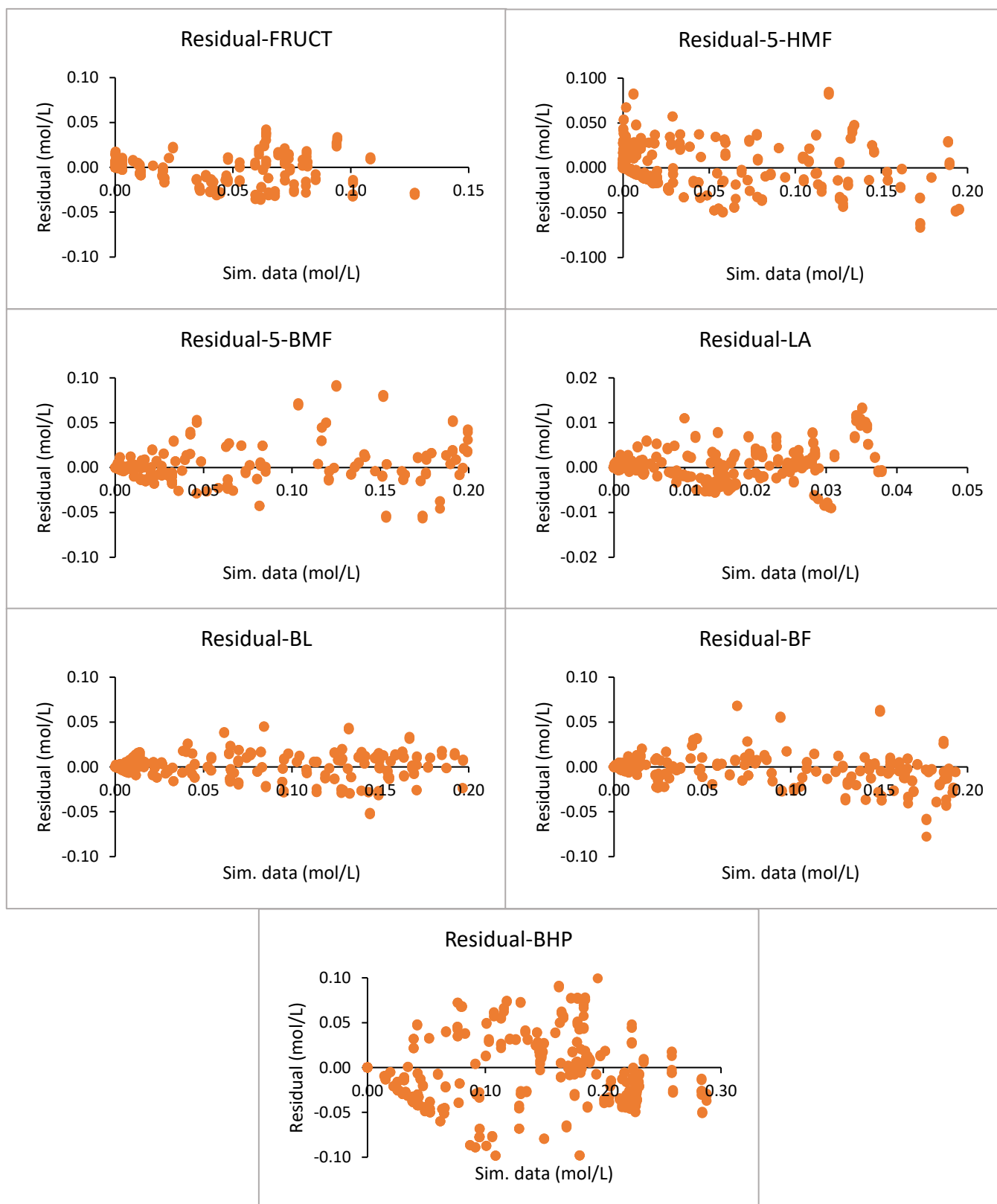


Fig. S2.3: Plot of residuals versus simulated data for Model 1

Table S2. 1: Estimated values at  $T_{ref} = 368\text{ K}$  and statistical data for Models 2 and 3.

	Model 2			Model 3		
	Estimates	HPD_%	Units	Estimates	HPD_%	Units
$\ln(k_0(T_{ref}))$	-2.34	0.11	L/mol/min	-2.29	1.03	L/mol/min
$\frac{E_{a0}}{R \cdot T_{ref}}$	18.7	3.33		14.8	3.66	
$\ln(k_1(T_{ref}))$	-4.39	0.66	L/mol/min	-4.42	0.78	L/mol/min
$\frac{E_{a1}}{R \cdot T_{ref}}$	20.0	3.78	-	19.4	4.48	-
$\ln(k_2(T_{ref}))$	4.99	0.00	L/mol/min	0.35	67.3	L <sup>2</sup> /mol <sup>2</sup> /min
$\frac{E_{a2}}{R \cdot T_{ref}}$	30.1	10.62	-	31.1	0.00	-
$\ln(k_3(T_{ref}))$	-6.51	1.27	L <sup>2</sup> /mol <sup>2</sup> /min	-6.61	1.29	L <sup>2</sup> /mol <sup>2</sup> /min
$\frac{E_{a3}}{R \cdot T_{ref}}$	0.1	0.00	-	1.00	0.00	-
$\ln(k_4(T_{ref}))$	-1.66	3.25	L <sup>2</sup> /mol <sup>2</sup> /min	0.004	164.0	L <sup>2</sup> /mol <sup>2</sup> /min
$\frac{E_{a4}}{R \cdot T_{ref}}$	14.2	15.39	-	10.2	36.49	-
$\ln(k_5(T_{ref}))$	-5.11	0.43	L <sup>2</sup> /mol <sup>2</sup> /min	-5.63	0.60	L <sup>2</sup> /mol <sup>2</sup> /min
$\frac{E_{a5}}{R \cdot T_{ref}}$	17.2	3.64	-	18.3	3.77	-
$\ln(k_6(T_{ref}))$	-8.02	1.27	L <sup>2</sup> /mol <sup>2</sup> /min	-8.03	1.29	L <sup>2</sup> /mol <sup>2</sup> /min
$\frac{E_{a6}}{R \cdot T_{ref}}$	21.2	10.79	-	21.7	10.73	-
$\ln(k_7(T_{ref}))$	4.98	1.06	L <sup>2</sup> /mol <sup>2</sup> /min	0.39	603.02	L <sup>2</sup> /mol <sup>2</sup> /min
$\frac{E_{a7}}{R \cdot T_{ref}}$	36.2	8.73	-	45.9	1.98	-
$\ln(k_8(T_{ref}))$	-7.37	1.18	L <sup>2</sup> /mol <sup>2</sup> /min	-7.17	1.30	L <sup>2</sup> /mol <sup>2</sup> /min
$\frac{E_{a8}}{R \cdot T_{ref}}$	5.38	52.87	-	5.26	58.24	-
$K_8$	0.028	4.09	-	0.026	3.72	
$\ln(k_9(T_{ref}))$	-3.04	1.87	L/mol/min	-	-	-

$\frac{E_{a9}}{R \cdot T_{ref}}$	2.61	78.27	-	-	-	-
$\ln(k_{10}(T_{ref}))$	-3.74	2.61	L/mol/min	-	-	-
$\frac{E_{a10}}{R \cdot T_{ref}}$	0.187	0.00	-	-	-	-
$\ln(k_{11}(T_{ref}))$	-	-	-	-3.65	0.01	L <sup>2</sup> /mol <sup>2</sup> /min
$\frac{E_{a11}}{R \cdot T_{ref}}$	-	-	-	49.6	0.91	-
$K_{11}$	-	-	-	0.05	2.49	
$\ln(k_{12}(T_{ref}))$	-	-	-	-1.63	0.07	L <sup>2</sup> /mol <sup>2</sup> /min
$\frac{E_{a12}}{R \cdot T_{ref}}$	-	-	-	0.03	169.92	-
$\ln(k_{humins-HMF}(T_{ref}))$	-60.0	0.00	L/mol/min	-60.0	0.00	L/mol/min
$\frac{E_{ahumins-HMF}}{R \cdot T_{ref}}$	2.00	0.00	-	2.00	0.00	-
$\ln(k_{humins-FRUCT}(T_{ref}))$	-20.1	0.00	L/mol/min	-4.50	2.47	L/mol/min
$\frac{E_{ahumins-FRUCT}}{R \cdot T_{ref}}$	3.47	0.00	-	9.92	33.30	-
$k_D$	0.021	0.00	L/mol/min	0.021	0.00	L/mol/min
$n$	1	0.00	-	1	0.00	-



Table S2.2: Correlation matrix of Model 1

	Lnk1	E1/RT	Lnk2	E2/RT	Lnk3	E3/RT	Lnk4	E4/RT	Lnk5	E5/RT	Lnk6	E6/RT	Lnk7	E7/RT	Inkhum1	Ehum1/RT	Lnkhum2	Ehum2/RT	Lnk0	E0/RT	Lnk8	E8/RT	K8	
Lnk1	1																							
E1/RT	-0.435	1																						
Lnk2	0.048	-0.104	1																					
E2/RT	0.00	0.00	0.00	0																				
Lnk3	-0.142	-0.022	0.006	0.00	1																			
E3/RT	0.00	0.00	0.00	0.00	0.00	0																		
Lnk4	-0.028	0.009	-0.044	0.00	0.123	0.00	1																	
E4/RT	0.024	-0.021	0.007	0.00	-0.037	0.00	-0.819	1																
Lnk5	0.209	0.034	-0.042	0.00	-0.038	0.00	-0.076	0.054	1															
E5/RT	0.034	0.4	-0.022	0.00	-0.033	0.00	0.026	-0.031	-0.256	1														
Lnk6	-0.655	0.371	-0.104	0.00	0.091	0.00	-0.037	0.018	0.34	-0.17	1													
E6/RT	0.574	-0.494	0.119	0.00	-0.058	0.00	0.035	-0.013	-0.295	0.224	-0.928	1												
Lnk7	0.052	-0.106	0.01	0.00	-0.009	0.00	-0.046	0.008	-0.039	-0.023	-0.105	0.12	1											
E7/RT	-0.172	0.167	-0.093	0.00	0.089	0.00	0.034	-0.024	-0.144	0.162	0.024	-0.036	-0.104	1										
Inkhum1	0.00	0.00	0.00	0.00	0.00	0.00	0.00	0.00	0.00	0.00	0.00	0.00	0.00	0.00	0									
Ehum1/RT	0.00	0.00	0.00	0.00	0.00	0.00	0.00	0.00	0.00	0.00	0.00	0.00	0.00	0.00	0.00	0								
Lnkhum2	-0.071	0.027	0.058	0.00	-0.006	0.00	-0.163	0.154	-0.053	-0.001	0.142	-0.125	0.054	0.02	0.00	0.00	1							
Ehum2/RT	0.034	-0.043	-0.246	0.00	0.023	0.00	0.156	-0.106	0.036	-0.054	-0.076	0.141	-0.243	0.533	0.00	0.00	-0.721	1						
Lnk0	0.038	0.068	-0.011	0.00	-0.009	0.00	-0.003	0.001	0.056	0.091	-0.001	0.001	-0.011	-0.142	0.00	0.00	-0.003	0.004	1					
E0/RT	0.002	-0.015	-0.03	0.00	-0.002	0.00	-0.017	-0.035	-0.051	0.109	-0.057	0.029	-0.031	0.67	0.00	0.00	-0.074	-0.147	0.005	1				
Lnk8	-0.135	0.019	-0.054	0.00	0.055	0.00	0.062	-0.059	-0.114	0.1	0.013	0.026	-0.054	0.344	0.00	0.00	-0.297	0.255	0.002	0.112	1			
E8/RT	0.055	-0.204	0.102	0.00	0.015	0.00	-0.075	0.059	0.108	-0.182	0.077	-0.057	0.102	0.721	0.00	0.00	0.363	-0.387	-0.012	0	-0.02	1		
K8	-0.098	0.062	-0.018	0.00	0.003	0.00	-0.024	0.029	-0.015	-0.028	-0.032	-0.017	-0.018	0.230	0.00	0.00	-0.046	0.009	-0.002	-0.04	-0.26	-0.356	1	

# Appendix S3: Additional Data-Chapter 5

This section contains some data on the evaluation of wind data:

Table S3. 1: Annual and seasonal average values of wind speed over the decade 2011-2021.

	Time (h)	2011	2012	2013	2014	2015	2016	2017	2018	2019	2020	2021
Mean Wind speed (m/s)	<b>0</b>	8.206	8.100	8.244	8.004	8.399	7.881	7.891	7.829	8.028	8.565	7.758
	<b>3</b>	8.056	8.005	8.097	7.909	8.392	7.840	7.885	7.748	8.114	8.473	7.628
	<b>6</b>	7.984	7.943	7.883	7.816	8.317	7.768	7.890	7.683	8.020	8.474	7.584
	<b>9</b>	7.901	7.829	7.776	7.790	8.252	7.636	7.647	7.564	7.843	8.461	7.529
	<b>12</b>	7.832	7.767	7.689	7.650	8.212	7.636	7.430	7.441	7.792	8.407	7.360
	<b>15</b>	8.042	7.986	8.030	7.966	8.580	7.924	7.714	7.859	8.125	8.877	7.609
	<b>18</b>	8.227	7.957	8.267	8.054	8.597	7.957	7.631	8.036	8.230	8.937	7.818
	<b>21</b>	8.227	7.957	8.267	8.054	8.597	7.957	7.631	8.036	8.230	8.937	7.818
	<b>Spring</b>	7.115	7.148	7.779	7.042	7.885	7.658	7.068	7.459	7.864	8.125	7.790
	<b>Summer</b>	7.028	7.172	6.975	6.348	6.944	6.834	6.812	6.195	6.595	7.021	6.205
	<b>Autumn</b>	8.344	7.982	8.243	7.527	8.815	7.328	8.028	7.880	8.744	8.731	7.579
	<b>Winter</b>	9.870	9.575	9.208	10.89	10.15	9.587	9.041	9.687	9.061	10.83	9.070

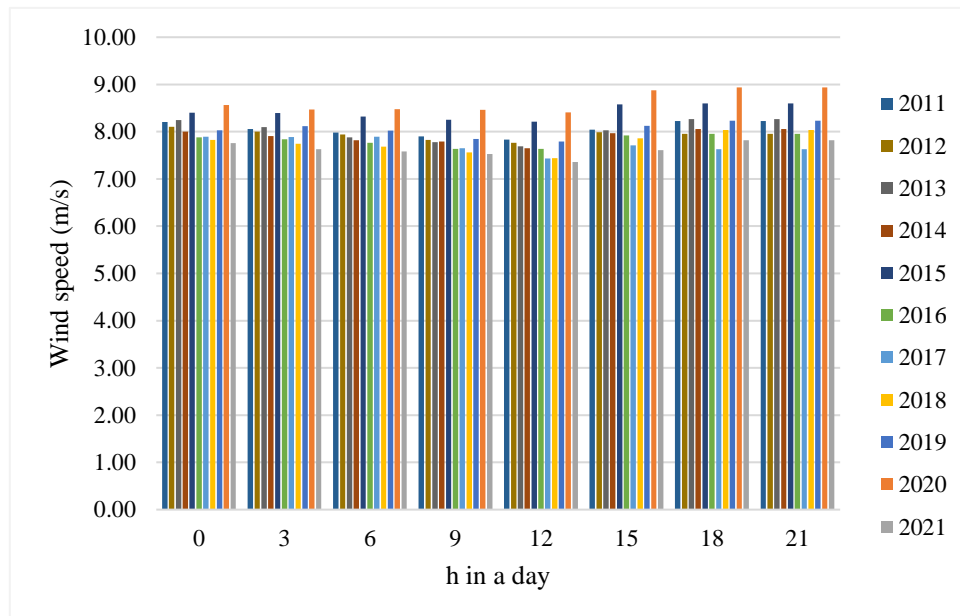


Fig. S3. 1: annual mean wind speed (2011-2021) each 3h in a day.

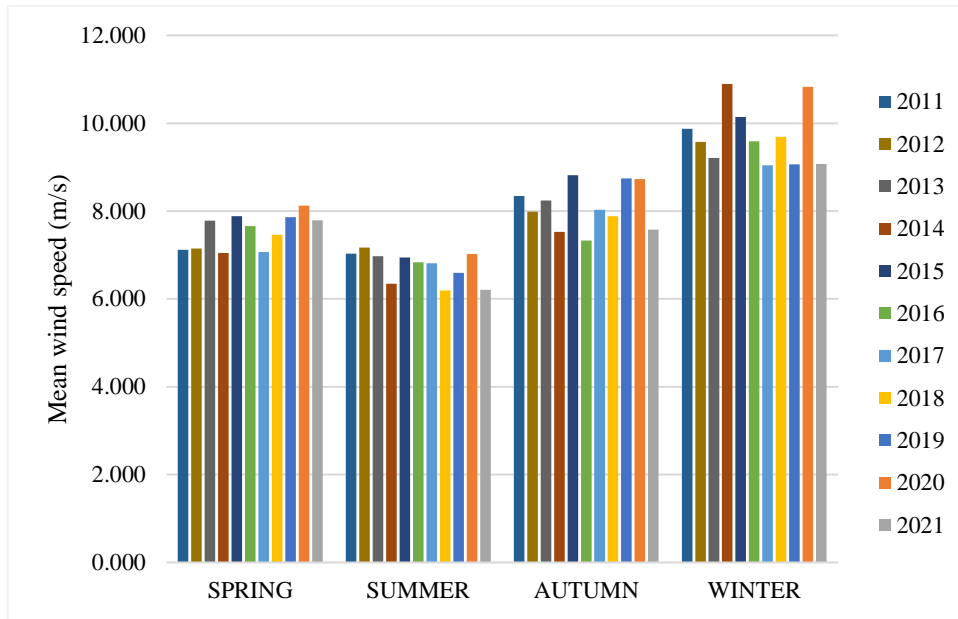


Fig. S3. 2: Mean wind speed for season

The table below (Table S3. 2) shows the average annual and seasonal wind power density, evaluated using a modified Eq. 5. 2:

Table S3. 2: Mean wind power density for season and annually.

		2011	2012	2013	2014	2015	2016	2017	2018	2019	2020	2021
Power density (W/m <sup>2</sup> )	SPRING	220.6	223.7	288.3	213.9	300.3	275.0	216.3	254.2	297.9	328.6	289.6
	SUMMER	212.6	225.9	207.8	156.7	205.1	195.5	193.6	145.6	175.7	212.0	146.3
	AUTUMN	355.8	311.5	343.0	261.2	419.6	241.1	316.9	299.7	409.5	407.7	266.7
	WINTER	588.9	537.7	478.2	791.6	639.6	539.8	452.6	556.8	455.6	778.2	456.9
	YEAR	344.5	324.7	329.3	355.8	391.1	312.8	294.8	314.1	334.7	431.6	289.9

Below are the summary tables for the assessment of damage distances associated with critical equipment in the inherent safety analysis. Condition and inventory data and DD-results for the human target and equipment are given.

Table S3. 3: Input data and DD calculation of the Major Hazard Equipment (MHE) in GVL-section (Human target).

Input Data				Damage Distances (m)					
Unit	T(°C)/p(bar)	Mass (Kg)	LOC	Flash Fire	Fire Ball	Jet Fire	Pool Fire	Explosion	Toxic Cloud
CRV-100	110/20	1126	1	26	0	32	59	29	26
			2	22	0	25	57	28	19
			3	16	0	0	36	48	15
CRV-101	150/20	1*	1	0	20	0	0	13	0
			2	0	0	0	0	0	0

\*Inventory with respect to volume of hydrogen in gas phase at the CRV-101 reactor.

			3	4	20	0	0	0	0
CRV-102	190/20.5	925	1	23	0	33	61	27	18
			2	15	0	26	57	15	0
			3	17	135	0	70	58	16
E-100	110/20	7.4	4	12	0	20	21	14	28
			5	26	0	121	24	31	34
E-102	150/20	1	4	0	0	0	0	0	0
			5	0	9	7	0	13	0
E-103	137/20	14	4	0	0	20	15	15	25
			5	27	20	145	26	34	37
E-104	120/1.1	1	4	0	3	0	0	0	0
			5	0	3	22	0	0	0
E-105	190/20	6.4	4	0	23	18	26	13	31
			5	22	24	140	50	32	47
E-106	176/1.5	1	4	0	3	0	0	0	0
			5	0	3	14	0	0	0
E-107	123.1.4	114	4	0	0	7	14	13	6
			5	23	18	5	19	29	28
Cond-100	120.1.1	1	4	0	7	0	0	0	0
			5	0	7	45	0	17	16
Cond-101	120/1.1	1	4	0	4	0	0	0	0
			5	0	4	15	17	0	0
Reb-102	136/1.85	1.5	4	0	6	0	0	0	0
			5	0	6	40	0	0	13
T-100	228/1.8	8	1	0	0	0	0	0	0
			2	0	0	0	0	0	0
			3	3	15	0	0	0	8
T-101	235.5/1.8	8	1	0	0	0	0	0	0
			2	0	0	0	0	0	0
			3	3	15	0	0	0	8
T-102	135/1.5	6	1	0	0	0	0	0	0
			2	0	0	0	0	0	0
			3	2	12	0	0	0	9
V-100	99.3/2.4	2410	1	0	0	17	55	0	16
			2	17	0	36	57	15	32

			3	95	0	0	55	55	286
V-101	40/1	961	1	0	0	0	42	0	0
			2	5	0	7	53	0	4
			3	4	0	0	34	0	17
V-102	80/1	1812	1	0	0	3	29	0	5
			2	8	0	12	50	29	31
			3	11	0	0	49	0	70
V-103	19.5/1	2644	1	0	0	0	30	0	0
			2	4	0	0	59	0	4
			3	3	0	0	58	0	7
P-100	39.5/20	-	4	0	0	21	10	0	0
			5	20	0	23	57	27	6
P-102	137/20	-	4	0	3	20	7	0	21
			5	0	0	27	0	16	30

Table S3. 4: Input data and DD calculation of the Major Hazard Equipment (MHE) in H2-section (Human target).

Input Data				Damage Distances (m)					
Unit	T(°C)/p(bar)	Mass (Kg)	LOC	Flash Fire	Fire Ball	Jet Fire	Pool Fire	Explosion	Toxic Cloud
AEL Stack (0.57MW)	80/30	0.1	4	0	9	5	0	13	0
			5	0	0	0	0	0	0
Buffer tank (3.8m <sup>3</sup> )	80/30	7.9	1	20	0	5	0	14	0
			2	6	0	0	0	0	0
			3	9	39	0	0	27	0
Compressor (13.5 kg/h)	30/200	0.1	4	0	0	0	0	0	0
			5	0	0	0	0	0	0
AEL Stack (2.2MW)	80/30	0.2	4	0	11	5	0	14	0
			5	0	0	0	0	0	0
Buffer tank (100m <sup>3</sup> )	80/30	209	1	20	0	5	0	14	0
			2	33	0	10	0	37	0
			3	29	110	0	0	84	0
Compressor (1000 kg/h)	30/200	0.1	4	19	28	8	0	25	0
			5	24	0	9	0	37	0

PEMFC Stack (2.7MW)	70/4	0.1	4	0	7	0	0	0	0
			5	0	0	0	0	12	0
PEMFC Stack (6.7MW)	70/4	0.1	4	0	7	4	0	13	0
			5	0	0	5	0	14	0
Tank 50m <sup>3</sup>	30/200	704	1	38	0	16	0	62	0
			2	44	0	20	0	64	0
			3	47	161	0	0	125	0
Tank 130m <sup>3</sup>	30/200	1598	1	36	0	15	0	51	0
			2	58	0	29	0	91	0
			3	63	208	0	0	165	0
Tank 150m <sup>3</sup>	30/200	2113	1	38	0	16	0	62	0
			2	64	0	33	0	105	0
			3	69	227	0	0	180	0
Tank 250m <sup>3</sup>	30/200	3522	1	38	0	16	0	62	0
			2	75	0	42	0	132	0
			3	84	267	0	0	214	0

Table S3. 5: Input data and DD calculation of the Major Hazard Equipment (MHE) in GVL-section (Equipment target).

Input Data				Atmospheric Equip.			Pressurized Equipment		
Unit	T(°C)/p(bar)	Mass (Kg)	LOC	Jet Fire	Pool Fire	Explosion	Jet Fire	Pool Fire	Explosion
CRV-100	110/20	1126	1	27	49	28	23	34	27
			2	24	47	27	20	32	26
			3	0	26	45	0	11	38
CRV-101	150/20	1*	1	0	0	13	0	0	12
			2	0	0	0	0	0	0
			3	0	0	0	0	0	0
CRV-102	190/20.5	925	1	28	53	26	23	41	25
			2	23	49	15	19	37	14
			3	0	63	53	0	53	45
E-100	110/20	7.4	4	17	20	14	15	0	13
			5	102	23	30	80	0	28
E-102	150/20	1	4	0	0	0	0	0	0
			5	6	0	13	0	0	12

E-103	137/20	14	4	17	13	14	15	0	13
			5	123	24	32	98	22	30
E-104	120/1.1	1	4	0	0	0	0	0	0
			5	19	0	0	7	0	0
E-105	190/20	6.4	4	15	25	13	13	0	12
			5	121	48	30	98	0	28
E-106	176/1.5	1	4	0	0	0	0	0	0
			5	11	0	0	0	0	0
E-107	123.1.4	114	4	6	11	0	0	6	0
			5	45	15	28	38	10	27
Cond-100	120.1.1	1	4	0	0	0	0	0	0
			5	41	0	0	35	0	0
Cond-101	120/1.1	1	4	0	0	0	0	0	0
			5	13	0	0	0	0	0
Reb-102	136/1.85	1.5	4	0	0	0	0	0	0
			5	31	0	0	18	0	0
T-100	228/1.8	8	1	0	0	0	0	0	0
			2	0	0	0	0	0	0
			3	0	0	0	0	0	0
T-101	235.5/1.8	8	1	0	0	0	0	0	0
			2	0	0	0	0	0	0
			3	0	0	0	0	0	0
T-102	135/1.5	6	1	0	0	0	0	0	0
			2	0	0	0	0	0	0
			3	0	0	0	0	0	0
V-100	99.3/2.4	2410	1	14	41	0	0	20	0
			2	30	43	15	28	22	14
			3	0	39	54	0	17	53
V-101	40/1	961	1	0	22	0	0	9	0
			2	0	28	0	0	13	0
			3	0	24	0	0	10	0
V-102	80/1	1812	1	0	21	0	0	9	0
			2	11	36	0	0	17	0
			3	0	36	0	0	16	0
V-103	19.5/1	2644	1	0	22	0	0	9	0

			2	0	43	0	0	20	0
			3	0	42	0	0	19	0
P-100	39.5/20	-	4	18	10	0	16	0	0
			5	19	46	26	17	30	25
P-102	137/20	-	4	17	7	0	15	0	0
			5	23	0	16	20	0	15

Table S3. 6: Input data and DD calculation of the Major Hazard Equipment (MHE) in H2-section (Equipment target).

Input Data				Atmospheric Equip.			Pressurized Equipment		
Unit	T(°C)/p(bar)	Mass (Kg)	LOC	Jet Fire	Pool Fire	Explosion	Jet Fire	Pool Fire	Explosion
AEL Stack (0.57MW)	80/30	0.1	4	0	0	0	0	0	0
			5	0	0	0	0	0	0
Buffer tank (3.8m <sup>3</sup> )	80/30	7.9	1	0	0	13	0	0	13
			2	0	0	0	0	0	0
			3	0	0	0	0	0	0
Compressor (13.5 kg/h)	30/200	0.1	4	0	0	0	0	0	0
			5	0	0	0	0	0	0
AEL Stack (2.2MW)	80/30	0.2	4	0	0	13	0	0	13
			5	0	0	0	0	0	0
Buffer tank (100m <sup>3</sup> )	80/30	209	1	0	0	13	0	0	13
			2	9	0	36	0	0	35
			3	0	0	77	0	0	66
Compressor (1000 kg/h)	30/200	0.1	4	7	0	25	0	0	24
			5	8	0	36	0	0	35
PEMFC Stack (2.7MW)	70/4	0.1	4	0	0	0	0	0	0
			5	0	0	12	0	0	12
PEMFC Stack (6.7MW)	70/4	0.1	4	0	0	13	0	0	12
			5	0	0	13	0	0	13
Tank 50m <sup>3</sup>	30/200	704	1	14	0	51	12	0	49
			2	18	0	63	15	0	60
			3	0	0	116	0	0	99
Tank 130m <sup>3</sup>	30/200	1598	1	14	0	50	12	0	48
			2	26	0	89	22	0	85



			3	0	0	152	0	0	131
Tank 150m <sup>3</sup>	30/200	2113	1	14	0	50	12	0	48
			2	30	0	103	25	0	98
			3	0	0	168	0	0	144
Tank 250m <sup>3</sup>	30/200	3522	1	15	0	61	12	0	59
			2	37	0	129	32	0	123
			3	0	0	199	0	0	172

# References

- I. D. Di Menno Di Bucchianico, Y. Wang, J.-C. Buvat, Y. Pan, V.C. Casson Moreno, S. Leveueur, Production of levulinic acid and alkyl levulinates: A process insight, *Green Chem.* (2021). <https://doi.org/10.1039/D1GC02457D>.
  - II. D. Di Menno Di Bucchianico, J.-C. Buvat, M. Mignot, V. Casson Moreno, S. Leveueur, Role of solvent in enhancing the production of butyl levulinate from fructose, *Fuel*. 318 (2022) 123703. <https://doi.org/10.1016/j.fuel.2022.123703>.
  - III. D. Di Menno Di Bucchianico, A. Cipolla, J.-C. Buvat, M. Mignot, V.C. Casson Moreno, S. Leveueur, Kinetic Study and Model Assessment for n-Butyl Levulinate Production from Alcoholysis of 5-(Hydroxymethyl)furfural over Amberlite IR-120, *Ind. Eng. Chem. Res.* 61 (2022) 10818–10836. <https://doi.org/10.1021/acs.iecr.2c01640>.
  - IV. D. Di Menno Di Bucchianico, J.-C. Buvat, M. Mignot, V. Casson Moreno, S. Leveueur, Role of solvent in enhancing the production of butyl levulinate from fructose, *Chemical Engineering Journal*. 465 (2023) 142914. <https://doi.org/10.1016/j.cej.2023.142914>.
- 
- [1] IEA, World Energy Balances: Overview, IEA, Paris, 2021. <https://www.iea.org/reports/world-energy-balances-overview>, License: CC BY 4.0.
  - [2] IEA, CO2 Emissions in 2022, IEA, Paris, 2023. <https://www.iea.org/reports/co2-emissions-in-2022>, License: CC BY 4.0.
  - [3] IEA, World Energy Outlook 2022, IEA, Paris, 2022. <https://www.iea.org/reports/world-energy-outlook-2022>, License: CC BY 4.0 (report); CC BY NC SA 4.0 (Annex A).
  - [4] EI, Statistical Review of World Energy 2023, (2023). <https://www.energyinst.org/statistical-review>.
  - [5] IEA, World Energy Investment 2023, (2023). <https://www.iea.org/reports/world-energy-investment-2023>, License: CC BY 4.0.
  - [6] IEA, Net Zero by 2050, IEA, Paris, 2021. <https://www.iea.org/reports/net-zero-by-2050>, License: CC BY 4.0.
  - [7] IEA, Tracking Clean Energy Progress 2023, IEA, Paris, 2023. <https://www.iea.org/reports/tracking-clean-energy-progress-2023>, License: CC BY 4.0.
  - [8] V. Ashokkumar, Recent advances in lignocellulosic biomass for biofuels and value-added bioproducts - A critical review, *Bioresource Technology*. (2022) 15.
  - [9] A. Corma, S. Iborra, A. Velty, Chemical Routes for the Transformation of Biomass into Chemicals, *Chem. Rev.* 107 (2007) 2411–2502. <https://doi.org/10.1021/cr050989d>.
  - [10] F. Cherubini, The biorefinery concept: Using biomass instead of oil for producing energy and chemicals, *Energy Conversion and Management*. 51 (2010) 1412–1421. <https://doi.org/10.1016/j.enconman.2010.01.015>.
  - [11] B. Kamm, P. Schönicke, Ch. Hille, Green biorefinery – Industrial implementation, *Food Chemistry*. 197 (2016) 1341–1345. <https://doi.org/10.1016/j.foodchem.2015.11.088>.
  - [12] R. Katakajwala, S.V. Mohan, A critical view on the environmental sustainability of biorefinery systems, *Current Opinion in Green and Sustainable Chemistry*. 27 (2021) 100392. <https://doi.org/10.1016/j.cogsc.2020.100392>.
  - [13] J. Lee, S. Kim, S. You, Y.-K. Park, Bioenergy generation from thermochemical conversion of lignocellulosic biomass-based integrated renewable energy systems, *Renewable and Sustainable Energy Reviews*. 178 (2023) 113240. <https://doi.org/10.1016/j.rser.2023.113240>.

- [14] M.A. Pellow, C.J.M. Emmott, C.J. Barnhart, S.M. Benson, Hydrogen or batteries for grid storage? A net energy analysis, *Energy Environ. Sci.* 8 (2015) 1938–1952. <https://doi.org/10.1039/C4EE04041D>.
- [15] IEA, *The Future of Hydrogen*, IEA, Paris, 2019. <https://www.iea.org/reports/the-future-of-hydrogen>, License: CC BY 4.0.
- [16] F. Dawood, M. Anda, G.M. Shafiullah, Hydrogen production for energy: An overview, *International Journal of Hydrogen Energy.* 45 (2020) 3847–3869. <https://doi.org/10.1016/j.ijhydene.2019.12.059>.
- [17] L.S. Ribeiro, J.J.M. Órfão, M.F.R. Pereira, An overview of the hydrolytic hydrogenation of lignocellulosic biomass using carbon-supported metal catalysts, *Materials Today Sustainability.* 11–12 (2021) 100058. <https://doi.org/10.1016/j.mtsust.2020.100058>.
- [18] A. Racha, C. Samanta, S. Sreekantan, B. Marimuthu, Review on Catalytic Hydrogenation of Biomass-Derived Furfural to Furfuryl Alcohol: Recent Advances and Future Trends, *Energy Fuels.* 37 (2023) 11475–11496. <https://doi.org/10.1021/acs.energyfuels.3c01174>.
- [19] S. Dutta, I.K.M. Yu, D.C.W. Tsang, Y.H. Ng, Y.S. Ok, J. Sherwood, J.H. Clark, Green synthesis of gamma-valerolactone (GVL) through hydrogenation of biomass-derived levulinic acid using non-noble metal catalysts: A critical review, *Chemical Engineering Journal.* 372 (2019) 992–1006. <https://doi.org/10.1016/j.cej.2019.04.199>.
- [20] E. Soszka, M. Jędrzejczyk, N. Keller, A.M. Ruppert, High yield production of 2-methyltetrahydrofuran biofuel with reusable Ni-Co catalysts, *Fuel.* 332 (2023) 126118. <https://doi.org/10.1016/j.fuel.2022.126118>.
- [21] P.M. Falcone, M. Hiete, A. Sapio, Hydrogen economy and sustainable development goals: Review and policy insights, *Current Opinion in Green and Sustainable Chemistry.* 31 (2021) 100506. <https://doi.org/10.1016/j.cogsc.2021.100506>.
- [22] G.D. Sharma, M. Verma, B. Taheri, R. Chopra, J.S. Parihar, Socio-economic aspects of hydrogen energy: An integrative review, *Technological Forecasting and Social Change.* 192 (2023) 122574. <https://doi.org/10.1016/j.techfore.2023.122574>.
- [23] N. Dahmen, I. Lewandowski, S. Zibek, A. Weidtmann, Integrated lignocellulosic value chains in a growing bioeconomy: Status quo and perspectives, *GCB Bioenergy.* 11 (2019) 107–117. <https://doi.org/10.1111/gcbb.12586>.
- [24] N. Scarlat, J.F. Dallemand, N. Taylor, M. Banja, *Brief on biomass for energy in the European Union*, Publications Office of the European Union. (2019). <https://publications.jrc.ec.europa.eu/repository/handle/JRC109354>.
- [25] Y.N. Guragain, P.V. Vadlani, Renewable Biomass Utilization: A Way Forward to Establish Sustainable Chemical and Processing Industries, *Clean Technol.* 3 (2021) 243–259. <https://doi.org/10.3390/cleantechnol3010014>.
- [26] J. Valentine, J. Clifton-Brown, A. Hastings, P. Robson, G. Allison, P. Smith, Food vs. fuel: the use of land for lignocellulosic ‘next generation’ energy crops that minimize competition with primary food production, *Global Change Biol Bioenergy.* 4 (2012) 1–19. <https://doi.org/10.1111/j.1757-1707.2011.01111.x>.
- [27] V. Menon, M. Rao, Trends in bioconversion of lignocellulose: Biofuels, platform chemicals & biorefinery concept, *Progress in Energy and Combustion Science.* 38 (2012) 522–550. <https://doi.org/10.1016/j.peccs.2012.02.002>.
- [28] S.G. Wettstein, D.M. Alonso, E.I. Gürbüz, J.A. Dumesic, A roadmap for conversion of lignocellulosic biomass to chemicals and fuels, *Current Opinion in Chemical Engineering.* 1 (2012) 218–224. <https://doi.org/10.1016/j.coche.2012.04.002>.
- [29] R.A. Sheldon, The Road to Biorenewables: Carbohydrates to Commodity Chemicals, *ACS Sustainable Chem. Eng.* 6 (2018) 4464–4480. <https://doi.org/10.1021/acssuschemeng.8b00376>.
- [30] S. Takkellapati, T. Li, M.A. Gonzalez, An overview of biorefinery-derived platform chemicals from a cellulose and hemicellulose biorefinery, *Clean Techn Environ Policy.* 20 (2018) 1615–1630. <https://doi.org/10.1007/s10098-018-1568-5>.
- [31] M.M. Cajnko, J. Oblak, M. Grilc, B. Likozar, Enzymatic bioconversion process of lignin: mechanisms, reactions and kinetics, *Bioresource Technology.* 340 (2021) 125655. <https://doi.org/10.1016/j.biortech.2021.125655>.

- [32] A. Morone, M. Apte, R.A. Pandey, Levulinic acid production from renewable waste resources: Bottlenecks, potential remedies, advancements and applications, *Renewable and Sustainable Energy Reviews*. 51 (2015) 548–565. <https://doi.org/10.1016/j.rser.2015.06.032>.
- [33] A.W. Bhutto, K. Qureshi, K. Harijan, R. Abro, T. Abbas, A.A. Bazmi, S. Karim, G. Yu, Insight into progress in pre-treatment of lignocellulosic biomass, *Energy*. 122 (2017) 724–745. <https://doi.org/10.1016/j.energy.2017.01.005>.
- [34] R. Kumar, V. Strezov, H. Weldekidan, J. He, S. Singh, T. Kan, B. Dastjerdi, Lignocellulose biomass pyrolysis for bio-oil production: A review of biomass pre-treatment methods for production of drop-in fuels, *Renewable and Sustainable Energy Reviews*. 123 (2020) 109763. <https://doi.org/10.1016/j.rser.2020.109763>.
- [35] A. Démolis, N. Essayem, F. Rataboul, Synthesis and Applications of Alkyl Levulinates, *ACS Sustainable Chem. Eng.* 2 (2014) 1338–1352. <https://doi.org/10.1021/sc500082n>.
- [36] I.T. Horváth, H. Mehdi, V. Fábos, L. Boda, L.T. Mika,  $\gamma$ -Valerolactone—a sustainable liquid for energy and carbon-based chemicals, *Green Chem.* 10 (2008) 238–242. <https://doi.org/10.1039/B712863K>.
- [37] L.E. Manzer, Preparation of Levulinic Acid Esters from  $\alpha$ -Angelica Lactone and Alcohols, Patent WO2005/075405, 2006.
- [38] A.P. Groves, C. Morley, J. Smith, P.A. Stevenson, Fuel Compositions Comprising a C4–8 Alkyl Levulinate, Patent WO2005044960, 2005.
- [39] W. Hodgson, A. Rae, Gasoline and Diesel Fuels Containing Alcohols, Alcohol Derivatives, and Levulinic Acid Derivatives, Patent WO2003002696, 2003.
- [40] M. Herskowitz, M. Landau, Y. Reizner, Diesel Fuel from Vegetable and Animal Oils Blended with Alkyl Levulinates, Patent WO2010106536, 2010.
- [41] S.J.C. Taylor, B.M. Adger, R. McCague, Preparation of Biodiesel Compositions from Fatty Acid Glycerides and Esters., Patent GB2478137A, 2011.
- [42] E. Christensen, A. Williams, S. Paul, S. Burton, R.L. McCormick, Properties and Performance of Levulinate Esters as Diesel Blend Components, *Energy Fuels*. 25 (2011) 5422–5428. <https://doi.org/10.1021/ef201229j>.
- [43] K. Alamgir Ahmad, M. Haider Siddiqui, K.K. Pant, K.D.P. Nigam, N.P. Shetti, T.M. Aminabhavi, E. Ahmad, A critical review on suitability and catalytic production of butyl levulinate as a blending molecule for green diesel, *Chemical Engineering Journal*. 447 (2022) 137550. <https://doi.org/10.1016/j.cej.2022.137550>.
- [44] M.A. Mellmer, C. Sener, J.M.R. Gallo, J.S. Luterbacher, D.M. Alonso, J.A. Dumesic, Solvent Effects in Acid-Catalyzed Biomass Conversion Reactions, *Angew. Chem. Int. Ed.* 53 (2014) 11872–11875. <https://doi.org/10.1002/anie.201408359>.
- [45] E.P. Dagnino, E.R. Chamorro, S.D. Romano, F.E. Felissia, M.C. Area, Optimization of the acid pretreatment of rice hulls to obtain fermentable sugars for bioethanol production, *Industrial Crops and Products*. 42 (2013) 363–368. <https://doi.org/10.1016/j.indcrop.2012.06.019>.
- [46] M. Germec, N.B. Bader, I. Turhan, Dilute acid and alkaline pretreatment of spent tea leaves to determine the potential of carbon sources., *Biomass Conv. Bioref.* 8 (2018) 529–544. <https://doi.org/10.1007/s13399-018-0301-2>.
- [47] C. Chang, X. Ma, P. Cen, Kinetics of Levulinic Acid Formation from Glucose Decomposition at High Temperature, *Chinese Journal of Chemical Engineering*. 14 (2006) 708–712. [https://doi.org/10.1016/S1004-9541\(06\)60139-0](https://doi.org/10.1016/S1004-9541(06)60139-0).
- [48] H.E. van Dam, A.P.G. Kieboom, H. van Bekkum, The Conversion of Fructose and Glucose in Acidic Media: Formation of Hydroxymethylfurfural, *Starch/Stärke*. 38 (1986) 95–101. <https://doi.org/10.1002/star.19860380308>.
- [49] O. Rosales-Calderon, V. Arantes, A review on commercial-scale high-value products that can be produced alongside cellulosic ethanol, *Biotechnol Biofuels*. 12 (2019) 240. <https://doi.org/10.1186/s13068-019-1529-1>.
- [50] D.W. Rackemann, J.P. Bartley, W.O.S. Doherty, Methanesulfonic acid-catalyzed conversion of glucose and xylose mixtures to levulinic acid and furfural, *Industrial Crops and Products*. 52 (2014) 46–57. <https://doi.org/10.1016/j.indcrop.2013.10.026>.

- [51] H. Heeres, R. Handana, D. Chunai, C. Borromeus Rasrendra, B. Girisuta, H. Jan Heeres, Combined dehydration/(transfer)-hydrogenation of C6-sugars (D-glucose and D-fructose) to  $\gamma$ -valerolactone using ruthenium catalysts, *Green Chem.* 11 (2009) 1247. <https://doi.org/10.1039/b904693c>.
- [52] M. Brasholz, K. von Kanel, C.H. Hornung, S. Saubern, J. Tsanaktsidis, Highly efficient dehydration of carbohydrates to 5-(chloromethyl)furfural (CMF), 5-(hydroxymethyl)furfural (HMF) and levulinic acid by biphasic continuous flow processing, *Green Chem.* 13 (2011) 1114–1117. <https://doi.org/10.1039/C1GC15107J>.
- [53] L. Peng, L. Lin, H. Li, Q. Yang, Conversion of carbohydrates biomass into levulinate esters using heterogeneous catalysts, *Applied Energy.* 88 (2011) 4590–4596. <https://doi.org/10.1016/j.apenergy.2011.05.049>.
- [54] V. Choudhary, S.H. Mushrif, C. Ho, A. Anderko, V. Nikolakis, N.S. Marinkovic, A.I. Frenkel, S.I. Sandler, D.G. Vlachos, Insights into the Interplay of Lewis and Brønsted Acid Catalysts in Glucose and Fructose Conversion to 5-(Hydroxymethyl)furfural and Levulinic Acid in Aqueous Media, *J. Am. Chem. Soc.* 135 (2013) 3997–4006. <https://doi.org/10.1021/ja3122763>.
- [55] M. Balakrishnan, E.R. Sacia, A.T. Bell, Etherification and reductive etherification of 5-(hydroxymethyl)furfural: 5-(alkoxymethyl)furfurals and 2,5-bis(alkoxymethyl)furans as potential bio-diesel candidates, *Green Chem.* 14 (2012) 1626. <https://doi.org/10.1039/c2gc35102a>.
- [56] L. Peng, L. Lin, H. Li, K. Chen, Acid-Catalyzed Direct Synthesis of Methyl Levulinate from Paper Sludge in Methanol Medium, *BioResources.* 8 (2013) 5895–5907. <https://doi.org/10.15376/biores.8.4.5895-5907>.
- [57] M.A. Tejero, E. Ramírez, C. Fité, J. Tejero, F. Cunill, Esterification of levulinic acid with butanol over ion exchange resins, *Applied Catalysis A: General.* 517 (2016) 56–66. <https://doi.org/10.1016/j.apcata.2016.02.032>.
- [58] W. Wei, S. Wu, Experimental and kinetic study of glucose conversion to levulinic acid in aqueous medium over Cr/HZSM-5 catalyst, *Fuel.* 225 (2018) 311–321. <https://doi.org/10.1016/j.fuel.2018.03.120>.
- [59] S. Kang, J. Yu, Maintenance of a Highly Active Solid Acid Catalyst in Sugar Beet Molasses for Levulinic Acid Production, *Sugar Tech.* 20 (2018) 182–193. <https://doi.org/10.1007/s12355-017-0543-5>.
- [60] T.C. Acharjee, Y.Y. Lee, Production of levulinic acid from glucose by dual solid-acid catalysts, *Environ. Prog. Sustainable Energy.* 37 (2018) 471–480. <https://doi.org/10.1002/ep.12659>.
- [61] R.A. Schraufnagel, H.F. Rase, Levulinic Acid from Sucrose Using Acidic Ion-Exchange Resins, *Product R&D.* 14 (1975) 40–44. <https://doi.org/10.1021/i360053a009>.
- [62] M.-R. Park, S.-K. Kim, G.-T. Jeong, Production of levulinic acid from glucosamine using zirconium oxychloride, *Journal of Industrial and Engineering Chemistry.* 61 (2018) 119–123. <https://doi.org/10.1016/j.jiec.2017.12.008>.
- [63] X. Zhang, X. Zhang, N. Sun, S. Wang, X. Wang, Z. Jiang, High production of levulinic acid from cellulosic feedstocks being catalyzed by temperature-responsive transition metal substituted heteropolyacids, *Renewable Energy.* 141 (2019) 802–813. <https://doi.org/10.1016/j.renene.2019.04.058>.
- [64] G. Xu, C. Chang, W.N. Zhu, B. Li, X.J. Ma, F.G. Du, A comparative study on direct production of ethyl levulinate from glucose in ethanol media catalysed by different acid catalysts, *Chem. Pap.* 67 (2013) 1355–1363. <https://doi.org/10.2478/s11696-013-0410-0>.
- [65] C.H. Kuo, A.S. Poyraz, L. Jin, Y. Meng, L. Pahalagedara, S.Y. Chen, D.A. Kriz, C. Guild, A. Gudz, S.L. Suib, Heterogeneous acidic TiO<sub>2</sub> nanoparticles for efficient conversion of biomass derived carbohydrates, *Green Chem.* (2014) 785–791. <https://doi.org/10.1039/C3GC40909K>.
- [66] L. Zhou, H. Zou, J. Nan, L. Wu, X. Yang, Y. Su, T. Lu, J. Xu, Conversion of carbohydrate biomass to methyl levulinate with Al<sub>2</sub>(SO<sub>4</sub>)<sub>3</sub> as a simple, cheap and efficient catalyst, *Catalysis Communications.* 50 (2014) 13–16. <https://doi.org/10.1016/j.catcom.2014.02.021>.
- [67] J. Liu, B.-B. Yang, X.-Q. Wang, C.-L. Liu, R.-Z. Yang, W.-S. Dong, Glucose conversion to methyl levulinate catalyzed by metal ion-exchanged montmorillonites, *Applied Clay Science.* 141 (2017) 118–124. <https://doi.org/10.1016/j.clay.2017.02.017>.
- [68] J. Heda, P. Niphadkar, V. Bokade, Efficient Synergetic Combination of H-USY and SnO<sub>2</sub> for Direct Conversion of Glucose into Ethyl Levulinate (Biofuel Additive), *Energy Fuels.* 33 (2019) 2319–2327. <https://doi.org/10.1021/acs.energyfuels.8b04395>.

- [69] C. Antonetti, D. Licursi, A.M. Raspolli Galletti, New Intensification Strategies for the Direct Conversion of Real Biomass into Platform and Fine Chemicals: What Are the Main Improvable Key Aspects?, *Catalysts*. 10 (2020) 961. <https://doi.org/10.3390/catal10090961>.
- [70] R. Liu, J. Chen, X. Huang, L. Chen, L. Ma, X. Li, Conversion of fructose into 5-hydroxymethylfurfural and alkyl levulinates catalyzed by sulfonic acid-functionalized carbon materials, *Green Chem.* 15 (2013) 2895. <https://doi.org/10.1039/c3gc41139g>.
- [71] E.-E. Oprescu, C.-E. Enascuta, R. Doukeh, C. Calin, V. Lavric, Characterizing and using a new bi-functional catalyst to sustainably synthesize methyl levulinate from biomass carbohydrates, *Renewable Energy*. 176 (2021) 651–662. <https://doi.org/10.1016/j.renene.2021.05.120>.
- [72] X. Xu, X. Zhang, W. Zou, H. Yue, G. Tian, S. Feng, Conversion of carbohydrates to methyl levulinate catalyzed by sulfated montmorillonite, *Catalysis Communications*. 62 (2015) 67–70. <https://doi.org/10.1016/j.catcom.2015.01.011>.
- [73] E. Ramírez, R. Bringué, C. Fité, M. Iborra, J. Tejero, F. Cunill, Assessment of ion exchange resins as catalysts for the direct transformation of fructose into butyl levulinate, *Applied Catalysis A: General*. 612 (2021) 117988. <https://doi.org/10.1016/j.apcata.2021.117988>.
- [74] X. Yang, J. Yang, B. Gao, T. Lu, L. Zhou, Conversion of glucose to methyl levulinate over Sn-Al- $\beta$  zeolite: Role of Sn and mesoporosity, *Catalysis Communications*. 130 (2019) 105783. <https://doi.org/10.1016/j.catcom.2019.105783>.
- [75] B. Chamnankid, C. Ratanatawanate, K. Faungnawakij, Conversion of xylose to levulinic acid over modified acid functions of alkaline-treated zeolite Y in hot-compressed water, *Chemical Engineering Journal*. 258 (2014) 341–347. <https://doi.org/10.1016/j.cej.2014.07.036>.
- [76] X. Hu, S. Jiang, L. Wu, S. Wang, C.-Z. Li, One-pot conversion of biomass-derived xylose and furfural into levulinate esters via acid catalysis, *Chem. Commun.* 53 (2017) 2938–2941. <https://doi.org/10.1039/C7CC01078H>.
- [77] B. Girisuta, L.P.B.M. Janssen, H.J. Heeres, Kinetic Study on the Acid-Catalyzed Hydrolysis of Cellulose to Levulinic Acid, *Ind. Eng. Chem. Res.* 46 (2007) 1696–1708. <https://doi.org/10.1021/ie061186z>.
- [78] N. Ya'aini, N.A.S. Amin, M. Asmadi, Optimization of levulinic acid from lignocellulosic biomass using a new hybrid catalyst, *Bioresource Technology*. 116 (2012) 58–65. <https://doi.org/10.1016/j.biortech.2012.03.097>.
- [79] P.P. Upare, J.-W. Yoon, M.Y. Kim, H.-Y. Kang, D.W. Hwang, Y.K. Hwang, H.H. Kung, J.-S. Chang, Chemical conversion of biomass-derived hexose sugars to levulinic acid over sulfonic acid-functionalized graphene oxide catalysts, *Green Chem.* 15 (2013) 2935. <https://doi.org/10.1039/c3gc40353j>.
- [80] J. Jow, G.L. Rorrer, M.C. Hawley, D.T.A. Lampton, Dehydration of d-fructose to levulinic acid over LZY zeolite catalyst, *Biomass*. 14 (1987) 185–194. [https://doi.org/10.1016/0144-4565\(87\)90046-1](https://doi.org/10.1016/0144-4565(87)90046-1).
- [81] C. Wang, Q. Zhang, Y. Chen, X. Zhang, F. Xu, Highly Efficient Conversion of Xylose Residues to Levulinic Acid over  $\text{FeCl}_3$  Catalyst in Green Salt Solutions, *ACS Sustainable Chem. Eng.* 6 (2018) 3154–3161. <https://doi.org/10.1021/acssuschemeng.7b03183>.
- [82] S. Saravanamurugan, O. Nguyen Van Buu, A. Riisager, Conversion of Mono- and Disaccharides to Ethyl Levulinate and Ethyl Pyranoside with Sulfonic Acid-Functionalized Ionic Liquids, *ChemSusChem*. 4 (2011) 723–726. <https://doi.org/10.1002/cssc.201100137>.
- [83] S. Saravanamurugan, A. Riisager, Zeolite Catalyzed Transformation of Carbohydrates to Alkyl Levulinates, *ChemCatChem*. 5 (2013) 1754–1757. <https://doi.org/10.1002/cctc.201300006>.
- [84] S. Saravanamurugan, A. Riisager, Solid acid catalysed formation of ethyl levulinate and ethyl glucopyranoside from mono- and disaccharides, *Catalysis Communications*. 17 (2012) 71–75. <https://doi.org/10.1016/j.catcom.2011.10.001>.
- [85] S. Zhao, G. Xu, J. Chang, C. Chang, J. Bai, S. Fang, Z. Liu, Direct Production of Ethyl Levulinate from Carbohydrates Catalyzed by H-ZSM-5 Supported Phosphotungstic Acid, *BioResources*. 10 (2015) 2223–2234. <https://doi.org/10.15376/biores.10.2.2223-2234>.
- [86] E.C. Njagi, H.C. Genuino, C.-H. Kuo, S. Dharmarathna, A. Gudz, S.L. Suib, High-yield selective conversion of carbohydrates to methyl levulinate using mesoporous sulfated titania-based catalysts, *Microporous and Mesoporous Materials*. 202 (2015) 68–72. <https://doi.org/10.1016/j.micromeso.2014.09.044>.

- [87] P.F. Pinheiro, D.M. Chaves, M.J. da Silva, One-pot synthesis of alkyl levulinates from biomass derivative carbohydrates in tin(II) exchanged silicotungstates-catalyzed reactions, *Cellulose*. 26 (2019) 7953–7969. <https://doi.org/10.1007/s10570-019-02665-w>.
- [88] S. Nazer, A. Najafi Chermahini, B.H. Monjezi, H.A. Dabbagh, Direct conversion of xylose to butyl levulinate over mesoporous zirconium silicates with an integrated dehydration alcoholysis process, *Journal of the Taiwan Institute of Chemical Engineers*. 114 (2020) 168–175. <https://doi.org/10.1016/j.jtice.2020.09.007>.
- [89] X. Lyu, Z. Zhang, F. Okejiri, H. Chen, M. Xu, X. Chen, S. Deng, X. Lu, Simultaneous Conversion of C<sub>5</sub> and C<sub>6</sub> Sugars into Methyl Levulinate with the Addition of 1,3,5-Trioxane, *ChemSusChem*. 12 (2019) 4400–4404. <https://doi.org/10.1002/cssc.201902096>.
- [90] C. Antonetti, D. Licursi, S. Fulignati, G. Valentini, A. Raspolli Galletti, New Frontiers in the Catalytic Synthesis of Levulinic Acid: From Sugars to Raw and Waste Biomass as Starting Feedstock, *Catalysts*. 6 (2016) 196. <https://doi.org/10.3390/catal6120196>.
- [91] C. Liu, X. Lu, Z. Yu, J. Xiong, H. Bai, R. Zhang, Production of Levulinic Acid from Cellulose and Cellulosic Biomass in Different Catalytic Systems, *Catalysts*. 10 (2020) 1006. <https://doi.org/10.3390/catal10091006>.
- [92] M. Signoretto, S. Taghavi, E. Ghedini, F. Menegazzo, Catalytic Production of Levulinic Acid (LA) from Actual Biomass., *Molecules*. 24 (2019) 2760. <https://doi.org/10.3390/molecules24152760>.
- [93] S.W. Fitzpatrick, *The Biofine Technology: A “Bio-Refinery” Concept Based on Thermochemical Conversion of Cellulosic Biomass*, ACS Symposium Series, 2006. 10.1021/bk-2006-0921.ch020.
- [94] B.D. Mullen, C.M. Leibig, L.A. Kapicak, D.L. Bunning, S.R. Strand, D.J. Brunelle, M.D. Rodwogin, R.P. Shirtum, A.J. Louwagie, D.J. Yontz, M.J. Tjosaas, PROCESS TO PREPARE LEVULINIC ACID, US10618864B2, 2020.
- [95] R.F.M.J. Parton, D. Santoro, de A. Rijke, PROCESS FOR THE ISOLATION OF LEVULINIC ACID, EP3115352A1, 2017.
- [96] B.D. Mullen, D.J. Yontz, C.M. Leibig, PROCESS TO PREPARE LEVULINIC ACID, US9073841B2, 2015.
- [97] GFBiochemicals, GFBiochemicals acquires leading levulinic acid derivatives producer Segetis and enters the US market, (2016). [http://www.gfbiochemicals.com/\\_media/Document/2017/4/26/\\_GFBiochemicals%20acquires%20leading%20levulinic%20acid%20derivatives%20producer%20Segetis.pdf](http://www.gfbiochemicals.com/_media/Document/2017/4/26/_GFBiochemicals%20acquires%20leading%20levulinic%20acid%20derivatives%20producer%20Segetis.pdf).
- [98] A.M. Raspolli Galletti, C. Antonetti, V. De Luise, D. Licursi, N. Nassi, LEVULINIC ACID PRODUCTION FROM WASTE BIOMASS, *BioResources*. 7 (2012) 1824–1835. <https://doi.org/10.15376/biores.7.2.1824-1835>.
- [99] D.B. Bevilaqua, M.K.D. Rambo, T.M. Rizzetti, A.L. Cardoso, A.F. Martins, Cleaner production: levulinic acid from rice husks, *Journal of Cleaner Production*. 47 (2013) 96–101. <https://doi.org/10.1016/j.jclepro.2013.01.035>.
- [100] C. Chang, P. Cen, X. Ma, Levulinic acid production from wheat straw, *Bioresource Technology*. 98 (2007) 1448–1453. <https://doi.org/10.1016/j.biortech.2006.03.031>.
- [101] L. Yan, N. Yang, H. Pang, B. Liao, Production of Levulinic Acid from Bagasse and Paddy Straw by Liquefaction in the Presence of Hydrochloride Acid, *Clean Soil Air Water*. 36 (2008) 158–163. <https://doi.org/10.1002/clen.200700100>.
- [102] D. Licursi, C. Antonetti, J. Bernardini, P. Cinelli, M.B. Coltelli, A. Lazzeri, M. Martinelli, A.M.R. Galletti, Characterization of the *Arundo Donax* L. solid residue from hydrothermal conversion: Comparison with technical lignins and application perspectives, *Industrial Crops and Products*. 76 (2015) 1008–1024. <https://doi.org/10.1016/j.indcrop.2015.08.007>.
- [103] S.G. Wettstein, D.M. Alonso, Y. Chong, J.A. Dumesic, Production of levulinic acid and gamma-valerolactone (GVL) from cellulose using GVL as a solvent in biphasic systems, *Energy Environ. Sci*. 5 (2012) 8199–8203. <https://doi.org/saravana>.
- [104] J. Feng, J. Jiang, J. Xu, Z. Yang, K. Wang, Q. Guan, S. Chen, Preparation of methyl levulinate from fractionation of direct liquefied bamboo biomass, *Applied Energy*. 154 (2015) 520–527. <https://doi.org/10.1016/j.apenergy.2015.04.115>.
- [105] J. Dai, L. Peng, H. Li, Intensified ethyl levulinate production from cellulose using a combination of low loading H<sub>2</sub>SO<sub>4</sub> and Al(OTf)<sub>3</sub>, *Catalysis Communications*. 103 (2018) 116–119. <https://doi.org/10.1016/j.catcom.2017.10.007>.

- [106] C. Chang, G. Xu, X. Jiang, Production of ethyl levulinate by direct conversion of wheat straw in ethanol media, *Bioresource Technology*. 121 (2012) 93–99. <https://doi.org/10.1016/j.biortech.2012.06.105>.
- [107] R. Le Van Mao, Q. Zhao, G. Dima, D. Petraccone, New Process for the Acid-Catalyzed Conversion of Cellulosic Biomass (AC3B) into Alkyl Levulinates and Other Esters Using a Unique One-Pot System of Reaction and Product Extraction, *Catal Lett*. 141 (2011) 271–276. <https://doi.org/10.1007/s10562-010-0493-y>.
- [108] S. Elumalai, B. Agarwal, T.M. Runge, R.S. Sangwan, Integrated two-stage chemically processing of rice straw cellulose to butyl levulinate, *Carbohydrate Polymers*. 150 (2016) 286–298. <https://doi.org/10.1016/j.carbpol.2016.04.122>.
- [109] Y. He, L. Zhang, Y. Liu, S. Yi, H. Yu, Y. Zhu, R. Sun, Sulfated complex metal oxides solid acids with dual Brønsted-Lewis acidic property for production of 5-ethoxymethylfurfural from biomass-derived carbohydrates, (2022) 132279. <https://doi.org/10.1016/j.cej.2021.132279>.
- [110] H. Chen, B. Yu, S. Jin, Production of levulinic acid from steam exploded rice straw via solid superacid, S<sub>2</sub>O<sub>8</sub><sup>2-</sup>/ZrO<sub>2</sub>-SiO<sub>2</sub>-Sm<sub>2</sub>O<sub>3</sub>, *Bioresource Technology*. 102 (2011) 3568–3570. <https://doi.org/10.1016/j.biortech.2010.10.018>.
- [111] M. Martínez Aguilar, X. Duret, T. Ghislain, D.P. Minh, A. Nzihou, J.-M. Lavoie, Production of fuel additives by direct conversion of softwood bark using a cheap metal salt, *Energy Conversion and Management: X*. 10 (2021) 100049. <https://doi.org/10.1016/j.ecmx.2020.100049>.
- [112] L. Peng, L. Lin, J. Zhang, J. Zhuang, B. Zhang, Y. Gong, Catalytic Conversion of Cellulose to Levulinic Acid by Metal Chlorides, *Molecules*. 15 (2010) 5258–5272. <https://doi.org/10.3390/molecules15085258>.
- [113] K. Lappalainen, N. Vogeler, J. Kärkkäinen, et al., Microwave-assisted conversion of novel biomass materials into levulinic acid, *Biomass Conv. Bioref.* 8 (2018) 965–970. <https://doi.org/10.1007/s13399-018-0334-6>.
- [114] J. Tan, Q. Liu, L. Chen, T. Wang, L. Ma, G. Chen, Efficient production of ethyl levulinate from cassava over Al<sub>2</sub>(SO<sub>4</sub>)<sub>3</sub> catalyst in ethanol–water system., *Journal of Energy Chemistry*. 26 (2017) 115–120. <https://doi.org/10.1016/j.jechem.2016.08.004>.
- [115] B. Velaga, R.P. Parde, J. Soni, N.R. Peela, Synthesized hierarchical mordenite zeolites for the biomass conversion to levulinic acid and the mechanistic insights into humins formation, *Microporous and Mesoporous Materials*. 287 (2019) 18–28. <https://doi.org/10.1016/j.micromeso.2019.05.049>.
- [116] J.M. Tukacs, M. Bohus, G. Dibó, L.T. Miki, Ruthenium-catalyzed solvent-free conversion of furfural to furfuryl alcohol, *RSC Adv.* 7 (2017) 3331–3335. <https://doi.org/10.1039/C6RA24723G>.
- [117] D.M. Alonso, J.M.R. Gallo, M.A. Mellmer, S.G. Wettstein, J.A. Dumesic, Direct conversion of cellulose to levulinic acid and gamma-valerolactone using solid acid catalysts, *Catal. Sci. Technol.* 3 (2013) 927–931. <https://doi.org/10.1039/C2CY20689G>.
- [118] A. Démolis, M. Eternot, N. Essayem, F. Rataboul, Influence of butanol isomers on the reactivity of cellulose towards the synthesis of butyl levulinates catalyzed by liquid and solid acid catalysts, *New J. Chem.* 40 (2016) 3747–3754. <https://doi.org/10.1039/C5NJ02493E>.
- [119] A.G. Laurenza, O. Losito, M. Casiello, C. Fusco, A. Nacci, V. Pantone, L. D'Accolti, Valorization of cigarette butts for synthesis of levulinic acid as top value-added chemicals, *Sci Rep.* 11 (2021) 15775. <https://doi.org/10.1038/s41598-021-95361-4>.
- [120] R. Behling, S. Valange, G. Chatel, Heterogeneous catalytic oxidation for lignin valorization into valuable chemicals: what results? What limitations? What trends?, *Green Chem.* 18 (2016) 1839–1854. <https://doi.org/10.1039/C5GC03061G>.
- [121] R. An, G. Xu, C. Chang, J. Bai, S. Fang, Efficient one-pot synthesis of n-butyl levulinate from carbohydrates catalyzed by Fe<sub>2</sub>(SO<sub>4</sub>)<sub>3</sub>, *Journal of Energy Chemistry*. 26 (2017) 556–563. <https://doi.org/10.1016/j.jechem.2016.11.015>.
- [122] H. Li, Z. Fang, J. Luo, S. Yang, Direct conversion of biomass components to the biofuel methyl levulinate catalyzed by acid-base bifunctional zirconia-zeolites, *Applied Catalysis B: Environmental*. 200 (2017) 182–191. <https://doi.org/10.1016/j.apcatb.2016.07.007>.
- [123] J. Heda, P. Niphadkar, S. Mudliar, V. Bokade, Highly efficient micro-meso acidic H-USY catalyst for one step conversion of wheat straw to ethyl levulinate (biofuel additive), *Microporous and Mesoporous Materials*. 306 (2020) 110474. <https://doi.org/10.1016/j.micromeso.2020.110474>.



- [124] S.S. Joshi, A.D. Zodge, K.V. Pandare, B.D. Kulkarni, Efficient Conversion of Cellulose to Levulinic Acid by Hydrothermal Treatment Using Zirconium Dioxide as a Recyclable Solid Acid Catalyst, *Ind. Eng. Chem. Res.* 53 (2014) 18796–18805. <https://doi.org/10.1021/ie5011838>.
- [125] D. Lai, L. Deng, Q. Guo, Y. Fu, Hydrolysis of biomass by magnetic solid acid, *Energy Environ. Sci.* 4 (2011) 3552. <https://doi.org/10.1039/c1ee01526e>.
- [126] D.M. Alonso, S.G. Wettstein, J.A. Dumesic, Gamma-valerolactone, a sustainable platform molecule derived from lignocellulosic biomass, *Green Chem.* 15 (2013) 584. <https://doi.org/10.1039/c3gc37065h>.
- [127] F. Kerker, M. Markiewicz, S. Stolte, E. Müller, W. Kunz, The green platform molecule gamma-valerolactone – ecotoxicity, biodegradability, solvent properties, and potential applications, *Green Chem.* 23 (2021) 2962–2976. <https://doi.org/10.1039/D0GC04353B>.
- [128] C.Y.Y. Wong, A.W.-T. Choi, M.Y. Lui, B. Fridrich, A.K. Horváth, L.T. Mika, I.T. Horváth, Stability of gamma-valerolactone under neutral, acidic, and basic conditions, *Struct Chem.* 28 (2017) 423–429. <https://doi.org/10.1007/s11224-016-0887-6>.
- [129] L.G. Covinich, N.M. Clauser, F.E. Felissia, M.E. Vallejos, M.C. Area, The challenge of converting biomass polysaccharides into levulinic acid through heterogeneous catalytic processes, *Biofuels, Bioprod. Bioref.* 14 (2020) 417–445. <https://doi.org/10.1002/bbb.2062>.
- [130] L. Qi, I.T. Horváth, Catalytic Conversion of Fructose to  $\gamma$ -Valerolactone in  $\gamma$ -Valerolactone, *ACS Catal.* 2 (2012) 2247–2249. <https://doi.org/10.1021/cs300428f>.
- [131] S. Capecci, Y. Wang, V. Casson Moreno, C. Held, S. Leveneur, Solvent effect on the kinetics of the hydrogenation of n-butyl levulinate to  $\gamma$ -valerolactone, *Chemical Engineering Science.* 231 (2021) 116315. <https://doi.org/10.1016/j.ces.2020.116315>.
- [132] A.M. Hengne, A.V. Malawadkar, N.S. Biradar, C.V. Rode, Surface synergism of an Ag–Ni/ZrO<sub>2</sub> nanocomposite for the catalytic transfer hydrogenation of bio-derived platform molecules, *RSC Adv.* 4 (2014) 9730. <https://doi.org/10.1039/c3ra46495d>.
- [133] M.G. Al-Shaal, W.R.H. Wright, R. Palkovits, Exploring the ruthenium catalysed synthesis of  $\gamma$ -valerolactone in alcohols and utilisation of mild solvent-free reaction conditions, *Green Chem.* 14 (2012) 1260. <https://doi.org/10.1039/c2gc16631c>.
- [134] M.H. Voges, R.M. Bullock, Catalytic ionic hydrogenations of ketones using molybdenum and tungsten complexes Based on the presentation given at Dalton Discussion No. 4, 10–13th January 2002, Kloster Banz, Germany., *J. Chem. Soc., Dalton Trans.* (2002) 759–770. <https://doi.org/10.1039/b107754f>.
- [135] E.V. Starodubtseva, O.V. Turova, M.G. Vinogradov, L.S. Gorshkova, V.A. Ferapontov, Enantioselective hydrogenation of levulinic acid esters in the presence of the RuII-BINAP-HCl catalytic system, *Russ Chem Bull.* 54 (2005) 2374–2378. <https://doi.org/10.1007/s11172-006-0125-2>.
- [136] S.S.R. Gupta, M.L. Kantam, Selective hydrogenation of levulinic acid into  $\gamma$ -valerolactone over Cu/Ni hydrotalcite-derived catalyst, *Catalysis Today.* 309 (2018) 189–194. <https://doi.org/10.1016/j.cattod.2017.08.007>.
- [137] M. Selva, M. Gottardo, A. Perosa, Upgrade of Biomass-Derived Levulinic Acid via Ru/C-Catalyzed Hydrogenation to  $\gamma$ -Valerolactone in Aqueous–Organic–Ionic Liquids Multiphase Systems, *ACS Sustainable Chem. Eng.* 1 (2013) 180–189. <https://doi.org/10.1021/sc300088j>.
- [138] A. Osatiashtiani, A.F. Lee, K. Wilson, Recent advances in the production of  $\gamma$ -valerolactone from biomass-derived feedstocks via heterogeneous catalytic transfer hydrogenation: Recent advances in  $\gamma$ -valerolactone production, *J. Chem. Technol. Biotechnol.* 92 (2017) 1125–1135. <https://doi.org/10.1002/jctb.5213>.
- [139] S. Kumaravel, S. Thiripuranthagan, M. Durai, E. Erusappan, T. Vembuli, Catalytic transfer hydrogenation of **biomass-derived** levulinic acid to  $\gamma$ -valerolactone over Sn/Al-SBA-15 catalysts, *New J. Chem.* 44 (2020) 8209–8222. <https://doi.org/10.1039/D0NJ01288B>.
- [140] M. Chia, J.A. Dumesic, Liquid-phase catalytic transfer hydrogenation and cyclization of levulinic acid and its esters to  $\gamma$ -valerolactone over metal oxide catalysts, *Chem. Commun.* 47 (2011) 12233. <https://doi.org/10.1039/c1cc14748j>.
- [141] J. Delgado, W.N. Vasquez Salcedo, G. Bronzetti, V. Casson Moreno, M. Mignot, J. Legros, C. Held, H. Grénman, S. Leveneur, Kinetic model assessment for the synthesis of  $\gamma$ -valerolactone from n-butyl levulinate and levulinic acid hydrogenation over the synergy effect of dual catalysts Ru/C

- and Amberlite IR-120, *Chemical Engineering Journal*. 430 (2022) 133053. <https://doi.org/10.1016/j.cej.2021.133053>.
- [142] M. Sudhakar, M. Lakshmi Kantam, V. Swarna Jaya, R. Kishore, K.V. Ramanujachary, A. Venugopal, Hydroxyapatite as a novel support for Ru in the hydrogenation of levulinic acid to  $\gamma$ -valerolactone, *Catalysis Communications*. 50 (2014) 101–104. <https://doi.org/10.1016/j.catcom.2014.03.005>.
- [143] W. Luo, U. Deka, A.M. Beale, E.R.H. Van Eck, P.C.A. Bruijninx, B.M. Weckhuysen, Ruthenium-catalyzed hydrogenation of levulinic acid: Influence of the support and solvent on catalyst selectivity and stability, *Journal of Catalysis*. 301 (2013) 175–186. <https://doi.org/10.1016/j.jcat.2013.02.003>.
- [144] K. Shimizu, S. Kanno, K. Kon, Hydrogenation of levulinic acid to  $\gamma$ -valerolactone by Ni and MoO<sub>x</sub> co-loaded carbon catalysts, *Green Chem*. 16 (2014) 3899–3903. <https://doi.org/10.1039/C4GC00735B>.
- [145] E.I. Gürbüz, D.M. Alonso, J.Q. Bond, J.A. Dumesic, Reactive Extraction of Levulinate Esters and Conversion to  $\gamma$ -Valerolactone for Production of Liquid Fuels, *ChemSusChem*. 4 (2011) 357–361. <https://doi.org/10.1002/cssc.201000396>.
- [146] L. Deng, Y. Zhao, J. Li, Y. Fu, B. Liao, Q.-X. Guo, Conversion of Levulinic Acid and Formic Acid into  $\gamma$ -Valerolactone over Heterogeneous Catalysts, *ChemSusChem*. 3 (2010) 1172–1175. <https://doi.org/10.1002/cssc.201000163>.
- [147] J. Yuan, S.-S. Li, L. Yu, Y.-M. Liu, Y. Cao, H.-Y. He, K.-N. Fan, Copper-based catalysts for the efficient conversion of carbohydrate biomass into  $\gamma$ -valerolactone in the absence of externally added hydrogen, *Energy Environ. Sci*. 6 (2013) 3308. <https://doi.org/10.1039/c3ee40857d>.
- [148] C. Ortiz-Cervantes, J.J. García, Hydrogenation of levulinic acid to  $\gamma$ -valerolactone using ruthenium nanoparticles, *Inorganica Chimica Acta*. 397 (2013) 124–128. <https://doi.org/10.1016/j.ica.2012.11.031>.
- [149] X.-L. Du, L. He, S. Zhao, Y.-M. Liu, Y. Cao, H.-Y. He, K.-N. Fan, Hydrogen-Independent Reductive Transformation of Carbohydrate Biomass into  $\gamma$ -Valerolactone and Pyrrolidone Derivatives with Supported Gold Catalysts, *Angew. Chem. Int. Ed*. 50 (2011) 7815–7819. <https://doi.org/10.1002/anie.201100102>.
- [150] J. He, H. Li, Y.-M. Lu, Y.-X. Liu, Z.-B. Wu, D.-Y. Hu, S. Yang, Cascade catalytic transfer hydrogenation–cyclization of ethyl levulinate to  $\gamma$ -valerolactone with Al–Zr mixed oxides, *Applied Catalysis A: General*. 510 (2016) 11–19. <https://doi.org/10.1016/j.apcata.2015.10.049>.
- [151] J. Song, L. Wu, B. Zhou, H. Zhou, H. Fan, Y. Yang, Q. Meng, B. Han, A new porous Zr-containing catalyst with a phenate group: an efficient catalyst for the catalytic transfer hydrogenation of ethyl levulinate to  $\gamma$ -valerolactone, *Green Chem*. 17 (2015) 1626–1632. <https://doi.org/10.1039/C4GC02104E>.
- [152] A. Bloess, W.-P. Schill, A. Zerrahn, Power-to-heat for renewable energy integration: A review of technologies, modeling approaches, and flexibility potentials, *Applied Energy*. 212 (2018) 1611–1626. <https://doi.org/10.1016/j.apenergy.2017.12.073>.
- [153] P.J. Megía, A.J. Vizcaíno, J.A. Calles, A. Carrero, Hydrogen Production Technologies: From Fossil Fuels toward Renewable Sources. A Mini Review, *Energy Fuels*. 35 (2021) 16403–16415. <https://doi.org/10.1021/acs.energyfuels.1c02501>.
- [154] IEA, Renewables 2022, IEA, Paris, 2022. <https://www.iea.org/reports/renewables-2022>.
- [155] IEA, Solar PV, (2023). <https://www.iea.org/energy-system/renewables/solar-pv#tracking>.
- [156] R. Nadda, A. Kumar, R. Maithani, Efficiency improvement of solar photovoltaic/solar air collectors by using impingement jets: A review, *Renewable and Sustainable Energy Reviews*. 93 (2018) 331–353. <https://doi.org/10.1016/j.rser.2018.05.025>.
- [157] Center for Sustainable Systems, Photovoltaic Energy Factsheet, University of Michigan, 2022.
- [158] C. Jung, D. Schindler, Efficiency and effectiveness of global onshore wind energy utilization, *Energy Conversion and Management*. 280 (2023) 116788. <https://doi.org/10.1016/j.enconman.2023.116788>.
- [159] P. Enevoldsen, M.Z. Jacobson, Data investigation of installed and output power densities of onshore and offshore wind turbines worldwide, *Energy for Sustainable Development*. 60 (2021) 40–51. <https://doi.org/10.1016/j.esd.2020.11.004>.
- [160] Center for Sustainable Systems, Wind Energy Factsheet, University of Michigan, 2022.

- [161] IRENA, Wind energy, (2023). <https://www.irena.org/Energy-Transition/Technology/Wind-energy>.
- [162] IEA, Wind, (2023).
- [163] L. Chang, H.B. Saydaliev, M.S. Meo, M. Mohsin, How renewable energy matter for environmental sustainability: Evidence from top-10 wind energy consumer countries of European Union, *Sustainable Energy, Grids and Networks*. 31 (2022) 100716. <https://doi.org/10.1016/j.segan.2022.100716>.
- [164] S.L. Dolan, G.A. Heath, Life Cycle Greenhouse Gas Emissions of Utility-Scale Wind Power: Systematic Review and Harmonization, *Journal of Industrial Ecology*. 16 (2012) S136–S154. <https://doi.org/10.1111/j.1530-9290.2012.00464.x>.
- [165] D.D. Hsu, P. O’Donoughue, V. Fthenakis, G.A. Heath, H.C. Kim, P. Sawyer, J.-K. Choi, D.E. Turney, Life Cycle Greenhouse Gas Emissions of Crystalline Silicon Photovoltaic Electricity Generation: Systematic Review and Harmonization, *Journal of Industrial Ecology*. 16 (2012) S122–S135. <https://doi.org/10.1111/j.1530-9290.2011.00439.x>.
- [166] M. Jacoby, Companies seek ways to reuse the retired giant structures rather than bury them, *C&EN*. 100 (2022) 26–30.
- [167] Y. Wang, J. Kowal, M. Leuthold, D.U. Sauer, Storage System of Renewable Energy Generated Hydrogen for Chemical Industry, *Energy Procedia*. 29 (2012) 657–667. <https://doi.org/10.1016/j.egypro.2012.09.076>.
- [168] H. Ishaq, I. Dincer, C. Crawford, A review on hydrogen production and utilization: Challenges and opportunities, *International Journal of Hydrogen Energy*. 47 (2022) 26238–26264. <https://doi.org/10.1016/j.ijhydene.2021.11.149>.
- [169] B. Greening, T. Braunholtz-Speight, R. Wood, M. Freer, Batteries and beyond: Multi-vector energy storage as a tool to decarbonise energy services, *Front. Energy Res.* 10 (2023) 1109997. <https://doi.org/10.3389/fenrg.2022.1109997>.
- [170] C. Acar, I. Dincer, Review and evaluation of hydrogen production options for better environment, *Journal of Cleaner Production*. 218 (2019) 835–849. <https://doi.org/10.1016/j.jclepro.2019.02.046>.
- [171] J. Incer-Valverde, A. Korayem, G. Tsatsaronis, T. Morosuk, “Colors” of hydrogen: Definitions and carbon intensity, *Energy Conversion and Management*. 291 (2023) 117294. <https://doi.org/10.1016/j.enconman.2023.117294>.
- [172] IEA, Hydrogen - “Tracking Hydrogen,” (2023). <https://www.iea.org/energy-system/low-emission-fuels/hydrogen>.
- [173] F. Ueckerdt, P.C. Verpoort, R. Anantharaman, C. Bauer, F. Beck, T. Longden, S. Roussanaly, On the cost competitiveness of blue and green hydrogen, (2022). <https://doi.org/10.21203/rs.3.rs-1436022/v1>.
- [174] G. Durakovic, P.C. Del Granado, A. Tomasgard, Are green and blue hydrogen competitive or complementary? Insights from a decarbonized European power system analysis, *Energy*. 282 (2023) 128282. <https://doi.org/10.1016/j.energy.2023.128282>.
- [175] S. Shiva Kumar, H. Lim, An overview of water electrolysis technologies for green hydrogen production, *Energy Reports*. 8 (2022) 13793–13813. <https://doi.org/10.1016/j.egy.2022.10.127>.
- [176] W. Kuckshinrichs, T. Ketelaer, J.C. Koj, Economic Analysis of Improved Alkaline Water Electrolysis, *Front. Energy Res.* 5 (2017). <https://doi.org/10.3389/fenrg.2017.00001>.
- [177] S.A. Grigoriev, V.N. Fateev, D.G. Bessarabov, P. Millet, Current status, research trends, and challenges in water electrolysis science and technology, *International Journal of Hydrogen Energy*. 45 (2020) 26036–26058. <https://doi.org/10.1016/j.ijhydene.2020.03.109>.
- [178] M. David, C. Ocampo-Martínez, R. Sánchez-Peña, Advances in alkaline water electrolyzers: A review, *Journal of Energy Storage*. 23 (2019) 392–403. <https://doi.org/10.1016/j.est.2019.03.001>.
- [179] IEA (2022), *Electrolysers*, IEA, Paris <https://www.iea.org/reports/electrolysers>, License: CC BY 4.0, (n.d.).
- [180] IRENA, Making the breakthrough: Green hydrogen policies and technology costs, (2021).
- [181] S. Shiva Kumar, S.U.B. Ramakrishna, S.V. Krishna, K. Srilatha, B.R. Devi, V. Himabindu, Synthesis of titanium (IV) oxide composite membrane for hydrogen production through alkaline water electrolysis, *South African Journal of Chemical Engineering*. 25 (2018) 54–61. <https://doi.org/10.1016/j.sajce.2017.12.004>.

- [182] O. Schmidt, A. Gambhir, I. Staffell, A. Hawkes, J. Nelson, S. Few, Future cost and performance of water electrolysis: An expert elicitation study, *International Journal of Hydrogen Energy*. 42 (2017) 30470–30492. <https://doi.org/10.1016/j.ijhydene.2017.10.045>.
- [183] S. Krishnan, V. Koning, M. Theodorus de Groot, A. de Groot, P.G. Mendoza, M. Junginger, G.J. Kramer, Present and future cost of alkaline and PEM electrolyser stacks, *International Journal of Hydrogen Energy*. (2023) S0360319923022590. <https://doi.org/10.1016/j.ijhydene.2023.05.031>.
- [184] M. Genovese, A. Schlüter, E. Scionti, F. Piraino, O. Corigliano, P. Fragiaco, Power-to-hydrogen and hydrogen-to-X energy systems for the industry of the future in Europe, *International Journal of Hydrogen Energy*. 48 (2023) 16545–16568. <https://doi.org/10.1016/j.ijhydene.2023.01.194>.
- [185] V. Cigolotti, M. Genovese, P. Fragiaco, Comprehensive Review on Fuel Cell Technology for Stationary Applications as Sustainable and Efficient Poly-Generation Energy Systems, *Energies*. 14 (2021) 4963. <https://doi.org/10.3390/en14164963>.
- [186] U.S. Department of energy. Energy Efficiency & Renewable Energy, Fuel Cells, (2015).
- [187] USA Office of Energy Efficiency & Renewable Energy, Hydrogen and Fuel Cell Technologies Office Multi-Year Research, Development, and Demonstration Plan | 3.2 Hydrogen Delivery, (2015) 1–29.
- [188] H. Barthelemy, M. Weber, F. Barbier, Hydrogen storage: Recent improvements and industrial perspectives, *International Journal of Hydrogen Energy*. 42 (2017) 7254–7262. <https://doi.org/10.1016/j.ijhydene.2016.03.178>.
- [189] J. Andersson, S. Grönkvist, Large-scale storage of hydrogen, *International Journal of Hydrogen Energy*. 44 (2019) 11901–11919. <https://doi.org/10.1016/j.ijhydene.2019.03.063>.
- [190] M. Li, Y. Bai, C. Zhang, Y. Song, S. Jiang, D. Grouset, M. Zhang, Review on the research of hydrogen storage system fast refueling in fuel cell vehicle, *International Journal of Hydrogen Energy*. 44 (2019) 10677–10693. <https://doi.org/10.1016/j.ijhydene.2019.02.208>.
- [191] Ø. Ulleberg, T. Nakken, A. Eté, The wind/hydrogen demonstration system at Utsira in Norway: Evaluation of system performance using operational data and updated hydrogen energy system modeling tools, *International Journal of Hydrogen Energy*. 35 (2010) 1841–1852. <https://doi.org/10.1016/j.ijhydene.2009.10.077>.
- [192] T. Egeland-Eriksen, A. Hajizadeh, S. Sartori, Hydrogen-based systems for integration of renewable energy in power systems: Achievements and perspectives, *International Journal of Hydrogen Energy*. 46 (2021) 31963–31983. <https://doi.org/10.1016/j.ijhydene.2021.06.218>.
- [193] M. Kopp, D. Coleman, C. Stiller, K. Scheffer, J. Aichinger, B. Scheppat, Energiepark Mainz: Technical and economic analysis of the worldwide largest Power-to-Gas plant with PEM electrolysis, *International Journal of Hydrogen Energy*. 42 (2017) 13311–13320. <https://doi.org/10.1016/j.ijhydene.2016.12.145>.
- [194] J.-M. Pierson, G. Baudic, S. Caux, B. Celik, G. Da Costa, L. Grange, M. Haddad, J. Lecuire, J.-M. Nicod, L. Philippe, V. Rehn-Sonigo, R. Roche, G. Rostirolla, A. Sayah, P. Stolf, M.-T. Thi, C. Varnier, DATAZERO: Datacenter With Zero Emission and Robust Management Using Renewable Energy, *IEEE Access*. 7 (2019) 103209–103230. <https://doi.org/10.1109/ACCESS.2019.2930368>.
- [195] European Commission, Project pipeline of the European Clean Hydrogen Alliance, (2021). [https://single-market-economy.ec.europa.eu/industry/strategy/industrial-alliances/european-clean-hydrogen-alliance/project-pipeline\\_en](https://single-market-economy.ec.europa.eu/industry/strategy/industrial-alliances/european-clean-hydrogen-alliance/project-pipeline_en).
- [196] G.J. Harmsen, Industrial best practices of conceptual process design, *Chemical Engineering and Processing: Process Intensification*. 43 (2004) 671–675. <https://doi.org/10.1016/j.cep.2003.02.003>.
- [197] D.K. Babi, J. Holtbruegge, P. Lutze, A. Gorak, J.M. Woodley, R. Gani, Sustainable process synthesis–intensification, *Computers & Chemical Engineering*. 81 (2015) 218–244. <https://doi.org/10.1016/j.compchemeng.2015.04.030>.
- [198] T. Van Gerven, A. Stankiewicz, Structure, Energy, Synergy, Time—The Fundamentals of Process Intensification, *Ind. Eng. Chem. Res.* 48 (2009) 2465–2474. <https://doi.org/10.1021/ie801501y>.
- [199] P. Glavič, Z.N. Pintarič, M. Bogataj, Process Design and Sustainable Development—A European Perspective, *Processes*. 9 (2021) 148. <https://doi.org/10.3390/pr9010148>.

- [200] P.T. Anastas, J.C. Warner, *Green Chemistry: Theory and Practice*, Oxford University Press: New York, 1998.
- [201] P. Pal, J. Nayak, Development and analysis of a sustainable technology in manufacturing acetic acid and whey protein from waste cheese whey, *Journal of Cleaner Production*. 112 (2016) 59–70. <https://doi.org/10.1016/j.jclepro.2015.07.085>.
- [202] A.C. Dimian, P. Iancu, V. Plesu, A.-E. Bonet-Ruiz, J. Bonet-Ruiz, Castor oil biorefinery: Conceptual process design, simulation and economic analysis, *Chemical Engineering Research and Design*. 141 (2019) 198–219. <https://doi.org/10.1016/j.cherd.2018.10.040>.
- [203] C.R. Vitasari, G.W. Meindersma, A.B. De Haan, Conceptual process design of an integrated bio-based acetic acid, glycolaldehyde, and acetol production in a pyrolysis oil-based biorefinery, *Chemical Engineering Research and Design*. 95 (2015) 133–143. <https://doi.org/10.1016/j.cherd.2015.01.010>.
- [204] T.S. Le, T.N. Nguyen, D.-K. Bui, T.D. Ngo, Optimal sizing of renewable energy storage: A techno-economic analysis of hydrogen, battery and hybrid systems considering degradation and seasonal storage, *Applied Energy*. 336 (2023) 120817. <https://doi.org/10.1016/j.apenergy.2023.120817>.
- [205] P. Gabrielli, F. Fürer, G. Mavromatidis, M. Mazzotti, Robust and optimal design of multi-energy systems with seasonal storage through uncertainty analysis, *Applied Energy*. 238 (2019) 1192–1210. <https://doi.org/10.1016/j.apenergy.2019.01.064>.
- [206] P. Gabrielli, M. Gazzani, E. Martelli, M. Mazzotti, Optimal design of multi-energy systems with seasonal storage, *Applied Energy*. 219 (2018) 408–424. <https://doi.org/10.1016/j.apenergy.2017.07.142>.
- [207] S. Sukumar, H. Mokhlis, S. Mekhilef, K. Naidu, M. Karimi, Mix-mode energy management strategy and battery sizing for economic operation of grid-tied microgrid, *Energy*. 118 (2017) 1322–1333. <https://doi.org/10.1016/j.energy.2016.11.018>.
- [208] B. Li, R. Roche, D. Paire, A. Miraoui, Sizing of a stand-alone microgrid considering electric power, cooling/heating, hydrogen loads and hydrogen storage degradation, *Applied Energy*. 205 (2017) 1244–1259. <https://doi.org/10.1016/j.apenergy.2017.08.142>.
- [209] M.J. Hadidian Moghaddam, A. Kalam, S.A. Nowdeh, A. Ahmadi, M. Babanezhad, S. Saha, Optimal sizing and energy management of stand-alone hybrid photovoltaic/wind system based on hydrogen storage considering LOEE and LOLE reliability indices using flower pollination algorithm, *Renewable Energy*. 135 (2019) 1412–1434. <https://doi.org/10.1016/j.renene.2018.09.078>.
- [210] S. Sanajaoba, Optimal sizing of off-grid hybrid energy system based on minimum cost of energy and reliability criteria using firefly algorithm, *Solar Energy*. 188 (2019) 655–666. <https://doi.org/10.1016/j.solener.2019.06.049>.
- [211] N. Afgan, Sustainability assessment of hydrogen energy systems, *International Journal of Hydrogen Energy*. 29 (2004) 1327–1342. <https://doi.org/10.1016/j.ijhydene.2004.01.005>.
- [212] B. Ness, E. Urbel-Piirsalu, S. Anderberg, L. Olsson, Categorising tools for sustainability assessment, *Ecological Economics*. 60 (2007) 498–508. <https://doi.org/10.1016/j.ecolecon.2006.07.023>.
- [213] H. Nautiyal, V. Goel, Sustainability assessment: Metrics and methods, in: *Methods in Sustainability Science*, Elsevier, 2021: pp. 27–46. <https://doi.org/10.1016/B978-0-12-823987-2.00017-9>.
- [214] A. Warhurst, *Sustainability Indicators and Sustainability Performance Management*, (n.d.).
- [215] R.K. Singh, H.R. Murty, S.K. Gupta, A.K. Dikshit, An overview of sustainability assessment methodologies, *Ecological Indicators*. 15 (2012) 281–299. <https://doi.org/10.1016/j.ecolind.2011.01.007>.
- [216] T. Waas, J. Hugé, T. Block, T. Wright, F. Benitez-Capistros, A. Verbruggen, Sustainability Assessment and Indicators: Tools in a Decision-Making Strategy for Sustainable Development, *Sustainability*. 6 (2014) 5512–5534. <https://doi.org/10.3390/su6095512>.
- [217] K.M. Kotb, M.R. Elkadeem, A. Khalil, S.M. Imam, M.A. Hamada, S.W. Sharshir, A. Dán, A fuzzy decision-making model for optimal design of solar, wind, diesel-based RO desalination integrating flow-battery and pumped-hydro storage: Case study in Baltim, Egypt, *Energy*

- Conversion and Management. 235 (2021) 113962. <https://doi.org/10.1016/j.enconman.2021.113962>.
- [218] O.S. Vaidya, S. Kumar, Analytic hierarchy process: An overview of applications, *European Journal of Operational Research*. 169 (2006) 1–29. <https://doi.org/10.1016/j.ejor.2004.04.028>.
- [219] M. Goumas, V. Lygerou, An extension of the PROMETHEE method for decision making in fuzzy environment: Ranking of alternative energy exploitation projects, *European Journal of Operational Research*. 123 (2000) 606–613. [https://doi.org/10.1016/S0377-2217\(99\)00093-4](https://doi.org/10.1016/S0377-2217(99)00093-4).
- [220] K. Hacatoglu, I. Dincer, M.A. Rosen, Sustainability assessment of a hybrid energy system with hydrogen-based storage, *International Journal of Hydrogen Energy*. 40 (2015) 1559–1568. <https://doi.org/10.1016/j.ijhydene.2014.11.079>.
- [221] A. Abu-Rayash, I. Dincer, Sustainability assessment of energy systems: A novel integrated model, *Journal of Cleaner Production*. 212 (2019) 1098–1116. <https://doi.org/10.1016/j.jclepro.2018.12.090>.
- [222] T. Weidner, V. Tulus, G. Guillén-Gosálbez, Environmental sustainability assessment of large-scale hydrogen production using prospective life cycle analysis, *International Journal of Hydrogen Energy*. 48 (2023) 8310–8327. <https://doi.org/10.1016/j.ijhydene.2022.11.044>.
- [223] M. Cipolletta, M. D'Ambrosio, V. Casson Moreno, V. Cozzani, Enhancing the sustainability of biodiesel fuels by inherently safer production processes, *Journal of Cleaner Production*. 344 (2022) 131075. <https://doi.org/10.1016/j.jclepro.2022.131075>.
- [224] R. An, G. Xu, C. Chang, J. Bai, S. Fang, Efficient one-pot synthesis of n-butyl levulinate from carbohydrates catalyzed by Fe<sub>2</sub>(SO<sub>4</sub>)<sub>3</sub>, *Journal of Energy Chemistry*. 26 (2017) 556–563. <https://doi.org/10.1016/J.JECHEM.2016.11.015>.
- [225] Y. Sun, K. Sun, L. Zhang, S. Zhang, Q. Liu, Y. Wang, T. Wei, G. Gao, X. Hu, Impacts of Solvents on the Stability of the Biomass-Derived Sugars and Furans, *Energy Fuels*. 34 (2020) 3250–3261. <https://doi.org/10.1021/acs.energyfuels.9b03921>.
- [226] A. Bagno, G. Scorrano, Selectivity in Proton Transfer, Hydrogen Bonding, and Solvation, *Acc. Chem. Res.* 33 (2000) 609–616. <https://doi.org/10.1021/ar990149j>.
- [227] H. Guo, A. Duereh, Y. Su, E.J.M. Hensen, X. Qi, R.L. Smith, Mechanistic role of protonated polar additives in ethanol for selective transformation of biomass-related compounds, *Applied Catalysis B: Environmental*. 264 (2020) 118509. <https://doi.org/10.1016/j.apcatb.2019.118509>.
- [228] H. Guo, Efficient conversion of fructose into 5-ethoxymethylfurfural with hydrogen sulfate ionic liquids as co-solvent and catalyst, *Chemical Engineering Journal*. (2017) 7.
- [229] S. Karnjanakom, P. Maneechakr, C. Samart, G. Guan, A facile way for sugar transformation catalyzed by carbon-based Lewis-Brønsted solid acid, *Molecular Catalysis*. 479 (2019) 110632. <https://doi.org/10.1016/j.mcat.2019.110632>.
- [230] Y. Wang, M. Cipolletta, L. Vernières-Hassimi, V. Casson-Moreno, S. Leveneur, Application of the concept of Linear Free Energy Relationships to the hydrogenation of levulinic acid and its corresponding esters, *Chemical Engineering Journal*. 374 (2019) 822–831. <https://doi.org/10.1016/j.cej.2019.05.218>.
- [231] V. Russo, R. Tesser, C. Rossano, T. Cogliano, R. Vitiello, S. Leveneur, M. Di Serio, Kinetic study of Amberlite IR120 catalyzed acid esterification of levulinic acid with ethanol: From batch to continuous operation, *Chemical Engineering Journal*. 401 (2020) 126126. <https://doi.org/10.1016/j.cej.2020.126126>.
- [232] C. Mukesh, D. Nikjoo, J.-P. Mikkola, Production of C-14 Levulinate Ester from Glucose Fermentation Liquors Catalyzed by Acidic Ionic Liquids in a Solvent-Free Self-Biphasic System, *ACS Omega*. 5 (2020) 4828–4835. <https://doi.org/10.1021/acsomega.9b03517>.
- [233] S. Leveneur, D.Yu. Murzin, T. Salmi, J.-P. Mikkola, N. Kumar, K. Eränen, L. Estel, Synthesis of peroxypropionic acid from propionic acid and hydrogen peroxide over heterogeneous catalysts, *Chemical Engineering Journal*. 147 (2009) 323–329. <https://doi.org/10.1016/j.cej.2008.11.045>.
- [234] R. Klaewkla, M. Arend, W. F., A Review of Mass Transfer Controlling the Reaction Rate in Heterogeneous Catalytic Systems, in: H. Nakajima (Ed.), *Mass Transfer - Advanced Aspects*, InTech, 2011. <https://doi.org/10.5772/22962>.
- [235] G.W. Bodamer, R. Kunin, Behavior of Ion Exchange Resins in Solvents Other Than Water - Swelling and Exchange Characteristics, *Ind. Eng. Chem.* 45 (1953) 2577–2580. <https://doi.org/10.1021/ie50527a057>.

- [236] E. Königsberger, Guidelines for the Measurement of Solid–Liquid Solubility, *Journal of Chemical & Engineering Data*. 64 (n.d.) 381–385. <https://doi.org/10.1021/acs.jced.8b01263>.
- [237] J.-M. Engasser, F. Chamouleau, L. Chebil, M. Ghoul, Kinetic modeling of glucose and fructose dissolution in 2-methyl 2-butanol, *Biochemical Engineering Journal*. 42 (2008) 159–165. <https://doi.org/10.1016/j.bej.2008.06.013>.
- [238] T. Flannelly, S. Dooley, J.J. Leahy, Reaction Pathway Analysis of Ethyl Levulinate and 5-Ethoxymethylfurfural from D-Fructose Acid Hydrolysis in Ethanol, *Energy Fuels*. 29 (2015) 7554–7565. <https://doi.org/10.1021/acs.energyfuels.5b01481>.
- [239] E. Ahmad, Md.I. Alam, K.K. Pant, M.A. Haider, Catalytic and mechanistic insights into the production of ethyl levulinate from biorenewable feedstocks, *Green Chem*. 18 (2016) 4804–4823. <https://doi.org/10.1039/C6GC01523A>.
- [240] M.A. Pérez-Maciá, D. Curcó, R. Bringué, M. Iborra, F. Rodríguez-Ropero, N.F.A. Van Der Vegt, C. Aleman, 1-Butanol absorption in poly(styrene-divinylbenzene) ion exchange resins for catalysis, *Soft Matter*. 11 (2015) 9144–9149. <https://doi.org/10.1039/C5SM02168E>.
- [241] E. du Toit, W. Nicol, The rate inhibiting effect of water as a product on reactions catalysed by cation exchange resins: formation of mesityl oxide from acetone as case study, *Applied Catalysis A: General*. 277 (2004) 219–225. <https://doi.org/10.1016/j.apcata.2004.09.015>.
- [242] M.A. Pérez, R. Bringué, M. Iborra, J. Tejero, F. Cunill, Ion exchange resins as catalysts for the liquid-phase dehydration of 1-butanol to di-n-butyl ether, *Applied Catalysis A: General*. 482 (2014) 38–48. <https://doi.org/10.1016/j.apcata.2014.05.017>.
- [243] S. Liu, Y. Zhu, Y. Liao, H. Wang, Q. Liu, L. Ma, C. Wang, Advances in understanding the humins: Formation, prevention and application, *Applications in Energy and Combustion Science*. 10 (2022) 100062. <https://doi.org/10.1016/j.jaecs.2022.100062>.
- [244] Y. Wang, Y. Huang, L. Liu, L. He, T. Li, C. Len, W. Yang, Molecular Oxygen-Promoted Synthesis of Methyl Levulinate from 5-Hydroxymethylfurfural, *ACS Sustainable Chem. Eng.* 8 (2020) 14576–14583. <https://doi.org/10.1021/acssuschemeng.0c05527>.
- [245] S. Quereshi, E. Ahmad, K.K. Pant, S. Dutta, Insights into the metal salt catalyzed ethyl levulinate synthesis from biorenewable feedstocks, *Catalysis Today*. 291 (2017) 187–194. <https://doi.org/10.1016/j.cattod.2016.12.019>.
- [246] B. Torres-Olea, I. Fúnez-Núñez, C. García-Sancho, J.A. Cecilia, R. Moreno-Tost, P. Maireles-Torres, Production of Biofuels by 5-Hydroxymethylfurfural Etherification Using Ion-Exchange Resins as Solid Acid Catalysts, *Chem. Proc.* 2 (2020). <https://doi.org/10.3390/ECCS2020-07587>.
- [247] C. P.A., S. Darbha, Catalytic conversion of HMF into ethyl levulinate – A biofuel over hierarchical zeolites, *Catalysis Communications*. 140 (2020) 105998. <https://doi.org/10.1016/j.catcom.2020.105998>.
- [248] B. Srinivasa Rao, P. Krishna Kumari, D. Dhana Lakshmi, N. Lingaiah, One pot selective transformation of biomass derived chemicals towards alkyl levulinates over titanium exchanged heteropoly tungstate catalysts, *Catalysis Today*. 309 (2018) 269–275. <https://doi.org/10.1016/j.cattod.2017.05.040>.
- [249] Z. Wang, Q. Chen, Conversion of 5-hydroxymethylfurfural into 5-ethoxymethylfurfural and ethyl levulinate catalyzed by MOF-based heteropolyacid materials, *Green Chem*. 18 (2016) 5884–5889. <https://doi.org/10.1039/C6GC01206J>.
- [250] I. van Zandvoort, Y. Wang, C.B. Rasrendra, E.R.H. van Eck, P.C.A. Bruijninx, H.J. Heeres, B.M. Weckhuysen, Formation, Molecular Structure, and Morphology of Humins in Biomass Conversion: Influence of Feedstock and Processing Conditions, *ChemSusChem*. 6 (2013) 1745–1758. <https://doi.org/10.1002/cssc.201300332>.
- [251] X. Zheng, X. Gu, Y. Ren, Z. Zhi, X. Lu, Production of 5-hydroxymethyl furfural and levulinic acid from lignocellulose in aqueous solution and different solvents, *Biofuels*, *Bioprod. Bioref.* 10 (2016) 917–931. <https://doi.org/10.1002/bbb.1720>.
- [252] Z. Zhang, Synthesis of  $\gamma$ -Valerolactone from Carbohydrates and its Applications, *ChemSusChem*. 9 (2016) 156–171. <https://doi.org/10.1002/cssc.201501089>.
- [253] J. Wang, H. Cui, J. Wang, Z. Li, M. Wang, W. Yi, Kinetic insight into glucose conversion to 5-hydroxymethyl furfural and levulinic acid in LiCl·3H<sub>2</sub>O without additional catalyst, *Chemical Engineering Journal*. 415 (2021) 128922. <https://doi.org/10.1016/j.cej.2021.128922>.

- [254] N. Nikbin, S. Caratzoulas, D.G. Vlachos, A First Principles-Based Microkinetic Model for the Conversion of Fructose to 5-Hydroxymethylfurfural, *ChemCatChem*. 4 (2012) 504–511. <https://doi.org/10.1002/cctc.201100444>.
- [255] Y. Yang, M.M. Abu-Omar, C. Hu, Heteropolyacid catalyzed conversion of fructose, sucrose, and inulin to 5-ethoxymethylfurfural, a liquid biofuel candidate, *Applied Energy*. 99 (2012) 80–84. <https://doi.org/10.1016/j.apenergy.2012.04.049>.
- [256] M. Iborra, J. Tejero, C. Fité, E. Ramírez, F. Cunill, Liquid-phase synthesis of butyl levulinate with simultaneous water removal catalyzed by acid ion exchange resins, *Journal of Industrial and Engineering Chemistry*. 78 (2019) 222–231. <https://doi.org/10.1016/j.jiec.2019.06.011>.
- [257] P. Delgado, M.T. Sanz, S. Beltrán, Kinetic study for esterification of lactic acid with ethanol and hydrolysis of ethyl lactate using an ion-exchange resin catalyst, *Chemical Engineering Journal*. 126 (2007) 111–118. <https://doi.org/10.1016/j.cej.2006.09.004>.
- [258] Y. Xu, W. Dou, Y. Zhao, G. Huang, X. Ma, Kinetics Study for Ion-Exchange-Resin Catalyzed Hydrolysis of Methyl Glycolate, *Ind. Eng. Chem. Res.* 51 (2012) 11653–11658. <https://doi.org/10.1021/ie3004489>.
- [259] A. Chakrabarti, M.M. Sharma, Cationic ion exchange resins as catalyst, *Reactive Polymers*. 20 (1993) 1–45. [https://doi.org/10.1016/0923-1137\(93\)90064-M](https://doi.org/10.1016/0923-1137(93)90064-M).
- [260] S. Leveneur, C.A. De Araujo Filho, L. Estel, T. Salmi, Modeling of a Liquid–Liquid–Solid Heterogeneous Reaction System: Model System and Peroxyvaleric Acid, *Ind. Eng. Chem. Res.* 51 (2012) 189–201. <https://doi.org/10.1021/ie2017064>.
- [261] H. Ariba, Y. Wang, C. Devouge-Boyer, R.P. Stateva, S. Leveneur, Physicochemical Properties for the Reaction Systems: Levulinic Acid, Its Esters, and  $\gamma$ -Valerolactone, *J. Chem. Eng. Data*. 65 (2020) 3008–3020. <https://doi.org/10.1021/acs.jced.9b00965>.
- [262] W.E. Stewart, M. Caracotsios, Athena Visual Studio., (n.d.). <https://athenavisual.com/>.
- [263] W.E. Stewart, M. Caracotsios, *Computer-Aided Modeling of Reactive Systems*, Wiley & Sons: Hoboken, NJ, 2008.
- [264] W.E. Stewart, M. Caracotsios, J.P. Sørensen, Parameter estimation from multiresponse data, *AIChE J.* 38 (1992) 641–650. <https://doi.org/10.1002/aic.690380502>.
- [265] M.A.J.S. Boekel, Statistical Aspects of Kinetic Modeling for Food Science Problems, *J Food Science*. 61 (1996) 477–486. <https://doi.org/10.1111/j.1365-2621.1996.tb13138.x>.
- [266] M. Caracotsios, W.E. Stewart, Sensitivity analysis of initial value problems with mixed odes and algebraic equations, *Computers & Chemical Engineering*. 9 (1985) 359–365. [https://doi.org/10.1016/0098-1354\(85\)85014-6](https://doi.org/10.1016/0098-1354(85)85014-6).
- [267] G. Buzzi-Ferraris, Planning of experiments and kinetic analysis, *Catalysis Today*. 52 (1999) 125–132. [https://doi.org/10.1016/S0920-5861\(99\)00070-X](https://doi.org/10.1016/S0920-5861(99)00070-X).
- [268] S. Capecci, Y. Wang, J. Delgado, V. Casson Moreno, M. Mignot, H. Grénman, D.Y. Murzin, S. Leveneur, Bayesian Statistics to Elucidate the Kinetics of  $\gamma$ -Valerolactone from n-Butyl Levulinate Hydrogenation over Ru/C, *Ind. Eng. Chem. Res.* 31 (2021) 11725–11736. <https://doi.org/10.1021/acs.iecr.1c02107>.
- [269] F.E. Turkheimer, R. Hinz, V.J. Cunningham, On the Undecidability among Kinetic Models: From Model Selection to Model Averaging, *J Cereb Blood Flow Metab.* 23 (2003) 490–498. <https://doi.org/10.1097/01.WCB.0000050065.57184.BB>.
- [270] G. James, D. Witten, T. Hastie, R. Tibshirani, *An Introduction to Statistical Learning: with Applications in R*, Springer US, New York, NY, 2021. <https://doi.org/10.1007/978-1-0716-1418-1>.
- [271] S. Leveneur, Kinetic modelling: Regression and validation stages, a compulsory tandem for kinetic model assessment, *Can J Chem Eng.* (2023) cjce.24956. <https://doi.org/10.1002/cjce.24956>.
- [272] S. Zhao, G. Xu, C. Chang, S. Fang, Z. Liu, F. Du, Direct Conversion of Carbohydrates into Ethyl Levulinate with Potassium Phosphotungstate as an Efficient Catalyst, *Catalysts*. 5 (2015) 1897–1910. <https://doi.org/10.3390/catal5041897>.
- [273] M.M. Zainol, M. Asmadi, P. Iskandar, W.A.N. Wan Ahmad, N.A.S. Amin, T.T. Hoe, Ethyl levulinate synthesis from biomass derivative chemicals using iron doped sulfonated carbon cryogel catalyst, *Journal of Cleaner Production*. 281 (2021) 124686. <https://doi.org/10.1016/j.jclepro.2020.124686>.
- [274] B.A. Fachri, R.M. Abdilla, H.H. van de Bovenkamp, C.B. Rasrendra, H.J. Heeres, Experimental and Kinetic Modeling Studies on the Sulfuric Acid Catalyzed Conversion of D -Fructose to 5-



- Hydroxymethylfurfural and Levulinic Acid in Water, *ACS Sustainable Chem. Eng.* 3 (2015) 3024–3034. <https://doi.org/10.1021/acssuschemeng.5b00023>.
- [275] M. Bicker, D. Kaiser, L. Ott, H. Vogel, Dehydration of d-fructose to hydroxymethylfurfural in sub- and supercritical fluids, *The Journal of Supercritical Fluids.* 36 (2005) 118–126. <https://doi.org/10.1016/j.supflu.2005.04.004>.
- [276] C. Moreau, R. Durand, S. Razigade, J. Duhamet, P. Faugeras, P. Rivalier, P. Ros, G. Avignon, Dehydration of fructose to 5-hydroxymethylfurfural over H-mordenites, *Applied Catalysis A: General.* 145 (1996) 211–224. [https://doi.org/10.1016/0926-860X\(96\)00136-6](https://doi.org/10.1016/0926-860X(96)00136-6).
- [277] R. Koppram, E. Tomás-Pejó, C. Xiros, L. Olsson, Lignocellulosic ethanol production at high-gravity: challenges and perspectives, *Trends in Biotechnology.* 32 (2014) 46–53. <https://doi.org/10.1016/j.tibtech.2013.10.003>.
- [278] S. Sadula, A. Athaley, W. Zheng, M. Ierapetritou, B. Saha, Process Intensification for Cellulosic Biorefineries, *ChemSusChem.* 10 (2017) 2566–2572. <https://doi.org/10.1002/cssc.201700183>.
- [279] C. Xiros, M. Janssen, R. Byström, B.T. Børresen, D. Cannella, H. Jørgensen, R. Koppram, C. Larsson, L. Olsson, A. Tillman, S. Wännström, Toward a sustainable biorefinery using high-gravity technology, *Biofuels, Bioprod. Bioref.* 11 (2017) 15–27. <https://doi.org/10.1002/bbb.1722>.
- [280] E.S. Lopes, J.F. Leal Silva, E.C. Rivera, A.P. Gomes, M.S. Lopes, R. Maciel Filho, L.P. Tovar, Challenges to Levulinic Acid and Humins Valuation in the Sugarcane Bagasse Biorefinery Concept, *Bioenerg. Res.* 13 (2020) 757–774. <https://doi.org/10.1007/s12155-020-10124-9>.
- [281] X. Yu, L. Peng, J. Dai, H. Li, C. Tao, F. Yang, J. Zhang, Ethylene glycol co-solvent enhances alkyl levulinate production from concentrated feeds of sugars in monohydric alcohols, *Fuel.* 304 (2021) 121471. <https://doi.org/10.1016/j.fuel.2021.121471>.
- [282] D.E. Joiner, J. Billeter, M.E.P. McNally, R.M. Hoffman, P.J. Gemperline, Comprehensive kinetic model for the dissolution, reaction, and crystallization processes involved in the synthesis of aspirin: Kinetic model for dissolution, reaction, and crystallization processes, *J. Chemometrics.* 28 (2014) 420–428. <https://doi.org/10.1002/cem.2605>.
- [283] R.S. Assary, T. Kim, J.J. Low, J. Greeley, L.A. Curtiss, Glucose and fructose to platform chemicals: understanding the thermodynamic landscapes of acid-catalysed reactions using high-level ab initio methods, *Phys. Chem. Chem. Phys.* 14 (2012) 16603. <https://doi.org/10.1039/c2cp41842h>.
- [284] W. Deng, Q. Zhang, Y. Wang, Catalytic transformations of cellulose and its derived carbohydrates into 5-hydroxymethylfurfural, levulinic acid, and lactic acid, *Sci. China Chem.* 58 (2015) 29–46. <https://doi.org/10.1007/s11426-014-5283-8>.
- [285] J. He, L. Lin, M. Liu, C. Miao, Z. Wu, R. Chen, S. Chen, T. Chen, Y. Su, T. Zhang, W. Luo, A durable Ni/La-Y catalyst for efficient hydrogenation of  $\gamma$ -valerolactone into pentanoic biofuels, *Journal of Energy Chemistry.* 70 (2022) 347–355. <https://doi.org/10.1016/j.jechem.2022.02.011>.
- [286] M.H. Tucker, R. Alamillo, A.J. Crisci, G.M. Gonzalez, S.L. Scott, J.A. Dumesic, Sustainable Solvent Systems for Use in Tandem Carbohydrate Dehydration Hydrogenation, *ACS Sustainable Chem. Eng.* 1 (2013) 554–560. <https://doi.org/10.1021/sc400044d>.
- [287] W. Weiqi, W. Shubin, Experimental and kinetic study of glucose conversion to levulinic acid catalyzed by synergy of Lewis and Brønsted acids, *Chemical Engineering Journal.* 307 (2017) 389–398. <https://doi.org/10.1016/j.cej.2016.08.099>.
- [288] M. Sajid, U. Farooq, G. Bary, M.M. Azim, X. Zhao, Sustainable production of levulinic acid and its derivatives for fuel additives and chemicals: progress, challenges, and prospects, *Green Chem.* 23 (2021) 9198–9238. <https://doi.org/10.1039/D1GC02919C>.
- [289] S. Jiang, M. Liu, L. Pan, Kinetic study for hydrolysis of methyl lactate catalyzed by cation-exchange resin, *Journal of the Taiwan Institute of Chemical Engineers.* 41 (2010) 190–194. <https://doi.org/10.1016/j.jtice.2009.06.006>.
- [290] M.T. Sanz, R. Murga, S. Beltrán, J.L. Cabezas, J. Coca, Kinetic Study for the Reactive System of Lactic Acid Esterification with Methanol: Methyl Lactate Hydrolysis Reaction, *Ind. Eng. Chem. Res.* 43 (2004) 2049–2053. <https://doi.org/10.1021/ie034031p>.
- [291] Z.-M. Xu, J.-Y. Luo, Y.-B. Huang, Recent advances in the chemical valorization of cellulose and its derivatives into ester compounds, *Green Chemistry.* 24 (2022) 3895–3921. <https://doi.org/10.1039/d2gc00377e>.

- [292] J. Kopyscinski, J. Choi, J.M. Hill, Comprehensive kinetic study for pyridine hydrodenitrogenation on (Ni)WP/SiO<sub>2</sub> catalysts, *Applied Catalysis A: General*. 445–446 (2012) 50–60. <https://doi.org/10.1016/j.apcata.2012.08.027>.
- [293] X. Qi, M. Watanabe, T.M. Aida, R.L. Smith, Selective Conversion of D -Fructose to 5-Hydroxymethylfurfural by Ion-Exchange Resin in Acetone/Dimethyl sulfoxide Solvent Mixtures, *Ind. Eng. Chem. Res.* 47 (2008) 9234–9239. <https://doi.org/10.1021/ie801016s>.
- [294] P. Carniti, A. Gervasini, S. Biella, A. Auroux, Niobic acid and niobium phosphate as highly acidic viable catalysts in aqueous medium: Fructose dehydration reaction, *Catalysis Today*. 118 (2006) 373–378. <https://doi.org/10.1016/j.cattod.2006.07.024>.
- [295] C. Ma, B. Cai, L. Zhang, J. Feng, H. Pan, Acid-Catalyzed Conversion of Cellulose Into Levulinic Acid With Biphasic Solvent System, *Front. Plant Sci.* 12 (2021) 630807. <https://doi.org/10.3389/fpls.2021.630807>.
- [296] R.-J. van Putten, J.C. van der Waal, E. de Jong, C.B. Rasrendra, H.J. Heeres, J.G. de Vries, Hydroxymethylfurfural, A Versatile Platform Chemical Made from Renewable Resources, *Chem. Rev.* 113 (2013) 1499–1597. <https://doi.org/10.1021/cr300182k>.
- [297] J. Kim, J. Han, Simulation study of a strategy to produce gamma-valerolactone from ethyl levulinate, *Energy*. 163 (2018) 986–991. <https://doi.org/10.1016/j.energy.2018.08.170>.
- [298] C. López-Aguado, D.M. Del Monte, M. Paniagua, G. Morales, J.A. Melero, Techno-Economic Assessment of Conceptual Design for Gamma-Valerolactone Production over a Bifunctional Zr–Al–Beta Catalyst, *Ind. Eng. Chem. Res.* 61 (2022) 5547–5556. <https://doi.org/10.1021/acs.iecr.1c04644>.
- [299] R.P. Bangalore Ashok, P. Oinas, S. Forssell, Techno-economic evaluation of a biorefinery to produce  $\gamma$ -valerolactone (GVL), 2-methyltetrahydrofuran (2-MTHF) and 5-hydroxymethylfurfural (5-HMF) from spruce, *Renewable Energy*. 190 (2022) 396–407. <https://doi.org/10.1016/j.renene.2022.03.128>.
- [300] J. Kim, J. Byun, J. Han, Process integration and economics of gamma-valerolactone using a cellulose-derived ethyl levulinate intermediate and ethanol solvent, *Energy*. 239 (2022) 121964. <https://doi.org/10.1016/j.energy.2021.121964>.
- [301] European Commission, Stepping up Europe’s 2030 climate ambition Investing in a climate-neutral future for the benefit of our people ., (2020). <https://eur-lex.europa.eu/legal-content/EN/TXT/?uri=CELEX%3A52020DC0562>.
- [302] F. Cuevas, J. Zhang, M. Latroche, The Vision of France, Germany, and the European Union on Future Hydrogen Energy Research and Innovation, *Engineering*. 7 (2021) 715–718. <https://doi.org/10.1016/j.eng.2021.04.010>.
- [303] Agriscopie, Le lin en Normandie, (2022). [https://normandie.chambres-agriculture.fr/fileadmin/user\\_upload/Normandie/506\\_Fichiers-communs/PDF/AGRISCOPIE/lin.pdf](https://normandie.chambres-agriculture.fr/fileadmin/user_upload/Normandie/506_Fichiers-communs/PDF/AGRISCOPIE/lin.pdf).
- [304] L. Nuez, J. Beaugrand, D.U. Shah, C. Mayer-Laigle, A. Bourmaud, P. D’Arras, C. Baley, The potential of flax shives as reinforcements for injection moulded polypropylene composites, *Industrial Crops and Products*. 148 (2020) 112324. <https://doi.org/10.1016/j.indcrop.2020.112324>.
- [305] K. Ross, G. Mazza, Characteristics of Lignin from Flax Shives as Affected by Extraction Conditions, *IJMS*. 11 (2010) 4035–4050. <https://doi.org/10.3390/ijms11104035>.
- [306] AgroscoPie, La forêt et la filière bois en Normandie, (2022). [https://normandie.chambres-agriculture.fr/fileadmin/user\\_upload/Normandie/506\\_Fichiers-communs/PDF/AGRISCOPIE/foret.pdf](https://normandie.chambres-agriculture.fr/fileadmin/user_upload/Normandie/506_Fichiers-communs/PDF/AGRISCOPIE/foret.pdf).
- [307] A. Le Floch, M. Jourdes, P.-L. Teissedre, Polysaccharides and lignin from oak wood used in cooperage: Composition, interest, assays: A review, *Carbohydrate Research*. 417 (2015) 94–102. <https://doi.org/10.1016/j.carres.2015.07.003>.
- [308] R. Bodîrlău, C.A. Teacă, I. Spiridon, Chemical modification of beech wood: Effect on thermal stability, *BioRes*. 3 (2008) 789–800. <https://doi.org/10.15376/biores.3.3.789-800>.
- [309] FranceAgriMer, Évaluation des ressources agricoles et agroalimentaires disponibles en France – édition 2020, (2020).
- [310] C. Wang, Y. Kong, R. Hu, G. Zhou, Miscanthus: A fast-growing crop for environmental remediation and biofuel production, *GCB Bioenergy*. 13 (2021) 58–69.

- [311] I. Adesina, A. Bhowmik, H. Sharma, A. Shahbazi, A Review on the Current State of Knowledge of Growing Conditions, Agronomic Soil Health Practices and Utilities of Hemp in the United States, *Agriculture*. 10 (2020) 129. <https://doi.org/10.3390/agriculture10040129>.
- [312] ADEME, INDDIGO, A. Vitré, J.-B. Robin, I. Leduc, REFERENTIEL NATIONAL DES COUTS DU SERVICE PUBLIC DE PREVENTION ET DE GESTION DES DECHETS (Edition 2019), (2016).
- [313] UpCycle, Livre Blanc - Mettre en place le tri et la valorisation des biodéchets, (2019). <https://facile.upcycle.org/livre-blanc-mettre-en-place-le-tri-et-la-valorisation-des-biodechets>.
- [314] Biomasse Normandie, Observatoire des déchets, de la ressource et de l'économie circulaire en Normandie, (2020). <https://www.biomasse-normandie.fr/nos-domaines-dintervention/dechets/observatoire-des-dechets-en-normandie/>.
- [315] Biomasse Normandie, Région Normandie, ADEME, Observatoire des déchets de Normandie - Les déchets ménagers et assimilés en Normandie - Année 2018, Observatoire des déchets de Normandie. (2020).
- [316] Clean Hydrogen Partnership, Hydrogen valleys - Normandy Hydrogen, (2023). <https://h2v.eu/hydrogen-valleys/normandy-hydrogen>.
- [317] Région Normandie, Normandie Hydrogen - AN AMBITIOUS INITIATIVE CONTRIBUTING TO THE ENERGY TRANSITION, (2022). [https://www.normandie.fr/sites/default/files/2020-11/exe\\_plaquette\\_normandie\\_hydro\\_gb\\_web2.pdf](https://www.normandie.fr/sites/default/files/2020-11/exe_plaquette_normandie_hydro_gb_web2.pdf).
- [318] Surface en aires protégées terrestres en Normandie, (2022). <https://www.anbdd.fr/biodiversite/connaissance/les-indicateurs-normands-de-la-biodiversite/surfaces-en-aires-protgees-terrestres-en-normandie/>.
- [319] Conseil national de l'industrie, NOTRE AMBITION POUR L'INDUSTRIE - Conseil national de l'industrie, (2018). <https://www.economie.gouv.fr/conseil-national-industrie-2018#>.
- [320] J. Tan, Y. Li, X. Tan, H. Wu, H. Li, S. Yang, Advances in Pretreatment of Straw Biomass for Sugar Production, *Front. Chem.* 9 (2021) 696030. <https://doi.org/10.3389/fchem.2021.696030>.
- [321] L. Ou, C. Dou, J. Yu, H. Kim, Y. Park, S. Park, S. Kelley, E.Y. Lee, Techno-economic analysis of sugar production from lignocellulosic biomass with utilization of hemicellulose and lignin for high-value co-products, *Biofuels, Bioprod. Bioref.* 15 (2021) 404–415. <https://doi.org/10.1002/bbb.2170>.
- [322] A.A. Marianou, C.M. Michailof, A. Pineda, E.F. Iliopoulou, K.S. Triantafyllidis, A.A. Lappas, Glucose to Fructose Isomerization in Aqueous Media over Homogeneous and Heterogeneous Catalysts, *ChemCatChem*. 8 (2016) 1100–1110. <https://doi.org/10.1002/cctc.201501203>.
- [323] T.H. Kwan, K.L. Ong, M.A. Haque, S. Kulkarni, C.S.K. Lin, Biorefinery of food and beverage waste valorisation for sugar syrups production: Techno-economic assessment, *Process Safety and Environmental Protection*. 121 (2019) 194–208. <https://doi.org/10.1016/j.psep.2018.10.018>.
- [324] J.A. Conti Silva, L.M. Grilo, M.H. Vasconcelos, T.M. Lacerda, 13 - Levulinic acid: perspectives of its biobased production and most promising derivatives, in: A.K. Chandel, F. Segato (Eds.), *Production of Top 12 Biochemicals Selected by USDOE from Renewable Resources*, Elsevier, 2022: pp. 387–414. <https://doi.org/10.1016/B978-0-12-823531-7.00002-0>.
- [325] Observatoire de l'éolien 2021 - Analyse du marché, des emplois et des enjeux de l'éolien en France, (2021). [https://fee.asso.fr/wp-content/uploads/2021/09/ObsEol\\_2021\\_web\\_HD.pdf](https://fee.asso.fr/wp-content/uploads/2021/09/ObsEol_2021_web_HD.pdf).
- [326] H. Hersbach, B. Bell, P. Berrisford, G. Biavati, A. Horányi, J. Muñoz Sabater, J. Nicolas, C. Peubey, R. Radu, I. Rozum, D. Schepers, A. Simmons, C. Soci, D. Dee, J.-N. Thépaut, ERA5 hourly data on single levels from 1940 to present., (2023). DOI: 10.24381/cds.adbb2d47 (Accessed on 01-2023).
- [327] Z.R. Shu, M. Jesson, Estimation of Weibull parameters for wind energy analysis across the UK, *Journal of Renewable and Sustainable Energy*. 13 (2021) 023303. <https://doi.org/10.1063/5.0038001>.
- [328] M. Jamil, S. Parsa, M. Majidi, Wind power statistics and an evaluation of wind energy density, *Renewable Energy*. 6 (1995) 623–628. [https://doi.org/10.1016/0960-1481\(95\)00041-H](https://doi.org/10.1016/0960-1481(95)00041-H).
- [329] T.P. Chang, Performance comparison of six numerical methods in estimating Weibull parameters for wind energy application, *Applied Energy*. 88 (2011) 272–282. <https://doi.org/10.1016/j.apenergy.2010.06.018>.

- [330] W. Zhou, H. Yang, Z. Fang, Wind power potential and characteristic analysis of the Pearl River Delta region, China, *Renewable Energy*. 31 (2006) 739–753. <https://doi.org/10.1016/j.renene.2005.05.006>.
- [331] S.A. Akdağ, A. Dinler, A new method to estimate Weibull parameters for wind energy applications, *Energy Conversion and Management*. 50 (2009) 1761–1766. <https://doi.org/10.1016/j.enconman.2009.03.020>.
- [332] K.S.R. Murthy, O.P. Rahi, Estimation of Weibull parameters using graphical method for wind energy applications, in: 2014 Eighteenth National Power Systems Conference (NPSC), IEEE, Guwahati, India, 2014: pp. 1–6. <https://doi.org/10.1109/NPSC.2014.7103858>.
- [333] E. Dallavalle, M. Cipolletta, V. Casson Moreno, V. Cozzani, B. Zanuttigh, Towards green transition of touristic islands through hybrid renewable energy systems. A case study in Tenerife, Canary Islands, *Renewable Energy*. 174 (2021) 426–443. <https://doi.org/10.1016/j.renene.2021.04.044>.
- [334] The MathWorks, Inc., Three-Parameter Weibull Distribution, (2023). <https://it.mathworks.com/help/stats/three-parameter-weibull-distribution.html>.
- [335] The MathWorks, Inc., MATLAB and Simulink - release R2023a, (2023). [https://it.mathworks.com/?s\\_tid=gn\\_logo](https://it.mathworks.com/?s_tid=gn_logo).
- [336] M. Huaiquan Zhang, Wind Resource Assessment and Micro-siting, Science and Engineering, China Machine Press, Singapore, 2015.
- [337] Éolien terrestre - Ministères Écologie Énergie Territoires, (n.d.). <https://www.ecologie.gouv.fr/eolien-terrestre>.
- [338] VESTAS, 2 MW platform -Datasheet, (2023). <https://www.vestas.com/en/products/2-mw-platform/V110-2-0-mw>.
- [339] G. Costanzo, G. Brindley, P. Cole, Wind energy in Europe - 2022 Statistics and the outlook for 2023-2027, (2023).
- [340] P.-S.E. Dai, L.D. Neff, K.L. Preston, R.-Y.J. Hwan, CATALYTIC DECOMPOSITION OF FORMATE IMPURITIES INTERTARY BUTYLALCOHOL AND METHYL TERTARY BUTYL ETHER STREAMS, Patent Number: 5,723,698, 1998.
- [341] T. Turek, D.L. Trimm, N.W. Cant, The Catalytic Hydrogenolysis of Esters to Alcohols, *Catalysis Reviews*. 36 (1994) 645–683. <https://doi.org/10.1080/01614949408013931>.
- [342] AspenTech, Aspen HYSYS, version 11, (2020). <https://www.aspentech.com/en/products/engineering/aspen-hysys>.
- [343] J.F. Leal Silva, A.P. Mariano, R. Maciel Filho, Economic potential of 2-methyltetrahydrofuran (MTHF) and ethyl levulinate (EL) produced from hemicelluloses-derived furfural, *Biomass and Bioenergy*. 119 (2018) 492–502. <https://doi.org/10.1016/j.biombioe.2018.10.008>.
- [344] W-tech, Axial Open Type Cooling Tower - datasheet, (2022). <https://www.w-tech.it/wp-content/uploads/2019/04/TC-TAA-ITA-ENG-R011-MAGNELIS.pdf>.
- [345] B. Esteves, U. Sen, H. Pereira, Influence of Chemical Composition on Heating Value of Biomass: A Review and Bibliometric Analysis, *Energies*. 16 (2023) 4226. <https://doi.org/10.3390/en16104226>.
- [346] A. Muralidhara, P. Tosi, A. Mija, N. Sbirrazzuoli, C. Len, V. Engelen, E. De Jong, G. Marlair, Insights on Thermal and Fire Hazards of Humins in Support of Their Sustainable Use in Advanced Biorefineries, *ACS Sustainable Chem. Eng.* 6 (2018) 16692–16701. <https://doi.org/10.1021/acssuschemeng.8b03971>.
- [347] Electricity Data Explorer-Open Source -Global Electricity Data Ember, EMBER. (2023). [ember-climate.org](https://ember-climate.org).
- [348] IEA, World Energy Outlook 2020, Paris, 2020. <https://www.iea.org/reports/world-energy-outlook-2020>.
- [349] Y. Xia, H. Cheng, H. He, W. Wei, Efficiency and consistency enhancement for alkaline electrolyzers driven by renewable energy sources, *Commun Eng.* 2 (2023) 22. <https://doi.org/10.1038/s44172-023-00070-7>.
- [350] J.C. Ehlers, A.A. Feidenhans'l, K.T. Therkildsen, G.O. Larrazábal, Affordable Green Hydrogen from Alkaline Water Electrolysis: Key Research Needs from an Industrial Perspective, *ACS Energy Lett.* 8 (2023) 1502–1509. <https://doi.org/10.1021/acsenenergylett.2c02897>.

- [351] R. Bhandari, C.A. Trudewind, P. Zapp, Life cycle assessment of hydrogen production via electrolysis – a review, *Journal of Cleaner Production*. 85 (2014) 151–163. <https://doi.org/10.1016/j.jclepro.2013.07.048>.
- [352] Hydrogen from renewable power: Technology outlook for the energy transition, IRENA, International Renewable Energy Agency, Abu Dhabi, 2018.
- [353] H.W. Langmi, N. Engelbrecht, P.M. Modisha, D. Bessarabov, Hydrogen storage, in: *Electrochemical Power Sources: Fundamentals, Systems, and Applications*, Elsevier, 2022: pp. 455–486. <https://doi.org/10.1016/B978-0-12-819424-9.00006-9>.
- [354] O. Rambert, L. Febvre, The challenges of Hydrogen Storage on a large scale, *International Conference on Hydrogen Safety*. (2021).
- [355] M.-R. Tahan, Recent advances in hydrogen compressors for use in large-scale renewable energy integration, *International Journal of Hydrogen Energy*. 47 (2022) 35275–35292. <https://doi.org/10.1016/j.ijhydene.2022.08.128>.
- [356] M. Gardiner, Energy requirements for hydrogen gas compression and liquefaction as related to vehicle storage needs, DOE, 2009.
- [357] Z. Abdin, C. Tang, Y. Liu, K. Catchpole, Large-scale stationary hydrogen storage via liquid organic hydrogen carriers, *iScience*. 24 (2021) 102966. <https://doi.org/10.1016/j.isci.2021.102966>.
- [358] M. Yue, H. Lambert, E. Pahon, R. Roche, S. Jemei, D. Hissel, Hydrogen energy systems: A critical review of technologies, applications, trends and challenges, *Renewable and Sustainable Energy Reviews*. 146 (2021) 111180. <https://doi.org/10.1016/j.rser.2021.111180>.
- [359] Zulfhazli, A.R. Keeley, S. Takeda, S. Managi, A systematic review of the techno-economic assessment of various hydrogen production methods of power generation, *Front. Sustain*. 3 (2022) 943145. <https://doi.org/10.3389/frsus.2022.943145>.
- [360] Y. Sanghai, Techno-Economic Analysis of Hydrogen Fuel Cell Systems Used as an Electricity Storage Technology in a Wind Farm with Large Amounts of Intermittent Energy, Masters Theses 1911 - February 2014, University of Massachusetts Amherst, 2013.
- [361] M. Patel, S. Roy, A.P. Roskilly, A. Smallbone, The techno-economics potential of hydrogen interconnectors for electrical energy transmission and storage, *Journal of Cleaner Production*. 335 (2022) 130045. <https://doi.org/10.1016/j.jclepro.2021.130045>.
- [362] D. McLarty, J. Brouwer, C. Ainscough, Economic analysis of fuel cell installations at commercial buildings including regional pricing and complementary technologies, *Energy and Buildings*. 113 (2016) 112–122. <https://doi.org/10.1016/j.enbuild.2015.12.029>.
- [363] J. Park, K.H. Law, Layout optimization for maximizing wind farm power production using sequential convex programming, *Applied Energy*. 151 (2015) 320–334. <https://doi.org/10.1016/j.apenergy.2015.03.139>.
- [364] G.P. Towler, R.K. Sinnott, *Chemical engineering design: principles, practice and economics of plant and process design*, Elsevier/Butterworth-Heinemann, Amsterdam ; Boston, 2008.
- [365] V. Casson Moreno, G. Iervolino, A. Tugnoli, V. Cozzani, Techno-economic and environmental sustainability of biomass waste conversion based on thermocatalytic reforming, *Waste Management*. 101 (2020) 106–115. <https://doi.org/10.1016/j.wasman.2019.10.002>.
- [366] M. Carlini, E. Mosconi, S. Castellucci, M. Villarini, A. Colantoni, An Economical Evaluation of Anaerobic Digestion Plants Fed with Organic Agro-Industrial Waste, *Energies*. 10 (2017) 1165. <https://doi.org/10.3390/en10081165>.
- [367] Discount rates for low-carbon and renewable generation technologies, Oxera, 2011.
- [368] Renewable energy discount rate survey results - 2018, Grant Thornton, 2018. <https://www.grantthornton.co.uk/insights/renewable-energy-discount-rate-survey/>.
- [369] IEA, Global average levelised cost of hydrogen production by energy source and technology, 2019 and 2050, IEA, Paris, n.d. <https://www.iea.org/data-and-statistics/charts/global-average-levelised-cost-of-hydrogen-production-by-energy-source-and-technology-2019-and-2050>.
- [370] Global hydrogen trade to meet the 1.5°C climate goal: Part III – Green hydrogen cost and potential, IRENA, International Renewable Energy Agency, Abu Dhabi, 2022.
- [371] Aspen Technology Inc, Aspen Process Economic Analyzer, (2023). <https://www.aspentech.com/en/products/engineering/aspen-process-economic-analyzer>.
- [372] S. Jenkins, 2022 CEPCI updates: June (prelim.) and May (final), *Chemical Engineering*. (2022). <https://www.chemengonline.com/2022-cepci-updates-june-prelim-and-may-final/>.

- [373] J. Haydary, *Chemical Process Design and Simulation: Aspen Plus and Aspen Hysys Applications*, John Wiley & Sons, Inc., Hoboken, NJ, USA, 2018. <https://doi.org/10.1002/9781119311478>.
- [374] T.A. Adams, *Learn Aspen Plus in 24 hours*, McGraw Education, New York, 2018.
- [375] M.S. Peters, K.D. Timmerhaus, *Plant Design and Economics for Chemical Engineers*, 4th Edition, McGraw Hill - International Editions, 1991.
- [376] *France 2030 : un plan d'investissement pour la France*, Gouvernement - Le ministère de l'Économie, des Finances et de la Souveraineté industrielle et numérique, 2022. <https://www.economie.gouv.fr/france-2030#>.
- [377] ADEME, *France 2030 – AAP AIDE A L'INVESTISSEMENT DE L'OFFRE INDUSTRIELLE DES ENERGIES RENOUVELABLES*, (2022). <https://agirpouurlatransition.ademe.fr/entreprises/aides-financieres/20220210/aide-a-linvestissement-loffre-industrielle-energies-renouvelables>.
- [378] Hourly labour costs EU, EUROSTAT, 2022. [https://ec.europa.eu/eurostat/statistics-explained/index.php?title=Hourly\\_labour\\_costs](https://ec.europa.eu/eurostat/statistics-explained/index.php?title=Hourly_labour_costs).
- [379] R. Wiser, M. Bolinger, B. Hoen, D. Millstein, J. Rand, G. Barbose, N. Darghouth, W. Gorman, S. Jeong, B. Paulos, *Land-Based Wind Market Report: 2022 Edition*, Office of the U.S. Department of Energy's Office of Energy Efficiency and Renewable Energy, 2022.
- [380] D. Feldman, V. Ramasamy, R. Fu, A. Ramdas, J. Desai, R. Margolis, *U.S. Solar Photovoltaic System and Energy Storage Cost Benchmark (Q1 2020)*, National Renewable Energy Laboratory, 2021. <https://doi.org/10.2172/1764908>.
- [381] N.R. Baral, A. Shah, *Techno-Economic Analysis of Cellulosic Butanol Production from Corn Stover through Acetone–Butanol–Ethanol Fermentation*, *Energy Fuels*. 30 (2016) 5779–5790. <https://doi.org/10.1021/acs.energyfuels.6b00819>.
- [382] J. Byun, J. Han, *Catalytic conversion of corn stover for  $\gamma$ -valerolactone production by two different solvent strategies: Techno-economic assessment*, *Energy*. 175 (2019) 546–553. <https://doi.org/10.1016/j.energy.2019.03.070>.
- [383] *Path to hydrogen competitiveness A cost perspective*, Hydrogen Council, 2020. [www.hydrogencouncil.com](http://www.hydrogencouncil.com).
- [384] M. Muron, G. Pawelec, S. Jackson, I.-P. Yovchev, *CLEAN HYDROGEN MONITOR*, Hydrogen Europe, 2022. <https://hydrogeneurope.eu/clean-hydrogen-monitor2022/>.
- [385] J. Fernández Méndez, F. Farfan Orozco, M. Ladero Galán, H. Grénman, *Techno-economic evaluation of obtaining valuable rare sugars from thermo-mechanical pulping side streams utilizing the latest technology*, *Chemical Engineering Journal*. 455 (2023) 140852. <https://doi.org/10.1016/j.cej.2022.140852>.
- [386] M. Wawrzkiwicz, E. Polska-Adach, *Physicochemical Interactions in Systems C.I. Direct Yellow 50—Weakly Basic Resins: Kinetic, Equilibrium, and Auxiliaries Addition Aspects*, *Water*. 13 (2021) 385. <https://doi.org/10.3390/w13030385>.
- [387] T. Ogawa, M. Yoshida, K. Ishihara N., *Techno-economic analysis on recent heterogeneous catalysts for ammonia synthesis*, *Chemistry*, 2022. <https://doi.org/10.26434/chemrxiv-2022-1vs9p>.
- [388] F.G. Baddour, L. Snowden-Swan, J.D. Super, K.M. Van Allsburg, *Estimating Precommercial Heterogeneous Catalyst Price: A Simple Step-Based Method*, *Org. Process Res. Dev.* 22 (2018) 1599–1605. <https://doi.org/10.1021/acs.oprd.8b00245>.
- [389] *Kisuma Chemicals – DHT-4A*, Kisuma Chemicals – Continuity through Innovation. (2023). <https://webshop.kisuma.com/dht-4a.html>.
- [390] *Electricity prices for non-household consumers, second half 2022*, (2022). [https://ec.europa.eu/eurostat/statistics-explained/index.php?title=Electricity\\_price\\_statistics#Electricity\\_prices\\_for\\_non-household\\_consumers](https://ec.europa.eu/eurostat/statistics-explained/index.php?title=Electricity_price_statistics#Electricity_prices_for_non-household_consumers).
- [391] *Natural gas prices for non-household consumers, second half 2022*, (2022). [https://ec.europa.eu/eurostat/statistics-explained/index.php?title=Natural\\_gas\\_price\\_statistics#Natural\\_gas\\_prices\\_for\\_non-household\\_consumers](https://ec.europa.eu/eurostat/statistics-explained/index.php?title=Natural_gas_price_statistics#Natural_gas_prices_for_non-household_consumers).

- [392] C. Kang, J.J. Liu, N. Woo, W. Won, Process Design for the Sustainable Production of Butyric Acid Using Techno-Economic Analysis and Life Cycle Assessment, *ACS Sustainable Chem. Eng.* 11 (2023) 4430–4440. <https://doi.org/10.1021/acssuschemeng.2c07372>.
- [393] W.D. Seider, J.D. Seader, D.R. Lewin, S. Widagolo, *Product and Process Design Principles - Synthesis, Analysis, and Evaluation*, 3rd Edition, John Wiley & Sons, Inc., United States of America, 2009.
- [394] A. Uihlein, L. Schebek, Environmental impacts of a lignocellulose feedstock biorefinery system: An assessment, *Biomass and Bioenergy*. 33 (2009) 793–802. <https://doi.org/10.1016/j.biombioe.2008.12.001>.
- [395] Z.J.N. Steinmann, A.M. Schipper, M. Hauck, M.A.J. Huijbregts, How Many Environmental Impact Indicators Are Needed in the Evaluation of Product Life Cycles?, *Environ. Sci. Technol.* 50 (2016) 3913–3919. <https://doi.org/10.1021/acs.est.5b05179>.
- [396] M.A.J. Huijbregts, S. Hellweg, R. Frischknecht, H.W.M. Hendriks, K. Hungerbühler, A.J. Hendriks, Cumulative Energy Demand As Predictor for the Environmental Burden of Commodity Production, *Environ. Sci. Technol.* 44 (2010) 2189–2196. <https://doi.org/10.1021/es902870s>.
- [397] F. Cherubini, G.P. Peters, T. Berntsen, A.H. Strømman, E. Hertwich, CO<sub>2</sub> emissions from biomass combustion for bioenergy: atmospheric decay and contribution to global warming: GLOBAL WARMING POTENTIAL OF CO<sub>2</sub> FROM BIOENERGY, *GCB Bioenergy*. 3 (2011) 413–426. <https://doi.org/10.1111/j.1757-1707.2011.01102.x>.
- [398] W. Liu, Z. Zhang, X. Xie, Z. Yu, K. Von Gadow, J. Xu, S. Zhao, Y. Yang, Analysis of the Global Warming Potential of Biogenic CO<sub>2</sub> Emission in Life Cycle Assessments, *Sci Rep.* 7 (2017) 39857. <https://doi.org/10.1038/srep39857>.
- [399] F. Cherubini, N.D. Bird, A. Cowie, G. Jungmeier, B. Schlamadinger, S. Woess-Gallasch, Energy- and greenhouse gas-based LCA of biofuel and bioenergy systems: Key issues, ranges and recommendations, *Resources, Conservation and Recycling*. 53 (2009) 434–447. <https://doi.org/10.1016/j.resconrec.2009.03.013>.
- [400] P. Garrett, P. Razdan, Life Cycle Assessment of Electricity Production From an Onshore V110-2.0 MW Wind Plant, Vestas Wind Systems A/S, Hedeager 42, Aarhus N, 8200, Denmark, 2015.
- [401] B. Parkinson, P. Balcombe, J.F. Speirs, A.D. Hawkes, K. Hellgardt, Levelized cost of CO<sub>2</sub> mitigation from hydrogen production routes, *Energy Environ. Sci.* 12 (2019) 19–40. <https://doi.org/10.1039/C8EE02079E>.
- [402] D.A. Notter, K. Kouravelou, T. Karachalios, M.K. Daletou, N.T. Haberland, Life cycle assessment of PEM FC applications: electric mobility and  $\mu$ -CHP, *Energy Environ. Sci.* 8 (2015) 1969–1985. <https://doi.org/10.1039/C5EE01082A>.
- [403] U.S. Environmental Protection Agency, Washington, DC. U.S. EPA, Annexes to the Inventory of U.S. GHG Emissions and Sinks: 1990-2020. Annex 2. Carbon Content Coefficients and Underlying Data for Petroleum Products, (2022).
- [404] J. Diab, L. Fulcheri, V. Hessel, V. Rohani, M. Frenklach, Why turquoise hydrogen will Be a game changer for the energy transition, *International Journal of Hydrogen Energy*. 47 (2022) 25831–25848. <https://doi.org/10.1016/j.ijhydene.2022.05.299>.
- [405] V. Casson Moreno, V. Cozzani, Major accident hazard in bioenergy production, *Journal of Loss Prevention in the Process Industries*. 35 (2015) 135–144. <https://doi.org/10.1016/j.jlp.2015.04.004>.
- [406] V.C. Casson Moreno, A.L. Garbetti, S. Leveneur, G. Antonioni, A consequences-based approach for the selection of relevant accident scenarios in emerging technologies, *Safety Science*. 112 (2019) 142–151. <https://doi.org/10.1016/j.ssci.2018.10.024>.
- [407] G.E. Scarponi, D. Guglielmi, V. Casson Moreno, V. Cozzani, Assessment of inherently safer alternatives in biogas production and upgrading, *AIChE J.* 62 (2016) 2713–2727. <https://doi.org/10.1002/aic.15224>.
- [408] A. Tugnoli, V. Cozzani, G. Landucci, A consequence based approach to the quantitative assessment of inherent safety, *AIChE J.* 53 (2007) 3171–3182. <https://doi.org/10.1002/aic.11315>.
- [409] P.A.M. Uijt de Haag, B.J.M. Ale, *Guidelines for Quantitative Risk Assessment (Purple Book)*, (1999).
- [410] C. Delvosalle, C. Fievez, A. Pipart, B. Debray, ARAMIS project: A comprehensive methodology for the identification of reference accident scenarios in process industries, *Journal of Hazardous Materials*. 130 (2006) 200–219. <https://doi.org/10.1016/j.jhazmat.2005.07.005>.

- [411] C.J.H. Van den Bosch, R.A.P.M. Weterings, *Methods for the Calculation of Physical Effects : Due to Releases of Hazardous Materials (Liquids and Gases)*. Yellow Book. CPR 14E, (1997).
- [412] C. Wulf, M. Haase, M. Baumann, P. Zapp, Weighting factor elicitation for sustainability assessment of energy technologies, *Sustainable Energy Fuels*. 7 (2023) 832–847. <https://doi.org/10.1039/D2SE01170K>.
- [413] I. Juwana, N. Muttill, B.J.C. Perera, Indicator-based water sustainability assessment — A review, *Science of The Total Environment*. 438 (2012) 357–371. <https://doi.org/10.1016/j.scitotenv.2012.08.093>.
- [414] H.V. Rowley, G.M. Peters, S. Lundie, S.J. Moore, Aggregating sustainability indicators: Beyond the weighted sum, *Journal of Environmental Management*. 111 (2012) 24–33. <https://doi.org/10.1016/j.jenvman.2012.05.004>.
- [415] N.L. Pollesch, V.H. Dale, Normalization in sustainability assessment: Methods and implications, *Ecological Economics*. 130 (2016) 195–208. <https://doi.org/10.1016/j.ecolecon.2016.06.018>.
- [416] S.R. Sousa, S.R. Soares, N.G. Moreira, R.M. Severis, L.A. De Santa-Eulalia, Internal Normalization Procedures in the Context of LCA: A Simulation-Based Comparative Analysis, *Environ Model Assess*. 26 (2021) 271–281. <https://doi.org/10.1007/s10666-021-09767-5>.
- [417] E. Ekener, J. Hansson, A. Larsson, P. Peck, Developing Life Cycle Sustainability Assessment methodology by applying values-based sustainability weighting - Tested on biomass based and fossil transportation fuels, *Journal of Cleaner Production*. 181 (2018) 337–351. <https://doi.org/10.1016/j.jclepro.2018.01.211>.
- [418] K. Hacatoglu, *A Systems Approach to Assessing the Sustainability of Hybrid Community Energy Systems*, (n.d.).
- [419] DNV-GL, PHAST - Process Hazards Analysis Software, version 8.4, (2021). <https://www.dnv.com/software/services/plant/consequence-analysis-phast.html>.
- [420] M.B. Kokare, R. V, C.S. Mathpati, Response surface optimization, kinetic study and process design of n-butyl levulinate synthesis, *Chemical Engineering Research and Design*. 137 (2018) 577–588. <https://doi.org/10.1016/j.cherd.2018.07.036>.
- [421] H.J. Bart, J. Reidetschlager, K. Schatka, A. Lehmann, Kinetics of esterification of levulinic acid with n-butanol by homogeneous catalysis, *Ind. Eng. Chem. Res*. 33 (1994) 21–25. <https://doi.org/10.1021/ie00025a004>.
- [422] R. Konaka, T. Takahashi, A Study of Reaction Rates. Esterification of Formic Acid with Ethanol, *Ind. Eng. Chem*. 52 (1960) 125–130. <https://doi.org/10.1021/ie50602a027>.
- [423] E.R. Sacia, M. Balakrishnan, A.T. Bell, Biomass conversion to diesel via the etherification of furanyl alcohols catalyzed by Amberlyst-15, *Journal of Catalysis*. 313 (2014) 70–79. <https://doi.org/10.1016/j.jcat.2014.02.012>.



# Symbols and Units

$AIC$	Akaike information criterion index
$\hat{C}_{iu}$	Estimated concentration of specie $i$ [mol/L]
$C_{iu}$	Experimental concentration of specie $I$ [mol/L]
$C_{v(K)}$	Cross-Validation (K-folds)
$E_{a_i}$	Activation energy of reaction $i$ [J/mol]
$k_i$	Rate constant of reaction $i$
$k_d$	Dissolution rate constant
$K_i$	Equilibrium constant of reaction $i$
$m_{\text{driedCat}}$	Dry catalyst mass [g]
$m_j$	Mass of $j$ [g]
$M_j$	Molecular weight of species $j$ [g/mol]
$[H^+]$	Molar concentration of protons [mol/L]
$[Prot]$	Proton concentration [mol/L]
$R_i$	Reaction rate $i$ [mol/L/min]
$r_d$	Dissolution reaction rate [mol/L/min]
$R$	Gas constant [J/K/mol]
$R^2$	Determination coefficient
$\rho_j$	Density of species $j$ [g/L]
$T$	Temperature [K]
$T_{\text{ref}}$	Reference temperature [K]
$V_{\text{Initial/Final}}$	Initial and final volume [L]
$V_{\text{Liquid}}$	Volume of reaction liquid [L]
$V_{\text{Reaction}}$	Reaction volume [L]
$v_{ij}$	Covariance matrix element
$ v $	Determinant of the covariance matrix of responses

$X_j$	Conversion of j
$Y_j$	Yield of j
$c$	Scale parameter (Weibull distribution) [m/s]
$C_f$	Credit factor
$CAPEX$	Capital cost [€]
$Deprec.$	Depreciation [€/y]
$f_{fossil}$	Fossil emission factor
$f_{biogenic}$	Biogenic emission factor
$F_n$	Cash flow [€/y]
$FHI$	Overall flammable inherent hazard index [m <sup>2</sup> /y]
$HI$	Overall inherent hazard index [m <sup>2</sup> /y]
$h_{i,j}$	Damage distance for the i-th PU and j-th LOC [m]
$f_{i,j}/t_{i,j}$	Flammability/Toxicity damage distance for the i-th PU and j-th LOC [m]
$k$	Shape parameter (Weibull distribution)
$LGHG$	Levelized greenhouse gas emission [t-CO <sub>2</sub> eq./Kg]
$OPEX$	Operating cost [€/y]
$NPV$	Net present value (€)
$CF$	Capacity Factor
$r$	Discount rate
$P$	Operation Probability (%)
$PI$	Overall potential hazard index [m <sup>2</sup> ]
$PUI$	Process unit inventory [m <sup>3</sup> ]
$Tax$	Taxation [€/y]
$THI$	Overall toxic inherent hazard index (m <sup>2</sup> /y)
$UPI_i$	Unit potential hazard index [m <sup>2</sup> ]
$UHI_i$	Unit inherent hazard index [m <sup>2</sup> /y]
$UFHI_i$	Unit flammable inherent hazard index [m <sup>2</sup> /y]

$UTHI_i$	Unit toxic inherent hazard index [ $m^2/y$ ]
$v$	Wind speed [m/s]
$v_c$	Wind cut-in speed [m/s]
$v_f$	Wind cut-off speed [m/s]
$v_{mean}$	Mean wind speed [m/s]
$v_r$	Rated wind speed [m/s]
$v_{mp}$	Most probable wind speed [m/s]
$v_{max-E}$	Maximum energy wind speed [m/s]
$\dot{V}_l$	Flow rate to the unit [ $m^3/s$ ]
$WPD$	Wind power density [ $W/m^2$ ]

# Abbreviations

AEL	Alkaline Electrolyzer
AIC	Akaike information criterion
AL	Alkyl Levulinate
ASI	Aggregated Sustainability Index
BF	Butyl formate
ButylFRUCT	Butylfructoside
BHP	Butyl-4-hydroxyvalerate
BL	Butyl levulinate
5-BMF/BMF	5-(butoxymethyl)furfural
BuOH	Butanol
Cat.	Catalyst (Amberlite IR120)
DD	Damage distance
5-EMF	5-(ethoxymethyl)furfural
Exp.	Experiment
FA	Formic acid
FRUCT	Fructose
FRUCTfur	Fructofuranose
GC	Gas chromatography
GVL	$\gamma$ -valerolactone
HydESS	Hydrogen Energy Storage System
HPD	High posterior density
HPS	Hybrid power System
5-HMF/HMF	5-(hydroxymethyl)furfural
HPLC	High-performance liquid chromatography
INT1	Intermediate 1

LA	Levulinic acid
LCB	Lignocellulosic Biomass
LOC	Loss of containment
MCDA	Multi criteria decision analysis
MILP	Mixed integer linear programming
ODEs	Ordinary differential equation system
OF	Objective function
PEM	Proton Exchange Membrane Electrolyzer
PEM-FC	Proton Exchange Membrane-Fuel Cell
Prot.	Protons
PSD	Particle size distribution
PtG	Power-to-Gas
PUI	Process unit inventory
Reg.	Regression
RES	Renewable energy source
SCEN	Scenario
Sim.	Simulation
SSR	Sum of squared residuals
SAT.	Saturation
Val.	Validation
WT(s)	Wind turbine(s)

# List of Figures

Fig. 1: (a)Global primary energy consumption [4]; (b) Global energy investment in clean and fossil energy, 2015-2023[5]	1
Fig. 2: Lignocellulosic biomass bio-components and conversion pathways.	4
Fig. 3: Conversion pathway via hexose sugars solvolysis	5
Fig. 4: Pentose sugars pathway to alkyl levulinates and levulinic acid	6
Fig. 5: Main pathway for GVL production by hydrogenation and its potential applications	16
Fig. 6: Hydrogen colours based on process and raw materials	22
Fig. 7: Figurative representation of a hydrogen energy storage system (HydESS).	26
Fig. 8: Setup of the autoclave for solvolysis experiment	36
Fig. 9: Reaction steps for the fructose alcoholysis in acid-catalyzed system.	40
Fig. 10: Effect of the stirring rate on the concentrations (normalized with respect to the fructose concentration at time zero): (A) fructose, (B) 5-HMF, (C) BMF, and (D) BL.	41
Fig. 11: Effect of catalyst PSD on the concentrations (normalized with respect to the fructose concentration at time zero): (A) fructose, (B) 5-HMF, (C) 5-BMF, and (D) BL	42
Fig. 12: Effect of water concentration on the concentrations (normalized with respect to the fructose concentration at time zero): (A) fructose, (B) 5-HMF, (C) 5-BMF, and (D) BL	44
Fig. 13: Effect of GVL concentration on the concentrations (normalized with respect to the fructose concentration at time zero): (A) fructose, (B) 5-HMF, (C) 5-BMF, and (D) BL.	46
Fig. 14: Effect of BuOH/GVL concentration on the concentrations (normalized with respect to the fructose concentration at time zero): (A) fructose, (B) 5-HMF, (C) BMF, and (D) BL	47
Fig. 15: Fructose dissolution in pure butanol and GVL/BuOH (30/70 wt%) solvents versus temperature	48
Fig. 16: Methodology adopted in Chapter 3	51
Fig. 17: Effect of temperature on the kinetics of 5-HMF solvolysis: (A) 5-HMF, (B) LA, (C) 5-BMF, (D) BL, (E) BF.	56
Fig. 18: Effect of catalyst loading on the kinetics of 5-HMF solvolysis: (A) 5-HMF, (B) LA, (C) 5-BMF, (D) BL, (E) BF	57
Fig. 19: Effect of 5-HMF loading on the kinetics of solvolysis: (A) 5-HMF, (B) LA, (C) 5-BMF, (D) BL, (E) BF	58
Fig. 20: Effect of temperature on LA and FA esterification kinetics.	59
Fig. 21: Simplified 6-step reaction mechanism for the butanolysis of 5-HMF.	60
Fig. 22: 8-step reaction mechanism for the butanolysis of 5-HMF with Int1	61
Fig. 23: Fit of Model 3 to experimental concentrations (Experiment 8); (A)5-HMF, 5-BMF; (B) LA, BF; (C) BL	68
Fig. 24: Fit of Model 3 to experimental concentrations (Experiment 3); (A)5-HMF, 5-BMF; (B) LA, BF; (C) BL	69
Fig. 25 Fit of Model 3 to experimental concentrations (Experiment 18); (A)5-HMF, 5-BMF; (B) LA, BF; (C) BL	69

Fig. 26: Fit of Model 3 to experimental concentrations (Experiment 14)	70
Fig. 27: overall graph of the 4 models against the 3 indices analyzed in the evaluation	72
Fig. 28: Methodology approach used in Chapter 4	75
Fig. 29: Schematic illustration of an apparatus for solubility.	79
Fig. 30. Effect of temperature on normalized compounds trends on fructose initial concentration. Fructose (A), 5-HMF (B), LA (C), 5-BMF (D), BL (E), BF (F).	81
Fig. 31. Effect of catalyst loadings on normalized compounds trends on fructose initial concentration. Fructose (A), 5-HMF (B), LA (C), 5-BMF (D), BL (E), BF (F)	82
Fig. 32. Effect of catalyst deactivation on normalized compounds trends on fructose initial concentration. Fructose (A), 5-HMF (B), LA (C), 5-BMF (D), BL (E), BF (F).	83
Fig. 33. Effect of fructose initial loadings on normalized compounds trends on fructose initial concentration. Fructose (A), 5-HMF (B), 5-BMF (C), LA (D),BL (E), BF (F).	85
Fig. 34. Variation of dissolved fructose concentration over time during the dissolution of solid fructose in butanol/GVL at different temperatures, and for an initial solid fructose content of 200 g/L.	86
Fig. 35: Repeating experiment 4. Fructose (A), 5-HMF (B), 5-BMF (C), LA (D),BL (E), BF (F)	87
Fig. 36: Repeating experiment 5. Fructose (A), 5-HMF (B), 5-BMF (C), LA (D), BL (E), BF (F)	88
Fig. 37. Main reaction mechanism for Fructose solvolysis to butyl levulinate, including the intermediate species Int1, and focus on the dehydration step of fructose.	90
Fig. 38: Focus on fructose conversion step: single-step fructose dehydration in Model 1; isomerization to fructofuranose in Model 2; alkylation to butylfructoside in Model 3	91
Fig. 39. Fit of model 1 to experimental concentration of Exp. 1, Fructose (A); BL (B), 5-HMF,5-BMF (C); LA, BF (D).	96
Fig. 40. Fit of model 1 to the experimental concentration of fructose and BL in Exp. 13, and Exp. 14. Fructose, BL (A-B); LA,BF (C-D); 5-HMF,5-BMF (E-F).	97
Fig. 41: Overall assessment among models respect with SSR and AIC indexes in regression and validation phases	98
Fig. 42. Simulation of the reaction conditions of experiment 1 with a reaction time of 24h. Simulation of fructose conc. (A); BL (B); 5-HMF, 5-BMF (C); LA, BF (D).	99
Fig. 43: Main aspects of the investigation in Chapter 5	102
Fig. 44: Flow chart of the proposed methodology for the conceptual design of the GVL process integrated with hybrid energy systems based on renewable sources and sustainability assessment steps.	105
Fig. 45: Potential site location in the Seine-Maritime department (Normandy) and summarized potential biomass info and wind exploitation in the region.	107
Fig. 46: Box plots of the annual and seasonal available wind power density in the location site (years 2011–2021).	109
Fig. 47: (A) Punctual values of wind speed data at the selected site in 2018; (B) Wind data according to Weibull distribution	110
Fig. 48: Overlay between wind speed frequency data and turbine device power curve	111
Fig. 49: Block diagram of the conceptual design of the GVL production process from fructose.	113
Fig. 50: Preliminary Process Flow Diagram for GVL-production from fructose	115

<i>Fig. 51 Preliminary process flow diagram for the production of GVL from fructose highlighting the different process sections</i>	116
<i>Fig. 52 Typical system design and balance of plant for an alkaline electrolyzer</i>	119
<i>Fig. 53 Figurative representation of scenarios including process sections and energy and material supply streams</i>	124
<i>Fig. 54: Flow chart of the optimal design algorithm for the wind farm-hydrogen energy storage configuration, minimising the objective function represented by the parameter %Energy-grid.</i>	126
<i>Fig. 55: System boundary for emission contributions for each process section.</i>	134
<i>Fig. 56: The critical Pus-MHE highlighted in the simplified diagram of the GVL production process.</i>	138
<i>Fig. 57: Illustration of the different stages of the sustainability index analysis.</i>	139
<i>Fig. 58: Profile schematisation of stakeholders in CT</i>	140
<i>Fig. 59: Optimal configuration design Scenario 6 - 2kty (A) variation of %Energy-Grid parameter as the number of WTs varies for different storage sizes (B) minimum number of WTs minimising the target term for each storage size</i>	144
<i>Fig. 60: Optimal configuration design Scenario 7 - 2kty (A) variation of %Energy-Grid parameter as the number of WTs varies for different storage sizes (B) minimum number of WTs minimising the target term for each storage size</i>	145
<i>Fig. 61: Optimal configuration design Scenario 6 and 7 - 4kty (A-A') variation of %Energy-Grid parameter as the number of WTs varies for different storage sizes (B-B') minimum number of WTs minimising the target term for each storage size</i>	147
<i>Fig. 62: NPV10 index value in Scenario 6 (expressed by colour) varying the price of GVL and hydrogen; (a) 5t-18WT, (b) 5t-35WT, (c) 7.5t-13WT (d) 7.5t-35WT.</i>	153
<i>Fig. 63: Comparison NPV10 index value in Scenario 6 (a) and Scenario 7 (b) varying the price of GVL and hydrogen;</i>	154
<i>Fig. 64: NPV10 index value in Scenario 7-4kty (expressed by colour) varying the price of GVL and hydrogen; (a) 2t-23WT, (b) 2t-35WT, (c) 5t-9WT (d) 5t-35WT.</i>	157
<i>Fig. 65: Contributions of each item to the CAPEX of each scenario configuration; (a) 2 kt/y, (b) 4 kt/y</i>	159
<i>Fig. 66: Contribution of GVL and hydrogen sales to total revenue for each scenario; (a) 2kt/y, (b) 4 kt/y.</i>	160
<i>Fig. 67: Contributions of each item to the OPEX of each scenario configuration; (a) 2 kt/y, (b) 4 kt/y</i>	161
<i>Fig. 68: LCOP GVL-H2(a) and SPmin GVL-H2 (b) values for each scenario and production size 2 kt/y</i>	162
<i>Fig. 69: LCOP GVL-H2(a) and SPmin GVL-H2 (b) values for each scenario and production size 4 kt/y</i>	162
<i>Fig. 70: NPV10 trend over 25 years, plant lifetime, for each scenario and relative to size 4 kt/y</i>	163
<i>Fig. 71: Cumulative probability trends related to sensitivity analysis on the NPV10 index;(a) 2kt/y, (b) 4kt/y</i>	165
<i>Fig. 72: Probability of occurrence of combinations of scenarios with respect to the NPV10 index value, i.e. the scenarios are in descending order of the index value in each combination; (a) 2 kt/y, (b) 4 kt/y.</i>	165
<i>Fig. 73: Probability of occurrence of each scenario as a first scenario in terms of NPV10; (a) 2 kt/y; (b) 4 kt/y.</i>	166
<i>Fig. 74: Probability of occurrence of each scenario as second scenario in terms of NPV10; (a) 2 kt/y; (b) 4 kt/y.</i>	166



Fig. 75: Effect of the variation ( $\pm 5\%$ ) of the main cost items on the NPV10 index; (a) Scenario 1, (b) Scenario 2, (c) Scenario 6, (d) Scenario 7	167
Fig. 76: (a) global emissions released per scenario (size 2 kt/y), considering fossil and biogenic contribution; (b) LGHG index for GVL, hydrogen and electricity per scenario and size 2kt/y.	168
Fig. 77 (a) Radar plot indicating emission contribution and GVL-LGHG; (b) Emissions saved per scenario compared to scenario 1 baseline.	169
Fig. 78: Overall view of LGHG index related to GVL for size 2 and 4 kt/y	170
Fig. 79: Cumulative probability trends related to sensitivity analysis on the LGHG index; (a) 2kt/y, (b) 4kt/y	171
Fig. 80: Effect of the variation ( $\pm 5\%$ ) of the main energy-resource demand on the LGHG index; (e) Scenario 5, (f) Scenario 6, (g) Scenario 7	173
Fig. 81: Overall of safety indexes on the target human	175
Fig. 82: Percentage contribution of the different accidental scenarios to the overall PI index	175
Fig. 83: Plot of the overall PI(a) and HI(b) indices for each scenario for target human, highlighting the contribution of the GVL production section, hydrogen production section, storage section.	178
Fig. 84 Overall indices for human and equipment (atm) target per scenario	179
Fig. 85 (a) Cumulative probability trends related to sensitivity analysis on the difference of HI among scenarios, (b) Probability of occurrence of scenarios combinations with respect to the HI index value.	180
Fig. 86: Performance of scenarios relative to normalized indices, in percentage terms.	181
Fig. 87: Graph of aggregated indices according to the different stakeholder profiles considered	182

# List of Tables

<i>Table 1: Production of levulinic acid from sugar monomers using various catalytic systems. Adapted from [I].</i>	10
<i>Table 2: Production of levulinate esters from sugar monomers using various catalytic systems. Adapted from [I].</i>	11
<i>Table 3: Production of levulinate esters from cellulose and raw biomass using various catalytic systems. Adapted from [I].</i>	14
<i>Table 4: Production of GVL from levulinic acid and alkyl levulinates using various catalytic systems</i>	18
<i>Table 5: Main advantages and disadvantages of alkaline electrolyzer and PEM systems</i>	24
<i>Table 6: Properties of Amberlite IR-120 according to the manufacturer (Acros Oganics).</i>	36
<i>Table 7: Experimental matrix for external and internal mass transfer experiments</i>	37
<i>Table 8: Experimental matrix for fructose solvolysis in different solvent systems (butanol, water and GVL).</i>	38
<i>Table 9: Results from swelling study of Amberlite IR-120 at room temperature.</i>	43
<i>Table 10: Comparison with literature data on fructose solvolysis to butyl levulinate.</i>	49
<i>Table 11: Experimental matrix</i>	54
<i>Table 12: Summary of modelling results of SSR and determinant coefficient</i>	66
<i>Table 13: Summary of kinetic constants and activation energies for each reaction step</i>	67
<i>Table 14: Distribution of experiments in 6 folds and evaluation of training and testing set of experiments</i>	71
<i>Table 15: Results of CV index for cross-validation</i>	72
<i>Table 16: Experimental matrix for kinetic solvolysis experiment from fructose to BL – Regression phase</i>	78
<i>Table 17: Experimental matrix for kinetic solvolysis experiment from fructose to BL – Validation phase</i>	79
<i>Table 18: Saturation molar concentration of fructose in isothermal conditions at different temperatures.</i>	86
<i>Table 19: Regression results for Model 1, Model 2, and Model 3</i>	94
<i>Table 20: Estimated parameters at <math>T_{ref} = 368</math> K and statistical data for Model 1</i>	95
<i>Table 21: Summary of validation stage results. SSRVal and AICval</i>	98
<i>Table 22: Simulation through Model 1 of the solvolysis system at different conditions.</i>	99
<i>Table 23: Characteristic data of wind distribution and power at the site considered</i>	110
<i>Table 24: Characteristics of the selected wind turbine V110-2.0 MW Vestas</i>	111
<i>Table 25: Equipment flowsheet legend</i>	115
<i>Table 26: Datasheet specification Alkaline electrolyzer</i>	120
<i>Table 27: Average data specification of PEMFC from literature</i>	122
<i>Table 28: Summary of scenarios defined according to electrical, thermal power and hydrogen supply.</i>	123
<i>Table 29: Cost assumptions for specific process items</i>	131
<i>Table 30: Cost assumptions for chemicals, catalysts, and utility.</i>	131
<i>Table 31: Assumptions employed in economic indicators analysis.</i>	132
<i>Table 32: Emission factor for environmental impact analysis</i>	134
<i>Table 33: Threshold Values assumed for the evaluation of damage distances</i>	136
<i>Table 34: Inherent Safety Key Performance Indicators (KPIs)</i>	137

<i>Table 35: Description of the different stakeholder profiles and corresponding priority among the sustainability perspectives used in this study.</i>	141
<i>Table 36: Weighting coefficients for the different stakeholder profiles considered.</i>	141
<i>Table 37: Equipment Design Configuration for Scenario 6 – Production size 2 kt/y</i>	144
<i>Table 38: Equipment Design Configuration for Scenario 7 – Production size 2 kt/y</i>	145
<i>Table 39: Equipment Design Configuration for Scenario 6 and 7 – Production size 4 kt/y</i>	147
<i>Table 40: Preliminary results economic evaluation: capital cost of the GVL scheme for production sizes 2 and 4 kt/y</i>	149
<i>Table 41: Preliminary results economic evaluation: partial OPEX cost of the GVL scheme for production sizes 2 and 4 kt/y</i>	150
<i>Table 42: LCOP values for Scenario 6 – 2 kt/y GVL production size.</i>	151
<i>Table 43: <math>SP_{min}</math> values for Scenario 6 – 2 kt/y GVL production size.</i>	152
<i>Table 44: LCOP values for Scenario 7 – 2 kt/y GVL production size.</i>	153
<i>Table 45: <math>SP_{min}</math> values for Scenario 7 – 2 kt/y GVL production size.</i>	154
<i>Table 46: LCOP values for Scenario 6 – 4 kt/y GVL production size.</i>	154
<i>Table 47: <math>SP_{min}</math> values for Scenario 6 – 4 kt/y GVL production size.</i>	155
<i>Table 48: LCOP values for Scenario 7 – 4 kt/y GVL production size.</i>	156
<i>Table 49: <math>SP_{min}</math> values for Scenario 7 – 4 kt/y GVL production size.</i>	156
<i>Table 50: Results of optimal system sizing of renewable energy integration, hydrogen production and storage for each scenario</i>	157
<i>Table 51: Variation of cost items with the major impact for sensitivity analysis</i>	164
<i>Table 52: Summary from the indices evaluated for the two different sizes</i>	170
<i>Table 53: Variation of material and energy demand with the major impact on emissions for sensitivity analysis</i>	171
<i>Table 54: Summary of inherent safety indices covered for critical equipment in the GVL scheme for target human</i>	174
<i>Table 55: Summary of inherent safety indices for PU in the GVL scheme for target <sup>a</sup>atmospheric, <sup>b</sup> pressurized equipment.</i>	176
<i>Table 56: Summary of inherent safety indices for PU in the H2 section for target human, <sup>a</sup>atmospheric, <sup>b</sup>pressurized equipment</i>	177
<i>Table 57: Summary global indices for each scenario and compared to human and equipment target</i>	178
<i>Table 58: Credit factor variation for sensitivity analysis</i>	180
<i>Table 59: Absolute and normalized (by internal normalization) values of global indices</i>	181
<i>Table 60: ASI for each scenario with linear aggregation (relative color scale for each profile/per column).</i>	182